AD A283596

CRITICAL ISSUES in the DEVELOPMENT of HIGH TEMPERATURE STRUCTURAL MATERIALS

94-26597

DTIC QUALITY INSPECTED 8

n For
CRA&I
TAB
nced
tion
By
Dist.ibution/
Availability Codes
Dist | Avail and/or Special
A-1

94 8 19 117

Best
Available
Copy

CRITICAL ISSUES
in the
DEVELOPMENT
of
HIGH TEMPERATURE STRUCTURAL MATERIALS

Proceedings from the Conference on Critical Issues
in the Development of High Temperature Structural Materials

held in Kona, Hawaii
March 7-14, 1993

EDITED BY

N.S. Stoloff, D.J. Duquette and A.F. Giamei

A Publication of

TMS
Minerals • Metals • Materials

A Publication of The Minerals, Metals & Materials Society
420 Commonwealth Drive
Warrendale, Pennsylvania 15086
(412) 776-9000

The Minerals, Metals & Materials Society is not responsible for statements or opinions and is absolved of liability due to misuse of information contained in this publication.

Printed in the United States of America
Library of Congress Catalog Number 93-86574
ISBN Number 0-87339-199-3

Authorization to photocopy items for internal or personal use, or the internal or personal use of specific clients, is granted by The Minerals, Metals & Materials Society for users registered with the Copyright Clearance Center (CCC) Transactional Reporting Service, provided that the base fee of $3.00 per copy is paid directly to Copyright Clearance Center, 27 Congress Street, Salem, Massachusetts 01970. For those organizations that have been granted a photocopy license by Copyright Clearance Center, a separate system of payment has been arranged.

TMS
Minerals • Metals • Materials

© 1993

If you are interested in purchasing a copy of this book, or if you would like to receive the latest TMS publications catalog, please telephone 1-800-759-4867.

FOREWORD

This Engineering Foundation Conference was devoted to discussion of the current status of research and development of superalloys, refractory metals, intermetallic compounds, ceramics and composites based upon ceramics or intermetallics. The Conference, held in Kona, Hawaii, March 7-14, 1993, was unique in that workers in these diverse fields rarely converse in a single forum. Coverage of these materials ranged from basic science through processing and mechanical properties as well as discussion of current applications (superalloys and refractory metals) and future applications (principally composites and intermetallics). In addition, the importance of reducing costs of development of new materials was cited in the Keynote address of Dr. Ben Wilcox of the recently renamed Advanced Research Projects Agency.

The attendees heard that nickel-base superalloys continue to be improved in strength and in permissible maximum operating temperatures, which now are in excess of 1120° C. New single crystal alloys containing up to 6% Re promise to raise this temperature still higher, providing a still more difficult target for designers of new competitive materials such as ceramic composites. Refractory metals and alloys compete with ceramics for some applications above 1350° C, but to date intermetallics provide the promise of lower density and higher thermal conductivity than superalloys or refractory metals at temperatures of 1000-1100° C. Moreover, if $MoSi_2$ can be successfully reinforced so as to simultaneously improve both toughness and creep resistance, such composites could provide useful strength and oxidation resistance to at least 1500° C.

It was reported that ultrafine microstructures provide some toughening in $MoSi_2$ composites, and that whiskers or fibers are better than particulates as reinforcements. Clearly, lack of low temperature ductility and toughness are the principal obstacles to applications of intermetallics. Creep rupture, fatigue and thermal properties of NiAl already match or exceed those of current superalloys, but designers appear to be unwilling to consider new materials with toughness much less than the 50-80 $MPa\sqrt{m}$ exhibited by superalloys at room temperature. However, it was pointed out that designers are not providing alloy developers with realistic minimum values of toughness that are required for turbine applications. It was suggested also that perhaps a fairer estimate of needed toughness might correspond to superalloy values at 760° C, near the well-known ductility minimum in superalloys. Another point in favor of NiAl is the finding that the toughness can be increased to the order of $15MPa\sqrt{m}$ by rapidly cooling from elevated temperatures to avoid segregation of interstitial impurities and subsequent strain aging, or by purification to eliminate the interstitials. However, most intermetallics are very sensitive to composition and, in addition, show marked sensitivity to moisture or hydrogen.

Ceramics and ceramic-matrix composites also have demonstrated improved toughness in recent years, although there was some dispute about the advisability of designing ceramic composites with pre- existing cracks. Also, concern was expressed about porosity and the presence of glassy phases of grain boundaries in powder processed ceramics, since both factors reduce mechanical properties. Another aspect of ceramic processing that offers the chance of matching ceramic and metal components was a discussion of functionally gradient materials (FGM). These can be made by four different processes and allow a

continuous range of properties from pure metallic to pure ceramic across a single component. However, the principal problems with all structural ceramics remained inadequate tensile strength and highly variable strength values.

The need was clearly identified to accelerate the time from conception of new materials to implementation. This would reduce costs and allow for more rapid iteration.

Management philosophy does not usually have the patience to sustain a ten to twenty year development program. An approach to the problem of rapid implementation is the partnership or consortium. This circumvents the possibility of an individual or institution working alone without the nurturing interactions of other companies, universities or government agencies. By having more input and allowing for more outlets of technology, the pace of progress is sure to quicken. In addition, the technology has advanced to such a high level in situations like gas turbine engines, that future advances will very likely call upon interdisciplinary skills. A new funding paradigm of in-kind funds by participants at least stretches scarce funds and shows management commitment. From the point of view of industry, this represents powerful leveraging and explains the great start-up success of the CRADA (Co-operative Research and Development Agreement) Program format. These agreements are for the purpose of fostering joint research efforts between national laboratories and industrial firms.

The Conference was noteworthy in several respects:

- diversity of materials covered
- range of physical and mechanical properties discussed
- inclusion of processing and environmental issues
- extensive discussion after each paper and in the panel period on issues ranging from basic scientific principles to economic considerations.
- openness of participants in discussing problems with, as well as, advantages of, each class of material.

The organizers, who included M. Nazmy, M. Yamaguchi and S. Suresh, are grateful to the Engineering Foundation for providing seed money to partially defray travel costs of Conferees. In addition, we acknowledge with thanks the financial support of the Army Research Office - Durham, Office of Naval Research; Center for Materials Science of Los Alamos National Laboratory and United Technologies Research Center. Finally, we are grateful to Mr. Jack Donaldson of the Engineering Foundation for handling all of the local arrangements in a highly capable manner.

N.S. Stoloff
D.J. Duquette
A.F. Giamei

Conference Co-Chairmen
June 14, 1993

TABLE OF CONTENTS

Keynote

High Temperature Materials: Processing and Application 1
B.A. Wilcox and M.A. Rigdon

SESSION I

Alloy Design I
(Theory)

Phase Stability and Alloy Design in High Temperature Intermetallics 15
J.H. Perepezko

Critical Issues in the Computational Materials Science for Structural Materials 29
M.H. Yoo and C.L. Fu

Alloy Design for High Temperature, Low Density Composite Materials 43
G.H. Reynolds and J.H. Norman

Advanced High-Temperature Alloys by Design Using
Rapid Solidification Processing 57
J.E. Flinn and T.F. Kelly

SESSION II

Alloy Design II
(Applications-Alloy Development)

Single Crystal Based Microstructure Design of Metal Matrix Composites
for High Temperature Applications 71
R. Raj

Ni-Based Superalloy Developments 87
G.L. Erickson

SESSION III

Advanced Processing

Advanced Materials Processing 109
A.F. Giamei

Synthesis and Property Attainment in Ceramic Matrix Composites 119
W.B. Hillig

The Effect of Processing on the Microstructure and Properties
of Advanced Materials 137
G.E. Fuchs

The Application of Combustion Synthesis in the Production of Titanium-Based
Ceramic and Ceramic-Metal Composites 151
H.J. Feng, K.R. Hunter and J.J. Moore

Improvement of Room-Temperature Ductility of Intermetallic Compounds
by Unidirectional Solidification 161
T. Hirano

SESSION IV
Strengthening/Toughening Mechanisms I
(Metals and Intermetallics)

Strengthening and Ductilization of Two Phase TiAl Alloys in Lamellar Form Ternary Alloying Additions 173
M. Yamaguchi and H. Inui

Strengthening and Toughening in Refractory Metal Alloys 189
J. Wadsworth, J. Wittenauer and T.G. Nieh

Precipitation in High Temperature Aluminides 203
M. Nemoto

Fracture Toughness of Gamma Base Titanium Aluminides with Ternary Additions at Room and Elevated Temperatures 217
R. Gnanamoorthy, Y. Mutoh, N. Masahashi and M. Mizuhara

Ductility of Ni_3Al Doped with Substitutional Elements 227
S. Hanada, A. Chiba, H.Z. Guo and S. Watanabe

SESSION V
Strengthening/Toughening Mechanisms II
(Ceramics and Composites)

Ceramic Matrix Composites: Challenges and Opportunities 239
A.G. Evans, J.-M. Domergue and E. Vaggagini

Plastic Anisotropy in MoSi2 Single Crystals 279
T.E. Mitchell and S.A. Maloy

Microstructural Effects on Creep Strengthening of $MoSi_2$ Matrix Composites 291
A.K. Ghosh and A. Basu

Fundamental Research on Functionally Gradient Materials (FGM) for Relaxation of Thermal Stress 303
I. Shiota

SESSION VI
Creep Resistance

Critical Aspects in the Development of Creep Resistant Superalloys & Intermetallics 321
M. Nazmy

Creep and Damage Process in Multi-Phase Ceramic Materials 333
D.S. Wilkinson

Designing for Improved High Temperature Strength, Creep, Oxydation, and Fatigue Resistance in Si_3N_4 349
G. Thomas

SESSION VII
Fatigue Resistance

Fatigue of Superalloys and Intermetallics 367
N.S. Stoloff

Creep Fracture and Creep-Fatigue Fracture in Ceramics and Ceramic Composites 385
S. Suresh

SESSION VIII
Environmental

Environmental Embrittlement of Ordered Intermetallics at Ambient Temperatures 399
T. Takasugi

High Temperature Corrosion of Intermetallics, Ceramics, and Carbon-Carbon Composites 415
G.H. Meier and F.S. Pettit

Environmental Resistance of Intermetallic Compounds and Composite Materials 431
D.J. Duquette

Environmental Effects on Elevated Temperature Subcritical Crack Growth of SiC/SiC Composites 445
C.H. Henager, Jr. and R.H. Jones

Hydrogen and Titanium Base Materials 455
H.G. Nelson

Plasticity Enhancement Mechanisms in Refractory Metals and Intermetallics 465
R. Gibala, H. Chang, C.M. Czarnik, K.M. Edwards and A. Misra

SESSION IX
Governmental Programs

Japanese National Project on Intermetallics 477
T. Maruo and M. Tomita

Advanced Structural Materials and Processes 491
A.H. Rosenstein

HIGH TEMPERATURE MATERIALS:

PROCESSING AND APPLICATION

Ben A. Wilcox* and Michael A. Rigdon**

* Advanced Research Projects Agency
3701 North Fairfax Drive
Arlington, Virginia 22203
and
** Institute for Defense Analyses
1801 N. Beauregard Street
Alexandria, Virginia 22311

Abstract

This paper discusses promising new processing technologies for producing improved high temperature structural materials. In addition issues are outlined which are beyond the normal technical realm that are required to move promising new materials into an application. Approaches to address affordability and shorten the time from discovery to application are described. New efforts to integrate basic and applied research to further reduce development cycle time and promote dual defense and civilian technology applications are discussed.

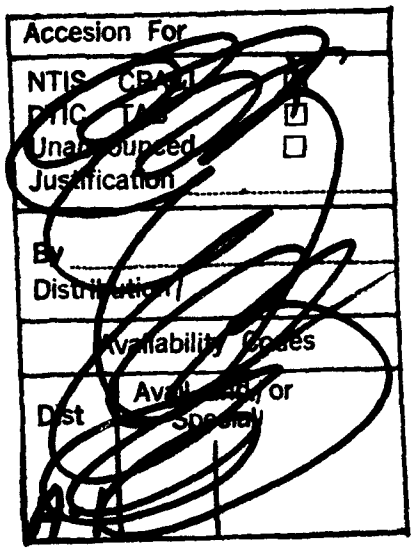

Critical Issues in the Development of High Temperature Structural Materials
Edited by N.S. Stoloff, D.J. Duquette and A.F. Giamei
The Minerals, Metals & Materials Society, 1993

Introduction

The search for high temperature structural materials continues to be an important area of research for the materials community. DoD, NASA, and DoE all have programs to advance the capability of gas turbine engines in defense, civil, and industrial applications specific to their missions. The DoE also has a Continuous Fiber Ceramic Composite (CFCC) program to develop the processing technology needed to take advantage of this class of materials in high temperature industrial processes. Even in this broad-based process development program, one of the major application areas is for gas turbine power generators. These programs and their goals are summarized in Table I.

At the present time, superalloys are the backbone of the gas turbine industry. These alloys have evolved over the past 50 years as illustrated in Figure 1. This figure contains several messages. First, the temperature capability of superalloys as measured by the 100 hour creep rupture time at 140 MPa stress has increased at about 8°C/year over the last 5 decades. Second, processes such as directional solidification and mechanical alloying have played a substantial role in recent increases in capability. Third, at >1100C, the temperature capability of current superalloys is approaching the 1395C melting point of Ni_3Al (a primary phase constituent of many superalloys) (References 2 and 7). As a result, much of the new research on high temperature materials is directed toward new classes of materials. This trend is illistrated by the papers on other classes of intermetallics, metal composites, and ceramic composites included in this conference. This shift in research emphasis is consistent with the circa 1989 projection for material usage in gas turbines shown in Figure 2. In general the usage of alloys is expected to decrease while the use of metal composites and ceramic composites is expected to increase as we move into the next century.

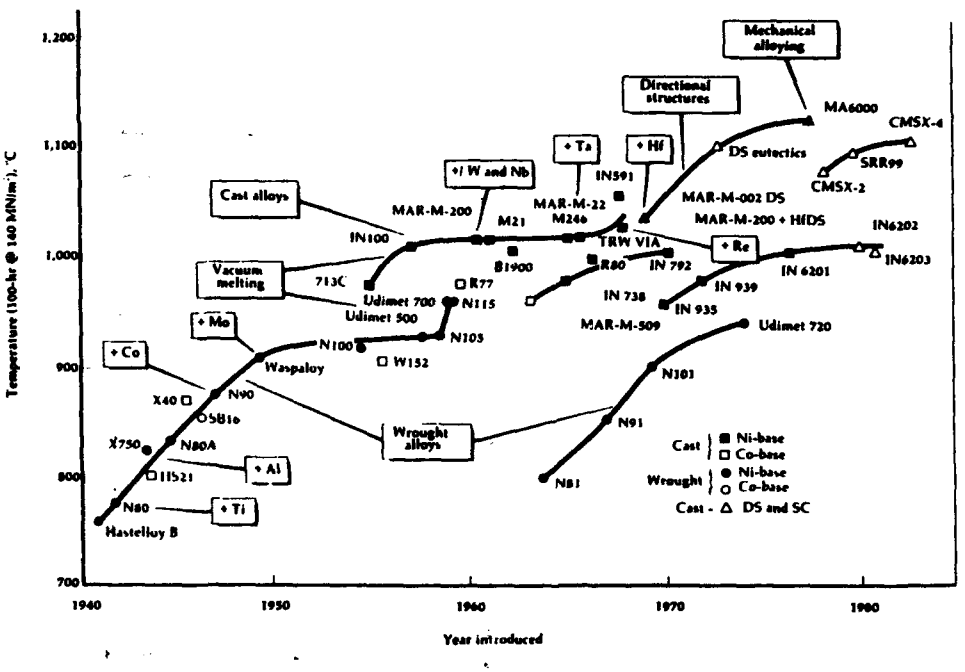

Figure 1 - History of 100-hr/140 MPa Stress Rupture Temperature Capability of Superalloys[1]

[1] Reprinted, with permission, from Advanced Materials and Processes, October 1990 (Reference 5).

Table I. Major High Temperature Materials Programs and Goals

AGENCY	PROGRAM	GOALS	REF.
DoD/NASA	INTEGRATED HIGH PERFORMANCE TURBINE ENGINE TECHNOLOGY (IHPTET)	25-30% INCREASE IN TURBINE TEMP. 30-40% DECREASE IN ENGINE WEIGHT 80-95% DECREASE IN COOLING AIR FLOW 20-40% DECREASE IN LIFECYCLE COSTS	(1)
	NATIONAL AEROSPACE PLANE (NASP)	≥ 800C SKIN TEMP	(2)
DoE	ADVANCED TURBINE SYSTEMS	~ 60% THERMAL EFFICIENCY (OVERALL SYSTEM) > 1425C FIRING TEMPERATURE EQUIVALANT REPAIR & MAINTENANCE	(3)
DoE	CONTINUOUS FIBER CERAMIC COMPOSITE (CFFC)	PROCESS DEVELOPMENT FOR HIGH TEMP. HEAT ENGINE, HEAT EXCHANGER AND HEAT GENERATION COMPONENTS	(4)
NASA	HIGH SPEED CIVIL TRANSPORT (HSCT) (ENABLING PROPULSION MTLS.)	≥1650C COMBUSTOR LINER TEMP. ≥1300C EXIT NOZZLE TEMP. NO FILM COOLING 18,000 HR LIFETIMES	(2)

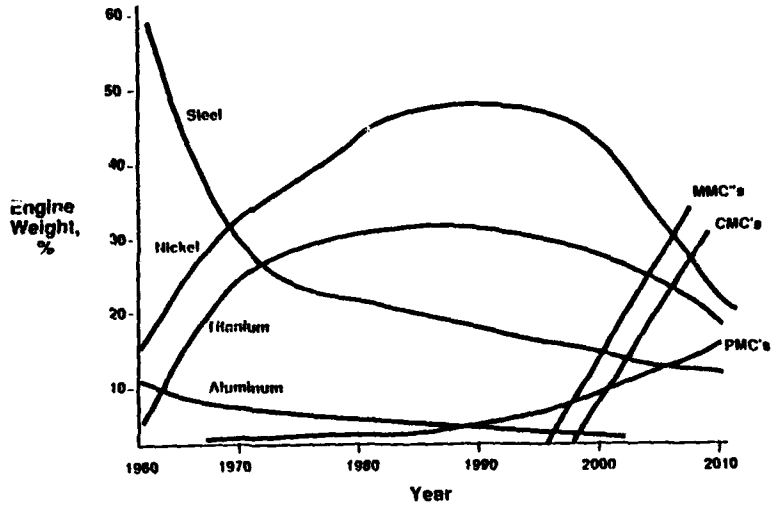

Figure 2 - Projected Usage of Materials Classes In Future Gas Turbine Engines (Reference 8)

If these projections are to be realized there are a number of steps that must be taken to get materials into a production application as illustrated in Figure 3. There are two critical issues associated with this process. First, it typically takes 15 to 20 years to progress through the steps illustrated in Figure 3. Much of the work that is the subject of this conference is focused on the search for and basic understanding of new high temperature materials and is relevant to the first two steps along the path to application. If these new materials are to begin entering use early in the next decade, a mechanism is needed to accelerate the process illustrated in Figure 3. Second, for a new material to make it into a production application, it must be affordable. In large part, affordability will be decided by the last four steps prior to product application in Figure 3. Of these four, the materials researcher has limited ability to address regulatory issues, competing materials, and capital investment. Regardless, these issues certainly have the ability to make the difference between just another good research program and the development of a new material that has economic impact.

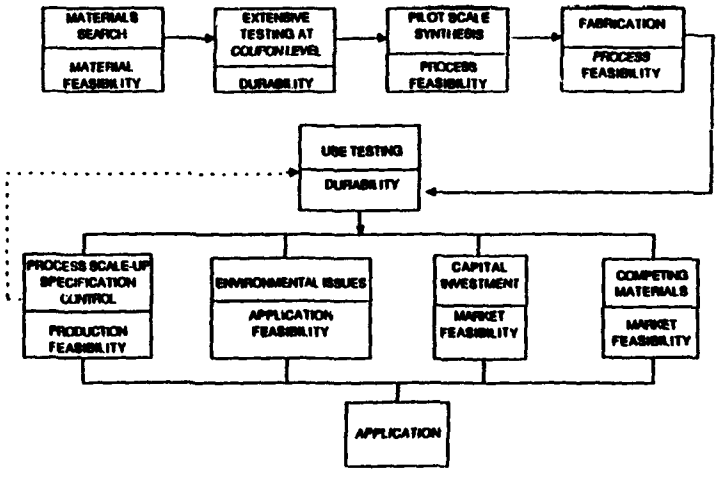

Figure 3 - Pathway from Discovery to Application

Processing Development Programs

One thing that technologists can do to impact affordability is to devise cost effective process routes to synthesize new classes of high temperature materials. This often involves a linkage between basic and applied researchers. As an example, the concept of designer microstructures (Figure 4a) containing whiskers for creep resistance, small hard particles for strength, and ductile phases for toughness was illustrated in 1988 (Reference 9). The theory was reduced to practice by Martin-Marietta Laboratories via an exothermic dispersion process under the XD trademark. The microstructure of the (Ti-Al)+TiB_2 alloy shown in Figure 4b closely resembles the model. Fabrication feasibility for various high temperature components via investment casting has been demonstrated (Reference 10). High temperature yield strength of the XD® Ti-Al is not a great deal different than that of an alloy such as Inconel 713C but the density is about half that of the nickel base alloy. The XD® Ti-Al alloy therefore provides the potential for significant weight savings.

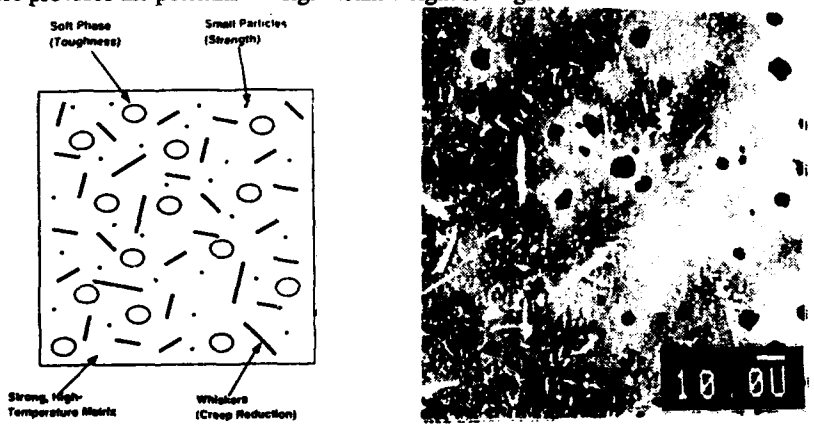

a. "Designer" Microstructure

b. Microstructure of XD® Titanium Aluminide

Figure 4 - Development of Designer Microstructure by XD® Process (Reference 9)

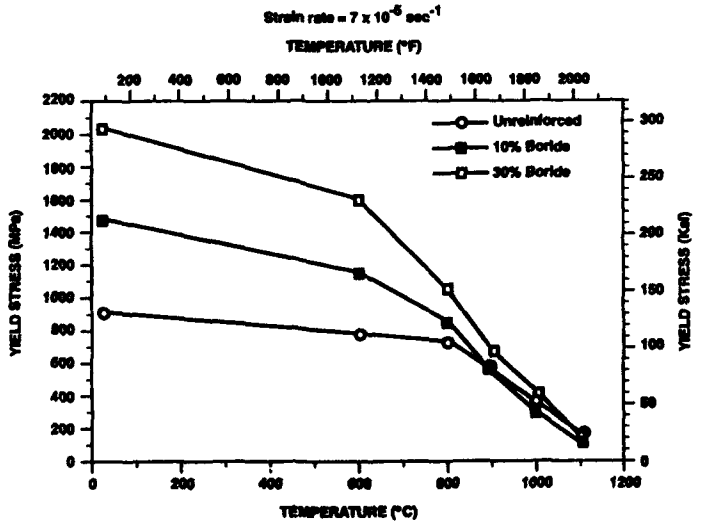

Figure 5 - Increase in Compressive Yield Strength of Nb-26 Ti-48 Al Through Addition of Nb and Ti Borides Via XD® Process (Reference 11)

A second example of linkage between basic and applied research to reduce processing cost is illustrated in Figures 6 and 7. Figure 6a illustrates that suitably prepared ceramic composites can exhibit considerably greater strain to failure (toughness) than monolithic ceramics. To accomplish this it is necessary to induce weak fiber/matrix interfaces such that interface debonding and crack bridging occurs as shown in Figure 6b. These concepts have been demonstrated by Lanxide Corporation as seen in Figure 7. The Dimox® process for producing ceramic matrix composites can result in greatly improved toughness for SiC fiber-reinforced Al_2O_3 compared with monolithic Al_2O_3. Figure 7b illustrates the considerable fiber pullout which has occurred.

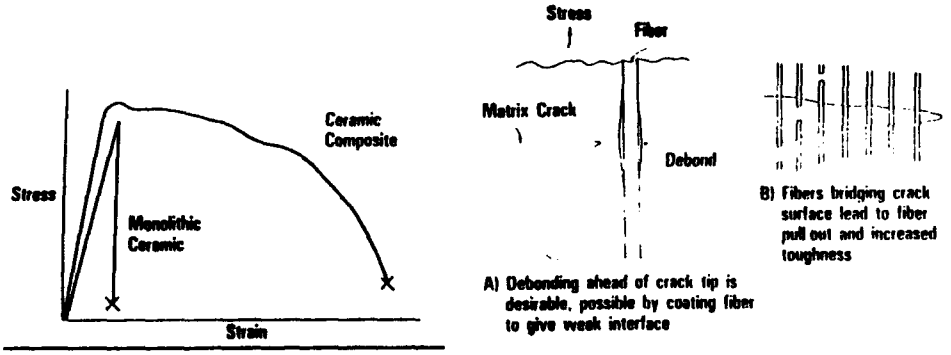

a. Strain-Strain Curves for Ideal Ceramic Matrix Composite, and Monolithic Ceramic

b. Control of Fiber-Matrix Interface Required to Optimize Toughness

Figure 6 -Theoretical Model of Desired Crack Growth Behavior (Reference 12)

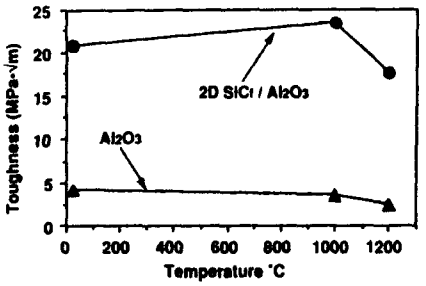

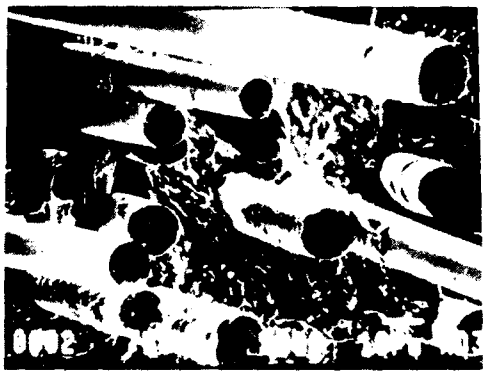

a. Toughness vs Temperature for Lanxide® 2D SiC Fiber-Reinforced Al_2O_3 and Conventional Al_2O_3

b. Fracture Surface of SiC/Al_2O_3 Composite that Demonstrates Fiber Pull-Out[2]

Figure 7 - Ceramic Matrix Composite that Exhibits Enhanced Fracture Toughness Through Fiber-Matrix Interface Control (Reference 13)

---

2 Micrograph provided courtesy of Lanxide Corporation, Newark, DE.

An extension of the linkage between modeling and processing embodied in the two previous examples is through the Intelligent Processing of Materials (IPM). The objective here is not only to obtain reductions in manufacturing costs but to simultaneously improve overall quality. Physical or experience-based models that relate finished properties with processing conditions are combined with process sensor data and control theory to make real time corrections to the manufacturing process. The goals are to increase yield and reduce inspection requirements of finished parts through real time control of manufacturing variables.

Titanium alloy matrices reinforced with SiC monofilaments have a distinct advantage in terms of specific tensile strength over the non-reinforced metal as shown in Figure 8. One of the traditional methods to prepare this material is hot pressed foil-fiber-foil layup. This process is labor intensive and time consuming. Synthesis of plasma sprayed SiC fiber reinforced titanium alloy matrix composite illustrated schematically in Figure 9a is an example of an IPM system with the potential to provide substantial reduction in synthesis cost. In this case various sensors and actuators are used to monitor and control droplet temperature, deposition temperature, and deposition rate. The result is a very uniform fiber spacing after consolidation, as shown by the micrograph in Figure 9b. This technology is limited to fabricating cylindrical shapes or sheets at present.

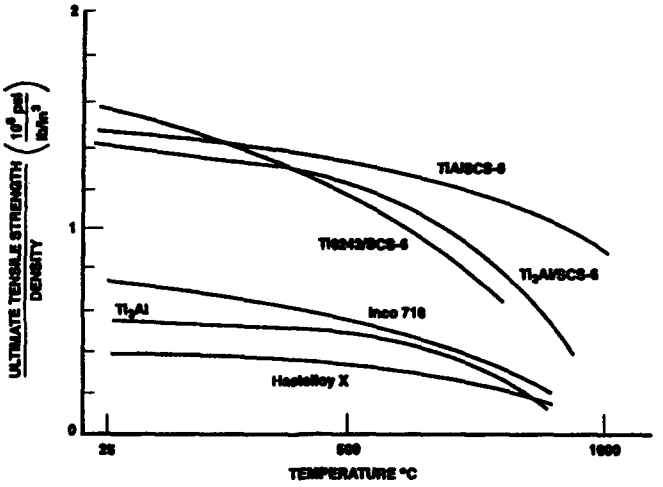

Figure 8 -Specific Tensile Strength versus Temperature for Selected Alloys and Composites (Reference 14)

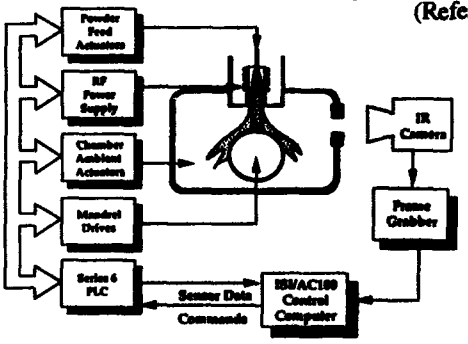

a. Process Diagram (Reference 15)

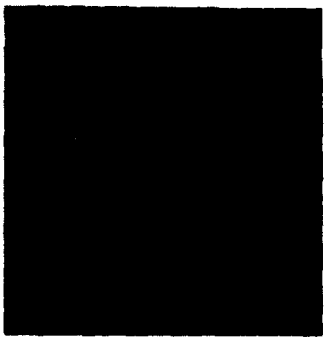

b. Resulting Microstructure After Hot Isostatic Pressing (Reference 14)

Figure 9 -Intelligent Processing of Materials (IPM) Applied to Plasma Sprayed SCS-6 Silicon Carbide Fiber Reinforced Ti-6-2-4-2

Recently a new technology, solid freeform manufacturing, has emerged as a means to rapidly manufacture complicated geometric shapes. This capability has two advantages important to both DoD and industry. First, CAD files can be converted directly to manufactured parts without the need for tooling or operator intervention. This will enable rapid acquisition of limited production parts. Second, solid freeform manufacturing is flexible in the sense that many different small volume production runs can be made on the same manufacturing line without extensive retooling. The status of solid freeform manufacturing for different materials classes is listed in Table II.

Figure 10 illustrates a method where a movable laser beam responding to a CAD file can sinter powders of ceramics and metals to produce solid objects.

Table II Status of Solid Freeform Manufacturing

Technique	Status
Plastic	Available, most mature (photolithography)
Wax	Demonstrated, investment casting
Metals	Indirect Capability
Ceramics	Demonstrated for molds and cores (laser sintering)
Composites	Metal matrix composites demonstrated from fabricated powder preforms
Functionally Gradient Materials	Variable composition capability; not demonstrated as yet
Machines	Assembly of discrete parts (i.e.. gear assemblies) has been demonstrated

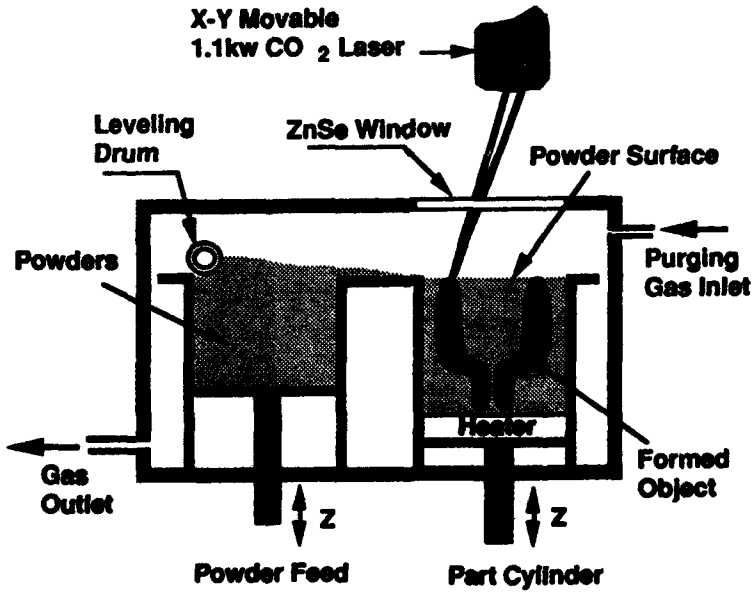

Figure 10 -Schematic Diagram of Solid Freeform Manufacturing via Selective Laser Sintering (Reference 16)

Use Testing

Thus far, discussion has been focused on development of processing routes to address the affordability issue associated with the introduction of new materials into application. In reference to Figure 3, these processes are at the pilot scale synthesis and fabrication level on the pathway to application. Another method of moving high temperature materials one step further along the path is to insert them into fielded applications: i.e., use testing. An example is the Ceramic Insertion Program initiated by ARPA. This activity will exploit the upgrade potential of military systems with components fabricated from state-of-the-art structural ceramics. One of the major goals of this effort is to attempt to shorten the discovery to application time cycle by creating a market pull for advanced ceramics rather than relying solely on technology push into the marketplace. Advanced ceramic gas turbine engine components, diesel engine components, rocket nozzles, gun tube components, bearings, and armor applications are being pursued. Success with this program may also provide incentives for company production investments that will further reduce the time to application.

Cooperative Efforts

Many of the promising high temperature materials are in the form of composites. High material cost, a large number of experimental and manufacturing variables, and the need for finished composites tailored to specific applications increases the cost of traversing the pathway to application (Figure 3). At the same time the concurrent downsizing of defense and the decline in commercial sales is resulting in reduced funding for research and development within the aerospace community. The net result is that high temperature composite material development is becoming too expensive for any one company to pursue alone.

Fortuitously, ARPA was granted an "agreements authority" in FY 91 to establish pre-competitive consortia or partnerships. This authority was expanded in FY 93 to include dual use (military-civilian) partnerships as part of the defense conversion and reinvestment strategy. The objective is to encourage companies who may normally compete with each other to cooperate on research and development when it is their mutual best interests. In addition to industry, consortia and partnerships can include academic, government, and national laboratory participants. The philosophy behind ARPA's agreements authority requires substantial (50%) cost sharing by the consortia participants. Thus, the consortia and partnerships typically create a vertical integration of laboratory with product-oriented research. They also generate an up-front financial commitment by the participants, resulting in application-oriented planning, corporate financial analysis, and work on more than one step at a time on the pathway to application (Figure 3). At this time ARPA has three partnerships devoted to high temperature composite materials, one partnership devoted to precision investment casting, and one consortium for the development of ceramic fibers for use in high temperature composites.

Of these, the Integrated High Performance Turbine Engine Technology (IHPTET) Ceramic Fiber Consortium has probably advanced the farthest. The overall objective is to develop fibers for use in ceramic, and possibly metal matrix composites that will operate at use temperatures up to 1650C and to have these fibers ready for commercial scale-up in 3 to 5 years. The organizational structure of this consortium is depicted in Figure 11.

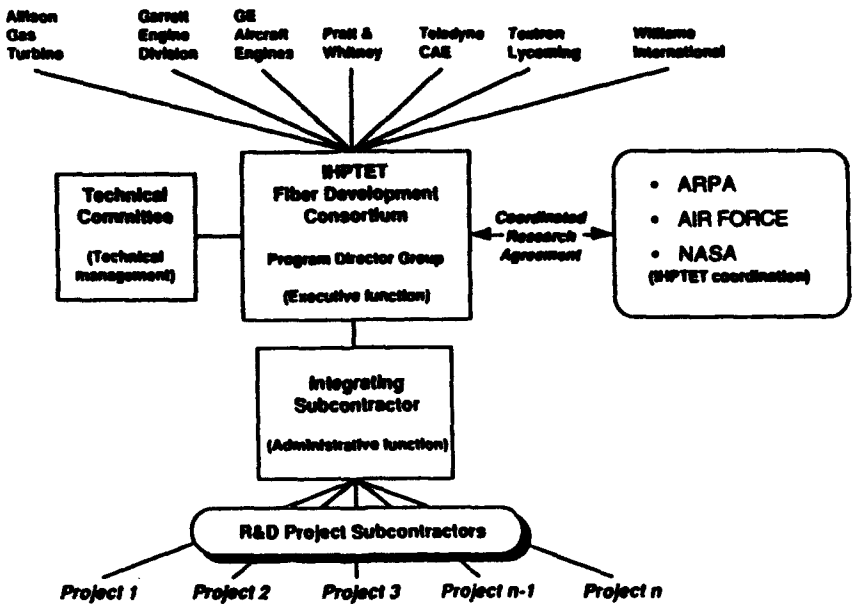

Figure 11 -Organizational Structure for the IHPTET Ceramic Fiber Consortium

Funding comes jointly from the seven engine company's IR&D and government (ARPA, Air Force, NASA). The program will run for five years, and research performers are being competitively chosen.

Summary

Critical issues in high temperature materials research extend beyond the search for better materials and basic understanding. Any new materials that will actually go into production will have to be affordable above all else. ARPA and other Federal Agencies have programs in place to address new manufacturing processes that will hopefully reduce the expense of some classes of emerging high temperature materials. Ultimately, the benefits these emerging materials offer, over currently available materials, must not be overcome by expense if they are to succeed.

The issue of affordability is also intertwined with health/safety/environmental and business/market issues. Materials that experience difficulty achieving acceptance due to problems in any of these areas are not likely to be produced in quantities that will be "affordable." While some of these affordability issues lie outside the technologists' sphere of influence, they must be kept in mind when planning new research initiatives.

The other critical issue of time-to-market is being addressed by ARPA in two ways. First, a ceramics technology insertion program is in place to gain field experience and generate a market pull for advanced structural ceramics technology. Second, partnerships that integrate laboratory and product-oriented research to meet specific industrial needs are getting underway. This concurrent approach to research along with shared financial commitment is expected to decrease the traditional 15 to 20 years of elapsed time needed to get from discovery to application.

Acknowledgements

The authors are grateful to Dr. William S. Coblenz, ARPA Defense Sciences Office, for valuable comments on this manuscript.

REFERENCES

1. Alan Katz, private communication with authors, Wright Laboratory, March 2, 1993.

2. J. Doychak, "Metal-and Intermetallic-Matrix Composites for Aerospace Propulsion and Power Systems," Journal of Metals, 44(6) (1992), 46-51.

3. R.A. Bajura, Holmes A. Webb, and William P. Parks, "Plan for an Advanced Turbine Systems Program," (Paper presented at the Workshop to Define Turbine System Research Needs-II, Greenville, South Carolina, 7-8 January 1992).

4. Michael A. Karnitz, Douglas F. Craig, and Scott L. Richlen, "Continuous Fiber Ceramic Composite Program," American Ceramic Society Bulletin 70(3) (1991) 430-435.

5. W.J. Molloy, "Investment-Cast Superalloys a Good Investment," Advanced Materials and Processes, 138(4) (1990), 23-30.

6. A.I. Taub and R.L. Fleischer, "Intermetallic Compounds for High Temperature Structural Use," Science, 243 (1989) 616-621.

7. J.K. Tien, G.E. Vignoul, and M.W. Kopp, "Materials for Elevated Temperature Applications," Materials Science and Engineering, A143 (1991) 43-49.

8. R.H. Jeal, "Ceramics File Flight Plan for Future Gas Turbines," Ceramic Industry, March (1989) 21-23.

9. A.R.C. Westwood, "Materials for Advanced Studies and Devices," Metallurgical Transactions B, 19B (1988), 155-164.

10. D.E. Larsen et. al., "Investment-Cast Processing of XD® Near-Gamma Titanium Aluminides," (Paper presented at ASM International Innovative Inorganic Composites Conference, Detroit, Michigan, October 1990).

11. L. Christodoulou and J.M. Brupbacher, "Metal Matrix Composite XD® Materials for Aerospace Applications," Materials Edge, November-December (1990), 29-33.

12. A.G. Evans, private communication with authors, University of California, Santa Barbara, 1990.

13. A.G. Fareed, et. al., "Mechanical Properties of 2-D Nicalon Fiber Reinforced LANXIDE Aluminum Oxide and Aluminum Nitride Matrix Composites," Ceramic Engineering Science Proceedings, 11 (7-8) (1990) 782-784.

14. D.R. Pank and J.J. Jackson, "Metal Matrix Composite Processing Technologies for Aircraft Engine Applications," Journal of Materials Engineering and Performance, to be published.

15. H.N.G. Wadley and W.E. Eckhart, eds., Intelligent Processing of Materials, The Minerals, Metals, and Materials Society, 1990, 17-39.

16. H.L. Marcus, et al. eds., Solid Freeform Fabrication Symposium Proceedings, The University of Texas at Austin, August, 1992, 72-85.

SESSION I

Alloy Design I
(Theory)

PHASE STABILITY AND ALLOY DESIGN IN HIGH TEMPERATURE INTERMETALLICS

J. H. Perepezko

Department of Materials Science and Engineering
University of Wisconsin-Madison
1509 University Avenue
Madison, WI 53706-1595

Abstract

In the development of high temperature intermetallics for structural applications, it is essential to consider the strong influence of materials processing. Among the fundamental data needed for effective processing are the relevant phase diagrams, the characteristic diffusivities and the possible solidification reaction pathways. In the Ti-Al system recent advances in the clarification of the phase diagram have had a direct impact on the analysis of phase stability and crystal growth processes. Building on the binary phase equilibria, it has been possible to develop new insight into several Ti-Al-X (X = Nb,Ta,Mo) ternary systems and the identification of ternary intermetallic phase reactions that are important for strengthening, toughening, and creep resistance. Similar developments have been demonstrated by alloy design modifications in other intermetallics such as $NbCr_2$ and NiAl. Monolithic alloy designs are also being supplemented by intermetallic matrix composites where again phase equilibria and interdiffusion reactions analyzed in diffusion couple studies provide an essential basis for an effective microstructural control and alloy design strategy.

Critical Issues in the Development of High Temperature Structural Materials
Edited by N.S. Stoloff, D.J. Duquette and A.F. Giamei
The Minerals, Metals & Materials Society, 1993

Introduction

In a high temperature environment, the essential requirements for structural materials include low density with high temperature strength, stiffness, and oxidation resistance, but adequate room temperature mechanical properties and cost effectiveness are also critical factors (1,2). High temperature service requires a thermal stability of the constituent phases which can be considered from several viewpoints. For example, a limited interaction with the service environment and compatibility with oxidation resistant coatings or reinforcement phases in composites are often basic requirements for survivability of a component at high temperature. In addition, application induced microstructural modification due to thermal cycling and the combined effects of temperature excursions under varying stress states are important to consider for a useful component. The underlying basis for the design and analysis of alloy synthesis and processing and the assessment of thermal stability is established to a significant extent by the relevant phase equilibria.

An important consideration in microstructural stability which is dominant throughout all treatments relates to the phase structure stability for a given compound. For different structures in disordered alloys, the relative stability is often determined by relatively small differences in energy (3,4). When the influence of ordering is considered as a perturbation on the energy differences, the relatively small differences making up phase stability determinations are again observed so that other influences due to strain, electronic and magnetic energetic terms can play a determining role in the actual structures observed in practice. The path of structural evolution and the rate of approach to the lowest energy structure or ground state are of course dictated by reaction kinetics. Moreover, the ordered nature of many intermetallic phases exposes new types of behavior that are not always evident in disordered systems. For instance, in ordered alloys diffusion can be sluggish due to the energetics of vacancy formation and also due to multiple site jump paths (5,6). For ordered systems the reaction kinetics involving a microstructural change depends on temperature through the usual Arrhenius function but also through the temperature dependence of the order parameter which tends to enhance the sensitivity of these materials to local structural defects (7).

One of the important attributes of intermetallics is their potential for prolonged thermal stability at elevated temperatures due in part to sluggish diffusion in an ordered lattice. Under such conditions the approach to equilibrium can be slow, and the reaction pathway can be sensitive to the prior thermal and deformation history. If this point is not considered and only a limited number of alloys are examined, then the observations can be incomplete and may even give a misleading assessment of the phase stability. Indeed, this is the inherent challenge in studying phase equilibria in intermetallic alloys. In the current work the evaluation of phase equilibria has been addressed by the systematic examination of numerous samples, sometimes with narrowly spaced compositions, after long term and often multiple annealing treatments which are terminated by either slow cooling or rapid quenching. Sometimes it is not possible to obtain elevated temperature phase equilibria information from bulk annealed samples due to unavoidable phase transformation(s) during the cooling of the samples. In that case diffusion couple experiments can play a major role in establishing the tie-lines. The sequence of phase reactions is also analyzed in terms of reaction temperatures obtained by thermal analysis and the structural changes associated with each reaction. However, by examining the changes in alloy constitution due to different treatments and relaxation of the phase structure and composition back to a common state in a given alloy at a set temperature, it is possible to judge the equilibrium arrangement at the set temperature.

Structural Stability

In order to provide a basis to consider the structural changes that can develop during phase transformation reactions associated with the processing treatments for intermetallic phase alloys, it is valuable to consider different stability rankings of the possible structures. This issue has received a fair amount attention and is currently under active study by a number of analysis methods ranging from empirical to phenomenological to atomistic level calculations (3,4,8-10). The essential features of these developments can be treated by following the highlights of a pairwise interaction model for the ground state structure in binary alloys but keeping in mind that other more detailed analysis is possible (11,12).

For a binary alloy the energy of solution in the model is assumed to be due only to interactions between the two kinds of atoms A and B of the system, with first and second neighbor pairwise interactions. All strain energy and interfacial energy effects are neglected in this analysis. If the bond energy of the ith neighbor A-A bond is denoted by E_i^{aa} and a similar symbol is used for the other bond energies then the ith neighbor interaction parameter V_i is given as $V_i = E_i^{AA} + E_i^{BB} - 2E_i^{AB}$. With this expression the energy of mixing is given only in terms of the V_i's. For the analysis V_1 is always considered positive, but V_2 maybe positive or negative and the results are expressed in terms of a ratio $V_2/V_1 = v$. The energy of mixing of a given structural state is defined as the difference between the configurational energy of that state and the reference state. The reference state is assumed as a two phase mixture of pure A and pure B, both with the same basic crystal structure. If the number of ith neighbor A-B bond is expressed by q_i the configurational energy of mixing is given by $E_m = \frac{1}{2} V_1 (q_1 + q_2 v)$ so that the problem of establishing the ground state is equivalent to minimizing the configurational energy of mixing. This type of analysis has been applied to a variety of systems (11,12). A useful comparison for selected values of v is shown in Fig. 1 where energy of mixing is presented as a function of composition for FCC based systems.

The appearance of second-nearest neighbor interactions is important because it leads to a more complete and realistic description of the superstructures possible. It also emphasizes that miscibility gaps which of course imply phase separation can occur naturally for second-nearest neighbor interactions. Thus, the alloying behavior of ordering and clustering are not mutually exclusive. Moreover, it is apparent that a variety of metastable transition states can occur during transformation from the disordered state to an equilibrium state following, for example, a quench from high temperature. In several cases it is apparent that disordered solutions are unstable to continuous ordering and that the transition kinetics can to be complex in such a system.

Reaction Kinetics-Decomposition Pathways

The full description of the various decomposition modes requires the analysis of the free energy as a function of ordering behavior as well, which is presented schematically in Fig. 2 from an analysis given by Soffa and Laughlin (13). For example in Fig. 2a, a free energy versus composition diagram is shown for an ordering alloy where the alloy of composition C_0 is a two phase mixture of ordered γ phase and disordered α phase for the given temperature, T_2, under equilibrium. If the alloy C_0 is quenched from the high temperature single phase α field to T_2 the as-quenched condition corresponds to point A' on the α disordered curve. Since A' is within the region where α is unstable with respect to continuous ordering, the reaction $A' \rightarrow B'$

proceeds without a nucleation barrier. The homogeneously ordered state at B' is still metastable with respect to the final equilibrium state at $\alpha_e + \gamma_e$. While the free energy versus composition diagram in Fig. 2a is useful, the underlying instability of the α phase at A' becomes clear when the free energy is also considered to be a function of the order parameter, η as in Fig. 2b. In this representation it is now clear that the state P indicated in Fig. 2a corresponding to composition C_0 at A' on the α disorder curve is indeed unstable with respect ordering to a state characterized by η_0^*. In addition, the disordered solution α outside of the hatched region in Fig. 2a is metastable with respect to ordering as indicated by Point P' since there is a free energy barrier. However, an ordering can take place without a change in composition but a discontinuous change in order parameter by the nucleation and growth of ordered regions and has been termed a congruent ordering process (7,14). Lastly, the stability of the as-quenched solution of the disordered a-phase when the composition is far from the ordering region such as at point R is also clearly evident.

When the kinetics of structural transitions in intermetallic phases are considered, the critical importance of examining all degrees of freedom that are available during the structural relaxation becomes apparent. For example, in the case discussed in Fig. 2 the free energy composition diagram does not indicate that the a disordered phase is unstable until the variation of the free-energy with order parameter is also examined. Indeed, this is the central issue in describing the kinetics of transitions involving ordered intermetallic phases. The rate of transition will normally be some function of a diffusion coefficient and a driving free energy, both of which are functions temperature, composition and order parameter (15). Therefore, the kinetic pathways need to be considered in terms of trajectories on a free-energy surface that can have a complex topology in general. As a consequence, the kinetic rates are also expected to be sensitive to processing effects such as quench-rate and the development of strain.

From atom movements in crystalline solids an atom vacancy exchange is the basic kinetic step. When the details of these types of exchanges are considered in ordered alloys, it is apparent that the atomistics of the specific structural types become very important in determining the jump pathway and the net frequency of atom exchange on different sublattices. An interesting example which appears to expose new types of kinetics behavior has been examined by Flutz (16,17) for a B2 equilibrium state. For different values of v other ordered arrangements such as DO_3 and B32 can develop in a transient manner during diffusion as the system encounters different states in the relaxation process towards final equilibrium. In some cases the transient states can persist for extended periods. Since the persistent transient states are not in metastable equilibrium, they have been termed pseudostable states (18) to reflect the slow relaxation kinetics.

Multiphase Microstructures

Microstructural control in intermetallic phases is of considerable importance to improving high temperature strength as well as low temperature ductility. The classic example of the benefits of careful microstructural control are the nickel-based superalloys which owe their high performance and versatility to microstructural designs based upon combinations of a Ni-rich disordered solid solution, γ and an ordered Ni_3Al ($L1_2$) based intermetallic phase, γ'. However, this experience has been repeated in the more recent development of titanium aluminides where Ti_3Al based alloys are a combination of $\alpha_2(DO_{19})$ and $\beta_0(B2)$ phases and TiAl based alloys are a combination of $\gamma(L1_0)$ and α_2 phases (2).

The development of multiphase microstructures in intermetallic alloys requires an optimum balance of compositions, volume fractions, sizes and distributions of constituent phases as guided by phase diagrams such as those in Fig. 3. If the coexisting phases exhibit similarities in crystal structure and compatible lattice parameters, then a phase equilibria such as that shown in Fig. 3a may develop and allow for the formation of a high volume fraction of a second phase either by a nucleation and growth process or by spinodal ordering. Other reaction pathways including solidification processing are also possible (Fig. 3b).

Although the reported experience has not been extensive, there are a few categories of microstructures approaches that have been examined systematically. For example, Naka, Thomas and Khan (19) have succeeded in developing two phase microstructures in pseudobinary Fe-Ni_2AlTi and Nb-Ti_2AlMo systems involving A2-$L2_1$ and A2-B2 type structures that are similar to the Al-$L1_2$ microstructures in nickel base superalloys (i.e. the disordered phase is the matrix) and show attractive performance. In a broad based and careful systematic study, Nemoto and coworkers (20,21) have examined a number of nickel and titanium aluminide intermetallic alloys with both ordered and disordered precipitate phases including precipitates based upon carbide or nitride phases which involve an intermetallic matrix that is saturated with carbon or nitrogen. Depending on the precipitate structure and coherency of the precipitate/matrix interface different types of dislocation/precipitate interactions contribute to strengthening.

In this regard it is useful to consider two examples which illustrate the guidance provided by the diagrams in Fig. 3. First, in the Ni-Al-Cu system for an alloy that lies in the NiAl-Cu_3Al section [i.e. (NiAl) - 25% (Cu_3Al)] a decomposition can be developed by a spinodal ordering process similar to that indicated in Fig. 3a. During aging of the quenched high temperature solid solution a spinodal-type microstructure developed (22) as indicated in Fig. 4a. In effect, the NiAl intermetallic phase is intermixed on a fine scale with a Cu-rich ductile phase. While the as-quenched solid solution exhibited extensive cracking during hardness testing, no cracking tendency was noted in the aged condition. In fact, in the aged state clear evidence of slip and plastic deformation was apparent which may be related to the plastic constraint imposed by the multiphase microstructure. Alternatively, for the situation depicted in Fig. 3b rapid solidification can be applied to extend the primary phase solubility which then allows for a high volume fraction of a dispersed phase to be developed during decomposition of the supersaturated solution. This is illustrated in Fig. 4b for a Nb-Cr alloy where the initial supersaturated bcc phase decomposed to a fine scale uniform two-phase bcc and $NbCr_2$ Laves phase microstructure (23).

Lattice Defects

Many of the most important and useful structural properties of alloys are determined by the crystal defect structure. In addition to defects such as dislocations and twins that control the deformation behavior, the departure from perfect order (i.e. $0 < \eta < 1$) is important in phase stability. The departure from perfect order can be accommodated by antiphase boundaries and also by constitutional defects. The role of constitutional defects has been examined extensively in the B2 structure where alloys such as NiAl, FeAl and CoAl have been shown to be quite sensitive to vacancy and antisite substitution defects (24). At the same time it is somewhat surprising that relatively little has been reported on other intermetallic phases and atomic defects. For example in the Laves phases which are the most populous class of intermetallic phases, the composition dependence of the lattice parameter for $NbCr_2$ shown in Fig. 5 suggests that a simple anti-structure substitution mechanism of Nb and Cr atoms on opposite

sites does not operate (25). In fact the substitution of the larger Nb atoms on Cr sites should be more difficult in the geometrically restrictive C15 lattice as compared to the substitution of the smaller Cr atoms on Nb sites. There is clearly much that remains to resolve in understanding the alloying and stability behavior within even single phase intermetallic structures.

Hierarchal Structures

It is apparent that there is a rich variety of transformation structures possible during the decomposition of ordered intermetallic phases, but there are also some constraints imposed by the crystallographic nature of the structures that can be applied to identify likely pathways or to eliminate others i.e., define a transformation hierarchy. The crystallographic symmetries of the precipitate phase and the matrix surrounding phase can provide basic information about the various allowed orientations and precipitate morphologies. With this approach, possible transformations between phases that can occur without long range diffusion or change of composition can be considered as displacive or chemical based transformations with a path that can be analyzed using a set group/super group symmetry relations (26). Transitions involving homogeneous deformations, shuffle transitions and chemical ordering can also be treated with this analysis. The approach will also suggest intermediate phases involved in the sequence of transformations that are likely to be metastable forms. The symmetry concepts are quite general and can be illustrated by considering the possible modes of structural transitions developed during cooling of an ordered B2 intermetallic phase in the Ti-Al-Nb system.

In the Ti-Al-Nb system two ternary phases the O(orthorhombic) and omega-type structure have been identified to develop from a high temperature cubic B2 phase as a result of displacive and chemical ordering during cooling. The transitions for these two-phases are represented by two fundamentally different modes. For the omega type phase as shown in Fig. 6 a collapse of the (111) planes in the [111] direction a (111) [111] type displacement wave is associated with the structural transformation sequence (27,28): $B2 \rightarrow \Omega' \rightarrow \Omega'' \rightarrow B8_2$

In the first stage, the partial collapse of (111) planes of the B2 phase (Fig. 6b) yields an Ω' structure which undergoes a reordering to the site occupancies of the B2 phase to yield a slightly modified Ω'' structure which has the same basic structure as Ω'. Subsequently, the $B8_2$ structure (Fig. 6d) forms by an additional reordering that is the 1A and 1B site occupancies which are different in Ω'' become identical in the $B8_2$ structure. A similar analysis can be developed for the $B2 \rightarrow O$ pathway (27).

Ti-Al-Nb System

There have been several studies (27-31) of some of the phase relationships in α_2 alloys with Nb additions which have revealed that at least two ternary phases, a B2 phase with a CsCl structure and an O phase with an orthorhombic structure, are present in this system. The B2 phase field may be quite extensive at high temperature, and yield alloys which exhibit a variety of decomposition products upon cooling including $B8_2$ and omega phases. An examination of the high temperature phase equilibria in the Ti-Al-Nb system has allowed for the determination of the 1200°C isothermal section (Figure 7). Some of the refinements of the previous preliminary diagram [32] are the extension of the bcc phase field over a large composition range, the clarification of the ternary (T2) phase region, and the smoothing of the composition variation of the $\gamma / \gamma + \alpha$ boundary.

The importance of the knowledge of an alloy's phase stability can be illustrated by considering the phase equilibria of alloys in the vicinity of the composition Ti-37Al-10Nb. At 1200°C under the equilibrium conditions, these alloys consist of two phases, α^* and B2 (figure 8a). However, on cooling these alloys undergo a series of reactions down to about 1185°C. During this cooling the α phase is transformed to the α_2 phase; a region of the α phase field stabilizes in the vicinity of Ti_4Al_3Nb and separates from the remaining α phase field [33]. As these transformations are occurring, the α and α_2 phase fields are undergoing compositional shifts to low aluminum concentration. The shift in composition of the α_2 phase field produces a dramatic alteration of the phase equilibria for this region of the ternary system in a temperature range of only about 50°C. This change in the phase equilibria upon cooling produces a change of almost 90° in the orientation of the tie-lines (figure 8b); the $\alpha+\beta$ two-phase field which is stable at 1200°C transforms into the $\alpha_2+\gamma$ two-phase field below 1185°C.

Furthermore, a systematic study utilizing thermal analysis and then coupling the results with a variety of heat treatments has allowed for the determination of the boundaries of the stable phase regions over a range of temperature. Such an analysis may allow for the establishment of processing schedules which can be used to avoid unwanted low temperature phases or reactions. Subsequent heat treatment can be used to dissolve the low temperature precipitates; however a complete removal may become a rather difficult and time consuming task. It is prudent to avoid such problems in the first place if at all possible. In addition to establishing processing schedules, knowledge of the phase equilibria may allow for the retention of the desired phase mixture through the appropriate addition of alloying elements.

Diffusional Interactions

Frequently, intermetallic phases are not considered as monolithic forms, but rather as constituents of a multi-phase alloy formed by in-situ processing reactions or as a constituent in a composite design produced through external processing (34). In the development of these alloy designs, often two basically dissimilar materials or phases with different mechanical and physical properties are combined to arrive at a final product with properties that are potentially superior to those of the individual constituent phases. The resultant alloy microstructure is often a complex multi-phase configuration. It is becoming increasingly clear that the performance of such designs and the elevated temperature stability are dominated by the characteristics of the internal interphases and the diffusional interactions. Among the most fundamental data needed to analyze these interactions are the relevant phase diagrams of stable and metastable conditions which are often at least of ternary order. From an analysis of phase equilibria it is possible to select combinations of phases which offer desirable properties in terms of phase interaction and high temperature thermal stability. In addition to phase diagram data, kinetic data such as the interdiffusion path and rates are required in order to understand and control the possible interactions at the interphases in multiphase systems.

The basic thermodynamic stability in a multiphase system can be evaluated following standard thermodynamic analysis involving the reaction of various two-phase and three-phase mixtures. This approach however, does not yield the reaction sequence between phases in a multiphase system. For example, as shown in Fig. 9 for a ternary system containing three intermediate phases α, β, and γ for an initial pairing of the phase mixture of γ and B, there are four possible pairings of reaction products, all of which represent stable pairings of the two-phase mixtures, but evolve through different phase sequencing pathways. In order to assess which of these pathways is selected, it is important to determine the interdiffusion path and reaction kinetics associated with the reduction in system free energy during reaction.

In order to illustrate some of the interdiffusion reaction kinetics features it is useful to consider the design of a intermetallic alloy phase in contact with a more ductile pure component which has been proposed as a toughening mechanism for a γ-TiAl intermetallic phase (35). A diffusion couple between pure Nb in contact with γ-TiAl was examined after an anneal of five days at 1200°C to yield the diffusion path illustrated in Fig. 10a. It is clear that Nb is not stable in contact with γ-TiAl and yields multiple-intermediate phase reaction layers as the result of the S-shaped diffusion path. The pathway trajectory immediately indicates that Al is the fastest diffusion species of feeding into Nb in order to develop the δ and σ phases and then crossing the line connecting the in points of the diffusion couple (i.e. the mass conservation condition) to form a ternary phase which has been identified to have a B2 structure and a phase before returning to the γ-TiAl composition. The application of this design did succeed in increasing the toughness by yielding intermediate layers of the δ and α phase which provided for weakly bonded interfaces. Building on this initial result, an alternate second phase dispersion design was examined by modifying the ductile phase composition through the addition of Ti. Again, diffusion couples between Ti-Nb alloys and γ-TiAl reveal the tendency of Al to be the fastest diffusing component producing an S-shaped diffusion pathway as indicated in Fig. 10b. In this case, the brittle intermediate reaction layers were avoided and strongly bonded interface was obtained. As result of the modified design further enhancements of toughening have been reported to remarkably high values (36). This illustration shows that even a rudimentary knowledge of the diffusion path can be used in a constructive design of second phase compositions and structures to promote a desired reaction sequence and interfacial bonding arrangement.

Concluding Remarks

In meeting the challenge to develop high temperature structural alloys with the required balance of mechanical properties and environmental resistance for engineering applications, alloy chemistries often evolve towards seemingly complex multicomponent arrangements. While it is usually not possible for the pace of a systematic phase equilibria determination to match the pace of alloy development efforts, the refinement and qualification of attractive alloy compositions in terms of the optimization of a desired microstructure configuration through annealing treatments or the long term structural stability at high temperature do require a phase equilibria database. Moreover, in the evaluation of multicomponent alloying selection strategies for a given intermetallic phase, it is often valuable to apply the guidance offered by the behavior of various alloying additions on the development of liquidus surfaces, solid solution solubility, intermediate phase reactions, and the stabilization of other phases. In this way the evolution of alloy chemistry can follow a more deliberate planned strategy.

Clearly, the processing of the advanced intermetallics, such as the titanium aluminides, requires a knowledge base with a foundation in phase equilibria, diffusion, and transformation kinetics; it can only be as effective as the depth of the knowledge base. The resources invested in acquiring this base do not slow down the real progress in alloy design but expedite it and expose new opportunities for processing.

Acknowledgment

The support of DARPA (ARO/DAAL 03-90-G-0183) is gratefully acknowledged.

References

1. R. L. Fleischer, D. M. Dimidnk and H. A. Lipsitt, Ann. Rev. Mater. Sci. 19 231 (1989).

2. D. M. Dimiduk, D. B. Miracle and C. H. Ward, Mat. Sci. and Tech. 8 367 (1992).

3. G. Inden and W. Pitsch, "Materials Science and Technology, Volume 5 Phase Transformations in Materials" ed. P. Haasen, (VCH, NY) p. 497 (1991).

4. A. Gonis, M. Sluiter, P. E. A. Turchi, G. M. Stocks and D. M. Nicholson, Jnl. Less Common Metals, 168 127 (1991).

5. H. Bakker and J. P. A. Westerveld, Phys. Stat. Sol. 145, 409 (1988).

6. H. Han, G. Frohberg and H. Wever, Phys. Stat. Sol. 79 559 (1983), N. Prinz and H. Wever, Phys. Stat. Sol. 61 505 (1980).

7. A. G. Khachtaturyan, Progr. Mat. Sci. 22 1 (1978).

8. E. S. Machlin, Acta Met. 24 543 (1976).

9. D. G. Pettifor, Mat. Sci. and Tech. 8 345 (1992).

10. T. Mohri, J. M. Sanchez and D. deFontaine, Acta Met. 33 1171 (1985).

11. M. J. Richards and J. W. Cahn, Acta Met. 19 1263 (1971).

12. S. M. Allen and J. W. Cahn, Acta Met. 20 423 (1972).

13. W. A. Soffa and D. E. Laughlin, Acta Met. 37 3019 (1989).

14. L.-Q. Chen and A. G. Khachaturyan, Acta Met. 39 2533 (1991).

15. H. Yamauchi and D. de Fontaine, in "Order-Disorder Transformations in Alloys" ed. H. Warlimont (Springer, NY) 148 (1974).

16. B. Flutz, Jnl. Less Common Metals, 168 145 (1991).

17. B. Flutz, Acta Met. 37 823 (1989).

18. R. Kikuchi, T. Mohri and B. Fultz, Mat. Res. Soc. Symp. Proc., 205 387 (1992).

19. S. Naka, M. Thomas and T. Khan, Mat. Sci. and Tech. 8 291 (1992).

20. W. H. Tian, T. Sano and M. Nemoto, Scripta Met. 20 933 (1986).

21. M. Nemoto, in "Critical Issues in the Development of High Temperature Structural Materials" eds. N. S. Stoloff, D. J. Duquette and A. F. Giamei (TMS Warrendale, PA) in press.

22. W. P. Allen, J. C. Foley, R. F. Cooper and J. H. Perepezko, Mat. Res. Soc. Symp. Proc. 194 405 (1990).

23. D. J. Thoma and J. H. Perepezko, Mat. Res. Soc. Symp. Proc., 194 105 (1990).

24. A. Taylor and D. J. Doyle, J. Appl. Cryst. 5 201 (1972).

25. D. J. Thoma and J. H. Perepezko, Mat. Sci. and Eng. A156 97 (1992).

26. J. W. Cahn, Acta Met. 25 721 (1977).

27. L. A. Bendersky, W. J. Boettinger, B. P. Burton, F. S. Biancamiello and C. B. Shoemarker, Acta Met. 38 931 (1990).

28. S. Banerjee and R. W. Cahn, Acta Met. 31 1721 (1983).

29. D. Banerjee, A. K. Gogia, T. K. Nandi and V. A. Joshi, Acta Met. 36 871 (1988).

30. L. A. Bendersky, W. J. Boettinger and A. Roytburd, Acta Met. 39 1959 (1991).

31. L. A. Bendersky, W. J. Boettinger and A. Roytburd, in "Intermetallic Compounds Structure and Mechanical Properties", ed. O. Izumi (Japan Inst. of Metals, Sendai) 845 (1991).

32. J. H. Perepezko, Y. A. Chang, L. E. Seitzman, J. C. Lin, N. R. Bonda, T. J. Jewett and J. C. Mishurda, in "High Temperature Aluminides and Intermetallics", eds. S. H. Whang, C. T. Liu, D. P. Pope and J. O. Stiegler, (TMS, Warrendale, PA) 19 (1990).

33. U. R. Kattner and W. J. Boettinger, Mat. Sci. and Eng. 152 9 (1992).

34. P. R. Smith and F. H. Froes, J. Metals (Mar.) 19 (1984).

35. L. S. Sigl, P. A. Mataga, B. J. Dalgleish, R. M. McMeeking and A. G. Evans, Acta Met. 36 945 (1988).

36. H. C. Cao, B. J. Dalgleish, H. E. Deve, C. Elliott, A. G. Evans, R. Mehrabian and G. R. Odette, Acta Met., 37 2969 (1989).

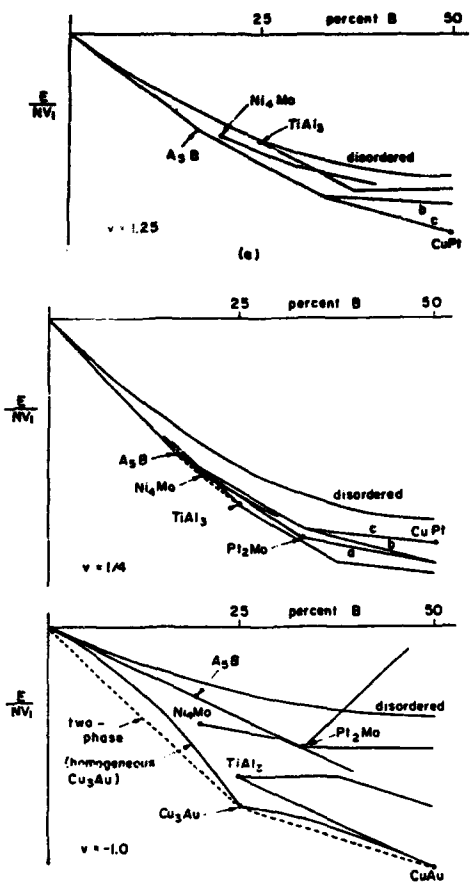

Fig. 1 Energy of mixing vs. composition of various states based on the fcc structure for three values of v (from (11)).

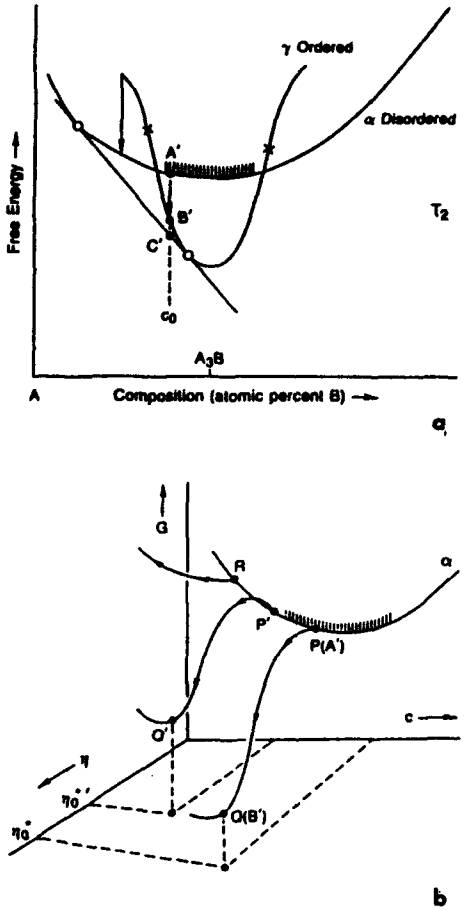

Fig. 2 a) Schematic free energy vs composition diagram for the ordered and disordered phases at T_2. The hatched segment of the free energy curve for the disordered phase corresponds to solutions which are unstable with respect to continuous ordering; b) Schematic free curves in G-c-η space. Points P, P' and R represent different states of thermodynamic stability of the disordered phase with respect to ordering (from (13)).

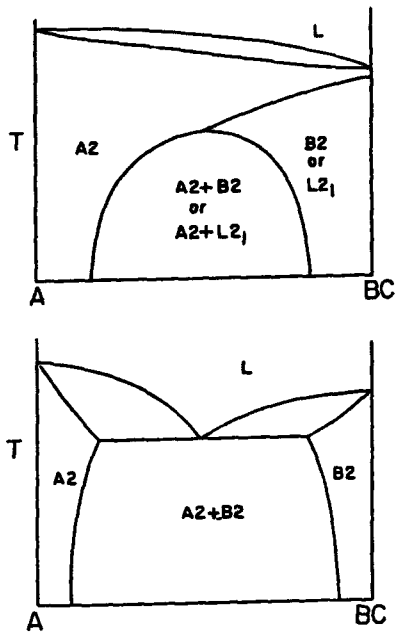

Fig. 3 Schematic phase diagrams for precipitation reactions in intermetallic alloys.

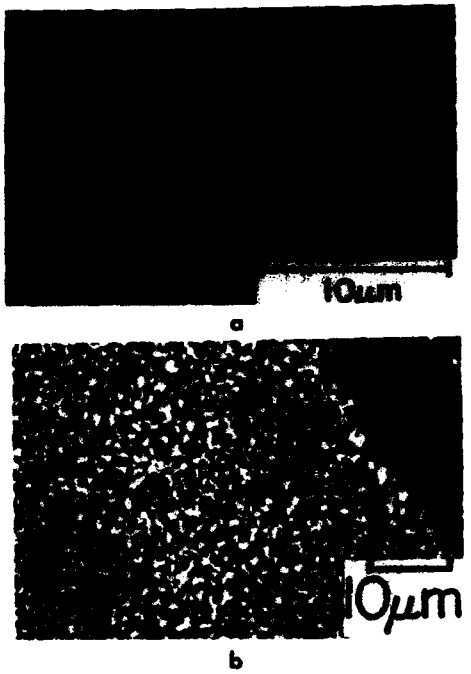

Fig. 4 a) Microstructure development in a Ni-40Al-30Cu alloy following solution treatment at 1000°C, quenching and then aging at 525°C for 1 day (SEM, backscatter mode) (22); b) Microstructure developed in a Nb-50 Cr alloy splat-quenched sample following a decomposition anneal at 1000°C (SEM, backscatter mode) 23.

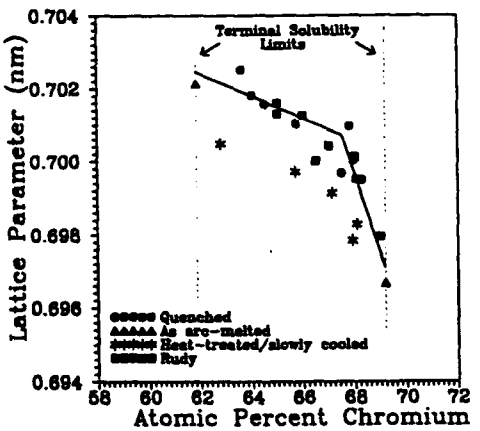

Fig. 5 Plot of the lattice parameter vs. composition for the C15 Laves phase in the Nb-Cr system (25).

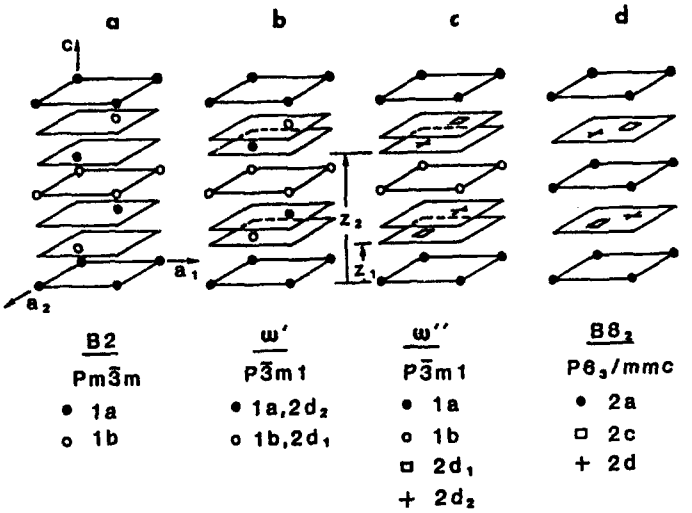

Fig. 6 Schematic drawing of (a) B2; (b) hypothetical ω'; (c) ω''; (d) $B8_2$ crystal structures. Different symbols represent different site occupancies (27).

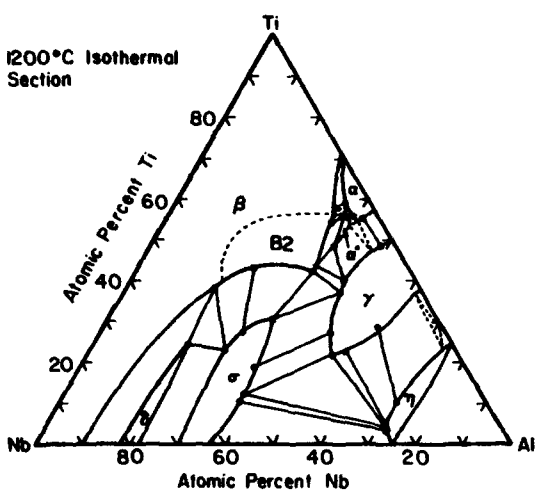

Fig. 7 The 1200°C isothermal section of the Ti-Al-Nb system.

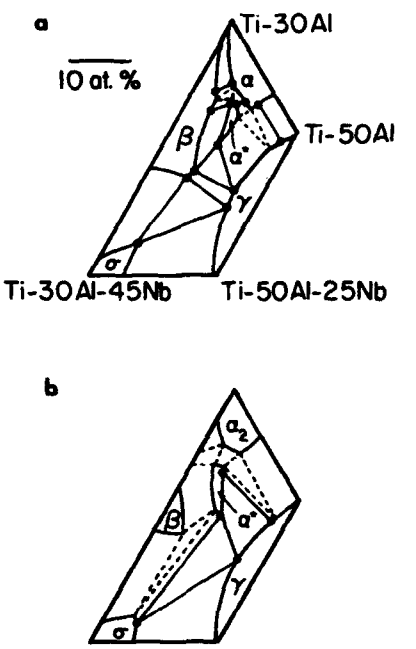

Fig. 8 Portions of the Ti-Al-Nb ternary isothermal sections near a) 1200°C and b) 1150°C.

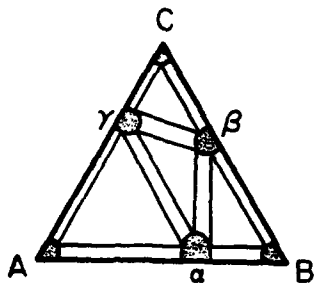

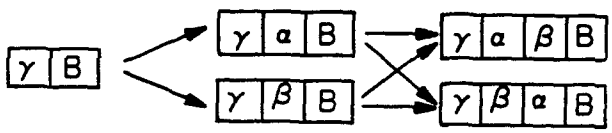

Fig. 9 Potential reaction layer formation in a γ/β diffusion couple involving stable pairings of phases.

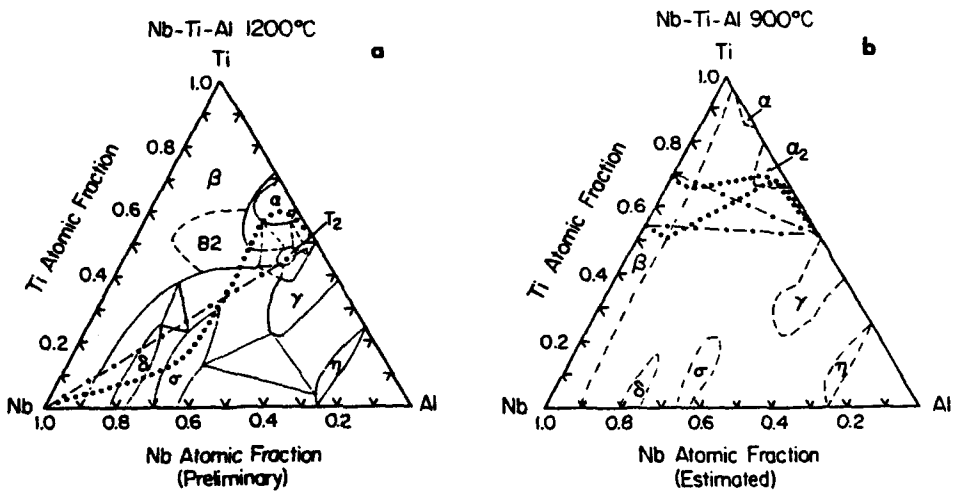

Fig. 10 a) Ti-Al-Nb isotherm at 1200°C indicating the diffusion path in a Nb/γ couple (dotted curve); b) Ti-Al-Nb isotherm at 900°C indicating the diffusion paths for two β/γ couples (dotted curve).

CRITICAL ISSUES IN THE COMPUTATIONAL MATERIALS SCIENCE FOR STRUCTURAL MATERIALS *

M. H. Yoo and C. L. Fu

Metals and Ceramics Division
Oak Ridge National Laboratory
Oak Ridge, TN 37831 (USA)

Abstract

Currently unresolved problems and critical issues in computational research on mechanical behavior of ordered intermetallics are assessed by reviewing the recent progress in the areas of first-principles quantum mechanical calculations, semi-empirical atomistic simulations, dislocation micromechanics and continuum mechanics. Significant improvements in theoretical and computational techniques have made the interpretive/predictive capability of computational materials science possible, especially the unique characteristics of strength and toughness in ordered intermetallic compounds. Future research areas of major importance in high-temperature structural materials are discussed.

* Research sponsored by the Division of Materials Sciences, U.S. Department of Energy, under contract DE-AC05-84OR21400 with Martin Marietta Energy Systems, Inc.

Critical Issues in the Development of High Temperature Structural Materials
Edited by N.S. Stoloff, D.J. Duquette and A.F. Giamei
The Minerals, Metals & Materials Society, 1993

Introduction

The mechanical properties of structural materials are known to be strongly influenced by the type of lattice defects present. In turn, the structure and properties of these defects are determined by the nature of atomic bonding. For this reason it is through the detailed study of the fundamental quantities at an atomic-level that the connection between atomistic and macroscopic properties can be made. Therefore, the so-called computational materials science for structural materials may be divided into the following aspects: (a) first-principles quantum mechanical calculations, (b) semi-empirical atomistic simulations, (c) micromechanical modeling, and (d) macroscopic continuum modeling. For example, some notable specific activities in these areas have been: (a) all-electron total energy calculations of bulk and defect properties based on the local density functional (LDF) theory, (b) simulation studies of dislocation cores and grain boundaries using the embedded atom method (EAM), (c) development of dislocation mechanisms for yield behavior using anisotropic elasticity theory, and (d) formulations of constitutive law and fracture toughness using continuum mechanics. While the interconnection is generally tenuous, due to the complexities introduced at intervening levels, there are cases where this link is at least qualitatively clear. For instance, one of the significant advances in intermetallics research, during the past five years, has been in the interpretive/predictive capability of computational materials science for intrinsic mechanical behavior of high-temperature ordered intermetallic alloys, e.g., see recent workshop reports (1-3).

It has been established that knowledge of the fundamental electronic structure and related properties is important for understanding the intrinsic and extrinsic factors that govern the mechanical behavior of ordered intermetallics. A comprehensive understanding of the bonding mechanism, point defect structure, yield strength anomaly, and brittle fracture behavior forms the basis for a better assessment of extrinsic effects on the strength and ductility of ordered intermetallics (e.g., B in Ni_3Al and H in FeAl), and provides a foundation for future alloy design strategies.

The purpose of this paper is to summarize unresolved problems and critical issues in computational research on mechanical behavior of ordered intermetallics and to discuss the knowledge base for potential answers to these problems. Future research areas of major importance in mechanical behavior of structural materials are also discussed.

Bonding Characteristics and Bulk Properties

Bonding Charge Density

When an intermetallic compound (A_3B) of the fcc based $L1_2$ structure is stable up to its melting point (e.g., Ni_3Al), the strong chemical ordering stems from the strong bonding between the dissimilar atoms (i.e., A-B bond). Such bonding behavior is best described by use of the so-called bonding charge density plot (Fig. 1). The bonding charge density is the response of the electron distribution, as referred to the atomic charge density, in the presence of the crystal field (4). The solid (dashed) lines in Fig. 1 denote contours of increased (decreased) electronic density as atoms are brought together to form a crystal. We find a depletion of electron density at the Al sites accompanied by a significant build-up of the directional d-bonding charge along the nearest neighbor Ni-Al direction. It is this directional d-bonding that gives rise to the strength of transition-metal aluminides. Thus, the bonding mechanisms of Ni_3Al can be best described by the combination of charge transfer and strong p (Al)-d(Ni) hybridization effects. A realistic interatomic potential used for atomistic simulation studies should properly take these effects into account. This issue will be discussed further in the following sections.

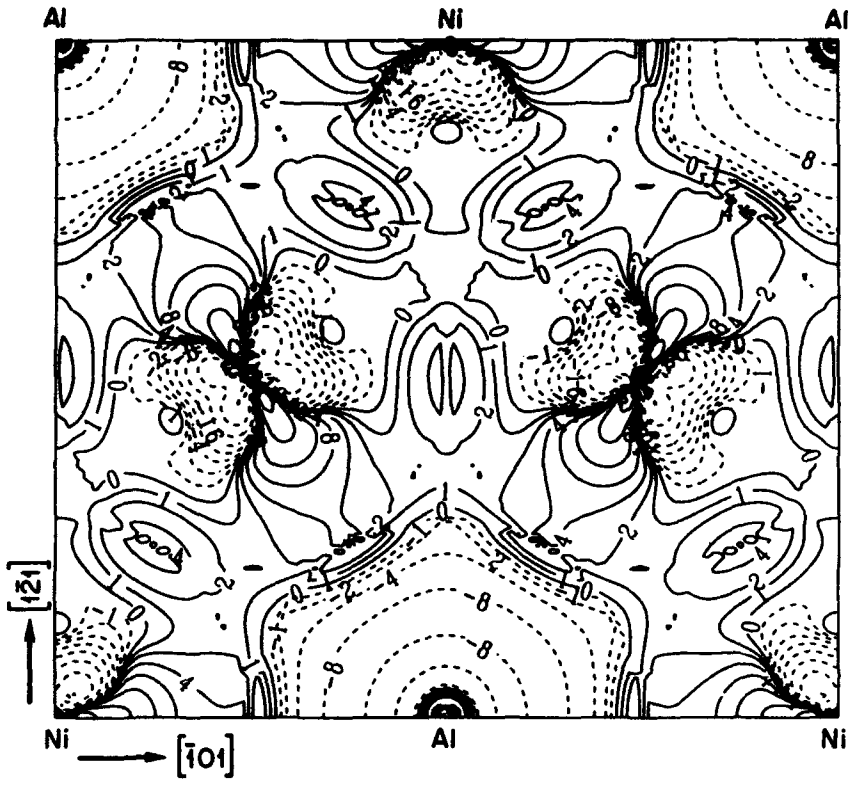

Figure 1 - The charge density difference between Ni_3Al and the superposition of neutral Ni and Al charge densities on the (111) plane [in units of 10^{-3} e/(a.u.)^3].

Elastic Constants

The single crystal elastic constants provide not only basic information on the nature of bonding forces in ordered intermetallics, but also the physical base for unusual mechanical behavior observed in some intermetallics. For example, in $L1_2$-type intermetallics, the elastic shear anisotropy, $A = 2C_{44}/(C_{11}-C_{12})$, is largely responsible for the anomalous (positive) temperature dependence of the yield stress (5).

First-principles total-energy calculations of the ground state elastic constants in intermetallic compounds were first performed by Fu and Yoo (6). The calculated values of the elastic constants of $L1_2$ alloys are listed in Table I. In the case of Ni_3Al, as was shown earlier in Fig. 5 of Ref. (7), the extrapolated values of experimental data are in good agreement with the calculated values. No experimental data are available for the remaining five alloys listed in Table I. As far as the calculated A values are concerned, the yield strength anomaly is likely for Ni_3Al and Ni_3Ti ($L1_2$), but not for Pt_3Al, Al_3Ti ($L1_2$), Al_3Sc, and Ni_3Si. The transition-metal trialuminides, Al_3Ti ($L1_2$) and Al_3Sc, show negative Cauchy pressures $(C_{12}-C_{44}) < 0$ which indicates that angular character to the atomic bonding is important in these intermetallics (8).

Table I. Calculated lattice parameters and elastic constants of $L1_2$ alloys at 0 K. B and G are bulk and shear moduli, and A and ν are Zener's shear anisotropy factor and Poisson's ratio

Alloy	a (nm)	(10^{11} N/m^2)					A	ν
		C_{11}	C_{12}	C_{44}	B	G		
Ni_3Al	0.349	2.35	1.45	1.32	1.75	0.88	2.93	0.38
Pt_3Al	0.385	4.36	2.20	1.40	2.92	1.26	1.30	0.34
Al_3Ti†	0.392	1.77	0.77	0.85	1.10	0.69	1.70	0.30
Al_3Sc	0.404	1.89	0.43	0.66	0.92	0.69	0.90	0.19
Ni_3Si	0.346	3.75	2.00	1.67	2.60	1.34	1.91	0.28
Ni_3Ti†	0.357	2.93	1.93	1.28	2.26	0.97	2.56	0.31

†Hypothetical $L1_2$ structure.

The six independent elastic constants of TiAl and $TiAl_3$ of the tetragonal $L1_0$ and $D0_{22}$ structures were calculated [9,10], and they are listed in Table II. A notable difference between C_{44} and C_{66} values of TiAl indicate the anisotropic character of atomic bonding between the (001) TiAl interlayer plane and the (010) Ti-Al mixed plane with respect to the [100] shear direction. The calculated values of shear and bulk moduli (Hill's average) are in excellent agreement with the experimental data at room temperature (11, 12). No experimental measurements of the elastic constants of TiAl have been reported yet.

Table II. Calculated elastic constants of tetragonal TiAl and $TiAl_3$ alloys of the $L1_0$ and $D0_{22}$ structures at 0 K

Alloy	(10^{11} N/m^2)							
	C_{11}	C_{12}	C_{13}	C_{33}	C_{44}	C_{66}	B	G
TiAl	1.90	1.05	0.90	1.85	1.20	0.50	1.25	0.70
$TiAl_3$	2.02	0.88	0.60	2.43	1.00	1.45	1.18	0.99

Strengthening Mechanisms

Yield Strength Anomaly

Although a large number of papers on modeling the yield strength anomaly in the $L1_2$ structure have appeared recently, e.g., in the recent conference proceedings (12, 13), the intrinsic physical source or the driving force for the positive temperature dependence of yield stress is not fully known. Any theory of the yield strength anomaly must explain not only the behavior of Ni3Al, but also the absence of it in other systems such as in Pt3Al

[6, 14]. In addition, a comparative analysis of the anomalous yield behavior between Ni_3Al and Ni_3Si may enable us to shed light on this critical issue.

First-principles total-energy calculations of shear (extended) fault energies, such as antiphase boundary (APB), superlattice intrinsic or extrinsic stacking fault (SISF or SESF), and complex stacking fault (CSF) energies, were performed using a super cell approach (7, 9, 10, 15). Table III shows the calculated results for Ni_3Al and Ni_3Si (16). According to the cross-slip-pinning model (5, 17), the energetic criterion for the thermally activated process of forming pinning centers along the leading superpartial is that the interaction torque and the APB energy anisotropy must be sufficiently large to have

$$\eta = \left(\frac{3A}{A+2}\right)\frac{\gamma_1}{\gamma_0} > \sqrt{3}, \qquad (1)$$

where γ_1 and γ_0 are the APB energies on (111) and (100) planes. According to the calculated results listed in Tables I and III, this criterion is satisfied for Ni_3Al, but not for Ni_3Si. Accordingly, a critical issue is to resolve the apparent contradiction between the theoretical prediction on stoichiometric Ni_3Si (15) and the experimental data on hypostoichiometric Ni_3Si (18).

The premise of micromechanical analyses for the CSP model (17) was the glissile-sessile transformation of <101> superdislocations in the $L1_2$ structure predicted on the basis of the atomistic calculations by Yamaguchi et al. (19) who used a central force model. The subsequent atomistic simulation studies by Yoo et al. (20) and Farkas and Savino (21), using the EAM potentials formulated for Ni_3Al by Foiles and Daw (22) and Voter et al. (23), respectively, confirmed the main conclusion of the central force model (19). That is, the stable equilibrium configurations of a superpartial dislocation core are a (111) planar splitting on the (111) APB plane and a (111) or ($1\bar{1}1$) nonplanar splitting on the (010) APB plane.

Table III. Calculated shear fault energies of $L1_2$ alloys at 0 K (in units of mJ/m^2)

Alloy	APB		SISF	CSF
	(100)	(111)		
Ni_3Al	140	175	40	225
Ni_3Al[a]	28	156	96	259
Ni_3Al[b]	33	142	13	121
Ni_3Si	707	625	460	710
Ni_3Ti	-160 (unstable)	550		
$Ni_3(Si,Ti)$[c]	360			

[a]EAM by Foiles and Daw (22).
[b]EAM by Voter and Chen (23).
[c]Assume every other Si site is replaced by Ti.

However, care should be exercised in using the EAM potentials, since the EAM-1 potentials (22) give too low a (100) APB energy and the EAM-2 potentials (23) predict a CSF energy lower than the (111) APB energy (c.f., Table III). The recent weak-beam transmission electron microscopy (TEM) investigation of $Ni_{76}Al_{24}$ reports the (111) APB and CSF energies of 180 and 206 mJ/m^2 (24), respectively, which are in good agreement with the results of first-principles calculations (Table III). Although these semi-empirical atomistic methods (e.g., the EAM) are still the current choice for large scale simulations, such as dislocation cores and crack tips, more thorough and careful construction of the "interatomic" potentials including the angular dependence of many body interactions should be developed (see Refs. 25 and 26).

Defect Hardening

In strongly ordered $L1_2$, B2 and $L1_0$ alloys (e.g., Ni_3Al, Ni_3Ga, NiAl, CoAl, and TiAl), the yield strength is known to increase as their compositions deviate from exact stoichiometry. First-principles total-energy calculations of the self (internal) energies of isolated single defects (antisite defects and constitutional vacancies) have been performed for NiAl, from which the temperature and composition dependencies of their equilibrium concentrations were determined by minimizing the grand potential (16). The calculated results of NiAl at 1300 K are shown in Fig. 2. Of the four possible point defects (two types of vacancies and two types of antisite defects), the calculations revealed that the concentration of vacancies on the Al sublattices was negligibly small and independent of the Al level. In addition to the substitutional antisite defects on Al sites, the vacancy concentration on the Ni sublattices, is about 10^{-5} for the Ni-rich side. On the Al-rich side, the major point defects are vacancies at the Ni sublattices and there is a two-orders of magnitude difference between the vacancy and antisite defect concentrations.

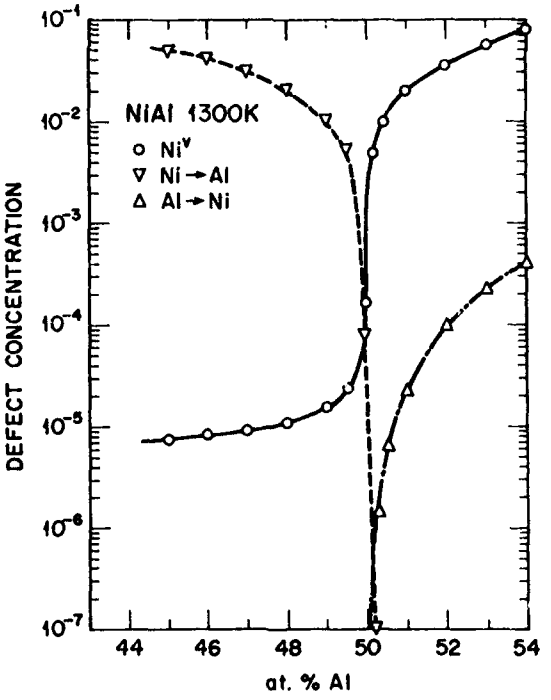

Figure 2 - The dependence of point defect configuration of NiAl on the aluminum concentration at 1300 K.

The atomic relaxation around a vacancy at the Ni sublattice on the Al-rich side is substantially larger than that associated with an antisite (Ni → Al) defect on the Ni-rich side. Thus, the experimental data on off-stoichiometric increase in microhardness (with a steeper composition dependence on the Al-rich side) compiled by Noebe et al. (27) are consistent with the point defect type and concentrations predicted by the first-principles calculations (16).

Solid Solution Hardening

In order to describe quantitatively the intrinsic strengthening mechanisms for the anomalous yield strength and defect hardening, it is essential to develop the capability of three-dimensional (3-D) atomistic simulations for the thermally activated dislocation configurations, such as cross-slip and climb of extended dislocations. The collective behavior of pinning segments along the superdislocations in the $L1_2$ structure has been treated recently (28). However, the problem of choosing appropriate boundary conditions for atomistically simulating kinks and jogs on dislocations remains largely an unsolved problem. Accordingly, solid solution hardening mechanisms in ordered alloys can be treated only qualitatively (29). Effects of solutes and impurities on the energetics of a system, such as the preferred interstitial absorption of boron in Ni3Al (4), the effect of Ti additions on the APB energies of Ni_3Si (15), and the surface energy reduction in FeAl caused by H (30), can be evaluated using the superlattice geometries. But, the effects of dilute (disordered) ternary additions are prohibitively difficult to model. Some progress has been made recently to calculate the effect of dilute alloying additions (or off-stoichiometry) on the shear fault energies of Ni_3Al and TiAl using an EAM simulation technique (29) and a quantum mechanical calculation based on coherent potential approximations (31).

Toughening Mechanisms

Cleavage Strength

The ideal cleavage (Griffith) energy, defined as the total surface energy of two cleaved surface planes ($G_C = 2\gamma_s$) can be determined from first-principles calculations by modeling of the surface by a single (free standing) slab or by a repeated supercell geometry (10). The Griffith strength, k_{IG}, defined as Irwin's stress-intensity factor for a Mode I crack is determined from the calculated G_C and elastic constants. The calculated results of G_C and k_{IG} for cubic ($L1_2$ and B2) and tetragonal ($L1_0$) transition-metal aluminides were given earlier (32). Table IV lists the calculated results for (111) and (100) cleavage planes in Ni3Al and Ni3Si. The ideal cleavage energy and strength of Ni3Si are predicted to be higher than those of Ni3Al.

It is generally recognized that the critical factor of dislocation behavior controlling the brittle-ductile transition (BDT) phenomena is the nucleation or emission of dislocations in metals and alloys, and the dislocation mobility in semiconductors and ceramics (33). In the case of ordered intermetallics, the critical factor(s) must depend closely on the intermetallic bonding characteristics of a given compound, in particular, whether its bonding behavior is more metallic or covalent. Therefore, the dislocation emission from a crack-tip may be important in Ni3Al, and probably the dislocation mobility in Ni3Si, for promoting crack-tip plasticity.

Table IV. Calculated ideal cleavage energies (G_c) and Griffith strength (k_{IG}) for the Mode I crack in Ni_3Al and Ni_3Si

	(hkl)	Gc (J/m^2)	[uvw]	k_{IG} (MPa $m^{1/2}$)
Ni_3Al	111	4.6	$1\bar{1}0$	1.06
			$11\bar{2}$	1.09
	100	5.8	001	1.11
			011	1.17
Ni_3Si	111	5.1	$1\bar{1}0$	1.37
			$11\bar{2}$	1.38
	100	7.2	001	1.56
			011	1.59

In extending the Rice-Thomson criteria for the BDT behavior, Rice has recently introduced a modified criterion (34, 35), for an edge dislocation parallel to the Mode I crack tip line, as

$$q = \frac{G_d}{G_c} = \frac{\gamma_{us}}{2\gamma_s f^2(\theta)}, \qquad (2)$$

where γ_{us}, called "unstable stacking energy", is defined as the maximum energy encountered in the rigid body shear process and $f(\theta) = \cos^2(\theta) \sin(\theta/2)$ for the case of elastic isotropy. Calculating γ_{us} for the Shockley partials in Ni_3Al from the EAM-1 (22), Sun et al., (34) predicted that Ni_3Al is more brittle than Ni in both (100) and (110) Mode I cracks. According to Foiles and Daw (22), the (100) Griffith energy of Ni_3Al is $G_C = 3.5$ J/m^2, which is the sum of 1.6 and 1.9 J/m^2 for the mixed composition and the pure Ni planes, respectively. This is considerably lower than the value of $G_C = 5.8$ J/m^2 obtained by the first-principles total-energy calculation (32). In addition, the anisotropic correction of $f(\theta)$ for the 1/6[112](1 11) partial slip at the Mode-I (001)[110] crack system (34), $\theta = 55°$, is from 0.36 to 0.30. This raises the value of G_d by a factor of 1.44, hence the brittleness increases.

The mobility of dislocations is expected to be strongly anisotropic owing to the coupling between the normal stress components and the shear response along the slip plane. Figure 3 show the anisotropic (linear elastic) coupling effect of σ_r and σ_θ on the elastic shear strain, which gives a substantial increase (25%) in $\varepsilon_{r\theta}$ from 0.37 to 0.46 for the case of 1/6<112>{111} partial dislocations. Nonlinear aspects of the anisotropic coupling effect can be investigated by atomistic simulation studies of the Peierls stress under the generalized applied stress state. Therefore, for a mechanistic understanding of crack-tip processes, a combined analysis using atomistic simulations and dislocation micromechanics is essential. In this regard, a challenging problem is not only to employ realistic interatomic potentials, but also to set up the proper boundary conditions at the interface between a discrete atomic region and the continuum around a crack tip.

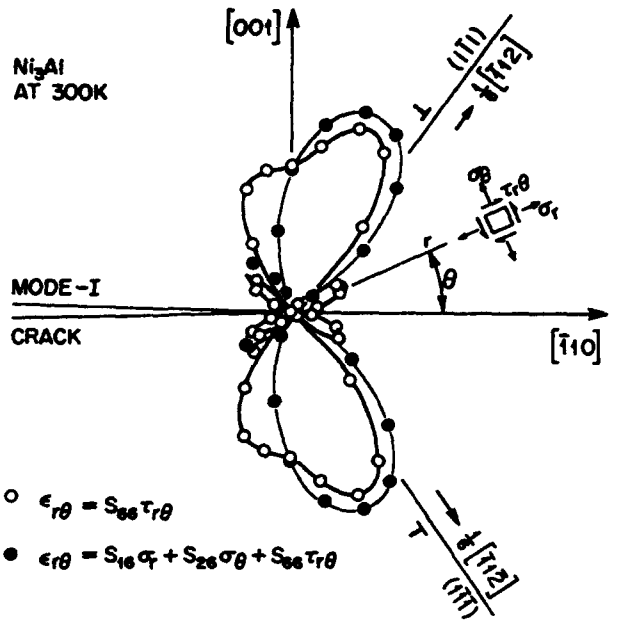

Figure 3 - Elastic shear strain field, $\varepsilon_{r\theta}$, at a Mode-I crack tip of (001)[110] type in Ni_3Al (in units of $1/\sqrt{2\pi r}$)

Interfacial Fracture

The foregoing description of ideal cleavage and crack-tip plasticity can be extended to the cases of intergranular fracture and heterophase interfacial fracture. According to atomistic simulation studies using the EAM, both at ground state (36) and at elevated temperatures by an equilibrium Monte Carlo technique (37), the cohesive energies of grain boundaries (GBs) of $\Sigma = 13$ twist and tilt and $\Sigma = 15$ tilt types are comparable for ductile Ni and 'brittle' Ni3Al. These results suggest that the 'intrinsic brittleness' of polycrystalline Ni3Al must be related not only to cohesive strength, but also to other factors such as the efficiency of inhomogeneous plastic deformation at/near GBs. On the other hand, the recent comparative analysis of Ni3Al and Cu3Au for a $\Sigma = 29$ symmetric tilt boundary by Yan et al. (38), using N-body potential of Finnis-Sinclair type (39), indicated that the formation of columnar "cavities" along the boundary in Ni3Al was related to its high ordering energy. If segregation of one of the alloy components occurs, the boundaries will disorder compositionally and a situation analogous to that found in weakly ordered alloys (e.g. Cu3Au) will ensue. However, this was not found in Ni3Al (38) and thus it suggests intrinsically brittle GBs. In view of the discrepancies in the shear fault and surface energies of Ni_3Al between semi-empirical atomistic simulation and *ab-intio* total energy methods, however, all of the simulation results should be interpreted only qualitatively as comparative analyses.

By use of first-principles total energy method, free surface energies of the low index planes have been determined for many transition-metal aluminides, including γ-TiAl (32), but no grain-boundary or heterophase interfacial energies have been obtained so far. In the case of the coherent (111) twin boundary in TiAl, the ideal work of interfacial separation, $G_i = 2\gamma_s - \gamma_b$, is obtained to be 4.44 J/m^2 from $G_c = 2\gamma_s = 4.5$ J/m^2 (40) and $\gamma_b = 60$ mJ/m^2 (9). This result indicates that in polysynthetically twinned (41) TiAl, the (111) twin interfacial mode of fracture is favored over the (111) cleavage mode only slightly, as far as the ideal work of fracture is concerned.

Hydrogen Embrittlement

Only recently, when a moisture-induced hydrogen embrittlement mechanism was identified in FeAl, was it realized that the test environment was a major cause of brittleness (42). The calculated results of hydrogen absorption effects on the (100) cleavage fracture of FeAl (30) are summarized in Table V. The effect of hydrogen absorption is a decrease in the cleavage energy, G_c, and also in the maximum cohesive strength, σ_m, as a result of strong electronic interaction between H and Fe atoms. No formal theory exists which can correctly take into account the crack-tip plasticity on an atomistic level. Nevertheless, one can obtain much insight into the relationship between k_{IG} and the experimentally measured fracture toughness, K_{IC}, by considering the phenomenological model developed by Gerberich et al. (43),

$$K_{IC} = \frac{1}{\beta}\exp\left(\frac{k_{IG}^2}{\alpha\sigma_y}\right), \qquad (3)$$

where σ_y is the yield strength (e.g., 360 MPa for FeAl) and α and ß are assumed to be material independent constants. The equation has been used widely in the analysis of fracture toughness and hydrogen embrittlement of Fe-base alloys. The important implication of Eq. (3) is that the macroscopic thresholds depend sensitively on the ideal cleavage energies through an exponentially dependent function. For instance, a decrease in k_{IG} by a factor of 2 lowers K_{IC} by a factor of 10^2. Thus, the goal of alloy design is to find those alloys with high values of k_{IG} and ways of trapping hydrogen so as to minimize the decrease in k_{IG}. The possible change in the yield strength due to hydrogen-dislocation interaction in ordered intermetallics is not understood and remains an open question.

Table V. Calculated cohesive strength, σ_m, and ideal cleavage energy, G_c, for (100) crack in FeAl

(100) crack	σ_m (GPa)	G_c (J/m^2)
FeAl	35	6.5
H in FeAl		
Low conc.	28	5.2
High conc.	11	1.7

Discussion and Summary

As was summarized in the recent workshop reports (1-3), there has been a significant advance collectively in all aspects of computational research on ordered intermetallic compounds in the past five years . Though limited to ground state properties, most of the fundamental bulk and defect properties relevant to mechanical behavior of intermetallic compounds can be determined by performing first-principles total-energy calculations based on the LDF theory. This predictive capability of first-principles computational techniques can make significant impacts in all other levels of computational materials science. First, future development of interatomic potentials can be made to be consistent with the result of first-principles calculations, not solely with the available experimental data as have been practiced in the past. Second, in certain established cases, the total energy calculations can provide direct input into micromechanical models, e.g., the defect self-energies into the thermodynamic calculations of defect concentrations, and the APB energy and elastic shear anisotropy factors into the dislocation model for yield strength anomaly. Third, the bulk and defect properties calculated for as-yet untested intermetallic compounds (e.g., bonding characteristics, specific elastic moduli, defect concentrations, and the input parameters to Eqs. 1-3) can furnish important insights to alloy designers who seek new-generation materials for high-temperature structural applications.

However, disorder and temperature effects are still largely unsolved problems. It is very difficult to handle structures and properties involving a large number (>50) of atoms per unit cell using first-principles approach (e.g., dislocation core structure, grain boundaries, crack tips, etc.). As the validity of interatomic potentials is improved and justified, semi-empirical atomistic methods (e.g., the EAM) will remain the current choice for large scale simulations. In such studies, however, extreme care must be exercised in setting the initial and boundary conditions to be in compliance with the displacement field given by the continuum theory.

In essence, all of the above discussion on ordered intermetallic compounds is also applicable for the ceramic compounds. Because of the more covalent nature of interatomic bonding in ceramics, as compared to intermetallics, the choice of relevant interatomic potentials would be, in general, more difficult but can be obtained (e.g., tight-binding approach). As for structural composites, first-principles and semi-empirical atomistic methods together could provide the necessary basic parameters for a given materials design strategy, such as the difference in bulk properties (elastic moduli and thermal expansion coefficients), interfacial and surface energies, and diffusion coefficients.

References

1. M. H. Yoo, S. L. Sass, C. L. Fu, M. J. Mills, D. M. Dimiduk and E. P. George, Acta Metall., 41 (1993), 987-1002.
2. M. I. Baskes, R. H. Hoagland, and A. Needleman, Mater. Sci. Eng. A159 (1992), 1-34.
3. C. T. Liu, R. W. Cahn, and G. Sauthoff, eds., Ordered Intermetallics - Physical Metallurgy and Mechanical Behavior, Kluwer-Academic Publ., Boston (1992).
4. C. L. Fu and M. H. Yoo, 155-164 in Ref. (3).
5. M. H. Yoo, Scripta Metall. 20 (1986), 915-920.
6. C. L. Fu and M. H. Yoo, Phil. Mag. Lett. 58 (1988), 199-204.
7. M. H. Yoo and C. L. Fu, ISIJ Int. 31 (1991), 1049-1061.
8. D. G. Pettifor, 47-59 of Ref. (3).
9. C. L. Fu and M. H. Yoo, Phil. Mag. Lett. 62 (1991), 159-165.
10. C. L. Fu, J. Mater. Res. 5 (1990), 971-979.
11. H. A. Lipsitt, D. Schechtman, and R. E. Schafrik, Metall. Trans. 6A (1975), 1991-1996.
12. D. Caillard, J. Thibault, and P. Veyssiére, eds., Mechanisms of Deformation and Strength of Advanced Materials, J. Phys. III, 1 (1991), 829-1166.
13. I. Baker, R. Darolia, J. D. Whittenberger, and M. H. Yoo, eds., High-Temperature Ordered Intermetallic Alloys V, MRS Symp. Proc., Vol. 288, MRS Pittsburgh, PA (1993).
14. G. Tichy, V. Vitek, and D. P. Pope, Phil. Mag. A53 (1986), 485-494.
15. C. L. Fu, Y. Y. Ye, and M. H. Yoo, Phil. Mag. Lett. 67 (1993), 179-185.
16. C. L. Fu, Y. Y. Ye, and M. H. Yoo, in Ref. (13).
17. V. Paidar, D. P. Pope, and V. Vitek, Acta Metall. 32 (1984), 435-448.
18. T. Suzuki, Y. Oya, and S. Ochiai, Metall. Trans. 15A (1984) 173-181.
19. M. Yamaguchi, V. Paidar, D. P. Pope, and V. Vitek, Phil. Mag A 45 (1982), 867-882.
20. M. H. Yoo, M. S. Daw, and M. I. Baskes, Atomistic Simulation of Materials - Beyond Pair Potentials, eds. V. Vitek and D. J. Srolovitz, Plenum Press, NY, 1989, 401-410.
21. D. Farkas and E. J. Savino, Scripta Metall. 22 (1988), 557-560.
22. S. M. Foiles and M. S. Daw, J. Mater. Res. 2 (1987), 5-15.
23. A. F. Voter and S. P. Chen, Characterization of Defects in Materials, eds. R.W. Siegel, J.R. Weestman and R. Sinclair, MRS Symp. Proc., Vol. 82, MRS, Pittsburgh, PA (1987) 175-180.

24. K. J. Hemker, B. Viguer, R. Schaüblin, and M. J. Mills, in Ref. (13).

25. A. E. Carlsson, Solid State Physics-Advances in Research and Applications, eds. H. Ehrenreich and D. Turnbull, Vol. 43, Academic Press, New York (1990), 1-91.

26. R. M. Nieminen, M. J. Puska, and M. J. Manninen, eds. Many-Atom Interactions in Solids, Springer-Verlag, Berlin (1990).

27. R. D. Noebe, R. R. Bowman, and M. V. Nathal, Intl. Mater. Rev. (to be published).

28. M. J. Mills and D. C. Chrzan, Acta Met. **40** (1992), 3051-3064.

29. D. M. Dimiduk, S. Rao, T.A. Parthasarathy, and C. Woodward, 237-256 in Ref. (3).

30. C. L. Fu and G. S. Painter, J. Mater. Res. **6** (1991), 719-723.

31. C. Woodward, J. M. MacLaren, and S. Rao, J. Mater. Res. **7** (1992), 1735-1750.

32. M. H. Yoo and C. L. Fu, Mater. Sci. Eng. **A153** (1992), 470-478.

33. A. George, 909-927 in Ref. (12).

34. Y. Sun, J. R. Rice and L. Truskinovsky, High-Temperature Ordered Intermetallic Alloys IV, eds., L. A. Johnson, D. P. Pope and J. O. Stiegler, MRS Symp. Proc. Vol. 213, MRS, Pittsburgh, PA (1991), 243-248.

35. J. R. Rice, J. Mech. Phys. Solids **40** (1992), 239-271.

36. S. P. Chen, A. F. Voter, and D. J. Srolovitz, High-Temperature Ordered Intermetallic Alloys II, eds. N.S. Stoloff, C. C. Koch, C. T. Liu, and O. Izumi, MRS Symp. Proc. Vol. 81, MRS, Pittsburgh, PA, (1987), 45-50.

37. S. M. Foiles, Ibid. 51-56.

38. M. Yan, V. Vitek, and G. J. Ackland, 335-353 in Ref. (3).

39. G. J. Ackland and V. Vitek, Phys. Rev. **B41** (1990), 10324-10333.

40. C. L. Fu and M. H. Yoo, Mater. Chem. Phys. **32** (1992), 25-36.

41. T. Fujiwara, A. Nakamura, M. Hosomi, S. R. Nishitani, Y. Shirai, and M. Yamaguchi, Phil. Mag. A **61** (1991), 591-606.

42. C. T. Liu, E. H. Lee, and C. G. McKamey, Scripta Met. **23** (1989), 875-880.

43. W. W. Gerberich, H. Huang, and P. G. Marsch, NASA Conf. on Advanced Earth-to-Orbit Propulsion Technology, Marshall Space Flight Center, Huntsville, Alabama, May 1992.

ALLOY DESIGN FOR HIGH TEMPERATURE, LOW DENSITY COMPOSITE MATERIALS

G.H. Reynolds and J.H. Norman

MSNW, Inc.
P.O. Box 865
San Marcos, CA 92079

Abstract

This paper considers the design of alloys or intermetallic compounds from the point of view of their utilization as composite matrices in combination with currently available filaments. Important criteria in this case would include both thermochemical and thermomechanical compatibility with available reinforcements, environmental resistance or amenability to being protected from the environment, and adequate levels of mechanical properties to serve effectively as composite matrices. Satisfying the compatibility and environmental resistance criteria can lead to very nontraditional matrix compositions and configurations, some of which may possess the requisite levels of mechanical properties. Examples resulting from a systematic analysis of compatibility of various materials with titanium-based alloys and titanium-containing intermetallic compounds which could form the basis for composite matrices reinforced with currently available filaments are discussed.

Critical Issues in the Development of High Temperature Structural Materials
Edited by N.S. Stoloff, D.J. Duquette and A.F. Giamei
The Minerals, Metals & Materials Society, 1993

Introduction

Our purpose is to discuss "compatibility" as a driver in the configuration of metal and intermetallic matrix composites using titanium and titanium aluminide matrices as model systems. We have arbitrarily considered only commercially available filaments, SiC, Al_2O_3 (sapphire), B, and C, as potential reinforcements since other, more developmental filaments are not likely to be available soon. With the constraints of matrix composition and filament composition three "compatibilities" then become of interest. The first is the chemical compatibility, or lack of it, between the filament and matrix which may necessitate the use of one or more interlayers, or chemical barriers, between the filament and matrix. The second is the chemical compatibility between the matrix and the environment, assumed here to be a high temperature, oxidizing atmosphere. This may necessitate the use of one or more interlayers, or chemical reaction barriers, between the matrix and the external environment. Finally, the mechanical compatibility between constituent materials combinations which satisfy the requirements of the first two types of compatibility will be briefly discussed.

Filament/Matrix Chemical Compatibility

Chemical reactions, i.e., the formation of discrete, new reaction product phases, between the filament and the matrix will likely result in a degradation of properties of both phases and the product composites. Considering the starting filament/matrix combinations being discussed here, Table I, which is based on several years of analytical and experimental studies (1-5), shows that only one starting material combination is thermochemically stable, Al_2O_3/TiAl, and even this combination becomes reactive at temperatures above about 1300°C. Clearly, for these starting materials combinations to be used, interlayers must be present to function as chemical reaction barriers. But what defines a suitable reaction barrier and what must be its dimensions to prevent reaction for the required length of time at the desired temperature? Let us consider the requirements.

Several questions must be addressed when examining filament/matrix chemical interactions. First, does the filament/matrix combination as it stands represent a chemically reactive system? Second, what interlayers will coexist, in a sequential manner if there is more than one interlayer, with both the matrix and the filament? Third, do these interlayers delay, to a sufficient exposure (time-temperature integral), filament/matrix chemical reactions? The first

question has been addressed through the observation of reaction products described in Table I. The second and third questions require examination of the transport rates in candidate interlayer materials.

Table I Filament/Matrix Material Combinations and Reaction Products

Filament	Matrix	Reaction Product Phases*
SiC	Ti	Ti_xSi_y, TiC
SiC	TiAl	Ti_xSi_y, TiC, Ti_2AlC, $TiAl_3$
Al_2O_3	Ti	Ti_xAl_yO, TiO_x
Al_2O_3	TiAl	None
C	Ti	TiC
C	TiAl	Ti_2AlC, $TiAl_3$
B	Ti	TiB, TiB_2
B	TiAl	TiB, TiB_2, $TiAl_3$

*Other compounds may be present in minor amounts.

The chemical barrier effectiveness of an unflawed interlayer or series of interlayers can be addressed as a function of transport rates of the various species through interlayers of a given thickness. The best barrier would be one in which the diffusion of a critical (i.e., potentially reactive) specie would be limited by the delay of that specie from completing transport through the barrier. A "delay time" is usually defined in terms of the diffusion coefficient, D, of that specie in the barrier material, the time over which the transport takes place, and the thickness, Δx, of the barrier. In this case, the "delay" time, t_d, for a barrier described by

$$6Dt_d = (\Delta x)^2$$

represents a time extrapolated from steady-state transport to zero transport. Of course, there is some finite amount of transport through the barrier at t_d elapsed time. Using the analysis of Crank (6), one obtains a formula for fluence (Q_t) in terms of $Q_t/c_1\Delta x$ where the barrier material is initially free of diffusant, the front face solubility of diffusant is c_1, and the barrier is backed by a perfect sink:

$$\frac{Q_t}{c_1 \Delta x} = \frac{Dt}{(\Delta x)^2} - \frac{1}{6} - \frac{2}{\pi^2} \sum_{n=1}^{\infty} \frac{(-1)^n}{n^2} \exp\left(-\frac{Dn^2\pi^2 t}{(\Delta x)^2}\right)$$

This is illustrated in Figure 1. Calculations at t_d, 0.6 t_d, and 0.3 t_d give $Q_t/c_1\Delta x$ as 0.039, 0.0079, and 0.00027, respectively. This indicates that the first Δx distance in the sink at t_d would contain $0.039c_1$ on the average if no diffusant escaped from this first Δx of the sink. For the shorter times considerably less of the diffusant has been transported to the sink. By a time of $2t_d$ the fluence is approximated well by the equation

$$\frac{Q_t}{c_1 \Delta x} = \frac{Dt}{(\Delta x)^2} - \frac{1}{6}$$

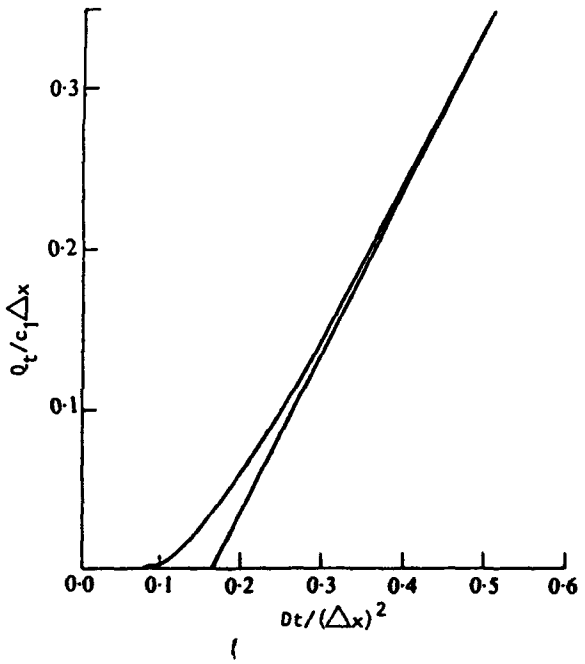

Figure 1. Approach to steady-state flux through a plane sheet.

Thus, when small fluences can be tolerated, this formula can be used to estimte how long a barrier will retard the fluence of diffusing species. If one estimates what a tolerable fluence might be, one can then estimate how long it would be before such a fluence occurred. Note also that low solubility of a

diffusant in the front face of the barrier (c_1) results in lower transport through the barrier.

An analysis of barrier effectiveness for steady-state flux conditions follows for the case of both one- and two-layer barriers assuming an infinite source and a perfect sink employing solubility limits at the barrier layer interfaces. The diffusion coefficients, $D_i(T)$, are taken as temperature dependent but concentration independent as a simplification for this treatment. Also, the exposure integral is utilized in the following equation derived from Fick's law:

$$\int_0^{t_e} J\,dt = \frac{\Delta c_i}{\Delta x} \int_0^{t_e} D_i(T)\,dt$$

assuming that Δc_i is temperature independent and where t_e is the total time of exposure and J is the flux. For simplicity, the exposure integral

$$\int_0^{t_e} D_i(T)\,dt$$

will be assumed to have occurred at some upper temperature limit for the exposure time since in many cases the high temperature exposure (such as during fabrication) dominates the integral.

Let us select an arbitrary exposure and an arbitrary barrier thickness and consider the case of a carbon filament protected by a TiC interlayer in a Ti matrix. If a one hour exposure at 1023°C (1300K) is selected, the transport of carbon through a 5 μm layer can be calculated using the following information:

C density in TiC = 0.99 g/cm^3
C density in $TiC_{0.6}$ = 0.59 g/cm^3
Δc = 0.4 g/cm^3
$D_i = 10^{-8.24}$ cm^2/sec

$$Jt_e = \frac{10^{-0.24} \cdot 0.4 \cdot 3600}{0.0005}\ g/cm^2 = 1.7 \times 10^{-2}\ g/cm^2$$

In this case 83 μm of carbon would have been lost by the source filament assuming that this carbon totally dissolved in the Ti matrix. Twice as thick a barrier would have halved this number as would half the exposure time. A 100K lower temperature would have reduced this number by a factor of 2.9. (The diffusion data for these calculations were taken from Ref. 7.)

This type of analysis can be made where solubilities (species densities) and diffusion coefficients are available. The general solution for steady-state transport in the case of a single barrier is

$$Jt_e = Dt_e \frac{(c_1 - c_2)}{\Delta x}$$

where c_1 and c_2 are the different concentrations (often employed in g/cm^3) in the barrier layer at the interfaces with the filament and matrix, respectively.

The two-barrier steady-state solution is somewhat more complicated to use but is almost as simple to express:

$$Jt_e = D_1 t_e \frac{(c_1 - c_2)}{\Delta x_1} = D_2 t_e \frac{(c_3 - c_4)}{\Delta x_2}$$

Note that c_2 and c_3 are not the same but represent the thermodynamic relationship between solubilities in medium 1 and medium 2, which can often be described by the ratio

$$\frac{c_2}{c_3} = \phi$$

Using the fluence equation for two barriers, one can solve for actual values of c_2 and c_3 given ϕ, D_1, D_2, Δx_1, Δx_2, c_1, and c_4. This solution then allows the calculation of Jt_e and thus evaluation of the effectiveness of the two-barrier resistance.

The previous calculations for transport for a single interlayer (TiC) on carbon filament in a Ti matrix indicate that to limit transport of filament or matrix

species to about 5 μm of filament loss, for example, one needs to obtain a Jt_e of <0.001 g/cm^2. With a 5 μm interlayer thickness, this means that the $Dt_e\Delta c$ term must be less than 5 x 10^{-7} g/cm. The burden of this term falls mainly on D. In the case of the TiC interlayer, the D value must be reduced by a factor of 17 to reach a satisfactory $10^{-9.5}$ cm^2/sec diffusion coefficient. Shorter times or, in some cases, lower solubilities can contribute to this reduction in fluence, but mainly it will be very dependent on exposure temperature. For example, a C surface coating on a commercial SiC filament becomes an effective TiC barrier in Ti matrices for the exposure time and temperatures used here.

While the system C-TiC-Ti appears to be a stable one, the relatively fast transport of C through TiC makes the use of such a "stable" system very questionable. One way of decreasing the transport is to put an additional interlayer between the C and the TiC that would further limit the C transport rate. WC, TaC, or MoC would achieve such an objective. For example, the diffusion coefficient of C in TaC at 1300K is 10^{-14} cm^2/sec versus 10^{-8} cm^2/sec in TiC. A 1 μm TaC layer slows C transport as much as would a meter of TiC according to these diffusion coefficients. W diffusion through TiC, a process that would destroy a WC interlayer for example, is described by a 10^{-18} cm^2/sec diffusion coefficient. Thus, a thin WC layer should be kinetically stable in contact with both C and TiC and should nearly prevent both Ti and C transport through it. This illustrates the importance of transport-limiting interlayers in increasing the lifetime of the composite by providing effective long-term chemical separation of reactive species originating with the filament and matrix.

Tables II and III represent an attempt to identify possible interlayers and combinations of interlayers on filaments that may allow the filament to coexist with Ti and/or γ-TiAl matrices; that is, adjacent layers do not react forming new phases. A list including more than two interlayers in appropriate sequence would be longer but would also represent a more hypothetical case than a real one. The listing in Tables II and III is a compilation of examples of stable phase combinations. The ability of a given combination to prevent filament/matrix reaction (wholesale chemical degradation) in the composite would be dependent on specific time-temperature exposure conditions and would be different for each combination.

Considering the SiC-Ti composite, the stable phase combinations can be recognized in the Ti-Si-C phase diagram (8) shown in Figure 2. This diagram

indicates that one single phase (TiC) forms a stable initial couple between SiC and Ti. However, as C transports through TiC, Si is left behind, destabilizing the system. It is more likely that a Ti-Ti_5Si_3-Ti_3SiC_2-SiC or a Ti-TiC-Ti_3SiC_2-SiC system is stable for longer times than the Ti-TiC-SiC system. Ti-Ti_5Si_3-$TiSi_2$-SiC seems a less likely candidate for long-term stability. The actual stable steady-state system will depend on Ti, C, and Si transport rates in the interlayers and also in the filament and matrix. Determining what interlayers are truly stable might be best accomplished through extended diffusion couple annealing experiments.

Table II Examples of Potential Single-Barrier Filament/Barrier/Matrix Combinations

Filament	Barrier Layer	Matrix
SiC	TiC	Ti
Al_2O_3	($xTiO \cdot Al_2O_3$)	Ti
Al_2O_3	Ti_5Si_3	Ti
Al_2O_3	(W,Ti)	Ti
C	TiC	Ti
C	W	Ti
C	WC	Ti
SiC	TiB_2	TiAl
SiC	Ti_2AlC	TiAl
SiC	Ti_3SiC_2	TiAl
SiC	$TiAl_3$	TiAl
Al_2O_3	None required	TiAl
C	Y_2O_3	TiAl
C	Al_2O_3	TiAl
C	RE_2O_3	TiAl
B	TiB_2	TiAl

Table III Examples of Potential Two-Barrier Filament/Barrier/Matrix Combinations

Filament	Inner Barrier	Outer Barrier	Matrix
SiC	$TiSi_2$	Ti_5Si_3	Ti
SiC	TiC	Ti_5Si_3	Ti
SiC	Ti_3SiC_2	TiC	Ti
SiC	Ti_3SiC_2	Ti_5Si_3	Ti
Al_2O_3	YAG	Y_2O_3	Ti
Al_2O_3	C	TiC	Ti
Al_2O_3	B	TiB	Ti
C	TiC	Ti_5Si_3	Ti
C	WC	TiC	Ti
C	TiC	Ti_3AlC	Ti
B	TiB_2	TiB	Ti
SiC	Ti_2AlC	TiB_2	TiAl
SiC	Ti_3CSi_2	TiB_2	TiAl
SiC	Ti_2AlC	Al_2O_3	TiAl
SiC	Ti_3CSi_2	Al_2O_3	TiAl
SiC	TiC	Ti_2AlC	TiAl
SiC	$TiSi_2$	Ti_5Si_3	TiAl
C	TiC	Ti_2AlC	TiAl
C	TiC	TiB_2	TiAl
C	TiC	Al_2O_3	TiAl
C	TiC	Y_2O_3	TiAl
B	TiB	Al_2O_3	TiAl
B	B_4C	Al_2O_3	TiAl
B	B_4C	TiB_2	TiAl

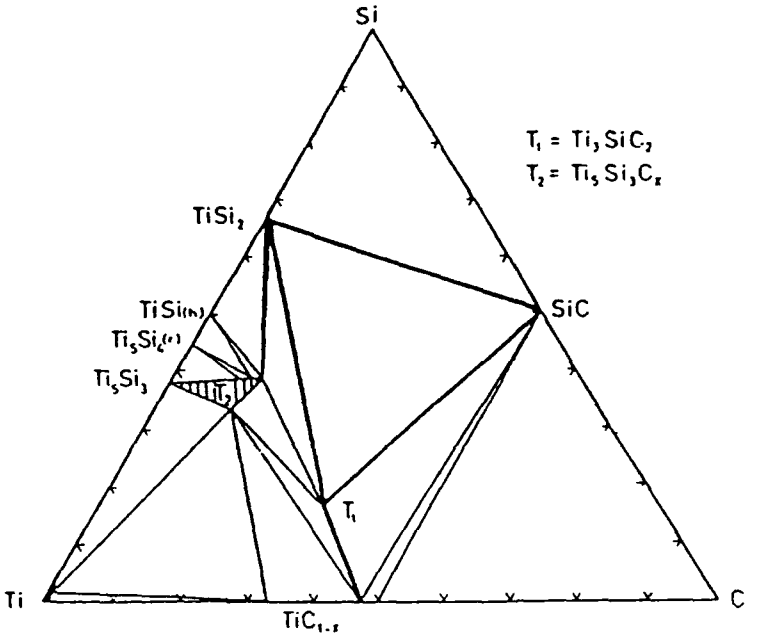

Figure 2 - Isothermal section of the phase diagram for the Ti-Si-C system at ~1200°C.

Environmental Compatibility

Environmental Protection of Ti and TiAl Composites

Ti and to a lesser extent γ-TiAl matrix materials are subject to reaction with the environment, particularly at high temperatures. At low temperatures Ti will self-protect by forming a TiO_2 coating. At high temperatures this coating dissolves in the Ti allowing oxidation to proceed rapidly. The oxidation properties of γ-TiAl are much better than those of pure Ti. Oxidation is best controlled in Ti alloys by deliberately applying protective coatings to the alloy. Those coatings that develop a stable Al_2O_3 surface phase during oxidation provide the best protection for Ti alloys. Aluminized Ti alloys on which a $TiAl_3$ layer forms provide a relatively stable system where Al_2O_3 protects the surface of the $TiAl_3$ coating from further oxidation. A $TiAl_3$ coating on γ-TiAl can be a chemically stable coating. Ti alloys which are reactive toward a $TiAl_3$ coating are better protected by an active Ti_5Si_3 interlayer between the $TiAl_3$ coating and the Ti alloy. This duplex coating also forms a protective Al_2O_3 layer with some SiO_2 and TiO_2 content. This duplex system functions

because of the very slow transport of Si through the Ti_5Si_3 to the Ti substrate and the slow dissolution of Si into the Ti. In experimental oxidation studies we have not observed the formation of Ti_3Si between the Ti_5Si_3 interlayer and Ti alloys. This situation is similar to the case in which no intermediate TiAl phases have been noted in the presence of a diffusion-produced $TiAl_3$ surface layer.

Oxides which have been used as barriers between Al_2O_3 and γ-TiAl, such as Y_2O_3 and YAG, could be used as external coatings if they exhibit low O and metal diffusivities and can remain crack-free. Other coatings that can be considered are metals with minimal or no reaction with environmental O_2. Gold, with a melting point of 1064°C, is the most inert. Pt can be used for higher temperature exposures but may oxidize at intermediate temperatures. Almost any metal used as a coating will need to be protected from reaction with Ti and γ-TiAl by an interlayer, however.

Mechanical Compatibility

The discriminator between alternative combinations of barrier layer materials for chemical reaction barriers either between filaments and matrices or between the matrix and the external oxidizing environment would likely be the mechanical "compatibility" between different materials combinations. By this is meant that since the barrier layers are rather thick and thus may represent a significant volume fraction of the product composite, microstructural design should attempt to minimize residual stresses in brittle constituent materials after fabrication and assure that residual stresses in at least the most brittle materials are compressive. For the model materials chosen, this probably means as a first approximation that one would choose at the outset interlayer materials for chemical barriers between the filament and matrix that have thermal expansion coefficients and elastic moduli in between those of the filament and composite substrate so that none serve as preferential crack initiation sites. Other considerations, such as the degree of preloading of filaments in compression, may modify these considerations, however. External environmental barriers would be chosen to have thermal and elastic properties as close to those of the composite substrate as practical. The micromechanical design of systems of the type described in this paper is currently in progress.

Summary

Consideration of some of the basic principles governing "compatibility" of constituents in titanium and titanium intermetallic matrix composites leads to an array of possible "functionally graded materials" microstructural designs which may offer long-term chemical and mechanical stability. The most surprising feature of such an array is that relatively few of the potential materials combinations are being actively researched at present.

References

1. G.H. Reynolds and J.H. Norman, "Fiber and Fiber Coating Development for Titanium Aluminide Metal Matrix Composite," in "Titanium Aluminide Composites, Proceedings of the Titanium Aluminide Composite Workshop, Orlando, FL, May 1990" (Report WL-TR-91-4020), 96-102.

2. G.H. Reynolds, J.H. Norman, and W.E. Bell, "Thermochemical Compatibility of Reinforcing Phases in Titanium Aluminide Metal Matrix Composites," in "Titanium Aluminide Composites, Proceedings of the Titanium Aluminide Composite Workshop, Orlando, FL, May 1990" (Report WL-TR-92-4020), 202-216.

3. G. Reynolds and P.W. Powell, "Experimental Studies of Fiber/Matrix Compatibility for Developmental Fibers," in "Titanium Aluminide Composites, Proceedings of the Titanium Aluminide Composite Workshop, Orlando, FL, May 1990" (Report WL-TR-92-4020), 217-232.

4. J.H. Norman, G.H. Reynolds, and L. Brewer, "Chemical Stability of Fiber-Metal Matrix Composites" Intermetallic Matrix Composites, ed. D.L. Anton et al. (Pittsburgh, PA: Materials Research Society, 1990), 369-377.

5. G.H. Reynolds, et al., "Status of Advanced Filament Development for Titanium Alloy and Titanium Intermetallic Matrix Composites - Part 1: Compositional and Compatibility Studies" in "Titanium Matrix Composites, Proceedings of the Titanium Matrix Composites Workshop, Orlando, FL, November 1991" (Report WL-TR-92-4035), 25-41.

6. J. Crank, The Mathematics of Diffusion (Oxford England: Clarendon Press, 1975).

7. O. Kubaschewski, "Diffusion," Atomic Energy Review, Special Issue No. 9, Titanium: Physico-Chemical Properties of Its Compounds and Alloys (1983), 441.

8. J.J. Nickl, K.K. Schweitzer, and P. Luxenberg, "Chemical Vapor Deposition of the Systems Ti-Si-C and Ti-Ge-C," Proceedings of the Third International Conference on Chemical Vapor Deposition, ed. F.A. Glosski, American Nuclear Society, April 24-27, 1972, Salt Lake City.

ADVANCED HIGH-TEMPERATURE ALLOYS BY DESIGN

USING RAPID SOLIDIFICATION PROCESSING

John E. Flinn, Idaho National Engineering Laboratory, EG&G Idaho, Inc., Idaho Falls, ID 83415-2218 and
Thomas F. Kelly, Department of Materials Science and Engineering, University of Wisconsin, Madison, WI 53706

Abstract

Rapid solidification processing (RSP) of metallic alloys has the potential for very significant improvements in high-temperature properties and performance. Results on microstructural fineness and stability and their influence on high-temperature mechanical properties are presented for several iron- and nickel-base alloys. A significant observation from the RSP studies is the important role of the interstitial elements of oxygen and nitrogen and to a lesser extent carbon in promoting and stabilizing microstructural features. The design of structural alloys needs to focus on effective utilization and control of the interstitial elements through composition adjustments and in association with RSP.

Critical Issues in the Development of High Temperature Structural Materials
Edited by N.S. Stoloff, D.J. Duquette and A.F. Giamei
The Minerals, Metals & Materials Society, 1993

Introduction

Benefits from rapid solidification processing (RSP) have not been fully explored for structural metallic alloys for high-temperature applications. Two features commonly observed from RSP of metallic alloys are composition homogeneity and fine microstructures (1-3). The concern for the last feature is stability after high-temperature exposures, e.g., powder consolidation, heat treatments, and certain applications. Both features, if retained, can impart very significant improvements in alloy properties and performance.

A considerable effort has been devoted by the authors to microstructure-property correlations for RSP iron- and nickel-base alloys and comparisons with their ingot metallurgy (IM) counterparts. Although significant progress has been made toward developing these correlations, there remains a number of issues that must be resolved to implement effective design of high-temperature metallic alloys using the RSP approach. This paper provides some important findings and interpretations observed for RSP alloys. Key issues that need to be resolved will also be addressed.

Observations

Microstructural Behavior

The authors have devoted considerable effort toward microstructural examinations and interpretation of the observations for a variety of iron- and nickel-base alloys prepared from RSP powders. The powders have been primarily prepared by centrifugal (CA) and inert gas atomization (IGA) methods (3-5). Recent studies have also involved nitrogen gas atomization. The microstructural examinations have mainly been performed on consolidated RSP powders; however, attention has also been given to the microstructure of the unconsolidated powders. Correlations have been and are continuing for the influence of microstructural features on mechanical properties of consolidated RSP powders.

One feature commonly observed for the RSP alloys is fine and stable grain sizes. An example of this behavior is shown in Figure 1 for five alloys (RSP and their IM counterparts) after a 1 h, 1100°C heat treatment. These results show that the RSP alloys retain fine and comparable grain sizes compared to IM. Parametric investigations involving atomization and consolidation methods and powder particle size show no discernable influence on grain size (3). The influence of powder particle size on grain size for several RSP alloys after extrusion consolidation and a 1 h, 1100°C heat treatment is shown in Figure 2. This behavior eliminates two particle size dependent features observed for the unconsolidated powders as being responsible for the fine and stable grain sizes. These features are the secondary dendritic solidification morphology, whose average spacing increases with particle size, and the oxide surface films acquired during powder processing (3). The surface film thickness is constant and independent of particle size for each alloy, which means that the volume fraction of the film increases with decreasing particle size. As a result, dispersion pinning of the grains after powder consolidation from oxide surface films is unlikely to be the source of the fine and stable sizes observed for the RSP alloys. The origin and stability of the fine grain sizes in RSP alloys will be addressed later in this paper.

Submicron microstructural features for several of the iron- and nickel-base alloys are being determined by high resolution transmission electron microscopy methods. Although at this time it is difficult to establish a consistent pattern for the submicron features of the RSP alloys, there are some features associated with RSP. The most extensive study has been performed on Type 304 SS (3,6-10). Powders prepared for this alloy by CA processing

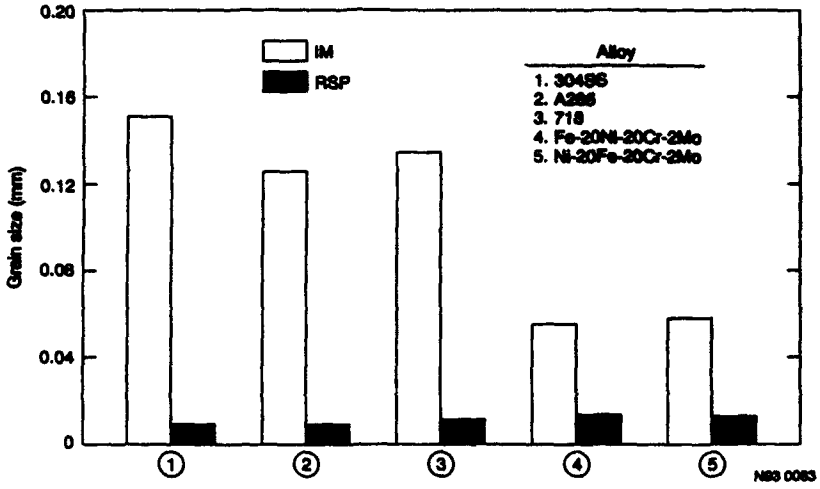

Figure 1 - Grain size after a 1 h, 1100°C heat treatment for RSP and IM iron- and nickel-base alloys.

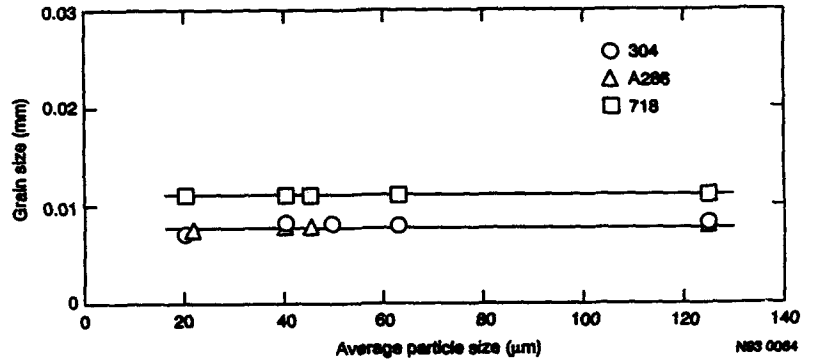

Figure 2 - Influence of powder particle size on grain size after powder consolidation and a 1 h, 1100°C heat treatment for RSP alloys.

show evidence of vacancy supersaturation (7). Vacancies in the consolidated powder after high-temperature heat treatments provide a large population of 8 nm hollow oxides shown in Figure 3. The hollow oxides serve as effective nucleation sites for carbides during aging heat treatments shown in Figure 4. In addition, a relatively high and stable dislocation population compared to its IM counterparts is retained in the RSP alloy after high-temperature heat treatments (3,8,10). Type 304 SS powders processed by IGA and consolidated show a high and stable dislocation density, but no nanometer-size, hollow oxides, i.e., no evidence of vacancy supersaturation (3). Although the solidification rates, based on secondary dendritic arm spacing, are comparable for the powders from the two atomization methods, IGA apparently does not promote the same level of vacancy trapping as does the CA process.

Mechanical Property Behavior

A large mechanical property database has been generated on consolidated RSP powders for iron- and nickel-base alloys. Some representative results from tests performed at higher temperatures will be shown to illustrate the effects from RSP. Results from IM-processed counterparts will be used for comparisons.

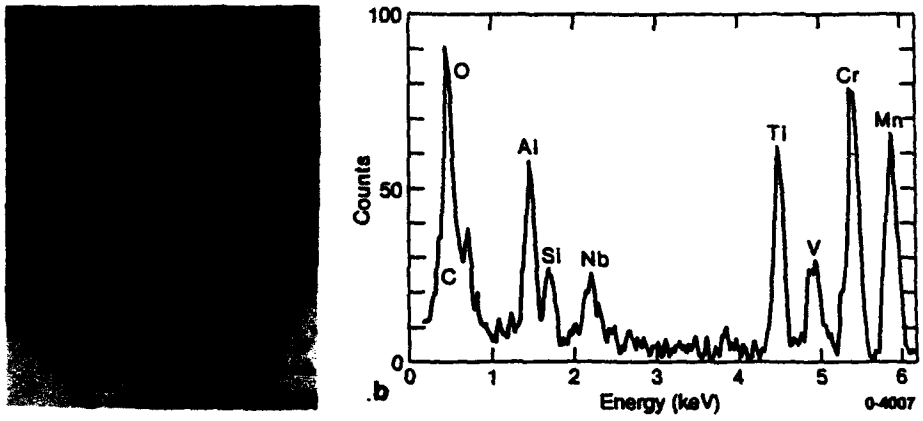

Figure 3 - 8 nm hollow oxides in RSP extruded 304 SS powder after a 1 h, 1200°C heat treatment: (a) bright-field overfocus and (b) x-ray spectrum.

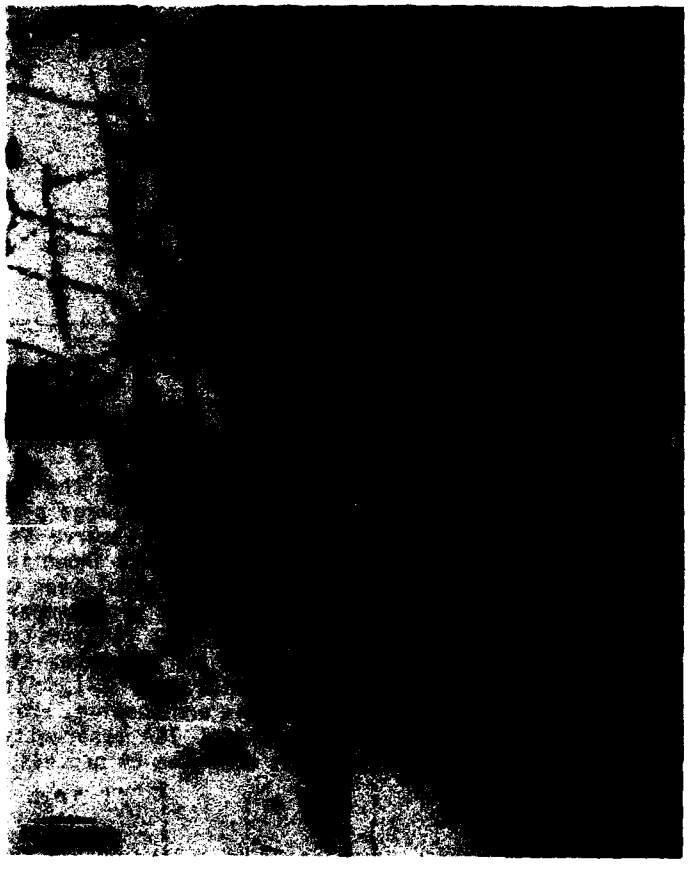

Figure 4 - RSP extruded 304 SS powder after aging: (a) overview of carbides-dislocations, (b) underfocus, and (c) overfocus bright-field image of 8 nm hollow oxide-carbide-dislocation interactions.

Examples of the tensile properties observed for RSP iron- and nickel-base alloys along with IM counterparts are given in Table I. These results show that significant tensile strengthening is associated with the RSP alloys, particularly in yield stress. In some cases the ductilities have decreased at the higher test temperatures. The increase in tensile strengths is primarily attributed to the fine grain size of the RSP alloys. This has been shown to be the case from tests performed at room temperatures (3).

The creep behavior of the RSP iron- and nickel-base alloys shows a mixed response in terms of improvements in creep resistance. Alloys investigated such as Fe-20Ni-20Cr-2Mo, Ni-20Fe-20Cr-2Mo, and 718, show slightly reduced creep resistance compared to their larger grain IM counterparts. The RSP A286 alloy shows a powder particle size dependence on the creep properties (3). For consolidated powder particle sizes <50 μm, creep resistance is slightly lower than the IM counterpart. However, larger particle sizes show more creep resistance. One of the alloys, Type 304 SS, has shown remarkable increases in creep resistance from rapid solidification processing (3). Creep curves of the Type 304 SS materials are shown in Figure 5 for consolidated CA and IGA processed powders as well as IM. Compositions of the three materials are identical. No improvement in creep resistance was observed for the IGA compared to the IM Type 304 SS material. The microstructure for the IGA and CA materials was identical, except, as stated earlier, no nanometer-size hollow oxides were observed in the IGA or IM Type 304 SS. The nanometer-size hollow oxides are responsible for the improved creep behavior for the consolidated CA processed Type 304 SS powders. In terms of creep performance equivalency with IGA or IM Type 304 SS, the CA alloy permits a 100°C increase in temperature or a two-fold increase in stress (3).

Table I. Tensile Properties for RSP and IM Iron- and Nickel-Base Alloys

Alloy	Test Temperature (°C)	Yield Stress (MPa)	Ultimate (MPa)	Total Elong. (%)
304:				
IM	600	79	320	47
RSP	600	157	409	39
Fe-20Ni-20Cr-2Mo:				
IM	600	112	405	42
RSP	600	181	457	26
A286*:				
IM	600	650	888	22
RSP	600	763	922	24
Ni-20Fe-20Cr-2Mo:				
IM	600	108	395	74
RSP	600	166	445	34
718**:				
IM	650	803	1035	23
RSP	650	925	1083	36

* Aged at 700°C for 100 h.
** Aged at 750°C for 4 h, then 650°C for 16 h.

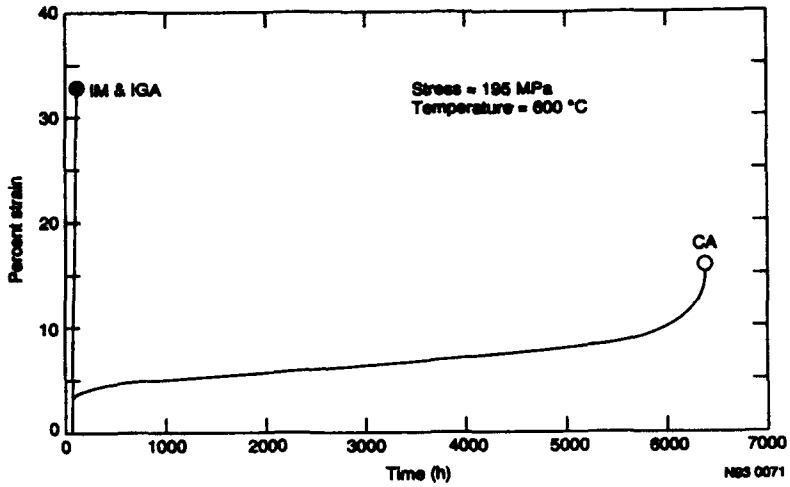

Figure 5 - Creep curves for Type 304 SS at 600°C and a stress of 195 MPa.

Modification of the gas atomization process to include melting under nitrogen and nitrogen atomization produces relatively high levels of entrained nitrogen for iron-base alloys. The influence of nitrogen on the creep properties of Type 304 SS RSP powders after consolidation is shown by the stress-time-to-rupture behavior in Figure 6. As a result, creep observations for RSP Type 304 SS show that oxygen and nitrogen can play a very important role in high-temperature strengthening, even though the material has small grain size.

Fatigue behavior of RSP iron- and nickel-base alloys has received limited attention. There is evidence that RSP can significantly improve fatigue resistance. An example is shown in Figure 7 for RSP A286 consolidated powder and its IM counterpart. Both materials were given before testing a 1 h, 1100°C solution anneal followed by a 100 h, 700°C aging treatment before testing. Failures at the lower stress ranges occurred in the threaded grip regions of the specimens. The A286 alloy is known for its notch sensitivity, and the true fatigue lifetime would be extended (indicated by the arrows in Figure 7) with a different specimen design. Apparent improvements in fatigue resistance for the RSP A286 compared to IM are attributed to fine grain size.

Origin of Fine Grains

Results presented show that RSP produces fine and stable grains. What is responsible for the fine grains from RSP and what produces their stabilization during high-temperature exposures are questions that need to be resolved. Recent studies on IGA processed A286 and 718 powders provide some insight into the origin of fine grains (11,12). The RSP process for the two alloys produces a primary and secondary dendritic solidification morphology. The primary dendrites emerge from nucleation sites predominately within the interior of the molten droplets. The size of the primary dendrites is not very dependent on particle size and is comparable to the grain sizes observed after powder consolidation. One-hour heat treatments on the particles show that homogenization of the secondary dendrite and the interdendritic region occurs at the higher temperatures; however, the primary dendrite boundaries remain (11,12). The average size of the primary dendrites does not change, and a shape change occurs at temperatures ≥1000°C. The shape change takes on the form of equiaxed grains. Measurements of the primary dendrite/grain size after the 1 h heat treatments for the A286 and 718 powders are shown in Figure 8.

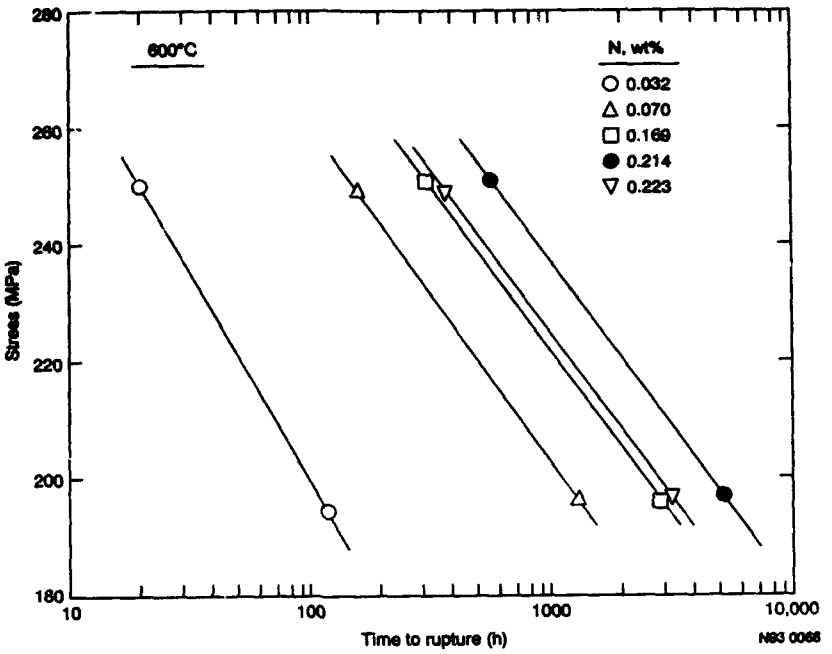

Figure 6 - Influence of nitrogen content on stress-time-to-rupture at 600°C for RSP Type 304 SS.

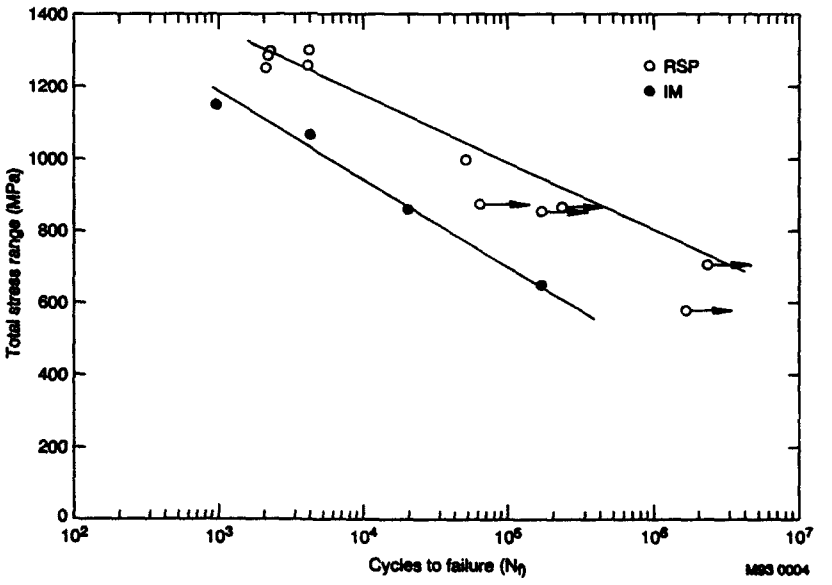

Figure 7 - Fatigue behavior at 600°C for IM and RSP A286 after aging at 700°C for 100 h.

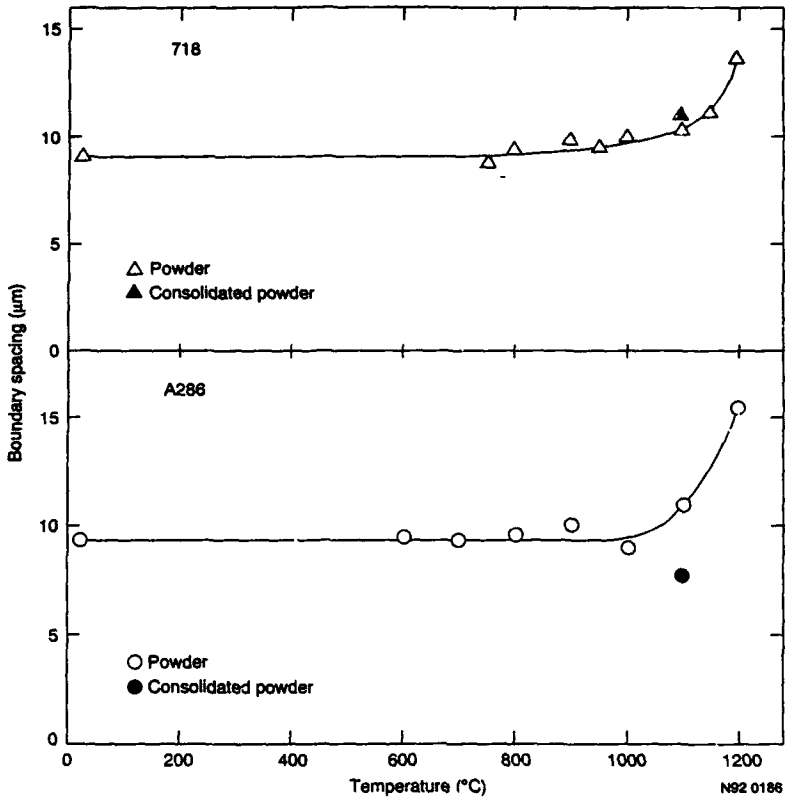

Figure 8 - Influence of 1 h heat treatments on the primary dendrite/grain size for RSP A286 and 718 powders.

Also shown is the grain size of the consolidated powders. It is difficult to believe that the primary dendrite size equivalency to the grain size after powder consolidation is just a coincidence. It should be noted that similar observations have also been observed for RSP Type 304 SS, Fe-20Ni-20Cr, and Fe-20Ni-20Cr-2Mo alloys (13). The mechanism responsible for the connection has yet to be resolved. However, implications strongly suggest that if the number of nucleation sites for the primary dendrites could be substantially increased, a much finer grain size could result.

A related feature to the origin of the fine grains from RSP is the grain stability when exposed to high temperatures. Growth retardation is also an issue that remains to be mechanistically resolved. A common perception is that a dispersed second phase is responsible for pinning the grain boundaries. High resolution microscopy examinations and dispersion pinning calculations on RSP iron-base alloys have not been convincing for resolving whether the grain growth retardation is due to second phase dispersions (3). The evidence seems to support that if the grain boundaries are pinned by second phase dispersions, they must be very small, i.e., <1 nm. Other explanations, such as impurity effects and significant reductions in primary dendrite and grain boundary energies from RSP, remain as options. A large effort needs to be devoted to high resolution analytical electron microscopy and atom probe studies of grain boundaries in RSP alloys. Since fine and stable grain sizes are features of RSP and appear to be a primary source for improved

strengthening, understanding and control of grain boundary makeup is extremely important for designing high-performance alloys. Although speculative, the authors believe that oxygen is important for the nucleation of primary dendrites (i.e., impurity clusters) and boundary stabilization. Studies are continuing to establish the role of oxygen in stabilizing fine grain sizes in RSP alloys.

Alloy Design Consideration

Studies to date have uncovered several features from RSP of iron- and nickel-base alloys that need to be exploited for opportunities to produce alloys with superior properties and performance. Evidence favors the interstitial elements, particularly oxygen and nitrogen, and to a lesser extent carbon, for providing fine and stable microstructures with corresponding enhancement in properties. However, research is needed to establish their role and how to achieve effective use and control from composition and RSP. It is reasonable to assume that the most effective use of the interstitial elements will come from their addition during the melting stage, just prior to atomization. The elements' presence in the melt will be best served if they remain dissociated, i.e., unreacted. Compound (e.g., oxides, nitrides, or carbides) formers with high free-energies of reaction with the interstitial elements should be restricted in their use as alloy additions. Examples are Al, Ti, and rare earths. Conceptually, the interstitials in the melt, particularly if significant superheats are involved, can be homogeneously suspended in solution in a dissociated state. Atomization of the melt into fine droplets and their rapid cooling through solidification will enable interstitial trapping to occur with minimal segregation. This procedure appears to be necessary to provide fine microstructural features. Stabilization of the features, particularly to high temperatures, is observed but remains an issue to be resolved in terms of understanding and control. It was noted earlier that oxygen in the alloys may be the key to stabilizing the microstructure. This was evident for the nanometer-size hollow oxides.

The design of high-temperature metallic alloys by RSP needs to focus on an effective combination for the three common forms of strengthening: (a) fine grain size, (b) solid solution, and (c) precipitation. Grain size appears to have its origin during solidification of the molten droplets after atomization. By increasing the number of nucleation sites, e.g., use of inoculants, for the primary dendrites, grain size should decrease. Solid solution strengthening for wrought nickel-base alloys has primarily focused on 1 to 3 wt% additions of refractory metal elements, e.g., Co, Mo, Nb, V, and W. Increasing the strengthening from these additions by incorporating RSP is not likely, even though one of the benefits attributed to RSP is extended solid solutions (1,2). For iron-base alloys, particularly the austenitic stainless steel series, the more potent solid solution strengthening elements are those interstitially dissolved, i.e., N, C, and B (14). Of these, nitrogen is the most effective. The ferrite forming elements, e.g., W, Mo, V, or Nb, provide significant substitutional solution strengthening in stainless steels, but not to the degree of interstitials. However, the effectiveness of solution strengthening from interstitial elements after high-temperature exposures below solution annealing temperatures is doubtful. This is particularly true for carbon, but nitrogen may be more effective at higher temperatures as a solid solution element as long as its concentration does not exceed solubility limits.

Additional strengthening from precipitates where RSP is involved appears to be centered on refractory-type dispersions, i.e., oxides, nitrides, and to a lesser extent, carbides. The RSP studies on A286 (3), which involves γ' strengthening, and 718 (15), which involves $\gamma'$and γ'' precipitates, show no improvements over their IM counterparts, except from grain size effects. As a

result, future efforts will need to focus on optimizing dispersion strengthening from the high-temperature refractory-type compounds.

High-temperature protection against oxidation/corrosion for iron- and nickel-base alloys may not be greatly enhanced from RSP. More studies are needed in this area. Without resorting to coatings /oxidation resistance for these base alloys is primarily improved (i.e., common knowledge) by Cr, Ni, Al, and Si additions. For certain corrosive environments, significant additions of nitrogen can greatly improve corrosion and wear resistance (16,17). However, its protection may be temperature limited, e.g., ≤900°C. To achieve the benefits of RSP, additions such as Al for oxidation/corrosion resistance need to be limited to obtain the maximum usage from interstitial elements.

Summary of Issues

The ability to improve high-temperature structural properties and performance of metallic alloys by rapid solidification processing (RSP) primarily is derived from composition homogenization and the fine and stable microstructural features. Control of the microstructure through a combination of alloy composition (particularly the minor elements) and RSP requires more study. Some key issues that need to be addressed are:

1. Establish methods for grain size refinement during solidification of atomized, molten droplets.

2. Determine the most effective utilization and control of interstitial elements during the powder processing cycle for microstructural stabilization.

3. Establish quantitative correlations between composition, properties, RSP parameters, and performance in applications.

4. In support of the items above, considerable effort needs to be devoted to high resolution analytical microscopy examinations and their interpretation.

5. The RSP approach needs to be scaled to commercial production of powders, and near-net-shape consolidation of the powders for retention of properties needs further study.

Acknowledgments

The authors appreciate the efforts provided by D. A. Cullen, B. P. King, and M. M. Siefken in preparing the manuscript. This work was supported by the Department of Interior's U.S. Bureau of Mines under Contract No. J0134035 and by the U.S. Department of Energy Advanced Industrial Concept Division Materials Program, both under DOE Contract No. DE-AC07-76ID01570.

References

1. M. Cohen, B. H. Kear, and R. Mehrabian in *Proceedings of the Second International Conference on Rapid Solidification Processing: Principles and Technologies II*, eds. R. Mehrabian, B. H. Kear, and M. Cohen (Baton Rouge, LA, Claitor Publ. Div., 1980) 1-12.

2. J. E. Flinn, *Rapid Solidification Technology for Reduced Consumption of Strategic Materials* (Park Ridge, NJ, Noyes Publ., 1985).

3. J. E. Flinn in *Rapid Solidification Technologies - An Engineers Guide*, eds. T. S. Srivatsan and T. S. Sudarshan (Lancaster, PA, Technomic Publ. Co., 1992) 127-256.

4. G. E. Korth, J. V. Burch, and V. W. Storhok in *Rapidly Solidified Materials: Properties and Processing*, eds. P. W. Lee and J. H. Moll (ASM International, Metals Park, OH, 1988) 213-220.

5. G. E. Korth, J. E. Flinn, and J. V. Burch in *Advances in Powder Metallurgy - 1990*, eds. E. R. Andreotti and P. J. McGeeham (Metal Powder Industries Federation, Princeton, NJ, 1990) 49-63.

6. R. N. Wright, J. C. Bae, T. F. Kelly, J. E. Flinn, and G. E. Korth, *Metall. Trans. A, 19A* (1988) 2399-2405.

7. J. C. Bae, T. F. Kelly, J. E. Flinn, and R. N. Wright, *Scripta Metall., 22* (1988) 691-696.

8. J. E. Flinn, J. C. Bae, and T. F. Kelly in *Heat Resistant Materials*, eds. K. Natesan and D. J. Tillack (ASM International, Metals Park, OH, 1991) 35-44.

9. J. E. Flinn, T. F. Kelly, and W. G. Wolfer, Ibid (Ref. 5) 65-79.

10. J. E. Flinn, J. C. Bae, T. F. Kelly and G. E. Korth, *Metall. Trans. A, 23A* (1992) 2557.

11. C. H. Sellers, J. E. Flinn, and G. L. Fletcher in *Advanced in Powder Metallurgy - 1992*, eds. J. M. Copus and R. M. German (Metal Powder Industries Federation, Princeton, NJ, 1992), *3*, 25.

12. J. E. Flinn, D. V. Miley, C. H. Sellers, and G. L. Fletcher in *Microstructural Sci., Vol. 20*, eds. M. R. Louthan, Jr. and W. R. Kanne, Jr. (ASM International, Materials Park, OH, in press).

13. J. E. Flinn, Idaho National Engineering Laboratory, EG&G Idaho, Inc., Idaho Falls, ID, unpublished results.

14. K. J. Irvine, D. T. Llwellyn, and F. B. Pickering, *J. of Iron and Steel Inst., 199* (1961) 153.

15. J. E. Flinn, K. Shin, and T. F. Kelly in *Superalloys 718, 625, and Various Derivatives*, ed. E. A. Loria (ASM International, Materials Park, OH, 1991) 251-260.

16. F. B. Pickering in *High Nitrogen Steels - 88*, eds. J. Foct and A. Hendry (The Institute of Methods, London, GB, 1989) 10-31.

17. J. Foct in *High Nitrogen Steels - 90*, eds. G. Stein and H. Witulski (Verlag Stahl Eisen, mbH, Dusseldorf, 1990) 1-21.

SESSION II

Alloy Design II
(Applications-Alloy Development)

SINGLE CRYSTAL BASED MICROSTRUCTURE DESIGN OF METAL MATRIX COMPOSITES FOR HIGH TEMPERATURE APPLICATIONS

Rishi Raj

Department of Materials Science and Engineering
Cornell University
Ithaca NY 14853-1501

Abstract

A microstructure design constructed from fibrous ceramic crystals embedded in a continuous metal matrix with the following features is proposed: ceramic crystals have an aspect ratio greater that 30, the diameter of the ceramic crystals is approximately 5μm, the metal volume fraction is the range 8-30%, the channel width of the metal layers is less than 1μm, and the metal-ceramic interface is coherent. Such a microstructure is likely to have good creep resistance, cavitation resistance and thermal shock resistance.

Introduction

The Design of Superalloys

Today's superalloys serve in structural applications at a higher fraction of their melting temperature than any other material. The highest temperature applications are found in turbine blades, which are in the form of single crystals, in jet engines for passenger aircraft[1].

There have been two major developments in the evolution of present day superalloys (Fig.1)[2],[3]. In the early fifties vacuum melting was introduced to lower the oxygen content resulting in greater resistance to intergranular cavitation. Then, in the mid-seventies, directional solidification was adopted to make high aspect ratio grain structures with boundaries aligned parallel to the loading axis. Different types of directional microstructures were explored, including directionally solidified eutectics. However, best properties were achieved where the entire component consisted of a single crystal[4].

In the single crystal approach the emphasis in basic research moved from the study of intergranular cavitation to the understanding of creep by dislocation mechanisms. Today, the superalloy single crystals consist of a solid solution strengthened nickel γ matrix reinforced by intermetallic γ'. The volume fraction of γ' can be greater than 70% and it is produced by precipitation.

The use of elongated grain structure is another way of obtaining single crystal like properties at high temperatures. This approach has been used effectively in the design of ODS alloys[5],[6], and also in the design of the tungsten filaments for incandescent lamps[7].

Critical Issues in the Development of High Temperature Structural Materials
Edited by N.S. Stoloff, D.J. Duquette and A.F. Giamei
The Minerals, Metals & Materials Society, 1993

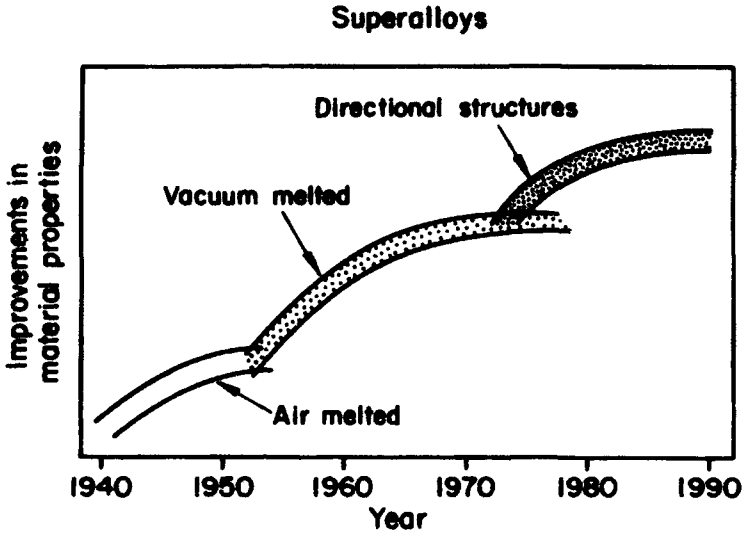

Figure 1: The three eras in the evolution of the superalloys. Directional solidification led first to the columnar grain structure and eventually to single crystal turbine blade. (After Refs 2 and 3).

The Design of Ceramic Reinforced Metal Matrix Composites

The highest possible service temperature of single crystal nickel base superalloys is limited by dislocation creep. The coarsening of the γ' precipitates and deformation of the intermetallic phase become significant above 1000°C. Thus higher service temperatures should be possible if the intermetallic γ' is replaced by an ceramic oxide.

The purpose of this paper is to consider the design guidelines for the microstructural features of the above ceramic reinforced metal-matrix composite. The criteria that must be considered in this design process are: (a) creep resistance, (b) cavitation fracture resistance of the metal-metal and the metal-ceramic interface, (c) resistance to thermal shock, and (d) resistance to environmental degradation.

In the following sections we consider the first three criteria. The first of these leads to the concept of a single crystal like structure consisting of elongated ceramic grains embedded in an interconnected metal matrix. The second and the third criteria lead to guidelines for the scale of the microstructure, the volume fraction of the interconnected metal phase, and the atomic structure and bonding of the metal/ceramic interface.

The choice of the metallic phase is limited by environmental stability. While refractory metals with their very high melting points and with thermal expansion coefficients close to those of oxides are interesting (the melting points are W-3410°C, Mo-2610°C, Ta-2996°C, and Nb-2468°C, and the thermal expansion coefficients in units of 10^{-6} are W-4.6, Mo-5.8, Ta-6.7 and Nb-8.3)[8], they suffer from poor oxidation resistance, especially Ta, Mo and W which form volatile oxides(#). In this context, it is interesting to note that the latest research in superalloys is concentrated in the development of oxide coatings that can serve as a barrier to thermal conduction, allowing higher inlet gas temperatures[9]. These coatings are often required to have the same properties that will be needed to protect the metal in the metal matrix composites from oxidation at very high temperatures.

Single Crystal Design for Creep Resistance

Two mechanisms, dislocation creep[10] and diffusional creep[11],[12], contribute to the deformation of structural materials at service temperatures. Dislocation creep is grain size independent and, therefore, important in "single crystal" designs. Diffusional creep is most easily suppressed by increasing the grain size. Both mechanisms are diffusion controlled; therefore, the use of dopants that bind to vacancies help to lower the rate of creep.

A study of the deformation mechanism maps of pure refractory metals with an equiaxed grain structure, for example niobium[13], shows that the creep rates by the dislocation mechanism are too fast for high temperature structural applications (in pure Nb the dislocation creep rate is nearly 0.1 s^{-1} at 1650°C for an applied stress of only 10 MPa), and that the diffusional creep rates can be reduced to an acceptable level (of approximately 10^{-8} s^{-1}) only if the grain size is larger than 100μm. An equiaxed, two phase

---

(#)However, niobium is a promising candidate. Its density is nearly the same as nickel, it does not suffer from a ductile to brittle transition, forms a solid oxide and has the potential of being hardened by precipitation of carbides or by solid solution strengthening. The thermal expansion coefficient of Nb matches that of alumina. It is also chemically compatible with alumina and probably with other oxides as well.

microstructure consisting of niobium and an oxide (such as alumina), however, is not likely to improve the creep resistance very significantly. Furthermore, crystal slip in the metal grains that are 100μm will produce large stress concentrations at the metal ceramic interface with a high probability of inducing interface fracture.

The "single crystal" microstructure that we propose for the metal matrix composite is similar to the design of the single crystal superalloy, consisting of elongated grains of a ceramic embedded in a metallic matrix. The two critical issues in the performance of this design are as follows:

(a) **The structure of the metal-ceramic interface**: The best properties will be obtained if the metal-ceramic interface is coherent, which would impart resistance to dislocation creep, to creep cavitation and to cleavage fracture at the metal/ceramic interface.
(b) **Thermal shock properties of the metal/ceramic composite**: A difference in the thermal expansion coefficients of the metal and the ceramic, and the anisotropy in the thermal expansion coefficient of the ceramic, can induce cleavage damage at the m/c interface. Microstructure designs that reduce the probability of this damage must be considered.

In the following sections the above issues are discussed one by one. The features of the microstructure that is proposed are shown by the schematic in Fig. 2. The ceramic grains are assumed to have a fibrous structure. The "unit cell" of the microstructure is defined by the transverse dimension d_t, the fiber diameter d_t, and the longitudinal dimension d_l. The other important microstructural parameters are v_m, the volume fraction of the metal phase, and w_m, the width of the metal channels confined in between the adjacent ceramic grains. Simple geometric analysis leads to the following relationship between these parameters:

$$\frac{w_m}{d_t} = \frac{1}{4}\left(v_m - \frac{1}{3A_r}\right) \tag{1}$$

Where the aspect ratio is defined as:

$$A_r = \frac{d_l}{d_t}. \tag{2}$$

Note that the right hand side in Eq.(1) must be greater than zero to obtain a continuous metal phase. The plot in Fig. 3 shows that the minimum volume required to obtain interconnectivity decreases with increasing aspect ratio. The width of metal film, w_m, varies with A_r, although it approaches a plateau for a fixed volume fraction as A_r becomes large. This limit, obtained from Eq. (1), is as following:

$$\lim_{A_r \to \infty} \left(\frac{w_m}{d_t}\right) = \frac{v_m}{4} \tag{3}$$

Equation (3) provides a useful guideline for microstructure design. For example suppose that the width of the metal films

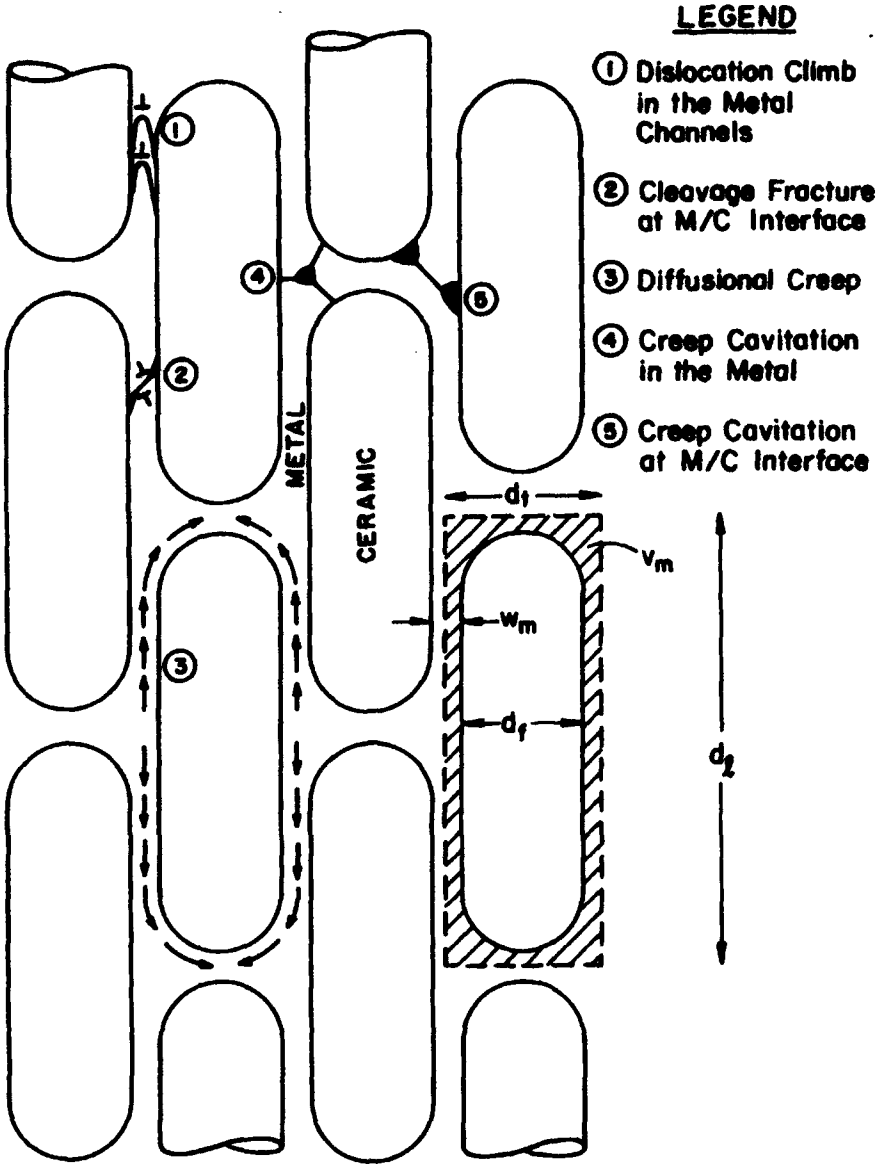

Figure 2: The geometrical parameters for the metal/ceramic composite. Item numbers 1 through 5 illustrate the possible deformation and fracture mechanisms in the composite.

must be less than 1μm (in order to achieve a sub-critical length of dislocation pile up), and that the diameter of the ceramic fiber is 50μm, then the volume fraction of the metal must be less than 8%. However, if the fiber diameter can be reduced to 10μm then the volume fraction of the metal may be as high as 36% (note that $d_c=d_f+w_m$).

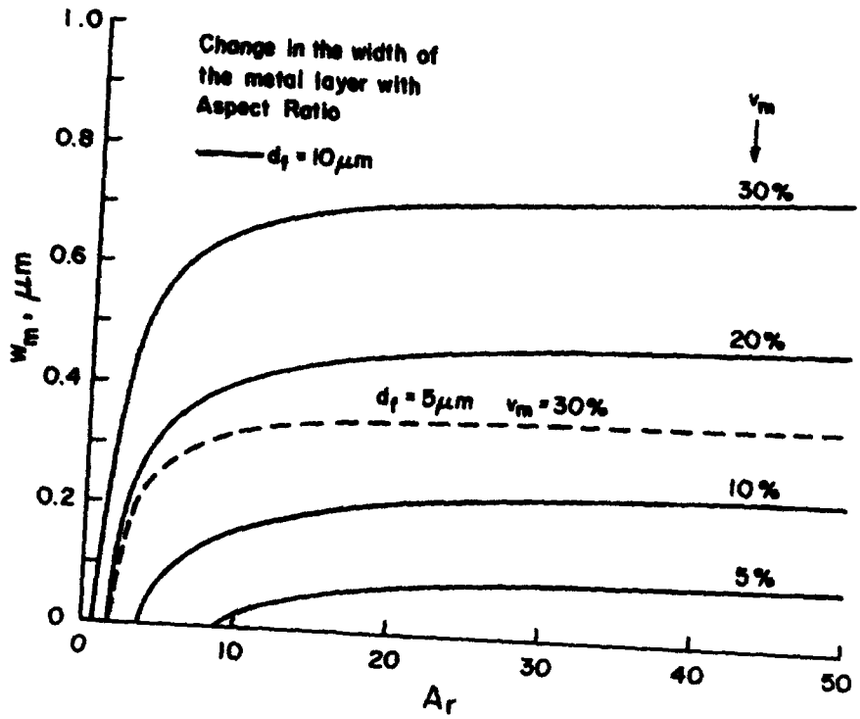

Figure 3: The relationship between the width of the metal layer and the aspect ratio of the ceramic crystals, for different volume fractions of the metal. Two cases of fiber diameters have been considered.

The properties of the conceptual microstructure sketched in Fig. 2 are discussed in the following sections. It is important to keep in mind that these properties depend critically on the atomic structure of the interface. The possible ways of envisioning this coupling between the atomic structure of the interface and the macroscopic behavior is discussed in the last section.

Diffusional Creep

Diffusional creep requires interfaces where atoms can be plated or removed[14] to produce a change in shape. If the entire composite structure is made of one single crystal then diffusional creep will be suppressed. The metal/ceramic interface cannot by itself serve both as a source and a sink of atoms if the inclusions are rigid(##). However, let us

(##) The transport of atoms around the inclusion from the longitudinal to the transverse interface can lead to transient creep that would accommodate the elastic stresses generated by the difference in the moduli of the metal and the ceramic, but it cannot lead to steady state creep. The total magnitude of the transient creep will be of the same order as the elastic

consider the more likely situation that the metal does contain interfaces so that diffusion by the path illustrated in Fig. 2 leads to creep. This mechanism can be analyzed approximately as follows. We assume that a tensile stress, σ, is applied along the longitudinal direction and that this stress drives diffusion from the longitudinal plane to the transverse plane, through the cross section of the metal layer of thickness w_m surrounding the rigid ceramic grains. Lattice diffusion through the metal is likely to be the dominant diffusion mechanism, and assuming the average diffusion distance to be $d_l/4$ the atom flux will be given by: $J_v = (D_v/\Omega kT)(4\sigma\Omega/d_l)$, where D_v is the lattice self diffusion coefficient of the metal, Ω is the atomic volume, and $\sigma\Omega$ is the maximum chemical potential difference between the atoms at the longitudinal and transverse interfaces. The flux is translated into strain rate using the equation that $\dot{\epsilon} = (J.\pi d_t w_m \Omega/2)(4/\pi d_t^2)(1/d_l)$, where the first term is the volume being plated on the transverse interface, the second term converts that into displacement rate and the third term converts it into strain rate. Substituting from Eq. (2) and (3) then leads to the following result:

$$\dot{\epsilon} = 2\frac{\sigma\Omega}{kT}\frac{v_m D_v}{A_r d_f^2} \qquad (4)$$

Acccording to Eq.(4) the strain rate is inversely proportional to the aspect ratio of the ceramic fibers and inversely proportional to the diameter of the ceramic fibers (assuming that $d_t \approx d_f$). The volume fraction of the metal phase has a minor influence on the strain rate: they are linearly proportional to each other.

A plot of Eq. (4) assuming that the metal is niobium (and the ceramic is a non-deforming constituent) is given in Fig. 4. The material constants for Nb were assumed to be as follows: $\Omega = 1.8\times10^{-29}$ m^3, and $D_v = 1.1\times10^{-4}\exp(-402\ \text{kJ mol}^{-1}/RT)$ m^{2}s^{-1}. The curves show that strain rate that can be expected at different temperatures assuming that the applied stress is 100 MPa, the aspect ratio of the ceramic fibers is 100, and the volume fraction of the metal is 30%. The results for three values of the fiber diameter 1, 5 and 10 μm are shown. Note that fiber diameters that are greater than 5 μm yield a strain rate of less than 10^{-9} s^{-1} at 1600°C.

Dislocation Creep

Single crystal nickel base γ/γ′ superalloys deform by dislocation creep. The mobility of dislocations has been studied in the literature, most recently by Pollock and Argon[15] who have investigated the mechanism by which the dislocations move through the γ phase channels formed in between the cuboidal γ′ precipitates. The width of the these channels is typically 0.1μm, which is less than the spacing between dislocations; thus, when forced to move the γ dislocations become pinned by walls of γ/γ′ interfaces. The

---

strain.

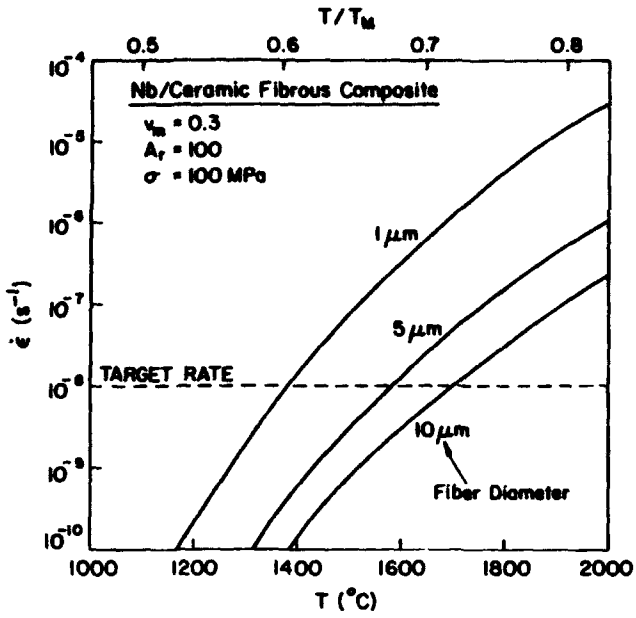

Figure 4: The predicted diffusional creep rates of a niobium/alumina composite as a function of temperature.

mechanism of pinning is likely to be related to the structure of the interface. The lattice mismatch between the γ and γ' has an influence on the creep behavior[16]. In low γ' volume fraction alloys the zero mismatch appears to give the lowest creep rate but in high volume fraction alloys a non-zero value of the mismatch gives the optimum creep performance[17],[18]. The first result may be rationalized on the basis of the lowest rate of coarsening of γ' precipitates, but the second result suggests a more complex role for the interface structure and bonding on the mobility of dislocations.

The lattice dislocation and the interface dislocation are two different entities with their own Burgers vector, which we call b_l and b_{gl}, respectively. They will be equal if the lattice dislocation does not disassociate when it enters the boundary; if it does, then we must invoke a vector equation: $b_l = b_{gl} + b_g$, where b_g is a dislocation that is totally embedded in the interface and its structure is related to the interface structure (for example, b_g could be a van der Merwe[19] dislocation that accommodates the misfit strain between the two lattices). This disassociation is illustrated by the schematic in Fig. 5.

The lattice and interface dislocations, b_g and b_{gl}, must move together. The leading and the lagging dislocation segments will have opposite curvatures in the moving configuration. The case where the interface dislocation has the lower mobility is illustrated in Fig. 6.

We now estimate the driving force for dislocation climb assuming that the interface dislocation is rate controlling. We

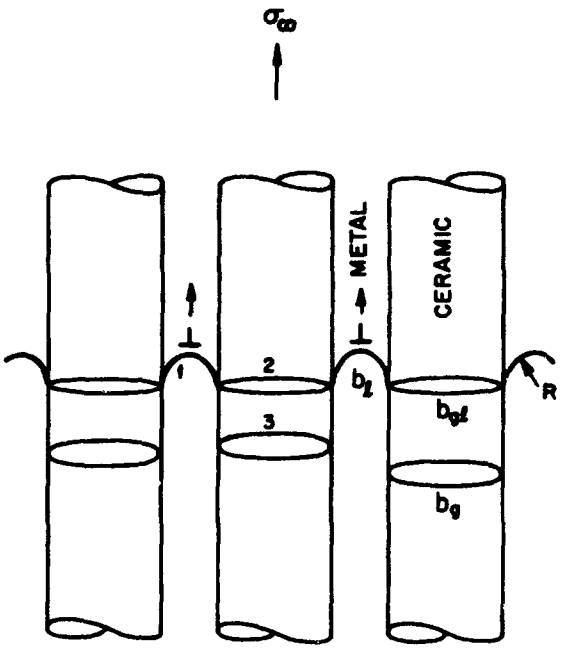

1. Lattice dislocation in the metal channel
2. Interface dislocation pinned to the lattice dislocation
3. The dissociated interface dislocation created by the reaction $\vec{b}_\ell = \vec{b}_{g\ell} + \vec{b}_g$

} Interface Structure Dependent

Figure 5: It is postulated that the lattice dislocation dissociates into two interface dislocations, one of whom, $b_{g\ell}$, is pinned to the lattice dislocation.

obtain an expression for the force on the interface dislocation loop represented by ($b_{g\ell}$, $\mathcal{E}_{g\ell}$) in Fig. 6. ($\mathcal{E}_{g\ell}$ and $\mathcal{E}_\ell$ are the line tensions for the interface and the lattice dislocations). The total force on the interface dislocation loop consists of two terms: (i) the force expressed on the loop directly by the applied stress, which is equal to $\sigma b_{g\ell}.\pi d_f$, where σ is the applied stress, and (ii) the pulling force exerted by the curved lattice dislocation, which would be equal to $2\mathcal{E}_\ell.\text{Cos}\theta$. The angle θ is related to the curvature in the lattice segment of the dislocation. It can be expressed in terms of the applied stress and the width of the metal channel, w_m, leading to the following expression for the driving force, F:

$$F = \sigma b_{g\ell}\pi d_f + \sigma b_\ell w_m \qquad (5)$$

Further simplification of the Eq. (5) results by expressing it in terms of the Orowan stress, $\sigma_{or}=\mathcal{E}_\ell/(b_\ell w_m)$, by assuming that $d_f \approx d_t$ and by substituting from Eq. (3), which gives that:

HIGH INTERFACE FRICTION

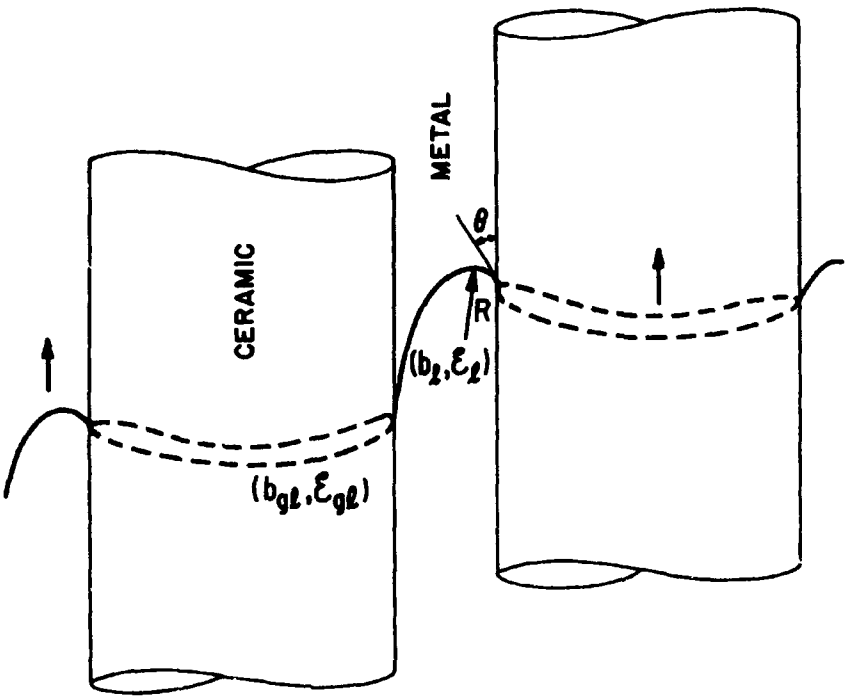

Figure 6: The moving configuration of a lattice and an interface dislocation where they are pinned to each other, and where the interface dislocation is assumed to be slower moving.

$$\frac{F}{\mathcal{E}_\ell} = \frac{2\sigma}{\sigma_{ow}}\left(\frac{4\pi}{v_m} \cdot \frac{b_{g\ell}}{b_\ell} + 1\right) \tag{6}$$

The second term in the above equation represents the pulling force on the loop from the lattice dislocation; this force reaches its maximum value when $\sigma \rightarrow \sigma_{ow}$, and becomes constant if the stress is increased further since the maximum possible force on the loop is reached when $\theta=0°$. The issue is not important since the first term will be generally greater than unity and, therefore, will dominate the force exerted on the interface loop. Thus, it appears as if the rate of creep is controlled not by the bowing out of the lattice dislocations but by the force exerted by the applied stress directly on the interface dislocations.

The analysis presented above assumes that the interface dislocations climb more slowly than lattice dislocations. The picture of dislocation movement presented in Figs 5 and 6 is consistent with the work of Pollock and Argon. The mobility of interface dislocations would depend greatly on the structure of

the interface and the diffusivity of point defects in the interface. In general, if the bonding at the metal/ceramic interface is strong then interface dislocations will have low mobility.

Resistance to Thermal Shock

Thermal shock, or more precisely, accumulative cyclic damage resulting from a difference in the thermal expansion of the metal and the ceramic will be a critical issue in the design of metal/ceramic composites. The figure of merit for thermal shock resistance in ceramics is given by:

$$\Delta T_c = B \frac{\sigma_f}{\alpha E} \tag{7}$$

where ΔT_c is the maximum step change in temperature that can be sustained without fracture damage, σ_f is the tensile fracture strength, α is the coefficient of linear thermal expansion, E is the Young's modulus, and B is a constant, called the Biot number, that depends on heat transfer parameters and sample size. In high volume fraction metal ceramic composites Eq. (7) is likely to provide reasonable guidelines for obtaining threshold values for safe and unsafe temperature excursions.

The detailed microstructure design of the metal/ceramic composite, however, must be based on fracture mechanism. The mechanism proposed here is slip induced interface fracture as illustrated in Fig. 2 by mechanism #2. There are three criteria that can be set for this type of microfracture: (i) a stress criterion that asks that the local stress concentration should be large enough to induce fracture, (ii) an elastic strain energy criterion that is equivalent to the Griffith condition, and (iii) a displacement criteria that is linked to the local strain that must be supplied in order to meet the need for physical opening of the cleavage crack. Below we evaluate these criteria to seek a threshold failure condition.

Criterion (iii) has been discussed in a fundamental way by Stroh[20] and applied specifically to slip induced cleavage initiation by Cottrell[21]. It requires a minimum amount of plastic strain. This condition cannot lead to a threshold since plastic strain may accumulate over several thermal cycles. However, a composite that has good ductility will also have better thermal shock resistance.

The local stress and the strain energy criterion depend on the scale and the morphology of the microstructure, represented by w_m and A_r in Fig. 2. The difference in the thermal expansion coefficient of the metal and the ceramic will give rise to spatially periodic tensile and compressive stresses, on the scale of d_t. Since fracture can occur only if the stress is tensile, the Griffith fracture condition must reflect the microstructural scale. Analysis[22] of this problem leads to the following threshold condition for failure:

$$d_f \leq \frac{4}{3} \frac{\gamma_{eff} F_B}{F_v E (\Delta T \Delta \alpha)^2}, \tag{8}$$

Here $\gamma_{eff} = \gamma_m + \gamma_c - \gamma_{mc}$ where the interface energies on the

right hand side refer to the free metal surface, free ceramic surface and the metal/ceramic interfaces, respectively. ΔT and $\Delta\alpha$ are the temperature excursion and the difference in coefficients of thermal expansion. E is the Young's modulus of the metal. The parameter F_s accounts for the shape of the crack (it may usually be assumed to be equal to $\pi/2$). F_v is the shape factor for the volume of one "unit cell" (see Fig. 2). For a fixed volume, a spherical shape will have the highest value, a needle shape an intermediate value, and a disc shape the smallest value of F_v[23]. Thus disc shaped ceramic inclusions are likely to have the best resistance to thermal shock. The magnitude of the right hand side in Eq. (8) is strongly material dependent, and may range from less than 1 μm to 50 μm. Certainly, composites made from thick ceramic fibers (d_f>100μm) are likely to have poor thermal shock resistance.

The largest stress concentration in the microstructure occur at the metal ceramic interface, where the thermal expansion coefficient is discontinuous. The design of the atomic structure of the interface, with the idea of creating graded interfaces that diffuse this stress concentration can enhance resistance to thermal shock. A first order analysis of the problem leads to the following guidelines: (a) the elastic moduli of the metal should be matched as far as possible to the elastic moduli of the ceramic, and (b) the magnitude of the interfacial shear stress, τ_{mc}, at the end corner of the ceramic fiber is related to geometry (assuming that the elastic moduli are matched), by the following equation[23]:

$$\frac{\tau_{mc}}{\Delta\alpha\Delta TE} = \sqrt{\frac{1}{3\left(v_m - \frac{1}{3A_r}\right)}} \qquad (9)$$

Equation (9) suggests that a large volume fraction of the metal and a large aspect ratio will reduce the stress concentration. If A_r gets very large then the right hand side becomes approximately $=\sqrt{1/(3v_m)}$. If we design for a stress concentration of about 2, then v_m should be greater than 8%.

The Role of the Atomic Bonding and Structure of M/C Interface

Throughout this paper the bonding and the structure of the metal ceramic interface have been an important issue. For example, the reaction between lattice dislocation and interface dislocations will depend on ther structure of the metal/ceramic interface. The climb of these interface dislocations, which is likely to control the rate of dislocation creep of the composite, will depend on interface diffusion which will be determined by atomic bonding at the interface.

Recent studies of metal ceramic interfaces by high resolution transmission electron microscopy and the modeling of the details of the defect structure of the interface is providing insights into the bonding character of the interface. For example, by this process the bonding at niobium/alumina interface is measured to be 2.5 to 3.5 times stronger than within the niobium metal.

A possible way of conceptualizing the relationship between the atomic structure of the m/c interface and physical

properties is to express it as shear modulus of the interface, G_g. The relative values of G_g and the shear modulus of the metal, G, will reflect the bonding at the interface relative to the bonding within the metal. The schematic in Fig. 7 identifies some of the properties that are likely to be influenced by the relative values G_g and G. Coherent interfaces and the existence of misfit dislocations with strong lattice bending are situations where G_g is likely to be greater than G. Incoherent interfaces are likely to have weak G_g. Recent work on the niobium/alumina interface discussed at the end of the preceding paragraph, suggests that mechanical properties of a composite made from these two materials would lie in the upper left section of Fig. 7.

Summary

The single crystal design of superalloy turbine blades represents the most advanced materials technology for reliable, high temperature structural applications. A next step in this evolution is to substitute the intermetallic phase in the superalloys by a ceramic. In this paper we have considered the influence of such a microstructure on diffusional creep, dislocation creep and thermal shock resistance. It is proposed that the volume fraction of the metal should be greater than 8%. The aspect ratio of the ceramic crystals should be greater than 30, and the transverse width of the crystals should lie in the range 1-10μm. For optimum thermal shock resistance the elastic moduli of the ceramic and the metal should be nearly equal. The bonding and the structure of the metal/ceramic interface is likely to control the mechanical properties of the composite, with the best properties being obtained if the elastic modulus of the interface is greater than the modulus of the metal, and if the interface is coherent.

The two most important general features of the above microstructure are the sub-micrometer scale of the metal channel layers and the coherency of the metal ceramic interface. The fine scale serves to provide immunity to thermal shock. The coherent interface pins the lattice dislocations and restricts climb, and therefore, lowers the rate of dislocation creep. The details of this creep mechanism depend on understanding of the splitting of lattice dislocations into interfacial dislocatons, and the climb of these dislocations together, as they remained pinned to one another.

Acknowledgements

This research was supported by the Air Force Office of Scientific Research, Grant No: AFOSR-90-0279, under the direction of Dr. A. H. Rosenstein.

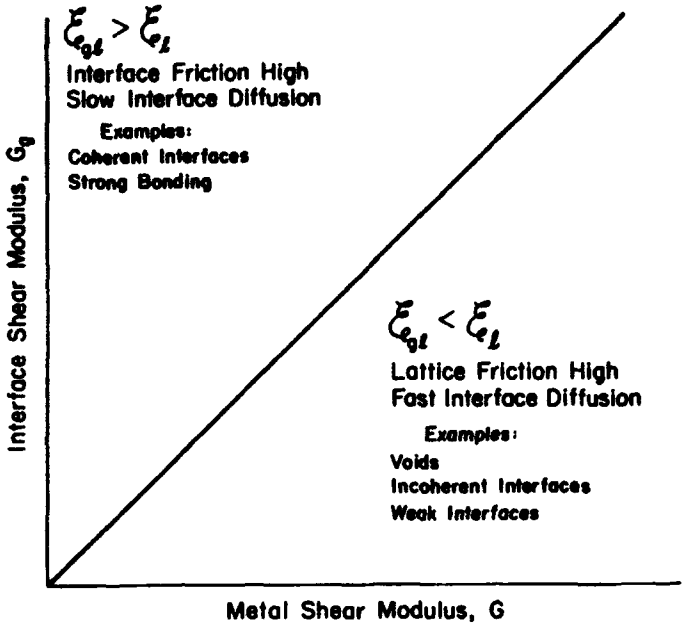

Figure 7: A representation of the relationship between interfacial bonding and other properties. G_g is the effective shear modulus of the interface and G is the modulus of bulk metal.

References

1. Sims C.T., Stoloff N.S., and Hagel J., eds., Superalloys II, (John Wiley and Sons, New York, 1987).

2. G. S. Hoppin III and W. P. Danesi, "Future of Superalloys", ibid. Ref. 1, pp. 549-561.

3. M. Gell and D. N. Duhl, "The Development of Single Crystal Superalloy Turbine Blades", in Processing and Properties of Advanced High Temperature Alloys, (eds) S. Allen, R. M. Pelloux and R. Widmer, (American Society for Metals, Metals Park, OH 1986), 97-131.

4. E. W. Ross and C. T. Sims, "Nickel-Base Alloys", ibid, Ref.1, 97-131.

5. B. A. Wilcox and A. H. Clauer, "High Temperature Creep of Ni-ThO_2 Alloys", in Oxide Dispersion Strengthening, (eds) G. S. Ansell, T. D. Cooper and F. V. Lenel, (Gordon and Breach, New York, 1968), 323-356.

6. E. Arzt and R. F. Singer, "The Effect of Grain Shape on Stress Rupture of the Oxide Dispersion Strengthened Superalloy MA6000", in Superalloys 1984, (eds) M. Gell et al., (The Metallurgical Society, 420 Commonwealth Drive, Warrendale, PA 1984), 361-371.

7. R. Raj and G. W. King, "Life Prediction of Tungsten Filaments in Incandescent Lamps", Metall. Trans. A, 9A (1978), 941-946.

8. R. G. Frank, "Recent Advances in Refractory Alloys", in Refractory Metal Alloys: Metallurgy and Technology, (eds) I. Machlin, R. T. Begley and E. T. Weisert, (Plenum, New York, 1968), 325-372.

9. J. H. Wood and E. H. Goldman, "Protective Coatings", ibid., Ref.1, 359-383.

10. A. K. Mukherjee, J. E. Bird and J. E. Dorn, "Experimental Correlations for High Temperature Creep", Trans. Amer. Soc. Met., 62 (1), (1969), 155-179.

11. C. Herring, "Diffusional Viscosity of Polycrystalline Solids", J. Appl. Phys., 21 (1950), 437-445.

12. R. L. Coble, "A Model for Boundary Diffusion Controlled Creep in Ceramic Materials", J. Appl. Phys., 34 (6) (1963), 1679-84.

13. H. J. Frost, Deformation Mechanism Maps, Ph.D. Thesis, Harvard University, Cambridge MA, January 1974.

14. R. W. Balluffi, "High Angle Grain Boundaries as Sources and Sinks for Point Defects", Grain Boundary Structure and Kinetics, (American Society for Metals, Metals park OH, 1980), 297-329.

15. T. M. Pollock and A. S. Argon, "Creep Resistance of CMSX-3 Nickel Base Superalloy Single Crystals", Acta Metall. Mater., 40 (1) (1992), 1-30.

16. I. L. Mirkin and O. D. Sancheev, Met. Sci. Heat Treatment, vol (1,2) (1967), p.10, referenced in "Fundamentals of Strengthening" by N. S. Stoloff, Ref. ibid 1, p 61.

17. C. C. Law and M. J. Blackburn, Metall. Trans. A, 11 (1980), 495.

18. F. Schubert, Superalloys Source Book, (ASM, Metals Park, OH 1984); referenced by S. Floreen in "Mechanical Behavior", ibid Ref. 1, p. 241.

19. J. H. van der Merwe, Surface Science, 31 (1972), 198.

20. A. N. Stroh, Advances in Physics, 6 (1957), 418.

21. A. H. Cottrell, "Theory of Brittle Fracture in Steel and Similar Metals", Trans. AIME, 208 (4) (1958), 192-203.

22. R. Raj, "The Design of the Interface Phase for Obtaining Thermal Shock Resistance in Silicon Nitride", International Conference on Thermal Shock, Schloss Ringberg in November 1992, eds., G. Petzow, G. Schneider and M. Hoffmann, to be published by the Kluwer Press, Netherlands (1993).

23. J. W. Christian, The Theory of Transformations in Metals and Alloys, (Pergamon Press, NY, 1965), 420.

Ni-Based Superalloy Developments

Gary L. Erickson

Cannon-Muskegon Corporation
2875 Lincoln Street
Muskegon, Michigan 49441

ABSTRACT

The need for higher performance materials for gas turbine engine hot section components continues. Interestingly, where much of the past Ni-based superalloy development activity was driven by the need to extend military aircraft altitude range and Mach number capability, todays efforts with this category material are increasingly impelled by the civil aircraft and industrial gas turbine industries.

Designing high thrust engines for the next generation widebody twins, turbine designers defined the need for higher strength Ni-based superalloys than the commercially available 2nd Generation class of single crystal materials (e.g., CMSX-4® and PWA 1484). This definition led to the recent development of 3rd Generation single crystal casting alloys and may also help stimulate activity toward 4th Generation SX alloy development.

Similarly, new turbine design activity in the industrial, land-based turbine industry has identified the need for the development of DS and SX casting alloys which provide an appropriate blending of large component castability, ease and efficiency of heat treatment, hot corrosion resistance and increased creep-rupture strength.

To this end, Ni-based superalloy development activity continues. This narrative describes the development of new DS and SX casting alloys for industrial and aero gas turbine usage, as well as the embryonic development of the ultra-high-strength 3rd and 4th Generation classes of single crystal superalloys. Alloy design concepts are reviewed in tandem with processing features and strengthening mechanisms. The desirable direction for future Ni-based superalloy development activity is provided.

Cannon-Muskegon Corporation is a subsidiary of SPS Technologies

Critical Issues in the Development of High Temperature Structural Materials
Edited by N.S. Stoloff, D.J. Duquette and A.F. Giamei
The Minerals, Metals & Materials Society, 1993

Introduction

Superalloys are a group of nickel-, iron-nickel, and cobalt-base materials that exhibit outstanding strength and surface stability at temperatures up to 85% of their melting points (0.85 T_m). They are generally used at temperatures above 540°C (1000°F). Having been initially developed for use in aircraft piston engine turbosuperchargers, superalloy development over the last 50 years has been paced by the demands of advancing gas turbine engine technology.

The first commercial nickel-base alloy developmental work, undertaken by the British in the early 1940s, led to the wrought Nimonic 75 and 80 alloys. Increased operating-temperature requirements for U.S. aircraft engines resulted in the use of aluminum plus titanium strengthened wrought materials during the same period of time. Component forgeability problems, however, led to the use of cast Vitallium (Co-27Cr-5.5Mo-2.5Ni-0.25C) until the shortages of cobalt supply experienced during the Korean War caused further research on nickel-base alloys.

Cast nickel-base alloy developments outpaced cobalt-base developmental work by the late 1950s because of their superior strengthening potential, that is, stable, coherent intermetallic compound γ' phase introduction. The introduction of commercial vacuum induction melting (VIM) and vacuum investment casting in the early 1950s provided further potential for γ' exploitation. Many nickel-base alloy developments resulted, continuing through the 1960s (Fig. 1).

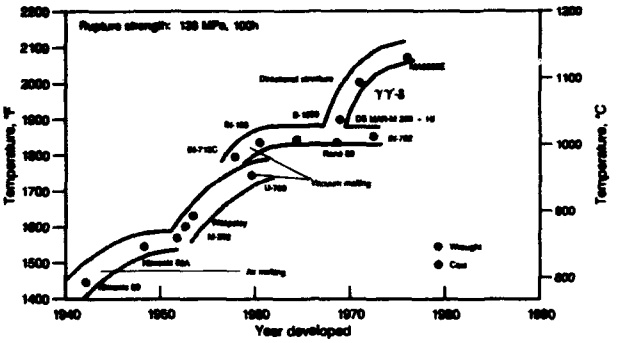

Figure 1 Progress in the high temperature capabilities of superalloys since the 1940's (1)

The development of new polycrystalline alloys continued through the 1970's, however, at a more moderate rate. Attention was concentrated instead on process development, with specific interest directed toward grain orientation and directional-solidification (DS) turbine blade and vane casting technology (Fig. 2).

Applied to turbine blades and vanes, the DS casting process results in the alignment of all component grain boundaries such that they are parallel to the blade/vane stacking axis, essentially eliminating transverse grain boundaries (Fig. 3). Because turbine blades/vanes encounter major operating stress in the direction which is near normal to the blade stacking axis, transverse grain boundaries provide relatively easy fracture paths. The elimination of these paths provides increased strain elasticity by virtue of the lower (001) elastic modulus, thereby creating opportunities for further exploitation of the nickel-base alloy potential, particularly in respect to creep and thermal fatigue resistance.

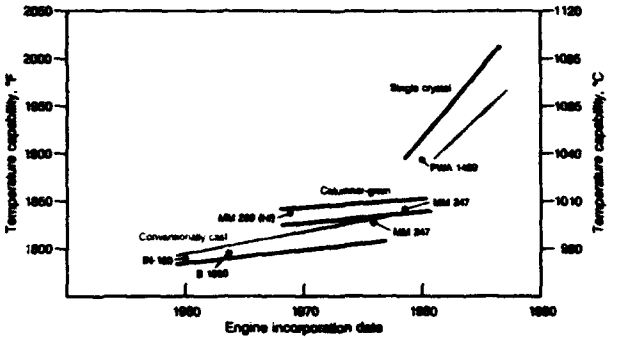

Figure 2 Advances in turbine blade materials and processes since 1960 (2)

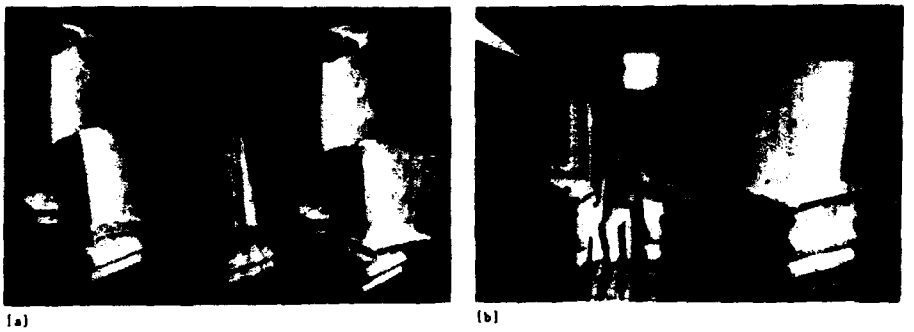

Figure 3 Turbine blade grain evolution. [a] From left, equiaxed, DS columnar and single crystal(3), [b] An exposed view of the internal cooling passages of an aircraft turbine blade(3), [c] Turbine blade cooling techniques

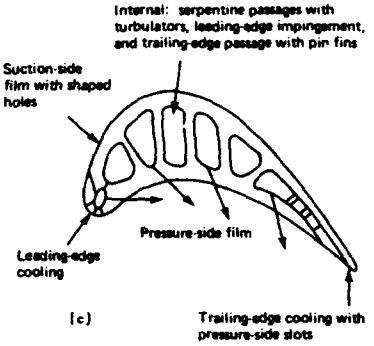

The logical progression to grain-boundary reduction is the total elimination thereof. Thus, single-crystal turbine blade/vane casting technology soon developed (Fig. 3), providing further opportunity for nickel-base alloy design innovation. Typical alloy performance improvements related to the directional casting technology are depicted in Figure 4.

The late 1970s, 1980s and early 1990s have, therefore, been a productive development period for nickel-base alloys designed specifically for directionally solidified columnar-grain and single crystal cast airfoil components. These new process technologies depicted in Figure 3, have contributed to dramatic improvements in gas turbine engine operating efficiency.

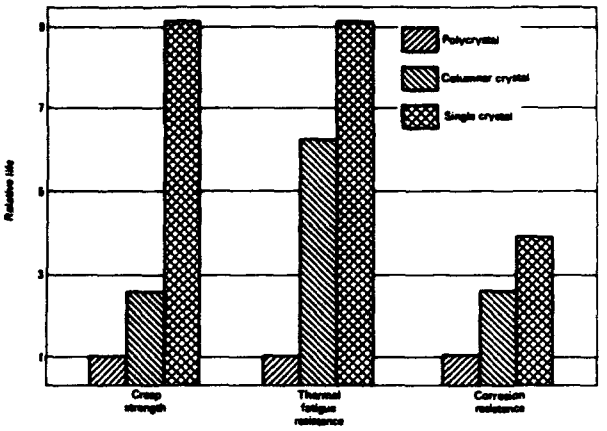

Figure 4 Comparative properties of polycrystal, DS columnar-crystal, and single-crystal superalloys (4)

Further engine efficiency improvements are apparent with recent SX process innovation undertaken at the Allison Gas Turbine Division of General Motors where Lamilloy® and CastCool™ turbine components (Fig. 5) have been developed. The unique components provide quasi-transpiration cooling schemes that allow much greater than 1649°C (3000°F) gas stream temperatures with existing Ni-based single crystal superalloys; this in contrast to the 1538°C (2800°F) capability conferred by the type of conventional air film cooling passages illustrated in Figures 3b and 3c.

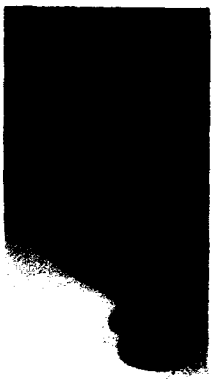

Figure 5 Allison gas turbine Castcool™ turbine blade (5)

The quasi-transpiration cooling is achieved through the adaptation of the Allison Lamilloy® component structure and bonding concepts to the casting process. Early process development consisted of casting individual "crystal-foil" halves, containing cast cooling holes, which when bonded together, resulted in highly efficient turbine blades. Current efforts involve casting Lamilloy structured components as total entities, thereby eliminating the bonding and associated processes.

Additional DS and SX casting process innovation is driven by the need to increase process thermal gradient characteristics for the higher strength, high refractory element containing Ni-based superalloys currently under development, along with the need to increase component casting lengths due to the developing industrial turbine producer interest in

DS and SX components which can range 15-63 cm (6-25 inches) in length. Process thermal gradient improvement may include the commercial development of liquid metal cooling schemes.

Associated alloy development is undertaken to help realize the full potential that these improved process capabilities provide. The newly developed materials are engineered to offer the balanced level of functional characteristics necessary for the emerging component applications. Interestingly, where much of the past Ni-based superalloy development activity was driven by the need to extend military aircraft capability, todays efforts with this category material are again, increasingly impelled by the civil aircraft and industrial gas turbine industries.

As such, this narrative discusses selected Ni-based alloy development activity which is primarily undertaken to serve the specific material requirements identified for emerging civil aero turbines and industrial engines.

Superalloy Design

Nickel-base superalloys have microstructures consisting of an austenitic face-centered cubic (fcc) matrix (γ), dispersed intermetallic fcc γ' $Ni_3(Al,Ti)$ precipitates coherent with the matrix (0 to 0.5% lattice mismatch), and carbides, borides, and other phases distributed throughout the matrix and along the grain boundaries. These complex alloys generally contain more than ten different alloying constituents. Various combinations of carbon, boron, zirconium, hafnium, cobalt, chromium, aluminum, titanium, vanadium, molybdenum, tungsten, niobium, tantalum, rhenium and yttrium result in the commercial alloys used in todays gas turbine engines.

Some alloying elements have single function importance, whereas others provide multiple functions. For example, chromium is primarily added to nickel-base alloys for sulfidation resistance (Cr_2O_3 protective scale formation), whereas aluminum not only is a strong γ' former but also helps provide oxidation resistance, when present in sufficient quantity, by forming a protective Al_2O_3 scale.

Many of the other alloying elements also have multiple roles titanium, while primarily partitioning to the γ', also participates in the formation of (MC) carbide, the hexagonal close-packed (hcp) eta (η) phase, and undesirable nitride and carbosulfide formation. Molybdenum, tungsten, tantalum, rhenium, cobalt and chromium additions promote solid-solution strengthening, but tantalum, tungsten, and rhenium may also partition to the γ' to varying degrees. Additionally, tantalum and rhenium are beneficial toward improving alloy environmental resistance properties.

Vanadium is a γ' partitioner, but it also promotes the formation of M_3B_2-type borides. Niobium forms the intermetallic phases delta (δ) (orthorhombic Ni_3Nb) and γ' (body-centered tetragonal Ni_3Nb), but it is also involved in the formation of Laves (Fe,Ni_2Nb) phase, carbides, borides and/or nitrides. Hafnium is a strong carbide former that is added to polycrystalline alloys to improve grain-boundary ductility. Furthermore, it increases the volume fraction of γ/γ' eutectic and improves oxidation resistance. Carbon, boron and zirconium are used at varying levels for grain boundary strengthening, while rare earth elements, like yttrium, are added to improve alloy oxidation resistance.

All of these constituents interact in various ways to provide high tensile, creep and fatigue strengths, plus oxidation and sulfidation resistance. Proper control of the cast microstructure and subsequent solutioning and aging treatments generally results in satisfactory component performance.

Under the extreme temperature/stress conditions in which superalloy components operate, however, microstructural features change, often with attendant property changes. The microstructural instabilities that may occur include (a) intermetallic phase precipitation (σ, μ, Laves), (b) phasial decomposition (carbides, borides, nitrides), (c) phase coalescence and coarsening (γ'), (d) phasial solutioning and reprecipitation (γ'), (e) order-disorder transition, (f) material oxidation, and (g) stress-corrosion cracking.

The formation of topologically close packed (TCP) phases (σ, μ and so on) can decrease creep-rupture properties. Their occurrence is controlled through chemistry adjustment and is fairly predictable through use of the commonly accepted methods of calculating the so-called electron vacancy number, N_v, of the given alloys. Different calculation methods exist; however, all provide a useful key to the prediction of TCP phase formation when proper reference points are known.

Although it occurs during both solidification and heat treatment, carbide precipitation is generally promoted during component heat treatment to effect an optimum grain-boundary carbide morphology and population. Discrete, blocky $M_{23}C_6$ particles in a discontinuous fashion are preferred. High-temperature, stressed exposure tends to cause carbide degeneration, often resulting in grain boundary overload and compromised rupture strength.

MC-type carbides generally occur during alloy solidification. Primary carbides are titanium-rich (MC-1) and/or tantalum rich (MC-2). With high temperature exposure, they may partially degenerate to form hafnium rich (MC-3) carbides and/or $M_{23}C_6$, M_7C_3, and M_6C carbides (secondary carbides); the specific type depending upon alloy chemistry and exposure temperature. The chromium rich $M_{23}C_6$ generally forms at the grain boundaries in polycrystalline materials, and when present as discrete, discontinuous particles, they provide the grain boundary strength and resistance to fracture needed to prolong service life.

Furthermore, carbide degeneration also releases titanium and tantalum to the solid solution matrix, resulting in further matrix saturation. Oversaturation can result in the formation of undesirable secondary phases such as μ (tungsten and/or molybdenum rich), α-W, α-Cr, and/or carbides and/or γ' grain boundary films, making chemistry balancing and controlled thermal treatment necessary for ultimate success.

Superalloy property attainment is principally a function of the amount and morphology of the γ' microstructural homogeneity, grain size and shape, plus carbide distribution. Early superalloys contained less than 25 vol% γ'. However, commercial vacuum induction refining and casting provided the opportunity for greater γ' volume fraction, to the extent that today's high strength cast superalloys generally contain approximately 65-70 vol% γ'.

This increased level of γ' results in greater alloy creep strength (Fig. 6), but it is fully exploited only in single crystal components, where full γ' solutioning is generally possible. For polycrystalline superalloy

components, high temperature strength is strongly influenced by the condition of the grain boundaries and, in particular, the grain boundary carbide morphology and distribution. Optimized properties can be achieved if solutioning and aging treatments are developed to attain discrete, globular carbide formation along the grain boundaries, in conjunction with optimized γ' volume fraction/morphology and component grain structure.

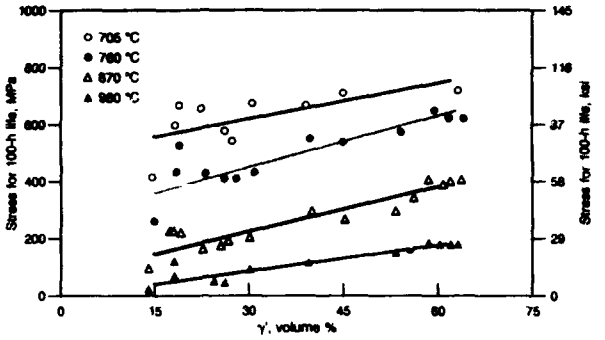

Figure 6 The relationship between γ' volume percent and stress-rupture strength for nickel-base superalloys (6)

Recent Superalloy Developments

Since polycrystalline cast superalloy process technology is relatively mature, very little effort is focused on the development of new Ni-based polycrystalline materials. However, there appears to be an interest for the use of relatively new high-strength DS materials for selected, critical polycrystalline castings, such as relatively large [100 cm (25 inch long)] industrial turbine blades and cast integral wheel components.

For example, the CM 247 LC® alloy is a candidate for large industrial turbine polycrystalline airfoil components since it offers better castability, higher strength, superior oxidation resistance, and improved process flexibility than typical of materials used previously, e.g., IN 738 C/LC, IN 792 and IN 939. Similarly, the Re-containing CM 186 LC® alloy is evaluated for advanced turbofan engine design where higher strength integral wheel components are required.

The chemical compositions for these dual-purpose materials are included within Table I, along with other first and second generation polycrystalline and DS columnar casting alloys which are commonly used in gas turbine hot sections. Of those provided, the high chromium containing materials (chromia formers) have primarily been used in industrial turbines, where Type II hot corrosion problems predominated, while the lower chrome, higher aluminum containing (alumina formers) have had greatest use in aero turbines, where engine gas stream temperatures tend to be much hotter, and oxidation thereby predominated the alloy protection consideration.

But today, the continuing need to increase engine operating temperatures, rotational speeds and component lives has affected the engine designers alloy selection criteria. For the industrial turbine designers, the higher gas stream temperatures drive the need to evaluate directionally solidified blade and vane components and associated materials offering a modified balance of hot corrosion/oxidation capability and processability, while the aero-turbine designers continue to specify

Table I Nominal compositions of selected first and second generation polycrystalline and DS columnar casting alloys

	C	Cr	Co	Mo	W	Re	Ta	Cb	Al	Ti	B	Zr	Hf	Ni
IN 738 LC	.010	16.0	8.4	1.7	2.5	-	1.7	0.7	3.6	3.4	.010	.05	-	BASE
IN 939	.15	22.5	19.0	-	2.0	-	1.4	1.0	1.9	3.7	.010	.10	-	BASE
IN 792	.14	12.7	9.0	2.0	4.2	-	4.2	-	3.4	4.1	.015	.05	1.0	BASE
René 80	.17	14.0	9.5	4.0	4.0	-	-	-	3.0	5.0	.015	.03	-	BASE
MM 002	.15	9.0	10.0	-	10.0	-	2.5	-	5.5	1.5	.015	.05	1.5	BASE
(7)(8) CM 247 LC	.07	8.1	9.2	.5	9.5	-	3.2	-	5.6	0.7	.015	.015	1.4	BASE
(9) CM 186 LC	.07	6.0	9.0	.5	8.0	3.0	3.0	-	5.7	0.7	.015	.005	1.4	BASE
MAR M 247	.15	8.0	10.0	.6	10.0	-	3.0	-	5.5	1.0	.015	.03	1.5	BASE
GTD 111	.10	14.0	9.4	1.5	3.7	-	3.0	-	3.0	5.0	.010	.01	.15	BASE

highly oxidation resistant components -- sometimes by means of rare earth element addition to the alloys used or sophisticated coatings protection -- and much higher strength DS columnar and single crystal casting alloys.

DS Columnar Casting Alloys for Industrial Turbines

Industrial gas turbine engines generally operate in temperature/pressure regime where Type II hot corrosion attack is an important materials design criteria (Fig. 7). The industry currently seeks highly creep-resistant materials able to be utilized in DS columnar casting processes since the newer engine designs are operated at significantly higher temperature/pressure levels. The alloys required must still offer good corrosion resistance with Type I corrosion beginning to dominate, while providing relatively higher creep-strength concurrent with large component producibility. DS modified versions of previously used equiaxed casting alloys have not been successful. Furthermore, industry efforts to develop new, high-strength materials for such application, have been mostly unsuccessful due to problems with DS castability, component transverse ductility and inadequate creep-rupture property attainment.

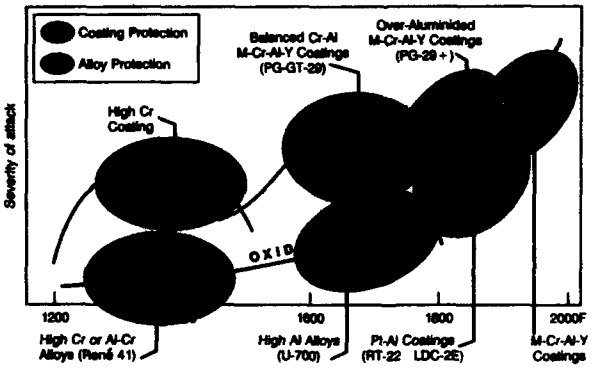

Figure 7 The protection scene (10)

The developmental materials should be designed with relatively high chromium content. Additionally, moderately higher refractory element content, appropriate Al/Ti ratio and very carefully balanced minor element constituents are important design considerations in trying to maximize the developmental materials overall functionality.

Relative to IN 738 C, current developmental materials should be able to provide at least 50°C (90°F) greater metal temperature capability

at the 138-207 MPa (20-30 ksi) stress level. In other words, some high chromium-containing developmental materials should be able to provide nearly DS CM 247 LC creep capability. It is expected that the new materials may be available for industry usage within the next 2-4 years.

CM 247 LC® Alloy

In the meantime, some industrial turbine producers have decided to utilize turbine blades and vanes produced with the CM 247 LC alloy in newly designed and uprated turbines. When cast into large DS components [(approximately 30-51 cm (12-20" long)] the alloy exhibits superior castability, solution characteristics and strength attainment. With a relatively ductile, high chromium-containing coating applied, components have exhibited extremely good resistance to hot corrosion attack. Furthermore, where natural gas is the predominant fuel, the material hot corrosion requirements are significantly less than those cases where low grade fuels containing corrosion accelerators such as vanadium, sulfur and sodium predominate, so that high temperature oxidation becomes the increasingly important environmental concern.

The CM 247 LC composition, presented in Table I, is derived from the base MAR M 247 composition. The primary CM 247 LC alloy design modifications are the reduction of carbon by approximately one-half to improve carbide microstructure, stability, and alloy ductility, plus the reduction of the Zr and Ti contents to improve DS grain boundary cracking resistance without sacrificing strength. Additionally, the alloy's W and Mo levels are reduced accordingly to minimize the formation of undesirable secondary M_6C platelets, μ phase and/or alpha W platelets or needles, resulting from the thermally induced degeneration of primary carbides. This degeneration of low parameter MC-1 (Ti-rich) and MC-2 (Ta-rich) carbides results in the formation of MC-3's (Hf-rich) with an associated release of Ta and Ti to the solid solution, thereby affecting the solubility of the W and Mo within the basic gamma solid solution; the result of which is the possible formation of thermally induced μ phase, alpha W and/or M_6C.

The alloy design results in extremely good DS castability; this being accomplished with the relatively low Hf ingot content of 1.4 wt. %. Furthermore, the alloy is capable of exhibiting similar functionality with a 1.0% Hf level in the DS castings (11), the significance of which is that alloys with higher levels of Hf (>1.5%) tend to be much more reactive with casting process related shell and core ceramics, thereby resulting in component-contained Hf-oxide/Hf silicate inclusions which deleteriously effect component fatigue strength and casting yield. Moreover, alloy tolerence to varied Hf content is important since it generally varies significantly from blade/vane top to bottom sections.

The CM 247 LC alloy can be fully γ' solutioned through multi-step treatment (12). The full solutioning provides an increased volume fraction of fine γ' particles, which positively influence the alloys creep-rupture response. Larson-Miller parameter representation of the CM 247 LC stress-rupture capability is provided in Figure 8, while the DS CM 247 LC vs. IN 738 LC 982°C (1800°F) stress-rupture properties are presented in log/log form in Figure 9. 1135°C (2075°F) Mach 1.0 oxidation results are presented in Figure 10.

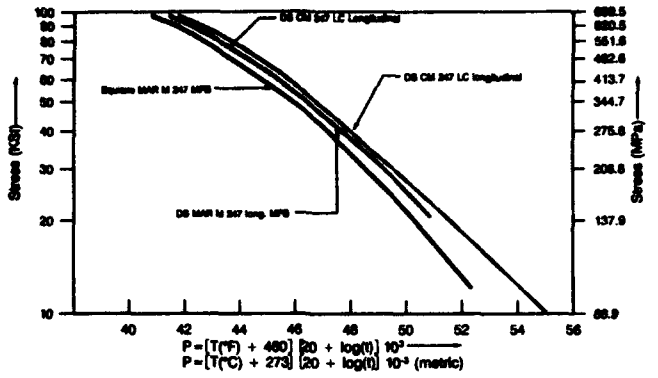

Figure 8 Stress-rupture strength of DS CM 247 LC vs. DS and equiaxed MAR M 247

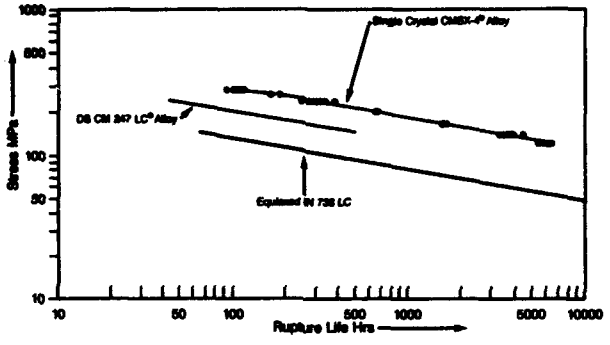

Figure 9 982°C (1800°F) stress-rupture for CMSX-4 vs. DS CM 247 LC vs. equiaxe IN 738 LC

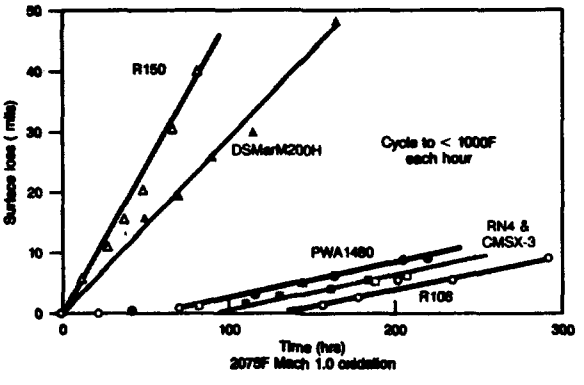

Figure 10 DS CM 247 LC (R 108) Mach 1.0 oxidation (13)

DS Columnar Casting Alloys for Aero Turbines

With the CM 247 LC alloy initially designed for aeroturbine usage, it has been specified in many turbine blade and vane applications throughout the industry. Significant production and turbine engine experience

confirms the alloys superior blending of castability, solutionability, creep, fatigue and environmental properties.

However, certain turbine designs require even greater strength and temperature capability from a DS material, since the component design renders it impractical to cast as a single crystal. For such application, then, the CM 186 LC® alloy is developed.

CM 186 LC® Alloy

The CM 186 LC alloy is a Re-containing derivative of the CM 247 LC alloy. It is primarily intended for DS columnar, complex-cooled vane segments and relatively large LP turbine blade components. Additionally, it is particularly attractive for use in components which are prone to recrystallization during solution heat treatment (resulting from residual casting stresses), since the alloy is used in the as-cast plus double aged condition.

The alloy exhibits excellent resistance to grain boundary cracking in casting complex-cored, thin wall turbine airfoils. It is fully solution heat treat capable, however, at the expense of transverse ductility. Hence, the specified use is an as-cast plus double aged condition.

In the as-cast plus double aged condition, CM 186 LC exhibits a 18°C (32°F) metal temperature advantage relative to fully solutioned DS CM 247 LC at the 982°C/248 MPa (1800°F/36.0 ksi) test condition, and 24°C (43°F) greater capability based on time to 1.0% plastic strain. This essentially equates to first generation single crystal alloy strength (CMSX-2®, CMSX-3®, PWA 1480, René N4, SRR99, AM1 ...). For higher temperature, the alloy strength is about midway between the DS CM 247 LC and CMSX-2/3 respective capabilities (Fig. 11).

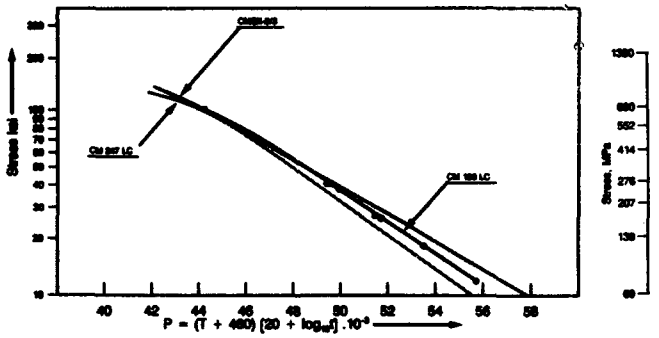

Figure 11 CM 186 LC vs. CM 247 LC vs. CMSX-2/3 (001) DS longitudinal Larson-Miller stress-rupture

Furthermore, the alloy typically exhibits 7-14% elongation in DS transverse stress-rupture tests performed between 871°C-1038°C (1600°F-1900°F), as illustrated in Table II. The CM 186 LC transverse strength is approximately 19°C (34°F) better than the DS CM 247 LC transverse rupture capability.

Table II DS CM 186 LC transverse stress-rupture data
As-cast plus double aged condition

Test Condition	Rupture (hrs.)	El (%) 4D	RA %
55.0 ksi/1800°F (379 MPa/871°C)	413.2	10.6	19.6
55.0 ksi/1800°F (379 MPa/871°C)	417.6	7.3	11.7
25.0 ksi/1800°F (172 MPa/982°C)	442.0	8.3	20.4
25.0 ksi/1800°F (172 MPa/982°C)	258.9	8.8	15.7
20.0 ksi/1900°F (138 MPa/1038°C)	161.5	13.9	20.6
20.0 ksi/1900°F (138 MPa/1038°C)	96.8	11.2	18.9

Table III presents the CM 186 LC chemical composition again, along with other 2nd generation DS superalloys. The most significant feature of the alloy is its 3.0% Re content. Rhenium addition to Ni-based alloys (3 wt. % level) has been shown to dramatically increase alloy creep strength due to its effect of reducing γ' particle coarsening rate (14), and the clustering of Re atoms which develop, thereby impeding dislocation movement (15).

Table III Second generation DS columnar casting alloys

		Nominal Composition, wt. %												
		C	Cr	Co	Mo	W	Ta	Re	Al	Ti	B	Zr	Hf	Ni
(9)	CM 186 LC	.07	6	9	.5	8	3	3	5.7	.7	.015	.005	1.4	BAL
(16)	PWA 1426	.1	6.5	10	1.7	6.5	4	3	6	-	.015	.1	1.5	BAL
(17)	René 142	.12	6.8	12	1.5	4.9	6.35	2.8	6.15	-	.015	.02	1.5	BAL

Following the Re addition, the alloy design concepts follow parallel to those already described for the CM 247 LC. It exhibits oxidation resistance which is superior to MM 002, while and hot corrosion properties are similar to MAR M 247, CM 247 LC and MM 002. Long term creep-rupture specimen review suggests adequate microstructural stability persists.

Single Crystal Casting Alloys for Industrial Turbines

Following extensive aeroturbine experience with single crystal cast superalloys, the industrial turbine designers seek to similarly employ single crystal casting materials for the combustion process efficiency benefits that they help create. Similar to their DS columnar counterparts, the single crystal materials/components are expected to help improve combustion cycle efficiency by virtue of their increased creep strength, mechanical/thermal fatigue resistance, temperature capability and resistance to environmental degradation.

Similar alloy design concepts are applied for single crystal as discussed for the DS alloy design. The exception, though, is that the intentional absence of grain boundaries from the cast components is desirable in order to allow the elimination of elements whose addition are intended primarily for grain boundary control, e.g., C, B, Zr, Hf. As these elements are melting point depressants, their removal should allow higher temperature solution cycles which result in an increased level of γ' and eutectic γ/γ' solutioning, plus greater alloy microstructural homogeneity; both of which improve alloy creep strength. Such features

should also provide further strength enhancing control of the γ' particle size, shape and distribution.

The alloy design flexibility that should be created by the elimination of grain boundary strengtheners simplifies the alloy design task. The corrosion resistant single crystal casting alloys should be developed to exhibit the following characteristics: (a) castability -- freedom from "freckles", spurious grain and sliver defects in large castings. Compatibility with existing core technology, (b) heat treatability -- wide solution heat treatment window, thereby accommodating the potential component chemistry variation experienced from bottom to top casting locations, (c) microstructural stability -- balanced chemistry which provides freedom from deleterious TCP phase formation during long term high temperature exposure, (d) creep strength -- similar to the CMSX-2 alloy capability, and (e) environmental resistance -- IN 738 type hot corrosion resistance. Moderate oxidation resistance. Excellent coatability.

This category material may be released for industry evaluation within the next 2 years.

In the meantime, though, some producers of relatively small and medium industrial turbines are either testing and/or committed to engine application of the 2nd generation, Re-containing single crystal superalloy, CMSX-4. One example of commitment is the turbine blading of the Solar® Turbines MARS T-14000 engine with CMSX-4; the successful application of which is described in (18). Additional alloy CMSX-4 detail follows.

Single Crystal Casting Alloys for Aero Turbines

The use of high strength single crystal components in turbine blade and vane application is partly responsible for the significant advances to engine output and efficiencies achieved in recent years. As earlier discussed, the single crystal process development ushered in an era of revitalized alloy development, which continues to thrive.

Selected first generation single crystal alloys developed during this renaissance are illustrated in Table IV. They all provide similar creep-rupture strength, however, with varying level of functionality, i.e., castability, heat treatability, resistance to recrystallizaton, fatigue strength and environmental properties resistance. Larson-Miller example of the CMSX-2/3 and CMSX-6 stress-rupture capabilities are illustrated in Figures 12 and 13, respectively.

Table IV First generation single crystal superalloys

	Nominal Composition, wt. %											Density
	Alloy	Cr	Co	Mo	W	Ta	V	Cb (Nb)	Al	Ti	Hf	Ni	kg/dm³
(19)	PWA 1480	10	5	-	4	12	-	-	5.0	1.5	-	BAL	8.70
(20)(21)	René N-4	9	8	2	6	4	-	.5	3.7	4.2	-	BAL	8.56
(22)(23)	SRR 99	8	5	-	10	3	-	-	5.5	2.2	-	BAL	8.56
(22)(23)	RR 2000	10	15	3	-	-	1	-	5.5	4.0	-	BAL	7.87
(24)	AM1	8	6	2	6	9	-	-	5.2	1.2	-	BAL	8.59
(25)	AM3	8	6	2	5	4	-	-	6.0	2.0	-	BAL	8.25
(26)	CMSX-2	8	5	.6	8	6	-	-	5.6	1.0	-	BAL	8.56
(26)	CMSX-3	8	5	.6	8	6	-	-	5.6	1.0	.1	BAL	8.56
(27)	CMSX-6	10	5	3	-	2	-	-	4.8	4.7	1	BAL	7.98
(28)	AF 56	12	8	2	4	5	-	-	3.4	4.2	-	BAL	8.25

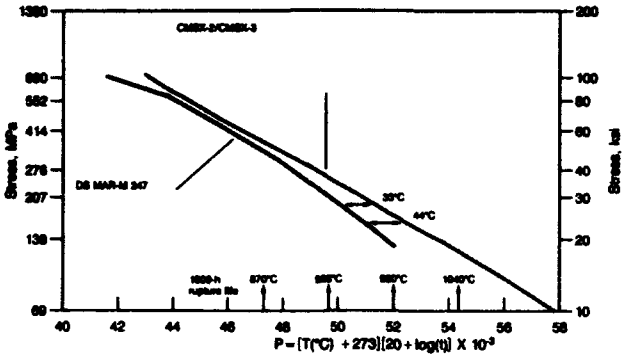

Figure 12 Larson-Miller stress-rupture strength of CMSX-2 vs. MAR M 247 (1.8 mm [0.070 in.] machined from blade specimens)

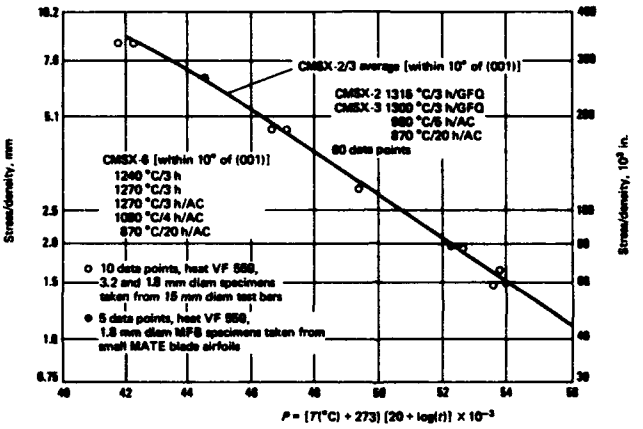

Figure 13 Larson-Miller specific stress-rupture stength of CMSX-6 vs. CMSX2/3

More recently developed, higher strength single crystal casting alloy compositions, referred to as 2nd Generation SX materials due to their 3.0% Re content (with the exception of MC-2) are provided in Table V. Again, the alloys exhibit similar creep-rupture properties with varied level of functionality.

Table V Selected second generation single crystal alloys

		Nominal Composition, wt. %										Density
		Cr	Co	Mo	W	Ta	Re	Al	Ti	Hf	Ni	kg/dm³
(29)	CMSX-4	6.5	9	.6	6	6.5	3	5.6	1.0	.1	BAL	8.70
(30)	PWA 1484	5	10	2	6	9	3	5.6	-	.1	BAL	8.85
	SC 180	5	10	2	5	8.5	3	5.2	1.0	.1	BAL	8.84
(31)	MC2	8	5	2	8	6	-	5.0	1.5	-	BAL	8.63

CMSX-4

The CMSX-4 alloy is Re-containing modification of the CMSX-2 alloy. It exhibits a balanced blend of characteristics desired for successful usage in the investment casting foundry, and ultimate properties attainment desired for advanced turbine blade and vane components.

Relative to CMSX-2, the material is necessarily designed with moderately lower Cr content to reduce the likelihood of alloy phasial instability, i.e., the thermally induced precipitation of undesirable Cr, W, Re-rich TCP phases. Similarly, W content is reduced, but the overall refractory element (W+Re+Mo+Ta) content is significantly increased. Cobalt content is increased to 9 wt. % to assist with alloy solid solubility, while the remainder of the elements essentially remain the same.

The resulting alloy is capable of full γ' solutioning and exhibits high stress-rupture strength [approximately 35°C (64°F) metal temperature advantage (density corrected) at 982°C/248 MPa (1800°F/36 ksi) condition] as illustrated in Figure 14. Interestingly, in relatively short term burner rig test at 899°C (1650°F) it also exhibits extremely good hot corrosion resistance (Fig. 15). Additionally, longer term hot corrosion burner rig tests confirm the alloy provides performance similar to IN 792, while 6000 hour stress-rupture tests at 982°C (1800°F) demonstrate adequate phasial stability.

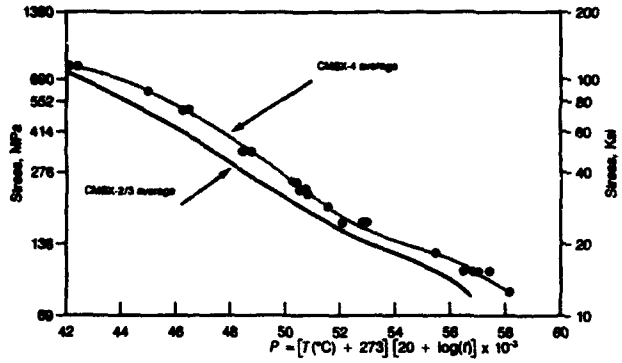

Figure 14 Average Larson-Miller stress-rupture strength of CMSX-4 vs. CMSX-2/3

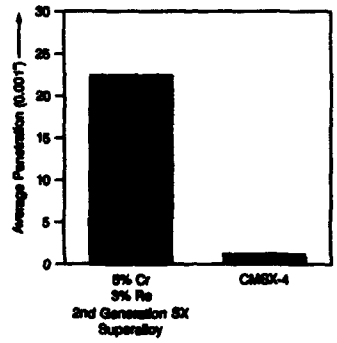

[uncoated, 899°C (1650°F), 1% sulfur, 10 ppm sea salt, 113 hour test]

Figure 15 Burner rig hot corrosion results for selected second generation SX superalloys (courtesy of Allison Gas Turbine)

Following solution heat treatment, the material is aged at sufficient temperature/duration to promote aligned γ' precipitates with an average 0.45 μm cubic dimension, with rounded corners, which tends to promote optimized creep rupture properties with the material. Examples of the desired γ' morphology/arrangement are provided in Figure 16.

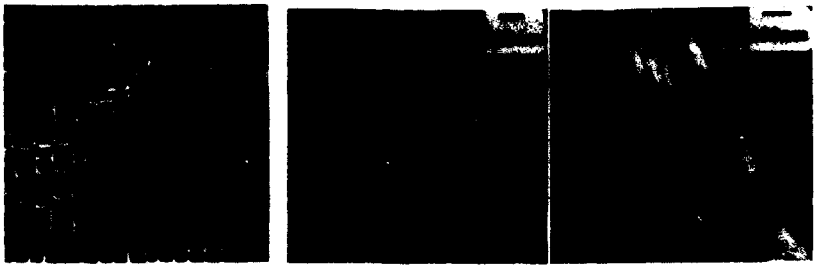

LE Airfoil Upper Longitudinal SEM Microstructure

TEM Microstructure

Figure 16 Typical alloy CMSX-4 cast turbine blade airfoil longitudinal microstructures (AGT 2nd stage solid blade)

The alloy also exhibits significantly better thermo-mechanical fatigue (TMF) properties relative to first-generation SX materials. Additionally, it appears that HIP treatment improves the higher refractory element containing alloys TMF properties by as much as 50%. Besides the obvious benefit achieved with pore closure, a portion of the improvement may be due to the resultant increase to alloy homogeneity.

Emerging environmental and thermal barrier coatings technology is expected to extend this category materials usefulness in the gas turbine engine for a minimum of 15 years into the future. Early work which illustrates the potential benefit achieved with an advanced overlay is provided in Figure 17.

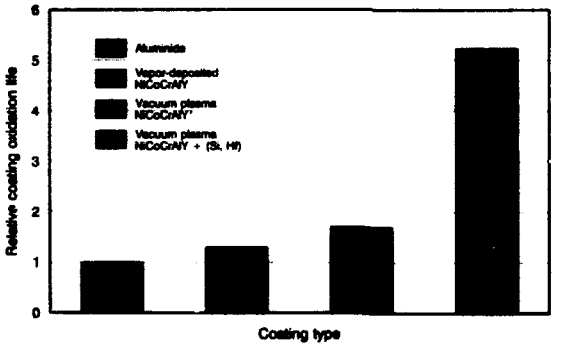

Figure 17 Coating performance of PWA 1480 at 1149°C (2100°F) [Burner rig oxidation] (4)

Similarly, low-level rare earth elemental addition to existing superalloys are shown to dramatically increase material bare oxidation resistance. Figure 18 shows the greater effectiveness of a moderate level of Y addition to the CMSX-3 (CMSX-3 MOD A) alloy in comparison to coating with an aluminide.

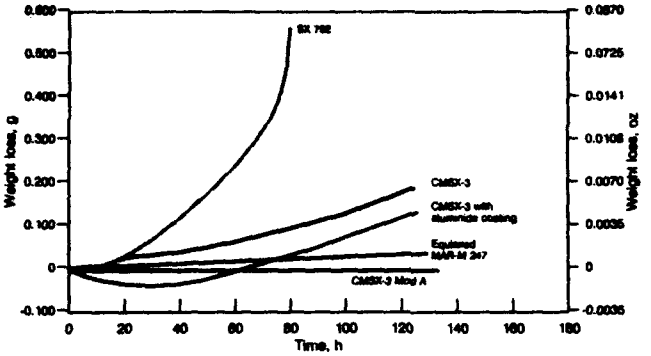

Figure 18 Dynamic, 1177°C (2150°F), cyclic oxidation (Courtesy of AGT)

3rd Generation SX Casting Alloys

Third generation single crystal casting materials should be designed with about 6 wt. % Re addition, which should result in much higher creep-rupture strength than attainable with 3% Re-containing alloys. Where the best 2nd Generation materials exhibit adequate γ' stability to 1149-1163°C (2100-2125°F), the 3rd Generation materials should exhibit a considerable extension of the capability.

With proper elemental balancing, the materials should exhibit CMSX-4-like castability, and should be capable of full γ' solutioning. They should be more dense than 2nd Generation materials, but the improved engineering properties achieved should tend to compensate the impact of the higher density.

They probably will not be as microstructurally stable as second generation single crystal materials at temperature above about 1079°C (1975°F), but should still offer extremely good ductility.

The typically desired increase to selected engineering properties sought to be achieved with 3rd Generation SX casting alloys follow: (a) creep strength -- 28°C (50°F) advantage to 1079°C (1975°F), relative to 2nd Generation SX materials. Similar creep strength at higher temperature, and then greater creep strength above 1163°C (2125°F), (b) hot corrosion -- Similar to 2nd Generation SX materials, (c) oxidation -- Similar to 2nd Generation SX, (d) tensile strength -- Similar or better than 2nd Generation SX, (e) impact strength -- Similar or better than 2nd Generation SX, (f) low cycle fatigue -- Relative to 2nd Generation SX, similar at low temperature, 2-3 times life at higher temperature, (g) notched low cycle fatigue -- Relative to 2nd Generation SX, 2-3 times better with high stress, similar with lower stress, and (h) high cycle fatigue -- 2-3 times better life than 2nd Generation SX.

Third generation single crystal superalloys will probably achieve aero turbine engine application within the next few years.

Future Superalloy Developments

DS columnar and SX alloy development efforts will continue to be stimulated by the aero and industrial turbine industry. The depth of activity will partially depend upon the investment casting industries ability to develop casting process improvements to make the production of large industrial components increasingly feasible.

The industry will expend considerable effort toward the turbine engine application of the second and third generation SX casting alloys during the next five years. Incremental improvements to second and third generation materials will maintain activity during this time period. Knowledge gained during the period could stimulate 4th Generation SX alloy development activity for specialized application, the result of which would be the further improvement to alloy creep-rupture and fatigue properties.

Summary

Superalloy development activity continues to provide the industrial and aeroturbine engine industries with new materials which exhibit capabilities extending improvement to turbine engine efficiency and output. The activity, coupled with process technology, minor element control and addition to superalloys, and coatings improvement, guarantee bountiful activity with superalloys into the 21st Century.

References

1. R.F. Decker, "Superalloys - Does Life Renew at 50?", 4th Int. Symp. on Superalloys (+ 1980) 2.
2. M. Gell and D.N. Duhl, "The Development of Single Crystal Superalloy Turbine Blades", Advanced High Temperature Alloys: Processing and Properties, American Society for Metals, 1986, 41-49.
3. L.E. Dardi, R.P. Dalal, and C. Yaker, "Metallurgical Advancements in Investment Casting Technology", Advanced High Temperature Alloys: Processing and Properties, American Society for Metals, 1986, 25-39.
4. M. Gell, D.N. Duhl, D.K. Gupta, and K.D. Sheffler, "Advanced Superalloy Airfoils", Journal of Metals, July 1987, 11-15.
5. F. Colucci, "Heat is Power", Aerospace Materials, Aug. 1992, 10-13.
6. R.F. Decker, "Strengthening Mechanisms in Nickel-Base Superalloys", (Paper presented at the Steel Strengthening Mechanisms Symposium, Zurich, 1969)
7. U.S. Patent Number 4,461,659 -- CM 247 LC Alloy.
8. K. Harris, G.L. Erickson, R.E. Schwer, "MAR M 247 Derivations: CM 247 LC DS Alloy, CMSX Single Crystal Alloys, Properties and Performance", 5th Int. Symp. on Superalloys (* 1984) 223-224.
9. U.S. Patent Number 5,069,873 -- CM 186 LC Alloy.
10. Chet T. Sims, private communications during tech mtg at CM, 1989.
11. G.L. Erickson, "Hf Effects in the CM 247 LC Alloy" (CM Product Evaluation Report, 1984)
12. G.L. Erickson, K. Harris, R.E. Schwer, "Directionally Solidified DS CM 247 LC - Optimized Mechanical Properties Resulting From Extensive Solutioning", (Paper presented at the 1985 ASME Gas Turbine Conference and Exhibit, Houston, TX, 18-21 March 1985)
13. E.W. Ross and K.S. O'Hara, "Rene 142: A High Strength, Oxidation Resistant DS Turbine Airfoil Alloy", 7th Int. Symp. on Superalloys (* 1992) 263.

14. G.L. Erickson, K. Harris, R.E. Schwer, "The Development of CMSX-5, A Third Generation High Strength Single Crystal Superalloy". (Paper presented at the 1985 TMS-AIME Annual Mtg, New York, NY, (Feb 1985)
15. D. Blavette, P. Caron, T. Khan, "An Atom-Probe Study of Some Fine-Scale Microstructural Features in Ni-Based Single Crystal Superalloys", 6th Int. Symp. on Superalloys (* 1988) 305-314.
16. A.D. Cetel, D.N. Duhl, "Second Generation Columnar Grain Nickel-Base Superalloy", 7th Int. Symp. on Superalloys (* 1992) 289.
17. Ibid. 13, 257-265.
18. K. Harris, G.L. Erickson, S.L. Sikkenga, W.D. Brentnall, J.M. Aurrecoechea, K.G. Kubarych, "Development of the Rhenium Containing Superalloys CMSX-4 and CM 186 LC for Single Crystal Blade and Directionally Solified Vane Applications in Advanced Turbine Engines", 7th Int. Symp. on Superalloys (* 1992) 297-306.
19. M. Gell, D.N. Duhl, A.F. Giamei, "The Development of Single Crystal Turbine Blades", 4th Int. Symp. on Superalloys, (+ 1980) 205-214.
20. C.S. Wukusick, (Final Report NAVAIR/N62269-78-C-0315, 25 Aug. 1980).
21. J.W. Holmes, K.S. O'Hara, ASTM STP 942, Phil., 1988, 672-691.
22. M.J. Goulette, P.D. Spilling, R.P. Arthey, "Cost Effective Single Crystals", 5th Int. Symp. on Superalloys (* 1984) 167-176.
23. D.A. Ford, R.P. Arthey, "Development of Single Crystal Alloys for Specific Engine Applications" 5th Int. Symp. * Oct. 1984 115-124.
24. E. Bachelet and G. Lamanthe, Paper presented at the National Symposium on SX Superalloys, Villard-de-Lans (France), 26-28 Feb. 1986.
25. T. Khan, M. Brun, Symp. on SX Alloys, MTU/SMCT, Munich, June 1989.
26. U.S. Patent Number 4,582,548 -- CMSX-2 Alloy.
27. U.S. Patent Number 4,721,540 -- CMSX-6 Alloy.
28. M. Doner, J.A. Heckler, (Paper presented at the Aerospace Tech. Conf., Long Beach., CA, Oct. 1985).
29. U.S. Patent Number 4,643,782 -- CMSX-4 Alloy.
30. A.D. Cetel, D.N. Duhl, "Second Generation Nickel-Base Single Crystal Superalloy", 6th Int. Symp. on Superalloys (* 1988) 235-244.
31. P. Caron and T. Khan, "Development of a New Nickel Based Single Crystal Turbine Blade Alloy for Very High Temperatures", (Paper presented at the First European Conference on Advanced Materials and Processes, Nov. 22-24, 1989 (Euromat '89), Aachen, FRG] Vol 1, 333-338.

+ Seven Springs Resort, Champion, PA, ASM,
* Seven Springs Resort, Champion, PA, TMS,

SESSION III

Advanced Processing

ADVANCED MATERIALS PROCESSING

by

Anthony F. Giamei

United Technologies Research Center MS 129-22, 400 Main Street,
East Hartford, CT 06108

Abstract

Advanced materials will require improved processing methods due to high melting points, low toughness or ductility values, high reactivity with air or ceramics and typically complex crystal structures with significant anisotropy in flow and/or fracture stress. Materials for structural applications at elevated temperature in critical systems will require processing with a high degree of control. This requires an improved understanding of the relationship between process variables and microstructure to enable control systems to achieve consistently high quality.

One avenue to the required level of understanding is computer simulation. Past attempts to do process modeling have been hampered by incomplete data regarding thermophysical or mechanical material behavior. Some of the required data can be calculated. Due to the advances in software and hardware, accuracy and costs are in the realm of acquiring experimental data. Such calculations can, for example, be done at an atomic level to compute lattice energy, fault energies, density of states and charge densities. These can lead to fundamental information about the competition between slip and fracture, anisotropy of bond strength (and therefore cleavage strength), cohesive strength, adhesive strength, elastic modulus, thermal expansion and possibly other quantities which are difficult (and therefore expensive to measure). Some of these quantities can be fed into a process model. It is probable that temperature dependencies can be derived numerically as well. Examples are given of the beginnings of such an approach for Ni_3Al and $MoSi_2$.

Solidification problems are examples of the state-of-the-art process modeling and adequately demonstrate the need for extensive input data. Such processes can be monitored in terms of interfacial position vs. time, cooling rate and thermal gradient. These quantities can then be used to predict dendrite sizes and solid state grain growth. Similar computations based on temperature compensated time can predict precipitation events or matrix phase change kinetics. This capability will lead to microstructural control as a primary objective of advanced materials processing.

Critical Issues in the Development of High Temperature Structural Materials
Edited by N.S. Stoloff, D.J. Duquette and A.F. Giamei
The Minerals, Metals & Materials Society, 1993

Introduction

Directional and single crystal solidification technology progressed rapidly in the 1970's due to the coalescence of the need for higher operating temperatures, a well structured set of processing trials leading to experimental thermal data and an improved understanding of the thermal environment. This understanding spanned the gaps from process variables to growth conditions to microstructure, and was due in large measure to computer simulations [1,2]. In particular, parameters such as superheat and withdrawal rate were shown to correlate strongly with thermal gradient, which controlled the columnar to equiaxed transition, thermosolutal convection and dendrite sizes [3]. During the eighties, models and post processing capabilities became much more sophisticated [4]. This occurrence was driven primarily by the improvement in computing power per dollar of investment in hardware and software. Applications were found for equiaxed castings as well [5].

Currently, welding is being investigated as a process for which we need improved understanding and control. This is an example of what can be accomplished today and clearly defines a path to the adaptive closed loop control systems which will be needed to process advanced materials for critical applications.

Computational Procedure

Finite Difference Method (FDM) welding analysis code described elsewhere [6] has been generated from the point of view of the welding engineer. The current version of this code (MICR13) has been specifically tailored to predict microstructural features as well as the macroscopic fusion zone widths on the upper and lower surfaces of a thin sheet. The calculations are done based on heat conduction within the plate. Convection in the liquid has been approximated by enhanced conduction. This approach was taken as convection was presumed not to dominate in this geometry. However, convection to the protective atmosphere (argon gas) and radiation to the environment are included. Temperature dependent thermal properties and the heat of fusion are incorporated. The heat input distribution can be either "top-hat" or gaussian in nature. The welding process is Gas-Tungsten-Arc (GTA) and vaporization effects from the Ti-6Al-4V alloy are included .

Calculations are typically full three dimensional transient computations including both heating and cool-down periods. Meshing is done automatically using a graduated rectilinear mesh according to one of three preselected procedures and datasets are archived. FDM calculations have been done for a test matrix of conditions; outputs consisted of screen output to monitor the run and visualization files for temperature, thermal gradient, cooling rate and grain size in the solid state (heat affected zone). Actual computing times run from one to ninety minutes per data set (depending on the fineness of the mesh), using a cluster size of six on the Alliant FX-2800 minisupercomputer and fully optimized code. Datasets have been built for austenitic stainless steel, Hastelloy-X and Ti-6Al-4V.

The code has routines for making preliminary estimates of the number of time steps required and to check out the input file for any errors or inconsistencies. The code was designed to be efficient, user-friendly and easy to compile (with various routines broken out and a makefile provided). The code is broken into "Chapters" to make it easier to follow the logic or to locate important sections. It also contains liberal comments, e.g. explanations of units. The data files have comments providing guidance for input data sequence and format. Typical cases can be run interactively in a Unix environment within minutes. A set of temperatures comes to the screen at a "survey point" to trace the progress of the solution. The code has been run on Convex, Stellar and DECstation platforms as well as on the Alliant system without difficulty.

The input is immediately archived and the output files are named in a consistent manner which allows easy reference to the archived input and gives the version number of the code used and data set letter for uniqueness, e.g. mv9b would refer to a volume file from version 9 of MICRO code, data set "b"; whereas ms6a would refer to version 6 of the MICRO code, data set "a" which would be archived as micr6a.inp. The runtime is saved in a "times" file with some salient comments about the unique features of the simulation. The user is encouraged to insert the date of the run as well. By convention, the "z" data set is for trials and can be overwritten to save space and the "t" data set is a timing data set for reference with different platforms, compilers, compilation levels and operating systems.

Output can be requested at all points within the volume at a given time ("volume" file) or at the top surface at all times ("surface" file). Much of the computed data is complex due to the dependence of scalar or vector quantities on both time and the three dimensional geometrical features. Scientific visualization has been an excellent tool to extract useful information from such simulations, e.g. weld penetration and mushy zone shape. Output can be requested in standard forms, which are compatible with several visualizers. Realistic colormaps, 3D graphics, varying degrees of transparency, specialized lighting effects and animation have been valuable tools to allow users to readily grasp meaning from large data files.

The "output" referred to above consists of two files; a co-ordinate file and a "quantities" data file. There are five quantities in the frequently used PLOT3D format being used; the first (Q1) is carried as a dummy with value 1, since it is used as a denominator to compute momentum vectors in viewers designed primarily for computational fluid dynamics datasets. There are three options for the remaining four quantities. The first is to carry dummy quantities of 2, 3, and 4 for Q2, Q3 and Q4 and set Q5 equal to the temperature at a grid point. The second is to compute the vector components of the scalar gradient field, G, and carry these as Q2 to Q4. The third procedure is to equate Q2 to the local grain size, Q3 to the local cooling rate and Q4 to the scalar temperature gradient, G as follows:

$$G = \mathrm{SQRT}\,(G_X{}^2 + G_Y{}^2 + G_Z{}^2) \qquad (1)$$

The "derivative quantities", thermal gradient and cooling rate, can be used to predict dendrite size [7], solidification microstructure [8] or welding defects [9]. The specific implementations are alloy dependent. The grain size calculation is done as a coarsening calculation based on diffusion control assuming a uniform initial grain size [9]. This data field provides a convenient record of temperature compensated time and can be modified to predict precipitate sizes or the shape of the "heat affected zone". Validation has been done by comparison with analytical solutions for the steady state problem, experimental data where available and with Finite Element Analysis using commercially available code [6].

In Fig. 1, an example is given of an isothermal surface at 1670 °K with a vector field attached to represent the thermal gradient using "icons", e. g. a set of arrows in this case. The mesh is shown as it intersects the isosurface to give an impression of the volume being modeled and to show the meshing strategy. This surface can be manually "walked" or automatically "swept" through to survey the data. The opening at the lower surface, for the case of the liquidus temperature isosurface, represents full penetration; this is considered as a desirable welding condition to achieve a joint with adequate strength and toughness. The MICRO welding code predicts instantaneous and smoothed upper and lower surface fusion zone widths, and these compare well with experiment for a variety of conditions [9]. Sectioning planes (x, y, z or any arbitrary orientation) can also be used to sample the data file. A user defined color map is used to provide realism in accordance with the colors associated with radiant heat. This feature improves the ability of the user to quickly relate to thermal data.

Figure 1. 1670 °K isothermal surface with thermal gradient vector "icons" attached.

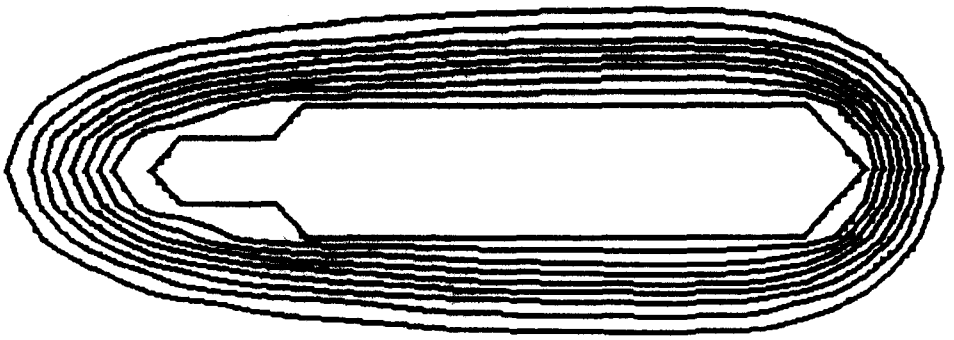

Figure 2. Grain size contour map for GTA welding simulation of Ti alloy thin plate (top view).

In Fig. 2, a grain size contour map is shown for the heat affected zone. These contours are similar to the isothermal contours, but do not collapse behind the heat source as it moves along. It appears that the GTA process comes to a near steady-state condition within a few seconds, and this is consistent with observation. Favorable comparisons have been made between computed and experimental grain size data for titanium alloys [9]. Fig. 3 shows a magnified isometric view of isograin size surfaces with some of the data "clipped" away for clarity. Data files are also generated for temperatures at preselected imaginary thermocouple locations in a "probe" file (for comparison with experimental data) and for the time dependence of grain size at any given survey point. An example of the latter data structure is shown in Fig. 4.

Future Process Modeling

The field of process simulation is maturing rapidly. The combination of advances in pre- and post-processing, analysis software and performance per unit price will broaden applications in the very near term. However, there are barriers as well as opportunities associated with wider use of process simulation in the manufacturing environment.

We need to recognize that modeling is done at several distinct levels, as shown in Table I. One barrier is human as well as digital communication between the various levels. The continuum, quantum and atomistic levels are relatively

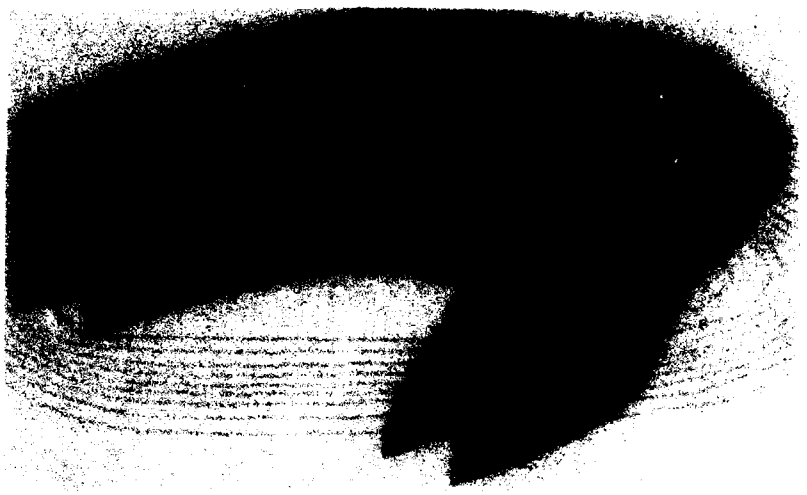

Figure 3. IsoGrainSize surfaces in heat affected zone (from 50 micron initial size).

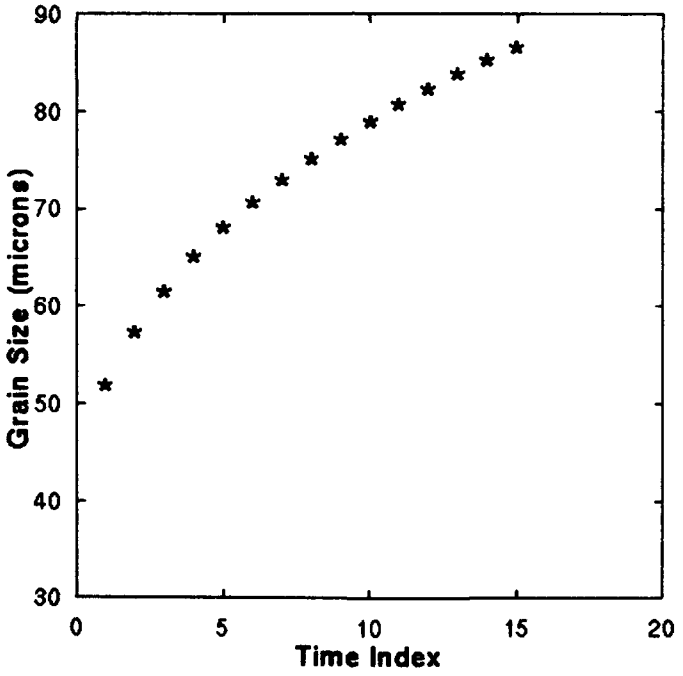

Figure 4. Time dependence of grain growth within heat affected zone.

mature at this point. However, the defect and grain levels need more emphasis. In some cases, available theories are inadequate as metallurgists and materials scientists have relied heavily on empirical correlations for many complex phenomena in the past. From the point of view of Materials Science, in order to predict the specific composition/process/structure/property relations, we need to improve microstructural models. This is particularly true in terms of predicting mechanical properties. Current mechanical models for material behavior are often inaccurate at large strain (above 3 to 5%). A physically based constitutive model would allow for simulation of large strain problems. Such problems are endemic in materials processing.

Table I. Levels of Modeling

TRANSPORT: Heat & Fluid Flow (Macro)
NON-UNIFORM: Composites (Meso)
MONOLITHIC/CONTINUUM: Solid Solutions (Meso)
MULTI-GRAIN: Texture (Micro)
DEFECT: Point/Line/Planar (Micro)
ATOMISTIC: Crystal Structure (Nano)
QUANTUM: Electrons (Pico)

We currently are able to compute the equilibrium crystal structure, lattice parameters, relative phase stability, thermal expansion coefficient, elastic compliance, Pierel's stress, Density of States, electron charge density (see Fig. 5), bond strength, diffusivity, activation energy, phase enthalpy, planar fault energies, residual stresses, specific heat, thermal conductivity, etc. from first principles or thermodynamics. The availability of these parameters has not pushed the technology sufficiently to have it applied routinely. What is needed is the PULL of application engineers, as was the case for single crystal superalloys. More effort is required in obtaining the temperature dependencies of thermophysical and mechanical properties.

Computed material properties can be used to "feed" process models. Most of these parameters are currently gathered from the literature or, in some cases, measured experimentally. Literature values are generally not available for the more complex systems. Laboratory measurements are typically time consuming and can be quite expensive. Both literature values and currently available measurements can be in error due to improperly prepared materials or non-standard techniques. At least simulated data will be systematic and consistent with known physical laws. Experimental data are still required for validation,however, but costs can be minimized.

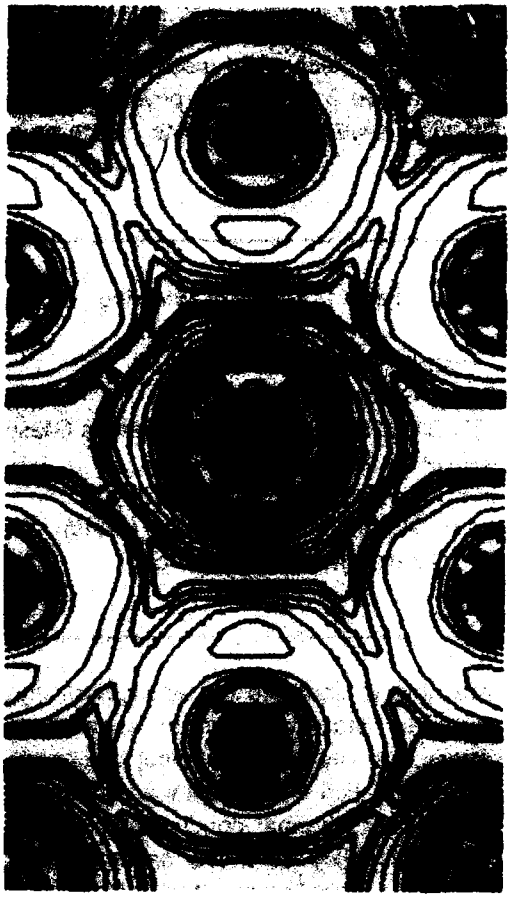

Figure 5. Electron charge density distribution on (110) plane.

Conclusions

A process control system requires a set of rules. Such rules can be extracted, at least in part, from simulations of the welding process. Welding is sufficiently complex so as to challenge current modeling capabilities. Nonetheless, predictions have been made for critical parameters, such as penetration and fusion zone taper as well as microstructural quantities, e.g. grain size in the heat affected zone. Simulations are consistent with experimental trends and can be tuned, where necessary, to provide a reasonably precise match. Heat conduction problems can be carried out very efficiently for a reasonably fine mesh. This approach seems to work well for thin plates and could be used to initialize an intelligent process control system. We are confident that other (simpler) processes can be accurately modeled as well in the near term.

The output of process simulation can be used to train a Knowledge Based System (KBS). The KBS can be very efficient, and can therefore drive a process control system. Currently, knowledge comes from experience or data. Conflicts within and between these sources of information must be resolved in order to establish unique linkage between input and output. In addition to data imperfections pointed out above, experience can be partially incorrect; and, of course simulations can be imperfect due to inadequate theory, inputs or numerical strategies. The KBS approach draws from the strengths of all three sources; it also circumvents discontinuities associated with vacation, shift change, retirement, etc. The KBS kernel can also draw from several sources of experience, for example. Thus it provides communication, continuity, accuracy and simplifies the path to optimization. This will replace the trial and error approach. Those that do not heed the call will not be competitive. Examples of the evolution of such a scenario already exist in the forging industry.

References

1) T. Pratt, F. Landis and A. Giamei, "Iterative Nonlinear Thermal Analysis of Directional Solidification Using a Fast Elliptic Solver", ASME Publication No. 80-HT-34 (1980).

2) A. Giamei, R. Mador, M. Duffy and P. Morris in Technology for Premium Quality Castings, TMS, Warrendale, PA (1988), pp. 15-28.

3) A. Giamei, E. Kraft and F. Lemkey in New Trends in Materials Processing, ASM, Metals Park, OH, (1976), pp 48-97

4) Modeling of Casting and Welding Processes IV, A. Giamei and R. Abbaschian, ed., TMS, Warrendale, PA (1988).

5) Modeling of Casting, Welding and Advanced Solidification Processes V, M. Rappaz, M. Ozgu and K. Mahin, ed., TMS, Warrendale, PA (1991).

6) A. F. Giamei, E. G-Miravete and J. H. Cowles, Jr., "A Comparison of Finite Difference vs. Finite Element Procedures for the Analysis of Three Dimensional Time Dependent Welding", in Proc. 3rd Int'l. Conf on Trends in Welding Research , Gaitinburg, TN, ASM, Materials Park, OH, (1992).

7) Kattamis, T. Z., Coughlin, J. C., and Flemings, M. C., "Influence of Coarsening on Dendrite Arm Spacing of Aluminum-Copper Alloys", Metallurgical Society of AIME Transactions, Trans. TMS-AIME, v. 239 No. 10, (1967), pp 1504-1511.

8) A. F. Giamei and E. G-Miravete, "Microstructural Predictors for Weld Processing", in MICRO/MACRO Scale Phenomena in Solidification, ASME Conf. Proc.AMD-Vol. 139, (1992) pp 121-125.

9) A. Giamei, E. G-Miravete, J. Cowles and M. Bruskotter in Modeling of Casting, Welding and Advanced Solidification Processes VI, T. Piwonka, V. Voller and L. Katgerman, ed., TMS, Warrendale, PA, (1993).

SYNTHESIS AND PROPERTY ATTAINMENT IN CERAMIC MATRIX COMPOSITES

William B. Hillig

Rensselaer Polytechnic Institute
Materials Engineering Department
Troy, NY 12180-3590

Abstract

Fiber reinforcement of ceramics is primarily intended to impart resistance to sudden catastrophic failure and increase toughness. Their incorporation complicates processing. All possible processes have significant limitations with respect to materials combinations and structures attainable. High temperature environmental considerations place further constaints. Performance data at elevated temperature is presented with emphasis on matrix cracking. Areas requiring further studied are recommended.

Critical Issues in the Development of High Temperature Structural Materials
Edited by N.S. Stoloff, D.J. Duquette and A.F. Giamei
The Minerals, Metals & Materials Society, 1993

Introduction and Background

Continuing progress towards more efficient, higher performance heat engines and other high temperature systems depends on the improvement of high temperature structural materials. Improved design is an equal partner to progress, but ultimately design becomes materials limited. There appears to be a nature-imposed temperature ceiling to the continuing evolution of "conventional" alloys. Intermetallics, ceramics and composites based on them offer promise in breaking through such a ceiling. If these new materials are to displace trusted conventional state-of-art materials, they must also show clear economic, or cost-effective performance advantage.

This paper considers the potential of ceramic matrix composites (CMCs) as structural materials. Monolithic ceramics typically offer high melting temperatures, low densities, oxidation resistance, and attractive elastic properties. Unfortunately, they usually fail in a catastrophic brittle mode. Very tough ceramics[1] have been produced by incorporating meta-stable ZrO_2 particulates into their structures. However, this enhanced toughness is only effective over a narrow temperature band. In contrast the toughening afforded by fiber reinforcement is not intrinsically limited by temperature. Hence, CMCs have attracted great interest. Translation of the potential of CMCs into practice will depend on how they fare in competition with other classes of materials, such as superalloys and metal matrix composites.

In the early 1970's fiber-reinforced glass and glass-ceramics were synthesized[2,3] that exhibited works-of-fracture comparable to that of brass. However, the toughness differs from that derived from ductility and involves some degree of matrix cracking. Nevertheless sudden catastrophic failure can be avoided and a minimum strength can be ensured. These early insights into ceramic toughening via fibers were not immediately embraced. Instead attention focussed on producing high performance, high reliability monolithic silicon carbide and silicon nitride ceramic turbines mainly for automobiles. However, these sophisticated materials remain vulnerable to accidental damage and catastrophic failure. The ultimate realization that tougher materials exhibiting "graceful failure" were needed has rekindled new attention on CMCs.

Great progress[4] has been made in understanding and predicting the toughness, strength and failure processes in ceramic composites based on micromechanical models. Refined experimental techniques continue to be developed to measure the basic physical properties required as inputs to these models. The present state of theoretical understanding outstrips the ability to produce ceramic composites that seriously challenge current state-of-art metallic structural systems. This is in part a tribute to designers and fabricators of metal parts which often have intricate labyrinth internal passages that allow efficient gas cooling. This approach has offset the need for materials having intrinsically higher temperature capabilities. However, as the properties, fabrication capabilities, and confidence in ceramic composites increases, and as the costs become competitive, the current state-of-art materials will be increasingly challenged and will ultimately be displaced.

This paper addresses those issues and barrier problems which are expected to pace that displacement. These include the limited palette of materials from which to produce the composites, processing limitations, and consensus as to what requirements are critical. Some limited data on mechanical performance are offered along with some commentary and recommendations for future emphasis.

Property Goals and Requirements

The performance advantages sought in CMCs relative to alternative materials are: (1) higher temperature capability in terms of strength, modulus, creep-resistance, thermal fatigue resistance, and environmental resistance; (2) lower density---if translatable into lower weight; (3) improved wear, corrosion, or radiation resistance; (4) reduced cost or reduced reliability on strategically scarce materials, such as chromium.

Although all of these goals are important, this paper takes the position that the most important contribution that ceramic composites can offer is to substantially extend the range of structural materials to higher temperatures than those imposed by nature on high temperature alloys. Such materials could open radically new design possibilities for high efficiency, high performance heat engines and other high temperature structures.

Composite Materials Options

Oxidation resistance and temperature capability *per se* are primary concerns. Thus, one strategy is to focus on the refractory oxides. Another is to seek out oxidation-resistant materials. The covalent silicides are high melting materials that are not only creep-resistant but also form very effective protective oxide layers. Hence, the refractory oxides and the covalent silicides have been attractive candidates for fibers and for matrices. The following sections discuss some of the constraints in producing suitable fibers for use in high temperature composites. Properties of reinforcing fiber are listed in Table 1.

Oxide Fibers

Continuous oxide fibers[5] for CMCs have been produced based on alumina, mullite, and zirconia among others. Fibers are typically spun from viscous colloidal suspensions and are later sintered to produce very fine-grained crystalline microstructures. The fibers can be produced in sufficiently fine diameters (3 to 20 μm) to be gathered into yarns and made into fabrics convenient for making laminated composites. However, the fine-grained structure of the fibers renders them prone to creep in accordance with the well-known proportionality[6] between the creep rate $d\epsilon/dt$ and $\sigma^n d^{-p}$ where σ is the applied stress, d is the grain size d, and n and p are exponents. Taking a stress of 200 MPa and a creep rate of 10^{-9}/sec as modest performance bounds for reinforcements for structural applications, then the upper use temperatures for the polycrystalline oxide fibers 1 is less than 1100°C as seen in Table I.

Single crystal oxide fibers can also be made as continuous fibers or as whiskers. Melt-grown single crystal sapphire fibers are relatively much larger in diameter 125 to 250 μm and more costly. This fiber exhibits substantially greater creep resistance[7], but must be processed by monofilament techniques.

Oxide fibers are intrinsically more susceptible to creep than are covalent non-oxide fibers. There has been an on-going search to identify and test compositions that may be more creep-resistant[8,9]. Yttrium aluminum garnet YAG appears to show promise[10] and melt grown fibers are just becoming available.

TABLE I Fibers for Ceramic Matrix Composites

Fiber	Diameter μm	Strength GPa	Modulus GPa	CTE 10^{-6} /°C	Approx. Max. Use Temp. °C
Al_2O_3(mono)	125-250	2.8	480	8.8	1450
Al_2O_3(poly)	20	1.4	380	9	<1100c
Al_2O_3/ZrO_2(poly)	20	2.1	380	9	<1100c
C	6-10	1.4-5.5	200-700	0	2200
Mullite(poly) (+B_2O_3)	10-12	1.9	220	5-6(est)	<1100c
SiO_2	10	1.4	70	0.5	1000
SiC(CVD)	140	3.5	425	4.5	1250±100(est)
SiC(Nicalon/ Tyranno)	10-1	2.4	190	3	1100-1300d
SiC(whiskers)	0.2-10	5-10	600	4.5	>1600

mono means monocrystal
poly mean polycrystal
c Temperature limit based on creep
d Temperature limit based on chemical degradation

Non-Oxide Fibers

The demonstration by Yajima[11] in 1975 that SiC could be produced by pyrolysis of a carbon and silicon containing resin was followed by a subsequent process for making fibers. These Nicalon TM silicocarbon fibers offered a higher temperature capability and high stiffness than other fibers then available and contributed significantly to the resurgence of interest in CMCs. These fibers are oxidation resistant, and are sufficiently fine in diameter to permit weaving. The processing causes these fibers to contain a considerable amount of internal oxygen, rendering them intrinsically thermodynamically unstable[12]. Thus, they begin to decompose and change microstructure at about 1100°C. Other fiber compositions such as Si-C-O-Ti, Si-O-N, Si-O-C-N have been produced, but all experience similar instability. The Nicalon fiber does creep once a temperature-dependent stress threshold is exceeded.

Silicon carbide itself is not subject to such instability problems. Various efforts to convert the starting resins into SiC fibers without the need to introduce oxygen into the system are showing promise. However, no fibers made by these approaches are yet available. Another route under development for producing SiC fibers is analogous to that for making polycrystalline oxide fibers, e.g., filaments are formed from a vehicle in which very fine SiC particulates are dispersed, followed by sintering.

Chemical vapor deposition CVD and whisker growth[13] by either vapor-liquid-solid VLS or vapor-solid VS offer further options for producing SiC filaments. The CVD process requires deposition of SiC from a suitable combination of reactive gases onto a hot filamental core. Accordingly, this process results in fibers, comparable in size to the single crystal sapphire fibers. Thus, composite fabrication with these CVD fibers requires their

handling as individual filaments. Although these fiber are thermodynamically stable, residual unreacted Si in the fibers appears to be responsible[14] for their creep above 1250°C.

A new process for making SiC whiskers, originally from rice hulls[15], has led to the ready availability of the whiskers as reinforcements in ceramic and metal matrix composites. Their diameters range from about 0.1 to 1 μm and their aspect ratios are of the order of 100. Limited quantities of larger, longer, more fiber-like SiC whiskers have been produced either as a by-product from the making of SiC, or as a result of carefully controlled laboratory processes. The low cost and availability of "rice hull" whiskers has had an impact on CMCs comparable to that of the polymer-derived silicocarbon fibers. These very fine whiskers are now recognized as being potent carcinogenic hazards.

Other reinforcements such as CVD TiC fibers and Si_3N_4 and Sialon whiskers have been produced, but these have not yet been widely used in CMCs.

Matrices and Coatings

Because of the limited fiber choices, matrices and processes must often be chosen to accommodate the fibers. If the fibers and the matrix are chemically reactive or mutually soluble, then a barrier layer coating is required to prevent damage to the fiber or to avoid sintering to the matrix. Considerations of interactions[16] under the additional influence of the environment, discussed later, indicate that in most composites both the fibers and the matrix should be either oxides or non-oxides, but not mixtures of the two.

Matching the thermal expansivities of the matrix and reinforcement are needed to minimize thermal stresses and thermal cycling problems. A mismatch of 1×10^{-6} in the expansivities results in a strain mismatch of about 0.1% during thermal excursions of the magnitude expected in high temperatures CMCs. Such strains can not only damage the composite, but also affect toughness of the composite via the fiber-matrix frictional coupling. Some of the possible fiber-matrix combinations can be considered by comparing Tables I and II.

Fiber coatings needed to prevent fiber degradation during processing or service must be benign towards the fiber and the matrix, and resist environmental attack. The coatings also affect the fiber-matrix coupling. Materials used for coatings[17] include carbon, SiC, BN, and SiO_2. These and other coatings can be deposited by chemical vapor deposition, sputtering, and other processes.

Fabrication

The effectiveness of "reinforcements" to improving the toughness and strength of ceramic composites increases in the order: particulates, discontinuous randomly oriented fibers, oriented fibers, and layered aligned continuous fibers. This is roughly the order of the difficulty of making the composites.

Pressureless sintering of compacted powder shapes is the most important process for making monolithic ceramics. This process necessitates substantial shrinkage of the porous starting shapes as the void space is eliminated. Although sintering is already some-what inhibited[18] by even small additions of second phase particulates, sintering can nevertheless take place.

Table II Matrices for Ceramic Composites

Material	Strength MPa	Modulus GPa	CTE 10^{-6} /°C	$K_{I,c}$ MPa $m^{1/2}$
Al_2O_3	350-700	480	8.8	3-5
ZrO_2	150-350	240	13.5	5.6-6.1
Mullite	180-200	145	5.3	2-3
Zircon	200-360	195	4.3	2.5
SiO_2 gl	---	70	0.5	1
Borosilicate gl	---	70	3.5	<1
SiC	500-800	425	4.5	3-6
Si_3N_4	600-850	385	3	4-7
LAS	50-250	84	2.0	2
CAS	---	88	5.0	2
$MoSi_2$	---	400	8.5	5

gl means glass
LAS means lithium aluminum silicate glass-ceramic
CAS means calcium aluminum silicate glass-ceramic

Introducing fibers (or platelets) that do not change dimensions during processing inhibits sintering even more. Thus, other techniques are often employed to achieve dense structures or to preserve the shape and size of the starting material. These processes include management of the aspect ratio of the "reinforcement" phase, pressure-assisted sintering, and various approaches for transporting material into the void spaces. These processes involve compromises which affect the properties, the range of feasible material systems, or the size and shape of the final composite. The processes can be categorized into (1) consolidation methods, and (2) infiltration methods.

Consolidation Methods

Aspect Ratio Management

Although fibers inhibit sintering, the smaller their aspect ratio, the closer they approximate particulate additions, and the greater the final density which is achievable by pressureless sintering. However, decreasing the fiber aspect ratio, for example by milling the fibers, can affect the composite toughness. The magnitude and sign of the effect depends on whether pull-out or crack deflection are the major toughening mechanisms. Thus, this approach depends on balancing the penalty in strength, toughness, and environmental encroachment, due to incomplete densification, against the possible loss in properties due to fiber shortening. Milewski[19] has studied the packing efficiency of solids consisting of mixtures of rods and sphere as a function of their volume fractions, sizes, and the aspect ratio of the rods. These results can provide useful guidelines for optimizing densification.

Pressure Assisted Sintering

Hot pressing HP and hot isostatic pressing HIP can produce dense composites. HP requires special high temperature dies and presses as well as controlled atmospheres. Both

HP and HIP work well depending on the creep-flow characteristics of the matrix and providing that the volume fraction of the reinforcement is not so large as cause the structure to "lock up." Excessive pressure can result in fiber failures. The shapes which can be made are limited by what die shapes are feasible.

HIP requires that the outer surface of the specimen be impermeable to the pressurizing gas. If the pores are closed then the specimen acts as its own envelope allowing considerable shape flexibility. Otherwise the sample must be "canned" in a suitable envelope which can restrict the shapes possible. Thus, under favorable conditions, shape integrity and predictable shrinkage may be achievable. In less favorable cases, a bulk shape is produced that requires further machining.

Infiltration Methods

Organometallic and Sol-Gel Precursor Infiltrations

Polymers[20] capable of being subsequently converted into a wide range of "ceramics" are under active exploration and development. The use of liquid phase chemistry to produce ceramics offers leads to compositional homogeneity, alloying flexibility, and processing possibilities and convenience not available by conventional powder-based technologies. These fluid precursor materials can also be used to produce the composites, for example, by infiltrating the resin into a porous compact comprised of the reinforcement.

Colloidal sols and ultrafine suspensions of ceramics offer much the same advantages and processing options as do the organic precursors and can also be used to provide composite matrices by infiltration[21] into porous preform structures. Such sols are often produced by hydrolysis of organometallic precursors such as tetraethylorthosilicate TEOS or aluminum alkoxides.

Because of the volumetric shrinkage that accompanies the conversion from the liquid precursor state to the ceramic, these processes do not lead to fully dense composites. The shrinkage often leads to internal matrix cracks and multiple reinfiltrations and conversions are required to achieve high densities.

Glass and Glass Ceramics

Because of their viscosity, glasses are particularly well suited for making fully dense composites[22]. By applying pressure to the glass and fiber reinforcement combination, in the working temperature range of the glass, the glass can be made to flow and to encapsulate the fibers. This technique is especially advantageous if the glass can be converted into a fine grained crystalline ceramic. The glass-ceramics selected are usually low thermal expansivity materials.

Among the various ways of combining the glass and the fibers is to coat the fibers with a slurry of powdered glass. The coated fibers are fixed in the desired arrangements, and then densified by heating. Another process is transfer molding: the dry fibers are placed in a die cavity and the molten glass is forced into the cavity under pressure, wetting and encapsulating the fibers. United Technology Corporation and Corning Glass Works, Inc. have both been actively developing these and related processes and have demonstrated remarkable property and process achievements. A wide range of carefully controlled and

reproducible shapes with specified fiber architectures can be produced.

The chief limitation of composites produce by this process arises from either the softening temperature of the glass, or the solidus temperature of the glass-ceramic at which point creep becomes a problem. The upper bound[23] of this temperature limit appears to be about 1150°C. It is possible that glass-ceramic compositions can be found having higher solidus temperatures

Chemical Vapor Deposition/Chemical Vapor Infiltration

Many matrix materials such as SiC, TiC, Al_2O_3, and ZrO_2 can be deposited from gases or combinations of gases under specific pressures, temperatures, and compositions, that are thermodynamically favorable. Thus, matrices can be introduced[24] into porous preform structures comprised of the reinforcement. This near-net-shape process has successfully produced large intricate shapes. For example turbine wheels of Nicalon fibers which are bonded by a CVI-produced SiC matrix have been achieved.

Such deposition requires transporting the gaseous reactants and by-products into and out of the pores. Because a continuing supply of gases is needed, fully dense structures cannot be produced by this process. Uniform deposition within the porous structure requires conditions under which the reaction is kinetically controlled at the deposition surface. Otherwise the process becomes choked off at the surface. Slow, carefully controlled processing is required. Reasonable production rates are achieved by batch processing in which many parts are infiltrated simultaneously over a long period of time.

The deposition rate has been shown to be substantially increased by means of forced gas flow, and temperature gradients. However, these techniques also impose limitations on the geometries which can be processed in this way.

Directed Oxidation

This process[25], also known as the Lanxide™ process, involves the simultaneous oxidation of a molten metal such as aluminum, and the simultaneous wicking of the molten metal through channels in the oxide layer. Thus, the oxidation occurs at, or on the continually replenished gas/melt interface. Alloying additions are found to enhance the kinetics and to modify the structure. If a porous mat of reinforcements, such as SiC fibers, is placed on the growing surface and constrained to a given geometry, the oxidation products can grow through the reinforcement enveloping it. Thus, this process can produce complex shapes of controlled size.

The process takes place at lower temperatures than are normally required for conventional sintering. Thus, some fibers, which might otherwise be degraded at higher sintering temperatures, can be used in this process. This process is restricted to those metals that show this kind of oxidative (or similar reactions with other gases such as nitrogen) behavior. Since capillarity is needed to maintain the supply of reactant to the surface, the resultant structures will either contain residual metal in channels, or porosity if the metal is later drained off.

Melt Infiltration

This near-net-shape process[26] for producing fully dense ceramic matrix composites is somewhat like the glass processes described above. However, the infiltrant typically is a single component material, having a sharp melting or decomposition temperature. The melt should be fluid and easily crystallizable with no tendency to form residual glasses.

In reactive melt infiltration, the porous preform reacts chemically with the melt, usually exothermally. In non-reactive infiltration no chemical interaction occurs. The reactive process has been used to make dense structures of siliconized SiC by infiltrating molten Si into a porous preform consisting of SiC and carbon particulates and/or fibers. The carbon becomes substantially converted to SiC. The non-reactive infiltration process has been demonstrated using by infiltrating various silicates and aluminosilicates, and refractory fluorides into porous SiC as well as aluminates into magnesium spinel.

The advantages of this generic process are the shape and dimensional flexibility and control, the expected absence or low content of glassy phases at high temperature, and the high solidus temperatures of the infiltrant, so that the appearance of creep-enhancing liquid phases at low temperatures is avoided. On the other hand because the infiltrants must be heated above their melting temperatures, the processing temperatures tend to be high compared with other processes. Thus, this process is limited by considerations of chemical compatibility, and matching of thermal expansivities between the preform and the infiltrants, and the sensitivity of the reinforcements to the processing temperatures.

Environment

High temperature structural materials will in most instances be exposed to chemically active gas environments. In reducing environments, bulk oxides such as Al_2O_3 may form volatile species; active oxidation of non-oxides such as SiC or Si_3N_4 may occur as a result of SiO volatilization instead of the formation of SiO_2 oxide films that normally slow down the oxidation process of various silicides. When the environment is oxidizing, self protecting oxide films form on such silicides as SiC or Si_3N_4 including SiC fibers.

However, when such silicides are combined with oxide constituents in a composite, the protective oxide barrier layer may be defeated because of interaction between the SiO_2 and the oxide constituent. This effect is attributable to an increase in the oxygen permeability of the oxidation product. For example, in composites[27] in which SiC was embedded in Al_2O_3 or in mullite matrices, the oxidation layer thickness formed in a given time ranged from 10 to about 50 times that of the layer on monolithic SiC. Enhanced oxidation of SiC has also been observed when the matrices were strontium silicate or strontium aluminum silicate. No such accelerated oxidation would occur in composites where both the reinforcement and the matrix are both silicides that oxidize to form only SiO_2, examples being SiC-reinforced $MoSi_2$ or Nicalon fibers embedded in a CVI-deposited SiC matrix. Oxidation is not an issue if both the reinforcements and the matrix are oxides.

Exposure of oxidizable fiber coatings to environmental attack can have dramatic effects on the fracture process and toughness. Such effects become prominent when the gas environment has access to the interior of the composite as a result of matrix cracking.

The above observations argue against composites in which the fibers and the matrix are mixed oxide/non-oxide systems. Such systems would appear to require an external oxygen barrier that envelopes the entire body.

Performance Experience

Prewo, Brennan and coworkers at the United Technology Research Center have produced[22] much of the most widely used systematic information available on mechanical and microstructural properties of CMCs. Their work demonstrated that tough CMCs can be made reproducibly, by practical processes, in a wide range of shapes, sizes, and fiber arrangements, and with impressive properties. Their optimized system of choice was a modified LAS glass-ceramic reinforced with continuous unidirectional Nicalon fibers or Nicalon fabric. Composites reinforced with layered fabric were shown to maintain a tensile strength of about 400 MPa up to 1400°C, and apparent failure strains of about 1.1% to at least 1000°C when tested in an inert environment. Such a large failure strain is indicative of significant toughening. However, both the strength and failure strain were found to be diminished when the tests were performed in air.

The LAS/Nicalon fiber system and related systems have been further studied by a number of independent workers and have provided the most comprehensive data against which theoretical models have been tested. In fact much effort is being directed at testing or providing basic information regarding either elastic property models or micro-mechanical models of toughness, matrix and fiber failure, and fiber-matrix coupling at room temperature.

Considerable information is also available on several glass matrix composites, SiC whisker reinforced ceramics, and composites produced by *CVI*. *CVI*-produced SiC matrix composites reinforced by a coated, layered Nicalon fabric have been extensively studied and made into a variety of complex shapes. These composites do not exhibit brittle failures. Testing in a non-oxidizing environment has given [ ] impressive apparent notched beam fracture toughness values in the range of 25 to 30 MPa $m^{1/2}$ independent of temperature up to 1400°C. The ultimate strengths dropped off above 1100°C presumable due to degradation of the unstable reinforcing fibers. The properties of the composite, which was about 70% dense and which had an open porosity of 10%, were seen to be sensitive to the test environment. The bend strength measured in air was temperature independent up to 1100°C, but dropped off markedly at higher temperature.
Other data have been reported from a few exploratory studies of new composite systems, as well as from characterizations of "practical" CMCs. These data typically are standard property measurements, usually obtained in flexure, such as elastic moduli, ultimate strength, and toughness.

Although matrix cracking has been theoretically studied in considerable depth[36,37,38] for idealized unidirectional fiber reinforced CMCs. Limited information[39] is available on the stress at which the matrix first fails. Mechanical property data as a function of temperature are even rarer.

Thus, the data of particular interest to this paper are the first matrix cracking stress (i.e., the stress at which matrix failure occurs, also known as the proportional limit), and mechanical properties as a function of time, and temperature. Table III is a compilation of composite properties of unidirectional composites, including first matrix cracking stress,

and as a function of temperature when available. Table IV summarizes data for laminated prototype CMCs. These latter data show the dichotomy between idealized structures suited for property modeling and composites based on processing convenience.

TABLE III Mechanical Properties of Unidirectional Ceramic Matrix Composites

Fiber/Matrix	Temp. °C	v_f GPa	E MPa	σ_o MPa	σ_u KJ/m^2	WOF MPa	$K_{I,c}$ m$^{\frac{1}{2}}$	Ref.
Nicalon/LAS	25	.50	130	290	640	---	16	27
	"	"	143*	290-370	---	---	---	28
Nicalon/CAS	"	.35	124	200	444	---	---	39
SCS-6/Boro-silicate glass	"	.17	120*	78	---	---	---	28
Nicalon/Boro-silicate glass	"	.49	120	---	1245	70	---	30
Carbon/Boro-silicate glass	"	.45	205*	360	572	---	---	28
SCS-6/RBSN	"	.30	193	227	682	---	---	38
SCS-6/Mullite	"	.25	87+8	---	730±50	---	---	34
SCS-6(w/BN)/ Mullite	"	.25	78±20	---	760±100	---	---	34
SCS-6/Zircon	25	.25	244±6	287±28	700±56	18±4	---	33
	1160	.25	281	248	348	3.8	---	"
	1315	.25	108	262	262	2.3	---	"
SCS-6(w/BN)/ Zircon	25	.25	235±26	357±43	681±36	25±5.6	---	33
	1160	.25	228	267	368	2.7	---	"
	1315	.25	147	---	315	2.9	---	"

σ_o is the first matrix cracking stress
σ_u is the ultimate strength of the composite
* Rule of mixtures value
SCS-6 is CVD SiC fiber
SCS-6(w/BN) is BN-coated CVD SiC fiber
RBSN is reaction bonded Si_3N_4

Discussion

Aside from the paucity of property data at high temperature, the most striking generalization evident from Tables 3 and 4 is that fracture toughness is markedly diminished either at high temperatures *per se* or by the combination of exposure to an oxidizing environment and high temperature. As discussed above, test environment has a significant effect in the LAS/Nicalon and the SiC/Nicalon composites. It appears that matrix cracking allows the environment to attack the fiber coating, allowing the fiber-matrix coupling to become much stronger.

On the other hand, the tests on SiC/zircon composites were done in an inert or slightly

reducing atmosphere, so that attack of the fiber-coating following matrix cracking would be suppressed or mitigated. Whereas the first matrix cracking stresses were only modestly reduced with increasing temperature, the works of fracture were reduced 5-fold. It is important to note that the experimental stress-strain curves remained continuous and did

TABLE IV Mechanical Properties of Lamellar or Cloth Reinforced Ceramic Matrix Composites Tested in Tension

Fiber/Matrix	Temp. °C	v_f GPa	E MPa	σ_o MPa	σ_u K/m^2	WOF MPa	$K_{I,c}$ m$^{\frac{1}{2}}$	Ref.
Nicalon/CAS $[0/\pm45/90]_s$	25	.40	115	37.5	125.6	---	---	29
Nicalon/CAS $[0/90]_{2s}$	25	.40	122.2	34.7	120.7	---	---	"
Nicalon/CAS $[\pm45]_{2s}$	25	.40	104.6	38.2	92.7	---	---	"
Nicalon/SiC Cloth; CVI	25	---	---	10	146	13±5	---	35
	1000*	---	---	35±25	62	0.25	---	"
Nicalon/SiC Cloth; CVI	25	---	---	12±10	127	10±1	---	35
	1000*	---	---	20±8	38	0.2	---	"
Mullite/SiC Cloth; CVI	25	---	---	7	43±5	0.15	---	35
	1000*	---	---	20±6	33±7	0.4	---	"
Nicalon/Si_3N_4 Cloth; CVI	25	---	---	5.5	81±5	3.8	---	35
	1000*	---	---	15.5	21±1	0.2	---	"
Mullite/Si_3N_4 Cloth; CVI	25	---	---	13±3	97±3	10	---	35
	1000*	---	---	5.5	22±6	9±2.5	---	"
Nicalon/CAS Cloth	25	---	---	21	200±10	28	---	35
	1000*	---	---	10.5	73±6	1	---	"
Nicalon/Al_2O_3 Cloth; D/O	25	---	---	14±4	236±50	26±11	---	35
	1000*	---	---	9	116±10	5.5±4.5	---	"

σ_o is the first matrix cracking stress
σ_u is the ultimate strength of the composite
* Heated RT to 1000°C over 1 hr. followed by 2 hr. hold at temperature in air.
D/O means directed oxidation

not show abrupt failure. The stress-strain dependence is expected to be a complex function of the fiber strength distribution and the fiber-matrix coupling. However, the relative insensitivity of the matrix cracking stress to temperature suggests that none of the parameters in Eq.1 is strongly affected by temperature. It would be surprising if the Weibull modulus for the fiber strength (i.e.flaw distribution) were a strong reversible function of temperature. Indeed the fibers had been previously exposed to the test temperatures during fabrication. Thus, the decrease in the work of fracture which suggests an increase in the fiber-matrix coupling with increasing temperature is at variance with the insensitivity of the matrix cracking stress.

This discussion points the need for (1) careful data on combined high temperature and environmental influences on the behavior or CMCs, and (2) further study of matrix failure. The latter failure allows ingress of the environment into the composite which in turn affects the failure of the overall composite. Comparison of the matrix failure stresses for Nicalon/LAS, Nicalon/CAS, and the carbon/borosilicate glass composites provide some deviations from the expectations based on Eq. 1, *viz.* the absolute values are about as expected, but not the ranking of the relative values. Thus, further critical examination of the matrix cracking phenomena is recommended.

The cloth laminate composites showed up to a 50-fold decrease in fracture energy when tested at high temperature in air after a two to three hour holding at temperature. However, in one case there was nearly no reduction. Because of the complex fiber geometry and the complications arising from oxidation effects, these results are difficult to reconcile quantitatively with theoretical models. However, the data point out that room temperature toughness does not automatically translate into toughness at high temperature.

Understanding and predicting matrix cracking and the processes affecting high temperature failure are extremely important. These issues will determine the realizable advantages of CMCs versus the competing materials. The potential of CMCs as a new generation of high temperature structural materials is not commensurate with the emphasis given to the relevant properties that are likely to determine the outcome of that competition. Whereas "graceful failure" and the reserve provided by the ultimate strength is important, it must be the integrity of the matrix, the crack-arresting capability and the environmental resistance all at high temperature that must be the primary concerns.

In ductile metals plastic deformation at the tip of an initially atomically sharp crack would in effect decrease the stress intensity factor at the crack tip, and may require an increase in the applied stress as the crack extends until a steady state tip geometry is attained. The analog in a composite is R curve behavior in which crack bridging increases as the crack advances , decreasing the stress intensity factor at the crack tip and energy is dissipated by fiber pullout . This increase in toughness with crack extension offers the nearest behavior to ductility. Modeling and predicting this R curve behavior is difficult. However, this phenomenon is recommended for special attention as it appears capable of leading to useful toughening capable of inhibiting matrix failure.

Conclusions and Summary

Assuming that the greatest advantage that CMCs offer is in the area of high temperature structural materials, it follows that they must ultimately compete with state-of-art superalloys with respect to (1) upper use temperature, (2) structural reliability, (3)

environmental resistance, (4) forming capability, and (5) cost.

These considerations are interconnected. Use temperature considerations suggest 1100°C as a lower bound. This temperature may be imposed by phase equilibrium considerations, the availability of satisfactory fibers, and other factors relating to (2), (3), and (4).

Structural reliability entails matrix integrity, damage tolerance, as well as other properties such as creep and fatigue resistance, which lie beyond the scope of this paper. Clearly the onset of matrix cracking must define the structural use limit of the composite. The energy consumed in "graceful failure" is of secondary interest to the use as a structural material.

As already discussed, combining oxidation resistant non-oxide constituents with oxide constituents may result in impaired environmental resistance to oxidation. Other considerations such as vulnerability to the ingress of environmental gases into open porosity and matrix cracks should influence the choice of constituents and the fabrication process.

Each of the processes for making CMCs has advantages and disadvantages and are better suited to some systems rather than others. If the focus is indeed to be on high temperature systems then some processes will be weeded out. Cost considerations will weed out others and may impose compromises with performance. There is great advantage to the capability of making a wide range of shapes, with specified fiber architectures, and with minimal subsequent finishing. At least four processes meet these requirements: glass-ceramics, melt infiltration, CVI and directed oxidation. The first two result in fully dense materials. However, the importance of a fully dense structure has not been clearly established.

References

1. A.G. Evans, and R.M. Cannon, "Toughening of Brittle Solids by Martensitic Transformations", Acta Metall. Mater., 34, 187-206 (1986).

2. I. Crivelli-Visconti and G.A. Copper, "Mechanical Properties of a New Carbon Fibre Material", Nature, 221, 754 (1969).

3. J. Aveston, "Strength and Toughness in Fibre Reinforced Ceramics", in Proceedings of Conference on Properties of Fibre Composites, 1971, IPC Science and Technology Press, Guildford, England.

4. W.B. Hillig, "Strength and Toughness of Ceramic Matrix Composites", Ann. Rev., Mater. Sci., 17, 341-383 (1987).

5. H.G. Sowman and D.D. Johnson, "Oxide Fibers from Chemical Ceramic Processes", in Fiber Reinforced Ceramic Composites, ed. K.S. Mazdiyasni, 1990, Noyes Publications, Park Ridge, NJ.

6. R.W. Cannon and T.G. Langdon, "Review of Creep in Ceramics", J. Mater. Sci., 18, 1-50 (1983).

7. L.E. Jones and R.E. Tressler, "The High Temperature Creep Behavior of Oxides and Oxide Fibers", NASA Contractor Rept. 187060, 1991.

8. G.S. Corman, "High Temperature Creep of Some Single Crystal Oxides", Ceram. Eng. Sci., Proc., 12, 1767-1773 (1991).

9. W.B. Hillig, "A Methodology for Estimating the Mechanical Properties of Oxides at High Temperatures", J. Am. Cer. Soc., 76, 129-138 (1993).

10. G.S. Corman, "Strength and Creep of Single Crystal YAG Fibers", Oral Presentation, 94th Annual Meeting of Amer. Ceram. Soc., Paper 64-S11-92.

11. S. Yajima, J. Hayashi and M. Omori, "Continuous Silicon Carbide Fiber of High Tensile Strength", Chem. Lett. 1975, 931.

12. K.L. Luthra, "Thermochemical Analysis of the Stability of Continuous SiC Fibers", J. Am. Cer. Soc., 69, C231-C233 (1986).

13. J.J. Petrovic and G.F. Hurley, "Vapor-Liquid-Solid (VLS) SiC Whiskers: Synthesis and Mechanical Properties", pp.93-120, see Ref. 4.

14. E. Lara-Curzio, "Thermomechanical Characterization of Silicon Carbide Fibers at Elevated Temperatures", Ph.D. Thesis, Rensselaer Polytechnic Institute, August 1992.

15. J.-G. Lee and I.B. Cutler, "Formation of Silicon Carbide from Rice Hulls", Am. Ceram. Soc. Bull., 54, 195-198 (1975).

16. K.L. Luthra, "Chemical Interactions in High-Temperature Ceramic Composites", J. Am. Cer. Soc., 71, 1114-1120 (1988).

17. J. Chin, "Application of Vapor Deposition Technology to the Development of Ceramic-Matrix Composites", pp.342-392, see Ref. 4.

18. M.N. Rahaman, "Science of Sintering Ceramic Matrix Composites", in Processing of Ceramic and Metal Matrix Composites, Vol. 17, Proceedings of the Canadian Institute of Mining and Metallurgy, pp.71-79, H. Mostaghaci, ed., 1989, Pergamon Press, New York.

19. J.V. Milewski, "Efficient Use of Whiskers in the Reinforcement of Ceramics", Adv. Ceram. Matls., 1, 36-41 (1986).

20. T. Mah, Y.F. Yu, E.E. Hermes and K.S. Mazdiyasni, "Ceramic Fiber Reinforced Metal-Organic Precursor Matrix Composites", pp.278-3120, see Ref. 4.

21. B.R. Marple, S.J. Glass and D.J. Green, "Ceramic Composites by Infiltration-Processing", pp.120-31, see Ref. 18.

22. K. Prewo, "Glass and Ceramic Matrix Composites Present and Future", in High Temperature/High Performance Composites, vol. 120, Materials Research Society Symposium Proceedings, 1988, pp.145-156, F.D. Lemkey, S.G. Fishman, A.G. Evans and J.R. Strife, Materials Research Society.

23. K.W. Prewo, J.J. Brennan and G.K. Layden, "Fiber Reinforced Glasses and Glass-Ceramics for High Performance Applications", Am. Ceram. Soc. Bull., 65, 305-313 (1986).

24. W.J. Lackey and T.L. Starr, "Fabrication of Fiber-Reinforced Ceramic Composites by Chemical Vapor Infiltration: Processing, Structure and Properties", pp.397-450, see Ref. 4.

25. M.S. Newkirk, A.W. Urquhart and H.R. Zwicker, "Formation of Lanxide™ Ceramic Composite Materials", J. Mat. Res., 1, 181-189 (1986).

26. W.B. Hillig, "Melt Infiltration Process for Making Ceramic Matrix Composites", pp.260-277, see Ref. 4.

27. K.L. Luthra and H.D. Park, "Oxidation of Silicon Carbide-Reinforced Oxide-Matrix Composites at 1375° to 1575°C", J. Ceram. Soc., 73, 1014-1023 (1990).

28. M.W. Barson, P. Kangutkar and A.S.D. Wang, "Matrix Crack Initiation in Ceramic Matrix Composites, Part I: Experiments and Test Results", Composites Sci. Tech., 44, 257-269 (1992).

29. S. Mall and R.Y. Kim, "Failure Mechanisms in Laminates of Silicon Carbide/Calcium Aluminosilicate Ceramic Composite", Composites, 23, 215-222 (1992).

30. D.M. Dawson, R.F. Preston and A. Purser, "Fabrication and Materials Evaluation of Higher Performance Aligned Ceramic Fiber-Reinforced Glass-Ceramic Composite", Ceram. Eng. Sci. Proc., 8, 815-821 (1987).

31. P.F. Becher, T.N. Tiegs and P. Angelini, "Whisker Toughened Ceramic Composites", pp.311-329, See Ref. 4.

32. R. Naslain, "CVI Composites", in Ceramic-Matrix Composites, pp.199-244, 1992, R. Warren, ed., Chapman and Hall, New York.

33. R.J. Singh, "High-Temperature Mechanical Properties of a Uniaxially reinforced Zircon-Silicon Carbide Composite", Ceram. Soc., 73, 2399-24-6 (1990).

34. R.N. Singh and A.R. Gaddipati, "Mechanical Properties of a Uniaxially Reinforced Mullite-Silicon Carbide Composite", J. Am. Ceram. Soc., 71, C100-C103 (1988).

35. D.A. Woodford, et al., "Tensile Properties of Ceramic Matrix Composites", to be published in J. Mater. Sci., May 1993.

36. J. Aveston, G.A. Cooper and A. Kelly, "Single and Multiple Fracture", pp.15-26, 1971, see Ref. 3.

37. B. Budianski, J.W. Hutchinson and A.G. Evans, "Matrix Fracture in Fiber-Reinforced Ceramics", J. Mech. Phys. solids, 34, 167-189 (1986).

38. M. Sutcu and W.B. Hillig, "The Effect of Fiber-Matrix Debond Energy on the Matrix Cracking Strength and the Debond Shear Strength", Acta Metall. Mater., 38, 2653-2662 (1990).

39. R.A. Shimansky and H.T. Hahn, "Effect of Interfacial Properties on Matrix Cracking Stress of Fiber Reinforced Ceramics", in Symposium on High Temperature Composites, pp.148-157, 1989 Proceedings of the American society for Composites, Technomic Publishing Co., Lancaster, PA.

40. A.G. Evans and D.B. Marshall, "Mechanical Behavior of Ceramic Matrix Composites", pp.1-39, see Ref. 4.

THE EFFECT OF PROCESSING ON THE MICROSTRUCTURE AND PROPERTIES OF ADVANCED MATERIALS

G. E. Fuchs
Knolls Atomic Power Laboratory
General Electric Company
P. O. Box 1072
Schenectady, New York 12301

ABSTRACT

Frequently, materials development programs attempt to optimize new materials based on alloy composition variations alone. The effect of the alloying additions on the microstructure and properties on the resulting materials is used to direct the alloy development. However, the role of processing is often overlooked. This paper will examine a variety of processing techniques, including powder metallurgy, casting, wrought processing and several hybrid/advanced techniques. The effect that these processing techniques have on the resulting microstructures and properties of superalloys, intermetallics and composites will be discussed. Whenever possible, the experimental variables will be limited to processing technique, alloy content or materials-type, in order to focus on the effect of processing on the microstructure and properties of advanced materials. The critical issues, limitations and advantages of each of these processing routes for advanced materials will also be discussed.

Critical Issues in the Development of High Temperature Structural Materials
Edited by N.S. Stoloff, D.J. Duquette and A.F. Giamei
The Minerals, Metals & Materials Society, 1993

INTRODUCTION

The need for lightweight materials which can withstand higher temperatures, more aggressive environments and longer lifetimes than current Ni-base superalloys is increasing. Programs initiated by DOD (Integrated High Performance Turbine Engine Technology - IHPTET), NASA (High Temperature Engine Materials Program - HITEMP), and NASP have been used to identify and develop lightweight, high temperature materials. The majority of these efforts have been focused on identifying candidate alloys, often intermetallic alloys, with properties that may be useful for high temperature applications. However, these programs have frequently stressed the effects of compositional variations, and alloying additions without examining the effect of processing. This paper will highlight the effect of processing of advanced materials, and will focus on monolithic and composite forms of Ni_3Al and TiAl.

MONOLITHIC ALUMINIDES

Ni_3Al-Based Alloys

Once the ductilization of polycrystalline Ni_3Al by boron was identified by Aoki and Izumi[1], and verified by Liu, et al [2,4] and Huang, et al [5,6], considerable effort was concentrated on alloy design. Although boron-doped Ni_3Al alloys exhibit good ductility at room temperature, elevated temperature testing indicated that the ductility at high temperature is sensitive to the test environment [7,8]. Additions of approximately 8 at% chromium significantly reduced this dynamic environmental embrittlement. Alloying additions of 0.2 - 1 at% Zr or Hf and/or 1-3 at% Mo are typically added to Ni_3Al + Cr + B alloys for increased elevated temperature strength and creep resistance [9]. Table 1 presents typical compositions for several Ni_3Al-based alloys developed by ORNL [10]. Some of these compositions have been optimized for a specific processing route. For example, IC-396M has been optimized for casting applications, such as diesel turbocharger impellers [11].

TABLE 1
COMPOSITION (WT%) OF ORNL DEVELOPED Ni_3Al-BASED ALLOYS

Alloy	Ni	Al	Cr	Zr	Mo	B
IC-50	BAL	11.3	--	0.6	--	0.02
IC-218	BAL	8.5	7.8	0.8	--	0.02
IC-218LZr	BAL	8.7	8.1	0.2	--	0.02
IC-221	BAL	8.5	7.8	1.7	--	0.02
IC-396M	BAL	7.98	7.74	1.7	1.43	0.008

ORNL has performed extensive studies on the fabricability of and the effect of processing on the properties of Ni_3Al-based alloys [10,12-14]. The work, which is summarized below, has primarily focused on alloys IC-50, IC-218, IC-218LZr and IC-221 (Table 1). Small laboratory heats of Ni_3Al-based alloys can readily be cold rolled to sheet. However, larger ingots are coarse grained and exhibit severe casting segregation.

Hot working ingot material requires care due to the low ductility at temperatures above approximately 900°C. Hot compression tests on IC-218LZr and IC-218 in the temperature range 1050°C-1200°C indicated that the low Zr alloy exhibited superior fabricability [13]. Currently, ingot breakdown is being performed by rotary forging and extrusion to minimize tensile strains. Once the cast structure has been reduced, the alloys can readily be cold or hot rolled. Fine grained ($\leq$ 10μm grain size) ingot metallurgy processed IC-218 was reported to exhibit superplasticity at temperatures in excess of 950°C [10]. Powder metallurgy processed (extrusion consolidated -1100°C/14:1) IC-218 has also exhibited superplasticity; however, this was at temperatures as low as 800°C [15]. This increase in the regime for superplasticity in powder metallurgy materials has been observed in other materials [16, 17] and is often attributed to the finer grain size, improved grain size control, and superior homogeneity of the powder metallurgy product.

Processing, in addition to affecting fabricability, also has a significant impact on the microstructure and properties of the material. Sikka and Loria [13] reported the effect of processing on the tensile and creep properties of IC-218 and IC-221 Ni_3Al-based alloys (Figure 1). The wrought alloys (extruded and cold rolled) and the powder metallurgy alloys (HIP + isothermal forge, CAP + extrude and rapid omni directional compacted) materials all exhibited grain sizes ranging from 9-21μm. A 727μm grain size was observed in the cast alloy. The coarse grained cast alloy exhibited the lowest strength and ductility at low test temperatures (< 700°C). At higher test temperatures, the cast alloy possessed a higher strength than the wrought and P/M alloys; however, the ductility was approximately equal to that of the P/M and I/M materials. Interestingly, it appears that the cast alloy exhibited an anomalous yield peak at a temperature approximately 200°C higher than the wrought and P/M products. Since no compositional variations in these alloys were evaluated, this difference in yield strength peak may be due to Hall-Petch strengthening at low temperatures in the much finer grained wrought and P/M alloys. Creep testing indicated that the cast alloy had significantly higher creep resistance than the I/M-wrought and P/M alloys (Figure 2). Although the P/M product might be expected to have lower creep strength, the creep resistance of the materials appeared to be more a function of grain size than processing. The P/M alloys also exhibited better creep rupture elongations and reductions in area, which could be utilized for improved fabricability and possibly superplastic forming.

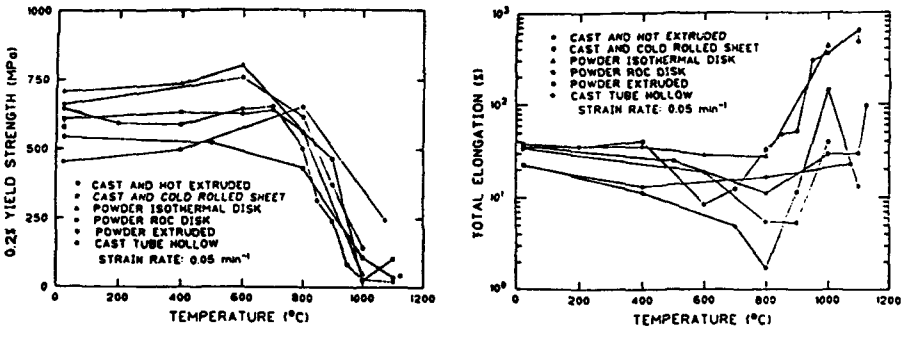

FIGURE 1 - Tensile Properties Comparison for IC-218 Alloys Processed by Six Different Processes. All Tests Were Conducted at a Strain Rate of 0.05/min. [13]

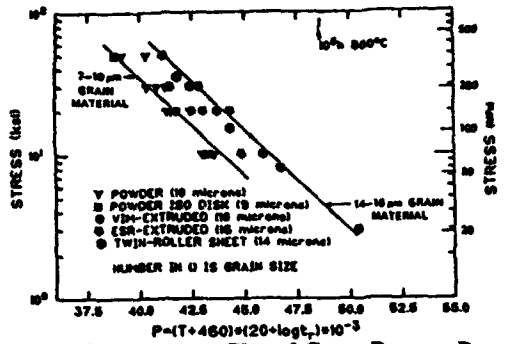

FIGURE 2 - Larson-Miller Parameter Plot of Creep Rupture Properties of IC-218 [13].

The high-cycle fatigue properties of powder metallurgy processed Ni_3Al + B and $Ni_3Al(Al,Mn)$ + B alloys were determined at room temperature and 500°C [18,19]. Both alloys (Figure 3) were evaluated in the as-HIP (1150°C/103MPa/4hrs) and HIP + extruded (1100°C/7:1) condition. In both cases and at both test temperatures, the HIP and extruded alloys exhibit superior fatigue strength in comparison with the as-HIP materials. The difference in fatigue resistance particularly noticeable at low stress amplitude/long life test conditions (10^7 cycle fatigue strength). The increased fatigue resistance observed in the extruded alloys was attributed to the grain refinement, homogenization and elimination of any residual porosity by extrusion processing. The effect of processing on the tensile and fatigue properties of IC-218 and IC-221 was determined at room temperature and 600°C [20,21]. The powder metallurgy processed alloy exhibited higher ductility and lower strength than ingot metallurgy processed material. The fatigue resistance of the ingot metallurgy alloys also appeared to be dependent on melting technique. An ESR-melted, extruded alloy possessed greater fatigue resistance than a VIM and extruded material.

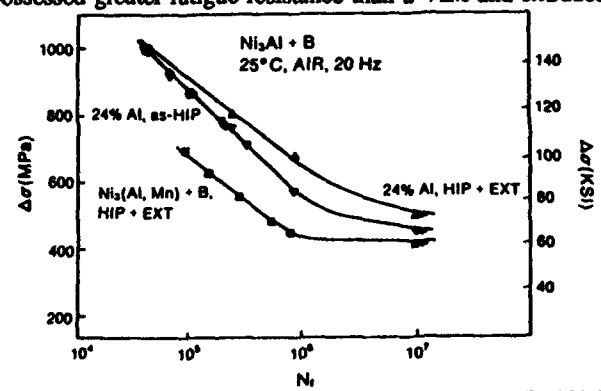

FIGURE 3 - High Cycle Fatigue Behavior of Ni_3Al + B and $Ni_3(Al,Mn)$ + B Alloys at Room Temperature [18].

A more recent powder metallurgy processing route employed for producing intermetallic compounds is self-heated high-temperature synthesis (SHS), often called reactive or exothermic processing. Unlike the previously discussed powder metallurgy

processes which utilized pre-alloyed powder, SHS processing utilizes elemental powders. In comparison with pre-alloyed powders, reactively sintered and reactively HIP'ed Ni_3Al + B alloys [22] exhibited higher strength but significantly lower ductility. The lower ductility of the reactively processed material was attributed to the inhomogeneities (pores and second phase) present in the microstructure (Table 2). Although boron-doped Ni_3Al alloys have been reactively processed, they would also be expected to exhibit the elevated temperature ductility minimum observed in cast, wrought and pre-alloyed powder metallurgy processed material. To date, no Cr alloyed Ni_3Al-based alloys have been processed by reactive processing. Since Cr is a necessary alloying addition to produce a structural alloy, alloys without Cr are of little commercial interest for elevated temperature applications.

TABLE 2
TENSILE PROPERTIES OF REACTIVE SINTERED AND PRE-ALLOYED POWER METALLURGY Ni_3Al + B ALLOYS

Processing	Y.S.	UTS	Elong.	Reference
Reactive Sinter	353 MPa	687 MPa	12%	[22]
RHIP	494MPa	677MPa	2%	[22]
HIP Pre-Alloyed	303MPa	1345MPa	34%	[18]
HIP + Ext	414MPa	1517MPa	34%	[18]

TiAl-Based Alloys

In 1956, McAndrew and Kessler identified the potential of γ-TiAl based alloys for elevated temperature structural applications [23]. However, limited low temperature ductility (700°C) and fabricability concerns of γ-TiAl alloys limited development efforts [24]. More recently, critical microstructural effects on mechanical properties have been identified in wrought binary alloys [25,26] which increased the room temperature ductility from essentially 0% tensile elongation to nearly 3%. However, the role of processing on the properties of binary alloys has not been examined. Ternary additions of Cr, Mn and V to hypo-stoichiometric alloys further increased low temperature ductility to approximately 3-4% elongation [27-29].

Although powder metallurgy methods were inititally used to fabricate materials [31, 32], the powders were stoichiometric and contained excessive impurities. More recent studies have almost exclusively examined cast and wrought materials. Several alloys have been developed and reported in the literature; however, the Ti-48Al-2Nb-2Cr at% alloy has received the most attention [33,34]. Microstructural evolution and mechanical properties in wrought alloys have been thoroughly summarized in a series of review articles [28,35-38]. However, only recently has the effect of processing on the properties of TiAl-based alloys been explored. Due to fabricability concerns with cast alloys [39,40], powder metallurgy processing has been identified as a potential method to improve workability. Powder metallurgy processing may also result in an alloy with improved properties due to increased homogeneity and refined microstructures. Concerns about compositional and impurity control and cost have limited the evaluation of powder metallurgy processing

routes. However, improved melting techniques have reduced impurity contents and increased reproducibility. The plasma rotating electrode process (PREP) has been an established method to make pre-alloyed Ti-based powders. Recently, though, gas atomization techniques have been developed [41,42] and the development of reactive sintering has increased the interest in powder metallurgy processing.

A comparison of Ti-48Al-2Nb-2Cr alloys processed by ingot metallurgy and powder metallurgy techniques indicated that processing has a significant effect on the properties evaluated [43,44]. PREP and gas atomization techniques were evaluated and compared with the properties of investment cast and wrought alloys [43]. The powder processed alloys, and in particular the gas atomized material, exhibited superior tensile properties in the temperature range 25°-1000°C (Figure 4). In addition, the fabricability (Figure 5) of the HIP consolidated powder processed Ti-48Al-2Nb-2Cr alloys was superior to the homogenized ingot metallurgy alloys [45]. Earlier studies of powder metallurgy processed

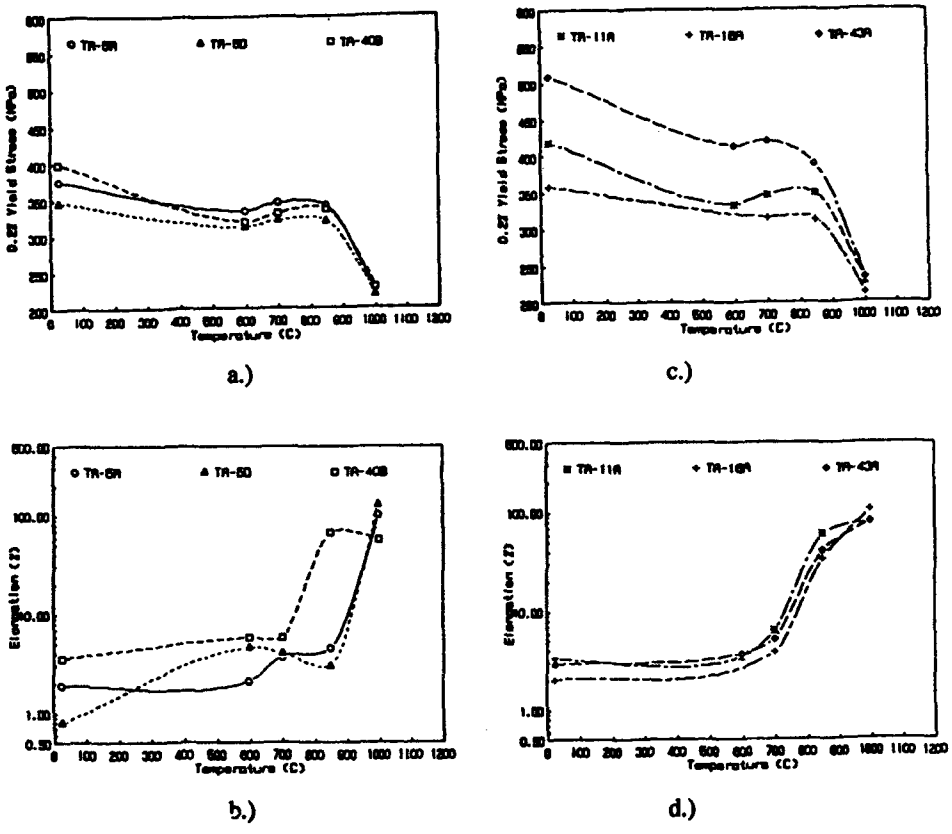

FIGURE 4 - The Effect of Temperatuare on the Yield Strenth and Ductility of Ti-48Al-2Nb-2Cr Alloys [43]. I/M Alloys -- TA-5A, TA-5D-Wrought, and TA-40B-Investment Cast. P/M Alloys -- TA-11A-Gas Atomized + HIP, TA-16A, PREP + HIP and TA-43A-Gas Atomized + Extrude

a.) I/M - Yield Stress
b.) I/M - Elongation
c.) P/M - Yield Stress
d.) P/M - Elongation

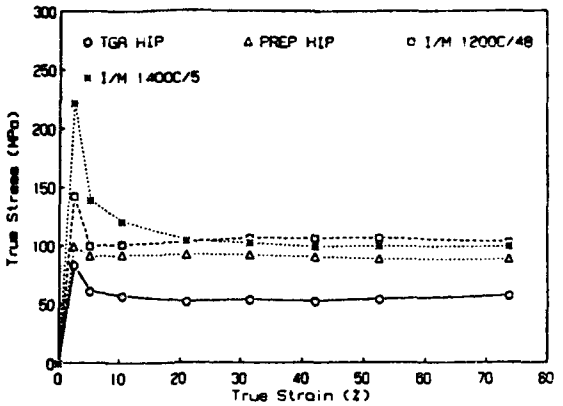

FIGURE 5 - Isothermal Forging of Ti-48Al-2Nb-2Cr Alloys at 1175°C/0.1 min^{-1}. TA-5A - Cast + Homogenized (1400°C/5 hrs.), TA-5D - Cast + Homogenized (1200°C/48 hrs.), TA-11A - Gas Atomized + HIP (1230°C/103 MPa/4 hrs.) and TA-16A - PREP + HIP (1230°C/103 MPa/4 hrs.) [45]

TiAl-based alloys reported limited ductility at room temperature [46] and emphasized HIP consolidation parameters to maintain the rapidly solidified microstructure [47]. The majority of these studies utilized low HIP temperatures based on studies that identified the lowest HIP temperatures and highest HIP pressures at which full density can be achieved. However, these HIP cycles have not necessarily been optimized for mechanical properties. The effects of HIP temperature and pressure on the tensile properties of a gas atomized Ti-48Al-2Nb-2Cr alloy was examined [45]. Although full density was achieved at all HIP conditions, material consolidated with HIP temperatures near the eutectoid temperature (~1125°C) in the $\alpha_2 + \gamma$ phase field (1090°C) and in the $\alpha + \gamma$ phase field (1140°C) exhibited low ductility at room temperature (Figure 6). In addition, evidence of prior particle boundary failure was observed on the fracture surface. HIP temperatures in the $\alpha + \gamma$ phase field (1230°C and 1300°C), exhibited the highest ductilities in the temperature range 25° - 1000°C. A variant on the gas atomization technique is to spray deposit Ti-based alloys [48]. However, additional work is required to optimize the system to minimize impurity pick-up.

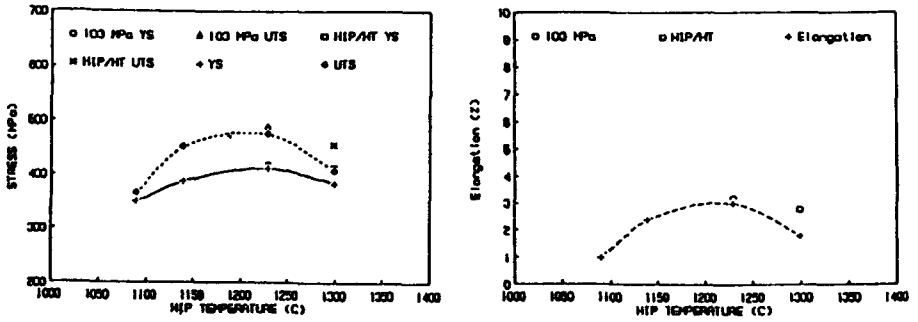

FIGURE 6 - The Effect of HIP Temperature and Pressure on the Room Temperature Tensile Properties of Gas Atomized Ti-48Al-2Nb-2Cr Alloys [45]

Although reactive processing to produce TiAl-based alloys has recently attracted much attention [49-51], Schafrik [52] produced a binary alloy from elemental powders. However, the alloys produced from elemental powders typically exhibit properties inferior to pre-alloyed powder and ingot metallurgy processing techniques. The reactively processed materials typically have significant oxygen contents, frequently greater than 1%, and exhibit low strength and ductility. The poor properties of reactively sintered materials also may be due to microstructural inhomogeneities resulting from the slow diffusion rate of Al in Ti [49].

Processing has been shown to have a significant effect on mechanical properties on laboratory scale heats. However, processing may have a greater effect on fabricability, particularly for scale-up from laboratory development to production. Chesnutt and Shih reported on wrought processing and scale-up of ingot metallurgy Ti-48Al-2Nb-2Cr alloys [53]. Isothermal forging of small laboratory samples (70 mm dia. x 50 mm) was accomplished without difficulty at 1175°C/0.1 min^{-1} on a 1.8 MN press. However, isothermal forging of large ingots (190 mm dia. x 114-229 mm) at 1066°-1149°C/0.1 min^{-1} was significantly more difficult. The large forgings required forces approaching the 71.2 MN limits of the press. In addition, the forged material did not respond to recrystallization heat treatments in all cases and exhibited edge cracking.

COMPOSITE MATERIALS

Ni_3Al-Based Composites

In order to improve high temperature strength and creep resistance, efforts are being made to utilize Ni_3Al-based alloys as matrices in composites. Both discontinuous and continuous reinforcements have been examined and a variety of approaches have been used to fabricate Ni_3Al-based composites. Consolidation of pre-alloyed powders with particulate reinforcement has been used extensively to fabricate intermetallic matrix composites. An IC-221 matrix was observed to react extensively with TiB_2; whereas, Al_2O_3 did not react with the matrix but exhibited limited matrix bonding [54,55]. TiC reinforcement exhibited only limited particle/matrix interaction, and, compared with similarly processed matrix samples, exhibited a significant increase in strength in the temperature range 25-1100°C. However, the 25 vol% TiC/IC-221 composite exhibited only limited ductility up to 1000°C. Additional testing indicated that the modulus of the composite was greater than the matrix at all test temperatures and greater than Ni-base superalloys up to approximately 800°C. Hot extrusions of pre-alloy powders of a modified IC-221 alloy, IC-396M, with 10% vol. additions of several candidate reinforcements were examined [56]. The ceramic reinforcements examined included TiN, NbC, HfO_2 and HfN. The HfN essentially dissolved into the IC-396M matrix, which resulted in a significant increase in strength due to solid solution strengthening of Hf in IC-396M. No reinforcement/matrix inter-reaction was observed in the composites fabricated with TiN, NbC and HfO_2. However, no significant strengthening was observed in any of these composites either.

Combining pre-alloyed powders with Al_2O_3 fibers has been used to fabricate the intermetallic matrix composites [57-60]. Both fiber FP and PRD-166 Al_2O_3 fibers have been used during composite preparation. The compatibility and mechanical properties of IC-15 (Ni-24Al-0.24B at%) and IC-218 matrices with Al_2O_3 was examined. Although the IC-15 did not react with the Al_2O_3, small ZrO_2 precipitates were observed at the IC-

218/Al_2O_3 interface. In comparison with the matrix, no increase in yield strength was observed in the composite. However, the composite exhibited a significant decrease in ductility and ultimate tensile strength. An IC-221/Al_2O_3 composite also exhibited excellent compatibility, and an increase in strength and creep resistance was observed at all test temperatures in the composite (Figure 7). Similar to the IC-218/Al_2O_3 and IC-15/Al_2O_3 composites, the ductility of the IC-221/Al_2O_3 composites exhibited reduced ductility, compared with the matrix.

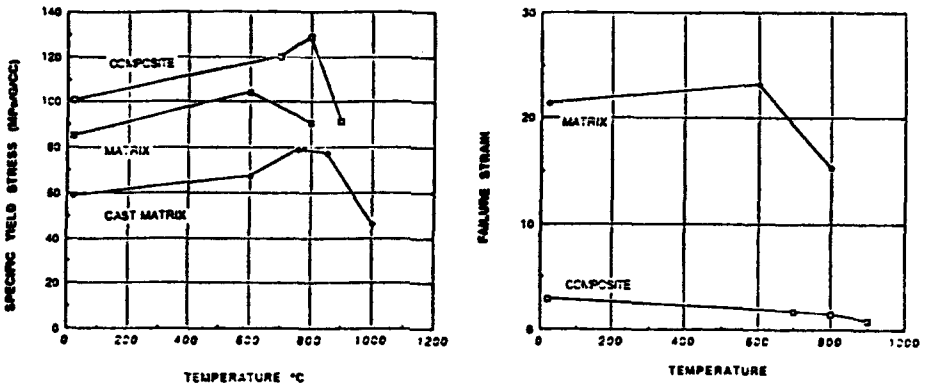

FIGURE 7 - The Effect of Temperature on the Specific Yield Strength and Ductility of an IC-221 Matrix Alloy and an Al_2O_3 Reinforced IC-221 Composite [59].

Vacuum hot pressing of IC-218 pre-alloyed powder with SCS-6 and Sigma SiC fibers produced samples for compatibility testing [61]. Both types of SiC fiber reacted extensively with the matrix. The Ni was observed to be the dominant diffusing species to form Ni-silicides. The interfacial reaction formed during consolidation and continued to grow during compatibility heat treatment studies. The authors concluded that diffusion barrier coatings would be required to develop Ni_3Al/SiC composites.

Instead of using pre-alloyed powders, reactive sintering of elemental powders combined with the ceramic reinforcement has also been used to produce the composite. Unlike the pre-alloyed powder matrices, the reactively sintered composites are almost exclusively fabricated with boron-doped binary Ni_3Al. Although the pre-alloyed powder metallurgy processing typically requires 1000°-1300°C for consolidation, reactive HIPing or sintering can be performed at 800°C. However, the actual temperature at the reaction front can approach 1500°C. Therefore, the compatibility of the matrix and reinforcement must consider the temperature and duration of the temperature rise. For this reason, SiC reinforcement must be coated with Y_2O_3 to protect the SiC from the molten Ni-Al solution [62]. Only minimal strengthening was observed in the composite due to the low volume fraction of the reinforcement. The fiber volume content, however, must be increased in order to obtain desirable strengthening effects from the reinforcements.

Pressure casting or melt infiltration has also been used to fabricate continuous Al_2O_3 fiber reinforced Ni_3Al composite. The process requires melt temperatures in the range 1400°-1700°C and 2.7MPa of argon pressure [63]. The key issue to melt infiltration is wetting of the fiber by the molten metal. Small additions (1-2 wt%) of Ti or Y can be added to the melt to facilitate melt infiltration [64]. No significant reaction was observed

to occur between the PRD-166 Al_2O_3 fiber and the Ni_3Al-based matrix. Measured modulus values of the composite were close to the rule-of-mixtures predictions along the fiber directions. Modulus measurements perpendicular to the fibers were significantly below the predictions. The tensile strengths and ductilities was significantly lower than the matrix alloy at room temperature and 1000°C. Additional work is required to achieve a composite with useful engineering properties.

TiAl-Based Composites

A significant amount of work has been performed on continuous fiber SiC reinforced α_2-Ti_3Al-based [65-68] and orthorhombic (Ti_2AlNb)-based [69-71] alloys. TiAl based alloys, which possess superior oxidation resistance and lower density, offer potentially higher use temperatures. Compatibility studies of potential γ-TiAl matrices with candidate reinforcements have often used pre-alloyed powders of the matrix alloys, consolidated around the reinforcement by HIP or hot processing. Saphikon (Al_2O_3) fibers combined with pre-alloyed powders with compositions Ti-48Al-1Ta(RSR), Ti-48Al-3V(RSR) and Ti-50Al-2Nb-0.3Ta(PREP) and consolidated the fibers by HIP [72]. The RSR alloys contained excessive oxygen and carbon levels and were two-phase α_2/γ alloys. Much lower interstitial contents were present in the PREP alloys and the Ti-50Al-2Nb-0.3Ta material is nearly a single phase γ-alloy. In all cases, very little matrix/Al_2O_3 reaction was observed. However, better matrix/Al_2O_3 stability was observed in the single phase alloy. Extensive reaction between pre-alloyed TiAl-5Nb(RSR) powder and SiC(SCS-6) fiber consolidated by HIP [73], was observed. After consolidation, the interfacial reaction continued during subsequent heat treatment. Application of a TiB_2 coating to a SiC(SCS-6) fiber prevented interaction with pre-alloyed Ti-47Al-2Ta powders during and after HIP consolidation [74]. A TiC coating on the SiC fiber, however, did not prevent matrix/fiber interaction. Although compatible matrix/fiber combinations have been identified, very few mechanical property data have been reported.

Ductile phase toughening of the low ductility γ-TiAl matrix has also been examined using powder metallurgy processing. Pre-alloyed powders of a single phase Ti-50.5Al(at%) alloy were combined with various volume fractions of TiNb powder, consolidated by hot pressing and then forged to a pancake [75]. The fracture toughness of the composite (40 MPa$\sqrt{m}$) was significantly higher than the monolithic alloy (8MPa$\sqrt{m}$). However, the fatigue crack growth rate and the fatigue crack threshold of the composite was inferior to the monolithic alloy. It should also be noted that, single phase γ-TiAl alloys have been reported to exhibit lower toughness and fatigue resistance than two-phase alloys [28]. In particular, near lamellar and fully transformed two-phase alloys exhibit toughness properties similar to the ductile phase toughened composite and fatigue resistance superior to the composite (Table 3). In addition, the long term thermal stability of the composite has not been established and may restrict the use temperature and/or lifetime.

Precipitation of second phase particles in a master alloy (XD processing) or during solidification of an ingot has been examined in several γ-TiAl alloys. TiAl-based alloys with TiB_2, $(TiNb)B_2$ and TiN particles (or Ti_2AlN) have been processed by XD techniques [76-78]. The composites are processed by ingot metallurgy techniques and are tested in the cast or hot worked condition. In all cases, the composites were reported to exhibit improved creep resistance, but the tensile ductility of the composites is significantly reduced. In addition, no improvements in fracture toughness were observed. Attempts to use powder metallurgy processing (PREP atomization followed by HIP) to refine the

TABLE 3
ROOM TEMPERATURE FRACTURE TOUGHNESS OF MONOLITHIC AND DUCTILE PHASE REINFORCED TiAl-BASED ALLOY

Alloy	Room Temperature Fracture Toughness (MPa√m)	Reference
Ti-50Al	8	[75]
Ti-50Al + 20vol% TiNb	40	[75]
Ti-48Al (Duplex)	10-20	[37]
Ti-48Al (Lamelar)	20-35	[37]

microstructure were successful [79]. However, improvement in the mechanical properties was observed and preparation of the PREP electrode was difficult and very costly. Precipitation of second phase particles during solidification of γ-TiAl based alloys has also been evaluated [80]. Additions of B, and Ta and B to a Ti-48Al alloy resulted in the formation of TiB_2 and (Ta,Ti)B, respectively. Although the creep resistance of the TiAl + Ta + B composite was superior to the monolithic TiAl alloy and the TiAl/TiB_2 composite, the major strengthening contribution arises from solute (Ta) hardening of the matrix.

SUMMARY

Processing has been shown to have a significant effect on the microstructure and properties of Ni_3Al and TiAl-based alloys and composites. In these materials, microstructural refinement and homogenization result in improved properties and fabricability. Both Ni_3Al and TiAl-based materials exhibit severe solidification segregation during ingot casting. Since laboratory scale development is often performed on small heats of material, the difficulties associated with segregation may not be manifest during the development stage. However, once scale-up from laboratory to production is initiated, the scale of segregation and the resulting problems may increase. As seen by the experience in the scale-up of Ni_3Al [13] and TiAl-based [53] alloys, these problems can be difficult to overcome without examining alternate production routes. In addition, alloy and process development and optimization without considering alternate routes for scale-up can be misleading. The improved fabricability of powder metallurgy processing may be the most important aspect, particularly when scale-up of a new material/process is limited by equipment capacity (e.g., forging). In addition, powder metallurgy, at this time, appears to be the optimum method to fabricate TiAl and Ni_3Al composites. Until foil processing of these materials is further commercialized, powder metallurgy processing that limits matrix/reinforcement exposure to solid-solid interactions will be the optimum route. Melt infiltration and reactive processing allow liquid metal to react with the reinforcement, which can often be catastrophic. The major limitations of powder processing are fiber fracture during consolidation, availability of matrix powders, purity of starting materials, and contamination during processing.

The advantages of powder metallurgy processing over ingot metallurgy processing for difficult to work and segregation prone materials, is well documented. High strength Ni-

base superalloys for aircraft gas turbine disk applications are almost exclusively processed by powder metallurgy routes. The powder metallurgy processing improves fabricability and mechanical properties in comparison with ingot metallurgy processing. For example, RENÉ95, when processed by powder metallurgy techniques (extrude + forge and HIP), exhibits refined microstructures and increased tensile properties [81] and fatigue resistance [82]. Similar considerations for the development of Ni_3Al and TiAl-based materials should be made. Examination of a single composition or a single processing route can not fully evaluate the potential of these and other advanced materials.

ACKNOWLEDGEMENTS

This work was performed at Knolls Atomic Power Laboratory, operated for the U.S. Department of Energy by the General Electric Company under Contract No. DE-AC12-76SN00052.

REFERENCES

1) K. Aoki and O. Izumi, Nippon Kinzoku Gakkaishi, 43 (1979), 1247-1250.
2) C. T. Liu and C. C. Koch, Technical Aspects of Critical Materials Used by the Steel Industry, Vol. IIB (The Electrochemical Society), 1983.
3) C. T. Liu, C. L. White, C. C. Koch, and E. H. Lee, IBID.
4) C. T. Liu, C. L. White, and J. A. Horton, Acta Met, 33 (1985), 213-219.
5) A. I. Taub, S. C. Huang, and K. M. Chang, Met Trans A, 15A (1984), 339.
6) S. C. Huang, A. I. Taub, and K. M. Chang, Acta Met, 32 (1984), 1703-1707.
7) C. T. Liu and C. L. White, Acta Met, 35 (1987), 643-649.
8) C. T. Liu, C. L. White, and E. H. Lee, Scripta Met, 19 (1985), 1247-1250.
9) J. H. Schneibel, G. F. Peterson, and C. T. Liu, J. Mat. Res., 1 (1986), 68-72.
10) V. K. Sikka, Proc. High Temp. Aluminides and Intermetallics, Eds. S. H. Whang, C. T. Liu, D. P. Pope, and J. O. Stiegler, (TMS, Warrendale, PA, 1990), 505-520.
11) J. W. Patten, IBID, 493-503.
12) C. T. Liu and V. K. Sikka, Journal of Metals, 44 (1986), 19-21.
13) V. K. Sikka and E. A. Loria, Proc. Superalloys 1988, Eds. S. Reichman, D. N. Duhl, G. Maurge, S. Antolovich, and C. Lund, (TMS, Warrendale, PA, 1988), 203-212.
14) V. K. Sikka, J. T. Mavity, and K. Anderson, Materials Science and Engineering, A153 (1992), 712-721.
15) V. K. Sikka, ORNL, Private Communications, 1988.
16) T. G. Nieh, C. M. Nally and J. Wadsworth, Journal of Metals, 45 (1989), 31-35.
17) T. G. Nieh and J. Wadsworth, Journal of American Ceramic Society, (1989).
18) G. E. Fuchs and N. S. Stoloff, Scripta Met, 21 (1987), 863-869.
19) G. E. Fuchs and N. S. Stoloff, Proc. Strength of Metals and Alloys, Eds., P. O. Kettunen, T. K. Lepisto, and M. E. Lehtonen, (Pergamon Press, NY, 1988), 665-670.
20) W. Matuszyk, RPI, Master's Thesis, 1988.
21) W. Matuszyk and N. S. Stoloff, Met Trans. 21A (1990), 2517-2524.
22) R. M. German, A. Bose, and N. S. Stoloff, MRS Symp. Proc., 133 (1989), 403-414.
23) J. B. McAndrew and H. D. Kessler, Journal of Metals, 8 (1956), 1348-1354.
24) H. A. Lipsitt, MRS Symp. Proc., 39 (1985), 351-364.
25) S. C. Huang and E. L. Hall, Met. Trans A, 22A (1991), 2619-2627.

26) S. C. Huang, E. L. Hall, and M. F. X. Gigliotti, MRS Symp. Proc., 81 (1987), 481-486.
27) S. C. Huang and E. L. Hall, MRS Symp. Proc., 133 (1989), 373-383.
28) Y. W. Kim, Journal of Metals, 41 (1989), 24-30.
29) T. Tsujimoto and K. Hashimoto, MRS Symp. Proc., 133 (1989), 391-396.
30) T. Kawabata, T. Tamuru, and O. Izumi, MRS Symp. Proc., 133 (1989), 329-334.
31) H. A. Lipsitt, D. Shechtman, and R. E. Schafrik, Met Trans, 6A (1975), 1991-1996.
32) S. M. L. Sastry and H. A. Lipsitt, Met Trans, 8A (1977), 299-304.
33) D. S. Shih, S. C. Huang, G. K. Scarr, H. Jang, and J. C. Chesnutt, Proc. Microstructure/Property Relationship in Ti Alloys and Aluminides, Eds Y. W. Kim and R. R. Boyer, (TMS, Warendale, PA, 1991), 135-389.
34) J. C. Chesnutt, Proc., Superalloys 1992, Eds. S. D. Antolovich, R. W. Staarud, R. A. McKay, D. L. Anton, T. Khan, R. D. Kissinger, and D. L. Klarstom, (TMS, Warrendale, PA, 1992), 381-389.
35) Y. W. Kim, and F. H. Froes, Proc. Hi Temp. Aluminides and Intermetallics, Eds. S. H. Whang, C. T. Liu, D. P. Pope, and J. O. Steigler, (TMS, Warrendale, PA, 1990), 465-472.
36) Y. W. Kim, MRS Symp. Proc., 213 (1991), 777-794.
37) Y. W. Kim and D. M. Dimiduk, J. of Metals, 43 (1991), 40-47.
38) Y. W. Kim, Proc. Microstructure/Property Relationship in Ti Alloys and Aluminides, Eds. Y. W. Kim and R. R. Boyer, (TMS, Warrendale, PA, 1991), 91-103.
39) S. L. Semiatin, N. Frey, S. M. El-Soudani, and J. D. Bryant, Met Trans A, 23A (1992), 1719-1735.
40) S. L. Semiatin, D. C. Vollmer, S. M. El-Soudani, and C. Su, Scripta Met, 24 (1990), 1409-1413.
41) J. H. Moll, C. F. Volton and B. J. McTiernan, Int'l. J. of Powder Met., 26 (1990), 149-155.
42) J. H. Moll and C. F. Yolton, Mod. Dev. in Powder Met., 18 (1988), 709-726.
43) G. E. Fuchs, Proc. 7th World Conf. on Ti, in Press.
44) C. F. Yolton and D. E. Eylon, Proc. 7th World Conf. on Ti, in Press.
45) G. E. Fuchs, Proc. MRS Symp., in Press.
46) M. A. Ohls, W. T. Nachbar, and P. R. Roberts, Proc. P/M in Aerospace and Defense Technologies, (MPIF, Princeton, NJ, 1991).
47) C. McCullough, J. J. Valencia, C. G. Levi, and R. Mehrabian, Acta Met, 37 (1989), 1321-1336.
48) D. G. Morris, M. A. Morris, S. Gunter, M. Leboeuf and G. Hollrigg, Scripta Met, 27 (1992), 1645-1650.
49) R. M. German, A. Boase and N. S. Stoloff, MRS Symp. Proc., 133 (1989), 403-414.
50) G. X. Wang and M. Dahms, Scripta Met, 26 (1991), 1469-1474.
51) G. X. Wang, M. Dahms, and B. Docan, Scripta Met, 27 (1992), 1651-1656.
52) R. E. Schafrik, Met Trans B, 7B (1976), 713-716.
53) J. C. Chesnutt and D. S. Shih, Proc. 7th World Conf. on Ti, in Press.
54) G. E. Fuchs, Proc. Metal and Ceramic Matrix Composites, Eds R. B. Bhagat, A. H. Clauger, P. K. Kumar and A. M. Ritter, (TMS, Warrendale, PA, 1990), 391-400.
55) G. E. Fuchs, J. Mat. Res, 5 (1990), 1649-1655.
56) C. G. McKamey and C. A. Carmichael, MRS Symp. Proc.,213 (1991), 1051-1056.
57) G. L. Povirk, J. A. Horton, C. G. McKamey, T. N. Tiegs and S. R. Nutt, J. Mat Sci, 23 (1988), 3945-3950.

58) C. G. McKamey, G. L. Puvirk, J. A. Horton, T. N. Tiegs, and E. K. Ohroner, MRS Symp. Proc., 133 (1989), 609-614.
59) P. C. Brennan, W. H. Kao, and J. M. Yang, J. Mat Sci, A153 (1992), 635-640.
60) A. Bose and R. M. German, Adv. Mat'ls and Proc., 3 (1988), 37-56.
61) J. M. Yang, W. H. Kao, and L. T. Liu, MRS Symp. Proc. 133 (1989), 453-458.
62) JA. Bose, B. Moore, R. M. German, and N. S. Stoloff, J. Metals, 43 (1988), 14-17.
63) S. Nourbakhsh, W. H. Rhee, O. Sahin, and H. Margolin, Mat Sci and Eng., A153 (1992), 619-627.
64) S. Nourbakhsh, F. L. Liang, and H. Margolin, MRS Symp. Proc. 133 (1989), 459-464.
65) K. R. Bain, J. L. Gambone, and R. D. Zoldan, MRS Symposium. Proc. 194 (1990), pp. 459-464
66) S. M. Jeng, C. J. Yang, J. M. Yang, D. G. Rosenthal, and J. Goeber, IBID, 277-284.
67) A. M. Ritter, E. L. Hall and N. Lewis, IBID, 413-422.
68) J. M. Larsen, W. C. Revelos, and M. L. Gambone, MRS Symp. Proc., 273 (1992), 3-166.
69) C. G. Rhodes, IBID, 17-29.
70) J. A. Graves, P. R. Smith, and C.G. Rhodes, IBID. 31-43.
71) P. R. Smith, J. A. Graves and C.G. Rhodes Ibid, 43 42. IBID
72) C. Das and S. Krishnamurthy, MRS Symp Proc., 273 (1992 93-13).
73) J.G. Das, Proc. Metal and Ceramic Matrix Composites, Eds., R. B. Bhagat, A. H. Clauer, P. Kumar, and A. M. Ritter, (TMS Warrendale, PA, 1990), 413-442.
74) D. E. Boss and J. M. Yang, MRS Symp. Proc., 194 (1990), 429-436.
75) K. T. Venkateswara Rao, and R. O. Ritchie, MRS Symp. Proc. 273 (1992) 127-133.
76) C. R. Feng, H. H. Smith, D. J. Michel and C. R. Crowe, MRS Symp. Proc. 194 (1990), 219-224.
77) S. L. Kampe, J. A. Clarke, and L. Chistodoulou, IBID, 225-232.
78) E. Robertson and P. L. Martin, IBID, 223-240.
79) L. Christodoulou, Martin Marietta Laboratory, Private Communications, 1990.
80) J. J. Valencia, J. P. A. Lofvandior, J. Rösler, C. G. Levi, and R. Mehrabian, MRS Symp. Proc., 194 (1990), 89-96.
81) R. V. Miner and J. Gadya, Int. J. Fat., 6 (1984), 189-195.
82) D. R. Chang, D. D. Kreugger and R. A. Sprague, Proc. superalloys 1984, (TMS, Warrendale, PA, Eds. M. Gell, C. S. Kortovich, R. H. Bricknell, W. B. Kent and J. F. Radavich, 1984), 245-273.

The Application of Combustion Synthesis in The Production of

Titanium-Based Ceramic and Ceramic-Metal Composites

H.J. Feng, K.R. Hunter, and J.J. Moore

Colorado Center for Advanced Ceramics
Department of Metallurgical and Materials Engineering
Golden, CO 80401

Abstract

This paper discusses the application of combustion synthesis in the production of dense, near net shape ceramic and ceramic-metal composites that could be used as high temperature structural materials. The current research program using this approach is described together with the existing data for the combustion synthesis of TiC-Al_2O_3-Al and TiC-Al_2O_3-Ti ceramic-metal composites from a TiO_2-C-Al exothermic reaction mix. This novel combustion synthesis approach utilizes an in-situ liquid metal infiltration together with a simultaneous hot pressing technique. The reaction stoichiometry generates a specific amount of liquid metal, ie. Al or Ti, which simultaneously infiltrates the pores of the TiC-Al_2O_3 ceramic matrix generated by the same combustion synthesis reaction. The effect of reaction parameters, eg. stoichiometry, green density, combustion mode, and hot pressing on the control of the synthesis reaction, product morphology and density is discussed, together with the major critical issues associated with using this novel approach to produce dense, near net shape ceramic-metal composite components.

Critical Issues in the Development of High Temperature Structural Materials
Edited by N.S. Stoloff, D.J. Duquette and A.F. Giamei
The Minerals, Metals & Materials Society, 1993

Introduction

Ceramic composites offer the greatest potential for applications at the highest service temperatures. However, susceptibility to brittleness created from nanoscale flaws seriously limits the current application of these materials. Incorporating a ductile metal network in ceramic composite materials offers considerable potential for the application of these ceramic-metal composites as structural materials. However, several critical issues in the synthesis and processing of these composite materials need to be resolved.
The application of a novel combustion synthesis technique for the economical production of these ceramic-metal composites is described in this paper. One of the major limitations of combustion synthesis or self propagating high temperature synthesis, SHS, is that relatively high levels of porosity, eg. 50%, remain in the product [1]. Figure 1 provides a schematic representation of the SHS reaction in which Tig is the ignition temperature and Tc is the combustion temperature. Under adiabatic conditions Tc will be the adiabatic temperature, Tad, and using the Kirchoff equation:

ie.

$$\Delta H(Tad) = \Delta H(To) + \int_{To}^{Ttrans} Cpdt \pm \Delta H(trans) + \int_{Ttrans}^{Tad} Cpdt = 0$$

where To is the initial or starting temperature, eg., 298K, Ttrans is the transition point of a reactant ($-\Delta H$) or a product ($+\Delta H$) and ΔH(trans) is the corresponding heat of transformation.

The propagating mode of combustion synthesis occurs when the exothermic reaction mixture is ignited locally and the heat generated is sufficient to propagate the reaction through the samples in 1 to 2 seconds. The simultaneous combustion mode is much faster and occurs when the whole of the reactant mixture is ignited at the same time, eg. placing it in a furnace above the ignition temperature of the SHS reaction.

Experimental Reaction Systems

Several model composite systems have been investigated in which an excess amount of Al is used both as a reductant in the reaction and as the metal component of the ceramic-metal composite [2-6] one example is given below:

$$3TiO_2 + 3C + (4 + x)Al = 3TiC + 2Al_2O_3 + xAl \quad (1)$$

where x was varied between O to 9 [2].

The excess amount of liquid Al is allowed to simultaneously infiltrate the pores in the ceramic composite, and hence improve the relative density. A variation of reaction (1) is given in reaction (2) in which the Al is used to reduce TiO_2 and generate an excess amount of Ti [6].

ie. $$(3 + x)TiO_2 + 3C + (4 + 4/3x)Al = 3TiC + (2 + 2/3x)Al_2O_5 + xTi \quad (2)$$

This ceramic-metal composite ($TiC-Al_2O_3-Ti$) will, therefore, provide a potential for increased operating temperatures.

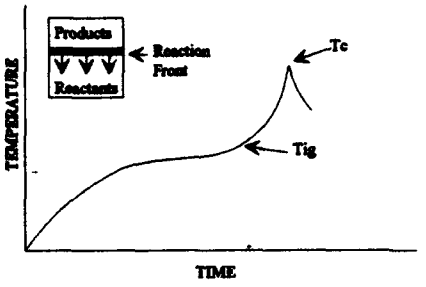

Figure 1. Schematic representation of the combustion synthesis reaction.

This novel approach, ie. SHS + in-situ liquid metal infiltration, has resulted in an increase in density of the composite from 45% theoretical to approximately 75% theoretical [2] in reaction (1). The enthalpy (H)-temperature (T) plots for these two reaction systems are given in Figure 2 in which Xr and Xp refer to the respective reactant and product H-T plots associated with the corresponding excess amount of Al or Ti, eg. Xr = 3, Xp = 3 refers to 3 moles of excess Al or Ti. Also indicated on these diagrams and in Table I are the corresponding melting and boiling points of reactants and products. It is apparent from Figure 2 that conducting these combustion synthesis reactions under adiabatic conditions with a Tig of 1000°C and a stoichiometry of x = 0 will exceed the melting points of Al, TiO_2, Al_2O_3, Ti and the boiling point of Al. These phase changes will affect the stability of the combustion front [7]. However, most SHS reactions are conducted under non-adiabatic conditions since heat is lost to the surroundings from the reactant pellet, ie. Tc<Tad. as indicated in Figure 2. Increasing x decreases Tad for both reaction systems. However, unlike reaction (1), reaction (2) becomes more exothermic as the amount of excess Ti (xTi) increases [Figure 2(b)].

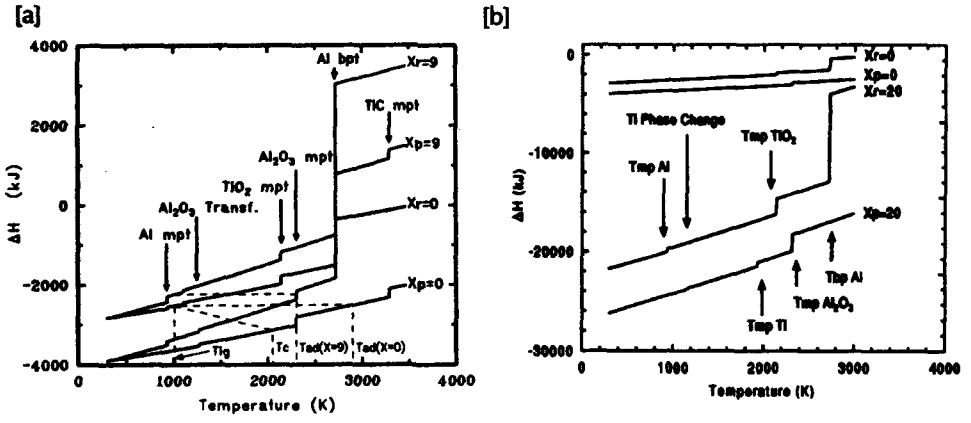

Figure 2. Enthalpy-temperature plots for reactants (Xr) and products (Xp) for [a] reaction (1) and [b] reaction (2) for various values of excess Al or Ti, ie., Xr = 9, Xp = 9 refers to an excess of 9 moles of Al or Ti in the reaction stoichiometry. Note that the heat of reaction for reaction (2) becomes more exothermic as xTi increases.

Experimental Procedure

The reactant powders (Table I) were thoroughly mixed using porcelain ball milling and pressed to various green densities, with varying values of x, into cylindrical compacts of 0.5 inches (12.7mm) in diameter and 1 inch (25.4mm) in length. These pellets were dried

for 1 hour at 120°C and ignited in either the propagating or simultaneous combustion modes using either a heated flat tungsten coil or a basket tungsten coil respectively in an argon [Figure 3]. The Tig was determined using a Pt-Pt/10%Rh thermocouple and Tc was determined using an Ircon Mirage two wavelength infrared pyrometer. A video camera was used in the propagating mode experiments to record the stability and rate of the combustion wave.

Table 1. Physical Properties of reactants and Products in Reactions (1)-(2)

Material	TiO_2	C	Al	TiC	Al_2O_3	Ti
Mpt°C	1830		660	3140	2050	1660
Bpt°C	3000		2467	4820	2980	3287
SG*	4.26	2.25	2.70	4.93	3.97	4.54
Size (μm)	-44	-44	-44			

*Specific Gravity

The ceramic-metal composites produced were examined using optical and scanning electron microscopy (SEM) interfaced with an energy dispersive spectroscopy (EDS) facility and also by x-ray diffraction (XRD). The density of the products was determined using an immersion in water technique.

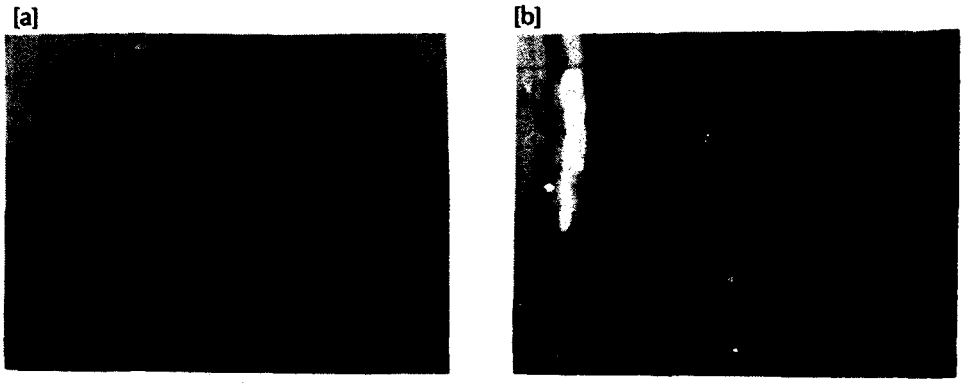

Figure 3. [a] coil configurations for propagating and [b] simultaneous combustion modes.

Results and Discussion

The ceramic-metal product densities increased with excess Al or Ti, eg. from 45% to 75% dense with x = 9 for reaction (1), while, in general, both Tig and Tc decreased with increase in xAl or xTi [2,6]. The effects of green density and excess Al on the stability of the combustion reaction conducted in the propagating mode were evaluated from examination of the slow motion video camera recording. A stable combustion front was one in which a steady state rate of propagation was observed. A semi-stable combustion front was one which oscillated, ie. the front slowed down, almost extinguished and subsequently increased. An unstable wave propagation was defined as that which

quenched out at some position along the pellet. Using these definitions, combustion synthesis stability diagrams were constructed for reactions (1) and (2) and are given in Figures 4(a) and (b) respectively. In general, increasing excess Al and green density for

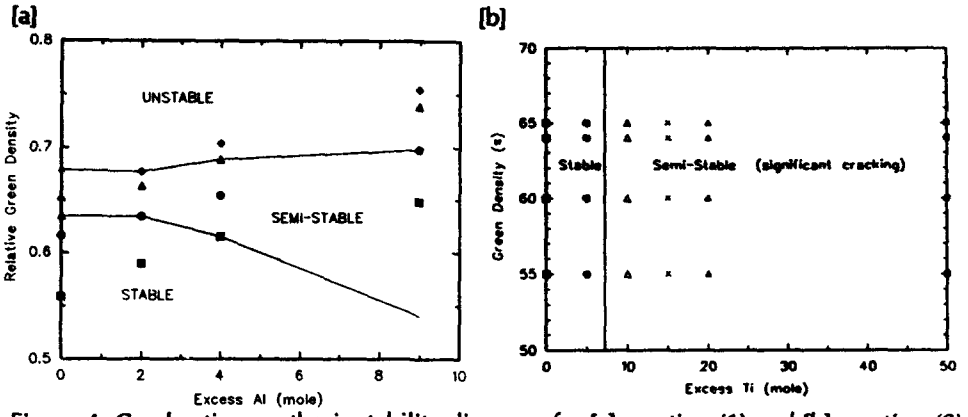

Figure 4. Combustion synthesis stability diagrams for [a] reaction (1) and [b] reaction (2)

reaction (1) resulted in decreased stability of the combustion front and eventually quenching out. This is the result of increased heat losses from the SHS reaction on account of increased thermal conductivity (increased green density) of the reactants ahead of the reaction front and latent heat of fusion (increased excess Al). Although no unstable fronts were observed in reaction (5), the combustion front became semi-stable on increasing xTi greater than 5. For values of $x>5$ severe cracking was observed to occur ahead of the combustion front [Figure 5] which was also coincidental with the onset of semi-stable propagation.

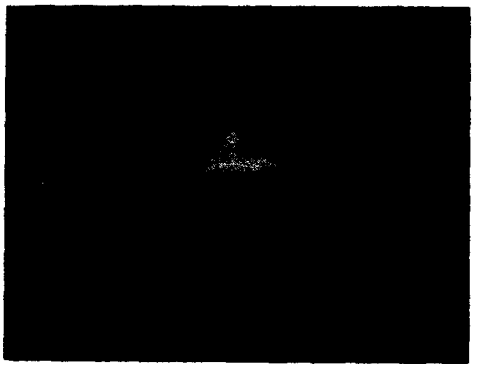

Figure 5. Observed cracking ahead of combustion front on reaction (2) for $x>5$.

Samples from reaction (2) were also produced by the simultaneous combustion mode. No cracking ahead of the front was observed. This is most likely a result of the lower thermal gradients that are present under this mode of ignition compared with the propagating mode. The increasing exothermicity of reaction (2) with increasing xTi [Figure 2] has aided in maintaining a semi-stable wave even up to xTi = 50.

XRD analysis of the products identified the expected product phases as TiC, Al_2O_3, and Al or Ti only. Typical product microstructures produced by both modes of combustion are given in Figure 6. The composite produced by the simultaneous combustion mode for reaction (2) exhibited less porosity than the propagating mode.

Although there is a considerable increase in density achieved by this SHS + in-situ liquid metal infiltration approach, maximum density and near net shape processing can be better

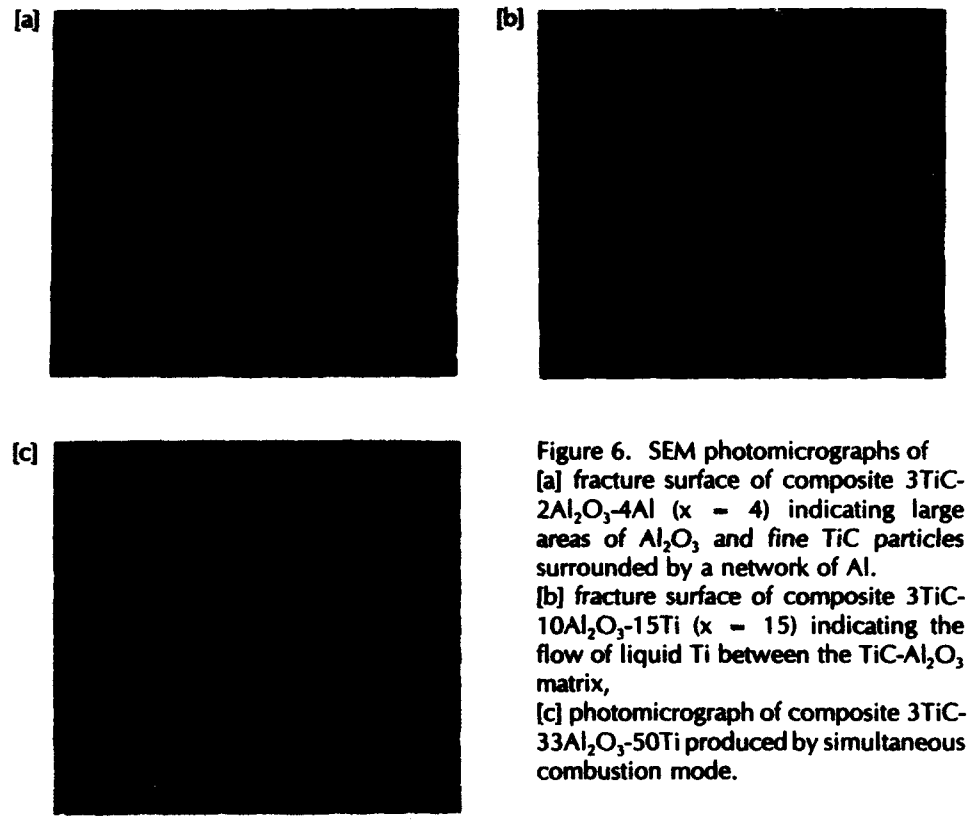

Figure 6. SEM photomicrographs of [a] fracture surface of composite 3TiC-$2Al_2O_3$-4Al (x = 4) indicating large areas of Al_2O_3 and fine TiC particles surrounded by a network of Al. [b] fracture surface of composite 3TiC-$10Al_2O_3$-15Ti (x = 15) indicating the flow of liquid Ti between the TiC-Al_2O_3 matrix, [c] photomicrograph of composite 3TiC-$33Al_2O_3$-50Ti produced by simultaneous combustion mode.

achieved by coupling this technique with simultaneous hot pressing. Applying a compressive load, simultaneously as the exothermic reaction is initiated has resulted in fully dense ceramic-metal composites of 3TiC-$2Al_2O_3$-9Al, ie. x = 9 [Figure 7] and achieved compressive strengths of 1.1x to 10^5 psi (758.4 MPa) [Figure 8]. The excellent distribution of a fine Al network between the fine TiC and Al_2O_3 particles is clearly evident in the fractured 3TiC-$2Al_2O_3$-xAl (x = 4) ceramic-metal composite shown in Figure 9. Increasing the relative density of the composite from 83% to 96% has produced a considerable increase in compressive strength and decrease in scatter of the data [Figure 8], even though the volume fraction of the soft ductile aluminum has increased. The terraced appearance of the fractured surface of the samples tested in the compression tests [Figure 9(c)] indicate a potential for increased toughness. However, no fracture toughness tests have been conducted as yet. Further improvement is possible by lowering Tc to avoid melting Al_2O_3. Fully dense TiC-Al_2O_3 ceramic composites have been achieved using small amounts of Al_2O_3 as a diluent and employing simultaneous hot pressing and SHS [Figure 10] in a graphite die. The volume fractions of reactants and products for reactions (1) and (2) for stoichiometries of x = 0 and y (diluent) Al_2O_3 in which y was varied from 0 to 6 are given in Figure 11.

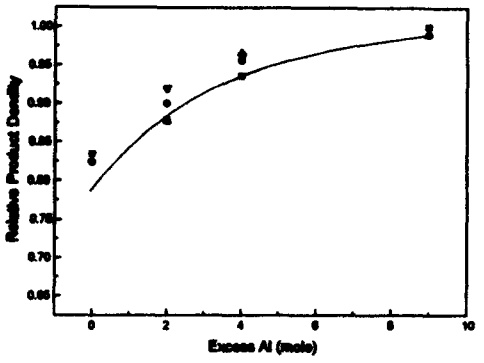

Figure 7. The effect of excess Al on the relative density of the TiC-Al_2O_3-Al ceramic-metal composite using the *simultaneous combustion mode* and a pressure of 3600 psi (24.8 MPa) applied to the reaction system in a graphite die

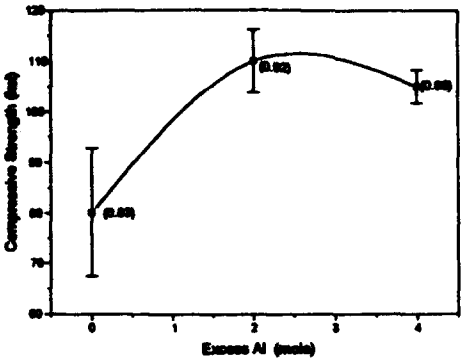

Figure 8. The effect of excess Al on compressive strength for TiC-Al_2O_3-Al ceramic-metal composites produced by *simultaneous hot pressing* and SHS in a graphite die, ie. same samples as given in Figure 7. The figures in parentheses indicate the theoretical density of the samples tested.

[a]

[b]

[c]

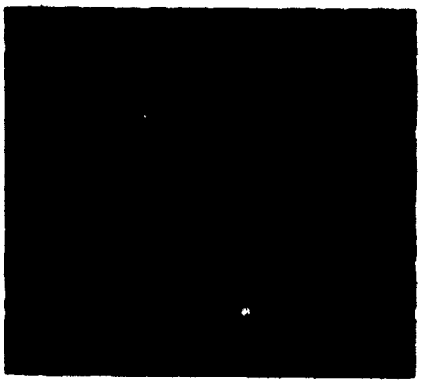

Figure 9. SEM photomicrograph of (a) 3TiC-$2Al_2O_3$ (x = 0), (b) 3TiC-$2Al_2O_3$-4Al (x = 4) and (c) fractured surface of 3TiC-$2Al_2O_3$-4Al after compression test.

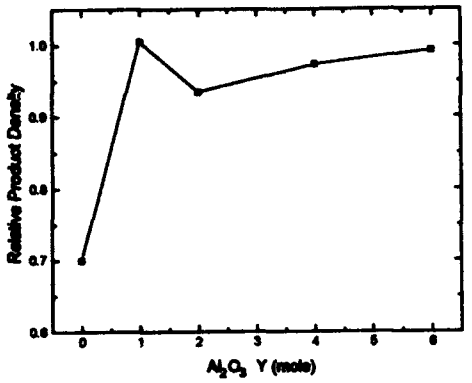

Figure 10. Effect of excess Al_2O_3 in the reaction stoichiometry for reactions (1) and (2) at x = 0 (no excess Al), ie. $3TiO_2 + 3C + 4Al + yAl_2O_3 = 3TiC + (2 + y)Al_2O_3$, on the relative density of the ceramic composite produced by simultaneous combustion and hot pressing (3600 psi, 24.8 MPa).

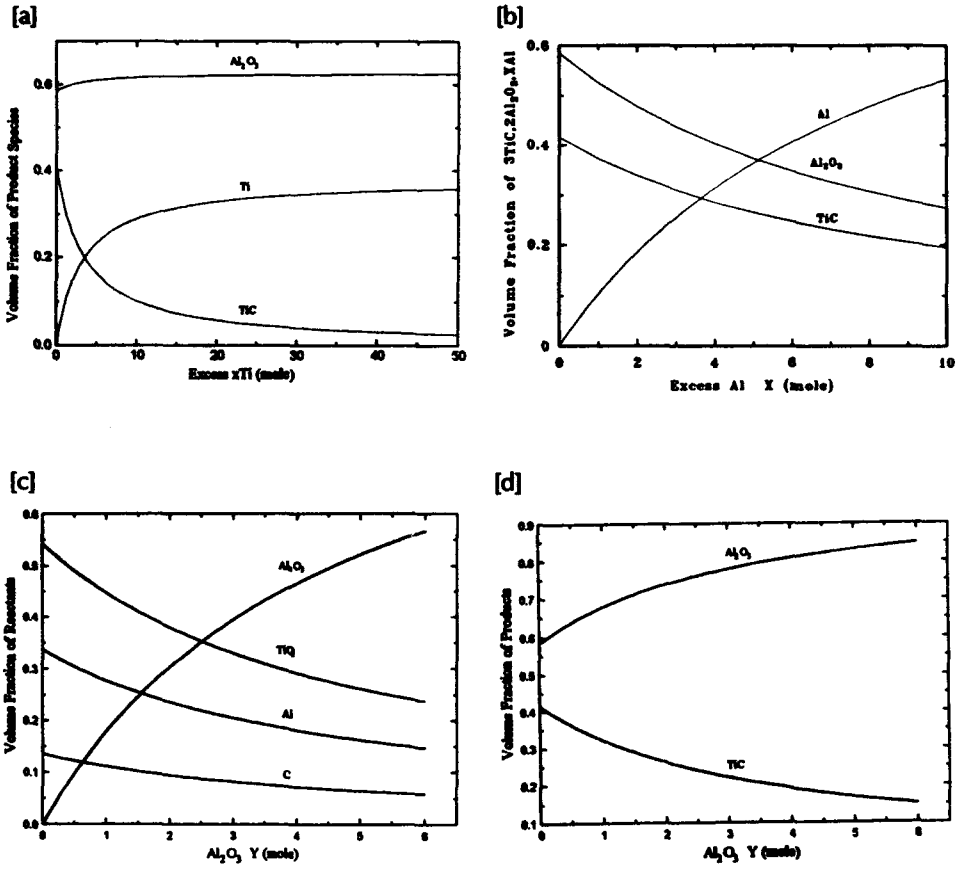

Figure 11. Effect of reaction stoichiometry on volume fractions of [a] products for reaction (1), [b] products for reaction (2) and [c] reactants and [d] products for reaction (1) when x = 0 and yAl_2O_3 is varied between 0 and 6.

Conclusions

It appears from these data, that the application of a simultaneously applied load during the SHS reaction is beneficial in improving the theoretical density and compressive strength of these ceramic and ceramic-metal composites. The addition of Al_2O_3 as a diluent lowers the combustion temperature and aids in control of the particle size of the product phases. The favorable distribution of a fine Al network in the ceramic-metal composite produced by this simultaneous SHS-in-situ liquid metal infiltration and hot pressing approach should result in improved fracture toughness and can be used in conjunction with the use of Al_2O_3 as a diluent to produce fully dense, near net shape, tough ceramic-metal composites. The critical issues to be resolved using this approach include a more fundamental understanding of the effect of the processing parameters on the ceramic-metal system, eg. green particle and compact processing; the effect of excess Al, Ti, and Al_2O_3 on Tc and density control and their effect on the mechanical properties of the composites; effect of loading on the reacting system; the level of oxygen in the excess Ti produced via reaction (2) and the reproducibility of microstructure and properties produced by this rapid synthesis and processing technique; and the elevated temperature properties for ceramic-Al and ceramic-Ti composites.

Acknowledgements

The authors are grateful for partial support of this work by NASA Microgravity Science Division - Code SN.

References

1. Z.A. Munir, Ceramic Bulletin, 67(2) (1988) 342.
2. H.J. Feng, J.J. Moore, D.G. Wirth, "The Combustion Synthesis of Ceramic-Metal Composites: The TiC-Al_2O_3-Al System", Met. Trans., 23A, 1992, pp 2373-2379.
3. H.J. Feng, J.J. Moore, D.G. Wirth, "Combustion Synthesis of TiB_2-Al_2O_3-Al Composite Materials" to be published in Proceedings of the Symposium on Developments in Ceramic and Metal Matrix Composites, TMS Annual Meeting, San Diego, March 1-5, 1992; pub by TMS, pp 219-239.
4. H.J. Feng, J.J. Moore, D.G. Wirth, "Combustion Synthesis of Ceramic Metal Composite Materials: The ZrB_2-Al_2O_5-Al System" International Journal Self-Propagating High Temperature Synthesis (SHS), 1, (2), 1992, pp 228-238.
5. H.J. Feng, J.J. Moore, D.G. Wirth, "The Combustion Synthesis of B_4C-Al_2O_3-Al Composite Materials" Proceedings of the Symposium on Synthesis and Processing of Ceramics: Scientific Issues MRS Fall Meeting, Boston, Dec 2-6, 2991; pub by MRS.
6. K.J. Hunter, J.J. Moore, D.G. Wirth, Proceedings of 6th International Titanium Conference, San Diego, CA, July 28 - Aug. 2, 1992; pub by TMS.
7. A.K. Filonenko V. 1. Vershinnikov, Combustion Explosion Shock Waves, 11 (1975) 301.

IMPROVEMENT OF ROOM-TEMPERATURE DUCTILITY OF INTERMETALLIC COMPOUNDS BY UNIDIRECTIONAL SOLIDIFICATION

TOSHIYUKI HIRANO

National Research Institute for Metals
1-2-1, Sengen, Tsukuba, Ibaraki 305 Japan

Abstract

A major drawback of intermetallic compounds is their poor ductility and low fracture toughness at room temperature. Considerable effort has been devoted to improve this drawback by micro-alloying and macro-alloying. This paper presents a promising alternative method. Unidirectional solidification using a floating zone method is found to improve the room-temperature ductility of Ni_3Al. Unidirectionally solidified Ni_3Al has a columnar-grained structure and exhibits a large tensile elongation of 60 % at room temperature. Intergranular fracture is suppressed. Solidification structure of Ni_3Al and its tensile properties are presented. Application of this method to TiAl is also presented.

Critical Issues in the Development of High Temperature Structural Materials
Edited by N.S. Stoloff, D.J. Duquette and A.F. Giamei
The Minerals, Metals & Materials Society, 1993

Introduction

Polycrystalline Ni_3Al is extremely brittle at room temperature because of intrinsic grain-boundary brittleness [1-3], and unless a small amount of boron is doped, it easily suffers from intergranular fracture, showing much limited ductility [4]. Very recently, Liu [5] and George et al. [6,7] pointed out that the brittleness is due to environmental effect, i.e. moisture-induced environmental embrittlement.

We recently found that unidirectional solidification (UDS) using a floating zone method (FZ) effectively overcomes this problem without boron doping. We call this method FZ-UDS [8,9]. The stoichiometric Ni_3Al grown by FZ-UDS has a columnar-grained structure and shows about 60% larger tensile elongation along the columnar structure at room temperature. It fractures transgranularly and intergranular fracture which occurs in brittle Ni_3Al is significantly suppressed [9]. Of particular interest is that it shows tensile ductility of about 15% even perpendicular to the columnar structure, with the fracture mode still being transgranular [10]. It indicates that the grain boundaries of Ni_3Al grown by FZ-UDS are resistant to intergranular cracking. In addition, FZ-UDS has an advantage of improving the ductility of Al-rich Ni_3Al [11], which is impossible for the boron-doping method [12]. This is favorable for high temperature structural applications since Al-rich Ni_3Al has higher strength at elevated temperatures than Ni-rich Ni_3Al [13]. Thus FZ-UDS is a promising way to improve the ductility of intermetallic compounds.

In this paper the FZ-UDS process, the solidification structure of Ni_3Al, and the room-temperature mechanical properties are presented. Application of FZ-UDS to TiAl is also presented.

FZ-UDS of Ni_3Al

Procedure

FZ-UDS is carried out in a flowing argon atmosphere by a floating zone method [8]. Infrared radiation from the double halogen lamps is used as the heating source. This method has an advantage of easy operation and permit us to control growth rate strictly. Forced convection is applied to the molten zone to reduce the temperature gradient in the radial direction and the concentration gradient in the molten zone: the feed rod and the grown alloy are rotated in opposite directions during the operation. The growth rate is the most important controlling factor of the solidification structure [8,9,14,15].

Solidification structure

Solidification structure of stoichiometric Ni_3Al is dependent on the growth rate, as shown in Fig.1 [14-16]. The structure grown at 25 mm/h is a columnar-grained single phase Ni_3Al which is ductile at room temperature as described below. A striking feature of this structure is high frequency of low energy boundaries, Σ1,3,9, and 19, as shown in Fig.2 [17]. In this figure, hatched bars indicate the experimentally determined values and open bars indicate the values predicted theoretically for randomly oriented grains. The frequency of low energy

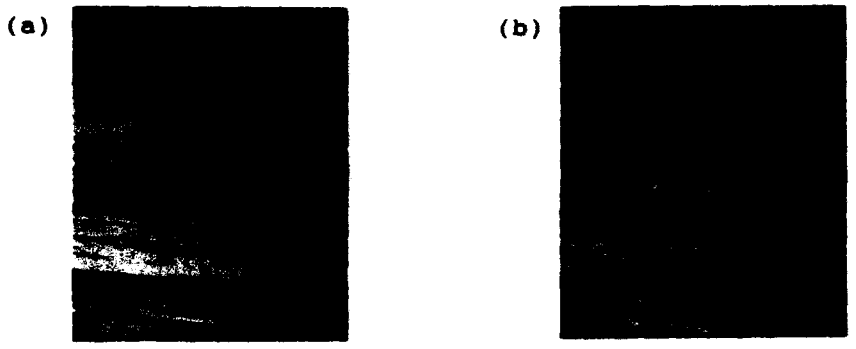

Figure 1- Optical micrographs of stoichiometric Ni3Al grown by FZ-UDS at the growth rate of (a) 25 mm/h and (b) 50 mm/h.

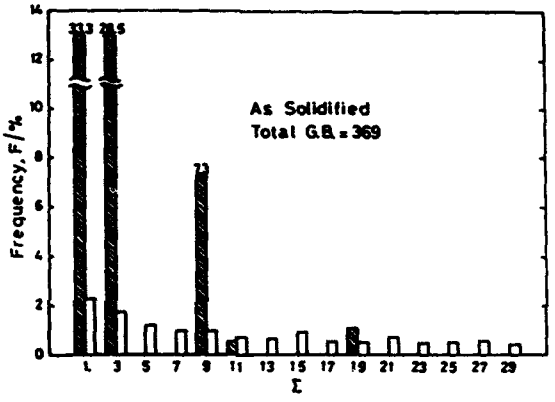

Figure 2- Frequency of coincidence boundaries as a function of Σ in the stoichiometric Ni3Al grown at 25 mm/h.

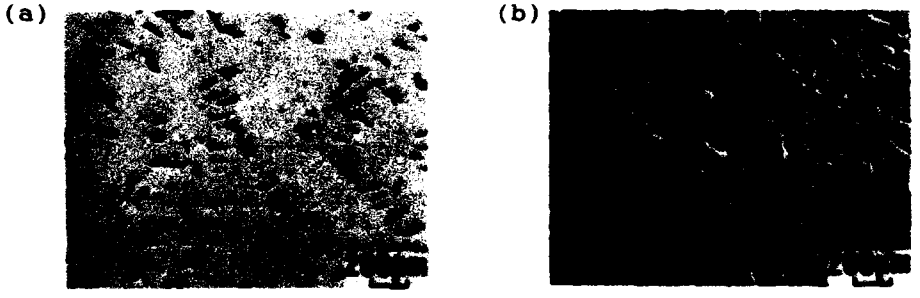

Figure 3- Optical micrographs of Al-rich Ni3Al grown by FZ-UDS at 25 mm/h. (a) Ni-26at%Al, (b) Ni-27at%Al.

boundaries exceeds 70 %. Therefore, the solidification structure has a texture. Several types of textures such as <100>, <110>, <111>, and <210> have been observed. With increasing the growth rate the structure becomes a duplex structure of Ni3Al and NiAl ($L1_0$-type β'-NiAl). Figure 1(b) shows that NiAl is precipitated dendritically in the columnar-grained Ni3Al matrix. At a lower growth rate below 10 mm/h it is difficult to keep the operation stable for long time and NiAl precipitate intermittently [8,9].

Al-rich Ni3Al shows a duplex structure of Ni3Al and NiAl at any growth rates. The precipitated NiAl is massive, as shown in Fig.3, which is different from that in stoichiometric Ni3Al [11].

Formation mechanism of the columnar-grained Ni3Al

Ni3Al and NiAl grow simultaneously from the liquid in the form of lamellar structure at the growth rate of 25 mm/h [14,16]. It is similar to eutectic alloys although stoichiometric Ni3Al undergoes peritectic reaction. The precipitated NiAl is not stable below solidification temperature and dissolves into the Ni3Al matrix when cooling starts after solidification. Resultantly the columnar-grained single phase Ni3Al is formed at room temperature.

Mechanical properties of stoichiometric Ni3Al at room temperature

Tensile properties

The columnar-grained single phase Ni3Al shows large tensile ductility along the columnar structure at room temperature, as shown in Fig.4 [9]. The total tensile elongation is larger than 60 %. Compare it with that of equiaxed and brittle Ni3Al which is fabricated by conventional casting.

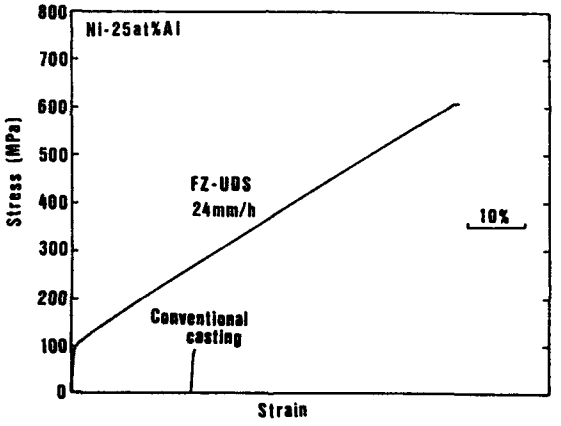

Figure 4- Tensile stress-strain curves of the columnar-grained single phase Ni3Al grown at 24 mm/h, comparing with that of equiaxed Ni3Al fabricated by conventional casting.

The tensile specimen is elongated uniformly throughout the entire gauge section. The stress-strain curve shows linear work hardening in the wide range of strain after yielding and then catastrophically fractures without necking. The linear working rate, which ranges from 1000 to 1250 MPa, is rather small compared with those of boron-nondoped [1] and boron-doped Ni3Al [4].

Of particular interest is that it shows about 15 % tensile elongation even perpendicular to the growth direction, as shown in Fig.5, indicating that the grain boundaries are resistant to

crack initiation. Liu and Oliver first tried to improve the room-temperature ductility of Ni3Al by directional levitation zone melting and obtained tensile elongation of 14.1 % in the longitudinal direction of the columnar-grained structure [18]. They pointed out that the effect is due to the grain shape, i.e. normal stress can be minimized along the columnar structure. However, the present results suggest that the effect of FZ-UDS is not due to the geometrical reason but due to the property of the grain boundary.

Very recently Liu and his gruop found that polycrystalline, B-free Ni3Al with and without Zr exhibit much larger room-temperture tensile ductility in oxygen than in air [5-7]. They used special specimens which were produced by careful cold working of polycrystalline ingots or single crystals and recrystallizing. They concluded that Ni3Al is intrisnsically ductile and suceptible to moisture-induced hydrogen embrittlement at ambient temperatures. The moisture-induced embrittlement may be suppressed in the Ni3Al grown by FZ-UDS. It may be related to the large amount of low energy boundaries in this alloy. However, there is a marked difference in fracture mode between Liu et al.'s Ni3Al and the FZ-UDS Ni3Al, as described below. The former Ni3Al fractures intergranularly independent of environment and the latter transgranularly. Additional study is therefore needed to clarify the cause of the large tensile ductility of the FZ-UDS Ni3Al.

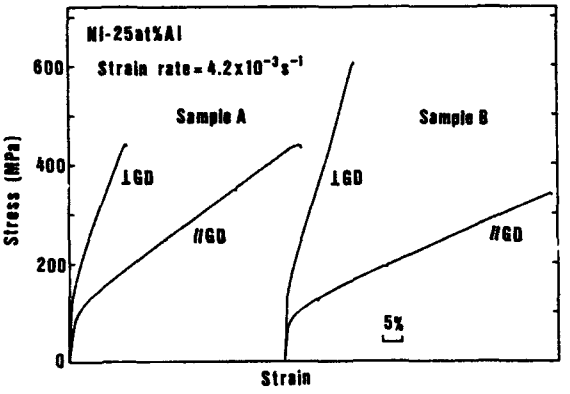

Figure 5- Room-temperature tensile stress-strain curves of the columnar-grained Ni3Al parallel and perpendicular to the growth direction.

Fracture mode

The fracture mode of the columnar-grained structure is transgranular type, as shown in Fig.6(a) [8,9]. Such fracture mode is quite similar to that of the born-doped ductile Ni3Al [4,9]. Many crystallographic slip traces are observed on the fracture surface. On the surface of the specimen surface it is seen that slip bands transferred across grain boundaries without crack initiation (Fig.6(b)), i.e. dislocations can move from one grain to the adjacent grain accompanying with accommodation slip in the grain boundary region. Intergranular fracture which is commonly observed in conventionally cast Ni3Al is suppressed in the columnar-grained Ni3Al. In other words, the grain boundary

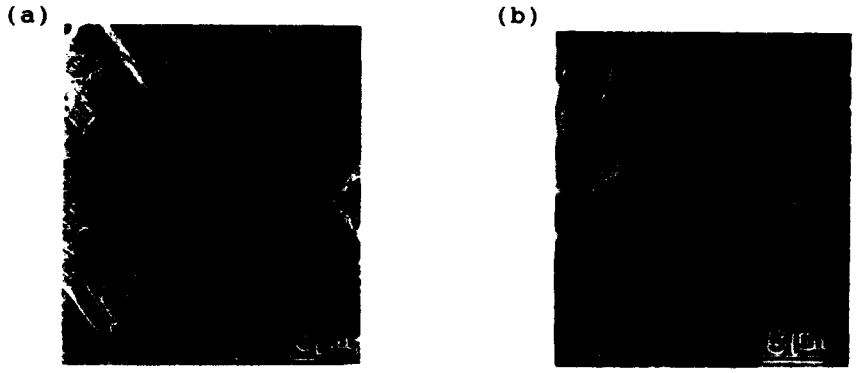

Figure 6- SEM micrographs of the (a) fracture surface and (b) side surface of the tensile-tested specimen grown at 24 mm/h.

brittleness of polycrystalline Ni3Al is substantially improved by FZ-UDS. Cold rolling of 25% is possible at room temperature without intermediate annealing in the same way as ductile metals [19].

Deformation microstructure

Primary and secondary slip systems of {111} are activated in tensile deformation. The specimen surface is corrugated after 3 % elongation and the surface corrugation develops into martensite-like plate with strain. Many stacking faults (SISF-type) are formed in the plate. This suggests a correlation between the formation of the SISF and the large tensile ductility [16].

Mechanical properties of Al-rich Ni3Al at room temperature

Tensile properties

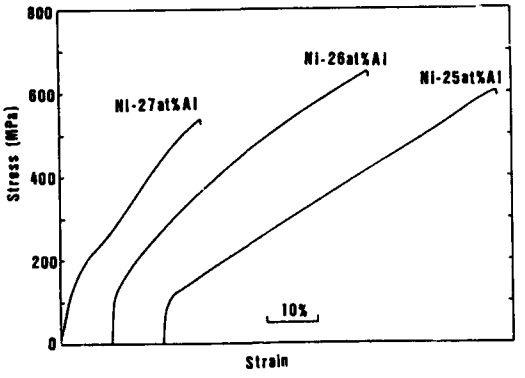

Figure 7- Room-temperature stress-strain curves of the stoichiometric and Al-rich Ni3Al.

It should be noted that Al-rich Ni3Al can be ductilized by FZ-UDS. Figure 7 shows the stress-strain curves of the stoichiometric and Al-rich Ni3Al [11]. As Al concentration increases, the yield stress and the work hardening rate increase and the tensile ductility, on the contrary, decreases.

Figure 8 plots the tensile elongation as a function of Al concentration, comparing with that of boron-doped Ni3Al [12]. It is well known that the effect of boron doping is strongly dependent on alloy stoichiometry [12]. The tensile elongation decreases with increasing Al concentration in Ni3Al and the boron doping is only effective in Ni-rich Ni3Al. Alloying elements such as Fe and Mn can also improve the ductility but this is also effective in Ni-rich Ni3Al [20]. In contrast with these micro- and macro-alloying, FZ-UDS can improve the ductility of stoichiometric and Al-rich Ni3Al. This is an advantage for high temperature structural applications since Al-rich Ni3Al has higher strength at elevated temperatures than Ni-rich Ni3Al [13]. Probably Al-rich Ni3Al is more resistant to

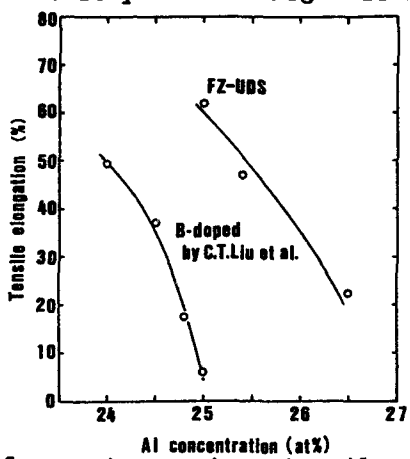

Figure 8- Plot of room-temperature tensile elongation as a function of Al concentration, comparing with the boron-doping effect [12].

oxidation than Ni-rich Ni3Al. The precipitated NiAl in Al-rich Ni3Al may increase the creep resistance.

Fracture mode

The Ni3Al matrix shows the same fracture mode as the stoichiometric Ni3Al, i.e. intergranular fracture. However, cracks initiate at the interface between the precipitated NiAl and the Ni3Al matrix, as shown in Fig.9 [11]. The precipitate NiAl themselves are brittle and show cleavage fracture.

Application of FZ-UDS to TiAl

FZ-UDS is also found to be effective in improving the room-temperature ductility of TiAl [21]. The solidification structure is strongly dependent on the growth rate and alloy composition similar to Ni3Al. Figure 10 shows the optical micrographs grown by FZ-UDS at several conditions. The alloys with 48 and 50 at % Al grown at 5 mm/h exhibit a single crystal-like

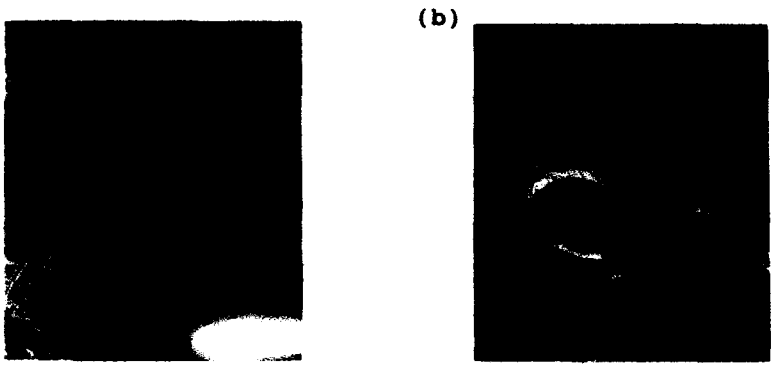

Figure 9- SEM micrographs of the (a) fracture surface and (b) side surface of the tensile-tested specimen of Ni-26at%Al

$Ti_3Al(\alpha_2)/TiAl(\gamma)$ layered structure. As the growth rate increases, the alloy with 48 and 50 at % Al exhibit a columnar-grained structure; however, the former consists of the layered structure, whereas the latter contains γ single-phase grains as well. The alloy with 52 at % Al exhibits a γ single phase, regardless of the growth rate.

The room-temperature tensile properties are shown in Fig.11 as function of alloy composition and growth rate. Concerning the tensile elongation, there are two attractive regions where the tensile elongation exhibits larger than 3 %. In particular, the region B where the alloy has columnar-grained structure is attractive because tensile ductility larger than 4 % and relatively high strength. It is considered that such attractive

Figure 10- Optical microstructures of Ti48 at % Al (a,b,c), 50 at % Al (d,e,f), and 52 at % Al (g,h) grown at 5 mm/h (a,d,g), 24 mm/h (b,e,h), and 70 mm/h (c,f).

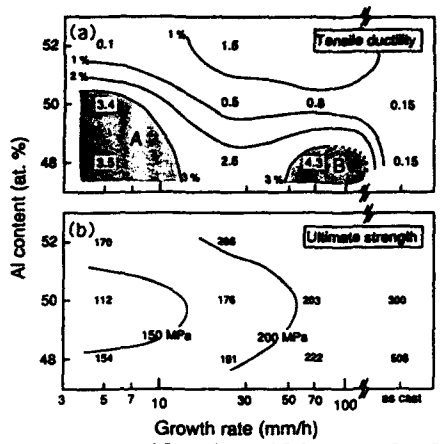

Figure 11- Changes in tensile ductility and ultimate strength with growth rate and alloy composition of TiAl grown by FZ-UDS.

properties are due to the columnar-grained structure with texture.

Summary

Improvement of the room-temperature ductility of Ni3Al and TiAl by FZ-UDS is presented. The experimental results indicate a possibility of improving brittle intermetallic compounds by controlling grain boundary character and texture, which are proposed by Watanabe [22]. FZ-UDS is a promising way to fabricate ductile intermetallic compounds.

Acknowledgment

The author would like to acknowledge Dr. T.Watanabe for his measurement of grain boundary character and helpful discussion. He also would like to Dr. M.Takeyama for his helpful discussion.

References

1. K.Aoki and O.Izumi, "On the Ductility of the Intermetallic Compound Ni3Al", Jpn.Inst. Metals, 19(1978),203-210.
2. T.Ogura,S.Hanada,T.Masumoto, and O.Izumi", Met.Trans. A, 16A(1985),441-443.
3. T.Takasugi,E.P.George,D.P.Pope, and O.Izumi, "Intergranular Fracture and Grain Boundary Chemistry of Ni3Al and Ni3Si", Scripta metall., 19(1985),551-556.
4. K.Aoki and O.Izumi, "Improvement in Room Temperature Ductility of the L12 type Intermetallic Compound Ni3Al by Boron Addition", J.Jpn.Inst. Metals, 43(1979),1190-1196.
5. C.T.Liu, "Environmental Embrittlement and Grain-Boundary Fracture in Ni3Al", Scripta metall.mater., 27(1992),25-28.
6. E.P.George,C.T.Liu, and D.P.Pope, "Environmental Embrittlement: The Major Cause of Room-Temperature Brittleness in Polycrystalline Ni3Al", Scripta metall.mater., 27(1992),365-370.
7. E.P.George,C.T.Liu, and D.P.Pope,"Intrinsic Ductility and Environmental Embrittlement of Binary Ni3Al", Scripta

metall.mater., 28(1993),857-862.
8. T.Hirano, "Improvement of Room Temperature Ductility of Stoichiometric Ni3Al by Unidirectional Solidification", Acta metall. mater., 38(1990),2667-2671.
9. T.Hirano and T.Kainuma, "Improvement of Room Temperature Ductility of Stoichiometric Ni3Al by Unidirectional Solidification", ISIJ International, 31(1991),1134-1138.
10. T.Hirano, "Tensile Ductility of Stoichiometric Ni3Al Grown by Unidirectional Solidification", Scripta metall.mater., 25(1991),1747-1750.
11. T.Hirano,Sea-Sung Chung,Y.Mishima, and T.Suzuki, "Improvement of Room Temperature Ductility of Ni3Al by Unidirectional Solidification", Mat.Res.Symp.Proc., 213(1991),635-640.
12. C.T.Liu,C.L.White, and J.A.Horton, "Effect of Boron on Grain-Boundaries in Ni3Al", Acta metall., 33(1985),213-229.
13. O.Noguchi,Y.Oya, and T.Suzuki,"The Effect of Nonstoichiometry on the Positive Temperature Dependence of Strength of Ni3Al and Ni3Ga", Met.Trans. A, 12A(1981), 1647-1653.
14. T.Hirano and T.Mawari, "Unidirectional Solidification of Ni3Al by a Floating Zone Method", Acta metall.mater. (in press).
15. T.Mawari and T.Hirano, (unpublished data).
16. T.Hirano and T.Mawari, "Microstructure and Room- Temperature Ductility of Unidirectionally Grown Ni3Al", Mater.Res.Symp.Proc., 288(1993), (in press).
17. T.Watanabe, "Toughening of Brittle Materials by Grain Boundary Design and Control", (Paper presented at the 6th Int. Conf. on Intergranular and Interphase Boundaries in Materials, Thessaloniki, Greece, 22-26 June 1992), Materials Science Forum, (in press).
18. C.T.Liu and B.F.Oliver, "Effect of Grain Shape on Environmental Embrittlement in Ni3Al Tested at Elevated Temperatures", J.Mater.Res., 4(1989),294-299.
19. T.Hirano and T.Mawari, "Cold Rolling of Boron-Free Polycrystalline Ni3Al Grown by Unidirectional Solidification", Scripta metall.mater., 26(1992),597-600.
20. T.Takasugi,O.Izumi, and N.Masahashi, "Electronic and Structural Studies of Grain Boundary Strength and Fracture in $L1_2$ Ordered Alloys-II. On the Effect of Third Elements in Ni3Al Alloy", Acta metall., 33(1985),1259-1269.
21. M.Takeyama,T.Hirano, and T.Tsujimoto, "Influence of Growth Rate on Microstructure and Tensile Properties of Directionally Solidified TiAl Alloys", (Proc. 6th Int. Synp. on the Intermetallic Compounds-Structure and Mechanical Properties-(JIMIS-6), Sendai, Japan, June 17-20, 1991, p.507-511).
22. T.Watanabe, "An Approach to Grain Boundary Design for Strong Ductile Polycrystal", Res. Mechanica, 11(1984), 47-84.

SESSION IV

Strengthening/Toughening Mechanisms I
(Metals and Intermetallics)

STRENGTHENING AND DUCTILIZATION OF TWO PHASE TiAl ALLOYS IN LAMELLAR FORM BY TERNARY ALLOYING ADDITIONS

Masaharu Yamaguchi and Haruyuki Inui

Department of Metal Science and Technology
Kyoto University
Sakyo-ku, Kyoto 606, Japan

Abstract

In two-phase TiAl alloys, the lamellar structures are of special interest and importance since they are so common and persistent, not only under as-cast conditions but also after thermal treatment. However, the lamellar structures are still poor in ductility, although they are beneficial for toughness and high-temperature strength. This article will review the recent progress made in understanding the basic mechanical properties of the gamma and alpha-2 phases which comprise the two-phase alloys in lamellar form, and discuss how an improved balance of strength and ductility in the lamellar form may be achieved.

Critical Issues in the Development of High Temperature Structural Materials
Edited by N.S. Stoloff, D.J. Duquette and A.F. Giamei
The Minerals, Metals & Materials Society, 1993

Introduction

Recently, there has been an enormous increase in the research and development activity on titanium aluminides , in particular on the TiAl compound since it has immense potential as a new high-temperature light-weight structural material (for a review, see Kim and Dimiduk [1]). The TiAl phase possesses a wide composition range. However, it extends primarily on the Al-rich side, and the TiAl compounds with nearly equiatomic or Ti-rich compositions exhibit a two-phase microstructure composed of the TiAl (gamma) phase and a small volume fraction of the Ti_3Al (alpha-2) phase . The so-called TiAl compounds to which a recent enormous increase in the research and development activity has been devoted, are such gamma/alpha-2 two-phase alloys rather than the Al-rich TiAl compounds with a gamma single-phase structure since the former alloys are more ductile and tougher than the latter compounds. In the last few years, marked improvements in the mechanical properties of the two-phase alloys in duplex form have been achieved through alloying with ternary elements and controlling their microstructure by thermomechanical processing [1-12]. However, the lamellar structures are still poor in ductility, although they are beneficial for toughness and high-temperature strength. Alloying elements such as Cr, V, and Mn have been reported to increase the room-temperature ductility of the two-phase alloys in duplex form. However, none of them is effective in ductilizing the two-phase alloys in lamellar form. This article will review the recent progress made in understanding the basic mechanical properties of the gamma and alpha-2 phases which comprise the two-phase alloys in lamellar form, and discuss how an improved balance of strength and ductility in the lamellar form may be achieved.

Lamellar structure

When two-phase TiAl alloys with near-equiatomic compositions are prepared by usual ingot-metallurgy methods, the gamma phase precipitates from the alpha phase producing a lamellar structure which is composed of the transformed gamma and remaining alpha lamellae. Gamma lamellae are formed in such a way that close-packed planes and directions in the gamma phase are parallel to the corresponding planes and directions in the alpha phase. However, three $\langle 1\bar{1}20\rangle$ directions on the (0001) basal plane of the hcp alpha phase are all equivalent while the $[1\bar{1}0]$ direction and other two $\langle 0\bar{1}1\rangle$ directions on the (111) plane of the gamma phase with the tetragonal $L1_0$ structure are not equivalent to each other. The gamma phase can thus be formed in six possible orientation variants corresponding to the six possible orientations of $[1\bar{1}0]$ on (111) in the gamma phase with respect to $\langle 1\bar{1}20\rangle$ on (0001) in the alpha phase [13-18]. The formation of stacking faults is believed to be a precursor of the alpha-to-gamma transformation in lamellar form [19,20] and the thinning/thickening of the alpha lamellae has been proposed to occur by the motion of ledges parallel to the interfaces [18,21-23]. However, more work is needed to elucidate it.

A typical lamellar structure in a unidirectionally solidified ingot of Ti - 49.3 at % Al revealed by transmission electron microscopy (TEM) is presented in Fig. 1[18]. The $[1\bar{1}0]$ and $\langle 0\bar{1}1\rangle$ net selected-area electron diffraction (SAED) patterns are schematically illustrated in A, B and C, D, respectively in the upper part of the figure and the types A - D of the SAED patters obtained from each individual lamella on the XY line in the figure are depicted in the bottom of the figure in order to differentiate the variety of domains. Between alpha-2 lamellae, gamma lamellae can be seen to form a lamellar domain structure and each gamma lamella corresponds to one of the six orientation variants. Gamma/gamma lamellar interfaces are therefore intervariant boundaries. When gamma lamellae with the SAED patter A or C border those with the pattern B or D, the two neighboring gamma lamellae are separated by an intervariant boundary of the true-twin type. The two neighboring gamma lamellae can be separated by intervariant boundaries of the pseudo-twin type(the SAED pattern A or C borders the pattern D or B) and the 120°-rotational type (A or B borders C or D). Of particular significance in Fig.1 is that the intervariant lamellar boundaries of the pseudo-twin and 120°-rotational types are commonly observed. The ratio of energies of intervariant lamellar boundaries of the three different types, the true-twin, pseudo-twin and 120°-rotational types, has been estimated to be in the range of 1 : 3 : 2 to 1: 7 : 6 on the basis of a hard-sphere model [18]. This is not in accordance with the results of TEM observations of intervariant lamellar boundaries in the gamma phase. Energies of the intervariant lamellar boundaries of the pseudo-twin and 120°-rotational types must be much

Figure 1: A typical example of the lamellar structure in an as-grown PST TiAl viewed along the $<110>_{TiAl}//<11\bar{2}0>_{Ti_3Al}$. Possible four types of SAED patterns (A-D) are illustrated in the upper part of the figure and the types of patterns obtained from each TiAl lamella are depicted at the bottom of the figure [18].

smaller than those estimated on the basis of a hard-sphere model and hence they are much close to the energy of the true-twin type boundary; otherwise the boundaries of the pseudo-twin and 120°-rotational types may not exist in the gamma phase because of their high energies. Recently, it has been suggested that the lattice mismatches would, if unrelaxed, generate huge elastic stresses at the intervariant lamellar boundaries of these two types [24]. These observations strongly suggest that significant relaxation of atoms occurs at these intervariant lamellar boundaries. This will be discussed again in the section on environmental embrittlement. Kad and Hazzledine [25] have proposed a dislocation model for the intervariant lamellar boundaries of the 120°-rotational type. They have reported some observations of screw dislocations which lie on the 120°-rotational intervariant lamellar boundaries and which are consistent with their being misfit dislocations forming shear boundaries.

Deformation and fracture at room temperature

Gamma phase

Ingots of two-phase alloys with nearly equiatomic compositions prepared by usual ingot-metallurgy methods have a microstructure composed of randomly oriented grains with the fully lamellar structure. However, when such ingots are remelted and unidirectionally solidified at an appropriate rate, single-crystal-like ingots derived from a single alpha-phase grain and composed of the lamellar structure, can be obtained [26-29]. Since numerous thin twin-related gamma phase lamellae are contained in the major constituent phase, we call these crystals polysynthetically twinned (PST) crystals from analogy with the phenomenon, polysynthetic twinning which is often observed in mineral crystals [30].
The yield stress and elongation of PST crystals are plotted as a function of the angle ϕ, at which the lamellar boundaries lie from the loading axis, in Fig.2 and Fig.3, respectively [26-29]. The results of other deformation experiments on PST TiAl show the same trend [31,32]. Similar lamellar orientation dependence of yield stress has been found also in tension and bending tests on polycrystalline specimens composed of the textured lamellar grains [33,34]. TEM observations of deformation structures have revealed that deformation twins of the (111)<112]-type, which do not disturb the $L1_0$ symmetry of the lattice, and dislocations with $\mathbf{b} = 1/2<110]$ exit abundantly, regardless of the angle ϕ and loading mode [35]. This indicates that ordered

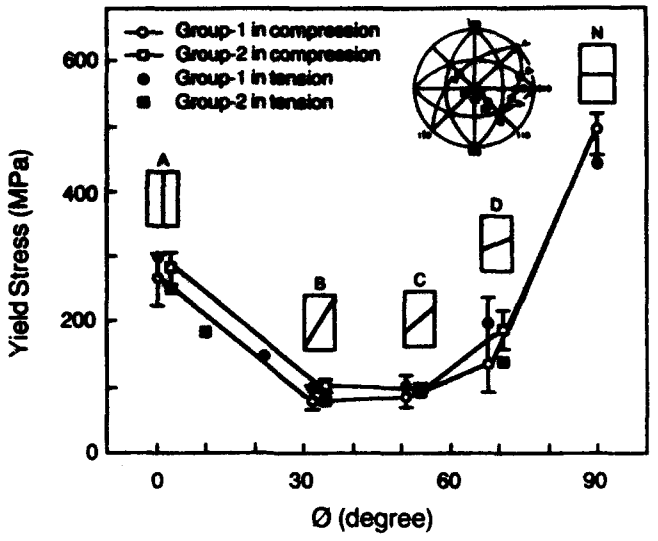

Figure 2: Yield stress of PST TiAl in tension and compression as a function of the angle ϕ [28]. The gauge section of tensile specimens is rectangular and has a dimension of 2mm in width and 0.2mm in thickness. The lamellar boundaries are perpendicular to the wide surface of specimens which is paralell to {112} (group 1) or {110} (group 2).

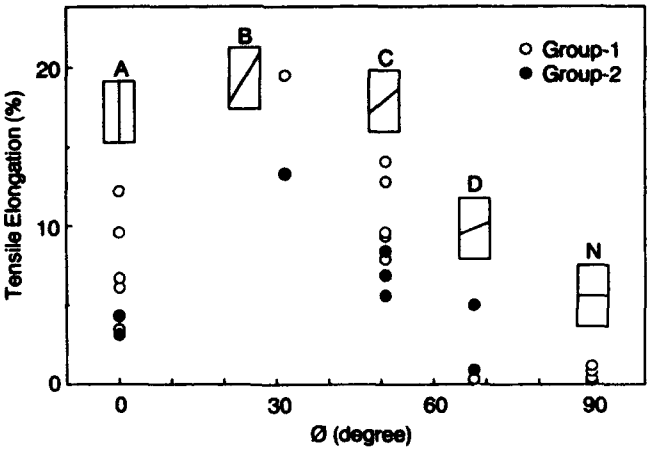

Figure 3: Elongation to fracture of PST TiAl as a function of the angle ϕ [28].The gauge section of tensile specimens is rectangular and has a dimension of 2mm in width and 0.2mm in thickness. The lamellar boundaries are perpendicular to the wide surface of specimens which is paralell to {112} (group 1) or {110} (group 2).

twinning and slip along <110] are the two major deformation modes of the gamma phase coexisting with the alpha-2 phase, as has been shown previously by Huang [3].

The yield stress and tensile elongation of PST crystals are highly dependent on the angle between the lamellar boundaries and loading axis (Figs.2 and 3). The yield stress is high when the lamellar boundaries are parallel or perpendicular to the loading axis, but it is very low for intermediate orientations.This is because when the lamellar boundaries are parallel or perpendicular to the loading axis, shear deformation proceeds on {111} planes intersecting the lamellar boundaries (the hard-type of deformation). On the other hand, for intermediate orientations, shear deformation occurs in the gamma lamellae parallel to the lamellar boundaries (the easy-type of deformation) and hence the lamellar boundaries and the lamellae of the alpha-2 phase do not give rise to direct obstacles to shear deformation of this type. In view of large elongation for the easy-type of deformation, whose characteristics are expected to directly reflect the deformation characteristics of the gamma lamellae, the gamma phase itself in equilibrium with the alpha-2 phase appears to be quite deformable.

However, regardless of the angle ϕ, fracture has been found to occur in a brittle manner without showing any local contraction even after deformed to more than 10% [28,29]. In particular, specimens with $\phi = 30° - 90°$ fail by a cleavage-like mode on a macroscopic habit plane parallel to the lamellar boundaries. Such fracture behavior, the very small plastic elongation for orientation N ($\phi = 90°$), and the asymmetrical orientation (ϕ) dependence of elongation with respect to $\phi = 45°$ suggest that the resolved normal stress on the lamellar boundaries plays an important role in the initiation of fracture. However, when the normal stresses calculated resolving the measured fracture stresses on the lamellar plane are plotted as a function of ϕ, a concave curve similar to that shown in Fig.2 is obtained [29]. This clearly suggests that some plastic deformation plays a role as a precursor to cleavage-like crack initiation. Orientation N exhibits a large compressive strain before fracture, while its tensile elongation is very limited. Nevertheless, the yield stress is the same in both compression and tension, which clearly indicates that yielding and therefore some plastic deformation precedes fracture also in tension. However, nothing has been known about the plastic precursor.

In general, no significant difference in yield stress between tension and compression is observed in PST TiAl. This is because of the existence of six orientation variants in the TiAl phase in lamellar form and the switching of the deformation mode from twinning to slip and vice versa in each variant corresponding to the change in loading mode.

The results of our recent preliminary study on the low-temperature deformation of PST crystals of TiAl have revealed that an abundance of faulted dipoles derived from superlattice dislocations, which are not observed in PST crystals deformed at room-temperature, exist in those deformed at liquid nitrogen temperature. This suggests that a slip-mode transition occurs below room-temperature. The faulted dipoles observed at liquid nitrogen temperature seem to be similar to those reported in studies on Al-rich single-phase TiAl compounds [36-40]. Lipsitt, Shechtman and Schafrik have suggested that the presence of the faulted ribbon is partially responsible for immobilizing the <101] superlattice dislocations up to about 630°C and the sessility of the superlattice dislocations is a major reason for brittleness of the Al-rich single-phase TiAl compounds below 700°C [36]. Huang and Hall [3] have performed room-temperature bend tests on consolidated bars produced from melt-spun ribbons, and have reported that 48 at % Al alloys with a two-phase microstructure, whose deformation occurs via ordered twinning of the {111}<112]-type and the motion of mobile 1/2<110] unit dislocations, are more ductile than 52 at % Al compounds with a single-phase gamma structure, which show a lower propensity of twinning and a relatively high density of sessile superlattice dislocations. However, PST crystals can be deformed to about 20% in tension even at liquid nitrogen temperature. Thus, the preponderance of superlattice dislocations and the existence of their faulted dipoles may not be directly related to the brittleness of TiAl compounds. An answer will be provided to the problem of brittleness in TiAl, in particular, in the two-phase TiAl alloys through understanding the plastic precursor to fracture initiation, that is the mechanisms of the nucleation of catastrophic brittle crack after some plastic deformation. The fracture behavior of PST TiAl will be discussed again in the section on environmental embrittlement.

Alpha-2 phase

The hard-type of deformation occurs for both A (ϕ = 0°) and N (ϕ = 90°) orientations. However, orientation N exhibits a higher yield stress and a much lower tensile elongation than orientation A. Recently, Inui, Toda and Yamaguchi [41] have grown single crystals of a $D0_{19}$ compound with an Al-rich composition, Ti - 36.5 at % Al, which is close to the composition of the alpha-2 phase in equilibrium with the gamma phase in the PST TiAl crystals, and performed tension and compression tests at room temperature. Figure 4 shows the orientation (ϕ) dependence of yield stress for single crystals of the $D0_{19}$ compound and PST TiAl crystals deformed in compression at room-temperature [41]. The specimens of the $D0_{19}$ compound are oriented so that their orientations correspond to those of the alpha-2 phase in PST crystals.The yield stress of the compound is higher than that of PST TiAl for all orientations except for orientation A where the yield stresses for the two materials are almost identical. Since the yield stress of the $D0_{19}$ compound rapidly increases as the angle ϕ increases, the difference in yield stress between the $D0_{19}$ compound and PST TiAl increases with increasing ϕ. Thus, as the angle ϕ increases, it becomes unlikely that the lamellae of the alpha-2 phase contribute to the plastic deformation of PST crystals of TiAl. In fact, it has been shown that the alpha-2 lamellae are not deformed at the yield stress, and hence large compatibility stresses are expected to develop in the regions along the alpha-2/gamma phase boundaries. This would be a reason for the difference in yield stress between the two hard orientations A and N. The ϕ dependence of yield stress of the $D0_{19}$ compound reflects the ϕ dependence of operative slip systems in the compound [41-43].

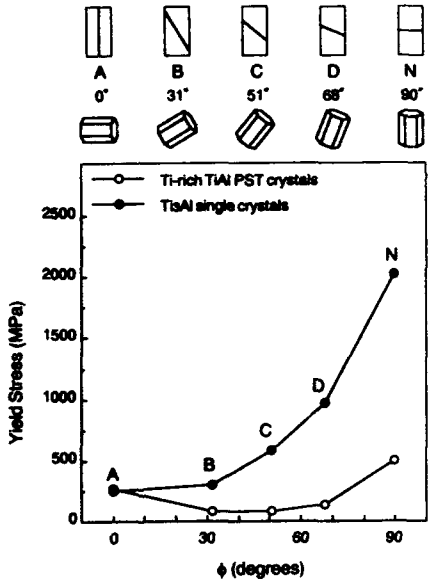

Figure 4: Orientation dependence of yield stress of single crystals of a $D0_{19}$ compound with a composition of Ti - 36.5 at % Al and PST TiAl [41].

Polycrystalline two-phase alloys

The room-temperature tensile properties of the polycrystalline two-phase alloys are directly related to their microstructure. The duplex microstructures result in tensile elongation of more than 2% in binary Ti - 48 at % Al and 4% in ternary alloys containing Mn, Cr and V [1-5]. Fully lamellar microstructures generally exhibit poor ductility, usually less than 1%, and hence a low strength due to premature fracture preceding yielding. Considering that PST TiAl with ϕ

= 0° - 50° shows tensile elongations as large as 10 - 20% at room temperature, the room temperature ductility of the polycrystalline two-phase alloys with fully lamellar structures would be expected to achieve higher values. A decrease in grain size is expected to result in an increase in ductility. However, there is reported to be a lower limit of 300 μm to the fully lamellar grain size that can be achieved by heat treatments [44]. A further decrease in grain size is believed to require special thermomechnical processing [44].

The fracture processes and properties of the two-phase alloys depend strongly on their microstructure. The K_{IC} value for the duplex structure depends on the volume ratio of equiaxed gamma grains to lamellar grains. It is is about 10 MPa$\sqrt{m}$ [45]. In contrast, the K_{IC} value for the lamellar structure, which increases with increasing lamellar grain size, ranges from 20 to 30 MPa$\sqrt{m}$ [45]. The microstructures consisting of equiaxed gamma grains have been found to exhibit a planar crack path and no tearing resistance. The dominant fracture process is the formation of transgranular cleavage and grain boundary cracks. On the other hand, the lamellar microstructure shows a tortuous crack path and a non-zero value of tearing modulus. The crack-tip fracture process has been reported to be dominated by the deflection of the main crack by the lamellae, the formation of a diffused zone of microcracks and ligaments ahead of the crack-tip, and the linkage of the microcracks with the main crack by shear fracture of the near-tip ligaments [45] (for a review, see Chan [46]). The microcracks are formed at boundaries of lamellar grains, along lamellar boundaries or at equiaxed gamma grains existing at lamellar grain boundaries.

The delamination of lamellar boundaries has been found to occur mostly along gamma/gamma interfaces (intervariant interfaces) at room temperature but along both gamma/gamma and gamma/alpha-2 interfaces at high temperatures [45,46]. The crack path deflection results in shear ligaments and a large plastic dissipation by fracturing of the lamellar ligaments. One of the major reasons for the high fracture resistance of the lamellar structure in comparison to the equiaxed gamma microstructure has been proposed to be the formation of such shear ligaments by mismatched crack planes [45-47]. The deformation feature of the ligament is somewhat similar to that of PST TiAl crystals with orientation A. Since yield stresses for the gamma and alpha-2 lamellae are almost identical for orientation A, the alpha-2 lamellae, which are much harder than the gamma lamellae in PST crystals with other orientations (see Fig.4) and hence do not contribute to the plastic deformation of PST crystals, can deform as the gamma lamellae deform, and thus PST crystals with orientation A exhibit a high yield stress and a large elongation of about 10 % at room temperature. This seems to support the shear ligament toughening of the lamellar microstructure.

Deformation at high temperatures

Our recent study of the high-temperature deformation of PST TiAl crystals shows that not only a slip-mode transition but also a change in the propensity for twinning occurs at 600° - 800°C for both the hard and easy types of deformation. At room temperature, deformation of PST crystals occurs by ordered-twinning of the {111}<112]-type and slip on {111}<110]. These twinning and slip systems are still operative at high temperatures. However, the propensity for the ordered-twinning was found to decrease at high temperatures [29].

Another important point concerns the activity of <101] superlattice dislocations. No <101] dislocations are observed in PST crystals of TiAl deformed at room temperature, while at 800°C <101] dislocations are frequently observed. This is indicative of an increased activity of <101] slip at high temperatures. Dislocations with b = 1/2<112] are found in specimens deformed at both room temperature and 800°C. However, they are not expected to play a major role in the plastic deformation of PST crystals of TiAl since their density is small even at 800°C. This is in agreement with the recent observations of deformation structures in Ti-49Al-3.4Nb (in at %) at 815°C and 982°C by Soboyejo, Schwartz and Sastry [48], whose observations show that twinning activity is limited and slip involves 1/2[110] unit dislocations and [101] and [112] superlattice dislocations. However, Huang and Kim [49] have reported that the dislocations in both gamma grains and gamma lamellae in lamellar grains in Ti-47Al-1Cr-1V-2.5Nb (in at %) deformed under creep conditions at 900°C are of the 1/2<110]-type and neither superlattice

dislocations nor any evidence of twin deformation is observed. Recently, Chan and Kim [45] have found that the amount of twins and dislocations in tensile specimens of Ti-47Al-2.6Nb-0.093Cr-0.85V (in at %) in lamellar form is considerably higher at 800°C than at 25°C. The reasons for the similarities and differences in these results are not yet clear. The high-temperature deformation mode of the gamma phase in equilibrium with the alpha-2 phase may sensitively depend on the deformation conditions and chemical compositions.

Alloying effects

Yield stress and ductility of PST crystals of TiAl

A number of alloying studies have been made on TiAl aimed at improving its mechanical properties, in particular, its ductility at room temperature. However, direct comparisons of these results often do not mean much since alloying additions produce a change in microstructure and processing route, which exerts an influence on the final microstructure, often varies with investigator. PST crystals have a great advantage in studying alloying effects on the mechanical properties of TiAl, in particular, on the mechanical properties of the gamma phase in equilibrium with the alpha-2 phase because of the following properties of PST crystals: (1) PST crystals of TiAl always have a fully lamellar microstructure, (2) when the loading axis is inclined at an intermediate angle between 0° and 90° to the lamellar boundaries, they deform via shear parallel to the lamellar boundaries (the easy-type of deformation of PST crystals), and (3) the easy-type of deformation occurs solely in the gamma lamellae and the coexisting alpha-2 lamellae have no direct influences on this type of deformation.

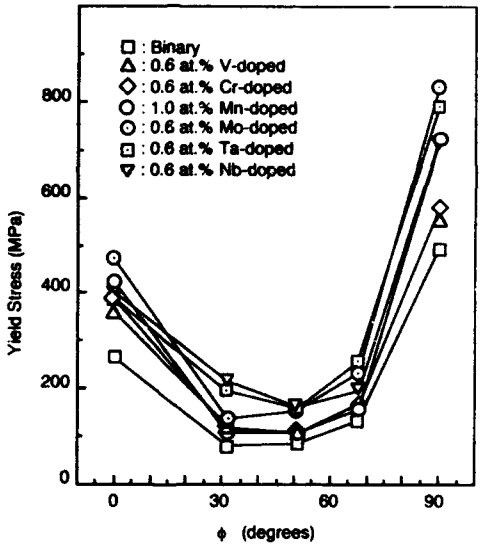

Figure 5: Yield stress of PST crystals of some ternary TiAl compounds as a function of the angle φ.

Figure 5 collectively shows the observed values of yield stress in compression of PST crystals containing six different ternary alloying elements, V, Cr, Mn, Mo, Ta and Nb. These alloying elements are added so that they substitute for 0.6 - 1.0 at % of the total number of atoms in the binary PST crystal with a nearly equiatomic composition of 49.3 at % Al. The amount of alloying elements is mostly 0.6 at %. This is because of the difficulty of growing PST crystals of ternary alloys containing alloying elements more than 1.0 at %, although the reasons for the difficulty are not known. The most notable feature of the figure is that the binary PST crystal shows the lowest yield stress regardless of the loading axis orientation with respect to the

lamellar boundaries. Mo, Ta and Nb seem to be more effective in hardening the gamma phase than V, Cr and Mn since yield stresses for the intermediate three orientations for PST crystals containing the former group of ternary elements are generally higher than those for PST crystals containing the latter group of ternary elements. Mo, Ta and Nb have much higher melting temperatures than V, Cr and Mn. This might be associated with the finding.

The results of X-ray microanalyses of Mn-, Cr- and Mo-bearing PST crystals in TEM show that Mo is enriched in the alpha-2 phase, while the atomic fraction of Cr and Mn in the alpha-2 phase is almost equal to or slightly higher than that in the gamma phase. Ternary phase diagrams for the Ti-Al-Ta, Ti-Al-Nb and Ti-Al-V systems [50-56] suggest that V and probably Ta as well behave similarly to Mo, while Nb is slightly enriched in the gamma phase. However, as far as we do not penetrate deeply into the ternary, the tie-lines in the (gamma+alpha-2) two-phase field may not be inclined too much with respect to the Ti-Al binary line, and thus the difference in the concentration of ternary element between the gamma and alpha-2 phases in the PST crystals is expected to be small. In fact, Mohandas and Beaven [57] have reported that in some near-gamma ternary alloys containing Nb, Mn, V and Cr homogenized at 1200°C for 48 hours, equilibrated at 1300°C and water quenched, no extensive partitioning of ternary alloying elements between the gamma and alpha phases occurs. More recently, Semiatin and McQuay have investigated the segregation and homogenization of a near gamma two-phase alloy with a composition of Ti-47Al-2.7Nb-0.3Ta (in at %) and found that the partitioning of the Nb and Ta solute between the gamma and alpha phases is almost equivalent [58]. Hence, the difference in yield stress between the ternary and binary PST crystals for the intermediate orientations can be regarded as the extent of solution-hardening of the gamma phase due to the corresponding ternary solute whose concentration is at the level of the nominal composition.

The alloying effect for $\phi = 0°$, where the lamellar boundaries are parallel to the loading axis, seems to be different from that for the easy-type deformation of the gamma lamellae. This may be because for this orientation, the alpha-2 lamellae can contribute to the plastic deformation of the PST crystals and thereby the alloying effect in the gamma phase and that in the alpha-2 phase, which are thought to be different from each other, are overlapped. For $\phi = 90°$, where the lamellar boundaries are perpendicular to the loading axis, the trend of the alloying effect is the same as that observed for the easy-type deformation of the gamma lamellae. This seems to be reasonable since the alpha-2 lamellae may not contribute to the plastic deformation of the PST crystals for this orientation. However, it is not understood why the increase in yield stress due to additions of Mo, Ta and Nb is much larger for this orientation than the yield stress increase observed in the intermediate orientations where the easy-type deformation of the gamma lamellae occurs.

The results of tensile tests of these ternary PST crystals with $\phi = 31°$ in air at room temperature show that their elongation is larger than that of the binary PST crystals. The Cr addition is the most effective in improving ductility of PST TiAl. Elongations as large as 30 % and 38 % have been observed for 0.6 at % and 1.0 at % Cr, respectively. Mo is next to Cr in the ductilizing effect. PST crystals containing other ternary elements show an elongation between those of the binary and Cr-bearing PST crystals. Such results may not be explained in terms of variations of intrinsic properties of the gamma phase such as lattice tetragonality, unit cell volume, site occupancy and twinning activity. For example, our recent ALCHEMI examination of the site occupation of Cr, Mo and Mn in the gamma lamellae in PST crystals indicates that these three elements favor the Al sublattice. Huang and Hall [59] have reported the same result on the site occupation of Cr in the gamma grains in a near gamma alloy with a duplex microstructure, although Mohandas and Beaven [57] have reported that Cr shows no apparent preference in the gamma grains in a two-phase alloy with about the same composition as that used by Huang and Hall. Mn is believed to favor the Al sublattice [2,57]. These observations seem to suggest that these three elements exhibit more or less the same site occupation behavior. Why, then, is Cr the most potent to ductilize the gamma phase? Nb is believed to favor the Ti sublattice [52-54,57,60]. However, Nb and Mn show a similar ductilizing effect in PST crystals. Thus, we may not find any significant correlation between the ductility of the gamma phase in the ternary PST crystals and the site occupation behavior of ternary alloying elements in the PST crystals. The alloying effects on the ductility of PST crystals should be understood

through taking account of some extrinsic factors such as "environmetal effect", as will be discussed in the section on environmental embrittlement.

Effects of Mn additions have been explained from the microstructural point of view [60]. At the same time, Mn additions have been reported to increase twinning activity [61]. There is little doubt that mechanical twinning in the gamma phase contributes to the toughening of the two-phase alloys [62-64]. However, deformation twins and dislocations with b = 1/2<110] are abundantly observed even in binary two-phase alloys deformed at room temperature and deformation substructures in ternary duplex alloys such as Cr- and V-bearing ones are essentially the same as those in the corresponding binary two-phase alloys [59]. Additions of ternary elements such as Cr, V, Mn and Nb seem to have relatively little effect on the deformation mode in the two-phase alloys. The intrinsic effect of these alloying elements has yet to be clarified.

Ductility of polycrystalline lamellar form

The polycrystalline lamellar structure is always brittle. This is closely associated with the brittleness of PST crystals with orientation N. If alloying elements effective in ductilizing PST crystals with orientation N are found, such alloying elements should be effective in ductilizing the polycrystalline lamellar form. One of the major reasons for the brittleness of PST crystals with orientation N is a large difference in deformability between the gamma and alpha-2 phases which results in large compatibility stresses at interphase boundaries (Fig.4). Not only in PST crystals but also in polycrystalline two-phase alloys with a lamellar microstructure, it has been generally observed that a large difference in the extent of deformation exists between the gamma and alpha-2 lamellae [65-67]. For example, Appel, Beaven and Wagner [66] have reported that propagation of twinning across the lamellar boundaries is generally halted at the gamma/alpha-2 interfaces and the stress field ahead of these terminated twins gives rise to the formation of cracks. To ductilize PST crystals with orientation N, we should thus make a search for ternary alloying elements which are preferentially soluble in the alpha-2 phase and cause significant changes in its mechanical properties, e.g. a considerable increase in the ease of pyramidal slip which is expected to reduce the large difference in deformability between the gamma and alpha-2 phases. Such alloying elements have yet to be searched.

Recently, an interesting microstructural effect of the addition of Si in combination with Cr has been reported in a two-phase alloy with a chemical composition of Ti-46Al-1Cr-0.2Si (in at %) [67,68]. The Cr concentration in the alpha-2 phase in the alloy has been found to be significantly higher than that in the gamma phase. This might suggest that the partitioning of the major alloying element Cr between the gamma and alpha-2 phases can be controlled by the minor alloying element Si. The Si and Cr bearing quarternary alloy is reported to exhibit high strength and good room-temperature ductility [67,68].

If we can control the partitioning of the major alloying elements such as Cr, V, Mn, Mo and Nb between the gamma and alpha-2 phases by adding a small amount of the fourth element, the mechanical properties of the two constituent phases in the two-phase alloys can be modified more or less independently and thereby the remarkable difference in strength between the gamma and alpha-2 lamellae in the fully-lamellar structures may be reduced, which may lead to ductiiization of the two-phase alloys in lamellar form.

Environmental embrittlement

Two-phase alloys in polycrystalline form

A number of intermetallic compounds including Ni_3Al, Co_3Al, FeAl and Fe_3Al show distinctly lower ductility at room temperature when tested in air than in vacuum as reviewed by Liu [69]. The influence of strain rate and environment on the flow and fracture behavior of two-phase TiAl alloys in polycrystalline form have been studied by several different research groups [70-76]. Nakamura, Hashimoto and Tsujimoto [72] have reported that Mn-bearing nearly equiatomic alloys in duplex form exhibit better ductility in vacuum than in air, although the observed environmental loss in ductility at room temperature is relatively small and no

significant difference in fracture mode is observed between specimens tested in air and in vacuum. Fracture of the polycrystalline duplex alloys at room temperature generally occurs in transgranular as well as intergranular modes in both air and vacuum.

Kim and Dimiduk [75] have investigated the influence of strain rate ($5x10^{-5}$ to $3x10^{-1}$ s^{-1}) on the room-temperature tensile properties of a near gamma two-phase alloy containing Cr, V and Nb in air. The ductility has been found to vary with specific microstructure and specimen surface condition. Electropolished duplex specimens show the most pronounced strain rate dependence of the ductility, while the fully-lamellar specimens reveal the least. They have observed a decrease in ductility with decreasing strain rate for the electropolished duplex specimens and suggested that some environmental effect is involved in the fracture process [75].

Two-phase binary alloys in PST form

Tensile tests of PST crystals with $\phi = 31°$ and those with $\phi = 0°$ have been carried out at room temperature. Tensile ductility and fracture stress, in particular, for $\phi = 31°$ have been found to be sensitive to test environment; they are higher when tested in vacuum or in dry air than in air or in hydrogen gas [76]. The tensile elongation and fracture stress are also sensitive to strain rate; they increase when tested in air or in hydrogen gas while they decrease when tested in vacuum with increasing strain rate.However, yield stress as well as work-hardening rate are almost insensitive to both test environment and strain rate. PST crystals with $\phi = 0°$ also exhibit similar environment and strain rate dependences of the tensile ductility and fracture stress, although the extent of the dependence is weaker than that for PST crystals with $\phi = 31°$. These results reveal that PST crystals of TiAl are susceptible to environmental embrittlement and also suggest that the embrittlement may be interpreted in terms of hydrogen embrittlement.

In the case of PST crystals with $\phi = 31°$, the fracture mode is directly related to the test environment and strain rate [76]. When they are tested in air or in hydrogen gas at lower strain rates at which the environmental loss in ductility is large, they fail in a cleavage-like mode with a habit plane (gamma/gamma interface) parallel to the lamellar boundaries, otherwise fracture occurs across the lamellar boundaries. Chan and Kim [45] have also reported in their study on the fracture behavior of a two-phase alloy in air that the majority of the delaminated interfaces observed at room temperature are gamma/gamma interfaces, with the gamma/alpha-2 interfaces less frequently observed. As mentioned in the section of microstructure, three different types of intervariant lamellar boundaries can exist in the gamma lamellae in the lamellar microstructures; (1) true-twin type, (2) pseudo-twin type and (3)120°-rotational order-fault type [18]. The ratio of energies of these three intervariant boundaries is in the range of 1: 3 : 2 to 1 : 7 : 6 [18]. To reduce the energies of the higher energy boundaries, relaxation of atoms in the close vicinity of the boundary planes is expected occur. Such relaxation of atoms is thought to have the potential to accept hydrogen along them, offering a preferential path for hydrogen penetration. Then, the bond strength of these boundaries will be reduced in the presence of hydrogen, resulting in a cleavage -like fracture along them [76].

Two-phase ternary alloys in PST form

The results of tensile tests of ternary PST crystals with $\phi = 31°$ in air and in vacuum at room temperature reveal that all the ternary PST crystals exhibit larger elongations in air and smaller elongations in vacuum than the binary PST crystal. Figure 6 shows stress-strain curves of PST crystals with $\phi = 31°$ containing 0.6 and 1.0 at % Cr at a strain rate of 2.0×10^{-4} in air and in vacuum at room temperature. Elongation increases in air, while it decreases in vacuum with increasing Cr content. The environmental loss in ductility is thus reduced by the addition of Cr. Fracture in binary PST crystals with intermediate values of ϕ in air occurs always along the lamellar boundaries, while the ternary PST crystals with $\phi = 31°$, in particular, those bearing Cr and Mo always fracture across the lamellar boundaries. These results suggest that the high energy intervariant lamellar boundaries are strengthened somehow by adding ternary alloying elements, and the alloying effect may not be attributed to their chemical nature since all the alloying elements investigated, which shows a wide variety of chemical nature, are effective in reducing the environmental loss in ductility.

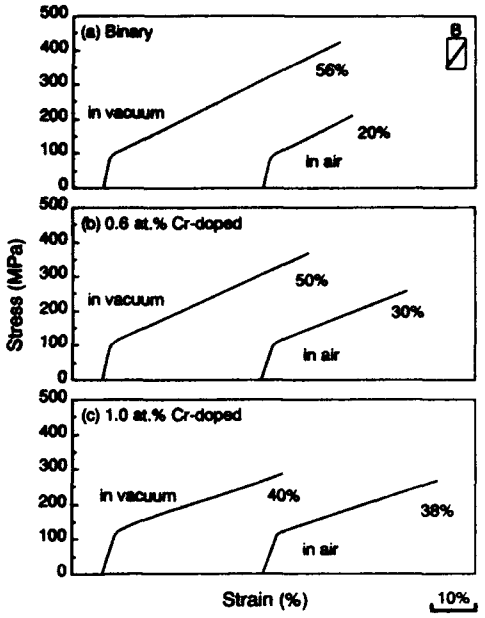

Figure 6: Tensile stress-strain curves of (a) binary, (b) 0.6 at % Cr-bearing and (c) 1.0 at % Cr-bearing TiAl PST crystals.

The alloying effect may be interpreted in terms of the preferential segregation of the ternary alloying elements to the pseudo-twin type and 120°-rotational type intervariant lamellar boundaries. We believe such segregation reduces the vulnerability of these high-energy boundaries to hydrogen attack. We have recently obtained direct evidence to indicate that the ternary alloying elements in PST crystals segregate preferentially to the high-energy intervariant lamellar boundaries, the details of which evidence will be described elsewhere [77]. Figure 7 shows the results of chemical analyses on true-twin type and pseudo-twin type intervariant lamellar boundaries in a Cr-bearing ternary PST crystal. These results have been obtained through HR TEM observations of the intervariant lamellar boundaries in the gamma lamellae in the ternary PST crystal using a high resolution electron microscope, JEOL-2010F equipped with a field emission gun and an EDS chemical analysis system. The radius of electron beam spot for chemical analysis was 0.5 nm. The preferential segregation of Cr is obvious in comparison of the results for the true-twin type and pseudo-twin type boundaries. We have made similar analyses on a Mo-bearing PST crystals and found similar preferential segregation of Mo on the high energy intervariant lamellar boundaries [77].

We may thus reduce environmental embrittlement in the two-phase TiAl alloys by alloying additions. However, the reduction in environmental embrittlement by alloying is not due to intrinsic changes in the mechanical properties of the gamma phase, but is due to a microstructural change, that is the segregation of alloying elements to the high energy intervariant lamellar boundaries. In fact, the results of tensile tests of ternary PST crystals in vacuum at room temperature reveal that all the alloying elements listed in Fig. 5 give rise to an increase in yield stress and a decrease in elongation. The intrinsic ductility of the gamma phase does not seem to be enhanced by adding such alloying elements. Of the alloying elements listed in Fig.5, Cr is the most effective in reducing the environmental loss in ductility. The addition of a small amount of Cr might enhance the formation of surface oxide film which is effective in increasing resistance to hydrogen attack. The addition of a small amount of Cr to the two-phase alloys is thus thought to result in (1) microstructural changes involving the increase in the volume fraction of transformed gamma phase and segregation of Cr to the high energy intervariant lamellar boundaries, and (2) a change in the chemical nature of surface. Good

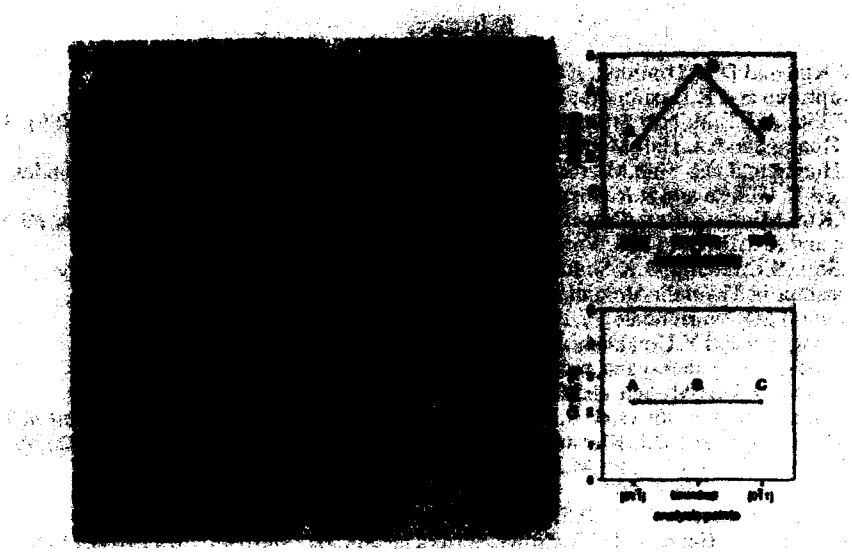

Figure 7: Micro-chemical analyses of the Cr concentration profile in the gamma/gamma intervariant lamellar boundary regions in a Cr-bearing PST TiAl: (a) for a pseudo-twin type intervariant boundary and (b) for a true-twin type intervariant boundary. Micro-chemical analyses were made on the spots indicated by A, B and C on the corresponding HREM images.

ductility of the two-phase alloys with Cr may be interpreted in terms of such changes in the microstructure and chemical nature of surface brought about by Cr additions.

The effect of alloying additions on the room-temperature ductility of PST crystals with $\phi = 90°$ is one of the subjects of our ongoing researches. Information on how the ductility of PST crystals with this lamellar orientation can be improved is badly needed to find a research route to improve the ductility of the two-phase alloys in lamellar form.

Summary and remarks

The lamellar structures are beneficial for toughness and high-temperature strength, however, they are poor in room-temperature ductility. Recently, significant progress has been made towards clarifying the basic mechanical properties of the gamma and alpha-2 phases coexisting in the two-phase alloys using polysynthetically twinned, PST crystals. In view of the large values of room-temperature tensile elongation shown by PST crystals, the ductility of the two-phase TiAl alloys in lamellar form would be expected to achieve higher values. We have suggested that the remarkable difference in strength between the gamma and alpha-2 lamellae, in particular, for the orientation where stress is applied perpendicularly to the lamellar boundaries should be reduced by alloying in order to improve the room-temperature ductility of the lamellar form. Alloying elements such as Cr, Mn and V have been reported to increase the room-temperature ductility of the two-phase alloys in duplex form. However, none of them is effective in ductilizing the two-phase alloys in lamellar form. Our knowledge of the specific role of a particular alloying element is still very limited. More extensive work in this field is required.

Acknowledgements

This work was supported by Grant-in-Aid for Scientific Research on the priority area "Intermetallic Compounds as New High Temperature Structural Materials" from The Ministry of Education, Science and Culture, Japan and in part by the research grants from NEDO and The R&D Institute of Metals and Composites for Future Industries.

References

1.Y-W.Kim and D.M.Dimiduk, JOM,43(8) (1991)40.
2.T.Tsujimoto and K.Hashimoto, High-Temperature Ordered Intermetallic Alloys III, ed.C.T.Liu, A.I.Taub,N.S.Stoloff and C.C.Koch, Vol.133 (MRS, Pittsburgh, Pa, 1989), 391.
3.S-C.Huang and E.L.Hall,Metall.Trans.,22A(1991)427.
4.S-C.Huang and D.S.Shih,Microstructure/Property Relationships in Titanium Aluminides and Alloys,ed.Y-W.Kim and R.R.Boyer(TMS,Warrendale,Pa,1991),105.
5.Y-W.Kim,Microstructure/Property Relationships in Titanium Aluminides and Alloys, ed.Y-W.Kim and R.R.Boyer(TMS,Warrendale,Pa,1991),91.
6.D.S.Shih,S.C.Huang,G.K.Scarr,H.Jang and J.C.Chestnut,Microstructure/Property Relationships in Titanium Aluminides and Alloys,ed.Y-W.Kim and R.R.Boyer(TMS,Warrendale,Pa,1991),135.
7.M.Yamaguchi and Y.Umakoshi,Prog.Mater.Sci.,34(1)(1990)1.
8.F.H.Froes,C.Suryanarayana and D.Eliezer,ISIJ International,31(10)(1991)1235.
9.D.M.Dimiduk,D.B.Miracle and C.H.Ward,Mater.Sci.Tech.,8(1992),367.
10.J.C.Chesnutt,Superalloys,ed.S.D.Antolovich,R.W.Stusrud,R.A.MacKay,D.L.Anton,T.Khan,R.D.Kissinger and D.L.Klarstrom(The Minerals,Metals & Materials Society,1992),381.
11.M.H.Yoo,S.L.Sass,C.L.Fu,M.J.Mills,D.M.Dimiduk and E.P.George,Acta metall.mater.,41(4)(1993),987.
12.C.T.Liu,MRS Symp.Proc.,288(1993)3.
13.C.R.Feng,D.J.Michel and C.R.Crowe,Scripta metall.,22(1988)1481; 23(1989),1135; Phil.Mag.Lett.,61(1990)95.
14.D.S.Schwartz and S.M.L.Sastry,Scripta metall.,23(1989)1621.
15.G.J.Mahon and J.M.Howe,Metall.Trans.,8A(1990),299.
16.Y.S.Yang and S.K.Wu,Phil.Mag.A,65(1)(1992)15.
17.H.Inui,A.Nakamura,M.H.Oh and M.Yamaguchi, Ultramicroscopy,39(1991)268.
18.H.Inui,A.Nakamura,M.H.Oh and M.Yamaguchi, Phil.Mag.A,66(1992)539.
19.J.A.Graves,L.A.Bendersky,F.S.Biancaniello,J.H.Perepezko and W.J.Boettinger,Mater.Sci.Eng.,98(1988)265.
20.S.A.Jones and M.J.Kaufman,Acta metall.mater.,41(2)(1993),387.
21.Y.S.Yang,S.K.Wu and J.Y.Wang,Phil.Mag.A,67(2)(1993)463.
22.B.K.Kad and H.L.Fraser,to be published in Phil.Mag.Lett.,1993.
23.S.R.Singh and J.M.Howe,Phil.Mag.A,66(5)(1992)739.
24.P.M.Hazzledine,B.K.Kad,H.L.Fraser and D.M.Dimiduk, MRS Symp.Proc.,273(1992)81.
25.B.K.Kad and P.M.Hazzledine,Phil.Mag.Lett.,66(1992)133.
26.T.Fujiwara,A.Nakamura,M.Hosomi,S.R.Nishitani,Y.Shirai andM.Yamaguchi, Phil.Mag.A,61(4)(1990)591.
27.M.H.Oh,H.Inui,A.Nakamura and M.Yamaguchi,Acta metall.mater.,40(1992)167.
28.H.Inui,M.H.Oh,A.Nakamura and M.Yamaguchi,Acta metall.mater.,40(11)(1992)3095.
29.M.Yamaguchi and H.Inui,Ordered Intermetallics-Physical Metallurgy and Mechanical Behavior(Proc.NATO Advanced Research Workshop),ed.C.T.Liu,R.W.Cahn and G.Sauthoff(Kluwer Academic Publishers, Dordrecht,1992),217.
30.C.S.Barrett and T.B.Massalski,Structure of Metals,3rd rev.edn.(Pergamon Press,Oxford,1980),406.
31.Y.Umakoshi and T.Nakano,Acta metall.mater.,41(1993)1155.
32.Y.Umakoshi,T.Nakano and T.Yamane,Mater.Sci.Eng.,A152(1992)81.
33.P.A.Beaven,F.Appel,B.Dogan and R.Wagner,Ordered Intermetallics-Physical Metallurgy and Mechanical Behavior (Proc.NATO Advanced Research Workshop), ed. C.T.Liu,R.W.Cahn and G.Sauthoff(Kluwer Academic Publishers, Dordrecht,1992),413.
34.J.Seeger,C.Hartig,A.Bartels and H.Mecking,MRS Symp.Proc.,213(1991)157.
35.H.Inui,A.Nakamura,M.H.Oh and M.Yamaguchi,Phil.Mag.A,66(4)(1992)557.
36.H.A.Lipsitt,D.Shechtman and R.E.Schafrik,Metall.Trans.,6A(11)(1975)1991.
37.D.Shechtman,M.J.Blackburn and H.A.Lipsitt,Metall.Trans.,5(6)(1974)1373.
38.G.Hug,A.Loiseau and A.Lasalmonie,Phil.Mag.A,54(1)(1986)47.
39.G.Hug,J.Douin and P.Veyssiere,MRS Symp.Proc.,133(1989)125.
40.S.H.Whang and Y.D.Hahn,High Temperature Aluminides and Intermetallics, ed.S.H.Whang,C.T.Liu,D.P.Pope and J.O.Stiegler(TMS,1990),91.
41.H.Inui,Y.Toda and M.Yamaguchi,to be published in Phil.Mag.A,1993.

42.Y.Minonishi,Phil.Mag.A,63(1991)1085.
43.Y.Umakoshi,T.Nakano,T.Takenaka,K.Sumitomo and T.Yamane,Acta metall.mater.,41(1993)1149.
44.Y-W.Kim,Acta metall.mater.,40(6)(1992)1121.
45.K.S.Chan and Y-W.Kim,Metall.Trans.,23A(1992)1663.
46.K.S.Chan,JOM,44(5)(1992)30.
47.H.E.Deve,A.G.Evans and D.S.Shih,Acta metall.mater.,40(6)(1992)1259.
48.W.O.Soboyejo,D.S.Schwartz and S.M.L.Sastry,Metall.Trans.,23A(1992)2039.
49.J.S.Huang and Y.W.Kim,Scrpta metall.mater.,25(8)(1991)1901.
50.A.Raman,Z.Metallkde.,57(1966)535.
51.S.Sridharan and H.Nowotny,Z.Metallkde,74(1983)468.
52.K.Kaltenbach,S.Gama,D.G.Pinatti,K.Schulze and E.T.Henig,Z.Metallkde,80(1989)535.
53.J.H.Perepezko,Y.A.Chang,L.E.Seitzman,J.C.Lin,N.R.Bonda,T.J.Jewett and J.C.Mishurda, High Temperature Aluminides and Intermetallics,ed.S.H.Whang,C.T.Liu,D.P.Pope and J.O.Stiegler(TMS,1990),10.
54.U.R.Kattner and W.J.Boettinger,Mater.Sci.Eng.,A152(1992)9.
55.K.Hashimoto,H.Doi and T.Tsujimoto,Trans.Japan Inst.Met.,27(1986)741.
56.T.Ahmed and H.M.Flower,Mater.Sci.Eng.,A152(1992)31.
57.E.Mohandas,P.A.Beaven,Scripta metall.mater.,25(9)(1991)2023.
58.S.L.Semiatin and P.A.McQuay,Metall.Trans.,23A(1992)149.
59.S.C.Huang and E.L.Hall,Metall.Trans.,22A(1991)2619; Acta metall.mater.,39(6)(1991)1053.
60.T.Tsujimoto and K.Hashimoto,MRS Symp.Proc.,133(1989)391.
61.T.Hanamura,R.Uemori and M.Tanino,J.Mater.Res.,3(4)(1988)656.
62.H.E.Deve and A.G.Evans,Acta metall.mater.,39(6)(1991)1171.
63.M.H.Yoo,C.L.Fu and J.K.Lee,J.Phys.III,1(6)(1991)1065.
64.C.L.Fu, Y.-Y.Ye and M.H.Yoo,MRS Symp.Proc.,288(1993)21.
65.L.Zhao and K.Tangri,Phil.Mag.A,65(5)(1992)1065.
66.F.Appel,P.A.Beaven and R.Wagner,Acta metall.mater.41(6)(1993)1721.
67.W.Wunderlich,Th.Kremser and G.Frommeyer,Acta metall.mater.,41(6)(1993)1791.
68.G.Frommeyer,W.Wunderlich,Th.Kremser and Z.G.Liu,Mater.Sci.Eng.,A152(1992)166.
69.C.T.Liu,Ordered Intermetallics-Physical Metallurgy and Mechanical Behaviour(Kluwer Academic Publishers, Dordrecht,1992),321.
70.C.T.Liu and Y.W.Kim,Scripta metall.mater.,27(1992)599.
71.T.Takasugi,S.Hanada and M.Yoshida,J.Mater.Res.,7(1992)2739.
72.M.Nakamura,K.Hashimoto and T.Tsujimoto,J.Mater.Res.,8(1)(1993)68.
73.K.S.Chan and Y-W.Kim,Metall.Trans.,24A(1993)113.
74.M.H.Oh,H.Inui,M.Misaki,M.Kobayashi and M.Yamaguchi,MRS Symp.Proc.,288(1993)1001.
75.Y-W.Kim and D.M.Dimiduk,MRS Symp.Proc.,288(1993)671.
76.M.H.Oh,H.Inui,M.Misaki and M.Yamaguchi,to be published in Acta metall.mater.,1993.
77.H.Inui and M.Yamaguchi,to be published.

STRENGTHENING AND TOUGHENING IN REFRACTORY METAL ALLOYS

J. Wadsworth*, J. Wittenauer†, and T. G. Nieh*

*Lawrence Livermore National Laboratory
Chemistry & Materials Science
P.O. Box 808, L-353, Livermore, CA 94550

†Lockheed Missiles and Space Co., Inc.
Lockheed Research and Development Division
3251 Hanover Street, Palo Alto, CA 94304-1187

Abstract

The development and application of refractory metal alloys for high-temperature aerospace structures is reviewed. Refractory metals are prime candidates for many high-temperature aerospace components because of their high melting points, fabricability, and inherent creep resistance. The use of refractory metals is often limited, however, by poor room temperature properties, inadequate oxidation resistance at elevated temperatures, or difficulties associated with joining, welding, or forming. Materials selection criteria for high-temperature structures are reviewed with an emphasis placed upon the distinctions between refractory metals and competing high-temperature materials - including carbon, ceramics, and intermetallics. Each class of materials has inherent limitations which govern their application. In some cases, materials limitations are being solved through the use of engineered materials hybrids such as ceramic-coated refractory metals or ceramics toughened with a ductile refractory metal phase. For many applications, use of ceramics and intermetallics is limited by their technological immaturity. For example, current understanding and application of molybdenum-based materials is based upon nearly 40 years of application experience in high-temperature structures. As an example of a materials development and qualification program, a brief synopsis of molybdenum alloy development is presented. Topics surveyed include recent advances in the understanding of the role of oxygen on the room temperature brittle behavior problem in molybdenum alloys.

Critical Issues in the Development of High Temperature Structural Materials
Edited by N.S. Stoloff, D.J. Duquette and A.F. Giamei
The Minerals, Metals & Materials Society, 1993

Introduction

For many high-temperature aerospace applications, refractory alloys based on niobium (Nb), molybdenum (Mo), tantalum (Ta), and tungsten (W) are the materials of choice. This is because, for applications requiring very high operating temperatures, strength levels are required that exceed the capabilities of conventional high temperature alloys such as stainless steels and superalloys. The Figure below shows some comparative selected data.

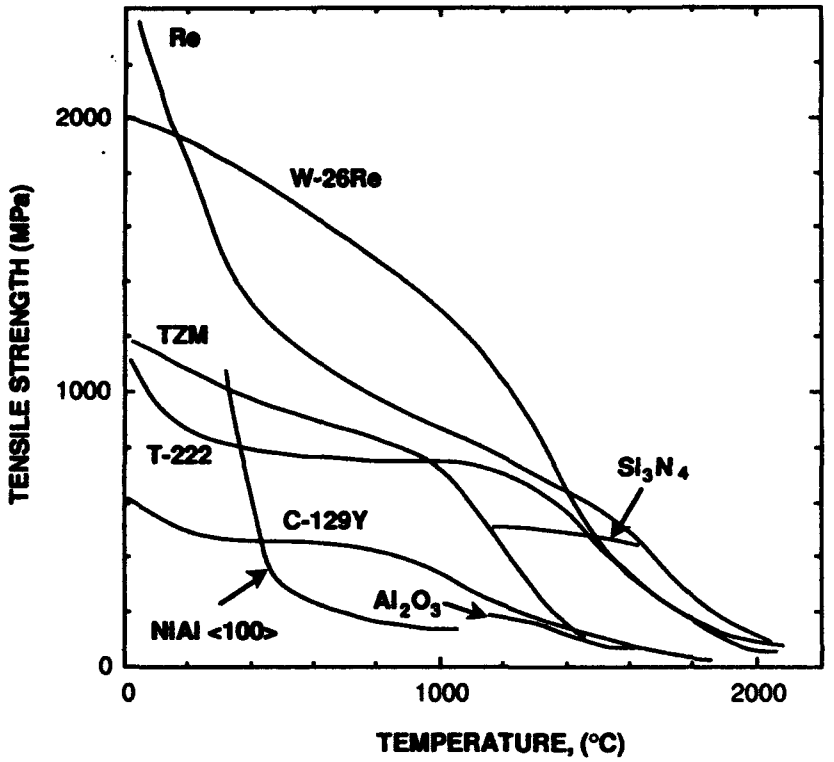

Fig. 1 Strength as a function of temperature for selected refractory metals, ceramics, and intermetallics

The favorable high-temperature strength properties of the refractory metals are in some cases offset by poor room temperature ductility and fabricability, embrittlement after welding or joining, and in some cases inadequate oxidation resistance. Despite these limitations, refractory metals are used successfully in a number of demanding high-temperature structural applications - principally in areas of propulsion and energy conversion. Selected data for the principal refractory metals are listed in Table I. As shown in Table I, the principal refractory metals have been available for engineering use for over 100 years and have been used for aerospace hardware for about 30 years. The refractory metals can boast a level of technological maturity which structural ceramics and intermetallics will not equal for some time to come. Also highlighted in Table I are the principal limitations of the refractory metals: catastrophic oxidation at a relatively low temperature and poor low temperature ductility (for Mo and W) that renders fabricability difficult.

By comparison, the production of alternative high-temperature structural materials (ceramics and intermetallics) has occurred over a much shorter time scale. Although ceramic "mill products" have been available for many years, it is only recently that the purity, density, and microstructural homogeneity of ceramics have allowed their consideration as useful high-temperature engineering structural materials. Key technological advances have included improved toughness, greater availability of product forms, the introduction of ceramic-matrix composites,

and gains in the area of superplastic forming. Intermetallic systems are at varying levels of technological maturity. Aluminides of Fe, Ni, and Ti are presently under consideration for high-temperature application while a host of other intermetallic systems (e.g. silicides and beryllides) remain at the stage of laboratory examination. Practically all intermetallic systems under investigation today are seen as potential replacements for superalloys. Thus far, no intermetallic materials have emerged to challenge the refractory metals and ceramics for high-temperature (T>1350°C) service. For this reason, the principal emphasis of this review is on ceramics and refractory metals.

Table I

Selected Data for the Principal Refractory Metals

	Nb	Ta	Mo	W
Melting Point (°C)	2468	2996	2617	3410
Oxide Melting Point (°C)	1490	1772	795	1500
Density (g/cm^3)	8.58	16.68	10.22	19.26
Ductile-Brittle Transition (°C)	-125	-273	30	300
Elastic Modulus (GPa)	110	186	324	405
U.S. Annual Consumption (mt)* [1]†	3425	387	18500	10275
U.S. Import Reliance (%) [1]†	100	86	0	75
Year of Isolation as Pure Element	1865	1865	1893	1783
Year of First Aerospace Application	~1965	~1970	~1960	~1960

*Only 10-20% is consumed annually as refractory metal mill products.
†Average 1988-92

Traditional areas of aerospace application for high-temperature materials such as rocket propulsion and re-entry systems have been supplanted in recent years by the demands of aerothermally-heated hypersonic vehicles, proposed high-Mach jet propulsion, and the development of thrust vector controls in advanced fighters. The demands of these fairly recent applications have yet to be met satisfactorily and a new look at available thermal technology is called for. With such applications in mind, the materials selection criteria for engineering structures which must withstand a high thermal loading are considered below.

Materials Selection for High Heat Flux Environments

As a framework for the evaluation of materials for high-temperature service, it is useful to consider failure modes associated with high-temperature structures. Optimum materials properties which mitigate these failure modes may then be discussed. In this way, the suitability of various metal, ceramic, and intermetallic solids may be ranked according to their basic physical, chemical, and mechanical properties. In constructing such a framework, the specific criteria are considered that are applicable to high thermal loading applications: rocket propulsion systems, aerothermally heated surfaces (i.e. hypersonic wing leading edges), and jet turbine hot stage environments.

Failure Modes Observed in High-Heat Flux Applications

Failure modes observed during the development of materials for high-heat flux applications may be generally classified as shown in the schematic below.

Under optimized conditions, many materials can withstand some of these failure modes. To withstand *all* of the above failure modes, however, requires a combination of an optimized high-temperature material and a thermally efficient design. Examples include:

- W-based rocket nozzles may be infiltrated with silver to allow for transpiration cooling as the silver vaporizes during use.
- Single-crystal superalloy turbine blades in the hot stage of modern jet engines contain integral cooling passages to allow for air-film cooling.

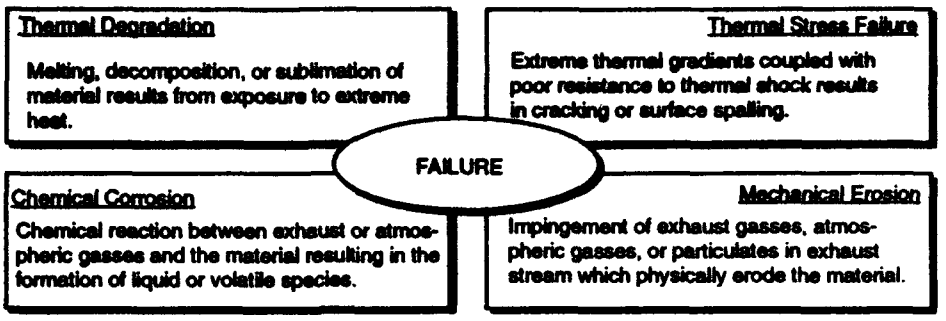

The materials properties which must be optimized to avoid the above four failure modes are described below. It is noted that other selection criteria may play a decisive role for some applications. These include density, cost, nuclear cross section, liquid alkali metal compatibility, and long-term creep strength. For purposes of simplicity, however, this review is restricted to the high-heat flux applications.

Materials Evaluation for High Heat Flux Applications

Thermal Degradation The susceptibility of a material to thermal degradation is determined by the *refractory limit* of the material. The refractory limit consists of two elements: 1) the decomposition temperature T_M at which melting, chemical dissociation, or sublimation occurs and 2) the thermal diffusivity. Thermal diffusivity - defined as the thermal conductivity k divided by the volume specific heat ρC_p - is a measure of the rate of heat removal from the material. Thus, if a material is to resist thermal degradation, it must have a high enough thermal diffusivity to conduct away the heat before the temperature rises to exceed its decomposition temperature. The relative importance of each of these factors will vary with the application. For an actively cooled structure, a high thermal diffusivity would be preferred; for a passive thermal barrier, low thermal diffusivity may be more desirable. The decomposition temperature and thermal diffusivity for a number of refractory metals, ceramics, and carbon are presented in Table II below. On the basis of the decomposition temperature T_M, structural ceramics compare favorably with the refractory metals. In terms of thermal diffusivity, metals have an advantage over oxides and nitrides - principally as a result of their high thermal conductivity. Graphite and the refractory metal carbides compare favorably with the refractory metals in terms of thermal diffusivity.

Thermal Stress Failure Upon exposure to rapid fluctuations in heat, ceramics and cermets typically respond by fracturing while metals do not. Since thermal stress failure occurs when local thermal expansion α is sufficient to overwhelm the strength of the material, materials with low thermal expansivity will be more tolerant to thermal shock. Since thermal strains are related to thermal stresses through the Young's Modulus E, a low-modulus material will be more tolerant to thermal shock than a high-modulus material. Since failure occurs when the local fracture strength σ is exceeded, a high-strength material will be more tolerant to thermal stress failure than a low-strength material. In this respect, modern ceramic materials have made impressive gains in the past decade. In the early 1960's when cermets and ceramics were originally evaluated as potential rocket thruster materials, it was not possible to obtain fully-dense material or to obtain the level of purity available in modern ceramics. Hence, strengths were low in these early studies. For this reason alone, ceramics deserve renewed consideration as high-temperature structural materials. A final material property affecting thermal shock resistance is the thermal conductivity k. Materials with a high thermal conductivity will have an ability to minimize formation of temperature peaks (hot spots) and thus contribute to the thermal shock tolerance of the material. For monolithic materials, these materials parameters are summed up by considering the thermal shock index $k \cdot \sigma / E \cdot \alpha$. Past studies have shown a direct correlation between this index and the tolerance of a material to thermal shock [7]. The thermal shock index for a variety of high-temperature materials is presented in Table II.

The data for the thermal shock index shown in Table II highlights what has historically been the greatest technological barrier to the application of ceramics for high-temperature structures. Of all the engineering properties of high temperature materials, resistance to thermal shock is the discriminator between those materials being utilized for high-temperature design (metals,

graphite) and those materials that are unsuitable (monolithic ceramics). Efforts to improve the thermal stress tolerance of ceramics have focussed on the engineered materials *cermets* and *ceramic-matrix composites.*

Table II

1500°C FAILURE INDICES FOR HIGH-TEMPERATURE MATERIALS [2-6]

	Thermal Degradation Indices:			↓	↓	Thermal Shock Index:			↓
	ρ (g/cm^3)	k W/cm·K	C_p W·s/g·K (x 10^{-2})	$k/\rho C_p$ cm^2/s^{-1} (x 10^{-2})	T_M °C	α cm/cm·K (x 10^{-6})	E^* GPa	σ^* MPa	$k\alpha/E\alpha$ W/cm
W	19.26	1.2†	0.908†	39.17	3410	5.8†	325†	135†	86.2
Re	21.03	0.48	0.956	13.63	3180	8.0	300	150	30.0
Ta	16.68	0.68	0.956	24.35	2996	8.6	150	95	50.1
Mo	10.28	1.0	1.96	28.34	2617	8.4	255	70	32.7
Nb	8.58	0.68	1.91	23.67	2468	9.6	70	40	40.5
HfC	10.021	0.18	1.72	5.96	3888	7.3	205	70	8.4
TaC	13.88	0.34	1.72	8.13	3875	8.1	175	70	16.8
NbC	7.616	0.32	3.11	7.72	3500	8.9	260	70	9.7
ZrC	5.932	0.39	3.11	12.08	3260	9.0	205	70	14.8
HfB_2	11.2	0.58	2.39	12.8	3377	8.3	170	70	28.8
ZrB_2	6.09	0.23	5.26	4.38	3247	8.3	170	70	11.4
BN	2.270	0.23	10.99	5.52	3000	8	30	20	19.1
AlN	3.26	0.18	7.17	4.61	2235	6.7	170	10	1.6
Si_3N_4	3.184	0.072	9.08	1.91	1900 *(s)*	4.0	35	10	5.1
ThO_2	9.62	0.015	1.84	0.484	3050	11.6	70	10	0.2
HfO_2	9.62	0.025	3.11	0.478	2812	10.9	70	10	0.3
ZrO_2	6.10	0.02	4.30	0.435	2700	12.0	125	10	0.1
BeO	2.886	0.15	12.42	2.38	2452	13.6	70	10	1.6
Al_2O_3	3.736	0.04	7.17	0.853	2072	10.9	140	10	0.3
$MoSi_2$	6.24	0.10	3.35	0.478	2030	10.0	280	20	0.7
C	2.020	1.0	10.76	26.28	3677 *(s)*	6.3	10	35	555.0

† All data are for 1500°C

** Estimated Values for Ceramic Materials [2]*

A cermet is a microcomposite with a continuous minority metal phase binding together the majority ceramic phase. The philosophy of extensive cermet research programs carried out in the 1950-60 era was to improve the thermal shock index of a structural ceramic through an increase in the thermal conductivity (continuous metal phase). Materials evaluated during this era included Cr-Al_2O_3, Co-B_4C, TiC-NiAl, and Cr_2B-Cr-Mo. Disappointingly, cermet research was largely abandoned by 1965 - it became increasingly apparent that cermets cannot withstand thermal cycling or thermal shock conditions. Further, the presence of a continuous metal phase did not always result in an increase for thermal conductivity relative to the monolithic ceramic. This has been attributed to the great increase in the number of microstructural interfaces in a cermet relative to a pure metal or ceramic.

Ceramic-matrix composites (CMCs) have the potential to exhibit improved resistance to thermal shock by providing for greatly improved strengths relative to monolithic ceramics. Although CMCs are a fairly recent development, they have already been successfully evaluated for engineering application in a rocket propulsion environment. An Al_2O_3/SiO_2 composite is used as high-temperature seal in missile applications. A C/SiC CMC nozzle has been successfully tested on the HM7 engine of the Ariane third stage [8]. This CMC boasts a 1400°C

flexural strength of 700 MPa - well in excess of the strengths for monolithic ceramics listed in Table II. Developments in CMC research and the closely related field of ductile-phase toughened ceramics now offer the potential for ceramics to be truly competitive with the refractory metals.

Chemical Corrosion Chemical corrosion is a material-specific and application-specific phenomenon - thus only a limited degree of generalization is possible. The following points, however, apply to all high-temperature materials:

- Materials may be judged for a particular application by considering which chemical reactions are thermodynamically *possible* at the temperature and environment in question; what is the exact service environment, i.e. the oxygen and carbon partial pressures? Oxide ceramics do not "oxidize" while carbides and metals do.
- Porosity is detrimental because high levels of porosity provide a larger amount of surface area for chemical reaction than does a fully dense body. Thus a plasma-sprayed coating is more likely to degrade in a corrosive environment than a fused slurry coating.
- Thermal diffusivity (Table I) should be optimized to minimize chemical attack. This is because the surface temperature (site of chemical reaction) can be moderated by the rate at which heat is conducted away.

Refractory metals are historically temperature-limited by their poor oxidation resistance. Fused silicide coatings have been developed for the principal refractory metals but extend the maximum operating temperature to only 1650°C - well below the useful strength limit of these metals. Of the various competing materials, borides begin to volatilize above about 800°C, and the carbides and graphite require oxidation protection. The oxide ceramics out-perform all high-temperature materials in resistance to hot corrosion. Unfortunately, the oxide ceramics are the poorest choice based upon thermal shock criteria. It appears that the problem of hot corrosion resistance cannot be completely overcome by materials selection at the present time. Rather, designs must be configured to limit maximum temperatures to within the safe operating range for coated refractory metal or carbon systems. (A further discussion of design concepts is offered at the close of this section.)

Mechanical Erosion Mechanical erosion is defined as erosion of the hot-structure surface by impingement of exhaust products or atmospheric species. Strength is the governing factor in defining the resistance of a material to mechanical erosion. Refractory metals and ceramics have generally higher erosion resistance than C-based materials. Tests with a rocket nozzle geometry showed that mechanical erosion of the nozzle throat is only evident in conjunction with surface spalling, chemical degradation, or melting [2]. In these instances, mechanical erosion simply assisted in the removal of decomposition products. In the case of refractory metals, a liquid oxide forms at elevated temperatures and mechanical erosion insures that a fresh metal surface is continually exposed - thus hastening the failure process. The same study showed that erosion resulting from simple mechanical impingement was not observed - the incident angle was too shallow for significant interaction. Other potential applications such as a thrust vector control system or a leading edge on a hypersonic aircraft may experience greater angles of impingement with a particulate stream. Thus, the mechanism of mechanical erosion may assume greater or lesser importance - depending upon the application.

Influence of Design Factors

In addition to optimization of materials properties for high-heat flux applications, described above, thermal design plays a critical role in preventing failure of high-temperature structures. For those applications where thermal shock resistance is a design driver, several steps can be taken to reduce the degree of thermal shock. Thermal shock failure occurs more readily in constrained bodies - whether constraint is provided by surrounding cooler material or by mechanical restraints. Thus a "tiled" design which confines expansion and contraction effects to discreet elements is less prone to thermal stress failure than a monolithic design. Similarly, thin-walled structures provide less constraint than bulk structures. A common design optimization comes through the integration of a metal backing sheet to a thin ceramic thermal or oxidation barrier. The metal sheet compensates for the poor thermal conductivity of the ceramic and helps to dissipate heat as well as to delocalize stress-inducing hot spots. The ceramic provides for resistance to erosion and chemical corrosion failure. Examples of this technology abound. Silicide coatings are applied to Nb alloy C-103 rocket thrusters for oxidation protection to

1650°C. Zirconia is plasma sprayed onto the Ni-based alloys and serves as a thermal and oxidation barrier in jet turbines [9]. At a development stage, oxide ceramics are being superplastically deformed and diffusion bonded to refractory metals to yield hybrid net-shaped structures for elevated-temperature service [10]. Thus, informed engineering design can utilize the advantages of both refractory metals and ceramic materials to yield a sound high-temperature structure.

The survey presented up to this point has necessarily been general in nature. Overlooked thus far has been the enormous effort required to actually qualify a material for engineering application. As shown in Table I, the principal refractory metals have been used for aerospace application since the dawn of the space age. For each of the refractory metals, the range of application has steadily expanded during this time as materials scientists have overcome problems associated with joining, fabricability, reproducibility of properties, and oxidation. Before emerging CMCs and intermetallics can qualify for engineering application, they will undoubtedly pass through a similar cycle. Thus, it is instructive to present a detailed case study of the developments with one material - Mo - which have occurred in the past 30-40 years. Although Mo has a long history of elevated-temperature application, it was not until the 1980's that fundamental factors which affect ductility and weldability in Mo were clearly understood. Some of the developments which have yielded the current state of the art in Mo-based materials are described in the sections which follow.

Case Study: Optimization of Mo Alloys for Aerospace Application

The history of refractory metal alloy research and development from 1950 to 1975 has been well reviewed recently by Perkins [11]. In summary, in the late 1950s tonnage quantities of mill products were produced. At that time, the spectrum and range of quality of refractory alloys were comparable to those of stainless steels and superalloys. Two decisions in the early 1970s altered this picture dramatically. One was the fact that work on nuclear space power systems was terminated in 1973 for an indefinite period. The second was the selection of reusable surface insulation (i.e., the Space Shuttle tile) instead of coated refractory metals for thermal protection of the Space Shuttle.

In the recent past, specifically the past three to four years, the above situation has changed suddenly for two reasons. First, advanced compact nuclear systems are being reconsidered as portable thermal and electrical power sources for possible aerospace applications. Second, the advent of exotic vehicle designs such as the National Aerospace Plane (or derivatives of this concept) demand the use of very high temperature materials that currently, quite simply, do not exist. The renewed interest in refractory metals for these applications merits a review of the current status of this group of materials.

Recent work on the brittle behavior of refractory metal alloys has been focused on molybdenum base alloys. Molybdenum and its alloys have specific advantages over the other refractory metals in terms of availability, high temperature specific strength, and oxidation resistance in certain propulsion systems. The major problem with molybdenum is its brittle behavior at room temperature and it is well accepted that poor room temperature ductility and toughness have limited widespread application of molybdenum base alloys. This brittle phenomenon can arise from a variety of sources.

The Group VI metals such as molybdenum, tungsten, and chromium are particularly susceptible to embrittlement by oxygen, nitrogen, and sometimes, carbon. Although this general observation is reasonably well documented, the details of oxygen effects in commercially important molybdenum alloys are not appreciated.

Kumar and Eyre [12] have been able to show that as little as 6 at. ppm of oxygen can totally embrittle molybdenum grain boundaries if the carbon content is very low (e.g., 0.4 at. ppm). In their work, it was also shown that carbon is effective in reducing the driving force for such oxygen segregation to grain boundaries. In this manner, carbon promotes ductile behavior. By varying the amount of carbon with respect to oxygen, Kumar and Eyre showed that at C/O atomic ratios greater than 2, oxygen segregation was severely limited during recrystallization or slow cooling from elevated temperatures. These key observations are shown in Fig. 2. In the

case of vacuum arc cast ingots of commercial unalloyed molybdenum, the atomic ratio for C/O is 4:1 if the alloy contains the maximum allowable C and O levels. Typically, the ratio is greater than this (often about 6) although for the cases where O is high and C is low, C/O atomic ratios of as low as 2 can be encountered. Based on the data of Kumar and Eyre, molybdenum alloys having this type of atomic ratio (2:1) could be susceptible to oxygen embrittlement. Furthermore, it should be pointed out that the oxygen levels in mill products of molybdenum alloys can increase, by comparison with initial ingot chemistries, as a result of oxygen contamination during processing.

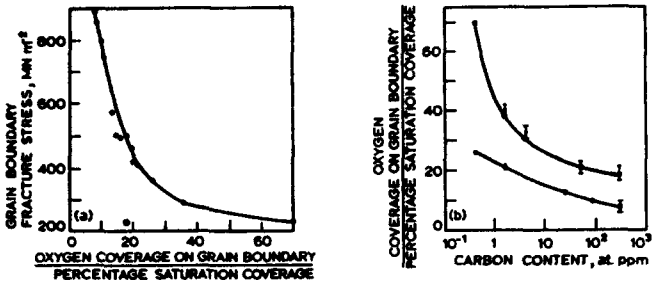

Fig. 2 (a) correlation of grain boundary fracture stress for molybdenum with oxygen coverage of grain boundaries and (b) effect of carbon content on oxygen coverage [12]. Oxygen monolayer coverage at molybdenum grain boundaries is severely embrittling but the degree of oxygen segregation can be controlled by increasing carbon content of alloys

Molybdenum Barstock

Although ductility in the longitudinal direction of commercial alloys of molybdenum extrusion products, barstock, and rods is usually excellent, extremely poor transverse ductility is invariably observed [13]. This latter property can be the limiting factor in components used in aerospace applications such as washers, nuts, and pistons. Traditionally, these components are manufactured by machining from products such as extrudate or barstock. Acceptance tests for these product forms are invariably based on longitudinal properties. During processing at room temperature, the components described above are often stressed in a circumferential or radial manner, and it is in these cases that brittle failures often manifest themselves.

The mechanical properties of unalloyed molybdenum and TZM (Mo-0.1Zr-0.5Ti) bars of a range of diameters were determined. The results of these tensile tests are that samples in the longitudinal direction showed excellent ductility (usually over 20%); those in the transverse direction, however, showed nil ductility.

The longitudinal metallographic sections of barstock show the expected microstructure for stress relieved, molybdenum alloy products, i.e., elongated grains containing a well developed subgrain structure. The transverse microstructure would normally be expected to consist of small equiaxed grains. However, the grains are irregular in shape and can be extremely wide and curved. This type of microstructure is associated with the development of a pronounced <110> fiber texture in bcc metals subjected to large strains during extrusion, swaging, bar rolling, and wire drawing.

In recent studies on molybdenum alloys, large numbers of grain boundaries were examined for the presence of cracks. An example is shown in Fig. 3. The presence of fractured carbides and associated cracks, distributed along grain boundaries, can be clearly observed. Such features are considered to be particularly undesirable in molybdenum and its alloys because of their extreme sensitivity to cracks and notches. Brittle behavior of molybdenum and molybdenum alloy barstock in the transverse direction has been concluded to be a result of these cracked carbide stringers.

An *in situ* Auger electron spectroscopy examination was carried out to isolate any influence of oxygen on the brittle failure of molybdenum barstock. No evidence was found to suggest that oxygen segregation to grain boundaries occurs in barstock of molybdenum or molybdenum alloys. This observation is in general agreement with the results described by Kumar and Eyre in terms of the C/O ratios.

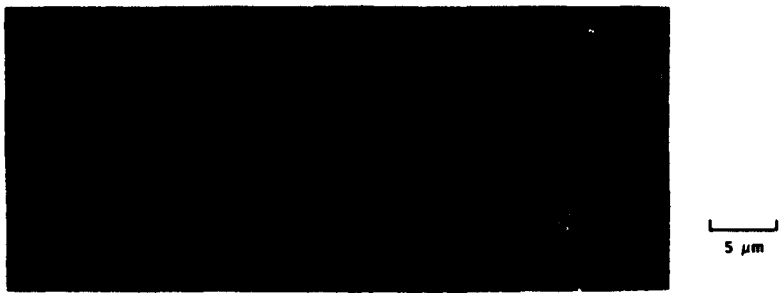

Fig. 3 Optical photomicrograph of grain boundaries from longitudinal sections of stress relieved 35 mm dia. low carbon, arc cast Mo barstock showing presence of fractured carbide crack stringers

It is possible, by careful consideration of recrystallization temperature effects on the reprecipitation of carbides on grain boundaries, combined with thermomechanical processing, to eliminate the above problem for molybdenum components such as flanges, washers, and nuts [13]. The microstructural changes resulting from recrystallization and thermomechanical processing procedures are fractured carbide crack stringers are no longer at grain boundaries, the grain size is considerably refined, and the orientations of the grain boundaries are rotated through 90° with respect to the stress direction to which components are typically subjected during fabrication. The improvement in mechanical properties by the use of this additional thermomechanical processing are dramatic for molybdenum and TZM; this is shown for Mo in Table III. For samples machined from recrystallized and upset forged discs, the tensile ductility is increased dramatically from zero to 27.5%. Improved values of yield and ultimate tensile strengths are observed, even by comparison with the longitudinal barstock values as a result of the grain size refinement that accompanies the recrystallization and forging process.

Table III
Property Comparison between extruded and upset forged Mo

	Yield stress, MPa	UTS, MPa	Elongation, %
Extruded bar			
Longitudinal	621	662	22
Transverse		450	0
Upset forged	683	787	27.5

Molybdenum-Rhenium Alloys

There is continuing interest in the development of a molybdenum base alloy that is ductile and insensitive to the subtle problems described above. A successful solution was suggested many years ago. This was the addition of rhenium to molybdenum [14]. In fact, two commercial alloys, Mo-42Re (Mo-27.2 at.%Re) and Mo-47Re (Mo-31.4 at.%Re), have been available since about 1960. By comparison with unalloyed molybdenum, however, these heavily alloyed compositions have increased density, complexity of production, and cost. The development of a dilute (i.e., less than about 20%Re (11.4 at.%Re)) Mo-Re alloy that demonstrates the same improvements as the above commercial Mo-Re alloys is an enticing one that has been considered in the past. Early work by Klopp and Witzke [15], for example, demonstrated that in dilute Mo-Re alloys, such benefits could be obtained in electron beam melted alloys. Recently, work by Lundberg and co-workers [16] has again raised the issue of dilute Mo-Re alloys and has purported to demonstrate improved properties. The preliminary evidence appears to show a

maximum in ductility in Mo-Re alloys at about 11-13%Re (6.0-7.1 at.%Re). Upon initial examination, the evidence presented by the above studies is convincing. As shown in Fig. 4, the tensile ductility of Mo-Re alloys appears to go through a maximum at about 11-13%Re (6.0-7.1 at.%Re). The increase in tensile ductility with additions of rhenium to molybdenum is attributed to a solute softening effect. Support for the solute softening effect also appeared convincing. Minima in yield strength and hardness were reported at intermediate rhenium contents (although these minima occurred at different rhenium levels for strength and hardness). Lundberg et al., also stated that elastic modulus measurements lend additional support to the concept that true solute softening takes place in the dilute Mo-Re alloys.

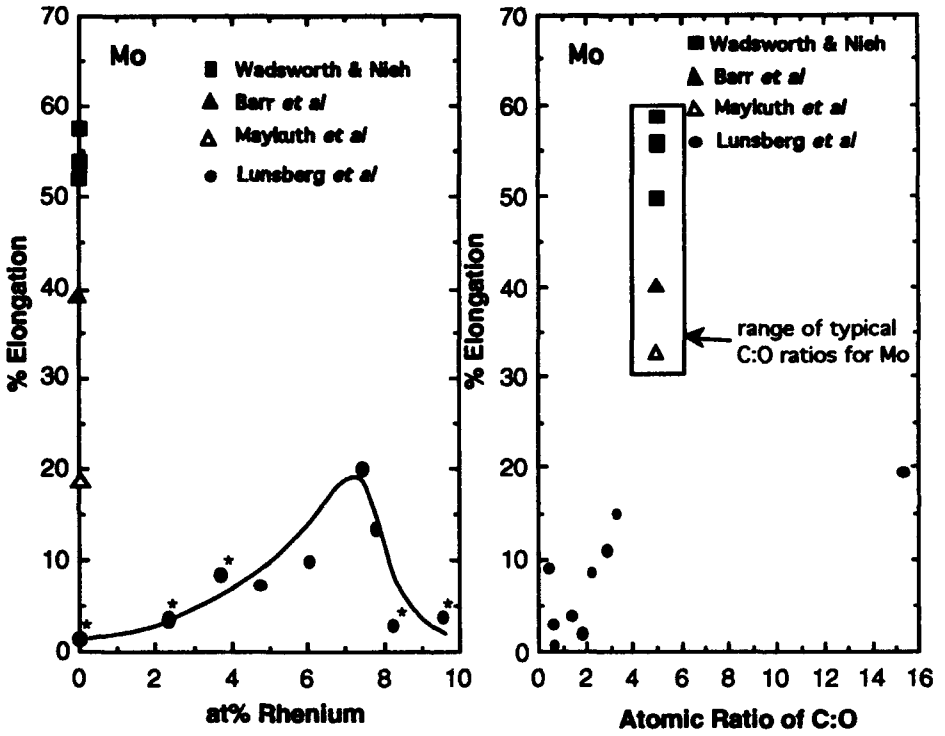

Fig. 4 Left: Room temperature percent elongation (closed symbols) and reduction in area (open symbols) for pure molybdenum and Mo-Re alloys as function of %Re; asterisks next to selected points indicate C/O atomic ratios of less than 2. Right: Room temperature percent elongation plotted as function of C/O atomic ratio for unalloyed molybdenum and Mo-Re alloys; typical range of C/O for commerical unalloyed molybdenum is indicated.

Subsequent work [17] has demonstrated that it is necessary to ensure that proper care has been taken to control the C/O atomic ratio. The published experimental results [16] indicate only about 1% tensile ductility for recrystallized unalloyed molybdenum. Recrystallized molybdenum can indeed exhibit low ductility; however, these low values can usually be attributed either to segregation of oxygen to grain boundaries as a result of an insufficiently high carbon level or to contaminated surface layers as a result of surface and grain boundary oxidation during recrystallization in conventional research vacuum systems. Commercial unalloyed molybdenum can readily be shown to exhibit tensile ductility values as high as 40% at room temperature for recrystallized unalloyed molybdenum have been reported.

In Fig. 4 ductility data from earlier work dating back to the 1960s are included with recent data on dilute Mo-Re alloys. These results indicate that the low ductility for unalloyed molybdenum cited by Lundberg is perhaps a result of oxygen embrittlement because of low ratios of C/O.

Data points with atomic ratios of C/O less than 2 are indicated with asterisks in Fig. 4. Note that all of the low ductility points in Fig. 4 are ones with C/O < 2, and that the highest ductility points, in the Mo-(10-13)Re (Mo-(5.4-7.1 at.%)Re) range, are those alloys with C/O > 2. The same trend is obtained by plotting percent elongation as a function of C/O, as shown in Fig. 4. Note that all the alloys with C/O ≤ 2 tend to have low ductility - independent of the amount of rhenium alloying addition. This suggests that the observed peak in ductility at 10-13%Re (5.4-7.1 at.%Re) is an artifact resulting from the inappropriately low values of ductility measured on alloy compositions outside the 10-13%Re (5.4-7.1 at.%Re) range.

Creep Resistance of Tungsten Alloys

Refractory metal alloys strengthened by HfC precipitation have been considered for applications at very high temperatures [18, 19]. This is because some of the highest strengths in metallic systems at high temperatures have been measured in these alloys and workers have observed that alloys containing equiatomic ratios of hafnium/carbon exhibit optimum properties. An unusual aspect of these alloys is that additions of excess hafnium or carbon over that required for complete combination, i.e. the equiatomic or stoichiometric ratio, instead of providing additional strengthening, have a weakening effect in both molybdenum base and tungsten base alloys. An example of this behavior is shown in Fig. 5. In these studies, hafnium and carbon were added to molybdenum- or tungsten-base alloys in amounts varying over a wide range to encompass both hafnium rich and carbon rich alloys. In the quantitative analyses of carbide precipitation in alloys in which there is a limited solubility of the carbon and carbide former in the matrix, it can be shown that the amount of carbide available for precipitation is sensitive to the 'excess' carbon or carbide former added to the alloy. Specifically, a maximum amount of precipitate is available in alloy compositions where the carbon is added to the carbide former in the exact ratio needed for complete or stoichiometric combination. This is because at the solution treatment temperature, excess carbon or carbide formers essentially use up part of the solubility product that governs the amounts that can go into solution.

Based on a description of carbide precipitation by Wadsworth [18], the high temperature creep and UTS data for molybdenum- and tungsten-base alloys containing various amounts of hafnium and carbon have been re-assessed [18,19]. Significant differences are found between the amounts of HfC assumed to be available for high temperature strengthening in the original analyses, and the amounts that are available as calculated using the recently developed approach. Also, by calculating trends in the HfC available for precipitation in tungsten-base alloys, it is possible to show that excess additions of hafnium or carbon to these alloys do not have a true weakening effect. It can instead be shown that additions of hafnium or carbon in excess of that required for stoichiometric combination, result in a decreased amount of HfC available for precipitation. It is this decrease in available precipitation that is the cause of reduced high temperature strength as shown in Fig. 5.

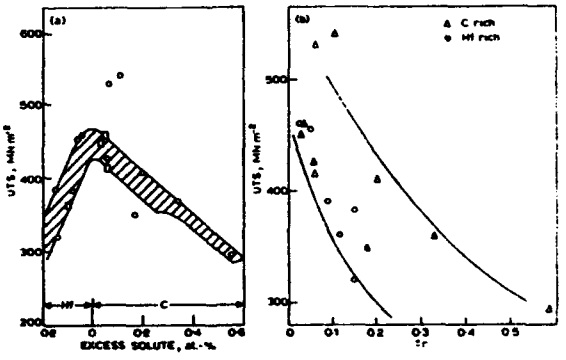

Fig. 5 Ultimate tensile strength of W-4Re-Hf-C alloys solution treated at 2204°C and tested at 1927°C. Left: UTS as function of excess solute added to alloys; Right: UTS as function of *r*, a measure of excess hafnium or carbon added to alloy that is proportional to amount of precipitate.

High Temperature Deformation of Niobium-based Alloys

During creep, metal alloys can exhibit Class I solid solution behavior. According to the original classification and description by Sherby and Burke [20] and Cannon and Sherby [21], Class I solid solutions are found in alloys that have relatively large atomic size mismatches for a given value of elastic modulus [22], although it has been pointed out that the solute concentration, stress level, and the ratio of climb to glide diffusivities are also important variables [23]. Often there is little or no subgrain formation [23], and the deformation behavior of the alloys does not exhibit a direct dependence on the stacking fault energy [21]. During creep, the alloys exhibit either little primary creep or an inversion of primary creep that often enters directly into tertiary, or accelerating, creep. The activation energy for creep in Class I solid solutions is for chemical interdiffusion and is often below the activation energy for self-diffusion of the matrix metal. In Class I solid solutions, creep behavior is believed to be controlled by solute drag on gliding dislocations. The law describing creep deformation can be written, in its simplest form, as $\dot{\varepsilon} = K \cdot \sigma^n$ where σ is the true flow stress, $\dot{\varepsilon}$ is the true strain rate, K is a material constant at a given temperature, and n is the stress exponent. In Class I solid solutions, n has a value of 3; this leads to an inherent high strain rate sensitivity of $m = 0.33$ in the equation $\sigma = k \cdot \dot{\varepsilon}^m$ where $m = 1/n$ and $k = 1/K$.

Niobium forms complete solid solutions (or exhibits extended mutual solid solubility) with most of the refractory metals. Many groups (Group IVB, VB, and VIB) of commercial niobium-based alloys have been manufactured and studied; these are the Nb-Hf, Nb-Zr, Nb-Ti, Nb-Ta, Nb-V, and Nb-W based systems. (The atomic size factors, $|\Omega|$, defined as: $|\Omega| = [\Omega_B - \Omega_A]/\Omega_A$, where Ω_B is the effective atomic volume of a solute B in a matrix A, and Ω_A is the effective atomic volume of solution A, that indicate the degree of atomic size mismatch, for these binary alloy systems are: 18.58, 27.11, 3.00, 0.26, 17.81, and 98.22, respectively [22].)

Recently, Wadsworth *et al.* [24] analyzed existing high-temperature data for a number of Nb alloys and pointed out that these alloys behave like Class I solid solution alloys during high temperature deformation. These alloys include binary Nb-Hf, Nb-Zr, Nb-Ti, Nb-Ta, Nb-V, and Nb-W, as well as some ternary alloys. For example, it was shown several years ago that a coarse-grained Nb-5.4Hf-2.0Ti[4] alloy (known commercially as C103) could exhibit large tensile elongations of over 200%; the phenomenon was observed at intermediate homologous temperatures (about 0.7 T_m, where T_m is the absolute melting temperature) and at intermediate strain rates (of about 10^{-3} s^{-1}). Other Nb-Hf based alloys include C129 (Nb-5.8Hf-5.6W) and WC-3009 (Nb-19Hf-6W). In a normalized form as diffusion-compensated strain rate versus modulus-compensated stress, data from C103, C129, and WC-3009 are depicted in Figure 6. It is evident that all alloys show a stress exponent value of 3 (i.e. $m = 0.33$). With respect to the role of alloying elements on determining Class I behavior, it may be inferred that the role of W does not appear to override that of Hf, or perhaps is equivalent to that of Hf. The maximum elongation-to-failure data are reported to be over 70% for C129, 200% for C103, and 164% for WC3009. The activation energies for C103, C129 and WC3009 are determined to be similar with a value of about 300 kJ/mol. The similarity amongst the activation energy values for all three alloys suggests that glide control by Hf atom drag is the controlling mechanism in each case. In addition to the Nb-Hf based alloys, other Nb alloys indicating the Class I solid solution behavior include D36 (Nb-18Ti-5Zr), Nb-18Ta-5W-0.8Zr, Cb753 (Nb-8.8V-1.2Zr), B66 (Nb-8.8V-4.6Mo-1.0Zr), and Cb752 (Nb-5W-3Zr). The significance of Class I solid solution behavior in these alloys is as follows.

The strain rate sensitivity is known to control the rate of neck formation in tensile tests at elevated temperatures [25]. Most ordinary metals and alloys have values of $m \leq 0.2$ and, as a result, show modest tensile ductilities (from 50 to 100%) even at very elevated temperatures. Superplastic alloys have values of m between about 0.4 to 0.6, although the methods for measuring m can lead to variations about this range [26]. The high values of m in superplastic metals account for their high tensile elongations; the largest reported value is about 8,000% [27] although more typical values are between 300 to 1000%. The strain rate sensitivity of $m = 0.33$ found in Class I solid solutions is intermediate between that for pure metals and superplastic alloys, and therefore extended ductility (150 to 600%) is predicted for these alloys.

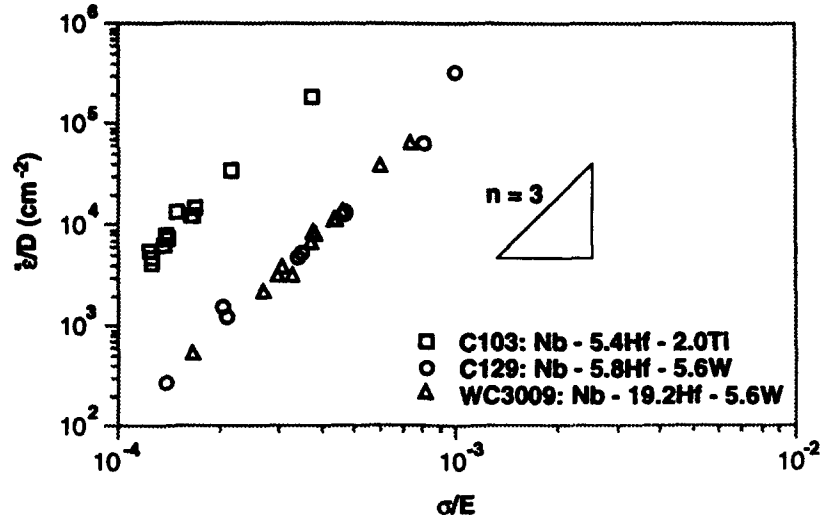

Fig. 5 Diffusion-compensated strain rate versus modulus-compensated stress for C103, C129, and WC3009.

It is pertinent to point out that in commercial superplastic forming operations, (a) tensile ductilities of over 200% are rarely required, (b) cavitation, as a result of grain boundary sliding, can become unacceptable without the application of back pressure at elongations greater than 200% (e.g., in the 7000 series aluminum alloys and in the Al-6Cu-0.5Zr commercial alloy), and (c) extremely high elongations are normally found at very low strain rates (~10^{-5} s^{-1}). In contrast, Class I solid solutions usually exhibit ductilities of 150% at reasonably high strain rates (10^{-2} s^{-1}). Cavitation should present less of a problem in Class I solid solutions, because the mechanism of flow is not based on grain boundary sliding. It would thus appear that complex forming operations with Class I solid solutions, such as refractory metals, should be feasible. Superplastic forming of these metals may also offer an additional advantage in that the special thermomechanical processing to produce the ultrafine, two-phase structures of superplastic alloys will not be required.

References

1 "Mineral Commodity Summaries 1993", (U.S. Bureau of Mines, MS 1040 Washington, D.C., 1993)

2 J.F. Lynch et. al., "Investigation of Nozzle Failure Mechanisms and of Parameters Affecting Nozzle Material Suitability in Solid-Propellant Rockets", (Air Force Report ASD-TDR-63-738, Prepared by Battelle Columbus, 1963).

3 R.J. Brook ed., Concise Encyclopedia of Advanced Ceramic Materials, (Oxford, UK: Pergamon Press, 1991).

4 R. Touloukian et. al. eds., Thermophysical Properties of Matter Vols. 1-8, (New York, NY: Plenum Press, 1973)

5 T.E. Tietz and J.W. Wilson, Behavior and Properties of Refractory Metals, (Stanford, CA: Stanford University Press, 1965).

6 D.M. Shah et. al., "Appraisal of Other Silicides as Structural Materials", Materials Sci. and Eng., A155 (1992), 45-57.

7 D.P.H. Hasselman, "Thermal Stress Resistance Parameters for Brittle Refractory Ceramics: A Compendium", Am. Ceram. Soc., Bull., 49 (1970), 1033-37.

8 S.K. El-Rahaiby, "C/SiC and SiC/SiC Ceramic Matrix Composites in France", Newsletter, U.S. Ceramics Information Analysis Center, 2(2) (1992), 1-5.

9 G.D. Smith and J.A.E. Bell in Physical Metallurgy of Controlled Expansion Invar-Type Alloys, (K.C. Russell and D.F. Smith eds., Warrendale, PA: The Metallurgical Society, 1990), 283-299.
10 J.P. Wittenauer, T.G. Nieh, and J. Wadsworth, "Superplastic Forming of a Zirconia Ceramic Sheet" in Processing, Fabrication, and Manufacturing of Advanced Materials for High-Temperature Applications II, (V.A. Ravi and T.S. Srivatsan eds., Warrendale, PA: The Metallurgical Society, 1993).
11 R. A. Perkins, in Proc. Conf. Advanced compact reactor systems, 282-325; 1982, Washington, DC, National Academy of Sciences, National Academy Press.
12 A. Kumar and B. L. Eyre, Proc. R. Soc., A370 (1980), 431-458.
13 J. Wadsworth, C. M. Packer, P. M. Chewy, and W. C. Coons, Metall. Trans., 15A (1984), 1741-1752.
14 R. I. Jaffee, D. J. Maykuth, and R. W. Douglass, in Refractory Metals and Alloys, (ed. M. Semchysen and J. J. Harwood), 383; 1961, New York, Interscience.
15 W. D. Klopp and W. R. Witzke, Metall. Trans., 4 (1973), 2006-2008.
16 L. B. Lundberg, J. Met., 37 (4) (1985), 44-47.
17 J. Wadsworth, T. G. Nieh, and J. J. Stephens, Scr. Metall., 20 (1986), 637-642.
18 J. Wadsworth, Metall. Trans., 14A (1983), 285-294.
19 J. Wadsworth and W. D. Klopp, in Physical Metallurgy and Technology of Molybdenum and its Alloys, (ed. K. H. Miska *et al.*), Ann Arbor, MI, 1985, AMAX Metals, 127-133.
20 O. D. Sherby and P. M. Burke, Prog. Mater. Sci. 13 (1967) 324 .
21 W. R. Cannon and O. D. Sherby, Metall. Trans.1 (1970) 1030.
22 H.W. King, Jour. Mat. Sci. 1 (1966) 79.
23 F.A. Mohamed and T.G. Langdon, Acta Met. 22 (1974) 779.
24 J. Wadsworth, P.A. Kramer, S.E. Dougherty, and T.G. Nieh, Scripta Metall. Mater., 27, (1992) 71-76.
25 D. A. Woodford, Trans. ASM Quarterly 62 (1969) 291.
26 J. W. Edington, K. N. Melton, and C.P. Cutler, "Superplasticity," Prog. Mater. Sci., 21 (1976) 61-170.
27 O.D. Sherby and J. Wadsworth, "New Superplastic Materials," in Superplasticity in Aerospace, Eds., H. C. Heikkenen and T. R. McNelly, The Metallurgical Society, Pennsylvania, PA, (1988), 3-27.

PRECIPITATION IN HIGH TEMPERATURE ALUMINIDES

M. Nemoto

Department of Materials Science and Engineering,
Faculty of Engineering 36, Kyushu University, 812 Fukuoka(Japan)

Abstract

Microstructural control to produce multiphase structure has received much attention to improve the high temperature strength as well as low temperature ductility of intermetallics. This paper describes the overall view of approaches to obtain various morphologies of multiphase intermetallics basing upon the phase diagrams. Special emphasis is to be laid on the microstructures formed by the decomposition of supersaturated intermetallics of NiAl(B2)-based, $Ni_3Al(L1_2)$-based and $TiAl(L1_0)$-based matrices. The strength of the multi-phase intermetallics is dependent on the mode of interaction between particles and dislocations. In the $L1_2$-phase strengthened by the precipitation of disordered coherent f.c.c. phase, dislocations are attracted into the disordered γ phase and cut through the particles during deformation, while in the alloys containing fine dispersion of partially coherent carbide particles, dislocations by-pass the particles during deformation.

Critical Issues in the Development of High Temperature Structural Materials
Edited by N.S. Stoloff, D.J. Duquette and A.F. Giamei
The Minerals, Metals & Materials Society, 1993

Introduction

Intermetallics composed of aluminium and other metallic components have received considerable interest as canditates for next generation high temperature structural materials because of their high melting points, low densities and possible high oxidation resistances. However most of them still suffer from lack of low temperature ductility and of enough high temperature strength.

Intermetallics based on the $L1_2$-ordered structure are attractive as high temperature structural materials because of their positive temperature dependence of yield strength. However, it has been known that "the creep strength anomaly" does not exis[1]. As creep strength is concerned, the single phase $Ni_3Al(\gamma')$-base intermetallics are inferior to recent two phase nickel-base superalloys. Khan et al.[2] compared the creep strength of the $\gamma - \gamma'$ CMSX-2 single crystal superalloy with that of its constituent γ' alloy and showed that the γ' alloy cannot compete with the parent alloy.

For B2-ordered NiAl, significant improvements in creep strengh were first demonstrated by Polvani et al.[3] by forming a two phase mixture of NiAl and Ni_2AlTi(Heusler phase). Similar Heusler phases and other phases such as Laves can be formed in NiAl by ternary additions such as Nb, Ta, Hf and V. The creep strength of these multi-phase intermetallics increased appreciably but not to the level of recent nickel-base superalloys[4]-[7]. It was proposed that optimizing the creep strength requires a balance of the compositions of the two phases, the precipitate volume fraction, the size and distribution of the precipitates by analogy to the nickel-base superalloys[8].

Much work has been performed also to improve the ductility of intermetallics since Aoki and Izumi[9] found the drastic effect of B on the ductility of Ni_3Al. The ductility of intermetallics could also be improved by macrostructural and microstructural control through heat treatments or processing in terms of powder metallurgy and fiber reinforcement. However there have been only a limited number of studies concerning the precipitation in intermetallics. The present paper describes the overall view to give the fine precipitation of second phases in $L1_2$-ordered Ni_3Al, B2-ordered NiAl and $L1_0$-ordered TiAl. The morphologies of deformation induced dislocations are also compaired.

Optimum Microstructure for High Temperature Intermetallics

There should be several ways by which the high temperature strength of intermetallics can be improved: elimination of grain boundaries, solid solution strengthening, precipitation strengthening and composite strengthening. The first two mechanisms are known to be essential to the high temperature materials but are already reported to be insufficient to exceed the strength of the nickel-based superalloys[2]. Therefore the introduction of multi-phase structures should be required also for intermetallics to attain higher strength over a wide temperature range.

Recently Naka and Khan[8][10] have been successful in creating a γ / γ' type two-phase microstructure which is very similar to that of nickel-based γ / γ' superalloys in the pseudo-binary Fe-Ni_2AlTi and Nb-Ti_2AlMo systems. Although the future of this approach looks promising, these alloys would be in the category of superalloys based upon different disordered matrix phases containing high volume fractions of ordered precipitates. It should be noted that the optimum microstructure for the intermetallic-based alloys might be different from that for the

disordered phase-based alloys. In the nickel base superalloys it has been known that most of deformation induced dislocations move predominantly in the disordered γ which forms narrow channels between γ '[11].

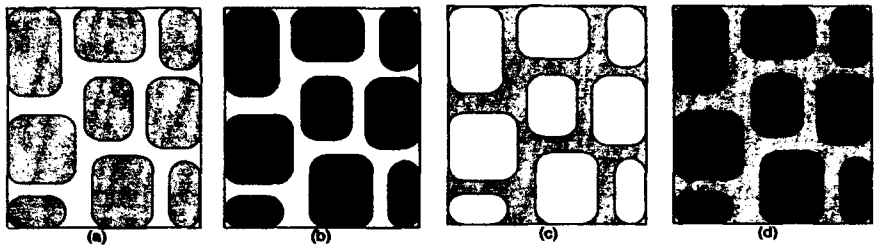

Figure 1 Microstructural variations of multi-phase intermetallics(b)-(d) as compaired to the Ni-base superalloy(a).

Figure 1 schematically shows the microstructural variations of nickel-base superalloys and of intermetallic-based alloys. In nickel-base superalloys, coherent $L1_2$-ordered γ ' is dispersed in disordered γ as shown in (a). The alloys proposed by Naka et al.[8][10] correspond to (b) where intremetallic phases different to γ ' are dispersed in a disordered matrix different to alloyed γ . The situation is reversed in intermetallic-based alloys as shown in (c) where a disordered phase is dispersed in an ordered phase. In (d), an intermetallic phase is dispersed in another intermetallic phase matrix. Other variations of multi-phase microstructures should also be possible. Therefore different behavior of dislocations can be expected in the intermetallic-based alloys. The optimum microstructure for the intermetallic-base alloys might be then different from that for the nickel-based superalloys.

Optimizing the multi-phase microstructures requires a balance of the compositions of the existing phases, the precipitate volume fraction, the size and distribution of the precipitates. The physical properties of the precipitate and of the matrix play primary roles to determine the mechanical properties of the intermetallic-based alloy since the contribution to the high temperature strength is dependent on the mode of interaction between particles and dislocations.

Precipitation in intermetallics can be attained basing upon the phase diagrams if the reliable diagrams are available. If the two phases facing each other in the phase diagram have fundamentally similar crystal structures and lattice parameters, extended solid solubility may be obtained at high temperatures. Then wide range of microstructural variations can be achieved.

Ductile Phase Toughning

Ductile phase toughning involves the incorporation of a ductile second phase in a brittle matrix[12]. The purpose of the ductile phase is to interact or interfere with the progression of cracks through the matrix phase or to lead to dislocation generation at the interphase interface of the ductile phase and of the brittle matrix. Such strain transfer can be facilitated by the presence of coherency or specific orientation relationships between two phases.

Ishida et al.[13] have been successful to improve drastically the ductility of NiAl-based alloys by the addition of alloying elements and by the control of microstructures. They found that a small amount of disordered phase formed by the addition of Fe, Co and Cr has a drastic effect

on the ductility. To avoid the strength decrease, Yang et al.[14] examined a number of alloys in a three phase field incorporationg β -NiAl, β '-Ni_2AlTi and γ '-Ni_3Al phases in the Ni-Al-Ti system. It was found that the presence of a substancial fraction of the relatively ductile γ ' phase in semicoherent epitaxy with β and β ' conferred several per cent of compressive plasticy on these alloys, where the β / β ' alloys are known to have a catastrophic room temperature brittleness. However even the improvement was achieved in the room temperature ductility by incorporating ductile phases, it should be necessary to disperse fine second phases to maintain the high temperature strength, especially creep strength.

Precipitation in Intermetallics

In most of structural alloys, intermetallic compounds exist as dispersoids. There have been surprisingly few studies on the phase decompositions in intermetallics. The mechanisms of precipcitation strengthning of intermetallic-based alloys have rarely investigated. As far as the present authors know, Ardell and Hovan[15] are the first who showed interest in strengthening the $L1_2$ ordered phase by a fine dispersion of coherent precipitates. They expected that dislocations in the Cu_3Al matrix will be attracted by the Co-rich precipitates for the same reason that unit dislocations in disordered alloys are attracted to precipitates which have a lower stacking fault energy than the matrix as discussed by Hirsch and Kelly[16] in their stacking fault strengthening theory. However, the effects of precipitation on the high temperature strength of ordered alloys have not been well investigated. Cu_3Au should not be sufficient for this purpose, because the order-disorder transition temperature is rather low(Tc=664 K).

Table 1 lists various combinations of precipitate and matrix phases investigated in our recent work to examine the microstructural characteristics of model alloys. Coherent or incoherent and ordered or disordered phases have been tried to disperse in Ni_3Al, NiAl and TiAl matrices. Some of our recent results will be reviewed below.

Table 1 Intermetallics with precipitates under investigation in the present work

matrix		precipitates	coherency*	alloy system
$L1_2$	Ni_3Al	γ -Ni(A1/fcc)	C	Ni-Al-Ti
		$M_{23}C_6$(cubic)	I	Ni-Al-Cr-C
B2	NiAl	α -Cr(A2/bcc)	C	Ni-Al-Cr
		α -Fe(A2/bcc)	C	Ni-Al-Fe
		β -Co(A1/fcc)	I	Ni-Al-Co
		$Ni_2lTi(L2_1)$	C	Ni-Al-Ti
$L2_1$	Ni_2AlTi	NiAl(B2)	C	Ni-Al-Ti
$L1_0$	TiAl	Ti_3AlC(cubic)	I	Ti-Al-C
		Ti_3AlN(cubic)	I	Ti-Al-N

* C: coherent, I: incoherent

Precipitation in Ni_3Al

Ni_3Al-disordered γ . A detailed examination of microstructure and strength of γ '-$Ni_3(Al,Ti)$-based two phase alloy has been performed by Tian et al.[17]-[19] and Nemoto et al[20]. They revealed a retrograde solubility of nickel in γ ', i.e., the solubility of nickel in γ ' has its maximum value at about 1373 K and decreases with decreasing as well as increasing

temperature as shown in Figure 2. It is possible to obtain a uniform supersaturated solid solution by quenching from this temperature and to disperse fine precipitates by aging. Actualy

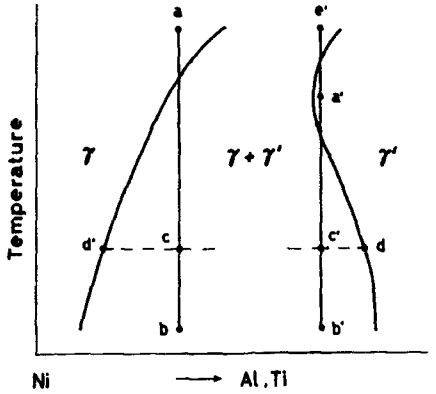

Figure 2 A schematic vertical cross section of Ni-Al-Ti phase diagram showing a retrograde solubility of γ in γ'.

Fig. 3 shows the variations of hardness of 78Ni18Al4Ti and 79Ni11.9Al9.1Ti γ/γ'-based alloy by aging at temperatures between 973 K and 1173 K after quenching from 1423 K[17].

Figures 4 (a) and (b) show the morphologies of precipitates in the peak-aged and over aged condition, respectively, taken by using the ordered lattice reflection from the matrix γ'. The precipitates are spherical or round-cubic shape in peak-aged condition,but are plates in over aged condition. High resolution electron microscopy revealed that the perfect lattice coherence is kept between the precipitate and matrix. The volume fraction of precipitates was estimated to be 4%.

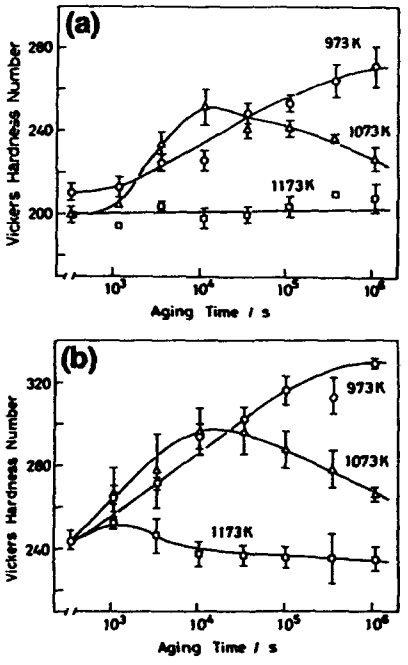

Figure 3 Variations of hardness 78Ni18Al4Ti and 79Ni12Al9Ti during aging.

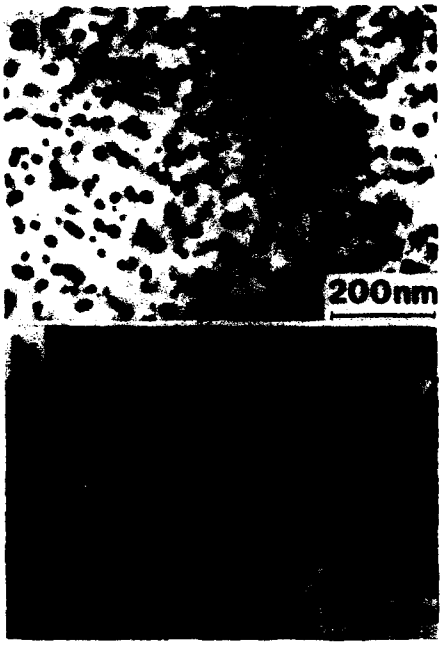

Figure 4 TEM micrographs of γ precipitates in Ni18Al4Ti. (a) aged at 1073 K for 1.08×10^4 s (3 h, peak-aged), (b) aged at 1073 Kfor 3.6×10^5 s (100 h)

Figure 5 is a $g=\bar{2}02$ dark field weak beam image of dislocations in a deformed single

Figure 5 TEM weak-beam image showing the dissociation of dislocations in the disordered particles at the peak aged condition in the Ni18Al4Ti aged at 973 K for 1.08×10^6 s and deformed 3% at 673 K.

crystal. The superlattice dislocations dissociate in the matrix and they tend to be uncorrelated by the absence of an APB, as they meet a disordered particle. The particles are not imaged in this dark field micrograph taken with the superimposed spot of matrix and precipitate reflections. A detailed TEM examination of the morphology of deformation induced dislocations revealed that the dislocations have dissociated on the (010) plane in the matrix and on the (111) in the particle. This observation strongly suggests that the fine dispersion of disordered γ' suppresses the cross slip of superdislocations from {111} to {001} and thus increasing the high temperature strength of γ'.

Ni_3Al-$M_{23}C_6$. When 0.5 mol% of carbon is added to $Ni_3(Al,Cr)$, hardening was observed by aging at temperatures around 1023 K. Figure 6 shows the variation of hardeness due to aging at 973 and 1073 K, respectively. Although the hardness increment is not very high, a typical age hardening and overage softening are recognized by aging at 1073 K.

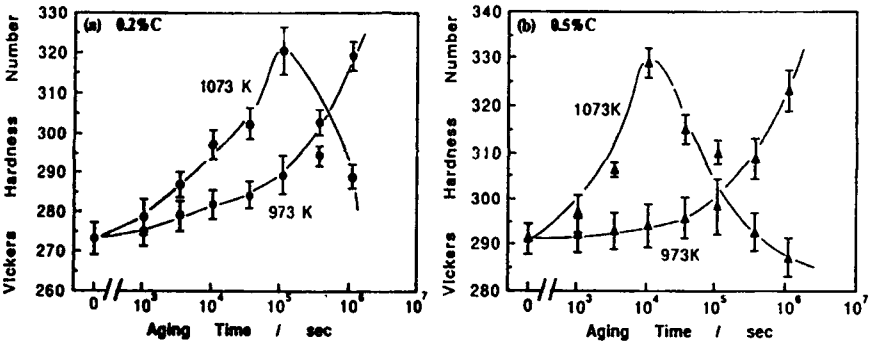

Figure 6 Variation of hardness of Ni24Al4Cr-0.2 and -0.5C alloy by aging at 973 and 1073 K.

Figures 7 (a) and (b) show the microstructures of the alloy aged at 973 K for 1.08×10^6 s and at 1073K for 1.08×10^5 s, respectively. The corresponding selected area electron diffraction (SAED) analysis revealed that the precipitate is an $M_{23}C_6$ type carbide and has the orientation relationship (100)-$M_{23}C_6$ parallel to (100)-γ' and [001]-$M_{23}C_6$ parallel to [001]-γ', i.e. cube-cube orientation relationship. $M_{23}C_6$ is a chromium-rich carbide which posses a complex cubic structure, containing 92 atoms per unit cell, with a lattice parameter of about 1.06 nm.

Figure 8 shows an example of high resolution image of $M_{23}C_6$ carbide observed from [110]-$M_{23}C_6$. It is evident that the surface of the particle is bounded by {111} and a periodical matching of lattice planes between the matrix and $M_{23}C_6$ is kept at the interface. The planer faults are observed to lie on the (111) planes of $M_{23}C_6$. These defects are characterized by a distinct displacement across the fault planes and considered to be growth defects.

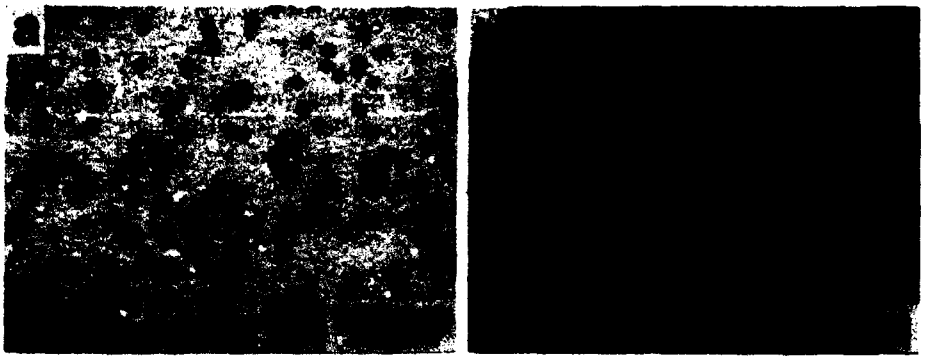

Figure 7 TEM micrographs of Ni24Al4Cr-0.5C aged (a) at 973 K for 1.08×10^6 s and (b) at 1073 K for 1.08×10^5 s (30 h).

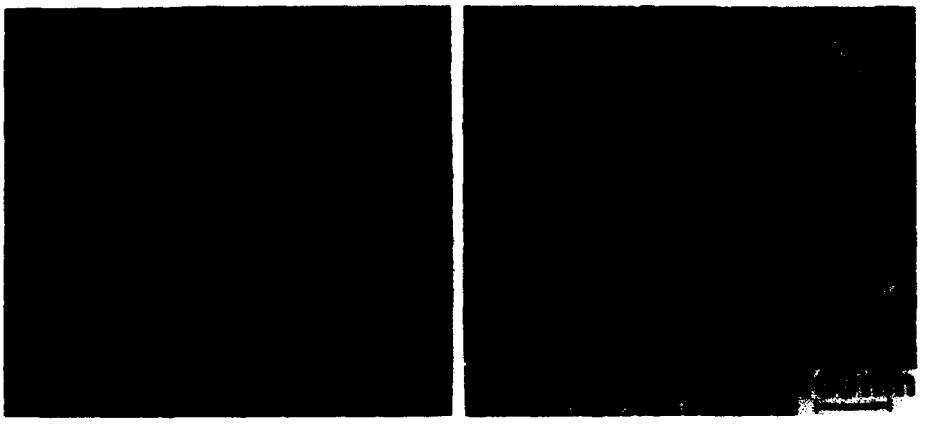

Figure 8 (left) High resolution image of the interface between $M_{23}C_6$ and Ni_3Al.

Figure 9 (right) Dislocations in the Ni24Al4Cr-0.5C alloy aged at K for 3.6×10^5 s (100 h) and deformed 3% at 573 K. Orowan loops are observed.

Figure 9 is a dark-field weak beam image of deformation induced dislocations in the alloy aged at 973 K for 3.6×10^5 s (100 h) and deformed 3% at 573 K. It is evident that the dislocations bypass the carbide particles leaving loops sorrounding them. The observesd morpholopgy of dislocations is quite different from that observed in the Ni_3Al with fine dispersion of coherent disordered γ', in which deformation induced dislocations are attracted into the particles and cut through them at any deformation temperatures.

Precipitation in NiAl

NiAl-Ni_2AlTi. Significant improvements in creep strengh were first demonstrated by Polvani et al.[3] by forming a two phase mixture of NiAl and Ni_2AlTi(Heusler phase). However because of the catastrophic room temperature brittleness this alloy has not been investigated so far. Field et al.[21] investigated the alloys along a line between the pseudo-binary NiAl and Ni_2AlTi system and obtained evidence for a spinodal ordering reaction in this system. Figure 10 shows the possibilitiy of the wide range of microstructural modification of this system by

controlling the heat treatments and by changing the alloy composition along the pseudo-binary line.

NiAl-Fe. Jung and Sauthoff[22] investigated the creep behavior of NiAl-Fe and Fe-NiAl systems and revealed that the effect of the α-Fe particles in B2-NiAl matrix was quite analogous to that of B2-NiAl particles in α-Fe matix. In both cases the particles act as dislocation obstacles because of the dislocation-particle interaction, and indeed adhering dislocations were observed at particles before detachment in the B2-NiAl case.

Phase transformation in the Fe-Al system depends strongly on the composition of the alloy. There is a possibility of the parallel reactions of ordering and phase separation[23][24]. Figure 11 shows the TEM microstructure of the alloys chosen along the line in the two phase region in the Fe-Ni-Al phase diagram shown in Figure 12. It can be known that the microstructure widely changes by heat treatments.TEM examination revealed the possibility of the coexistence of α-Fe and two kind of B2-ordered phases which have been observed by Liu et al.[25] in an Fe-23.2Al-4.1Ni alloy. The microstructure of this system is still to be clarified.

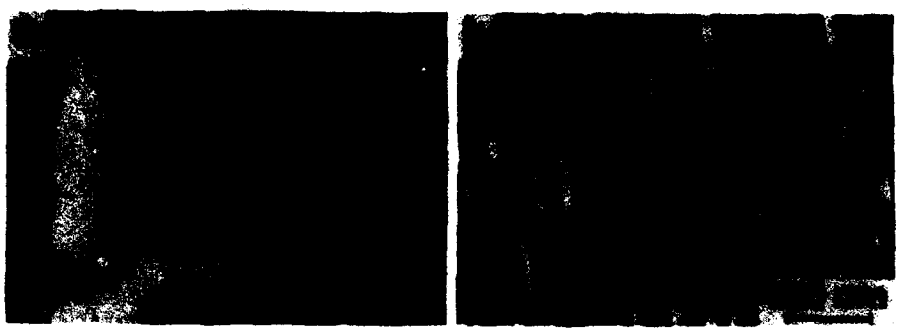

Figure 10 TEM micrographs of (a) 50Ni40Al10Ti alloy aged at 1273K and (b) 50Ni43Al7Ti aged at 1173K for 3.6×10^5 s (100 h) showing the precipitate of Ni_2AlTi in NiAl.

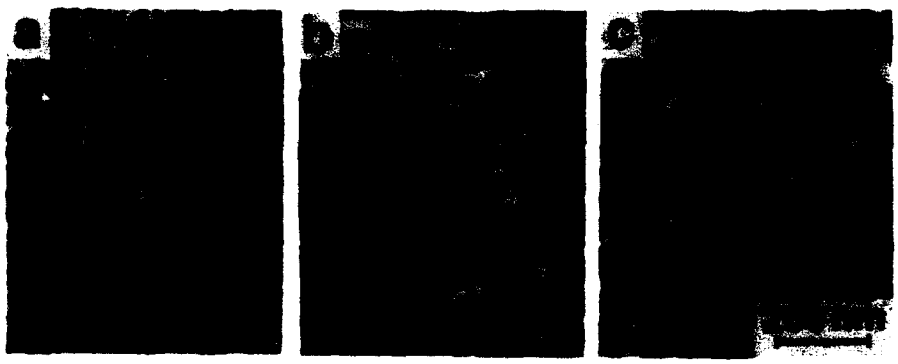

Figure 11 TEM micrographs of (a) 40Ni40Al20Fe, (b) 28Ni28Al44Fe and (c) 10Ni15Al75Fe aged at 973K for 1.08×10^5 s (30h).

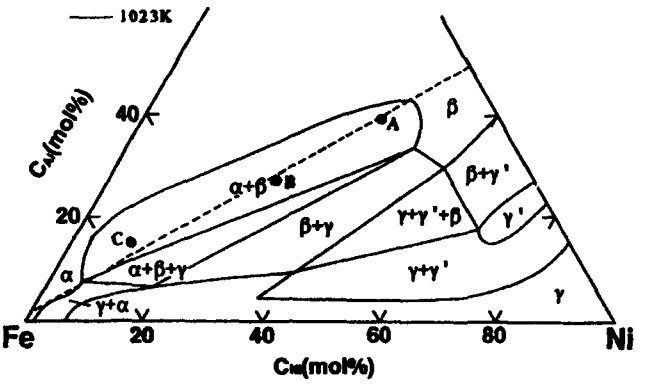

Figure 12 Partial isothermal section of Ni-Al-Fe phase diagram with the alloys of Figure 11.

NiAl-Cr. Among the alloying elements examined to improve the ductility of NiAl, Cr is interesting because theoretical calculations indicate that the APB energy can be significantly reduced[26]. In the study of the modification of slip behavior of NiAl single crystals, Miracle et al.[27] and Field et al.[28] found the precipitation of α-Cr particles having cube-cube orientation relationship with the matrix. Figure 13 shows the partial section of Ni-Al-Cr ternary phase diagram in which phase regions at 1298 K and 1423 K are indicated[29]. It must be immediately known that the α-Cr phase precipitates from the β-NiAl matrix during aging after solution annealing.

Figure 14 shows the variation of hardness of NiAl with different Cr contents during aging at 973 K and 1173 K. It should be noted that the NiAl hardenes appreciably by aging at 973 K and also that the amount of hardening is strongly dependent on the Cr contents and the sites of atom replacement. The amount of hardening is larger in NiAl containing higher amount of Cr and smaller in NiAl in which the equal amounts of Ni and Al are replaced by Cr.

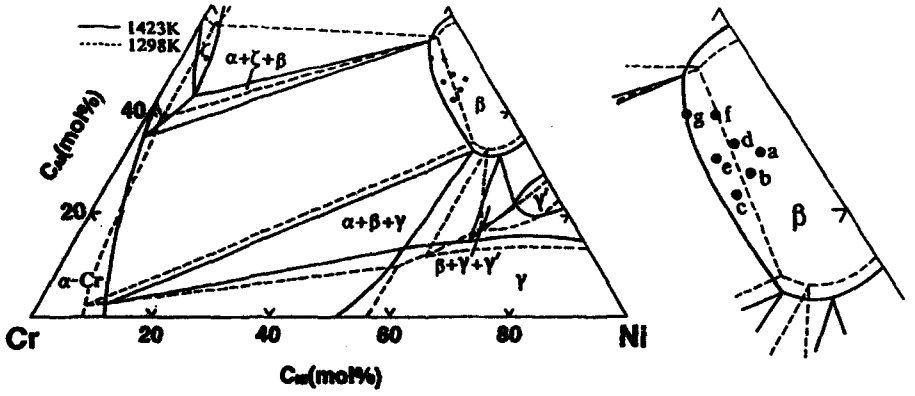

Figure 13 Partial isothermal section of Ni-Al-Cr phase diagram with the alloys in Figures 14 and 15.

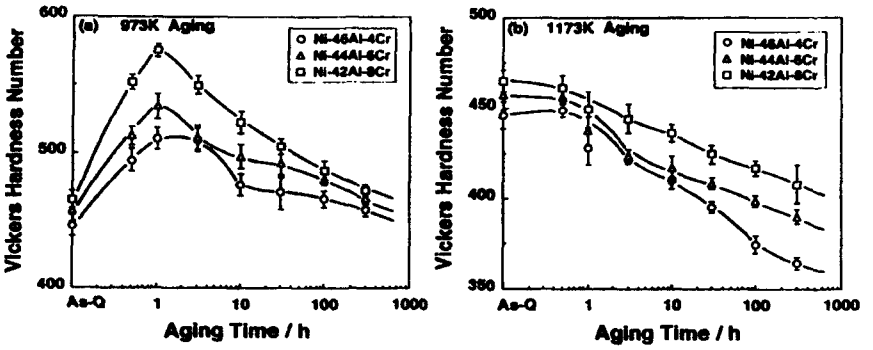

Figure 14 Variation of the hardness of B2-ordered NiAl-Cr alloy by aging at 973 and 1173 K after quenching from 1423 K.

Figure 15(a) shows spherical precipitates formed in 50Ni42Al-8Cr aged at 1173 K for 3.6×10^6 s (1000 h) observed from the [111] direction of the matrix. The high resolution electron micrograph of the interface between the α -Cr precipitate and B2-ordered NiAl shown in Figure 15(b) reveales that the precipitate lattice have a perfect coherency with the matrix lattice. The loss of coherency of α -Cr precipitates occurs only after prolonged aging. No punching of loops would be expected for α -Cr because the misfit between the α -Cr and the NiAl matrix lattices is only 0.8%[27]. After prolonged aging dislocations in the matrix might climb over the particles leaving misfit dislocation loops at the interfaces. Deatiled analysis of the nature of the misfit dislocations in unidirectionally solidified NiAl-Cr eutectic composites has already been reported[30][31].

High temperature compression tests indicated that the fine precipitation of α -Cr in NiAl increases the strength of NiAl appreciably at intermediate temeratures but the strength of NiAl-Cr decreases gradually with increasing temperature and approaches to nearly the same level of monolithic NiAl with nonstoichiometry[32]. TEM examination of deformation induced dislocations suggested that the dislocations bypass the α -Cr particles during deformation involving cross-slip at the particles.

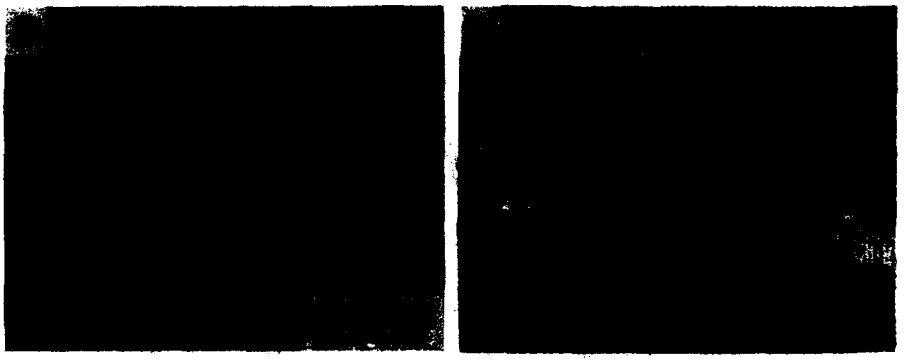

Figure 15 (a) TEM micrograph of NiAl-Cr alloy aged at 1173 K for 3.6×10^6 s (1000 h) showing the precipitation of spherical α -Cr, (b) HREM.

NiAl-Co. Figure 16 shows the partial Ni-Al-Co ternary phase diagram in which phase regions

at 1373 K and 1573 K are indicated[33]. Ishida et al.[13] have shown that the ductility of B2-ordered NiAl can be significantly improved by composing a multi-phase microstructure between NiAl and the disordered f.c.c. Co phase. The phase diagram aloso shows the various possibilities of microstructural variation. For example, an ordinal precipitation of NiAl must be expected in disordered Co. On the other hand, the precipitation of disordered-Co phase in β - NiAl is also expected in NiAl. In the bimodal alloy used by Ishida et al.[13] the precipitations of Co in NiAl and NiAl in Co are expected by apropriate heat treatments.

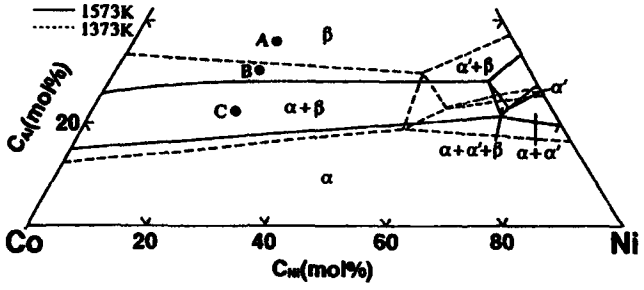

Figure 16 Partial section of Ni-Al-Co phase diagram with the alloys in Figure 17.

Figure 17 shows the variations of hardness and yield strength of NiAl with chemical compositions shown in Fig.16 by aging at different temperatures. Both the monolythic and bimodal NiAl harden appreciably by aging at temperatures around 1073 K. TEM examination revealed that he β -Co precipitates are platelet in shape lying parallel to the {110} planes of NiAl and have the Kurdjumov-Sachs orientation relationship.

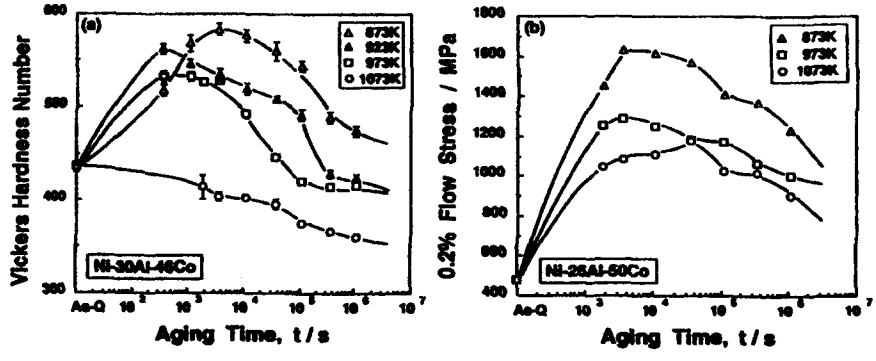

Figure 17 (a)Variation of the hardness and (b) compressive yield strength of NiAl-Co by aging at 873~1073K.

Precipitation of Carbide and Nitride in TiAl

According to the Ti-Al-C ternary phase diagram reported by Schuster et al.[34], Ti_2AlC(H-phase) is in equilibrium with TiC, Ti_3Al and TiAl, and Ti_3AlC(P-phase) with TiC, Ti_3Al and α

-Ti at 1273 K. However, the morphologies of these carbides in TiAl or Ti_3Al have not been reported. Figure 18 shows typical age hardening and over age softening observed for both the alloys containing 0.5 mol% of carbon or nitrogen. The increment of yield strength of TiAl-N, however, is smaller than that obtained in TiAl-C possibly because of the loss of the solid solution strengthening in TiAl-N during aging.

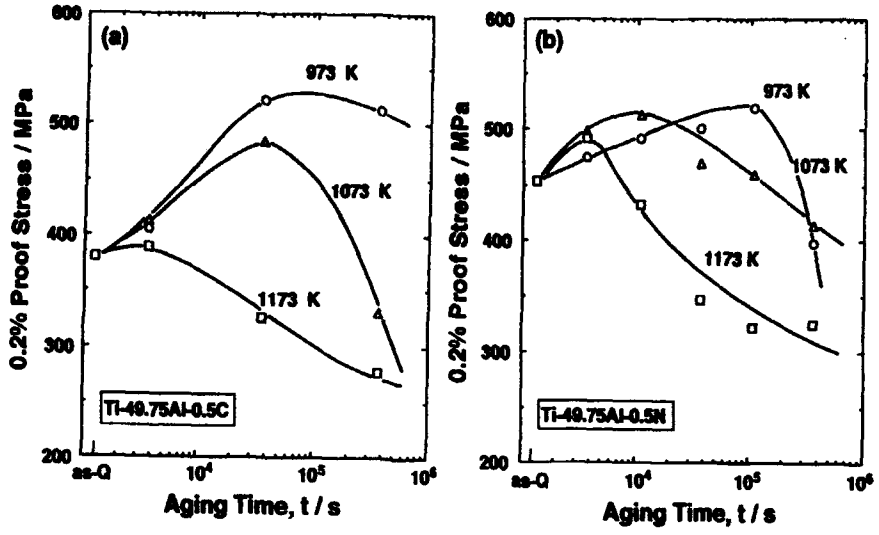

Figure 18 Variation of compressive yield strength of TiAl-0.5C(a) and TiAl-0.5N(b) by aging at 973 K, 1073 K and 1173 K, respectively.

TEM exmination revealed the fine precipitation of needle-shaped carbide and nitride at dislocations and in the matrix during aging. Figure 19 shows the precipitates formed in TiAl-2N by aging at 1173 K for $3.6x10^5$ s (100 h). A tilting experiment easily revealed that the precipitates have a needle-like shape and the square cross-section with the sides parallel to [010] and [100] directions of the matrix lattice. SAED analyses indicated that the crystal structure of the precipitates are of the perovskite type in which the carbon atoms occupy the octahedral sites of $L1_2$ structure. It should be noted that the needle-like precipitates are formed only in one direction parallel to the [001] axis of the TiAl matrix.

When the alloys were aged at lower temperatures, weak extra-spots appeared in the SAED patterns for the precipitates. Try-and-error procedure basing upon the SAED patterns indicated the formation of carbon-vacancy long-range ordering, where the carbon atoms and vacancies make rows along the [100] direction in a needle-shaped perovskite carbide. The carbon atom rows are considered to be neighbored with the vacancy columns resulting in an anisotropic atom arrangement in the (001) plane of the perovskite carbide. Figure 20 shows schematically the structure of the needle in which the domains A and B are repeated along the axis of the needle. It should be noted that almost similar morphologies and structures has been observed in the TiAl-N. Figure 21 shows the weak beam dark field image of dislocations in Ti51Al-0.3C aged at 1073 K for $3.6x10^4$ s (10 h) and deformed 3% at 673K indicating that the dislocations bypass the needle-shaped carbide during deformation.

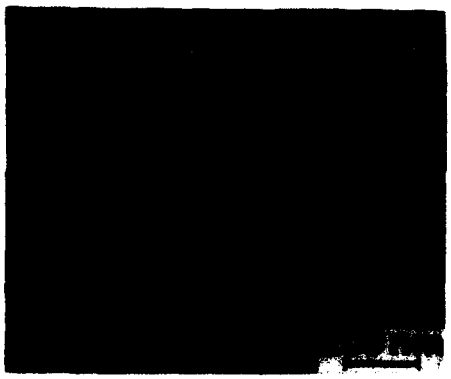

Figure 19 Transmission electron micrographs of TiAl-2N aged at 1073 K for 1.08×10^5 s.

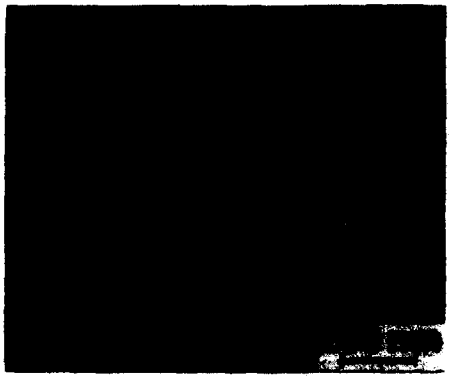

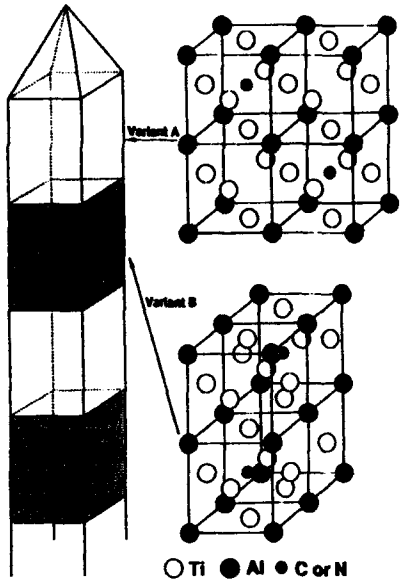

Figure 20 A schematic illustration of the repeated two variants of long range ordering in a needle precipitate.

Figure 21 (left) Dark field image of dislocations in Ti51Al-0.3C aged at 1073 K for 1.08×10^5 s and deformed about 3% at 673 K.

Summary

To satisfy the requirements to improve the room temperature ductility and the high temperature strength of intrmetallics, microstructural modifications in terms of phase decomposition should be important. The work on the $L1_2$-ordered Ni_3Al, B2-ordered NiAl and $L1_0$-ordered TiAl-based alloys has shown various possibilities of precipitation of fine particles in the ordered matrix. For example, fine precipitations of disordered γ and $M_{23}C_6$ carbide in Ni_3Al-based intermetallics, disordered α-Cr and β-Co in NiAl and a perovskite type carbide and nitride in TiAl-based intermetallics are obtained. Behavior of dislocations in these intermetallics differs appreciably. In Ni_3Al with a fine dispersion of disordered γ, superlattice dislocations dissociate in the matrix and they are strongly attracted to the disordered particles. In $Ni_3(Al,Cr)$ with $M_{23}C_6$ dispersoids dislocations bypass the carbide particles leaving loops sorrounding them. The strong attractive interaction might effectively contribute to increases the high temperature strength of intermetallics. Further work is required on the relation between multiphase structures and high temperature strength of intermetallics.

Acknowledgements

This research was supported by the Grant-in-Aid for Scientific Research from the Ministry of Education, Science and Culture, Japan, under project numbers (C) 03650580.

References

1. J.H.Schneibel and P.M.Hazzledine, Ordered Intermetallics-Physical Metallurgy and Mechanical Behaviour, ed. C.T.Liu, R.W.Cahn and G.Sauthoff, NATO ASI Series E, Vol.213, Kluwer Academic Publ., Dordrecht, (1992), 565-581.
2. T.Khan, P.Caron and S.Naka, High Temperature Aluminides and Intermetallics, ed. S.H.Whang et al.TMS, Warrendahle, 1990, 219-241.
3. R.S.Polvani, W.S.Tzeng and P.R.Strutt, Metall.Trans., 7A(1976), 33-40.
4. M.V.Nathal, Ordered Intermetallics-Physical Metallurgy and Mechanical Behaviour, ed. C.T.Liu, R.W.Cahn and G.Sauthoff, NATO ASI Series E, Vol.213, Kluwer Academic Publ., Dordrecht, (1992), 541-563.
5. R.Darolia et al., ibid., 679-678.
6. G.Sauthoff, Z.Metallkde., 77(1986), 655-666.
7. G.Sauthoff, Ordered Intermetallics-Physical Metallurgy and Mechanical Behaviour, ed. C.T.Liu, R.W.Cahn and G.Sauthoff, NATO ASI Series E, Vol.213, Kluwer Academic Publ., Dordrecht, (1992), 525-539.
8. S.Naka, M.Thomas and T.Khan, ibid., 645-662.
9. K.Aoki and O.Izumi,"On the Ductility of the Intermetallic Compound Ni_3Al", J.Japan Inst.Metals, 43(1979), 170-175.
10. S.Naka and T.Khan, Proc.Intern.Symp. on Intermetallic Compounds-Strength and Mechanical Properties, JIMIS-6, ed. O. Izumi, The Japan Inst. Metals, Sendai, (1991),16-171.
11. C.Carry et al., Metall.Trans., 10A (1979), 855-860.
12. R.D.Noebe, A.Misra and R.Gibala, ISIJ International, 31(1991), 1172-1185.
13. K.Ishida, R.Kainuma, N.Ueno and T.Nishizawa, Metall.Trans., 22A(1991), 441-446.
14. R.Yang, J.A.Leake and R.W.Cahn, Mater.Sci.Eng., A152(1992), 227-236.
15. A.J.Ardell and M.J.Hovan, Mater. Sci. Eng., 9(1972) 163-174.
16. P.B.Hirsch and A.Kelly, Philos.Mag., 12(1965) 881-900.
17. W.H.Tian, T.Sano and M.Nemoto, Scripta Metall., 20(1986), 933-936.
18. W.H.Tian, T.Sano and M.Nemoto, J.Japan Inst.Metals, 53(1989) 1013-1021, 1022-1028, 1029-1034.
19. W.H.Tian, T.Sano and M.Nemoto, J.Japan Inst.Metals, 54(1990), 276-284, 285-291.
20. M.Nemoto, W.H.Tian and T.Sano, J. de Physique., 1(1991), 1099-1117.
21. R.D.Field, R.Darolia and D.F.Lahrman, Scripta Metall., 23(1989), 1469-1474.
22. L.Jung and G.Sauthoff, Z.Metallkde, 80(1989), 484-489.
23. S.M.Allen and J.W.Cahn, Acta Metall., 24(1976), 425-437.
24. P.R.Swann, W.R.Duff and R.M.Fisher, Metall.Trans., 3(1972), 409-419.
25. T.F.Liu, S.C.Jeng and C.C.Wu, Metall.Trans., 23A(1992), 1395-1401.
26. T.Hong and A.J.Freeman, High Temperature Ordered Intermetallic Alloys III, ed. C.T.Liu, et al. Mater.Res.Soc.Symp.Proc.,Vol.133, Materials Research Society, Pittsburg, (1989), 75-80.
27. D.B.Miracle, S.Russell and C.C.Law, ibid. 225-230.
28. R.D.Field, D.F.Lahrman and R.Darolia, Acta metall.Mater., 39(1991), 2961-2969.
29. P.Rogl, Ternary Alloys, Vol.4, ed. G.Petzow and G.Effenberg, VCH, Weinheim, (1991), 400-415.
30. J.L.Walter, H.E.Cline and E.F.Kock, Trans.Met.Soc.AIME, 245(1969), 2073-2079.
31. H.E.Cline, J.L.Walter, E.F.Koch and L.M.Osika, Acta Met., 19(1971), 405-414.
32. R.T.Pascoe and C.W.A.Newey, Metal Sci. J., 2(1968), 138-143.
33. M.Hubert-Protopotescu and H.Hubert, Ternary Alloys, Vol.4, ed. G.Petzow and G.Effenberg, VCH, Weinheim, (1991), 234-244.
34. J.C.Schuster, H.Nowotny and C.Vaccaro, J.Solid State Chem., 32(1980), 213-219.

FRACTURE TOUGHNESS OF GAMMA BASE TITANIUM ALUMINIDES

TERNARY ADDITIONS AT ROOM AND ELEVATED TEMPERATURES

R. Gnanamoorthy, Y. Mutoh, N. Masahashi*, and M. Mizuhara*

Nagaoka University of Technology, Nagaoka, Japan.
*Nippon Steel Corporation, Kawasaki, Japan.

Abstract

Titanium aluminide base intermetallics posses excellent high temperature strength and low density. However, low room temperature ductility and toughness restrict the application of titanium aluminide base intermetallics for structural components. Effect of aluminium content and ternary addition on the fracture toughness of gamma base titanium aluminides were investigated at room and elevated temperatures. From the experimental results, it was found that microstructure has strong influence on the room and elevated temperature fracture toughness while ternary addition has no effect on the room temperature fracture toughness but affect at high temperatures. Fracture surface morphology depended on the microstructure and test temperature and had strong correlation with the fracture toughness.

Critical Issues in the Development of High Temperature Structural Materials
Edited by N.S. Stoloff, D.J. Duquette and A.F. Giamei
The Minerals, Metals & Materials Society, 1993

Introduction

Attractive high temperature properties and light weight of gamma base titanium aluminide intermetallic compounds make them most suitable for elevated temperature applications provided their low room temperature ductility and toughness are improved [1–6]. Aluminium concentration, microstructure, ternary additions, processing condition etc., have strong influence on the mechanical properties of titanium aluminides [1]. Alloys with composition ranging from 48 to 52 % Al[1] have appreciable plasticity [2]. The fracture toughness of gamma base titanium aluminide increases with increasing amount of lamellar colonies and binary Ti–48Al with lamellar microstructure exhibit maximum room temperature strength and fracture toughness [2,4]. However, fully transformed lamellar microstructure exhibits poor ductility compared to duplex microstructure. Duplex microstructure have good balance of mechanical properties compared to single phase microstructures [1,2]. Addition of ternary elements such as chromium, manganese, vanadium, and niobium affects the mechanical properties considerably. Ductility as high as 4% has been achieved due to addition of ternary elements [1]. Still, the maximum room temperature ductility and toughness achieved are below the acceptable limits for practical applications. Detailed knowledge about the fracture mechanisms and characteristics values of fracture toughness such as K_{Ic}, J_{Ic} etc., is necessary for designing alloys with improved fracture toughness. So for many investigations have been carried out for better understanding of the fracture mechanisms of binary titanium aluminides [7,8]. However, those of ternary titanium aluminides and the effect of ternary elements on the fracture toughness have not yet been studied in detail. Hence, the object of the present investigation, is to study the effect of microstructure and ternary addition on the room and elevated temperature fracture toughness and fracture behavior of gamma base titanium aluminides.

Materials and Experimental Procedure

Test Materials

Gamma base Ti–50Al, Ti–46Al, Ti–47Al–3Cr and Ti–47Al–3Nb were used for the current investigation. High purity ingots were prepared by plasma arc melting. The ingots were homogenized for 96 hours at 1050°C in vacuum (4 mPa). The nominal composition and microstructural details of the cast materials are shown in Table I. The heat treated Ti–50Al contained mostly γ phase with very little α_2 phase. A nearly lamellar (α_2/γ) microstructure was obtained after homogenization treatment of Ti–46Al. Heat treated Ti–47Al–3Cr contained both equiaxed γ grains and lamellar α_2/γ colonies. X–ray diffraction studies carried out on the samples indicated the presence of β–phase in addition to α_2 and γ phases. Detailed TEM investigations performed also confirmed the presence of third phase (β–bcc) in Ti–47Al–3Cr [9]. A fully transformed lamellar microstructure was obtained in the case of Ti–47Al–3Nb after homogenization treatment. Final microstructures of test materials are shown in Figure 1. Test specimens were made by multi–wire cutting and then machining to required dimensions and surface finish.

Experimental Procedure

[1] All compositions are mentioned in atomic percent.

Table I Composition and Microstructural Details of Test Materials

Material	Chemical Composition					Second Phase	Grain size
	Ti	Al	Cr/Nb	O	H		
	(in at. pct)			(in wt. ppm)			μm
Ti–50Al	49.1	50.9	–	170	5.0	α_2	200
Ti–46Al	55.3	44.7	–	120	1.6	α_2	500
Ti–47Al–3Cr	48.1	49.2	2.75	250	7.0	$\alpha_2+\beta$	60
Ti–47Al–3Nb	53.5	43.5	3.06	170	8.9	α_2	60

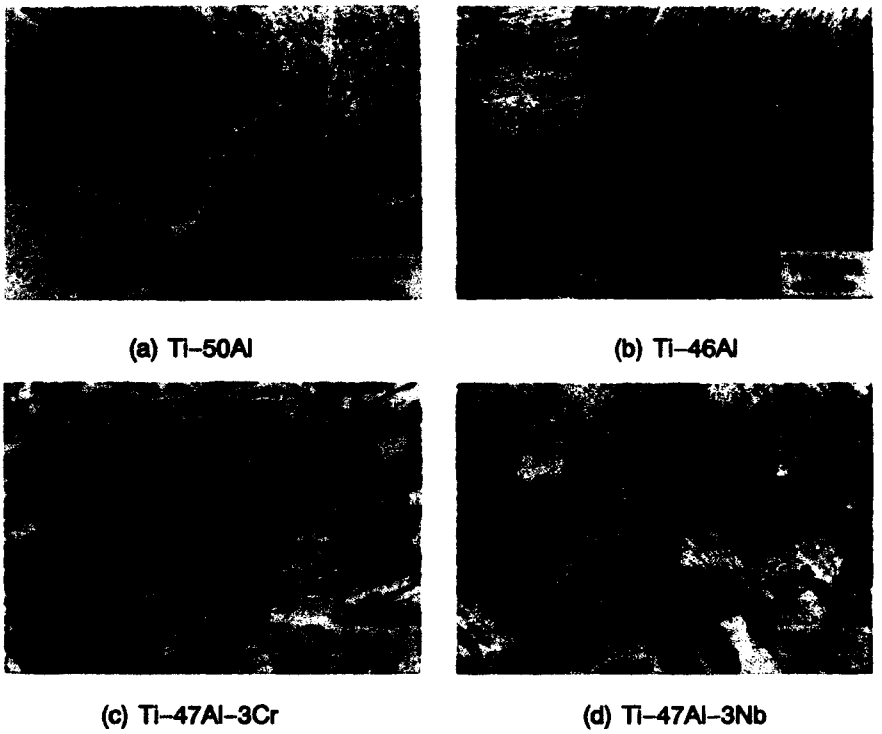

(a) Ti–50Al (b) Ti–46Al

(c) Ti–47Al–3Cr (d) Ti–47Al–3Nb

Figure 1 – Microstructures of Test Materials.

Fracture toughness tests using 20 mm thick CT specimens [10] were carried out for Ti–47Al–3Cr to estimate K_{Ic} fracture toughness value. Chevron notched CT specimens were fatigue precracked and fracture toughness values were estimated according to the ASTM test standard for evaluating K_{Ic}. At high temperatures, valid plane strain fracture toughness (K_{Ic}) values are impossible to estimate for the test materials because of the

non-linearity in the load-displacement curve due to large plastic deformation and stable crack growth. So, it is essential to estimate the fracture toughness using the elastic-plastic fracture parameter, J-Integral. A convenient J_{ic} test method using side-grooved single specimen [11] of dimensions 5x10x55 mm^3 was followed to estimate the fracture toughness at room and elevated temperatures. The introduction of side-groove makes the crack initiation point coincided to the maximum load point and enables to measure the crack initiation fracture toughness value [11]. A fatigue precrack was introduced up to a/W ratio of about 0.55 using a sinusoidal wave of 10 Hz and stress ratio of 0.1 from electro discharge machine notch. Precracked specimens were side-grooved using fine diamond cutter of 0.3 mm thickness to a depth of about 25% of the specimen thickness and then fracture toughness tests were performed. Specimens were soaked in test temperature for 15 min and in a vacuum of better than 4 mPa before testing. Fractographical studies were performed using SEM.

Results and Discussion

Room temperature fracture toughness (K_{ic}) estimated using sufficiently thick Ti-47Al-3Cr CT specimens yielded an average value of 34.8 $MPam^{0.5}$. The apparent fracture toughness (K_Q) values obtained using side-grooved bend specimens were almost equal to those obtained using CT specimens (Figure 2). Thus, this relatively simple technique using side-grooved single specimen for estimating a acceptable fracture toughness value, which can be considered to be the plane strain fracture toughness, is found satisfactory at room temperature. Estimated J_{ic} fracture toughness at room and elevated temperature are shown in Figure 3.

Fracture Toughness of Binary Gamma Base TiAl

In spite of similar heat treatment conditions, difference in aluminium content in gamma base titanium aluminides resulted in different microstructures (Figure 1(a) & (b)). At room temperature, the fracture toughness of Ti-46Al with lamellar microstructure was very high compared to the equiaxed Ti-50Al. This is consistent with the results of previous investigations [3,4]. Kampe et al [4] have reported decreasing fracture toughness with increasing volume fraction of equiaxed grains. The initiation fracture toughness values strongly depend on the microstructure in the crack-tip region. In the case of equiaxed material, this effect is negligible and have no influence on the fracture toughness values. But, in Ti-46Al, the alignment of hard α_2 laths to the crack plane in the crack-tip region decides the stress required to fracture and thus the fracture toughness values. When the crack plane is nearly perpendicular to the α_2/γ lath, toughening due to crack-tip blunting plays a significant role. When the crack plane is at an angle to the α_2/γ lath, the crack tip is not straight and the deflected crack tip increases the fracture toughness. In addition, a straight fatigue precrack was obtained in the case of Ti-50Al compared to Ti-46Al in spite of similar precracking conditions. A large number of interlocking and bridging between crack surfaces in the fatigue precrack region which induces the stress shielding effect, may also contribute to the fracture toughness of Ti-46Al.

Fracture surface morphology of the binary materials are shown in Figure 4. For the binary Ti-50Al, the room temperature fracture was totally transgranular cleavage with typical 'river-patterns' (Figure 4(a)) indicating very brittle nature of fracture associated with low fracture toughness. The fracture surface of Ti-46Al showed different fracture

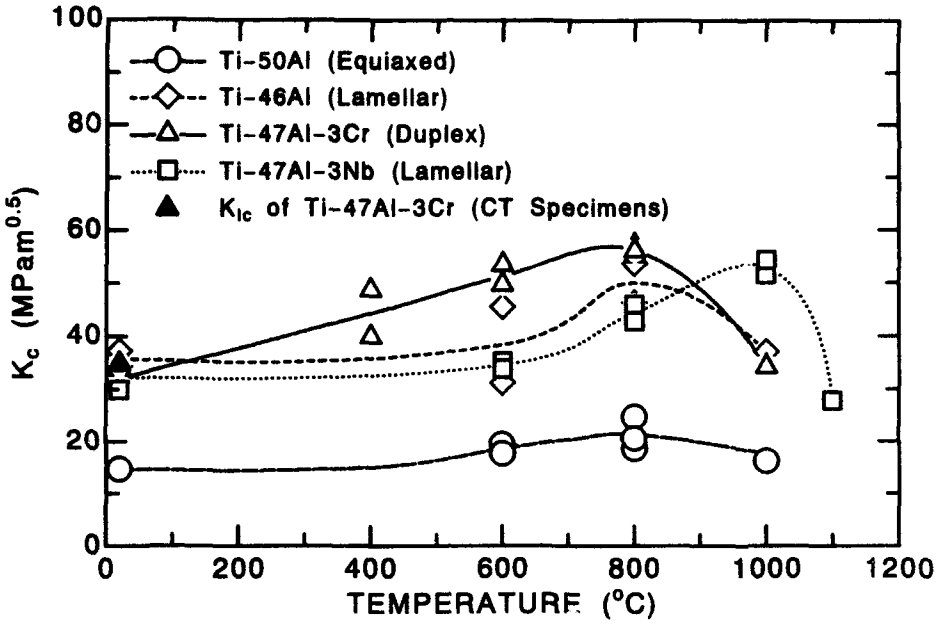

Figure 2 - Fracture Toughness (K_c) vs Temperature using Side-grooved Bend Specimens.

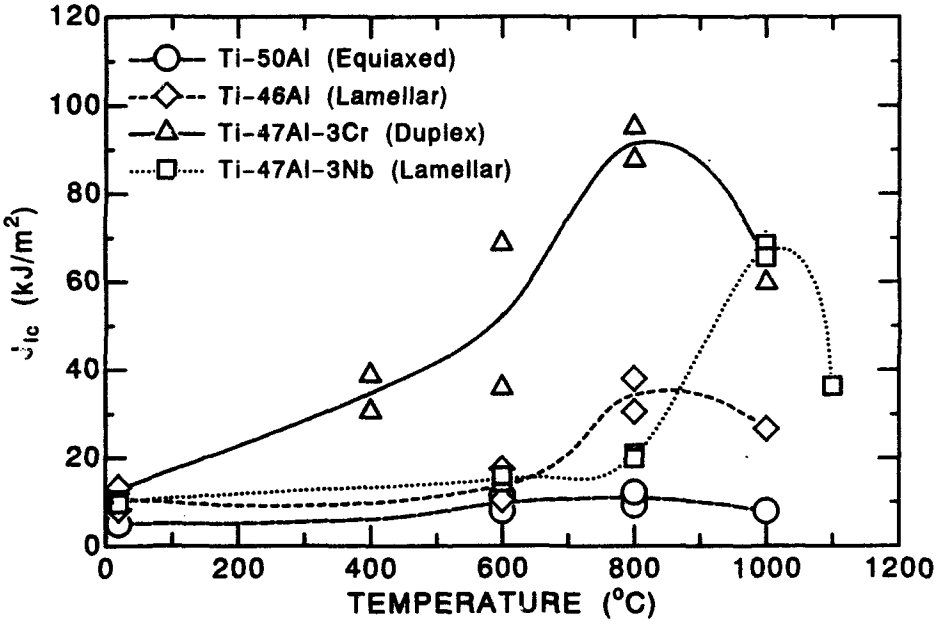

Figure 3 - Fracture Toughness (J_{Ic}) vs Temperature.

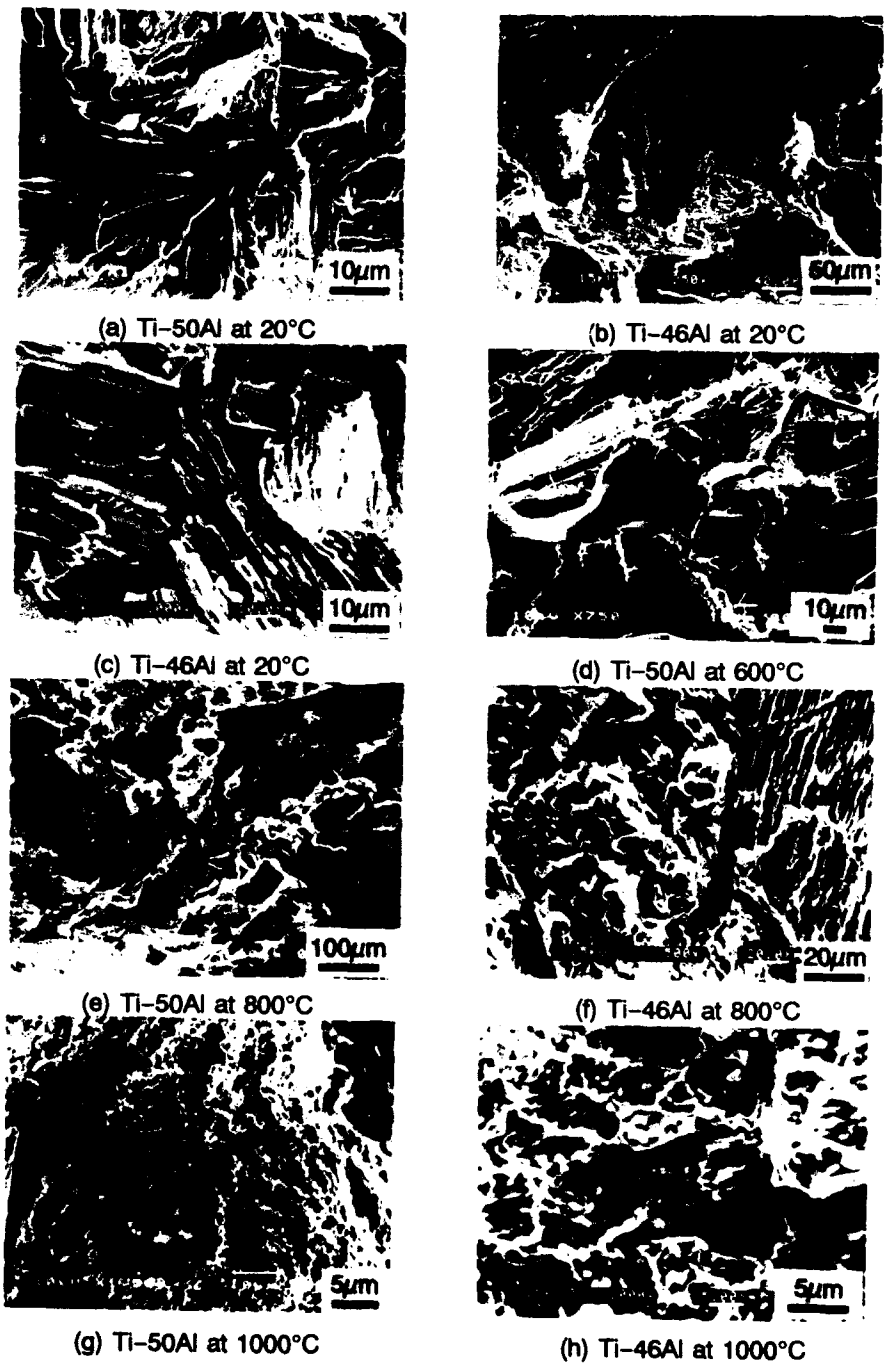

Figure 4 – Fractographs of binary γ–base titanium aluminides

morphology depending up on the orientation of the lamellar lath to the fracture plane.

intralamellar (along lamellar lath as shown in Figure 4(b)) and translamellar (across lamellar α_2/γ interphase as shown in Figure 4(c)) fracture were observed.

The fracture toughness of binary materials was more or less constant up to 600°C. Fracture surfaces of the Ti–50Al specimens tested at 600°C were also characterized by dominant transgranular cleavage mode of fracture. The slip–plane fracture with saw toothed zigzag planes were also observed (Figure 4(d)).

With further increase in temperature, fracture toughness increased up to a critical temperature and then decreased for both the binary materials. Lipsitt et al [8] have investigated the deformation substructure of TiAl up to 900°C and suggested that the mobility of dislocation controls the plasticity of TiAl. Dislocations are immobilized below 700°C by an unknown obstacle [8] and results in low fracture toughness below 700°C. Above this temperature, the increase in the mobility of dislocations increases ductility and fracture toughness. At intermediate temperatures (around 800°C), intergranular fracture dominates for both the binary aluminides (Figure 4(e) & (f)). In the case of Ti–50Al with mostly equiaxed γ grains, the grain boundaries are straight and offers less resistance to fracture. But, in the case of Ti–46Al with lamellar microstructure, the grain boundary is serrated and this increases resistance to fracture. In addition, interstitial oxygen content in Ti–46Al was low compared to Ti–50Al (Table I) and this generally increases the grain boundary cohesion. This high grain boundary cohesive strength of Ti–46Al results in higher fracture toughness compared to Ti–50Al at 800°C. The maximum fracture toughness was obtained at the same temperature about 800°C for the binary materials. Ductile dimple fracture was dominant at 1000°C in both the binary materials (Figure 4(g) & (h)). Recrystallization may be the one reason for the softening at 1000°C and causes decrease in strength and toughness of the material.

Effects of Chromium Addition

The room temperature fracture toughness of Ti–47Al–3Cr was very high compared to the binary Ti–50Al. Presence of hard lamellar colonies in Ti–47Al–3Cr increases the fracture toughness. The fracture toughness of chromium alloyed material is more or less equal to that of lamellar Ti–46Al at room temperature and the fractographs revealed dominant transgranular cleavage type of fracture as shown in Figure 5 (a). The high room temperature fracture toughness can be attributed to increased slip and twinning activity due to the addition of chromium, niobium and vanadium to gamma base titanium aluminides [1]. Addition of chromium also strengthens and stabilizes the α_2 phase [12] and permits easy mobility of dislocations. This increase in mobility of dislocations contributes for the improvement in toughness. In addition, small amounts of ductile β phase contained in Ti–47Al–3Cr also contribute for increasing fracture toughness.

With increasing temperature the fracture toughness increased dramatically compared to other materials investigated and the maximum fracture toughness was obtained at about 800°C. Grain boundary separation was dominant mode of fracture in the specimens fractured at 600°C, which indicates that the addition of chromium increases the tendency of intergranular fracture in the material investigated. But in the case of bend specimens [10], cavities or dimples were also observed on the fracture surfaces. Generally, it is considered as cavities are nucleated from the second phase material or point defects, either vacant lattice sites or interstitial atoms at higher temperatures. From the shape and size of cavities, it is clear that the cavities might

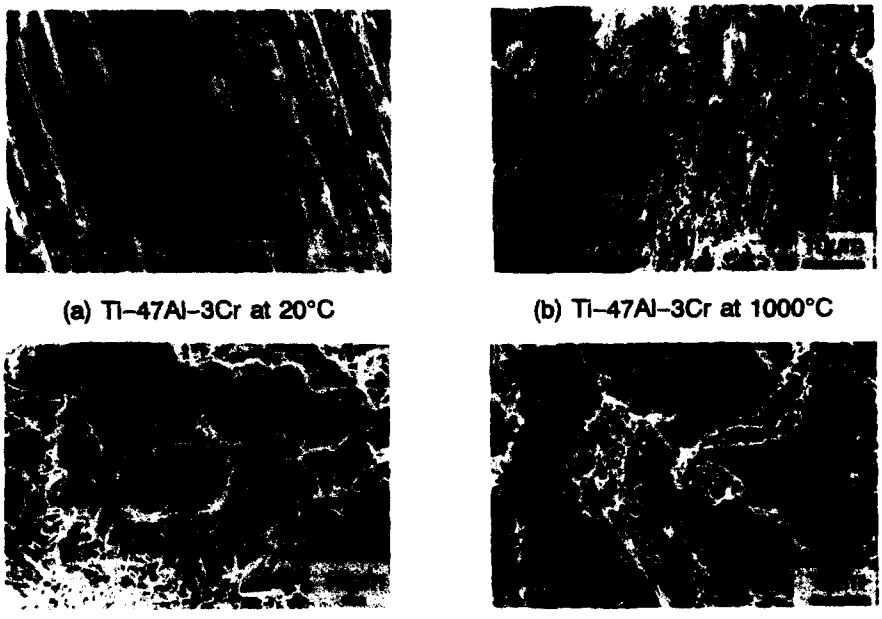

(a) Ti–47Al–3Cr at 20°C

(b) Ti–47Al–3Cr at 1000°C

(c) Ti–47Al–3Nb at 600°C

(d) Ti–47Al–3Nb at 1000°C

Figure 5 – Fractographs of ternary γ–base titanium aluminides.

have been formed due to the intergranular fracture of β grains from the base material. The increase in the amount of second phase and impurities in Ti–47Al–3Cr might have accelerated the cavity nucleation process. The plasticity of the β phase [9] also contributes to the increased fracture toughness. This type of fracture feature was not observed in the other materials investigated. With further increase in temperature, the concentration of cavities considerably increased and at 1000°C the specimen exhibited entirely ductile dimple like fracture (Figure 5(b)). No effect of chromium addition on the transition temperature, which coincided with those in Ti–50Al and Ti–46Al was found.

Effects of Niobium Addition

In spite of similar processing conditions, the final microstructure resulted after homogenization treatment for the niobium alloyed material was fully lamellar compared to the equiaxed microstructure for the Ti–50Al and the duplex microstructure for the Ti–47Al–3Cr. An increased amount of α_2 phase was obtained in Ti–47Al–3Nb compared to Ti–47Al–3Cr. The presence of hard α_2 laths results in increased fracture toughness compared to binary Ti–50Al. The fracture toughness of Ti–47Al–3Nb was more or less equal to that of Ti–46Al which also has the similar lamellar microstructure but with coarse grains. Increased slip activity due to addition of niobium might have resulted in high fracture toughness for Ti–47Al–3Nb [1,6]. The room temperature fracture surface of Ti–47Al–3Nb was characterized by transgranular cleavage type of fracture similar to Ti–46Al.

The fracture toughness of Ti–47Al–3Nb was more or less constant up to 600°C similar to the binary materials. Increased grain boundary fracture was observed in the niobium alloyed material at low temperatures (Figure 5(c)). The fracture surface of the material tested below 800°C, revealed mixed transgranular cleavage and intergranular fracture mode. The fracture toughness of Ti–47Al–3Nb increased dramatically above 800°C. The fracture toughness was maximum at 1000°C and thereafter decreased. Sobeyojo et al [6] have reported the increased dislocation density in niobium alloyed material compared to the binary material. Increased slip activity above 800°C increases ductility and fracture toughness of the niobium alloyed material. In addition, curvature of lamellae was observed by Sobeyojo et al [6] in the niobium alloyed material above 982°C. The extensive bowing of lamellae was attributed to the sliding between lamellae interfaces [6]. Fine lamellae thickness (lath thickness≈0.2 μm) also enhance the lamellae bowing in the niobium alloyed materials. This causes high fracture toughness in niobium alloyed material above 800°C and increases the brittle–ductile transition temperature. The fracture surface of fracture toughness specimens tested at 1000°C revealed ductile tearing as the dominant mode of fracture (Figure 5(d)).

Conclusions

Fracture toughness experiments were carried out at different temperatures for binary and ternary gamma base titanium aluminides. Based on the above investigations following conclusions were obtained.

1) The room temperature fracture was entirely transgranular cleavage for the binary material and increased α_2 phase resulted in a 'lamellar–type' fracture mode. The fracture mode changed from dominant low temperature transgranular cleavage to intergranular fracture at intermediate temperatures. At high temperatures, ductile tearing was observed in the materials investigated.

2) Fracture toughness of gamma base titanium aluminides strongly depend on the microstructure and composition. Materials with lamellar microstructure possessed high room temperature fracture toughness.

3) The fracture toughness of three phase ($\gamma+\alpha_2+\beta$) Ti–47Al–3Cr material was high compared to two phase ($\gamma+\alpha_2$) titanium aluminides and fracture toughness increased drastically at lower temperatures compared to other materials investigated.

4) Niobium addition has no effect on low temperature fracture toughness of the gamma base titanium aluminides but increases the fracture toughness above 800°C.

5) With increasing temperature, the fracture toughness increased up to a critical temperature depending up on the composition and then decreased. The brittle–ductile transition temperature was affected due to addition of niobium, while chromium addition had no influence on the brittle–ductile transition temperature.

Acknowledgment

Support for one of the authors (RG) from the Ministry of Education, Science and culture, Japan is gratefully acknowledged.

References

1. Y. W. Kim, "Intermetallic Alloys Based on Gamma Titanium Aluminide" JOM, 41 (7) (1989), 24–30.

2. S. C. Huang and E. L. Hall, "Plastic Deformation and Fracture of Binary TiAl-Base Alloys," Metall. Trans. 22A (2) (1991), 427-439.

3. W. O. Soboyejo et al., "Microstructure and the Fracture Behavior of a Gamma Alloy," Microstructure/Property Relationships in Titanium Aluminides and Alloys, eds. Y. W. Kim and R. R. Boyer, (The Minerals, Metals and Materials Society, 1991), 197-211.

4. S. L. Kampe et al., "Microstructure Morphology Effects on Fracture Toughness of a Near-Gamma Titanium Aluminide Alloy", Microstructure/Property Relationships in Titanium Aluminides and Alloys, eds. Y. W. Kim and R. R. Boyer, (The Minerals, Metals and Materials Society, 1991), 313-322.

5. S. C. Huang and E. L. Hall, "The Effects of Cr Addition to Binary TiAl-Base Alloys," Metall. Trans., 22A (11) (1991), 2619-2627.

6. W. O. Soboyejo, D. S. Schwartz, and S. M. L. Sastry, "An Investigation of the Fracture Behavior of γ Based Titanium Aluminides; Effects of Annealing in the $\alpha+\gamma$ and $\alpha_2+\gamma$ Phase Fields", Metall. Trans., 23A (10) (1992), 2039-2059.

7. S. A. Court, V. K. Vasudevan, and H. L. Fraser, "Deformation Mechanisms in the Intermetallic Compound TiAl", Phil. Mag. A., 61 (1) (1990), 141-158.

8. H. A. Lipsitt, D. Shechtman, and R. E. Schafrik, "The Deformation and Fracture of TiAl at Elevated Temperatures", Metall. Trans., 6A (11) (1975), 1991-1996.

9. N. Masahashi et al., "Ternary Alloying of Gamma Titanium Aluminides for Hot-Workability", Proceedings of Material Research Society Symposium, (Material Research Society, 213 (1991)), 795-800.

10. R. Gnanamoorthy et al., "High Temperature Strength and Fracture Toughness in Gamma Phase Titanium Aluminides", Submitted for publication to J. Mat. Sci.,

11. Y. Mutoh, "A Simple J_{Ic} Test Method Using a Side-grooved Charpy Size Specimen", Role of Fracture Mechanics in Modern Technology, eds. G. C. Sih, H. Nisitani, and T. Ishihara, (Elsevier Science Publ, North Holland, 1987), 503-513.

12. W. Wunderlich, T. Kremser, and G. Frommeyer, "Enhanced Plasticity by Deformation Twinning of TiAl Base Alloys with Cr and Si", Z. Metallkd., 81 (1990), 802-808.

DUCTILITY OF Ni_3Al DOPED WITH SUBSTITUTIONAL ELEMENTS

S.Hanada, A.Chiba, H.Z.Guo and S.Watanabe

Institute for Materials Research
Tohoku University, Sendai 980, Japan

Abstract

This paper reports on ductility of B-free Ni_3Al alloys. Recrystallized Ni_3Al binary alloys with Ni-rich compositions show appreciable ductility when an environmental effect is eliminated, while the alloys with stoichiometric and Al-rich compositions remain brittle. The ductility in the Ni-rich Ni_3Al alloys is associated with low ordering energy.

The additions of ternary elements, which are classified as γ formers, ductilize ternary Ni_3Al alloys(Ni-23 at%Al-2 at%X, X=Pd, Pt, Cu and Co), whereas the additions of γ' formers embrittle ternary Ni_3Al alloys(Ni-23 at%Al-2 at%X, X=Ta, Mo, Nb, Zr, Hf, V, Ti and Si). The additions of small amounts (less than 1 at%) of γ' formers such as Zr and Hf also ductilize as-cast ternary Ni_3Al alloys. Ductility of Ni_3Al alloys doped with substitutional elements is discussed in terms of ordering energy and microstructure.

Critical Issues in the Development of High Temperature Structural Materials
Edited by N.S. Stoloff, D.J. Duquette and A.F. Giamei
The Minerals, Metals & Materials Society, 1993

Introduction

It has been found that Ni_3Al alloys are ductilized both by microalloying with B[1] and by macroalloying with Pd, Pt, Cu and Co [2-4]. Extensive studies have revealed that the ductilization by microalloying is interpreted in terms of high cohesive strength at grain boundaries caused by B segregation, while the ductilization by macroalloying is associated with lowering ordering energy. Aoki and Izumi reported that Ni_3Al alloys are ductilized not only by the addition of B but also by the addition of a substitutional element such as Zr [5,6]. Guo et al.[7] and George et al.[8] also found ductilization of Ni_3Al alloys by Zr additions. The addition of Zr to Ni_3Al has been revealed experimentally and theoretically to raise ordering energy. Therefore, the ductilization by Zr addition can not be explained in terms of ordering energy.

It is widely known that ductile nickel-base superalloys contain the minor elements such as B, C, Zr and Hf [9]. The additions of these elements to nickel-base superalloys are generally believed to increase grain boundary strength and cohesion and eventually to suppress intergranular fracture, although the underlying mechanisms are not well understood. Among these minor elements, it has been confirmed that B additions are effective in ductilizing Ni_3Al alloys[1,10], while C additions have little effect [11]. However, ductilization of Zr- and Hf-doped Ni_3Al ternary alloys has not been systematically studied.

This paper aims to describe the relation between ductility of Ni_3Al alloys and ordering energy and to demonstrate the effect of Zr and Hf additions on ductility of Ni_3Al alloys in comparison with nickel-base superalloys for the better understanding of Zr and Hf behavior in the alloys.

Effect of Ordering Energy on Ductility of Ni_3Al Alloys

It has been found that ductility of binary Ni_3Al alloys in the composition range from 23 to 26 at%Al increases with decreasing Al concentration, using recrystallized samples with an average grain size of approximately 100 μm which were prepared by repeated cold forging and annealing [12]. A single phase of Ni_3Al was found in this composition range by optical and transmission electron microscopy in agreement with the result on the phase diagram of the Ni-Al system [13]. Tensile tests performed at 290 K in a vacuum of 10^{-2} Pa revealed that ductility indicates a pronounced alloy stoichiometry effect. However, recent studies on environmental embrittlement have shown that the vacuum of 10^{-5} Pa is insufficient for suppression of the embrittlement [14], suggesting that tensile properties without environmental embrittlement should be examined in a vacuum of at least less than 10^{-6} Pa. Otherwise it may be a convenient way to measure ductility of Ni_3Al alloys in liquid nitrogen, since water in air is frozen at 77 K and the chemical reaction between Al and H_2O, which is considered to cause the environmental embrittlement, is suppressed. The result is shown in Fig.1, where ductility at 290 K in a vacuum of 10^{-2} Pa [12] is also included. It is evident that elongation is much larger at 77 K than at 290 K in the composition range tested. This suggests that the elongation at 290 K is affected by moisture-induced environmental embrittlement. It should be noted in Fig.1 that ductility increases with decreasing Al concentration. Recently, Liu [15] have reported that binary Ni_3Al alloys containing 24 and 23.5 at%Al show tensile ductility of 7.2 and 8.2% at room temperature in dry oxygen. These results indicate that tensile ductility in binary Ni_3Al alloys depends on the composition.

Cahn et al. [16] have shown from the experiments of thermal dilatometry and high temperature X-ray diffractometry that the order-disorder transition temperature for binary Ni_3Al alloys decreases with decreasing Al concentration. On the basis of the cluster variation method Enomoto and Harada [17] have also reported the similar tendency to Cahn et al. Chiba et al. [18] have more recently observed the domain structures of melt spun binary Ni_3Al ribbons. No apparent anti-phase domain (APD) was observed in Ni-26 and 25 at%Al, while APDs were

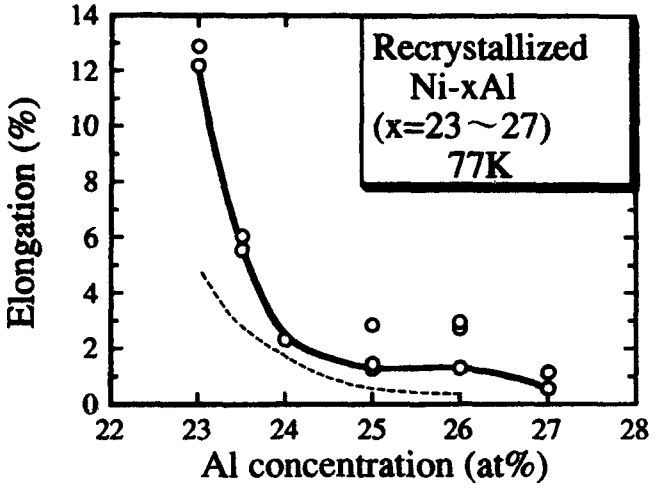

Fig.1 Ductility of recrystallized Ni_3Al binary alloys at 77 K as a function of Al concentration.The dotted line indicates ductility at 290 K in a vacuum of 10^{-2} Pa.

distinctly seen in Ni-rich Ni_3Al alloys. The domain size was found to become fine with increasing Ni concentration. These observations imply that ductilization of B-free Ni-rich Ni_3Al alloys is attributed to lowering ordering energy.

Ackland and Vitek [19] have calculated the atomic structures of grain boundaries in $L1_2$ ordered alloys. They found that grain boundaries in strongly ordered alloys show very little relaxation, resulting in the presence of columns of cavities in the boundaries, whereas grain boundaries in weakly ordered alloys show extensive relaxation, leading to much more homogeneous structures. This implies that a Ni-rich Ni_3Al alloy with low ordering energy is ductilized because of high cohesive strength at grain boundaries. Besides the structural change in grain boundaries, dislocation reactions at grain boundaries are facilitated by lowering ordering energy. Consequently, a great number of dislocation reactions become available. This leads to the relaxation of stress concentration at grain boundaries produced by piling-up of dislocations and to ductility improvement. King and Yoo [20] have calculated numbers of allowed dislocation reactions between glide dislocations and grain boundary dislocations in ordered alloys. They revealed that the number of available reactions is always larger at grain boundaries of disordered alloys than at grain boundaries of ordered alloys. Thus, a Ni_3Al alloy with low ordering energy is ductilized because of the ease of dislocation reactions at grain boundaries

It is suggested from the results described above that a ternary Ni_3Al alloy is ductilized if the addition of a ternary element lowers the ordering energy. The change of ordering energy due to the addition of a ternary element has been discussed on the basis of thermodynamic calculation [21], cluster variation method [17], experimental and thermodynamic investigation [13] and microstructural observation of APDs [22]. These results are consistent with each other. One of the results, obtained by Jia [13], is shown in Fig.2(a), where the interaction parameter between Ni and a ternary element X, V_{NiX}, is plotted against V_{AlX}, the interaction parameter between Al and X. He concluded that ternary elements added to Ni_3Al alloys are classified as γ formers and γ' formers. Furthermore, he showed that when an alloying element X tends to substitute for the Al site in Ni_3Al, the addition of X stabilizes the γ' phase(γ' former), whereas when X tends to substitute for the Ni site, the γ phase is stabilized by

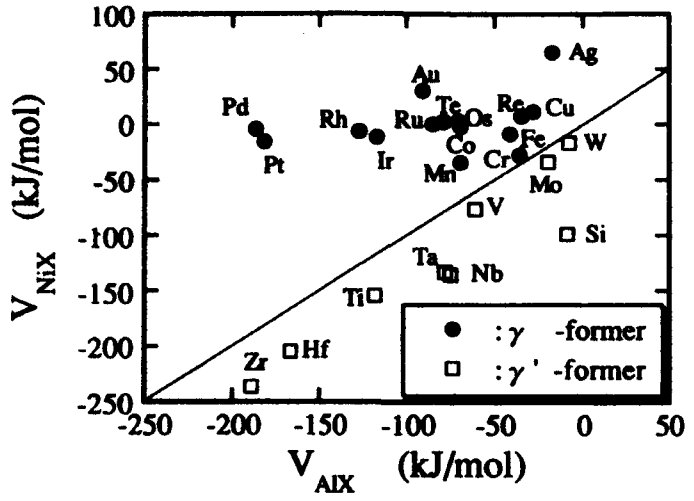

Fig.2(a) Relation between the interaction parameters V_{NiX} and V_{AlX} [13].

the addition of X (γ former). Therefore, it is suggested that the stronger the tendency for a ternary element to substitute for the Ni site, the more the ordering energy of Ni_3Al decreases. As shown in Fig.2(a), Pd is situated farthest above the divided line. This means that Pd has the strongest tendency to substitute for the Ni site. Recent results on ALCHEMI have confirmed this preferential substitution [23] .

Several elements in Fig.2(a) were added to Ni_3Al in compositions of Ni-23 at%Al-2 at%X(X=Pt, Pd, Cu, Co, Cr, Fe, Mn, Ta, Mo, Nb, Zr, Hf, V, Ti and Si) and arc-melted alloys were tensile tested at room temperature in a vacuum of 10^{-2} Pa. Results are summarized in Fig.2(b). Ductilization and embrittlement caused by the ternary additions are estimated by

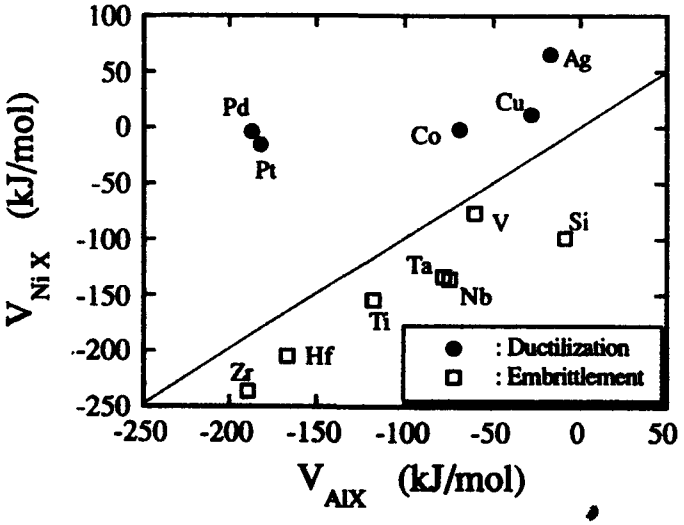

Fig.2(b) Effect of ternary additions on ductility.

comparing ductility in ternary alloys with ductility in the binary Ni-23 at%Al alloy. It is obvious that Ni_3Al is ductilized by the addition of γ formers, whereas the embrittlement appears by the addition of γ' formers. No significant change in ductility was observed in the ternary alloys doped with Cr, Fe and Mn which are located near the divided line, although they are classified as γ -formers. To rule out a possibility that the ductility improvement by ternary additions is not intrinsic but it results from suppression of environmental embrittlement, ductility of Pd-doped Ni_3Al was investigated in different environments. Fig.3 shows stress-strain curves for recrystallized Ni-23 at%Al-2 at%Pd with an average grain size of about 50 μ m. The alloy exhibits evidently environmental embrittlement. It should be noted, however, that 18% elongation in oxygen is larger than 13% elongation of recrystallized Ni-23 at%Al in oxygen. Also, ductility was higher in as-cast Ni-23 at%Al-2 at%Pd than in as-cast Ni-23 at%Al. Thus, it is concluded that ductility in Ni_3Al alloys is related to ordering energy.

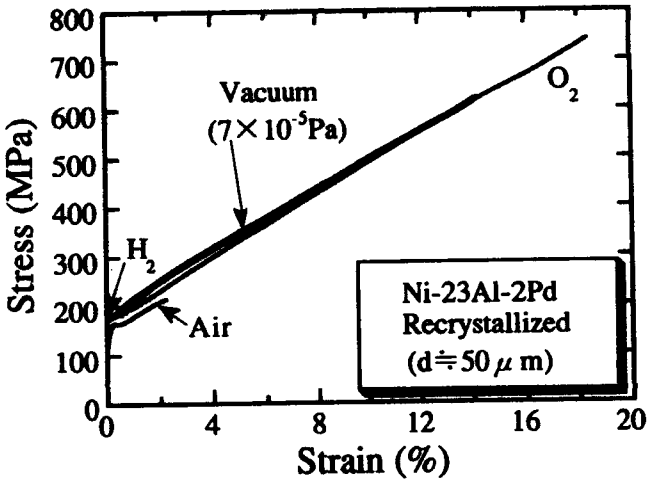

Fig.3 Stress-strain curves for recrystallized Ni-23 at%Al-2 at%Pd in different environments.

Ductility of Zr- and Hf-doped Ni_3Al Alloys

Fig.4 shows composition dependence of elongation and yield stress of as-cast Ni-23 at%Al alloys doped with Zr at room temperature in dry oxygen. Elongation increases remarkably with increasing Zr concentration and exhibits a peak of approximately 30% at 0.4 at%Zr, although yield stress increases gradually. Elongation of as-cast Ni_3Al alloys doped with 0.4 at%Zr is plotted in Fig.5 as a function of Al concentration. One can see a pronounced alloy stoichiometry effect. Very little ductility, which is equivalent to that of binary Ni_3Al alloys, is obtained at 24~26 at%Al. With further decreasing Al concentration elongation increases rapidly and reaches 35% elongation at 22 at%Al in contrast to binary Ni-23 at%Al which showed 5% elongation at 23 at%Al.

Recrystallized Zr-doped Ni_3Al alloys with an average grain size of about 100 μ m were prepared by repeated cold forging and annealing. Yield stress and elongation are plotted in Fig.6 as a function of Zr concentration. It is evident that ductility of Zr-doped Ni_3Al alloys is slightly less than the binary alloy and decreases with increasing Zr concentration. Surprisingly, elongation is larger in the as-cast Zr-doped alloys (Fig.4) than in the recrystallized alloys at compositions higher than 0.2 at%Zr. Low ductility of the atter might be explained by the

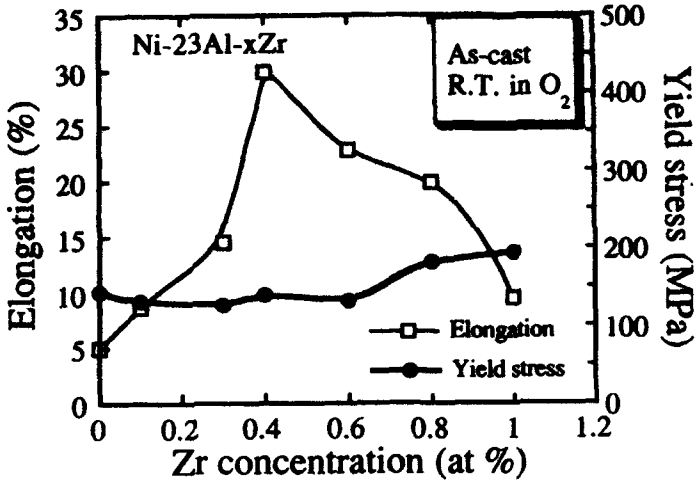

Fig.4 Ductility and yield stress of as-cast Ni-23 at%Al alloys doped with Zr at room temperature in dry oxygen as a function of Zr concentration.

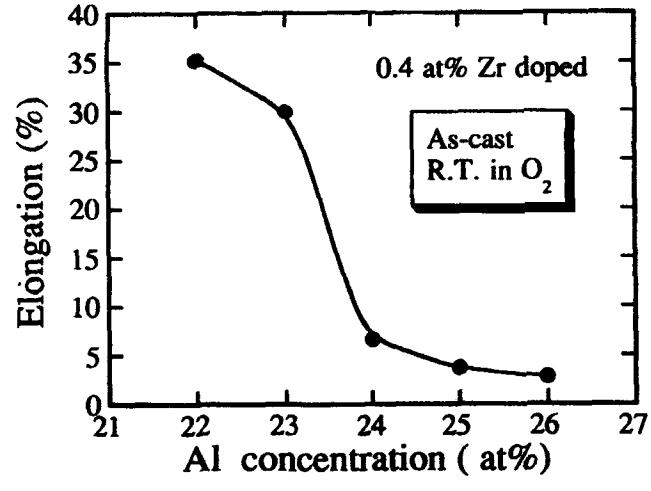

Fig.5 Ductility of as-cast Ni_3Al alloys doped with 0.4 at%Zr at room temperature in dry oxygen as function of Al concentration.

introduction of microcracks during cold forging which is associated with initiation of failure in tensile tests. However, since the decrease in ductility of the latter is gradual with Zr concentration in contrast to the rapid increase and subsequent decrease in ductility of the former, less ductility of the recrystallized alloys is considered to be intrinsic. In the preceding section it was illustrated that the ductility of the ternary Ni_3Al alloys can be interpreted in terms of ordering energy. Zr is classified as a γ'-former whose addition to Ni_3Al raises ordering energy and

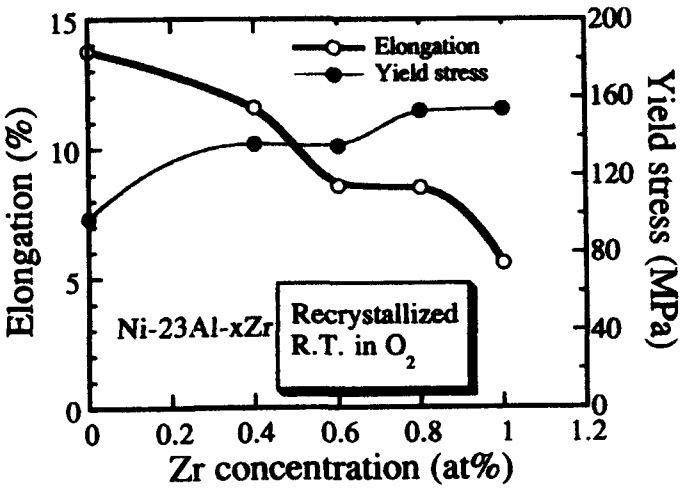

Fig.6 Ductility and yield stress of recrystallized Ni-23 at%Al alloys doped with Zr at room temperature in dry oxygen as a function of Zr concentration.

embrittles the alloys. Therefore, the decrease in ductility of the recrystallized Zr-doped Ni_3Al alloys with increasing Zr concentration is consistent with the explanation based on the ordering energy.

Fig.7 shows the SEM fractograph of the as-cast Ni-23 at%Al-0.4 at%Zr, consisting predominantly of very irregular intergranular facets and of few transgranular surfaces. Auger

Fig.7 SEM fractograph of as-cast Ni-23 at%Al 0.4 at%Zr.

electron spectroscopy from the intergranular fracture indicated Zr segregation at grain boundaries. There was no evidence of impurity segregation. Thus, the ductility improvement of the as-cast Zr-doped Ni_3Al alloys may be attributed to Zr segregation and/or grain boundary morphology.

To check this, the cast alloys were annealed at 1373 K for 24 h. According to Auger analyses flat grain boundaries without Zr segregation were produced and ductility of the 0.4 at%Zr-doped alloy became to be equivalent to that of the as-cast binary alloy. It is now recognized that a Zr addition ductilizes Ni and Ni-base superalloys by inhibiting segregation of impurities such as S to grain boundaries through sulfide formation. Using Auger analysis, Liu et al. [10] have detected slight concentrations of S on grain boundaries of Ni-24 at%Al. Therefore, the ductilization of the as-cast Zr-doped Ni_3Al alloys may be explained partly by supression of S segregation to grain boundaries. The effect of Zr segregation in the as-cast Ni_3Al alloys on ductility is not clear at present.

Lozinskiy et al. have systematically investigated the concentration dependence of the ductility in S- and Zr-doped Ni and found the ductility improvement by Zr additions [24]. Doherty et al. [25] have studied ductility improvement of a superalloy by small additions of minor elements, and they found that Hf has the same effect as Zr. That is, the ductility against Zr and Hf concentrations shows a pronounced peak. They explained that the occurrence of the peak in the ductility against dopant concentration is due to a combination of ductility improvement caused by the suppression of S segregation to grain boundaries and the embrittlement from the formation of intermetallic phases, e.g. Ni_5Hf, Ni_5Zr, etc. at grain boundaries. Referring to their results, the effect of small additions of Hf to Ni_3Al alloys was investigated as a function of Hf concentration. The results are plotted in Figs. 8 and 9 for as-cast and recrystallized Ni_3Al

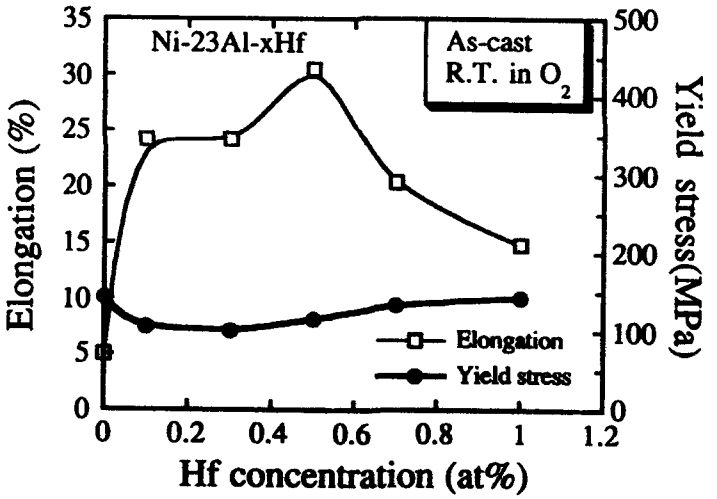

Fig.8 Ductility an dyield stress of as-cast Ni-23 at%Al alloys doped with Hf at room temperature in dry oxygen as a function of Hf concentration.

alloys. It is apparent from the comparison with Figs.4 and 6 that the concentration dependence of ductility in the Hf-doped Ni_3Al alloys is very similar to that in the Zr-doped ones. Zr and Hf are reported to dissolve substitutionally in Ni_3Al. The solubility limit at 1273K is in excess of at least 1 at%. This means that no intermetallic phase forms by the additions of Zr and Hf in concentrations up to 1 at% of this work. Therefore, embrittlement of Zr- and Hf-doped Ni_3Al alloys is attributable to high ordering energy. Thus, it is suggested that various factors are concerned with the ductility of as-cast Zr- and Hf-doped Ni_3Al alloys; i) elimination of S segregation at grain boundaries and ii) morphology change in grain boundary , which result in

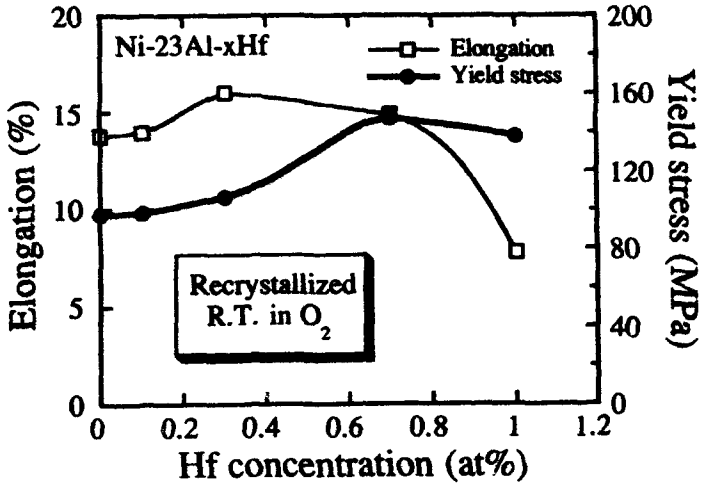

Fig.9 Ductility and yield stress of recrystallized Ni-23 at%Al alloys doped with Hf at room temperature in dry oxygen as a function of Hf concentration.

ductility improvement, iii) increase in ordering energy, which leads to embrittlement. On the other hand Hf additions to Ni-base superalloys are believed to increase cohesive strength at grain boundaries [25]. More detailed studies on chemistry, structure and morphology of grain boundaries are now in progress.

Summary

Ductility of binary and ternary Ni_3Al alloys was investigated under conditions where environmental embrittlement is eliminated. The obtained results are summarized as follows.

(1) Ductility of B-undoped Ni_3Al binary alloys exhibits a marked alloy stoichiometry effect, that is, ductility increases with decreasing Al concentration.

(2) 2 at% additions of γ formers such as Pd, Pt, Cu and Co to Ni-23 at%Al ductilize the ternary alloys, whereas 2 at% additions of γ' such as Ta, Mo, Nb, Zr, Hf, V, Ti and Si embrittle the alloys. No significant change in ductility appears by the additions of weak γ formers such as Fe, Mn and Cr.

(3) Ductility of binary and ternary Ni_3Al alloys is interpreted in terms of ordering energy.

(4) Zr and Hf additions less than 1 at% ductilize as-cast Ni_3Al alloys probably by roughening grain boundaries and suppressing S segregation to grain boundaries. The ductilization disappears after recrystallization.

Acknowledgment

This work is supported in part by Grant-in-Aid for Scientific Research on Priority Area from the Ministry of Education, Science and Culture, Japan.

References

1. K.Aoki and O.Izumi, Nippon Kinzoku Gakkaishi, 43(12) (1979), 1190-1196.
2. A.Chiba, S.Hanada, and S.Watanabe, Mater. Trans., JIM, 31(9) (1990), 824-827.
3. A.Chiba, S.Hanada, and S.Watanabe, Scripta metall. mater., 25(2) (1991), 303-307.

4. A.Chiba, S.Hanada, and S.Watanabe, Acta metall.mater., 39(8) (1991), 1799-1805.
5. K.Aoki and O.Izumi, Nikkei Mechanical, 7.21(1980), 52-57.
6. K.Aoki, Mater.Trans., JIM, 31(6) (1990), 443-448.
7. J.T.Guo et al., to be published. Proc. 1st Pacific RIM Inter.Conf. on Advanced Materials and Processing, (1992).
8. E.P.George, C.T.Liu and D.P.Pope, Scripta metall. mater., 27(3) (1992), 365-370.
9. D.M.Shah and D.N. Duhl, Superalloys 1988 (Warrendale, PA: The Metallurgical Society, (1988), 693-702.
10. C.T.Liu, C.L.White, and J.A.Horton, Acta metall.mater., 33(2) (1985), 213-229.
11. M.Masahashi, T.Takasugi, and O.Izumi, Acta metall., 36(7) (1988) 1823-1836.
12. A.Chiba, S.Hanada, and S.Watanabe, Mater.Trans., JIM, 33(5) (1992), 503-508.
13. C.-C.Jia, (Ph.D.thesis, Tohoku University, 1990), 11-27.
14. N.Nakayama, (Master thesis, Tohoku University, 1993).
15. C.T.Liu, Scripta metall. mater., 27(1) (1992), 25-28.
16. R.W.Cahn et al., Acta metall., 35(11) (1987), 2737-2751.
17. M.Enomoto and H.Harada, Metall. Trans., 20A(4) (1989), 649-664.
18. A.Chiba, S.Hanada, S.Watanabe, Nippon Kinzoku Gakkaiho, 30(1)(1991), 12-18.
19. G.J.Ackland and V.Vitek, High-Temperature Ordered Intermetallic Alloys III (Pittsburgh, PA: Materials Research Society, 1989), 105-111.
20. A.H.King and M.H.Yoo, Scripta Metall., 21(8) (1987), 1115-1119.
21. S.Ochiai, Y.Oya, and T.Suzuki, Acta metall., 32(2) (1984), 289-298.
22. A.Chiba, S.Hanada and S.Watanabe, Mater.Sci.Eng., A152 (1992), 108-113.
23. A.Chiba, D.Shindo, and S.Hanada, Acta metall.mater., 39(1) (1991), 13-18.
24. M.G.Lozinskiy, G.M.Volkogon, and N.Z.Pertsovskiy, Russ.Met., 5(1967), 65-72.
25. J.E.Doherty, A.F.Giamei, and B.H.Kear, Canad.Metall.Quart., 13(1) (1974), 229-236.
26. D.N.Duhl and C.P.Sullivan, J.Metals, 23(7) (1971), 38-40.

SESSION V

Strengthening/Toughening Mechanisms II
(Ceramics and Composites)

CERAMIC MATRIX COMPOSITES: CHALLENGES AND OPPORTUNITIES

by

A. G. Evans, J. M. Domergue and E. Vagaggini

Materials Department
College of Engineering
University of California
Santa Barbara, California 93106-5050

ABSTRACT

A methodology for the straightforward and consistent evaluation of the constituent properties of CMCs is summarized, based on analyses from the literature. The results provide a constitutive law capable of simulating the stress/strain behavior of these materials. The approach is illustrated using data for two CMCs: SiC/CAS and SiC/SiC. The constituent properties are also used as input to mechanics procedures that characterize stress redistribution and predict the effect of strain concentrations on macroscopic performance.

Critical Issues in the Development of High Temperature Structural Materials
Edited by N.S. Stoloff, D.J. Duquette and A.F. Giamei
The Minerals, Metals & Materials Society, 1993

1. INTRODUCTION

For the structural application of ceramic matrix composites (CMCs), it is necessary to have a methodology that prescribes the influence of strain concentrations, such as notches, on tensile properties. Ideally, this methodology should have explicit connections to the constituent properties (fibers, matrix, interface), such that efficient design procedures can be implemented. This article contributes toward this objective by surveying the tensile properties of CMCs and the mechanisms that govern their properties, in a manner that leads to a methodology for relating macroscopic behavior to constituent properties. A mechanics approach that addresses the influence of strain concentrations is then summarized and compared with preliminary experimental results.

CMCs usually have substantially lower notch sensitivity than monolithic brittle materials[1-4] and, in several cases, exhibit notch insensitive behavior.[5-7] This desirable characteristic of CMCs arises because the material may *redistribute stresses* around strain concentration sites. There are two fundamental mechanisms of stress redistribution:[8-12] (i) distributed *matrix cracking* and (ii) fiber failure involving *pull-out*. An understanding of these effects provides a basis for devising a methodology to characterize and predict properties. In most CMCs, the Linear Elastic Fracture Mechanics (LEFM) methodology successfully devised for metals cannot be used,[2,8,12-14] because failure does not occur by the propagation of a dominant mode I crack. Alternative mechanics are needed, based on the actual mechanisms of failure. A more relevant mechanics is that based on the Large-Scale Bridging of matrix cracks by fibers[8,13-15] (LSBM). However, even LSBM is inadequate. It must be augmented by Continuum Damage Mechanics (CDM)[16] in order to establish a rigorous methodology.

The basic approach has the following features. An informed background needed for progress is provided by experimental results used in conjunction with models of

matrix cracking and fiber failure. The matrix cracking and fiber failure observations are conducted on 2-D materials in tension and shear. Large-Scale Bridging Mechanics are used to rationalize the observed damage mechanisms. The tensile properties measured in the presence of holes notches, when combined with damage observations, establish the mechanics approach needed to rationalize the influence of strain concentrations.

The strategy is facilitated by devising *mechanism maps* that use *non-dimensional parameters*, which combine the basic constituent properties listed on Table I in mechanistically relevant ways. A list of these parameters is presented in Table II. The most successful methodology will be that using the *minimum* number of constituent properties needed to represent the constitutive behavior. At mechanism transitions, the mechanics needed to characterize composite behavior often change.[12,17]

2. BASIC RESULTS FOR 1-D MATERIALS

2.1 Phenomenology

Models for a range of damage phenomena found in 1-D CMCs, have been established and validated by experiment.[18-40] These models provide the basis upon which the behavior of 2-D and 3-D CMCs can be addressed. The underlying phenomenology involves matrix cracking and fiber failure. *Matrix cracks* form first and interact with predominantly intact fibers,[2,18-24] subject to interfaces that debond, at energy Γ_i, and then slide at a constant shear stress, τ.‡ This process commences at a lower bound stress, $\bar{\sigma}_{mc}$. The crack density increases with increase in stress above $\bar{\sigma}_{mc}$ and may eventually attain a saturation spacing, $\bar{\ell}_s$. The details of crack evolution are governed by the distribution of matrix flaws. The matrix cracks reduce the elastic

‡ More rigorous debonding and sliding behaviors have been analyzed,[21] but have not yet been found necessary for the derivation of useful constitutive laws.

modulus, $\bar{E}$, cause hysteresis in the presence of sliding interfaces, and also induce a permanent strain, ε_p. These matrix cracking effects are schematically illustrated in Fig. 1. The intent is to relate these quantities to the constituent properties (Table I) through non-dimensional parameters (Table II).

The matrix cracks may enhance the stress on the fibers and encourage fiber failure.[8,15] However, when a fiber fails, the stress does not reduce to zero everywhere along that fiber. Load transfer can still occur through the sliding stress, τ, even though the matrix has many cracks.[25-27] As a result, the ultimate tensile strength (UTS) may exceed the value expected for a 'dry bundle' (fibers with no matrix). Two bounds appear to be involved. When failed fibers and matrix cracks do not induce a significant *stress concentration* within *intact* fibers, global load sharing (GLS) applies.[25] Then, the effective gauge length relevant to fiber failure is governed by the load transfer length. Consequently, the UTS becomes independent of the actual gauge length. Conversely, when an unbridged segment of matrix crack exists (because of processing flaws, etc.), the stress concentration induced within the fibers reduces the UTS.[8,15] In this case, fiber pull-out appears to control the UTS.[41] Constituent properties that lead to this transition in behavior will be discussed below.

2.2 Matrix Cracks

A summary of the matrix cracking results is presented, which apply to materials with relatively small debond energies (SDE). More complete results are presented elsewhere.[21,24] *Long* matrix cracks interacting with fibers are subject to a steady-state condition, which leads to a *lower bound* cracking stress, given by[2,18,19]

$$\frac{\bar{\sigma}_{mc}}{E_L} = \left[\frac{6\tau\Gamma_m f^2 E_f}{(1-f)E_m^2 R E_L}\right]^{1/3} - q/E_m \qquad (1a)$$

where q is the residual axial stress in the matrix, which is related to the misfit strain, Ω^*, by;[19]

$$q/E_m = \beta\left[E_f/E_L(1-\nu)\right]f\Omega \tag{1b}$$

with $\beta = 1$. The first important non-dimensional relationship is thus (Table II),

$$\bar{\sigma}_{mc}/E_L = M^{1/3} - \beta Q \tag{1c}$$

As multiple matrix cracking develops, the slip zones from neighboring cracks overlap and produce a *shielding* effect.[20,22] When the shielding proceeds to completion, a *saturation* crack density results. This occurs at stress $\bar{\sigma}_s$, with an associated spacing, $\bar{\ell}_s$, given by[20]

$$\bar{\ell}_s/R = \chi\left[\Gamma_m(1-f)^2E_fE_m/f\tau^2E_LR\right]^{1/3} \tag{2a}$$

The coefficient χ depends on crack evolution: periodic, random, etc. Recent estimates[22] indicate that, $\chi = 1.6$. The second important non-dimensional formula is thus (Table II),

$$\bar{\ell}_s/R = \chi L^{1/3} \tag{2b}$$

The actual *evolution of matrix cracks* at stresses above σ_{mc} is governed by the size and spatial distribution of matrix flaws. If this distribution is known, the evolution can

---

* Ω may be related to the thermal expansion coefficients of fiber α_f and matrix α_m by , $\Omega = (\alpha_m - \alpha_f)\Delta T$, where ΔT is the cooling range, taken as a positive quantity. However, in some cases, there are additional contributions from phase transformation, 'intrinsic' stress, etc.

be simulated[20] (Fig. 2).‡ A simple formula that can be used to approximate crack evolution is[9]

$$\bar{\ell} = \bar{\ell}_s \frac{[\bar{\sigma}_s/\bar{\sigma}_{mc} - 1]}{[\bar{\sigma}/\bar{\sigma}_{mc} - 1]} \tag{3}$$

Direct application of Eqns. (1) to (3) requires that the elastic properties be known and, moreover, that the constituent properties (τ, Γ_m and Ω) be independently measured.[9,30] However, it would be more convenient if a methodology existed that related the constituent properties to *readily measured macroscopic features*. With this objective, a series of formulae have been derived from basic solutions for debonding and sliding at interfaces, as matrix cracks evolve.[21,24,31] Matrix cracks *increase* the elastic compliance. Numerical calculations indicate that the *unloading elastic modulus*, E^*, is given by[31]

$$E_L/E^* - 1 = (R/\bar{\ell})\,\alpha[f, E_f/E_m] \tag{4}$$

where α is another non-dimensional function (Fig. 3). Initial unloading occurs with modulus, E^*. However, the displacements caused by reverse sliding soon dominate.[32,33] These lead to an effective unloading/reloading modulus, $\bar{E}_r$, and generate a hysteresis loop, width $\delta\varepsilon$. When the stress $\bar{\sigma}_p$ is below $\bar{\sigma}_s$, such that limited slip zone overlap occurs, the unloading modulus and the loop width (Fig. 1) are independent of the misfit strain, Ω, but relate to the sliding stress, τ. They are also independent of Γ_i, for SDE.[24,32] The unloading modulus is given by[23,24,31,32]

‡ In some cases, *small* matrix cracks can form at stresses below $\bar{\sigma}_{mc}$.[28,29] These occur either within matrix-rich regions or around processing flaws. However, the non-linear composite properties are usually dominated by fully-developed matrix cracks that form at stresses above $\bar{\sigma}_{mc}$ (Fig. 1).

$$E^*/E_L = 1 + \mathcal{H} E^*/\bar{\sigma}_p \tag{5}$$

where $\mathcal{H}$ is the third important non-dimensional parameter (Table II), given by

$$\mathcal{H} = b_2(1 - a_1 f)^2 R\bar{\sigma}_p^2/4\bar{l}\tau E_m f^2 \tag{6}$$

The width of the hysterisis loop $\delta\varepsilon$ is[24,32]

$$\delta\varepsilon = 2\mathcal{H}\left(\bar{\sigma}/\bar{\sigma}_p\right)\left[1 - \bar{\sigma}/\bar{\sigma}_p\right] \tag{7a}$$

such that the loop width at half maximum, $\delta\varepsilon_{1/2}$ (at $\bar{\sigma} = \bar{\sigma}_p/2$), is

$$\delta\varepsilon_{1/2} = \mathcal{H}/2 \tag{7b}$$

The *permanent strain*, ε_p, is sensitive to the sliding stress and the misfit, as well as the debond energy. It is given by,[21,24,32]

$$\varepsilon_p = 2\mathcal{H}\left[1 - \Sigma_i\right]\left[1 - \Sigma_i + 2\Sigma_T\right] + \varepsilon^* \tag{8}$$

where Σ_i and Σ_T are two non-dimensional parameters (Table II) that introduce the influence of the debond energy Γ_i and the misfit strain Ω, given by[21,24,32]

$$\begin{aligned} \Sigma_T &\equiv \frac{\bar{\sigma}_T}{\bar{\sigma}_p} = (c_2/c_1)E_m\Omega/\bar{\sigma}_p \\ \Sigma_i &\equiv \frac{\bar{\sigma}_i}{\bar{\sigma}_p} = (1/c_1)\sqrt{E_m\Gamma_i/R\bar{\sigma}_p^2} - \Sigma_T \end{aligned} \tag{9}$$

and ε^* is the extension associated with relief of the residual stress caused by matrix cracks, in the absence of interface sliding,[31]

$$\varepsilon^* = (E_m \Omega/E)\left[f a_2/(1 - a_1 f)\right]\left[E/E_c - 1\right] \tag{10}$$

The above results can be combined to give an expression for the secant modulus, $\bar{E}_s$.[24] The resulting constitutive law may be used to simulate stress/strain curves.[24] The results may also be used to evaluate τ, Γ_i and Ω, provided that $\bar{l}_s$ has been measured, as elaborated below.

At stresses above $\bar{\sigma}_s$, the behavior is less well-documented. It has generally been assumed that the tangent modulus $\bar{E}_t$ is that associated exclusively with the fibers,[18]

$$\bar{E}_t = f E_f \tag{11}$$

However, deviations from Eqn. (11) often arise.[22]

Finally, it is noted that certain matrices (especially oxides) are susceptible to stress corrosion cracking.[25] This phenomenon leads to time-dependent matrix cracking, which can occur at stresses below $\bar{\sigma}_{mc}$.

2.3 Fiber Failure

Several factors are important concerning fiber failures within a composite matrix. (i) Fibers begin to fail prior to the UTS.[25-27] At the UTS, the fraction of failed fibers within the characteristic length, δ_c, is sufficient that the remaining intact fibers are unable to support the load. (ii) The stochastic nature of fiber failure dictates that the fiber failure sites have a *spatial* distribution around the fracture plane. Consequently, a frictional *pull-out resistance* exists. This resistance allows the material to sustain load, beyond the UTS. The associated pull-out strength S_p is an important property of the

composite. (iii) When unbridged flaws exist in the material, the matrix cracks introduce stress concentrations within intact fibers. This effect may lead to a reduced UTS.[8,15]

The basic stochastics of fiber failure have identified two non-dimensional parameters: a characteristic strength[25,36]

$$S_c = S_o \left[\tau L_o / R S_o\right]^{\gamma(m+1)} \tag{12a}$$

and a characteristic length

$$\delta_c = L_o \left[S_o R / \tau L_o\right]^{\gamma(m+1)} \tag{12b}$$

related by

$$S_c = \tau \delta_c / R \tag{12c}$$

When multiple matrix cracking precedes composite failure, and when GLS applies, the UTS is gauge length independent at large lengths ($L_g \gtrsim \delta_c$). The UTS is given by[25]

$$S_u = f S_c F(m) \tag{13}$$

where

$$F(m) = \left[2/(m+2)\right]^{\gamma(m+1)} \left[(m+1)/(m+2)\right]$$

At shorter gauge lengths ($L_g < \delta_c$), the UTS increases as L_g decreases[26] (Fig. 4).

In principle, it is possible for composite failure to be preceded by relatively few matrix cracks, with GLS still applicable. Then, because the average stress on the fibers is

lower, the UTS is predicted to be higher than S_u. In the limit wherein only *one* matrix crack has formed, the UTS (subject to GLS) is

$$S_u^* = f S_c G(m) \tag{14}$$

where

$$G(m) \approx \left[(5m+1)/5m\right]\exp\left[-1/(m+1)\right]$$

The spatial distribution of the fiber failures that occur upon loading results in fiber pull-out on the matrix fracture plane. The mean pull-out length, $\bar{h}$ (for $L_g > \delta_c$), has the non-dimensional form[25,36]

$$\bar{h}\tau/RS_c = \lambda(m) \tag{15}$$

There are two bounding solutions for the function λ (Fig. 5). Composite failure subject to *multiple matrix cracking* gives the *upper bound*. Failure in the presence of *a single crack* gives the *lower bound*.

Because of pull-out, the system has a *residual* strength, S_p, (Fig. 6a) given by

$$\begin{aligned} S_p &= 2\tau f \bar{h}/R \\ &\equiv 2 f S_c \lambda(m) \end{aligned} \tag{16}$$

The preceding results are applicable provided that there are no unbridged segments along the matrix crack. Unbridged regions concentrate the stress in the adjacent fibers and weaken the composite. The effect can be addressed using Large-

Scale Bridging Mechanics (LSBM). Simple linear scaling considerations require that the strength S^* depend on a non-dimensional *flaw index*[8,15] (Table II),

$$\mathcal{A} = a_o S^2/E_L \Gamma_o \tag{17}$$

where Γ_o is the area under the stress/displacement curve for the bridging fibers, S is the fully-bridged UTS and $2a_o$ is the length of the unbridged segment. The flaw index $\mathcal{A}$ must be specified for each bridging law, based on Γ_o. The functional dependence of strength S^* on $\mathcal{A}$ has been determined by numerical analysis for two limiting cases.[37] A *lower bound* arises in the presence of bridging without pull-out ($S = S_u$, $S_p = 0$), with flaw index[8,15] (Table II),

$$\mathcal{A}_b = 3\left[f/(1-f)\right]^2 \left(E_f E_L/E_m^2\right)\left(a_o \tau/RS\right) \tag{18a}$$

The dependence of the UTS on $\mathcal{A}_b$ is plotted on Fig. 6a. An *upper bound* obtains when the UTS is pull-out dominated ($S = S_p$), with flaw index[8,37,41] (Table II),

$$\mathcal{A}_p = 2\left(a_o/\bar{h}\right)\left(S_p/E_L\right) \tag{18b}$$

The degradation is plotted on Fig. 6b. The behavior between the bounds has not been well-established. It involves coupled bridging and pull-out. One result[37] (plotted on Fig. 6a) suggests that the lower bound is more relevant when $\mathcal{A}_b \lesssim 0.3$, whereas the upper bound is a reasonable approximation when $\mathcal{A}_b > 1.5$.

Experimental validation of the above results requires independent measurement of S_c, and m. Tests conducted on pristine fibers are *not relevant*, because fiber degradation usually occurs upon composite processing.[10,38,42] Two approaches have been used. One approach entails removal of the matrix, by dissolution,[1] which is only feasible if further

fiber degradation does not occur. The second approach involves *fracture mirror* measurements on failed fibers, after tensile testing of the composite.[10,38,39,42]

3. CHARACTERISTICS OF 2-D MATERIALS

3.1 Matrix Cracking

General comparison between the stress/strain, $\sigma(\varepsilon)$, curves measured for 1-D and 2-D materials[41] (Figs. 7 and 8) provides important perspective. It is found that $\sigma(\varepsilon)$ for 2-D materials is quite closely matched by simply scaling down the 1-D curve from S to S/2. The behavior of 2-D materials must, therefore, be *dominated* by the 0° plies,‡ which provide a fiber volume fraction in the loading direction about half that present in 1-D material.

The only significant 2-D effects occur at the initial deviation from linearity. At this stage, matrix cracks that form either in matrix-rich regions or in 90° plies evolve at somewhat lower stresses than cracks in 1-D materials.[29,30] However, the associated non-linearities are usually slight and do not normally contribute in an important manner to the overall non-linear response of the material. For example, matrix cracking in the 90° plies often proceeds by a tunneling mechanism[9,43,44] (Fig. 9). Tunnel cracking occurs subject to a lower bound stress[11,43,44]

$$\sigma_t = \left[\Gamma_m E/gt\right]^{1/2} - J_R\left(E_L + E_T\right)/2E_T \qquad (19)$$

where g is a function that ranges between 1/3 and 2/3.[44] The unloading modulus associated with tunnel cracks is[44]

‡ Furthermore, since some of the 2-D materials are woven, the S/2 scaling infers that the curvatures introduced by weaving have minimal effect on the stress/strain behaviors.

$$\bar{E}/E = h\left(E_f/E_m, f, t/\bar{L}\right) \tag{20}$$

with $\bar{L}$ being the mean crack spacing in the 90° plies. The function h varies between 1 and ~ 0.6 as $t/\bar{L}$ changes from ~ 0 to > 1. The corresponding permanent strain is[44]

$$\varepsilon_p = \left(1 - E_T \nu^2/E_L\right)\sigma_R/E_L \tag{21}$$

The actual evolution of cracks at stresses above σ_τ depends on the availability of flaws in the 90° plies.

Extension of these tunnel cracks into the matrix of the 0° plies results in behavior similar to that found in 1-D material. Moreover, if the stress $\bar{\sigma}_0$ acting on the 0° plies is known, the 1-D solutions may be used directly. Otherwise, this stress must be estimated. For a typical 0/90 system, $\bar{\sigma}_0$ ranges between $\bar{\sigma}$ and $2\bar{\sigma}$, depending upon the extent of matrix cracking in the 90° plies and upon E_T/E_L.[44] Preliminary analysis has been conducted below using, $\bar{\sigma}_0 = 2\bar{\sigma}$, as implied by the comparison between 1-D and 2-D stress/strain curves (Fig. 8). Additional modelling is required on this topic.

3.2 Fiber Failure

The matrix cracks that originate in the 90° plies and extend through the 0° plies must induce a stress concentration in the fibers. The phenomenon is analogous to that considered above for 1-D material containing unbridged segments. When the stress concentration is small, the UTS should be given by Eqn. (13), but with f replaced by f_ℓ. In a typical case ($f_\ell/f = 1/2$), the UTS would be $S_u/2$, consistent with experimental findings on several CMCs (Fig. 8). In other cases, the stress concentration is important and the UTS is significantly smaller than $S_u/2$.

Major factors governing the stress concentration are the modulus ratio, E_T/E_L, the crack spacing, $\bar{L}$, and τ. That is, small values of E_T/E_L, $\bar{L}$ and τ alleviate the stress concentration.[41]

3.3 Shear Damage

When loaded in shear, 2-D CMCs are subject to non-linear deformation.[45] The deformations are governed primarily by matrix cracks. Typical shear stress/strain, $T(\gamma)$ curves (Fig. 10) indicate that CMCs can normally sustain larger shear strains than tensile strains prior to failure. The matrix damage often consists of cracks oriented at 45° to the fiber axis. Since fiber sliding is inhibited in shear loading, the elastic compliance of the composite with matrix cracks may be a useful upper bound for the shear strength. Consequently, when normalized by the shear modulus of the composite (Fig. 10), the $T(\gamma)$ curves found for a range of CMCs tend to converge into a band.

4. TEST METHODOLOGY

The preceding characteristics suggest a methodology that can be used to efficiently evaluate constituent properties, which may then be used to make predictions about composite performance. The basic philosophy is that straightforward procedures be used, with consistency demonstrated between independent measurement approaches. The measurements that are experimentally convenient include: the fiber pull-out length, $\bar{h}$, the matrix crack spacing at saturation, $\bar{l}_s$, the stress/strain (σ, ε) behavior, the fracture mirror dimensions and the bending deformation of a bilayer (Table I).

The steps are as follows. Generally, the fiber modulus is known, whereupon E_m can be evaluated from the measured initial composite modulus. Both S_c and m are known, provided that fracture mirror measurements have been made. Curvature measurements made on bilayer provide Ω. At this stage, measurements of pull-out,

saturation crack spacing and unloading/reloading hysteresis are used to determine τ, Γ_i and Γ_m, as well as to provide checks on the magnitudes of S_c and Ω.[24,34] Specifically, the magnitude of τ is obtained from the hysteresis loop width at half maximum, $\delta\varepsilon_{1/2}$, measured as a function of $\bar{\sigma}_p$ (Eqn. 7b) and checked using the unloading modulus, $\bar{E}$ (Eqn. 5). Typical results are shown in Figs. 11 and 12. Then, the misfit strain, Ω, and the debond energy, Γ_i, are evaluated from the permanent strain ε_p (Fig. 13) by using Eqn. (8). Additional procedures have been devised to determine Ω.[24] The misfit is compared with the bilayer measurements. Thereafter, the fiber pull-out lengths are used to provide consistency checks on τ and S_c, by using Eqn. (15), with the appropriate bound for λ.

When the preceding measurements provide consistent information, two other results can be used. The saturation crack spacing, $\bar{l}_s$, allows estimation of Γ_m (Eqn. 2), which may be compared with values found for the monolithic matrix material. The same value of Γ_m can be used to calculate the matrix cracking stress, $\bar{\sigma}_{mc}$ (Eqn. 1), which can be compared with the onset of linearity found in the stress/strain curves.

Finally, with S_c and m known, the UTS may be compared with the strengths predicted from global load sharing analysis (Eqn. 13) and fiber pull-out analysis (Eqn. 16). This comparison gives insight about the influence of matrix flaws on stress concentrations expected in the fibers.

The procedure is briefly illustrated by referring to a comprehensive set of results obtained on both SiC/CAS[6,9,24,30] and SiC/SiC[29,34,46] (see Figs. 11–13). The constituent properties for these two CMC systems obtained using the above methodology are summarized in Table III. More complete assessments are provided elsewhere.[24,34] The comparison between these two systems is interesting, because the constituent properties are very different. (i) In the SiC/SiC system, the fibers have clearly been degraded during processing. (ii) The large difference in τ indicates that the C coating placed on the fibers in the SiC/SiC material (by vapor deposition) has very different properties

than the C interphase in the CAS system, which is governed by reaction during processing. The high stiffness of the SiC matrix may also have an important influence on τ. (iii) The SiC/SiC system has a substantially larger debond energy, Γ_i, which is the origin of the relatively small permanent strain.

5. SIMULATIONS

When the constituent properties have been evaluated in a consistent manner, the stress/strain curves, for SDE materials, at stresses prior to saturation may be simulated by using Eqns. (1) to (10).[24,34] The procedure is straightforward for 1-D material, provided that Eqn. (3) is a reasonable representation of matrix crack evolution. Some examples are presented in Fig. 14a.[24] Further work is needed to predict the behavior above $\bar{\sigma}_s$. The simulation capability for 2-D material depends on the assumption made about the stress $\bar{\sigma}_0$ acting on the 0° plies. If this stress is considered to be, $\bar{\sigma}_0 = 2\bar{\sigma}$, the simulations for SDE materials, based on SiC/CAS (Fig. 14b), agree quite well with experiments except at small plastic strain.[34] Further research is needed to understand the behaviors at small plastic strains.

6. EFFECTS OF STRAIN CONCENTRATIONS

6.1 General Considerations

When either holes or notches (or other strain concentrating sites) are introduced, experimental results have indicated that CMCs can exhibit (at least) three classes of behavior,[12,40] as sketched in Fig. 15. Class I materials exhibit a dominant (mode I) crack emanating from the notch, with fiber failures occurring as the crack extends across the material. Class II materials experience multiple (mode I) matrix cracking from the notch. These cracks usually extend across the net section prior to fiber failure. In class III

materials, shear damage occurs from the notch and extends normal to the notch plane prior to composite failure. In all three cases, *stresses are redistributed* by matrix cracking as well as by fiber pull-out.

The characterization of notch effects for CMCs exhibiting these three classes of behavior appears to require different *mechanics*, because the stress redistribution mechanism within each class operates over different physical scales. Class I behavior involves stress redistribution by fiber bridging/pull-out, which occurs along the crack plane. Large-Scale Bridging Mechanics (LSBM) is preferred for such materials.[8,13-15] Class II behavior allows stress redistribution by large-scale matrix cracking. Consequently, a mechanism-based, Continuum Damage Mechanics (CDM) is regarded as most appropriate.[16] Class III behavior involves material responses similar to those found in metals,[12,40,41] and a comparable mechanics might be used: either LEFM for small-scale yielding or non-linear fracture mechanics for large-scale yielding. Since a unified mechanics has not yet been identified, it is necessary to devise *mechanism maps* that distinguish the various classes, through constituent properties. Initial attempts are elaborated below.

6.2 Mechanism Transitions

The transition between class I and class II behaviors involves considerations of both matrix crack growth and fiber failure. One hypothesis for the transition may be analyzed using LSBM. Such analysis allows the condition for fiber failure at the end of an unbridged crack segment to be solved simultaneously with the energy release rate of the matrix front. The latter is equated to the matrix fracture energy.[15] By using this solution to specify that fiber failure occurs *before the matrix crack extends into steady-state*, class I behavior is presumed to ensue. Conversely, class II behavior is assigned when the steady-state matrix cracking condition is achieved prior to fiber failure. The resulting mechanism map involves two indices:[15]

$$S = (RS/a_o\tau)(E_m^2/E_L E_f)[(1-f)/f]^2 \equiv 3/\mathcal{A}_b \quad (24a)$$

and

$$C_m = \sigma_{mc}/S \quad (24b)$$

With S and C_m as coordinates, a mechanism map may be constructed that distinguishes class I and class II behavior (Fig. 16). While this map has qualitative features consistent with experience, the experiments required for validation have not been completed. In practice, the mechanism transition in CMCs must involve additional considerations.

The incidence of class III behavior is found at relatively small magnitudes of the ratio of shear strength, T, to tensile strength S. When T/S is small, a shear band develops at the notch front and extends normal to the notch plane.[10,40] Furthermore, since T is related to G (Fig. 10), the parameter G/S is selected as the ordinate of a mechanism map.[12,41] Experimental results suggest that class III behavior arises when $G/S \lesssim 50$ (Fig. 17).

6.3 Mechanics Methodology

i) Class I Materials

The class I mechanism, when dominant, has features compatible with LSBM. These mechanics may be used to characterize effects of notches, holes and manufacturing flaws on tensile properties, whenever a single matrix crack is prevalent. For cases wherein the flaw or notch is small compared with specimen dimensions, the tensile strength may be plotted as functions of *both* flaw indices: $\mathcal{A}_b$ and $\mathcal{A}_p$ (Fig. 6). For the former, the results are sensitive to the ratio of the pull-out strength S_p to the UTS. These

results should be used whenever the unnotched tensile properties are compatible with global load sharing. Conversely, $\mathcal{A}_p$ should be used as the notch index when the unnotched properties appear to be pull-out dominated.

When the notch and hole have dimensions that are significant fraction of the plate width ($a_o/w > 0$), *net section* effects must be included.[8,37] Some results (Fig. 18) illustrate the behavior.

Complete experimental validation of LSBM for class I materials has not been undertaken. Partial results for the material, SiC/C_B, are compatible with LSBM, as shown for data obtained with center notches and center holes[12] (Fig. 17), with $\mathcal{A} \approx 0.8$. For this material, the unnotched properties appear to be pull-out controlled,[10,12] and the constituent properties give a pull-out notch index, $\mathcal{A}_p \approx 0.76$.

ii) Class II Materials

The non-linear stress/strain behavior governed by matrix cracking, expressed through $\bar{E}$ (Eqn. 5) and ε_p (Eqn. 8) provide a basis for a Damage Mechanics approach that may be used to predict the effects of notches and holes. Such developments are in progress. An important factor that dictates whether continuum or discrete methods are used concerns the ratio of the matrix crack spacing to the radius of curvature of the notch.

In practice, several class II CMCs have been shown to exhibit notch insensitive behavior for holes and notches in the size range: 1–5 mm (Fig. 19). These materials include: SiC/CAS[6] and SiC/glass (1070).[7] The non-linearity provided by the matrix cracks thus appears to allow stress redistribution to an extent that essentially *eliminates* the stress concentration.[7,47] The elimination of the stress concentration has been established both by notch strength measurement[6,7] and by thermoelastic emission tests.[46]

iii) Class III Materials

Class III behavior has been found in several C matrix composites[10,12] (Fig. 16). In these materials, the extent of the shear deformation zone ℓ_p is found to be predictable from measured shear strengths, T, in approximate accordance with[12]

$$\ell_p/a_o \approx \sigma/T \tag{25}$$

Calculations have indicated that this shear zone diminishes the stress ahead of the notch,[12] analogous to the *effect of a plastic zone in metals,* and provides good notch properties. For several C/C materials, it has been found that the shear band lengths are small enough that LEFM characterizes the experimental data over a range of notch lengths. For edge notched specimens, it is found that,[12] $K_{IC} \approx 16$ MPa$\sqrt{m}$ (Fig. 20). However, conditions must exist where LEFM is violated. For example, when $\ell_p/a_o \lesssim 4$, the stress concentration is essentially eliminated and the material must then become notch insensitive.[12] Further work is needed to identify parameters that bound the applicability of LEFM, as well as establish the requirements for notch insensitivity.

7. SUMMARY

Test methods have been described that relate constituent properties to macroscopic behaviors in a consistent manner. The approach has been illustrated for two CMC systems. It is expected that the methodology will be used to predict stress/strain curves and examine their sensitivity to constituent properties. These properties may be used to delineate mechanism maps that represent transitions in macroscopic performance, especially in the presence of strain concentrations. Mechanics procedures for each mechanism have been described in a preliminary manner. A concerted effort is needed

to further develop and validate the mechanics, which should have applicability to a wide range of technologically important CMCs.

ACKNOWLEDGEMENTS

This work was supported by the Defense Advanced Research Projects Agency through the University Research Initiative under Office of Naval Research Contract No. N-00014-86-K-0753.

TABLE I

Measurement Methods

CONSTITUENT PROPERTY	MEASUREMENT
Sliding Stress, τ	• Pull-Out Length, $\bar{h}$[25,36] • Saturation Crack Spacing, $\bar{l}_s$[20,22] • Hysteresis Loop, $\delta\varepsilon_{1/2}$[23,24] • Unloading Modulus, $\bar{E}_L$[23,24]
Characteristic Strength, S_c, m	• Fracture Mirrors[38,39] • Ultimate Strength, S[25]
Misfit Strain , Ω	• Bilayer Distortion[9] • Permanent Strain, ε_p[23,24] • Residual Crack Opening[32]
Matrix Fracture Energy, Γ_m	• Monolithic Material • Saturation Crack Spacing, $\bar{l}_s$[22] • Matrix Cracking Stress, $\bar{\sigma}_{mc}$[19]
Debond Energy, Γ_i	• Permanent Strain, ε_p[21,24] • Residual Crack Opening[21,24]

TABLE II

Summary of Non-Dimensional Coefficients

$$\Sigma_T \equiv \frac{\overline{\sigma}_T}{\overline{\sigma}_p} = (c_2/c_1)E_m\Omega/\overline{\sigma}_p, \quad \text{Misfit Index}^{21,24,32}$$

$$\Sigma_i \equiv \frac{\overline{\sigma}_i}{\overline{\sigma}_p} = (1/c_1)\sqrt{E_m\Gamma_i/R\overline{\sigma}_p^2} - \Sigma_T, \quad \text{Debond Index}^{21,24}$$

$$\mathcal{H} = b_2(1-a_1 f)^2 R\overline{\sigma}_p^2/4\overline{\ell}\tau E_m f^2, \quad \text{Hysteresis Index}^{24,32}$$

$$\mathcal{L} = \Gamma_m(1-f)^2 E_f E_m/f\tau^2 E_L R, \quad \text{Crack Spacing Index}^{22}$$

$$\mathcal{M} = 6\tau\Gamma_m f^2 E_f/(1-f)E_m^2 R E_L, \quad \text{Matrix Cracking Index}^{2,18,19}$$

$$\mathcal{Q} = E_f f\Omega/E_L(1-\nu), \quad \text{Residual Stress Index}^{19,24}$$

$$\mathcal{A} = a_o S^2/E_L\Gamma, \quad \text{Flaw Index}^{8}$$

$$\mathcal{A}_b = \left[f/(1-f)\right]^2\left(E_f E_L/E_m^2\right)\left(a_o\tau/RS_u\right), \quad \text{Flaw Index for Bridging}^{8,15}$$

$$\mathcal{A}_p = \left(a_o/\overline{h}\right)\left(S_p/E_L\right), \quad \text{Flaw Index for Pull-Out}^{37,41}$$

TABLE III

Important Constituent Properties For CMCs:
Comparison Between SiC/SiC and SiC/CAS

PROPERTY		MATERIAL	
		SiC/CAS	SiC/SiC
CONSTITUENTS	Matrix Modulus, E_m (GPa)	100	400
	Fiber Modulus, E_f (GPa)	200	200
	Sliding Stress, τ (MPa)	15–20	100–150
	Residual Stress, q (MPa)	80–100	50–100
	Fiber Strength, S_c (GPa)	2.0–2.2	1.3–1.6
	Shape Parameter, m	3.3–3.8	4.2–4.7
	Matrix Fracture Energy, Γ_m (Jm^{-2})	20–25	5–10
	Debond Energy, Γ_i (Jm^{-2})	~ 0.1	~ 2
DEPENDENT PROPERTIES	Matrix Cracking Stress, σ_{mc} (MPa)	140–160	200–220
	Saturation Crack Spacing , $\bar{d}_s$ (μm)	110–130	15–20
	Pull-out Length $\bar{h}$ (μm)	250–350	25–40

REFERENCES

[1] K.M. Prewo and J.J. Brennan, *J. Mater. Sci.*, 17 (1982) 1201–06.

[2] D.B. Marshall, B.N. Cox and A.G. Evans, *Acta Metall.*, 33 (1985) 2013.

[3] J.J. Brennan and K.M. Prewo, *J. Mater. Sci.*, 17 (1982) 2371–83.

[4] M. Bouquet, J.-M. Birbis, J.-M. Quenisset and R. Naslain, ICCM-VI, Elsevier, London. Vol. 2 (1987) p. 248–49.

[5] J.M. Domergue, H.C. Cao, A.G. Evans and D. Petrak, *J. Am. Ceram. Soc.*, to be published.

[6] C. Cady and A.G. Evans, *J. Am. Ceram. Soc.*, to be published.

[7] S. Mall, D.E. Bullock and J.J. Pernot, to be published.

[8] G. Bao and Z. Suo, ASME Book No. AMR118, *Appl. Mech. Rev.*, 45 (1992) 355–66.

[9] D. Beyerle, S.M. Spearing and A.G. Evans, *J. Am. Ceram. Soc.*, 75 (1992) 3321–30.

[10] F.E. Heredia, S.M. Spearing, P. Mosher, A.G. Evans and W.A. Curtin, *J. Am. Ceram. Soc.*, 75 (1992) 3017–25.

[11] N. Laws and G. Dvorak, *Jnl. Composite Mtls.*, 22 (1980) 900.

[12] F.E. Heredia, S.M. Spearing, M.Y. He, T.J. Mackin, P.A. Brøndsted, A.G. Evans and P. Mosher, *J. Am. Ceram. Soc.*, to be published.

[13] B.N. Cox and D.B. Marshall, *Fatigue and Fracture of Eng. Mtls.*, 14 (1991) 847.

[14] B.N. Cox and C.S. Lo, *Acta Metall. Mater.*, 40 (1992) 69.

[15] L. Cui and B. Budiansky, to be published.

[16] D. Hayhurst, F.A. Leckie and A.G. Evans, *Proc. Roy. Soc.*, London, A434 (1991) 369.

[17] A.G. Evans and F.W. Zok, *Topics In Fracture and Fatigue* (ed. A.S. Argon) 1992, pp. 271–308.

[18] J. Aveston, G.A. Cooper and A. Kelly, in *The Properties of Fiber Composites*, NPL Conf. Proc., pp. 15–26.

[19] B. Budiansky, J.W. Hutchinson and A.G. Evans, *J. Mech. Phys. Solids*, 34 (1986) 167.

[20] F.W. Zok and S.M. Spearing, *Acta Metall. Mater.*, **40** (1992) 2033.

[21] J.W. Hutchinson and H. Jensen, *Mech. of Mtls.*, **9**, (1990) 139.

[22] S.M. Spearing and F.W. Zok, *Jnl. Eng. Mtls. Tech.*, in press.

[23] A.W. Pryce and P. Smith, *J. Mater. Sci.*, **27** (1992) 2695–2704.

[24] E. Vagaggini, J.M. Domergue and A.G. Evans, *J. Am. Ceram. Soc.*, to be published.

[25] W.A. Curtin, *J. Am. Ceram. Soc.*, **74** (1991) 2837–45.

[26] L. Phoenix and R. Raj, *Acta Metall. Mater.*, **40** (1992) 2813–28.

[27] F. Hild, J.M. Domergue, F.A. Leckie and A.G. Evans, *Intl. Jnl. Solids Structures*, to be published.

[28] B.Y. Kim and N. Pagano, *J. Am. Ceram. Soc.*, **74** (1991) 1082–90.

[29] X. Aubart, Thèse de Doctorat de L'Université de Paris (Nov. 1991), "Modélisation et Identification du Comportement de Composites à Matrice Céramique."

[30] D. Beyerle, S.M. Spearing, F.W. Zok and A.G. Evans, *J. Am. Ceram. Soc.*, **75** (1992) 7519.

[31] M.Y. He, B.-X. Wu, A.G. Evans and J.W. Hutchinson, *Mech. of Mtls.*, to be published.

[32] D.B. Marshall, *Acta Metall. Mater.*, **40** (1992) 427–41.

[33] T.J. Kotil, J.W. Holmes and M. Cominou, *J. Am. Ceram. Soc.*, **73** (1990) 1879.

[34] J.M. Domergue, E. Vagaggini, A.G. Evans and D. Roach, *J. Am. Ceram. Soc.*, to be published.

[35] S.M. Spearing, F.W. Zok and A.G. Evans, *J. Am. Ceram. Soc.*, in press.

[36] M.D. Thouless and A.G. Evans, *Acta Metall.*, **36** (1988) 517.

[37] Z. Suo, S. Ho and X. Gong, *J. Matl. Engr. Tech.*, in press.

[38] A.J. Eckel and R.C. Bradt, *J. Am. Ceram. Soc.*, **72** (1989) 435.

[39] J.F. Jamet, D. Lewis and E.Y. Luh, *Ceram. Eng. Sci. Proc.*, **5** (1984) 625.

[40] A.G. Evans, *Mat. Sci. Eng.*, **A143** (1991) 63.

[41] A.G. Evans, F.W. Zok and T.J. Mackin, to be published.

[42] H.C. Cao, E. Bischoff, M. Rühle, A.G. Evans, D.B. Marshall and J.J. Brennan, *J. Am. Ceram. Soc.*, **73** (1990) 1691.

[43] J.W. Hutchinson and Z. Suo, *Appl. Mech. Rev.*, **28** (1991).

[44] C. Xia, R.R. Carr and J.W. Hutchinson, *Harvard Univ. Report Mech-202* (1992) to be published.

[45] P.A. Brøndsted, F.E. Heredia and A.G. Evans, *J. Am. Ceram. Soc.*, to be published.

[46] T.J. Mackin, A.G. Evans and T.E. Purcell, to be published.

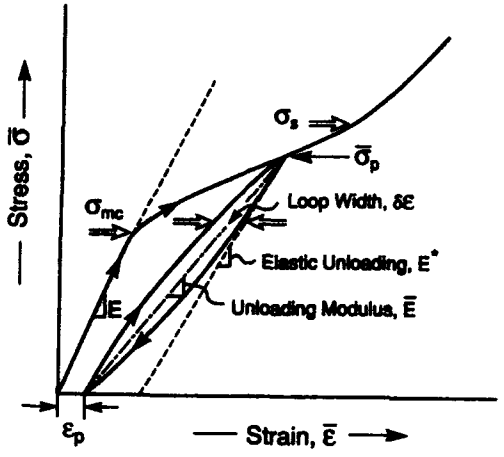

Figure 1

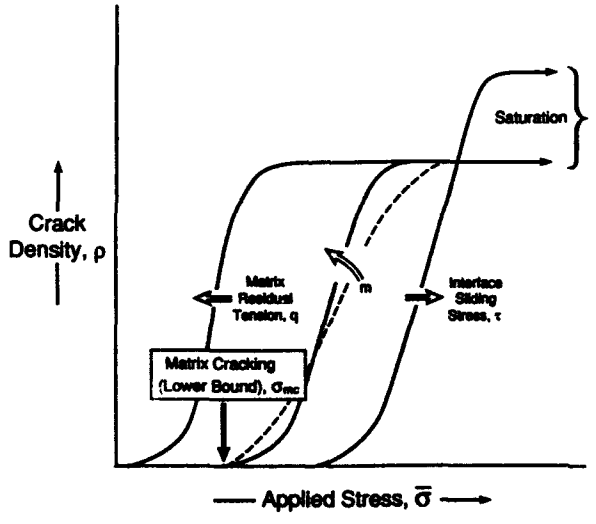

Figure 2

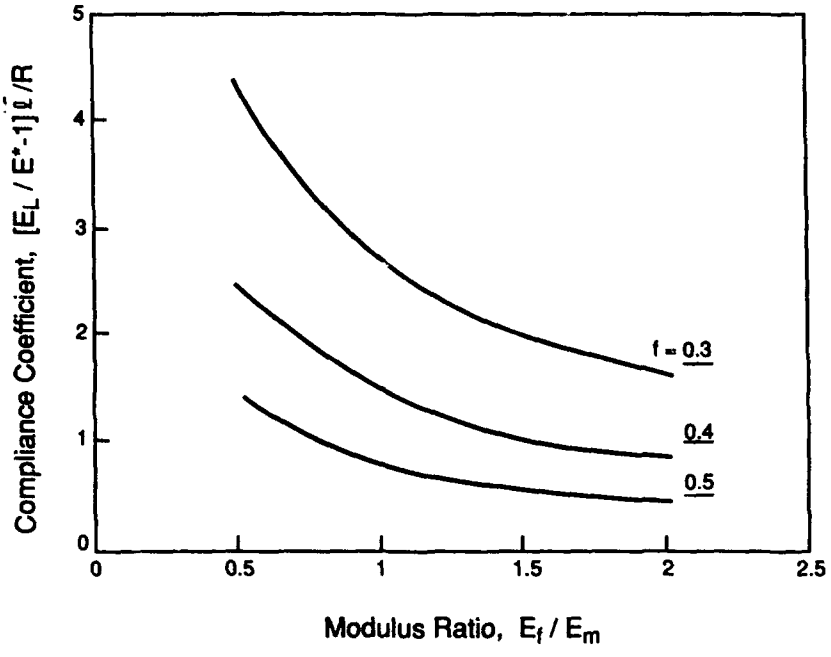

Figure 3

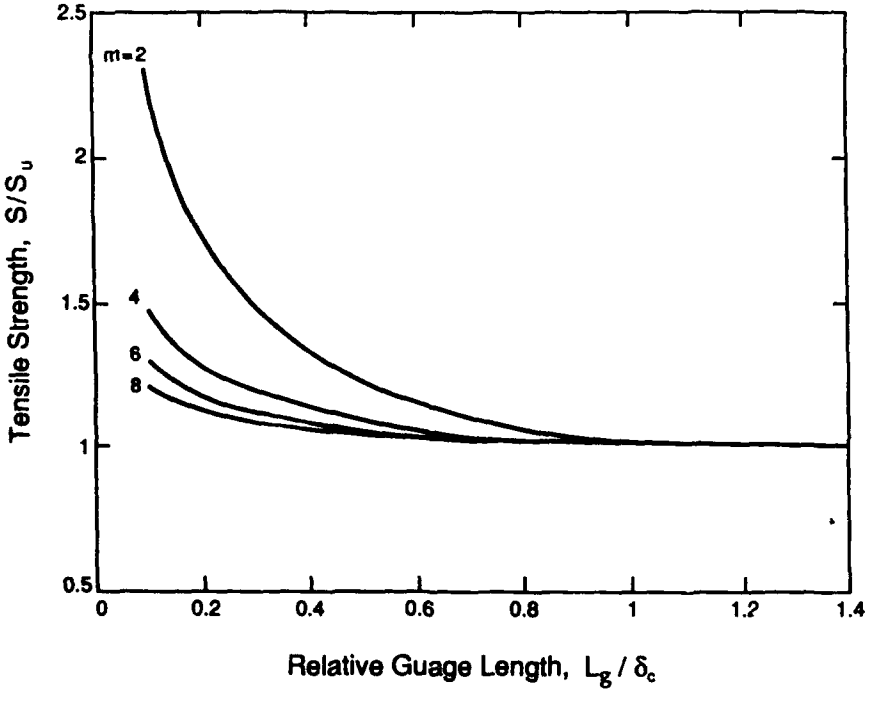

Figure 4

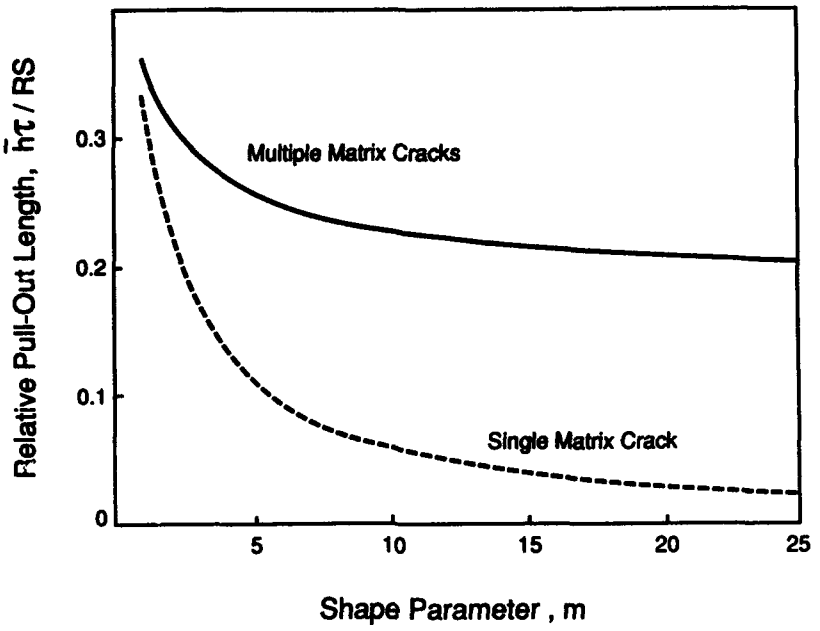

Figure 5

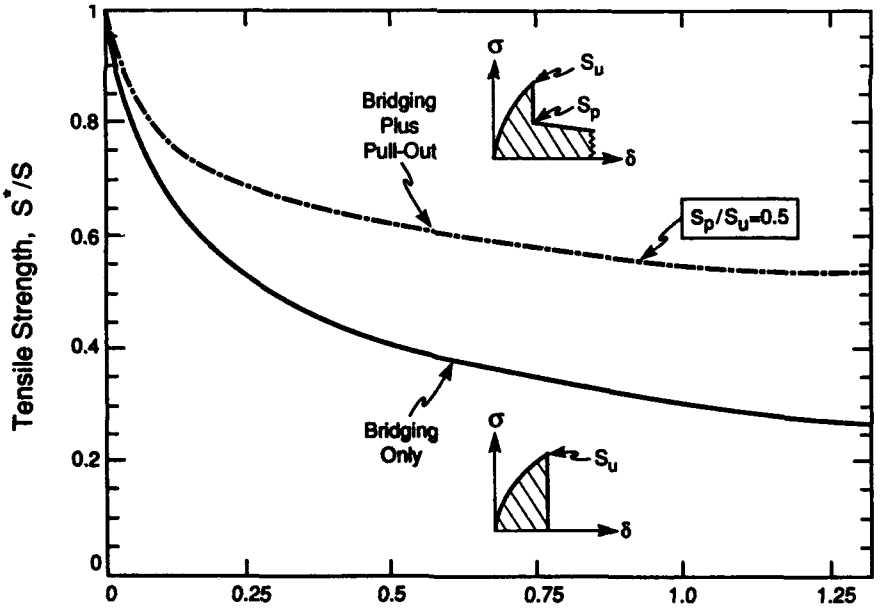

Figure 6a

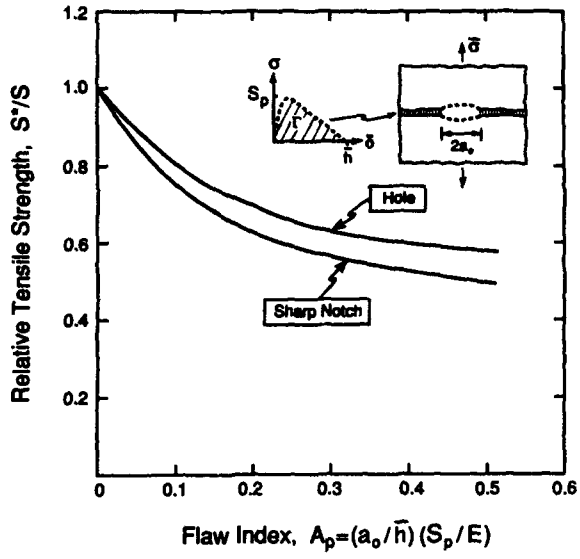

Figure 6b

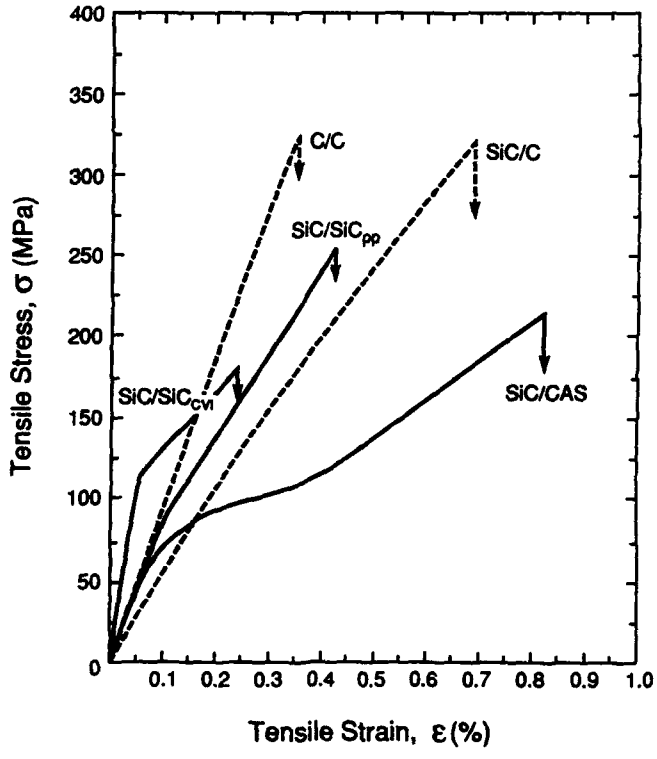

Figure 7

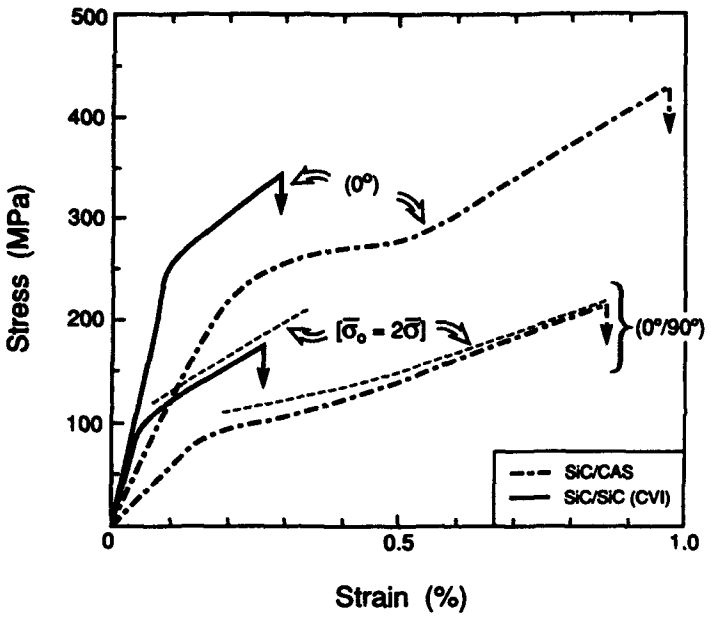

Figure 8

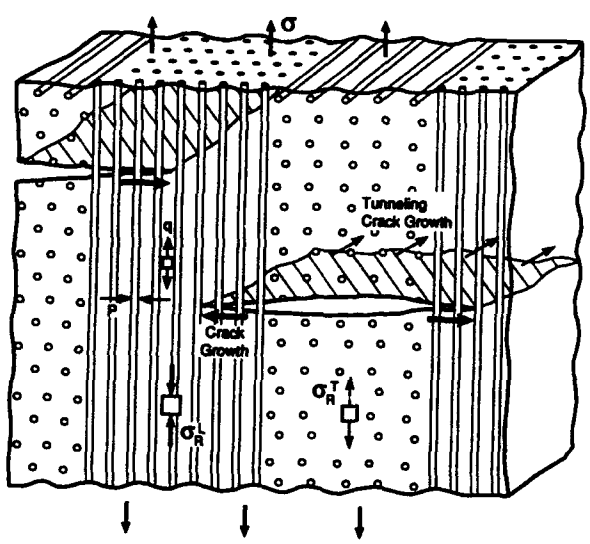

Figure 9

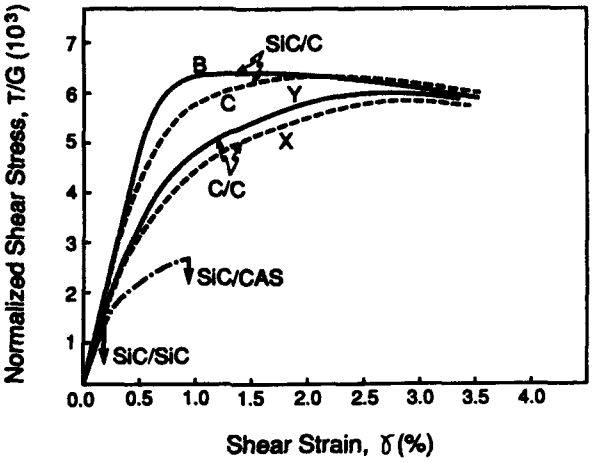

Figure 10

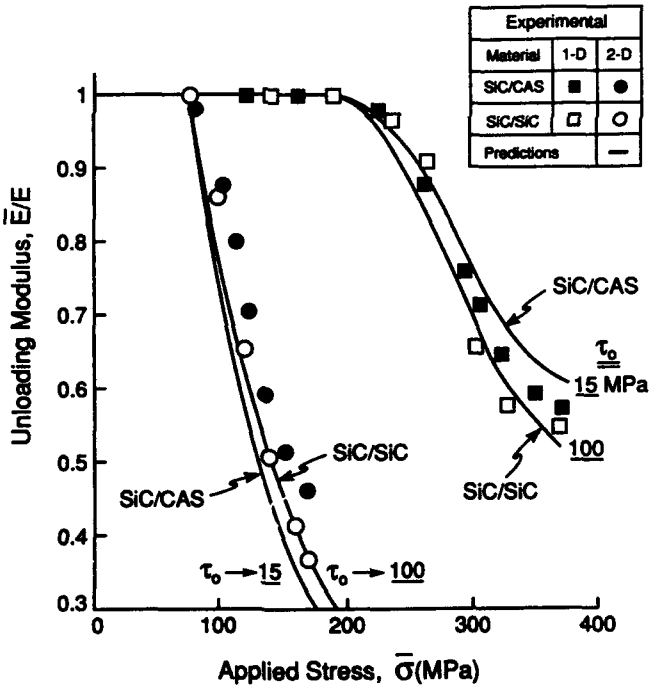

Figure 11

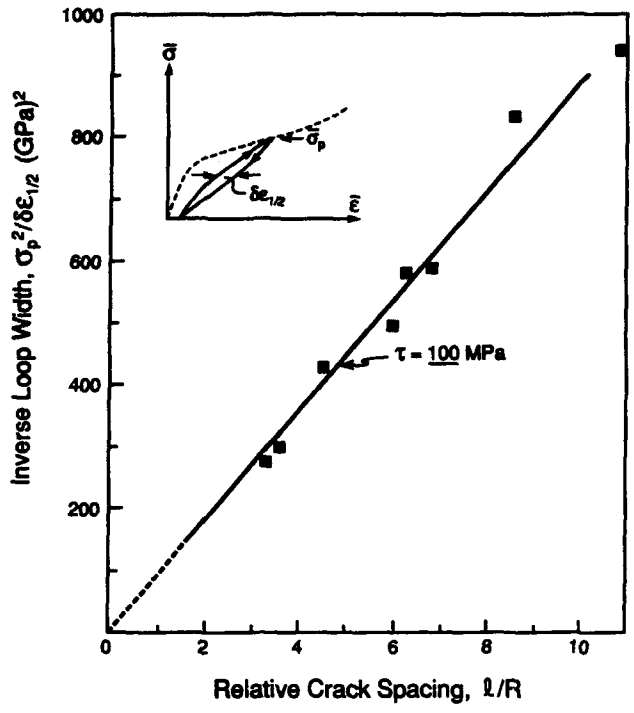

Figure 12

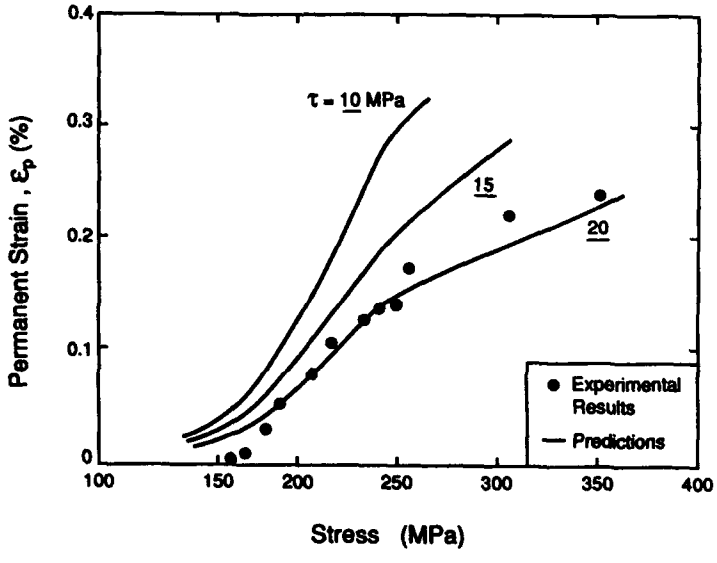

Figure 13

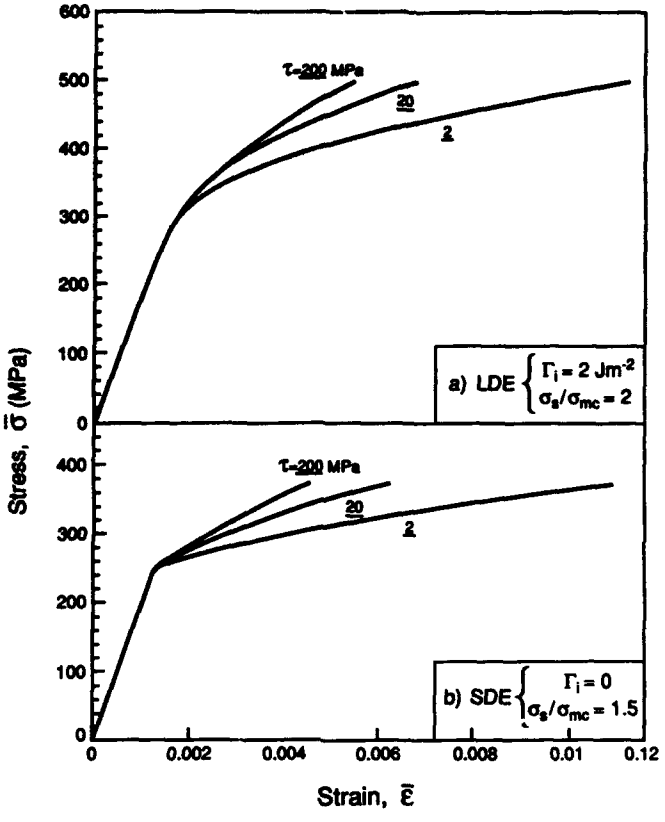

Figure 14a

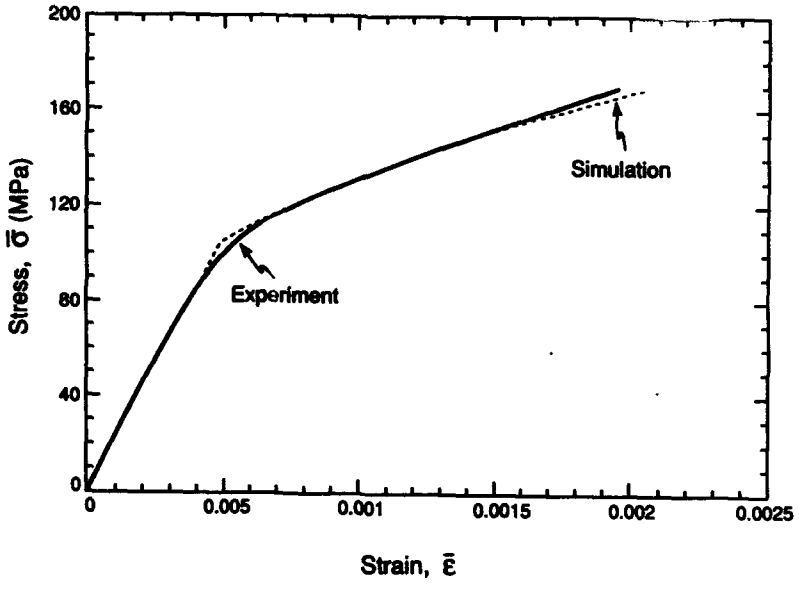

Figure 14b

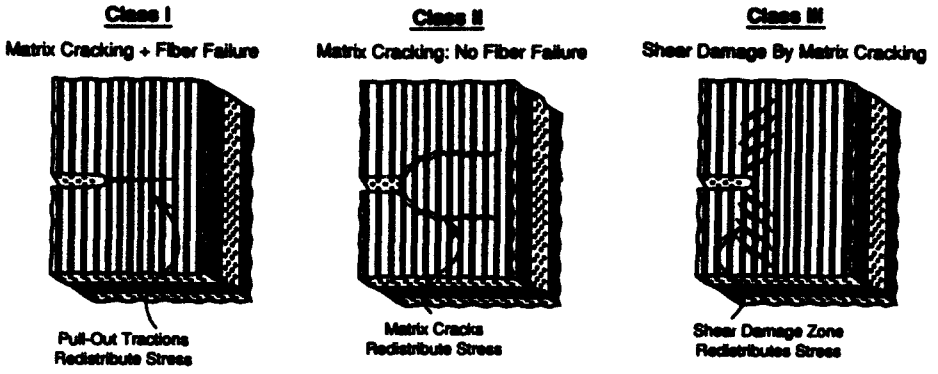

Figure 15

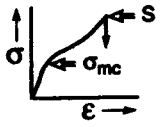

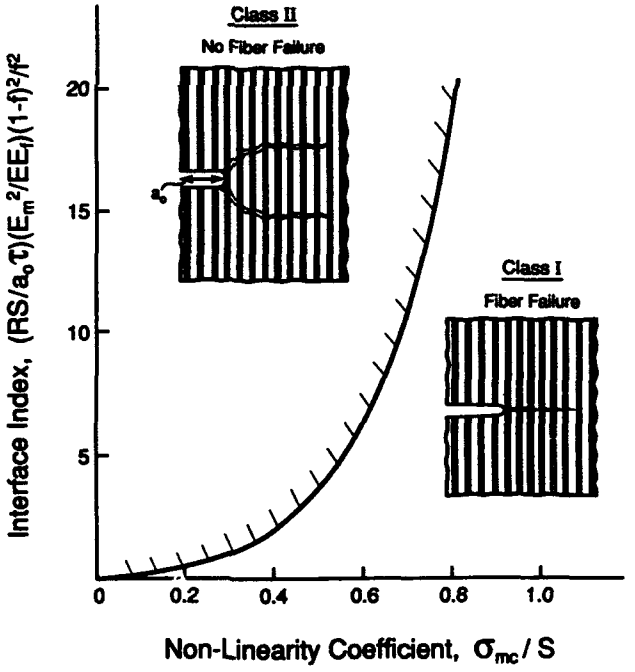

Figure 16

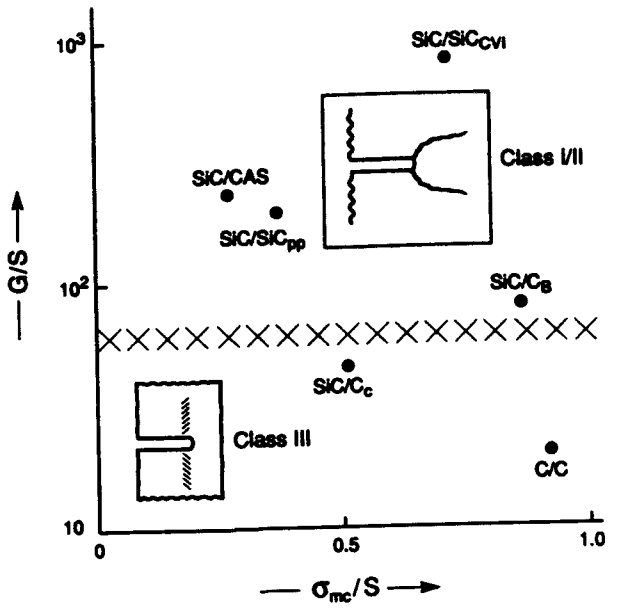

Figure 17

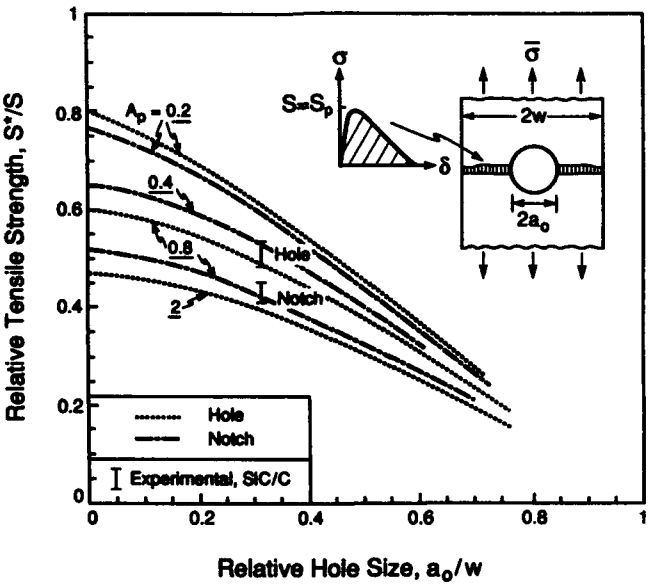

Figure 18

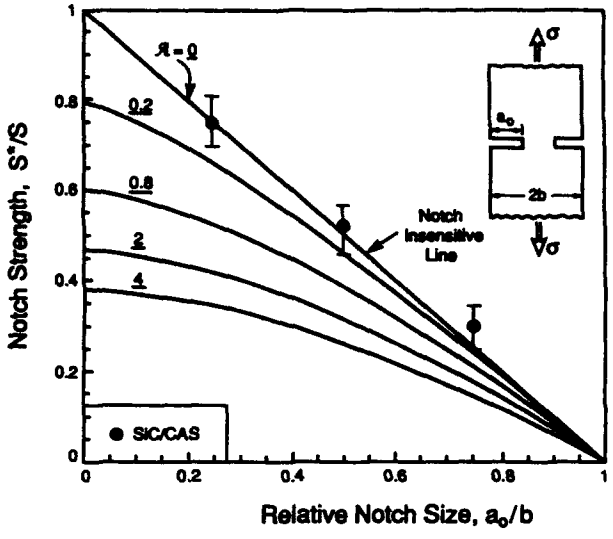

Figure 19

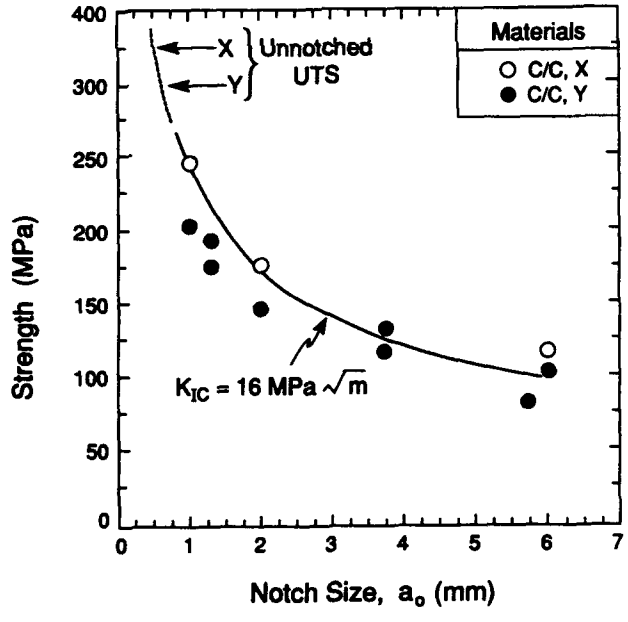

Figure 20

FIGURE CAPTIONS

Fig. 1. A schematic indicating the consequence of matrix cracking in CMCs on the stress/strain behavior.

Fig. 2. A schematic indicating the parameters that influence the evolution of matrix cracks in 1-D CMCs.[30]

Fig. 3. Effects of matrix crack density on the elastic compliance of 1-D CMCs.[31]

Fig. 4. Effects of gauge length on the ultimate tensile strength predicted by global load sharing analysis.[27]

Fig. 5. Bounding solutions for the non-dimensional fiber pull-out length.[25]

Fig. 6. Strength degradation in elastically isotropic CMCs subject to unbridged segments (length $2a_o$) a) combined bridging and pull-out; b) pull-out.[8,37]

Fig. 7. A comparison of stress/strain curves for 2-D CMCs all reinforced with Nicalon fibers (with $f \approx 0.4$). The SiC/CAS is a laminate, the SiC/SiC_{CVI} has a plain weave: the other materials have a 8-harness satin weave.[41]

Fig. 8. A comparison of 1-D and 2-D CMC tensile properties obtained for SiC/CAS and SiC/SiC_{CVI}. The lines marked (1/2)1-D are the results for 1-D material reduced in scale by (1/2).[41]

Fig. 9. A typical matrix cracking mode in 2-D CMCs.[9]

Fig. 10. The shear strength of various CMCs normalized by the composite shear modulus.[45]

Fig. 11. The unloading modulus measured for 1-D and 2-D SiC/CAS and SiC/SiC_{CVI} showing comparisons with the model (Eqn. 5) for various sliding stresses.[24,34]

Fig. 12. Variations in the relative hysteresis loop width with crack density obtained for 2-D SiC/SiC_{CVI} showing comparisons with the model (Eqn. 7) for various sliding stresses.[24]

Fig. 13. Variation in permanent strain for a 1-D SiC/CAS material showing comparisons with the model (Eqn. 8) for various values of the sliding stress, using an independently determined value for the misfit strain, with ($\Gamma_i \approx 0$).[30]

Fig. 14. Simulated stress, strain curves for SDE material a) 1-D material with notational constituent properties. b) 2-D material simulation obtained by assuming $\bar{\sigma}_o = 2\bar{\sigma}$, compared with experimental measurements (constituent properties relevant to SiC/CAS).

Fig. 15. The three classes of behavior found in CMCs and the associated mechanisms of stress redistribution.[40,41]

Fig. 16. A proposed mechanism map for the transition between class I and class II behaviors.[15,41]

Fig. 17. A proposed mechanism map for the transition to class III behavior.[45]

Fig. 18. Effects of holes and notches on the tensile strength predicted using LSBM. Also included are results obtained for SiC/C$_B$.[12]

Fig. 19. The notch strength of a 2-D SiC/CAS composite revealing that this is a notch insensitive material.[6]

Fig. 20. Use of LEFM to characterize the notch strength of C/C composites.[12]

NOMENCLATURE

a_i parameters found in the paper by Hutchinson and Jensen[21]
a_o length of unbridged matrix crack
b_i parameters found in the paper by Hutchinson and Jensen[21]
c_i parameters found in the paper by Hutchinson and Jensen[21]
f fiber volume fraction
f_ℓ fiber volume fraction in loading direction
$\bar{h}$ mean fiber pull-out length
ℓ_p plastic zone size
$\bar{\ell}$ mean matrix crack spacing
$\bar{\ell}_s$ mean saturation crack spacing
m shape parameter for fiber strength distribution
q residual stress in matrix in axial orientation
t ply thickness
2w plate width
E Young's modulus of composite
E_* Young's modulus of material with matrix cracks
E_f Young's modulus of fiber
E_L ply modulus in longitudinal orientation
E_m Young's modulus of matrix
E_L ply modulus in longitudinal orientation
E_s secant modulus
E_T ply modulus in transverse orientation
$\bar{E}_L$ unloading modulus
$\bar{E}_t$ tangent modulus
L mean crack spacing in 90° plies
L_g gauge length
L_o reference length
R fiber radius
S tensile strength
S_c characteristic fiber strength
S_o scale factor for fiber strength
S_p pull-out 'strength'
S_u UTS subject to global load sharing
S_* tensile strength in presence of a flaw or notch

T shear strength

α compliance coefficient
β residual stress coefficient
γ shear strain
δ displacement
δ_c characteristic length
$\delta\varepsilon$ hysteresis loop width
ε strain
ε_e elastic strain
ε_p permanent strain
ε^* contribution to permanent strain caused by matrix cracks
ν Poisson's ratio (assumed to be the same for fiber and matrix)
λ pull-out coefficient
σ stress
σ_R residual stress in 0/90 material along fiber axis
σ_τ lower bound stress for tunnel cracking
$\bar{\sigma}_i$ debond stress
$\bar{\sigma}_{mc}$ matrix cracking stress
$\bar{\sigma}_o$ stress acting on 0° plies in a 2-D material
$\bar{\sigma}_p$ peak stress
$\bar{\sigma}_s$ saturation stress
$\bar{\sigma}_T$ misfit stress
τ interface sliding resistance
χ matrix cracking coefficient
Γ fracture energy
Γ_i interface debond energy
Γ_o dissipation associated with traction law
Γ_m matrix fracture energy
Ω misfit strain

PLASTIC ANISOTROPY IN $MoSi_2$ SINGLE CRYSTALS

T. E. Mitchell and S. A. Maloy

Center for Materials Science
Los Alamos National Laboratory
Los Alamos, New Mexico 87545

Abstract

Single crystals of $MoSi_2$ are an order of magnitude stronger when compressed along [001] than along any other orientation. This is because the easy slip systems, {011}<100> and {110}<111>, have a zero Schmid factor acting on them so that harder slip systems are forced into operation. We find that [001] crystals compressed at 1000°C yield by slip on {103}<331>. TEM shows that the 1/2<331> dislocations tend to decompose into 1/2<111> and <110> dislocations. This decomposition process apparently inhibits the mobility of 1/2<331> dislocations at higher temperatures and another system, {101}<111>, becomes operative at 1300°C and above. [021] crystals have been tested for comparison and are found to yield at much lower stresses on the easy systems. In the design of advanced high temperature structural materials based on $MoSi_2$, the large plastic anisotropy should be used to advantage.

This research was supported by the US Department of Energy, Office of Basic Energy Sciences.

Critical Issues in the Development of High Temperature Structural Materials
Edited by N.S. Stoloff, D.J. Duquette and A.F. Giamei
The Minerals, Metals & Materials Society, 1993

Introduction

Molybdenum disilicide ($MoSi_2$) has attracted considerable interest in recent years because of its potential as a high temperature structural material due to its good oxidation resistance and strength at high temperatures[1]. It is brittle at low temperatures with a modest fracture toughness of around 3 MPa $m^{1/2}$; this can be improved by a factor of 2 or 3 by additions of ZrO_2 or SiC[1]. $MoSi_2$ is generally reported to become ductile at temperatures above ~1000°C. However, Aikin[2] reports a brittle-to-ductile transition temperature of 1400°C; it is likely that the transition temperature depends on the silica content at the grain boundaries[3].

Crystallography

$MoSi_2$ has the tetragonal $C11_b$ structure, space group I4/mmm, with unit cell parameters a=3.204Å and c=7.848Å. Each Mo atom is surrounded by 10 Si atoms at a distance of 2.616Å and each Si atom is surrounded by 5 Mo atoms and 5 Si atoms also at a distance of 2.616Å; the crystal structure is illustrated in Figure 1. Elementary dislocation theory suggests that mobile dislocations should have Burgers vectors with the shortest lattice vectors and move on the closest packed planes[4]. Burgers vectors of possible perfect dislocations are given in Table I[5].

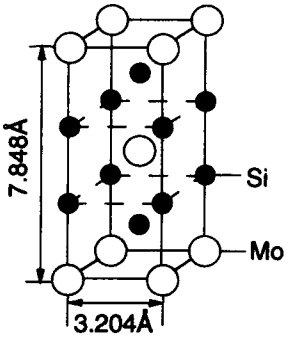

Figure 1 - Tetragonal unit cell of $MoSi_2$.

Table I Burgers Vectors of Possible Perfect Dislocations in $MoSi_2$

Burgers Vector	|b| (Å)	Possible slip planes
<100>	3.204	{011}, {013}, {010}, (001)
1/2<111>	4.531	$\{1\bar{1}0\}$, $\{0\bar{1}1\}$
<110>	4.531	$\{1\bar{1}0\}$, (001)
1/2<331>	7.848	$\{1\bar{1}0\}$, $\{0\bar{1}3\}$
[001]	7.848	{100}, {110}

The <100> dislocations have by far the shortest Burgers vectors and these dislocations are indeed commonly observed in deformed $MoSi_2$. However, other dislocations are required to fulfill the Von Mises criterion in polycrystalline materials[6] or single crystal orientations where the Schmid factor is zero (e. g., [001]). The next two Burgers vectors in Table I, 1/2<111> and <110>, have identical magnitudes, as do the last two, 1/2<331> and [001]. The reason for the identical magnitudes is that the c/a ratio in $MoSi_2$ is essentially exactly $\sqrt{6}$ and the {110} planes

have hexagonal symmetry, as illustrated in Figure 2. (The unit cell has overall tetragonal symmetry because the AB stacking of the {110} planes destroys the hexagonal symmetry). 1/2<111> and <110> dislocations have both been reported, although the latter probably occur by dislocation reactions[5, 6]. The occurrence of 1/2<331> dislocations has also been documented, in spite of their long Burgers vectors[7, 8]. An early description of [001] dislocations[9] has not been confirmed. Table I also gives potential slip planes for each of these dislocations and their spacings are listed in Table II.

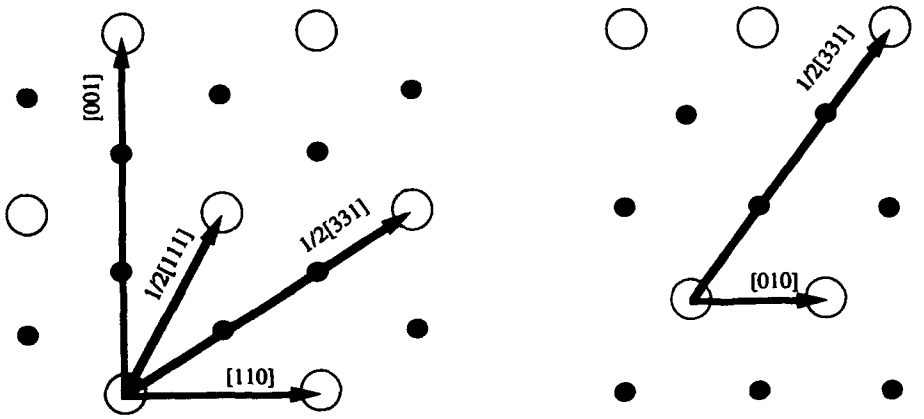

Figure 2 - {110} and {103} planes of $MoSi_2$. Both are stoichiometric and {110} has hexagonal symmetry.

Table II Spacings of Possible Slip Planes in $MoSi_2$

Slip Plane	Stoichiometric?	Spacing(Å)	Possible Burgers Vectors
{1$\bar{1}$0}	Yes	2.266	1/2<111>, <110>, 1/2<331>, [001]
{0$\bar{1}$3}	Yes	2.026	<100>, 1/2<331>
{100}	Yes	1.602	<010>, [001]
(001)	No	1.308	<100>, <110>
{011}	No	0.988	<100>, 1/2<111>

Table II also indicates whether the plane is stoichiometric, i. e., whether a given plane contains atoms in the correct $MoSi_2$ proportion or consists of alternate layers of Mo and Si atoms. The choice of slip systems is still not intuitively obvious from Tables I and II. Dislocations with <100> Burgers vectors might be expected to glide on {013} planes, which have the largest available spacing, followed by {010} and (001): instead they choose to glide on {011} planes[6, 10]. Dislocations with 1/2<111> Burgers vectors should and in fact do glide on {110} planes; we report below that they may also glide on {011} planes at high temperatures for [001] crystals. Dislocations with 1/2<331> Burgers vectors have available to them the widely spaced stoichiometric {110} and {013} glide planes; both of these planes have been reported in the literature[7], although recent observations on [001] crystals deformed at 1000°C and on polycrystalline material deformed at 900°C suggest that {013} is the operative slip plane[8, 11].

Figure 3 shows diagrams of some likely slip systems in $MoSi_2$ - {011}<100>, {1$\bar{1}$0}<111>, {0$\bar{1}$3}<331> and {0$\bar{1}$1}<111>. As will be shown in the present paper, each of these systems operates in different regimes of orientation and temperature. In particular, for $MoSi_2$ crystals with the [001] orientation, the first two easy systems are suppressed, necessitating the operation of other systems. Because of this, $MoSi_2$ is highly anisotropic and, as first shown by Umakoshi et al[7], [001] crystals have a much higher yield stress. Here we will extend these measurements of yield stress anisotropy, using transmission electron microscopy to unfathom some of the mysteries of dislocation behavior in $MoSi_2$.

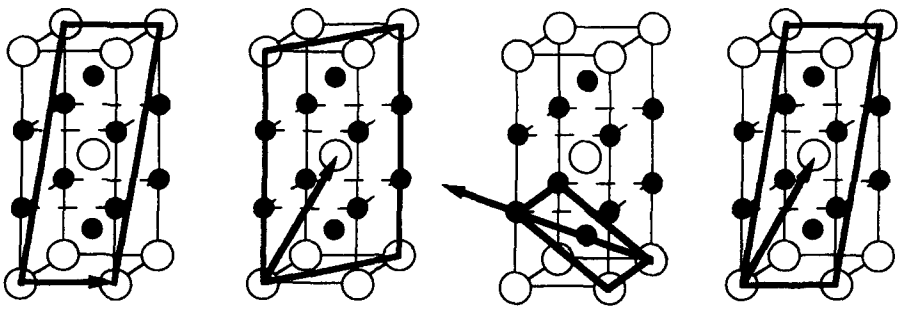

Figure 3 - Some possible slip systems in $MoSi_2$.

Experimental

Single crystals of $MoSi_2$ were grown by J. Garrett of McMaster University using the Czochralski technique at a rate of 180 mm/h. Specimens were oriented by the Laue back-reflection x-ray technique and cut into parallelepiped compression samples 1.5mmx1.5mmx5mm with a diamond saw; final polishing of the faces was with 1μm grade diamond. The compression axis was selected to be the hard [001] orientation for one set of samples and a soft [021] orientation for another set. These orientations are shown in the stereographic projection in Figure 4 which also includes the poles of all the possible slip planes and directions. In addition, one sample was 10° off the [001] orientation towards [110]. Compression testing was performed under displacement control at temperatures from 1000 to 1600°C using one of two rigs. One compression rig had alumina rams and single crystal YAG pads and was operated in argon with a strain rate of $10^{-5}s^{-1}$.The other rig was made of thoriated tungsten, had SiC pads, operated in vacuum and gave a strain rate of $10^{-4}s^{-1}$. TEM thin foils were prepared using standard techniques and examined in a Philips CM30 transmission electron microscope operating at 300kV in order to characterize the dislocation microstructures.

Results and Discussion

Yield Stresses

Yield stresses for all of the crystals tested to date are shown plotted against temperature in Figure 5; included are data for the two orientations, [001] and [021], and the two strain rates, 10^{-4} and $10^{-5}s^{-1}$.The data are complicated and detailed discussion will be given below. However, some general observations can be made at this point. Firstly, the [001] specimens are an order of magnitude stronger than the [021] specimens (this is even more anisotropic than the data reported by Umakoshi et al[7]). Secondly, the yield stresses decrease steeply with increasing temperature, except for complications between 1000 and 1300°C for the [001] orientation to be discussed later. Thirdly, the yield stresses for the [001] orientation are highly dependent on strain rate with a factor of two or more difference in stress level between 10^{-4} and $10^{-5}s^{-1}$; such a strain rate dependence corresponds to a stress exponent of around 3.

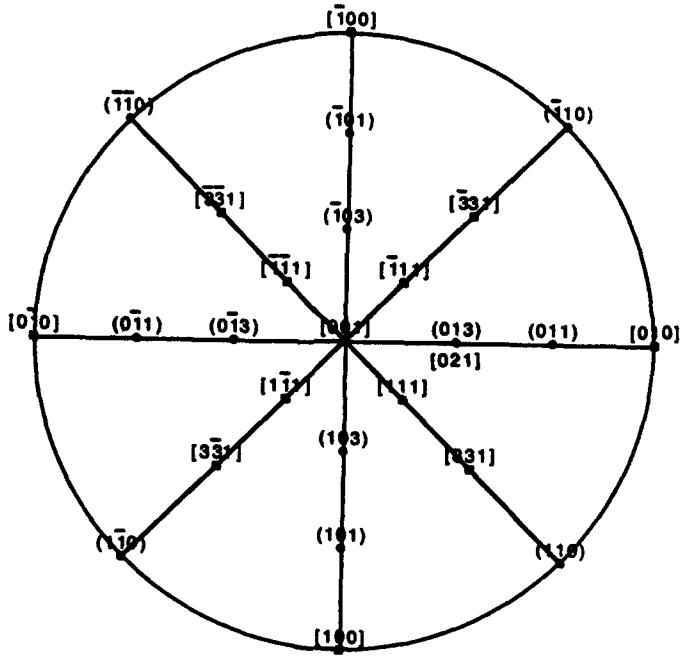

Figure 4 - Stereographic projection of $MoSi_2$, showing the [001] and [021] compression axes and the poles of the slip planes (filled-in circles) and slip directions (squares).

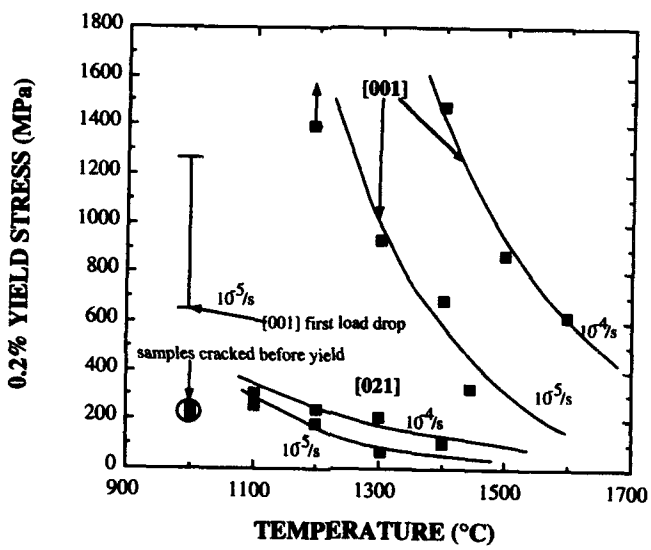

Figure 5 - Yield stress plotted against temperature for two orientations and the two strain rates.

Observations on Individual Specimens

[001] Specimen Tested at 1000°C. This specimen was tested at a strain rate of $10^{-5}s^{-1}$. It yielded with a small load drop at 700 MPa, followed by increased stress and further load drops until the load limit of the testing machine was reached at a stress of 1400 MPa. The total strain was

measured after the test to be only 0.3% and so the yield stress is indicated in Figure 5 as a bar extending from 700 MPa at the first load drop to 1400 MPa at the load limit. Slip lines were detected on the surface corresponding to {013} planes. Dislocations with 1/2<331> Burgers vectors were found by TEM (see below) and so the slip system is concluded to be {013}1/2<331>. This system has a Schmid factor of 0.39 for the [001] compression axis while the easy {011}<100> and {110}1/2<111> systems have zero Schmid factors. A thin foil was cut parallel to the ($\bar{1}03$) slip plane and a typical area is shown in Figure 6. A **g.b** analysis was conducted and the results are indicated in Figure 6.

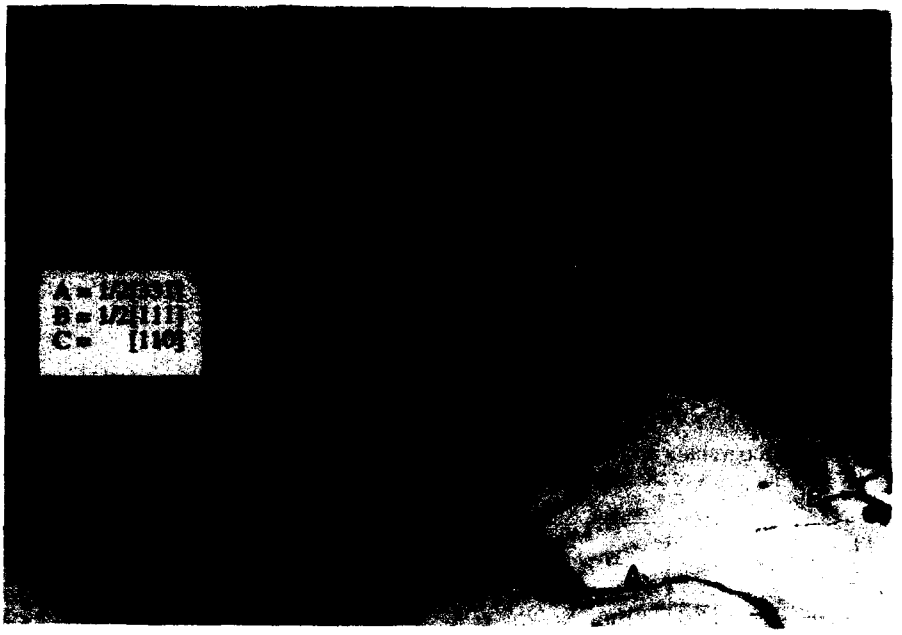

Figure 6 - Dislocation microstructure in the ($\bar{1}03$) slip plane of [001] $MoSi_2$ deformed at 1000°C.

It is seen that the microstructure consists of dislocations with 1/2[331], 1/2[111] and [110] Burgers vectors. The 1/2[331] dislocations mostly lie in the [331] direction, i. e., they are screw dislocations. Many of the 1/2[111] and [110] dislocations lie in pairs along the [010] direction which are connected to the 1/2[331] screw dislocations. It is concluded that the 1/2[331] dislocations decompose by a reaction of the type:

$$1/2\langle 331\rangle \dashrightarrow 1/2\langle 111\rangle + \langle 110\rangle \qquad (1)$$

This reaction is energetically favorable because the angle between the Burgers vectors of the product dislocations is 120°. We call equation (1) a decomposition reaction rather than a dissociation reaction because all of the dislocations have perfect Burgers vectors and no faults are involved. The highly angular nature of the dislocations in Figure 6 with dislocations lying along the [331] and [010] directions indicates that glide is controlled by a strong Peierls stress. The decomposition presumably occurs after the 1/2[331] dislocations have stopped gliding. The dislocation products tend to stay in pairs because they have low mobility even though they repel each other; the [110] dislocations have a zero resolved stress acting on them while the 1/2[111] dislocations have a zero Schmid factor in their preferred ($1\bar{1}0$) plane and must have a very high Peierls stress opposing their motion in the ($\bar{1}01$) plane. Other features in Figure 6 are the prominent rows of dislocation loops which were analysed to have [100] Burgers vectors and lie along the [010] direction. This is shown even more clearly in Figure 7 which is from a foil cut

perpendicular to the slip plane. The strings of loops evidently form from dipoles and we envision the following series of steps in their formation:

1. 1/2[331] dipoles form by self-trapping of dislocations of opposite sign lying along [010].
2. The decomposition reaction (1) occurs.
3. The 1/2[111] dislocations of opposite sign annihilate by glide on the ($\bar{1}$01) plane leaving a [110] dipole.
4. The decomposition reaction [110] ---> [100] + [010] occurs which is energetically neutral.
5. The [010] dislocations which are screw in character glide in the (101) plane to annihilate and leave a [100] pure edge dipole.
6. The [100] dipole undergoes fluctuations induced by pipe diffusion and self-climb to produce a string of loops lying along the [010] direction.

Note that this process involves only localized diffusion rather than bulk diffusion such as occurs at higher temperatures, as described below.

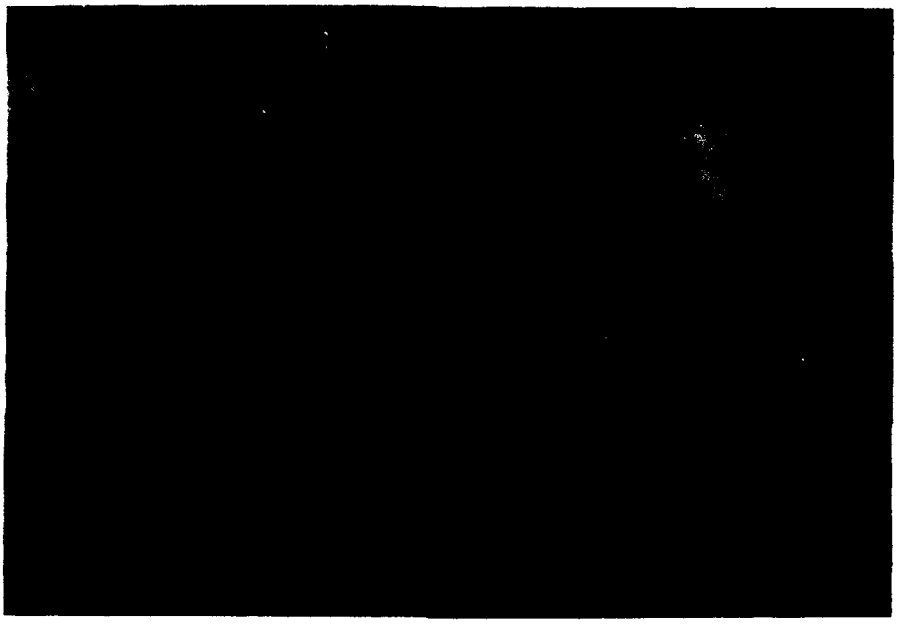

Figure 7 - [001] $MoSi_2$ deformed at 1000°C viewed perpendicular to the ($\bar{1}$03) slip plane.

[001] Specimens Deformed at 1200°C. Specimens compressed at this temperature showed no signs of yielding even when taken to the limit of the testing machine corresponding to a stress of 1400 MPa, as indicated by the arrow in Figure 4. This surprising result suggests that the mobility of the 1/2<331> dislocations decreases with increasing temperature. A possible explanation for this is that the the decomposition reaction (1) occurs before a significant amount of glide can occur. As pointed out before, the <100> dislocations have no resolved stress acting on them and the 1/2<111> dislocations are required to move on {011} where they evidently experience a high Peierls stress. It is also worth returning to the observation that yielding at 1000°C occurs in a series of load drops, suggesting that 1/2<331> dislocations nucleate at the surface and move into the specimen in bursts. The nucleation event itself may be inhibited by the decomposition reaction at higher temperatures, thus preventing plastic flow. The key to understanding this behavior is that the 1/2<111> dislocations only become mobile at temperatures of 1300°C and above, as described next.

[001] Specimens Deformed at 1300 to 1600°C. Specimens compressed in the high temperature regime yielded smoothly with none of the load drops characteristic of the 1000°C test. Figure 4 shows that the yield stresses are very high but decrease rapidly with increasing temperature from

950 MPa at 1300°C to 300 MPa at 1500°C for the $10^{-5}s^{-1}$ strain rate and from 1500 MPa at 1400°C to 600 MPa at 1600°C for the $10^{-4}s^{-1}$ strain rate. Surprisingly, slip lines could not be detected on the surfaces of the crystals after each test, implying that slip occurs on a fine scale. Figure 8 shows a typical microstructure for a crystal compressed at 1500°C. Dislocations occur mostly in small-angle tilt boundaries and **g.b** analysis shows that the Burgers vectors are all either <100> or <110>. Thus the boundaries are on {100} or {110} planes and consist of <100> or <110> edge dislocations respectively. However, both <100> and <110> dislocations have zero Schmid factors for the [001] compression axis and so they must have formed by dislocation reaction. In view of the observation that the 1/2<331> dislocations are only mobile at temperatures around 1000°C, we propose that deformation is being produced by the motion of 1/2<111> dislocations, most probably on {101} planes. There are 8 of these slip systems, all equally stressed for the [001] compression axis, with a Schmid factor of 0.33. The <100> and <110> dislocations then arise from interactions such as

$$1/2[1\bar{1}1] + 1/2[11\bar{1}] \text{ ---> } [100] \qquad (2)$$

and

$$1/2[111] + 1/2[11\bar{1}] \text{ ---> } [110] \qquad (3)$$

Both reactions (2) and (3) are energetically favorable and and can give rise to sessile edge dislocations. For example, in reaction (2), if the reacting dislocations lie respectively on $(\bar{1}01)$ and (101), then the product [100] dislocation will lie along [010]; these are therefore pure edge dislocations which can then climb into low energy tilt boundaries to produce the observed microstructure.

Figure 8 - Microstructure in [001] $MoSi_2$ deformed 1% at 1500°C and $10^{-4}s^{-1}$, (001) foil.

[021] Specimens Deformed at 1000 to 1200°C. Specimens compressed at 1000°C were always found to crack before yielding. However, at 1100°C and above, yielding took place smoothly and stresses an order of magnitude below those for [001] crystals. Slip traces were detectable and were found to correspond to the {110} slip plane. A typical dislocation microstructure is shown in Figure 9 for a [021] crystal deformed 1% at 1100°C; the foil was cut parallel to the observed

$(1\bar{1}0)$ slip traces. Two sets of dislocations were identified in Figure 9 by **g.b** analysis: the dislocations in one set have a 1/2[111] Burgers vector and lie along [110], corresponding to the expected $(1\bar{1}0)$ slip plane; the others have a [010] Burgers vector and lie along [101], which means that they are pure edge dislocations with a $(\bar{1}01)$ slip plane. It is concluded that [021] is a suitable orientation to activate both the {110}1/2<111> and {101}<010> slip systems. The latter has a lower Schmid factor, implying that it has a lower critical resolved shear stress, as discussed later.

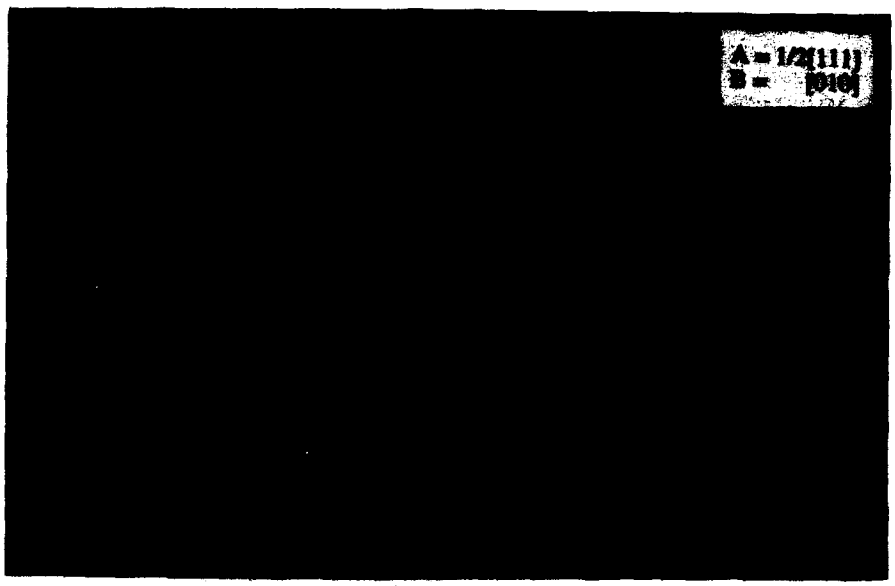

Figure 9 - Microstructure in [021] $MoSi_2$ deformed 1% at 1100°C, $10^{-5}s^{-1}$, $(1\bar{1}0)$ foil.

[021] Specimens Deformed at 1300 and 1400°C. With increasing temperature, a greater proportion of <100> dislocations were found and less 1/2<111> dislocations. A typical microstructure for a crystal deformed at 1300°C is shown in Figure 10. The dislocations are

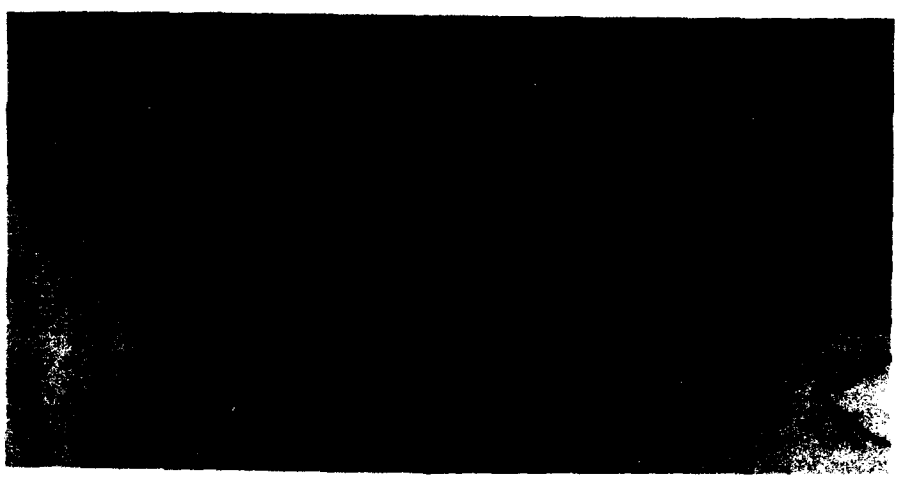

Figure 10 - Dislocation Microstructure in [021] $MoSi_2$ deformed 1% at 1300°C, $10^{-5}s^{-1}$.

much less angular than at 1100°C, indicating an increase in the amount of climb. In fact, the [010] dislocations tend to lie parallel to [100] at 1300°C, compared with [101] at 1100°C; this could mean that the glide plane has switched to (001) at the higher temperature but climb seems a more likely explanation in view of the tilt boundaries that are produced in the [001] specimens at the same temperature.

Specimen 10° off [001] Deformed at 1400°C. The compression axis of this specimen was 10° off the [001] orientation towards [110] and was prepared in order to test the sensitivity of the slip behavior to the exact orientation. The specimen was tested at a strain rate of $10^{-4}s^{-1}$ and yielded at a stress of 1200 MPa followed by a drop in stress to 1000 MPa; this compares with 1500 MPa for the exact [001] specimen in Figure 4. A typical dislocation microstructure is shown in Figure 11. All of the dislocations were found by **g.b** analysis to have 1/2[111] Burgers vectors (except for the partial dislocations described below). They lie largely along the [110] direction, implying that the slip plane is $(1\bar{1}0)$. The Schmid factor for the $(1\bar{1}0)1/2[111]$ system is zero for an exact [001] compression axis but it is 0.15 for the actual axis 10° off [001]. Because of the large disparity between the critical resolved shear stresses for the motion of 1/2<111> dislocations on $\{1\bar{1}0\}$ and $\{\bar{1}01\}$ planes, this Schmid factor is enough to activate the easier system in spite of the low resolved stress acting on it. The observation of partial dislocations and stacking faults in Figure 11 is unique to this investigation; attempts were made to image dissociated dislocations by weak-beam microscopy in all the previous specimens, without success. The partials in Figure 11 were identified by **g.b** analysis and the following dissociation reactions were found:

$$1/2[111] \text{ ---> } 1/3[001] + 1/6[331] \quad (4)$$

and

$$1/2[111] \text{ ---> } 1/6[\bar{3}01] + 1/3[001] + 1/2[010] \quad (5)$$

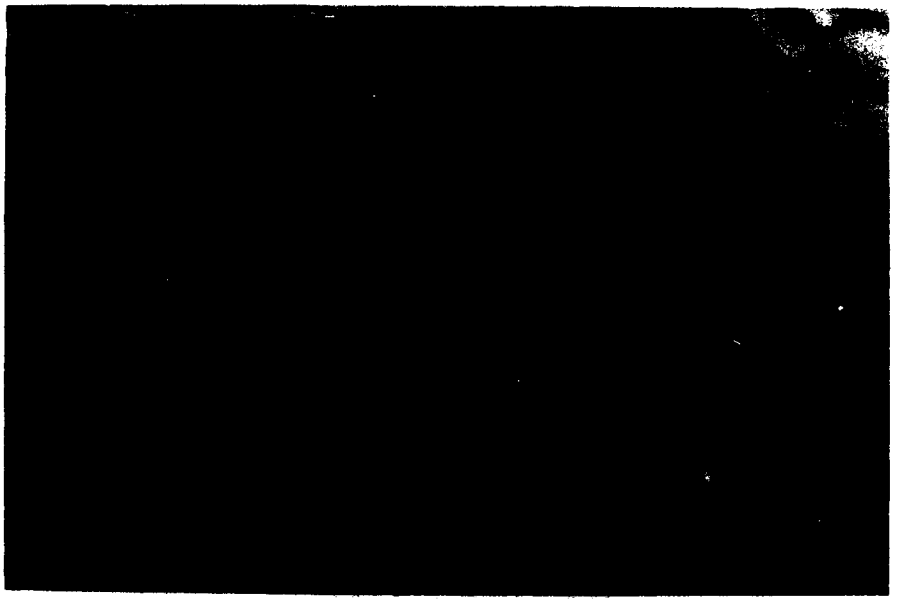

Figure 11 - Dislocation microstructure in $MoSi_2$ oriented 10° off [001] deformed 4% at 1400°C

Reactions (4) and (5) are illustrated in Figure 12; both involve a decrease in energy and both have faults associated with them. The partials in reaction (1) have Burgers vectors joining Mo and Si atoms and so the fault is an anti-phase boundary(APB). The outer partials in reaction (5) produce complex stacking faults. In addition, both of the dissociations are produced by climb; for example, the APB in (4) lies in the (001) plane and so the 1/3[001] partials must have moved by

climb. These dissociations are still under study but our present conclusion is that they occur after the 1/2<111> dislocations have become immobilized and are probably unimportant to the glide process.

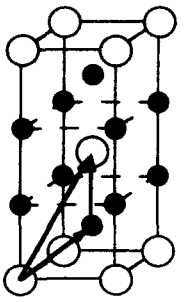

1/2<111> ->1/6<331>+1/3<001>

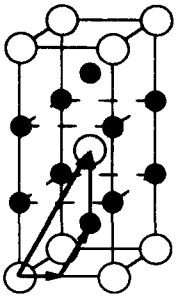

1/2<111> -> 1/2<010> + 1/3<001> + 1/6<301>

Figure 12 - Unit cell of $MoSi_2$ showing the partials in reactions (4) and (5).

Critical Resolved Shear Stresses

It is apparent that glide occurs under various circumstances on four systems - {011}<100>, {110}1/2<111>, {013}1/2<331> and {011}1/2<111>. It is therefore important to know the critical resolved shear stress (CRSS) for each of these systems as a function of temperature, in order to be able to predict the slip behavior as a function of orientation. CRSS values have been calculated from the yield stresses in Figure 4 by using the appropriate Schmid factor and the slip system inferred from the TEM investigations. The results are shown in Figure 13 where CRSS is plotted against temperature for the four slip systems.

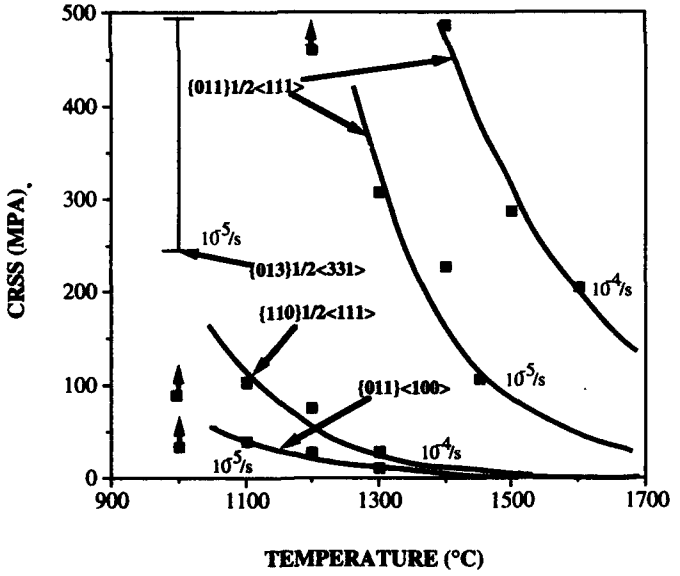

Figure 13 - CRSS versus temperature for the four slip systems in $MoSi_2$

Several assumptions have been made in calculating the CRSS data in Figure 13:

1. For the [021] orientation, {011}<100> and {110}1/2<111> slip are equally activated by the applied stress so that, because {011}<100> has the lower Schmid factor, it has the lower CRSS.

2. Slip on the {013}1/2<331> system only occurs around 1000°C for the exact [001] orientation and the effective CRSS probably increases with increasing temperature because of the instability of the 1/2<331> dislocation.

3. At some temperature between 1000°C and 1300°C, {011}1/2<111> slip becomes easier than {013}1/2<331> slip and becomes dominant for [001] compression at higher temperatures.

The data in Figures 4 and 13 illustrate the tremendous plastic anisotropy in $MoSi_2$. The [001] compression axis is much stronger than any other orientation but it is essential to maintain the orientation to within a few degrees to avoid activating any of the easy systems. This is true not only for single crystal $MoSi_2$ but also for polycrystalline material with a strong [001] texture produced by some suitable mechanical or melt processing technique. This is a preliminary report and the investigation of the mechanical properties and slip behavior of single crystal $MoSi_2$ is continuing[12].

References

1. A. K. Vasudevan and J. J. Petrovic, "A Comparative Overview of Molybdenum Composites," Mater. Sci. Eng., A155 (1992), 1-17.

2. R. M. Aikin, 1992, "On the Ductile-to-Brittle Transition in $MoSi_2$," Scripta metall. mater., 26 (1992), 1025-1030.

3. S. R. Srinivasan, R. B. Schwarz and J. D. Embury, "Ductile-to-Brittle Transition in $MoSi_2$,"High Temperature Ordered Intermetallic Alloys V, ed. I. Baker, J. D. Whittenberger, R. Darolia and M. H. Yoo (Pittsburgh: Materials Research Society, 1993).

4. J. P. Hirth and J. Lothe, Theory of Dislocations (New York: Wiley, 1982).

5. O. Unal, J. J. Petrovic, D. H. Carter and T. E. Mitchell, "Dislocations and Plastic Deformation In Molybdenum Disilicide," J. Amer. Ceram. Soc., 73 (1990), 1752-1757.

6. S. A. Maloy, A. H. Heuer, J. J. Lewandowski and T. E. Mitchell, "On the Slip Systems in $MoSi_2$," Acta metall. mater., 40 (1992), 3159-3165.

7. Y. Umakoshi, T. Sakagami, T. Hirano and T. Yamane, 1990, "High Temperature Deformation of $MoSi_2$ Single Crystals with the $C11_b$ Structure," Acta metall. mater., 38 (1990), 909-915.

8. S. A. Maloy, T. E. Mitchell, J. J. Lewandowski and A. H. Heuer, "{103}<331> Slip in $MoSi_2$," Phil. Mag. Lett., in press(1993).

9. F. W. Vahldiek and S. A. Mersol, "Phase Relations and Substructure in Single-Crystal $MoSi_2$," J. Less-Common Metals, 15 (1968), 165-171.

10. P. H. Boldt, J. D. Embury and G. C. Weatherly, "Room Temperature Microindentation of Single-Crystal $MoSi_2$," Mater. Sci. Eng., A155 (1992), 251-258.

11. H. Kung, A. Basu and A. K. Ghosh, "Dislocation Structures of Monolithic MoSi2 Developed during High Temperature Deformation," Scripta metall. mater., submitted (1993).

12. S. A. Maloy, "Dislocations and Mechanical Properties of Molybdenum Disilicide Single Crystals," Ph. D. Thesis (Cleveland, Ohio: Case Western Reserve University, 1993).

MICROSTRUCTURAL EFFECTS ON CREEP STRENGTHENING OF $MoSi_2$ MATRIX COMPOSITES

Amit K. Ghosh and Ajoy Basu
Department of Materials Science & Engineering,
University of Michigan, Ann Arbor, MI 48109-2136

Abstract

$MoSi_2$ intermetallics, in monolithic form or reinforced with SiC particulates and whiskers, have potential application in future gas turbine engines. In this paper we have examined the creep strengthening mechanism in these materials, and the influence of microstructural size, the distribution of SiC reinforcements, and the effect of stress state within the temperature range of 1100 to 1400°C. The matrix grain size has been found to have a significant effect on creep rate for grain sizes less than 30 μm. A model proposed to explain this behavior suggests that intense deformation occurs in grain corners during the boundary sliding process. Results obtained from tension and compression tests indicate that while creep by dislocation climb-glide dominates the matrix behavior as in a metallic material, progressive microcracking within the reinforcement phase, the associated grain boundary cavitation and glassy phases at the grain boundary can introduce a weakening effect. Studies with the particulate and whisker reinforced materials have revealed a reinforcement aspect ratio effect on creep strengthening.

Introduction

The silicides of refractory metals such as Mo, Nb and W have potential as high temperature structural materials as well as matrix materials for composites with service capabilities above 1000°C. Of these materials, molybdenum disilicide exhibits excellent high temperature oxidation resistance, approaching that of SiC, because of the formation of a protective silica film [1-2]. In spite of its high melting point (2030°C), at ~1000°C $MoSi_2$ begins to yield and exhibit dislocation motion like metals do [3]. At an even higher temperature (~1200°C), the yield strength of $MoSi_2$ drops further and its creep resistance is also reduced [4]. Aikin and others have claimed that grain boundary SiO_2 (a viscous layer) is responsible for lower strength of these materials [5-6]. Consequently, attempts are being made to produce clean alloys by addition of SiO_2 removers (e.g., C, Er, CaO, etc.) [7-10] and to improve the mechanical properties of $MoSi_2$ by synthesizing composites with hard ceramic phases as well as ductile metallic phases [10-12]. SiC reinforcement has shown excellent bonding characteristics with $MoSi_2$ [9], and it also rids the SiO_2 inclusions from $MoSi_2$ grain boundaries via chemical reaction. Furthermore, SiC whiskers have been previously shown to have potential for creep strengthening of $MoSi_2$ [13-14]. It was also shown that grain boundary microcracks can be present within such composites [9], thus suggesting that the creep behavior might be a function of the imposed stress state - tensile vs. compressive. When reinforcements are distributed in a fine scale through the microstructure, they can change the grain size of the matrix material as well. The objectives of this study were to examine the effects of reinforcement type, damage, and the microstructural scale in $MoSi_2$ composites containing SiC particulate and whisker reinforcements, and their effects on tensile and compression creep behavior.

Experimental Work

Material Synthesis

$MoSi_2$ powder (-325 mesh) from Cerac was used for consolidating monolithic $MoSi_2$. Particulate and whisker reinforced composites were prepared by mixing $MoSi_2$ powder respectively with powders and whiskers of SiC, (20 vol% in each case). Table 1 lists the

Critical Issues in the Development of High Temperature Structural Materials
Edited by N.S. Stoloff, D.J. Duquette and A.F. Giamei
The Minerals, Metals & Materials Society, 1993

source of the constituents and their particle size. For the SiC_p composites, a slurry milling approach was used to develop a homogeneous intimate mixture of fine scale constituents. In the case of SiC whisker reinforcement, ultrasonic blending was used which led to greater agglomeration of reinforcements and a larger interparticle spacing. The powder mixtures were hot pressed in a graphite die at 1700°C for 2 hours under 28 MPa pressure. Hot pressed billets were cut and a portion HIP'ed at 1700°C for 90 min under 200 MPa pressure. The oxygen content of the monolithic and SiC_p composites were respectively 0.6 wt% and 4 wt%.

TABLE I.
SIZE AND SOURCE OF MATRIX AND REINFORCEMENTS

MATERIAL	AVE. PARTICLE SIZE	SOURCE
$MoSi_2$	5 μm	Cerac, Inc. Milwaukee, WI
SiC_p	0.7 μm	H.C. Stark Germany
SiC_w	0.5 μm dia. 50 μm length	Tateho Chemical Japan

Characterization of Microstructure

The optical micrographs of $MoSi_2$ and the two composites are shown in Fig. 1. Grain boundaries were revealed in cross-polarized light. The average grain size of monolithic $MoSi_2$ was 30 μm, that of SiC_p reinforced material was 3 μm, and SiC_w reinforced material was 7 μm. The monolithic material showed small spherical SiO_2 particles (not a continuous film) on the grain boundaries and a small amount of porosity, the total volume of both was approximately 5%. Previous work with high resolution TEM showed that the interface between SiC and $MoSi_2$ is free from contaminants without a special orientation relationship. The reinforcement agglomerates were always located on grain boundaries and a considerable amount of void formation was found within the agglomerated regions (see Fig. 2). The void density was approximately 6%.

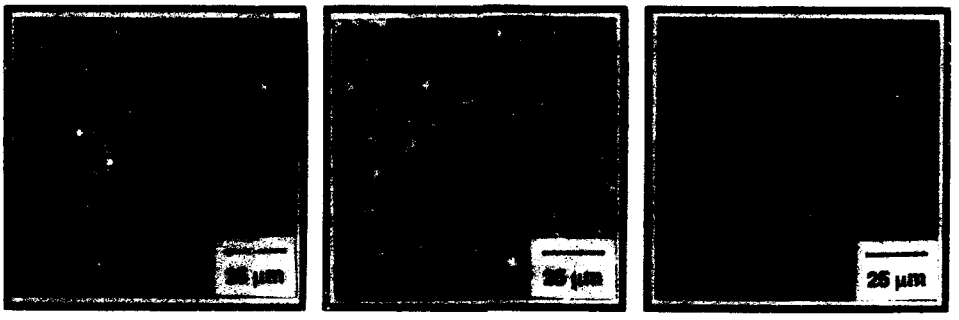

Fig. 1. Microstructures of hot-pressed $MoSi_2$ and $MoSi_2$/SiC composites.

Compression Tests

Rectangular samples, 3 mm x 3 mm x 6 mm, were cut from the billets and two types of compression tests were conducted in the temperature range of 1100-1400°C by pressing the samples between rigid SiC platens in an argon environment. The tests were conducted on an Instron machine fitted with a Centorr furnace also in a high purity argon environment. The first set of tests were step strain rate tests in which the samples were first strained at a strain rate of $10^{-4}s^{-1}$ to a steady level of stress, followed by decremental step strain rate tests. Steady stress values were achieved at each strain rate level which were subsequently used to plot log (strain rate) vs. log (stress) plots. Constant stress creep tests were also performed by subjecting separate samples to controlled load levels. A constant stress on the creeping specimen was maintained by increasing this load with continued creep strain under the assumption of constant specimen volume. Crosshead displacement corrected for machine compliance was used to determine sample strain. Normal creep curves with primary, secondary and tertiary regions were observed. Minimum creep rates were determined from the strain-time plots, and plotted as a function of stress.

Tensile Tests

From the cylindrical billets, slices were cut perpendicular to their axes and a gauge section with large grip tabs was fabricated by diamond grinding. The specimen cross-section was 3 mm x 3 mm and the gauge length was 6 mm. A special SiC grip was fabricated to pull the tabs from beneath them (i.e. loading on edge not face). Constant stress creep tests were conducted in a manner described previously for the compression tests. Typically several load levels were explored from each specimen. The onset of tertiary creep (or fracture) was found to occur at much smaller strain levels and more abruptly than in compression.

Fig. 2. SEM photograph of $MoSi_2/SiC_p$ composite showing microvoids within regions of SiC_p agglomerates.

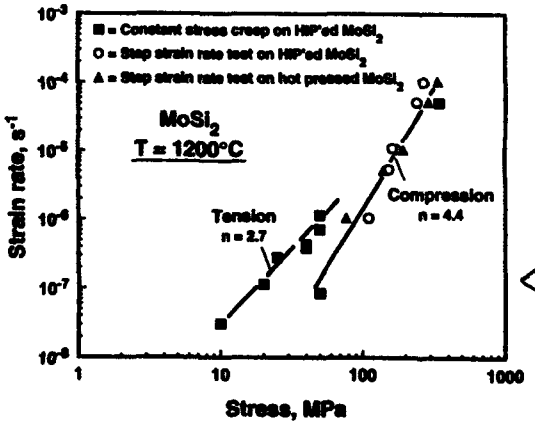

Fig. 3. Step strain rate and creep test results for $MoSi_2$ under compression and tension loading at 1200°C.

Experimental Results and Discussion

Creep Behavior and Mechanisms

Figure 3 shows strain rate vs. stress data for $MoSi_2$ at 1200°C from compression creep and step-strain rate tests as well as from tension creep tests. The results include hot-pressed and HIP'd materials, and exhibit some degree of scatter. An average curve drawn through the compression data points shows a stress exponent (n) for creep of about 4.3 at high stresses and 3.0 at the low stresses, which is indicative of dislocation creep [15-16]. The tension data shows a 40-50% weakening relative to compression, and it has an n value of 2.7 (at low stresses). The lower n for tension may be a result of concurrent grain boundary microcracking which was observed in this material (Fig. 4). Such microcracking in the form of wedge cracks is possibly diffusion assisted. Fig. 5 shows step-strain rate test data for 1100°C, 1300°C, and 1400°C as compared with the compression curve for 1200°C from Fig. 2. This family of curves clearly illustrates a decreasing n with increasing temperature. However, at 1100 and 1200°C (homologous temperatures of 0.60-0.65), the observed creep behavior fits climb-controlled creep models of Weertman [15], and Weertman and Weertman [16] and also viscous glide models with stress exponents varying in the range of 3 to 4.5. A value of n = 3 was also found by Umakoshi et al. for single crystal $MoSi_2$ [17]. Transmission Electron Microscopy of dislocation structure of specimens deformed at

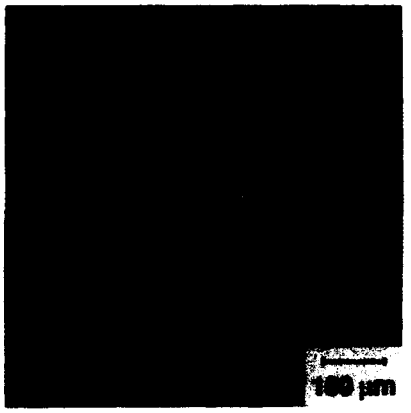

Fig. 4. Intergranular cracking during tensile creep of $MoSi_2$ at 1200°C creep strain ~ 0.9% at 50 MPa. Failure occurred when the sample was loaded to 100 MPa.

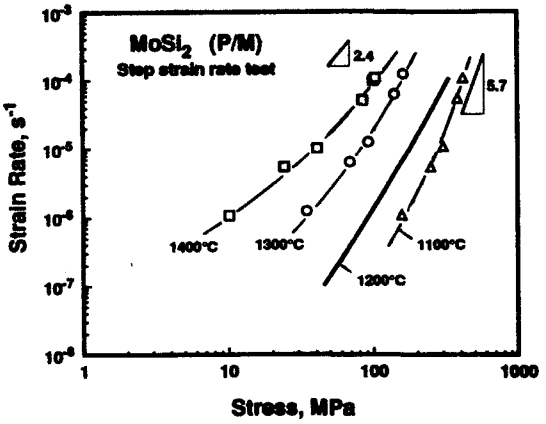

Fig. 5. Step strain rate test data in compression for $MoSi_2$ at several temperatures, compared with the curve for compression from Fig. 3. Stress exponents (n) at $10^{-4}s^{-1}$ are: 5.7 (1100°C), 3.8 (1200°C), 3.5 (1300°C) and 2.4 (1400°C).

1300°C indicated the formation of dislocation cells and subgrains (Fig. 6) as further evidence for the glide-climb process. Subgrain size was in the range of 0.5-0.2 μm and the dislocations which have been identified with this structure are {010}<100>, {011}<100>, {013}<100>, {001}<110> and {101}1/2<111>. (These results are from H. Kung of the University of Michigan) All of the high temperature data from Fig. 5 and those from Refs. [13] and [18] are plotted in the form of Zener-Hollomon parameter ($Z = \dot{\varepsilon} \exp(Q/RT)$ in Fig. 7. The data lie in a narrow band exhibiting an activation energy for creep of about 372 kJ/mol. This latter value compares with 433 kJ/mol as found by Sadananda et al. [13] and 230 kJ/mol of Alman et al.[19]. The two segments of this curve show values of n = 4.4 for the higher stress range and n = 1.7 for the lower stress range, as in Ref. [13]. The material in the present work has, however, a higher strength level. These observations strongly suggest that dislocation climb-glide creep in this material is accompanied by grain boundary sliding, and at low stresses and above 1300°C sliding is possibly accommodated by diffusional processes and occurs concurrently with cavity growth.

The effect of reinforcements on composite strength is shown in Fig. 8. Composite test results are indicated by data points along with other data shown by curves. A significant weakening relative to $MoSi_2$ (solid line) was observed for the 20% SiC_p reinforced

Fig. 6. TEM bright field micrograph of $MoSi_2$ deformed at 1300°C in compression which shows the formation of dislocation cells and subgrains. (Photo Courtesy of H. Kung.)

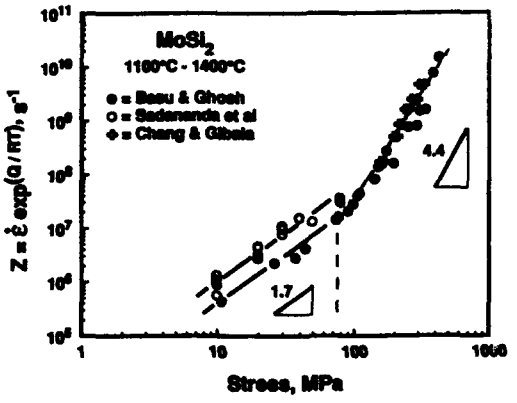

Fig. 7. Zener-Hollomon parameter, plotted against stress for all compression data on $MoSi_2$ shown in Figs. 3 and 5. The data of Sadananda et al. [13] and Chang and Gibala [18] are included for comparison. A lower value of n occurs at stresses below 72 MPa.

composite. SiC_w (20%) produced a somewhat lesser weakening effect. The data of Sadanda et al. [13] is cross-plotted to indicate that this whisker-reinforced material (fabricated at Los Alamos National Laboratory) showed substantial strengthening over monolithic $MoSi_2$. Furthermore, the data of Mason and Van Aken [20] is shown for their arc-melted $MoSi_2$-Mo_5Si_3 interlocking script microstructure eutectic composite. This also shows strengthening over the P/M $MoSi_2$ matrix. The values of n for the composites were not significantly different from that of the matrix and were in the range of 3 to 3.4.

Matrix Effects

The apparently unusual composite weakening effect in this study as well as Ref. [9] may be partly rationalized as a result of particle agglomeration, and the presence of voids or damage within the SiC clusters. However, this can account for no more than 20% loss in creep strength. Possible sources for the large strength discrepancy might then be: (i) a greater amount of grain boundary silica leading to viscous sliding of grains, and/or (ii) a grain size effect (not normally expected in the dislocation creep regime). To examine these possibilities, we plotted in Fig. 9 a collection of strain rate vs. stress data for the $MoSi_2$ matrix (without reinforcement) for various grain sizes and oxygen content from a number of sources [5, 10, 13,]. The P/M material data from Aikin [5] falls on present data (solid line), and his supercleaned XD-processed $MoSi_2$ (extremely low oxygen) [5] shows slight strengthening. Srinivasan and Schwartz [18] produced fine grain $MoSi_2$ (~ 3 μm g.s.) by mechanical milling in an inert environment. With only 0.15 wt% oxygen, the strength of

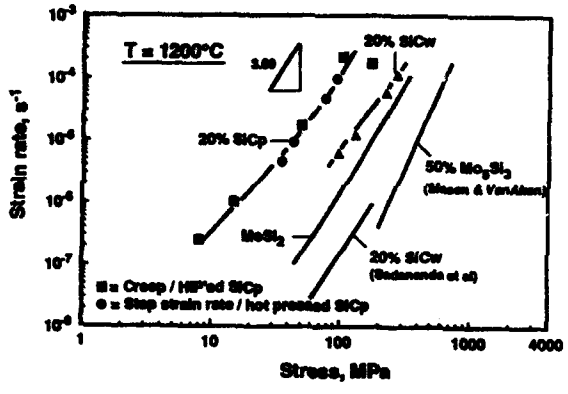

Fig. 8. Step strain rate and creep test results in compression (1200°C) for $MoSi_2$/20%SiC_p and $MoSi_2$/20%SiC_w composites (data points) compared with monolithic $MoSi_2$ from Fig. 3 and from Refs. 13 and 20.

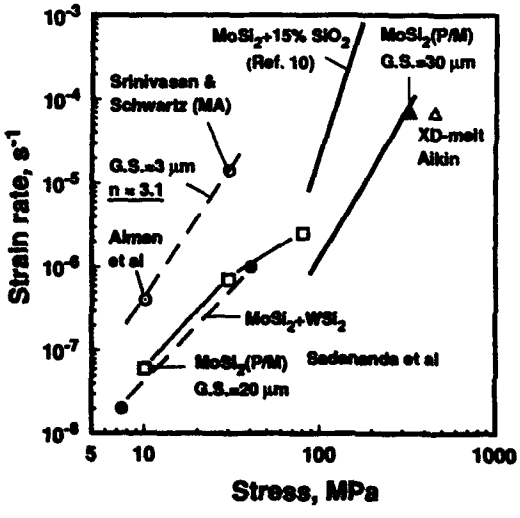

Fig. 9. A collection of strain rate vs. stress data for $MoSi_2$ at 1200°C -- solid line (30 μm g.s.) is from Fig. 3. Data for different grain sizes and SiO_2 content (see text) are from Refs. 5, 10, 13, 19 and 21. Closed triangle is for P/M $MoSi_2$ from Ref. 5.

their material is found to be an order of magnitude lower than that of our $MoSi_2$ matrix material which contains 0.6 wt% oxygen. The data of Alman et al. [21] is also for a grain size of about 3 μm. The oxygen content is not known in this case, but the line joining the last two data points exhibits a stress exponent of about 3.1, which is not significantly different from that of the matrix. The 3 μm grain size $MoSi_2$ is, however, at least an order of magnitude weaker than the 30 μm g.s. material investigated in this work. Furthermore, the data of Sadananda et al. [13] shows lower creep strength in comparison to that from the present work even though their oxygen content (0.3-0.5 wt%) is lower than ours. The creep behavior of $MoSi_2$ containing 15% grain boundary $SiO_2$was previously studied [10] which showed weakening by about 80%, but not by an order of magnitude. This curve is also included in Fig. 9 for comparison. Thus, oxygen (or SiO_2) content by itself may not be the major contributor to the lowering of creep strength in $MoSi_2$. Furthermore, when SiO_2 is present at the grain boundary, a viscous SiO_2 layer is expected to produce a stress exponent value between 1 and 2, which is significantly less than what is observed here. Despite one unusual data point of Sadananda et al. [13], Fig. 9 clearly shows an overall effect of grain size on creep strength, i.e., increasing grain size leading to higher creep strength without significantly influencing the stress exponent. The additional data for $MoSi_2/WSi_2$ solid solution alloy [13] indicates that even with refractory additions the strengthening achieved is less than the overall grain size effect. It must be emphasized that this overwhelming grain size effect on creep strength is found primarily in the dislocation climb-glide regime, albeit in concurrence with grain boundary sliding, an effect which is not commonly recognized.

To investigate the universality of this matrix grain size effect on dislocation climb-glide creep, we plot in Fig. 10 stress for a fixed strain rate as a function of grain size taken from the literature [22-24]. A number of intermetallic alloy systems are represented at a homologous temperature of about 0.6, within the climb-controlled creep ($3.4 \leq n \leq 5.7$) regime. A grain size dependence is visible for each intermetallic alloy. Using a simple relationship $\sigma = BdP$, where σ is stress for a fixed creep strain rate $\dot{e}$, d = grain size, and B = a temperature dependent constant, the grain size exponent, p, is found to be within the range 0.43-0.76. It should be noted that similar grain size dependence at 0.5 Tm was found by Barrett, Lytton and Sherby [25] for copper for grain sizes below 100 μm. Here also, the effect seems to become smaller for grain sizes larger than 100 μm.

With grain size dependence of the matrix behavior in mind, the creep strength for $MoSi_2$ and its composites at $\dot{e} = 10^{-5}s^{-1}$ is plotted in Fig. 11 as a function of grain size. All composites are found to be stronger relative to their own matrices, (i.e., for the same grain size). SiC_w reinforcements appear to provide greater strengthening relative to the matrix than either SiC_p and Mo_5Si_3. The efficiency of strengthening expressed as $(\Delta\sigma/\sigma_m)/v_f$, where $\Delta\sigma$ = strength enhancement, σ_m = matrix strength, v_f = reinforcement vol fraction is 2 for SiC_p, 2.4 for SiC_w (this work), 3.8 for SiC_w [Ref. 13] and 1.52 for Mo_5Si_3. The lower strengthening efficiency of SiC_w in this work is possibly due to the microstructural damage present.

A Creep Deformation Model for Matrix

A simple model has been developed to explain the grain size dependence of dislocation creep rate. The basic concept was proposed by Gifkins [26] in which grain boundary sliding is accommodated by triple-point fold formation. Whether or not folds form, significant stress and strain concentration can be present near triple points during grain boundary sliding. Even though some diffusional stress relaxation [27-28] can occur in this region, at lower temperatures where dislocation creep is the primary deformation mechanism, relaxation is incomplete. In ordered intermetallics, the grain interior can maintain strong directional bonding and lower diffusivity in comparison to the disordered grain boundary and triple-point corner regions. Fig. 12 schematically shows a two-dimensional grain boundary inclined at 45° to the compression axis. A state of compression, resolved into shear plus biaxial compression when applied on the segment of the boundary, will lead to sliding tendency under superimposed pressure. Deformation of the grain corners must take place to accommodate any sliding which can occur. Thus the sliding shear rate, $\dot{\gamma} \propto \dot{e}_{lc}$, where $\dot{e}_{lc}$ = local strain rate in grain corners, which is greater than that within grain interior due to a stress concentration factor, k. The dislocation creep rate in grain corners can follow the same general stress dependence as the grain interior except that dislocation sources are numerous and easily activated. Thus, if the general grain creep law is given by $\dot{e}_g = A\sigma^n$, the constant A can be higher and stress exponent n can be

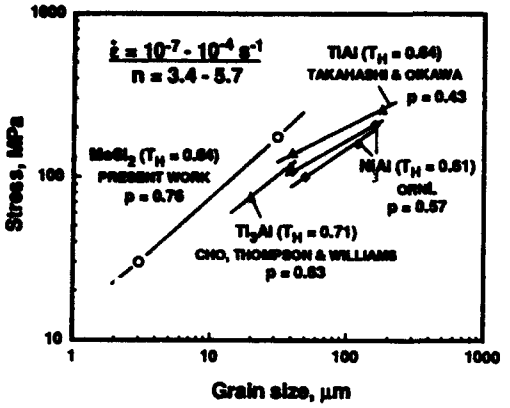

Fig. 10. Creep strength at constant strain rate as a function of grain size for a variety of intermetallic alloys from Refs. 22, 23, and 24 are compared against $MoSi_2$ data (1200°C) from Fig. 9. (T_H = homologous temperature; for Ti_3Al β-transus is used for normalization.) The slope, p (grain size exponent) values are shown.

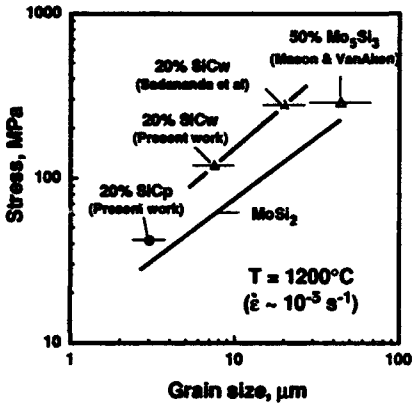

Fig. 11. Stress vs. grain size data, at a strain rate of $10^{-5}s^{-1}$ for monolithic $MoSi_2$ from Fig. 10, compared with data for various composites from Fig. 8 for the same strain rate.

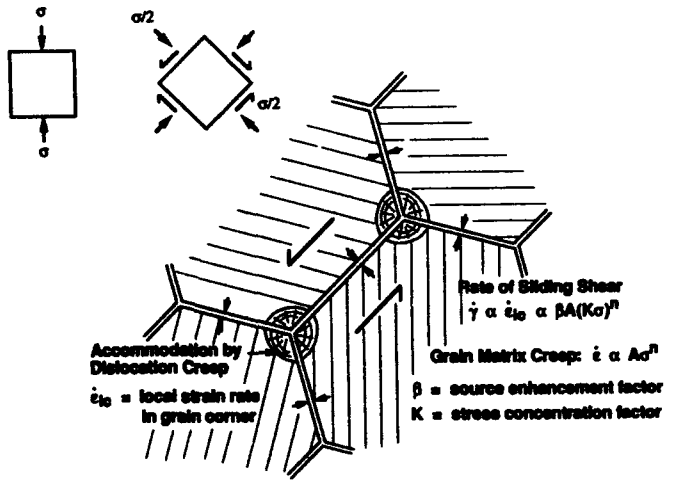

Fig. 12. Schematic of a simple model of creep in compression showing intense deformation zones in grain corners which control the rate of grain boundary sliding. Background creep in the grain matrix is described by power law: $\dot{\varepsilon} = A\,\sigma^n$.

lower for the triple-point regions. If we neglect any change in n, but consider a source enhancement factor, β, the local strain rate in the corner becomes

$$\dot{e}_{lc} = \beta A(k\sigma)^n = (\beta A k^n)\sigma^n \quad (1)$$

Since grain boundary sliding contribution to overall strain rate, $\dot{e}_{gbs}$, is proportional to sliding shear rate $\dot{\gamma}$, and the number of active grain corners per unit volume,

$$\dot{e}_{gbs} \propto \dot{\gamma} \cdot \left(N_c / d^3\right) \propto \dot{e}_{lc} \left(N_c / d^3\right) \quad (2)$$

where N_c = the number of active corners/grain (diameter = d).

Substituting Eq (1) in Eq (2), the total strain rate can be given by:

$$\dot{e} = \dot{e}_g + \dot{e}_{gbs} = A\sigma^n + \alpha\ N_c \beta A k^n \left(\sigma^n / d^3\right) \quad (3)$$

where α = a constant of proportionality. Eq (3) can be expressed in a simple form as

$$\dot{e} = \left(A + A_1 / d^3\right)\sigma^n \quad (4)$$

where the constant $A_1 = \alpha N_c \beta A k^n$. Thus, the creep Eq (4) combines a strongly grain size dependent part with a grain size independent part in an overall dislocation creep framework.

Using the matrix creep data for 3 μm and 30 μm grain size materials from Fig. 9, the constants A and A_1, in Eq (4), can be determined and then the strain rate vs. stress plots for a number of other grain sizes, 7 μm and 18 μm and 100 μm, can be calculated (linear plots) as shown in Fig. 13. Composite strength data (points) from Fig. 8 are cross-plotted in Fig. 13 to demonstrate strengthening effect in each composite. This extent of strengthening can be explained by existing composite creep models [29-30].

Damage also plays an important role in composite strength. Pre-existing voids and microcracking during creep can decrease the strength level if no superimposed pressure exists on the grain boundaries. In tensile tests, there is a net tensile stress component normal to the grain boundaries aiding in the boundary opening up during grain stretching and boundary sliding. The strain increment from this provides enhanced creep rate as shown in Fig. 14 for both the matrix and SiC_p reinforced composite. This strength differential effect is greater for composites since the initial damage is much greater for composites. It is interesting to note that while tensile specimens fail with virtually zero creep ductility, under compression the fine grain composites can undergo significantly higher creep strain than $MoSi_2$ matrix before fracture. Thus, grain refinement can impart greater toughness at the expense of creep strength.

Conclusions

1. Monolithic $MoSi_2$ in the 1100-1400°C temperature range deforms primarily by dislocation climb-controlled creep, with concurrent grain boundary sliding. Creep stress exponents vary between 4 and 2. Sliding is accommodated by dislocation creep at 1100 and 1200°C, and diffusional creep at higher temperatures. Dislocation cells and subgrains form during primary creep at higher temperatures. The activation energy for creep is about 374 kJ/mol.

2. A grain size dependence of creep strength is observed for grain sizes 30 μm and less with an exponent of 0.76 for grain size. Thus, creep strength increases with increasing grain size, eventually saturating around 100 μm size, a behavior common with other intermetallics and some metals.

3. A dislocation climb-glide creep model with concurrent grain boundary sliding which is accommodated by intense deformation at grain corners is found to explain the observed grain size dependence.

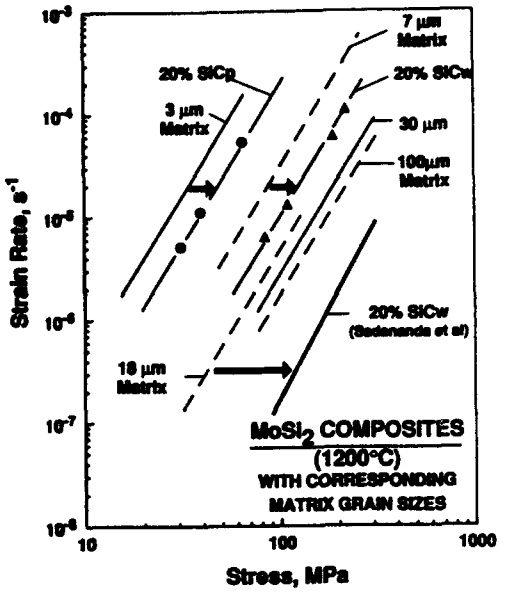

Fig. 13. Calculated strain rate vs. stress plots for matrices with different grain sizes (dashed lines) compared with composite data for the same grain sizes. The solid lines are for 3 and 30 μm g.s. $MoSi_2$ are from Fig. 9. The large arrows indicate the extent of composite strengthening relative to matrix.

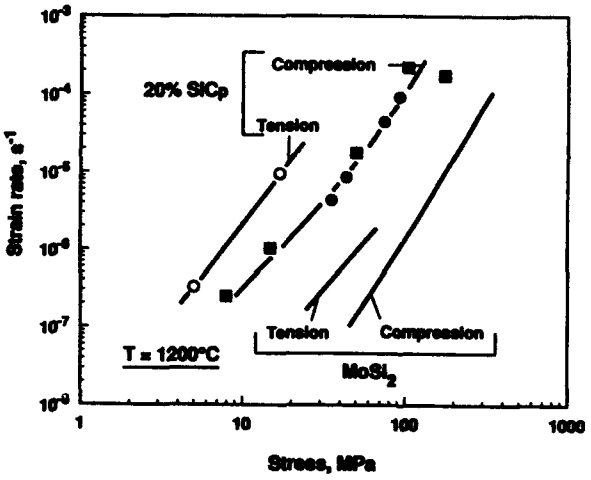

Fig. 14. Strain rate vs. stress data for $MoSi_2/20\%SiC_p$ in compression and tension at 1200°C compared with similar data on monolithic $MoSi_2$.

4. Addition of SiC_p and SiC_w reinforcements to $MoSi_2$ matrix produce creep strengthening relative to the matrix present within the composites. However, relative to coarse grain matrix, weakening often occurs because reinforcement addition can cause significant grain refinement.

5. Creep strengths of $MoSi_2$ and its composites are lower in tension than in compression because grain boundaries are prevented from separating readily during compression testing. Composites with a greater flaw density within reinforcement regions are more sensitive to this strength differential effect.

Acknowledgements

The authors acknowledge the financial support of this work through the U.S. Air Force URI Grant No. DOD-G-AFOSR-90-0141 (Dr. A.H. Rosenstein, Grant Monitor).

References

1. E. Fitzer and W. Remmele, presented at the Fifth International Conference on Composite Materials, (ICCM-5) p. 515 (1985).
2. J.B. Berkowitz-Mattuck, M. Rossetti and D.W. Lee, *Met. Trans.*, **1**, 479 (1970).
3. W.A. Maxwell, Report No. NACA RM E9G01 (1949).
4. R.A. Long, Report No. NACA RM E50F22 (1950).
5. R.M. Aikin, *Scr. Metall.*, **26**, 1025 (1992).
6. J.J. Petrovic, Private communications (1993).
7. S. Maloy, J.J. Lewandowski, A.H. Heuer and J.J. Petrovic, *J. Mater. Sci. and Eng.*, **A155**, 159 (1992).
8. D.P. Mason and D.C. VanAken, Mat. Res. Soc. Symp. Proc., **273**, p. 289 (1992).
9. A.K. Ghosh, A. Basu and H. Kung, Mat. Res. Soc. Symp. Proc., **273**, p. 259 (1992).
10. A. Basu and A. Ghosh, Proc. Int. Symp. on Advanced Metal Matrix Composites for Elevated Temperatures, ASM International, Metals Park, OH, p. 41 (1991).
11. M.J. Maloney, DARPA Contract Report, No. N00014-8-7-C-0862, High Temperature Materials Workshop, Wright Patterson AFB, Feb.,1991.
12. L. Xiao and R. Abascian, Proc. Int. Symp. on Advanced Metal Matrix Composites for Elevated Temperatures, ASM International, Metals Park, OH, p. 21 (1991).
13. K. Sadananda, C.R. Feng, H. Jones and J.J. Petrovic, *J. Mater. Sci. and Eng.*, **A155**, p. 227 (1992).
14. S.M. Wiederhorn, R.J. Gettings, D.E. Roberts, C. Osterag and J.J. Petrovic, *Mater. Sci. and Eng.*, **A155** (1992).
15. J. Weertman, *J. Applied Phys.*, **28**, p. 362 (1957).
16. J. Weertman and J.R. Weertman, Physical Metallurgy, R.W. Cahn Ed. North Holland, Amsterdam, p. 736 (1965).
17. Y. Umakoshi, J. Sennami and T. Yamane, Proc. Fall Meeting of Jap. Inst. Metals, p. 279 (1990).
18. H. Chang, H. Kung and R. Gibala, Mat. Res. Soc. Symp. Proc., **273**, p. 253 (1992).
19. D.E. Alman, K.G. Shaw, N.S. Stoloff and K. Rajan, *Mater. Sci. and Eng.*, **A155**, p. 85 (1992).
20. D.P. Mason and D.C. VanAken, Mat. Res. Soc. Symp. Proc., (1992) In print.
21. S.R. Srinivasan and R.B. Schwarz, *Advances in Powder Metallurgy*, **7**, p. 345 (1992).
22. Oak Ridge National Lab Report, ORNL-DWG 85-16426.
23. T. Takahashi and H. Oikawa, Mat. Res. Soc. Symp. Proc., **213**, p. 721 (1991).
24. W. Cho, A.W. Thompson and J.C. Williams, *Met. Trans.* A, vol. 21A, p. 641 (1990).

25. C.R. Barrett, J.L. Lytton and O.D. Sherby, *Trans. of AIME*, **239**, p. 170 (1967).

26. R.C. Gifkins, *J. Aust. Inst. of Metals*, **18**, p. 137 (1973).

27. A.G. Evans, J.R. Rice and J.P. Hirth, *J. Am. Ceram. Soc.*, p. 369 (1980).

28. C.W. Lau and A.S. Argon, Fracture D.M.R. Taplin Ed. Univ. of Waterloo Press, Waterloo, Ontario, Canada, p. 595 (1977).

29. M. Mclean, *Comp. Sci. and Technol.*, **23**, p. 37 (1985).

30. T.H. Courtney, Mechanical Behavior of Materials, Mc-Graw Hill, p. 245 (1990).

Fundamental Research on Functionally Gradient Materials (FGM)

for Relaxation of Thermal Stress

Ichiro SHIOTA

National Research Institute for Metals
3–12, 2–chome, Nakameguro, Meguro–ku,
Tokyo 153, JAPAN

Abstract

A planned space plane will fly at speeds in excess of Mach 10. It is estimated that the surface of the fuselage will be subjected to a very high temperature, 2000K, by aerodynamic heating. High performance jet and rocket engines for the space plane also will be subjected to very high temperatures. Therefore, the surfaces of the fuselage and engine parts should have a proper thermal barrier.

Ceramics as thermal barrier coatings on a metal part form a kind of composite. However, if an ordinary composite is heated, internal stresses with a sharp peak due to the thermal coefficients difference may cause cracks or spalling. If we eliminate the interface by gradually changing the composition from ceramic to metal, the internal stress will be reduced, as there is no stress concentration present. Such a material is called a functionally gradient material (FGM).

Science and Technology Agency (STA) of the Japanese Government had started a 5–year national project to develop FGMs since 1987. Roughly classified, four processes; i.e., gaseous, powder configuration, spraying and self–propagating high temperature synthesis (SHS) were applied to fabricate FGMs in the project. A 300 mm square panel of FGM and FGMs with several curves were fabricated, and the project successfully ended in March 1992. The concept of FGM can also be applied to fiber–reinforced plastics, electronics, biomaterials, etc. New national project to develop energy conversion FGMs will be started in April, 1993, by STA.

Introduction

The space plane will be designed to fly from Japan to Europe or U.S.A. in a few hours. Flying path is not decided yet, as it depends on the performance of the materials and designing of the plane. It is expected to fly at speeds of over Mach 10 in rather dense air, and fly at a speed of Mach 25 in a vacuum orbit. When the space plane is flying in air, the speed is much faster than a

Critical Issues in the Development of High Temperature Structural Materials
Edited by N.S. Stoloff, D.J. Duquette and A.F. Giamei
The Minerals, Metals & Materials Society, 1993

traditional space shuttle. It is anticipated that the fuselage is subjected to intense heat. The nose cone and the air inlet of the engine of a space plane may be exposed to 2000K, which is a much higher temperature than that encountered by the space shuttle (1700K). No monolithic material is available which has sufficient toughness and heat resistivity to withstand this high temperature.

Generally speaking, ceramics are heat resistive, and metals are tough for a structural member. Thus thermal barrier of ceramics is often coated or stuck on a metal member. In the case of a space shuttle, two kinds of ceramic tiles are applied on the fuselage, forming a composite. All properties, such as heat resistivity, thermal expansion coefficient, Young's modulus, etc. have a large discontinuity at the interface between ceramics and a metal member as shown in Fig. 1.a). When such the composite is heated, thermal stresses with sharp gradients are induced at the interface due to the difference of coefficients of thermal expansion (CTE) between two different materials. The stress often causes delamination or spalling of the coated ceramics. It is well known that ceramics tile often debond from the fuselage of the space shuttle.

At such elevated temperatures, no traditional heat protective system is reliable at a reasonable stress level at the interface as described above. Then the space plane should have a proper thermal barrier on the surface of the fuselage.

A shuttle has small engines on board, but they are used only to control the position. This is because the shuttle is launched by a huge rocket. Then the engines on the shuttle need not to be used at severe operating condition. In the case of the space plane, it has to fly by itself. The turbo–jet engine will be used at a speed of up to Mach 4, a scram–jet engine is used at a speed between Mach 4 to Mach 7 and a rocket engine is for over Mach 7. Then all the engine parts such as turbine blades, combustion chambers, etc., will be subjected to severe condition. Then highly heat resistive materials should be applied not only to the fuselage, but also to the parts in high performance jet– and rocket engines.

Relaxing the stress, which is introduced by the difference of CTEs, is the most essential to construct the space plane. If we eliminate the interface by changing the composition gradually from ceramics to metal, every property will change continuously in the material. Then it does not have sharp stress concentrations, because every functionality changes continuously as the internal composition varies gradually from ceramics on the face to metal on back side as shown in Fig. 1.b). Such the material is a functionally gradient materials, FGM. At the moment, FGM is highly promising materials for the space plane. Three main groups of designing, fabrication and evaluation, cooperate with each other.

Designing

Designing of FGM was mainly performed by Tokyo Institute of Technology group (1) and Daikin Co. group (2). The procedure is as follows; At first, a thin layer (dz) in an FGM is assumed to have a uniform composition as shown in Fig. 2. As the illustration, it was considered that a ceramic–metal gradient material in the form of a thin plate, in which compositional graduation occurs along the thin layer direction (the z–axis). The plate is now assumed to be in a stationary state under a prescribed thermal gradient field. Thermomechanical analysis of the plate was conducted. Then the shape of the dispersoids is assumed as ellipsoid, and when the ratio of x_1 axis and $x_2(x_3)$ axis is changed, and the x_1 is much longer than the others, the dispersoids are cylindrical. If the x_1 axis and $x_2(x_3)$ are the same, the dispersoids are spherical, and if the x_1 axis is much shorter than $x_2(x_3)$, the dispersoids are platelet. Besides the

shape of the dispersoids, the orientation of the dispersoids can be determined by determining the axis, if need.

Thus the properties of the thin layer can be determined from the properties of constituent materials by using well known rule of mixtures.

Assuming that the constituents of FGM compromise phase A(ceramic), phase B(metal), and micro–pore, the fraction volumes for constituents, expressed as V_A, V_B, V_P respectively, satisfy the following equation as shown in Fig. 3(a).

$$V_A + V_B + V_P = 1 \tag{1}$$

In order to simplify the treatment, the nondimensional parameter is introduced as follows:

$$V_B' = V_B / (V_A + V_B) \tag{2}$$

As shown in Fig. 3(b), we define the distribution function for V_B' with non–dimensional thickness z.

$$V_B' = f(z) = \begin{cases} f_o & 0 \le z \le z_o \\ (f_1 - f_o)\left[\dfrac{z - z_o}{z_1 - z_o}\right]^n & z_o \le z \le z_1 \\ f_1 & z_1 \le z \le 1 \end{cases} \tag{3}$$

Then, the fractional volumes of the constituents A and B can be expressed as functions of V_B' and an independent distribution V_P, as follows:

$$\begin{aligned} V_A &= (1 - V_P)(1 - V_B') \\ V_B &= (1 - V_P)V_B' \end{aligned} \tag{4}$$

Estimation of Effective Properties

In order to calculate the temperature distribution and the thermal stress distribution in the FGM, effective material properties, such as the thermal conductivity λ, the coefficient of thermal expansion α, and the elastic constants including Young's modulus E and Poisson's ratio ν, for intermediate compositions of the FGM are required. There are several ways implemented in the system for estimating the effective material properties of the intermediate compositions, which are classified into two different categories, that is, heuristic and theoretical approaches.

Heuristic Approach

In the field of composite materials, different types of rules of mixture have been proposed theoretically or experimentally with respect to rather simpler microstructures. We implemented these rules for the required material properties based upon the microstructure. These rules are all expressed generally in the following form:

$$P(z) = V_A(z)P_A + V_B(z)P_B + V_B(z)V_B(z)Q_{AB} \tag{5}$$

In these equation, P denotes any one of the properties, P_A and P_B correspond to the basic properties of each constitutent phase, and Q_{AB} is a

function of V_A, V_B, P_A, P_B and V_P.

Micromechanical Approach

Eshelby (3) solved the general problem of the elastic field of an ellipsoidal inclusion embedded in an infinite homogeneous medium (called a " matrix").

In order to treat practical situations of composite materials, Wakashima et al. (4) extended Eshelby's equivalent inclusion method for a single ellipsoid to the case of numerous inhomogeneity having many different shapes (called " fillers"). Wakashima (5) also developed the generalized Eshelby's approach which can calculate thermo–elastic properties using the ellipsoidal inclusion model. This approach was adopted as the alternative way to calculate the effective properties of intermediate compositions with complex microstructures.

Let the fillers in the FGM be modeled with an ellipsoid which has independent parameters of aspect ratio L (=c/a) and orientation angles (θ,ϕ) as shown in Fig. 4. Then, effective properties such as the compliance tensor M can be obtained from the following equation.

$$M - M_o = \Sigma V_r (M_r - M_o) B_r \qquad (6)$$

where M denotes the global compliance tensor. The subscript o refers to a matrix phase and the subscript $_r$ refers filler phases. B_r denotes the phase stress concentration–factor tensor, and the elements of B_r are functions of ellipsoidal parameters as well as elastic constants of matrix and filler. Micro–pores can be considered as one of the filler phases.

Fuzzy Transition in Phase Composition

In any type of rule of mixture or micromechanical constitutive theory, there exists distinction between the matrix phase and the filler phase, and these phases are not necessarily interchangeable. However, it is not clear at what fractional volume the matrix phase changes into a filler phase. Sometimes, the microstructure changes from one type to another in some intermediate compositions. To overcome this uncertainty, we introduce " Fuzzy Set Theory" for the treatment of the fuzzy transition in phase composition and microstructure.

Consider a material combination of A and B in which there appears many different microstructures ranging i (i=1 to ℓ). We define the probable effective properties, such as the global compliance, with fuzzy membership functions μ_i as follows:

$$M = \Sigma \mu_i(V_B')M_i \qquad (7)$$

where M_i denotes the global effective properties calculated from equation 6 for i–th microstructure at the value of V_B'. Note that the membership functions can be controlled by the position of microstructural change p_j and by the width d_j (j=1 to $1-\ell$) as shown in Fig.5.

For example, a material combination of zirconia (ZrO_2) and nickel (Ni) is examined. The effective material properties of the FGM fabricated by plasma spraying was investigated in the paper (6), in which spherical particles were assumed as the microstructure:

i. Spherical Ni particles embedded in the ZrO_2 matrix.
ii. Spherical ZrO_2 particles embedded in the Ni matrix.

The calculated results revealed that, except for effective thermal conductivity, the effective material properties display almost linear variations with the volume fraction of Ni because the Q_{AB} term in equation 5 had little contribution. The effective thermal conductivities calculated for the two different microstructures, indicated as types i and ii, are shown in Fig. 6(b).

Here, we consider the probable situation, in which the miocrostructure changes from the type i to the type ii as the volume fraction of Ni increases:

iii. Microstructureal transition from type i to type ii at p_1=0.5 and the transition width d_1=0.4.

The membership functions for the two different microstructures are shown in Fig.6(a), and the probable effective thermal conductivites calculated from equation 7 are plotted in Fig.6(b) with a solid line. Because the higher order membership functions are employed, the effecticve property shows quite smooth transitions. The fuzzy transition parameters herein proposed are heuristic variables. Therefore extensive experimental investigations should be carried out for a variety of material compositions and microstructures.

Then whole properties, including internal stress of FGM can be estimated by lamination of the thin layers with different compositions. If we vary the compositional gradient in FGM, we can estimate the optimum compositional gradient to minimize the internal stress. The information of the optimum gradient is supplied to fabrication group.

Fabrication and Structures

The processes adopted to fabricate FGMs in the project can be classified into four groups: gaseous process, powder configuration process, spraying process and SHS (Self–propagating High temperature Synthesis) process.

Gaseous Process

In the case of the gaseous process, PVD (physical vapor deposition) and CVD (chemical vapor deposition), the grain size of the crystals in the FGM is submicron. Then these processes are suitable to form a thin FGM. We can obtain an smooth compositional change from ceramics to metal, even total thickness is less than 10 μm. This process is suitable to form a thin FGM which might be subjected to a high temperature gradient, as the deposition rate is rather slow, especially in PVD process.

PVD process Fabrication of FGM was carried out by NRIM group (7) and Sumitomo Electric Industries Co. group (8). An HCD (Hollow Cathode Discharge) type instrument was used. A schematic illustration of the instrument is shown in Fig. 7. The Ar plasma generated by high DC current heats the source metal in the water cooled copper crucible. Then the metal evaporates and migrates to the substrate. The metal vapor can be ionized by the Ar plasma, and easily forms a ceramic such as carbide, nitride or oxide by introducing reaction gas such as hydrocarbon, nitrogen, or oxygen, respectively. Deposition rate of the metal or ceramics depends on electric power, vapor pressure of the metal in the crucible, surface area and temperature of the metal. In the case of Cr, which has rather high vapor pressure, deposition rate of the metal or its compounds is approximately 100 μm an hour, and 30 μm an hour for Ti. An example of the FGM structure obtained by this method is shown in Fig. 8. No interface between Ti and TiN can be observed in the figure. However, we can understand the gradual

compositional change from the gradual change of the indentation size by Knoop test.

CVD process CVD process was attempted mainly by Tohoku University group (9) and Nippon Oil Co. group (10). The experimental set-up is illustrated in Fig. 9. A $SiCl_4$–CH_4–H_2 system was adopted and the substrate was heated in a hot-wall type reaction chamber. The $SiCl_4$ reservoir was kept at 293K and its vapor was carried into the furnace by bubbling hydrogen carrier gas. The gas flow rate and the ratio of $SiCl_4$ to CH_4 were controlled by a program controller. The deposition conditions are shown in Table 1. The deposition temperature (T_{dep}) was selected between 1673 to 1773K. The total gas pressure (P_{tot}) was 1.3 kPa. Deposition time (t_{dep}) was kept at 9 ksec. The change of gas composition during deposition is shown in Fig. 10.

The specimen obtained by deposition at 1773K and 1.3kPa with pattern A had many pores throughout the film. The specimen resulting from deposition at 1673K and 1.3kPa with pattern B had pores near the substrate. A plate-like deposit having a compositional gradient from C to SiC was fabricated by controlling the SiC/C ratio in the gas phase during deposition. The CVD conditions having a compositional distribution resulting in minimum thermal stress were 1773K and 1.3kPa (pattern B), and 1673K and 1.3kPa (pattern A). Fig. 11 shows a cross-sectional profile of SiC/C FGM fabricated at 1773K and 1.3kPa (pattern B). Though the structure changes to the thickness direction, Si content, which means SiC content, increased gradually from the bottom to the top of the FGM.

Powder Configuration Process

This process is classified into two methods. One is " Direct Method" , in which powder mixtures with different composition are piled up directly. The other is " Thin Sheet Method" in which sheets of powder mixtures with different composition are once formed, and they are piled up in the compositional order.

Direct method This method was performed mainly by Tohoku University group (11).

In the case of powder configuration process, the grain size of the crystals in an FGM depends on initial powder size. A step FGM is usually obtained, when layers with various composition are stacked manually. The thickness of FGM of more than 10 mm can be obtained easily by this process, but the size of panel area is limited by the hot-pressing or sintering equipment. At the beginning, it was difficult to obtain a thin FGM with continuous compositional change. However, a very thin layer can be recently formed by using computerized equipment, then compositional change became practically continuous. Simultaneous sintering by using laser beam during preparing powder mixture is also attempted. Sintering balance is the most essential for sound FGM, as proper sintering temperature for metal is usually lower than one for ceramics. Then temperature gradient sintering is sometimes required. The device is shown in Fig. 12. The beam emitted by the YAG (yttrium-aluminium-garnet) laser of 300W rating is passed through the focusing lens to regulate the beam diameter, then reflected by the oscillating mirror, after which it is led through a quartz glass window into the furnace chamber, to irradiate the sample. The furnace chamber is equipped with a molybdenum heater for uniformly pre-heating the sample. Also, while not used in the present experiment, the furnace can as necessary be further arranged to cool the sample from the reverse side.

An example of microstructure cross section is shown in Fig. 13. No cracks of visible size are observed, which is indicative of quite good quality sinter.

Thin sheet lamination method This method was attempted mainly by NKK group (12). The flow chart of the thin sheet lamination method is shown in Fig. 14. Slurry, mixture of the powders and the organic additives such as binder, deflocculant, plasticizer and solvent, is flattened by a blade to form a sheet on the moving film. Appropriate volume fraction of the organic additives in the sheet is almost proportional to the surface area per unit volume of the powder. This process is called as " doctor-blade sheet forming process" . The thickness is controlled by adjusting the gap between the edge of the blade and the film. The produced sheet is called as " green sheet" .

Two methods are used to form a multi-layer sheet. One is pressing the sheets with different composition, which are formed separately, to make one body. The other is piling up the slurries one after another in order of composition.

The multi-layer sheet is dried, and all the organic additives and solvent were vaporized by heating to 723K at the rate of 5K/h (dewaxing) before sintering. The sheet was sintered at 1623K for 2 hours in Ar-10%H_2 atmosphere.

To avoid the distortion and the cracking during dewaxing and sintering, the shrinkage of each layer of the sheet should be equal. In Fig. 15, the linear shrinkage of bodies from fine ZrO_2 powder (average diameter of 0.03 μm) and Ni powder (4 μm) are shown by a thick line. A coarse powder of ZrO_2 (15 μm) is added in the raw material to control the shrinkage, and the results are shown in the same figure by thin lines. Fig. 16 is the microstructure of FGM produced according to this idea. However, it is clear that the body made from the coarse powder have more porosity than one without the coarse powder.

Spraying Process

Fabrication of FGM by spraying was carried out by NRIM group (13) and Nippon Steel Co. group (14). The former group adopted " Twin torches method" and the latter adopted " One torch method" . Fig. 17 shows the schematic illustration of the twin torches method. Ni-base alloy (Ni-Cr-Al-Y) and ZrO_2-base ceramic (ZrO_2-8%Y_2O_3, by the name of 8YSZ) powders with particle size of 10 to 44 μm were used in this study.

The graded coating of 0.3 to 0.4 mm thickness were tried with the established spraying conditions by pre-experiment. The microstructures of graded coatings are shown in Fig. 18. It is obvious in twin torches method to get the graded coatings easily by programming of feeding rate of each powder.

Pores in the coating may decrease the tensile strength and corrosion resistance of coating but some extent of porosity were improve the thermal resistance. So, the porosity of monolayer coatings of Ni-Cr-Al-Y and 8YSZ coatings was observed by buoyancy method. The results revealed that almost no recognizable difference in porosity of Ni-Cr-Al-Y coatings as for the change of operating current and powder feeding rate in this experiments (these values are apparent values). Porosity of 8YSZ coating slightly decrease with increase of operating current, but there is no difference in regard to the change of powder feeding rate.

Fine grain size in FGM is obtained, when the initial powder is fine. However smallest size of the powder is limited by capability of feeding to the spraying torch, as too fine powder is difficult to feed. Approximately 0.3-1 mm of thickness can be obtained easily. This process can be applied to obtain a large area size of a panel. Simultaneous sintering by using laser beam during spraying is also attempted.

SHS Process

Fabrication of FGM by this method was performed mainly by Osaka university group (15) and GIRI Tohoku group (16). In the case of SHS process, large heat is generated during chemical reaction to form TiC from Ti and C or TiB_2 from Ti and B. The reaction was initiated by electric ignition. Such heat is the driving force of sintering. HIP or hydrostatic-pressing was applied to eliminate pores during sintering. Ni to TiC and Cu to TiB_2 FGMs are obtained by this process.

In the case of the TiC, it generates a high formation energy of 185 kJ/mol, which gives the adiabatic combustion temperature (T_{ad}) reaching to its melting point of 3343K. The Ni addition can dilute the reaction heat and reduce the T_{ad}. Fig. 19 shows the variation of T_{ad} as a function of Ni content. Solid line is the thermodynamically calculated temperature and open circles are the measured ones. A good coincidence between theoretical and measured temperatures means that the combustion reaction propagated in a adiabatic state. The T_{ad} is a useful parameter to control the microstructure, although it does not correspond to the reaction temperature at the combustion sintering because the ignition agent supplies additional exothermic heat. The T_{ad} under pre-heating condition can be easily calculated. The addition of TiC ceramic powder is a useful way to control the microstructure without changing the composition. It can act not only to reduce the reaction temperature, but to prevent grain growth of TiC. When the reaction temperature exceeded the boiling point of Ni (3000K), the sintered body frequently included large pores. On the other hand, the combustion synthesis hardly occurred when Ni content was higher than 50 wt%, but fine TiC crystals were formed in the Ni matrix, which was probably caused by precipitation from the Ni solution at the cooling. Based on these experiments on densification and microstructure control for non-graded TiC-Ni, the test samples of FGM were fabricated. Fig. 20 shows the green composition, microstructure and elements distribution for an FGM of TiC-Ni, which eleven layers of reactant with a thickness of 1 mm were laminated to 100% Ni. Different contents of TiC powders were added to each layer to keep T_{ad} constant at 1600K for Ni compositions less than 80 wt%. The structure considered of small and uniform size TiC grains through the FGM, but the Ni phase diffused to the surface of TiC side. The compositional change was being optimized to withstand a surface temperature change through FGM of 1000K. Computer aided design using heat transfer and thermal stress analyses was being conducted to optimize the FGM structure for high temperature use.

Evaluation Method and Properties

Important properties of FGMs are strength and heat resistivity. We have to know the properties of every elemental part in FGM to decide an optimum structural or compositional graduation.

Mechanical Properties

Mechanical properties were measured mainly by Tohoku University group (17) and MEL (MITI) group (18). The strength of one part is different from the other part, as the structure in an FGM is not uniform. If internal stress exceeds the failure strength at a certain part, the FGM will be broken. Then we have to know the strength of every part. In the case of metal and ceramics, there are established testing methods to check the strength. We usually use tensile test for metal, and bending test for ceramics. It is difficult to compare both data each other. However, there are ceramics part and metal part in one body of an

FGM. Then, it should be established that a new method which can decide the strength of whole range from brittle ceramics to ductile metal. Takahashi and Hasbida developed a new " small punch test (SP-Test)" , which can decide fracture strength and Young's modulus. Originally, small punch (SP) testing procedure has been developed for the evaluation of ductile-brittle transition temperature on radiation damage for fusion reactor structural steels and material degradation in power plant. The specimen is uniformly fastened between the upper and lower die.

In this project, the SP-test is modified to obtain good reproducibility for FGMs. A schematic illustration of the MSP-testing equipment is shown in Fig. 21. The sample size is 10 mm x 10 mm, and the thickness is 0.5 to 1.0 mm. The sample is supported by the ring shape lower die. Load is applied to the sample by the upper puncher. The deflection of the sample during the test was detected by a high accurate transducer which is connected at the bottom of the Al_2O_3 rod. An example of the MSP-test is shown in Fig. 22. As shown in the figure, absorbed energy decreased monotonically as increasing ceramic content.

It is very difficult to observe the internal stress in FGM directly. X-ray technique or ultrasonic method are not useful, as the constitution and structure in an FGM are inhomogeneous. Then estimation by using FEM method was adopted. An example of the results is shown in Fig. 23. The internal stress in the FGM is obviously less than one in the directly joined sample.

Thermal Properties

Thermal properties were observed mainly by Tohoku University group (19), Shizuoka University group (20) and NAL (21).

Laser shot test for thermal shock resistance and measurements of thermal properties such as thermal conductivity, thermal expansion coefficient and so on are carried out by evaluation group.

A schematic illustration of thermal shock testing device is shown in Fig. 24. Irradiation time was controlled by using the chopper. Thermal shock failure was detected by using AE during irradiation. An example of the results is shown in Table 2. NFGMs (Non-FGMs) suffered cracks or debonding, while the FGM did not.

Thermal stability is also important, as an FGM is thermodynamically non-equilibrium because of heterogeneous structure. On that point of view, NRIM group carried out to reveal the thermal stability of FGMs (22-23). The stability is influenced by its structure, which can be roughly classified into two types. One of them consists of sub-micron crystals, which are often found in FGMs by gaseous processes. The other type has larger crystals than over 1 μm, which is obtained by processes using powders for starting materials such as powder metallurgy, SHS and plasma spraying process. In the former case, it was revealed that fine size and random orientation of the crystals were most essential to improve the stability. While less porosity was important for latter type. It was also revealed that the substrate metal without affinity to the elements in FGM was preferable (7).

All processes succeeded to fabricate flat FGMs of 30 mm in diameter by the end of March, 1990. On the bases of the results, we also succeeded in fabricating an FGM panel of 300 mm square, an FGM with a curved surface, as a hemisphere with 50 mm in diameter and a pipe of 10 mm in diameter and 200 mm long by the end of March, 1992. The large panel is assumed to apply to the fuselage. The hemisphere with 50 mm in diameter is for the nose cone of space plane and the pipe or half of a pipe is for leading edge. Sometime, we need to apply a cooling panel at the back of the FGM. A cooling panel is joined at the

back of an FGM by brazing. In the case of a pipe and half of a pipe, FGM is formed on a cooling pipe. Sometime, we cannot apply a cooling system. These FGMs have been exposed to rocket combustion gas for heat resistance test simulating the real environment, which revealed higher heat resistivity than ordinal TBC.

Thermal fatigue of SiC/C FGM under cyclic heating was also carried out. Decrease of the effective thermal conductivity of SiC NFGM and SiC/C FGM was observed after 30 to 40 cycles of heating and cooling. This was caused by vertical cracking which was observed in the SiC NFGM. This cracking thought to be due to the thermal stress under cyclic heating. On the other hand, SiC/C FGM did not suffer such cracking under the same condition.

Large area heating by Xenon lamp and exposing FGMs in rocket combustion gas are also carried out by NAL group. All data indicate the FGMs are much more highly heat resistive than traditional thermal barriers.

Other Promising Applications of FGM

In a case of a plastics with FRP (fiber reinforced plastics) skin, delamination is the most serious problem. The delamination can be eliminated by gradual change of volume fraction of reinforcements at the interface.

In the case of electronics field, FGMs can be applied to joining of electrodes or sensors. For example, temperature or flow rate of hot liquid or hot gas in a pipe is often required. Usually ceramics insulator is applied between electrodes and the pipe. However, thermal cycle by flowing of hot fluid may cause a gap between them. The gap can be eliminated by using FGM. The FGM can be applied in a sensor-built-in-mount, which is tough to thermal cycling. The sensor is useful to detect deformation or temperature of the surface of certain hot container such as a boiler.

If an FGM is applied to porcelain tooth, it may have a strong and compact core, and porous and bio-compatible ceramics on the surface. Then tissue will grow into the pores. Synthetic bones may have the similar structure.

The concept of FGM is useful not only in the field of thermal stress relaxation but also in other various fields as described above. The FGM is applicable to every parts which may have problems due to interface.

References

1. Wakashima,K. and Tsukamoto,H., Proc. 1st Intnl. Symp. FGM, Sendai, Japan, Oct.(1990)19-26
2. Hirano,T., Teraki,J. and Yamada,T., ibid, 5-10
3. Eshelby,J.D., Proc. R. Soc. London A241(1957)376-396
4. Wakashima,K., Otsuka,M. and Umekawa,S., J.Compos. Mater. 8(1974)391-404
5. Wakashima,K.,Tsukamoto,H. and Choi,B.H.,Proc.Korea-Japan Metals Symp. Comp. Mater. (1988)102-115
6. Wakashima,K., Hirano,T. and Niino,M., Proc. ESA Symp.(1990)
7. Shiota,I., Shinohara,Y., Imai,Y. and Ikeno,S., Proc.1st Intnl. Symp. FGM, Sendai,J apan, Oct.(1990)19-224
8. Kawai,C., Wakamatsu,S., Sakagami,S. and Igarashi,T, ibid., 77-82
9. Sasaki,M. and Hirai,T., ibid, 83-88
10. Uemura,S., Sohda,Y and Kude,Y., ibid, 237-242
11. Kawasaki,A. and Watanabe,R.,ibid, 197-202
12. Takemura,M., Yoshitake,A., Hayakawa,H., Hyakuba,T. and Tamura,M., ibid, 97-100
13. Fukushima,T., Kuroda,S. and Kitahara,S., ibid, 145-150
14. Shimoda,N., Kitaguchi,S., Saito,T., Takigawa,H. and Koga,M., ibid, 151-156

15.Miyamoto,Y., Nakanishi,H., Tanaka,I., Okamoto,T. and Yamada,O., ibid, 257–262
16.Yanagisawa,N., Sata,N. and Sanada,N., ibid, 179–184
17.Saito,M. and Takahashi,H., ibid, 297–306
18.Hirano,K. and Suzuki,T., ibid, 313–320
19.Hashida,T. and Takahashi,H., ibid, 365–374
20.Araki,N., Mihara,J. and Makino,A., ibid, 345–350
21.Kunsakawa,A., Sasaki,M., Takahashi,M., Niino,M., Adachi,N. and Arikawa,H., ibid, 291–296
22.Shinohara,Y., Imai,Y., Ikeno,S. and Shiota,I., ibid, 225–230
23.Shinohara,Y., Imai,Y., Ikeno,S. and Shiota,I., Proc. 4th Symp.FGM, (1991) 173–179 (in Japanese),
24.Yuki,M., Maruyama,T., Irisawa,T., Kawasaki,A. and Watanabe,R., Proc.1st Intnl. Symp. FGM, Sendai, Japan,Oct.(1990)203–208

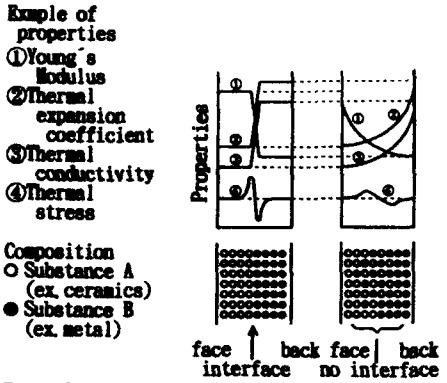

Fig. 1 Compositional and properties change in TBC and FGM

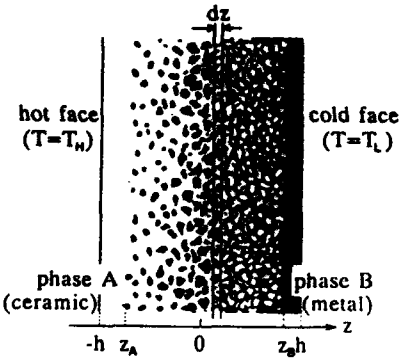

Fig. 2 Schematic representation of a ceramic-metal gradient material. (Ref. 1)

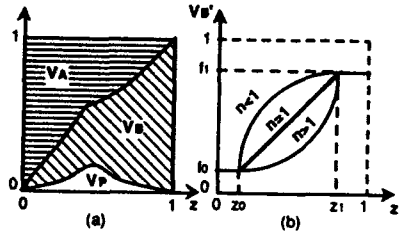

FIGURE 3
Distribution Functions (Ref. 2)

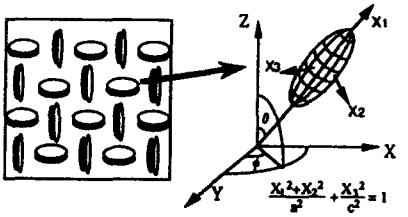

FIGURE 4
Ellipsoidal Model for Micromechanics (Ref. 2)

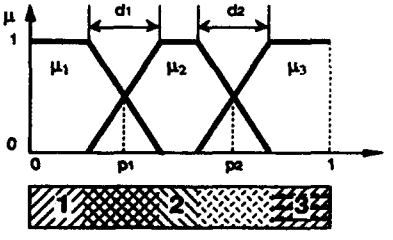

FIGURE 5
Fuzzy Membership Functions (Ref. 2)

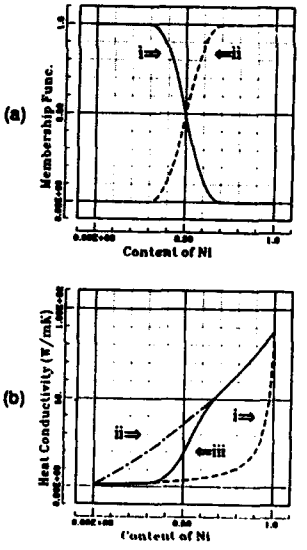

FIGURE 6
Assumed Membership Functions and Calculated Effective Thermal Conductivity of ZrO2/Ni FGM (Ref. 2)

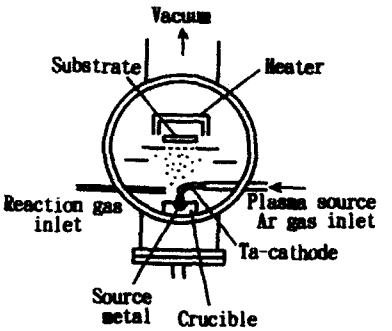

Fig. 7 HCD type PVD instrument

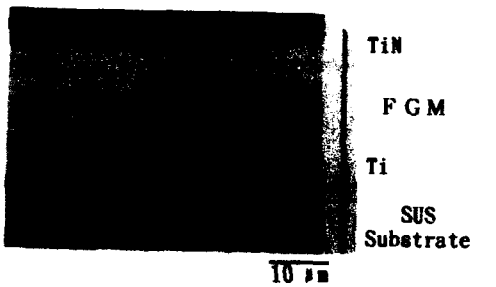

Fig. 8 Cross section of Ti/TiN FGM obtained by HCD method
(Diamond shape: Knoop indents)

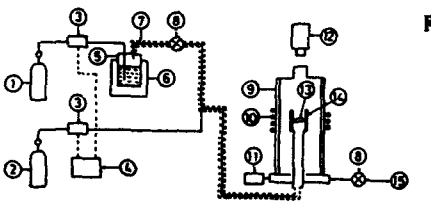

Fig. 9 Schematic diagram of the CVD apparatus
1. H2 gas 2. CH4 gas 3. mass flow meter
4. program controller 5. SiCl4 reservoir
6. const. temp. bath 7. heater
8. pressure regulator 9. reaction chamber
10. work coil 11. pressure gauge
12. optical pyrometer 13. substrate
14. graphite heater 15. pump
(Ref. 9)

Table 1 CVD conditions for SiC/C FGM (Ref. 9)

Deposition temperature (T_{dep}), K:	1673 1773
Total gas pressure (P_{tot}), kPa:	1.3
Gas flow rate $10^{-6}m^3sec^{-1}$	
$SiCl_4$	: 0 to 1.7
CH_4	: 6.7 to 1.3
H_2	: 0 to 5.0
Deposition time (t_{dep}), ksec:	9

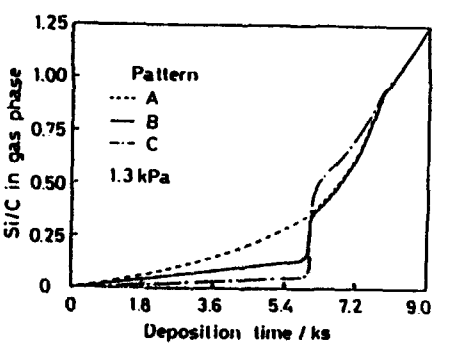

Fig. 10 Change of the ratio of Si/C in gas phase vs. depositon time (Ref. 9)

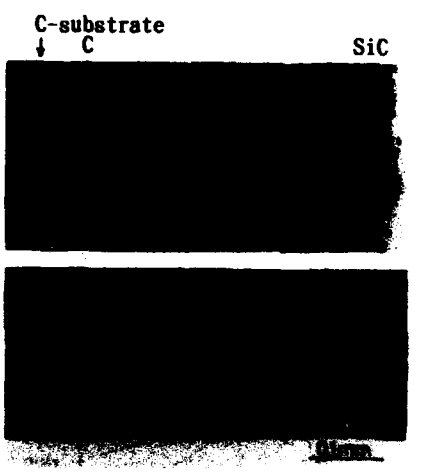

Fig. 11 Cross section of SiC/C FGM obtained by CVD
(upper: stractural change
lower: compositional change of Si)
(by M. Sasaki and T. Hirai)

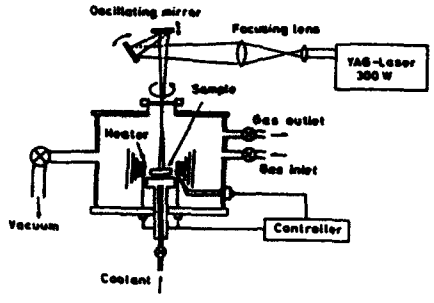

Fig. 12 Device of temperature gradient sintering by laser beam irradiation (Ref. 24)

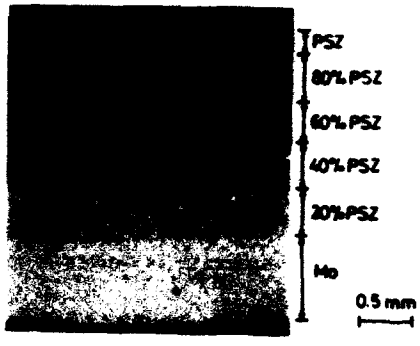

Fig. 13 Sectional microstructure of PSZ/Mo graded FGM sintered under temperature gradient by laser irradiation. 170W P_{max}, 60 sec. t_{keep} (Ref. 24)

Binder
Ceramic Powder } — Mixing — Deforming —
Metal Powder

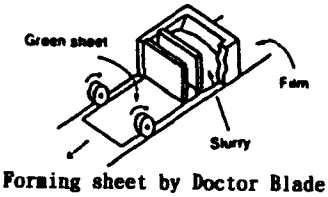

Forming sheet by Doctor Blade

— Lamination — Debinder — Sintering — F G M

Fig. 14 Flow chart of thin sheet lamination method (Ref. 12)

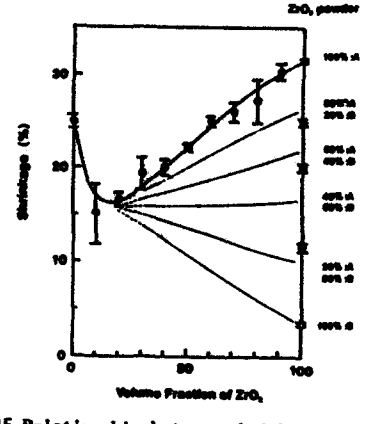

Fig. 15 Relationship between shrinkage and volume fraction of ZrO2 (A: Ave. diameter=0.03μm, B: Ave. dia. =15μm) (Ref. 12)

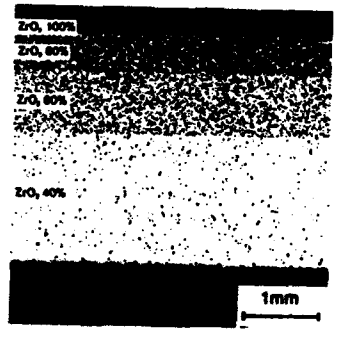

FiG. 16 Microstructure of FGM. The thickness of each composition was recommended by designing group. (Ref. 12)

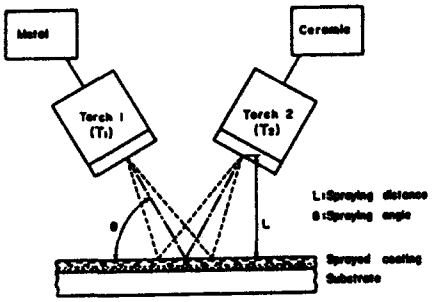

Fig. 17 Schematic illustration of twin torches method for graded coating (Ref. 13)

Fig. 18 Structure of Ni-Cr-Al-Y/PSZ FGM by twin torch method
(Ni-Cr-Al-Y: 800Å, PSZ: 1200Å
Gas flow rate: 45ℓ /min
Spraying angle: 71 deg.)
(Ref. 13)

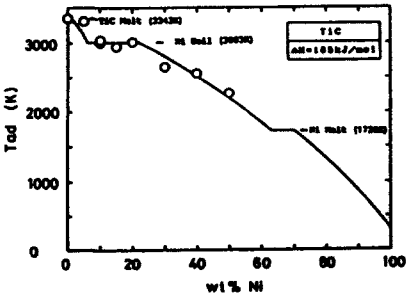

Fig. 19 Adiabatic combustion temperature for the mixed reactants of TiC+C+Ni as a function of Ni content, (Solid line:calculated, open circles:obs.) (Ref. 15)

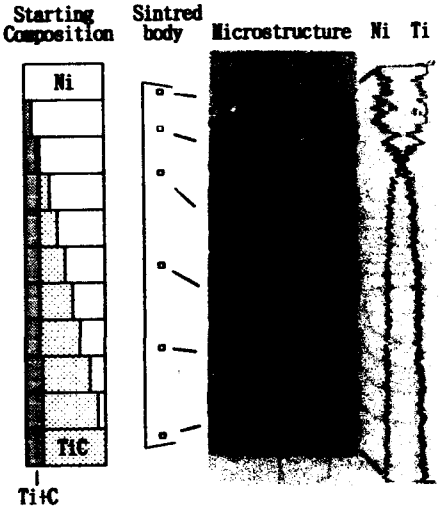

Fig. 20 Structure and element distribution of the TiC-Ni FGM with o-100% composition The Tad was controlled at 1600K through the body by adding TiC powder. (Ref. 15)

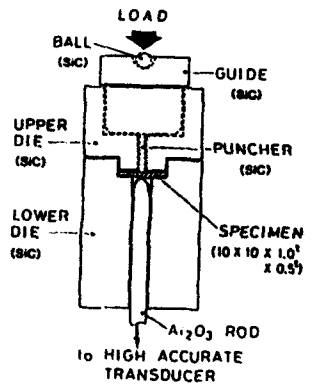

Fig. 21 Schematic diagram of HSP test at very high temperature (Ref. 17)

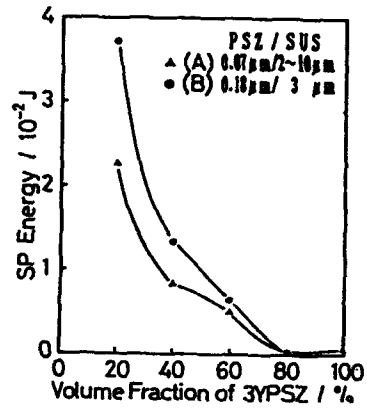

Fig. 22 Absorbed SP energy as the function of volume fraction of 3YPSZ(%) (by R. Watanabe H. Takahashi & coworkers)

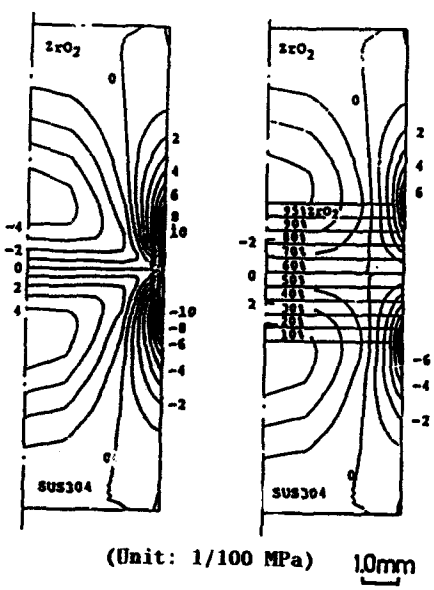

Fig. 23 Calculated internal stress between ZrO2 and SUS304
a) direct joint, b) FGM
(by A. Kawasaki & R. Watanabe)

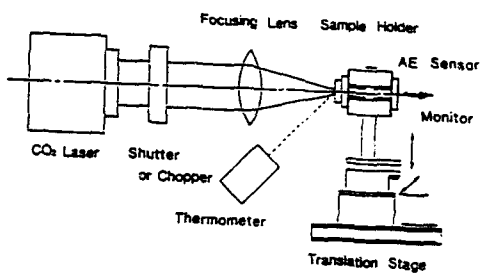

Fig. 24 Experimental setup for laser heating test (Ref. 19)

Table 2. Thermal Shock Test for SiC/C Composites
(by T. Hirai, H. Takahashi & coworkers)

Material		Quick Heating*	Quenching**
		Cracking	Debonding of Film
NFGM	SiC	Yes	Yes
	SiC+30mol%C	No	Yes
	SiC / SiC+30mol%C	Yes	Yes
FGM	SiC/C	No	No

*Laser Heating: 6sec ON - 6sec OFF (780sec)

**Water Quenching: Holding at 1123K for 5min
-Quenched in water at 273K

SESSION VI

Creep Resistance

Critical Aspects in the Development

of Creep Resistant Superalloys & Intermetallics

M. Nazmy
Materials Technology Dept.
ABB Power Generation Ltd.
Baden, Switzerland

Abstract

A major thrust in the development and use of gas turbines is the efficiency through better life-cycle management as well as by using higher turbine entry temperature. The continuous effort of developing improved creep resistant nickel-base superalloys has been driven by the need of achieving higher turbine entry temperature. The possibility of further development in the nickel-base superalloys field, to achieve larger jumps in the temperature capability of these alloys, is getting smaller by approaching the incipient melting in nickel-base alloys. The emergence of intermetallics class of materials gives a new dimension for the development process of creep resistant materials. This paper will present and discuss the limitations in the development of creep resistant nickel-base superalloys taking into consideration the possible strengthening mechanisms and the relevant requirements for the applications. The prospects of developing creep resistant intermetallics suitable for gas turbine applications will be investigated in the light of the state-of-the-art and the inherent advantages and limitations of such class of materials.

Critical Issues in the Development of High Temperature Structural Materials
Edited by N.S. Stoloff, D.J. Duquette and A.F. Giamei
The Minerals, Metals & Materials Society, 1993

Introduction

Increased operating temperatures and improved efficiencies are primary goals in the continuing development of aircraft and land based gas turbines. A more efficient turbine is required to achieve lower fuel consumption. Higher turbine inlet temperature and increased stage loading, with fewer operative stages, result in fewer parts, shorter engine lengths and reduced weight (1). The continuous effort of developing improved creep resistant nickel-base superalloys has been driven by the need of achieving higher turbine entry temperatures. The possibility of further development in the nickel-base superalloys field, to achieve larger jumps in the temperature capability of these alloys, is getting smaller by approaching the incipient melting of these alloys. Additional limitations are partly due to microstructural effectiveness of the strengthening mechanisms with increased temperatures. Processing limitations include the maximum size of the component that can be manufactured in single crystal (SC) and directionally solidified (DS) forms. An obvious physical limitation for all of the nickel-base super-alloys is the continuous increase of density with increasing the temperature capability due to the alloying with heavy refractory elements.
The intermetallic class of materials emerged as a candidate to replace nickel-base superalloys in specific applications due to intrinsic advantages for intermetallics. Such advantages can be physical such as lower density or higher melting point. The application of intermetallics as replacement of superalloys is faced with a number of limitations. These limitations can be related to processing intermetallics or to sensitivity to environmental effects in some cases or their unusually lower ambient ductility and lower fracture toughness in other cases.
In the present paper the critical issues and prospects in the further development of nickel-base superalloys and the limitations for the development of potential candidates of intermetallics will be presented and discussed.

Development of Creep Resistant Nickel-Base Superalloys

Micro- and Macrostructure characteristics

A typical conventionally cast (CC) nickel-base superalloy exhibits ~mm equiaxed grain structure and consists of an FCC solid solution strengthened matrix γ with precipitated γ' particles. The γ' precipitates have an ordered FCC structure and are coherent with the surrounding matrix. In addition to the γ' particles, the CC nickel-base superalloys, contain different types of carbides located on the grain boundaries as well as inside the grains. A full account on the detailed microstructure characteristics and the role of the different microstructural constituents in the strengthening mechanisms of the alloy is given elsewhere (2). Creep and thermal fracture in both wrought and cast alloys that have equiaxed grain structures are always associated with grain boundaries that are transverse to the applied stress. Versnyder and co-workers reasoned that by controlling the grain shape to reduce the density of transverse grain boundaries i.e. by producing elongated grains parallel to the stress axis, grain boundary fracture might be inhibited and ductility increased (3). The approach of DS was applied to nickel-base alloys by Versnyder and Guard who showed a correlation between the elongated structure and improved high temperature mechanical properties (4).
Although the principal motivation for the development of DS was to control the grain morphology of superalloys, the process also influences several other microstructural characteristics. Thus, a sharp crystallographic texture is obtained due to dominance of the fast growing <100> crystal orientation parallel to the direction of solidification. The dendrites are similarly aligned.
After it has been realized that the creep rupture life is controlled by the volume fraction of fine γ', work on SC was resumed (5). In CC high-strength superalloys, even when heat treated very close to the incipient melting temperature, γ' is only partially solutioned, i.e. substantial amounts of coarse as-cast γ-γ' eutectic remain. Thus, the melting point limitation actually hinders realization of the full strengthening potential. The SC structure allows the removal of grain boundary strengthening elements such as B, Hf, Zr and C, which results in an appreciable increase of the incipient melting point of the alloy (6).

The mechanical alloying (MA) process was developed to produce complex nickel-base superalloys strengthened with oxide particles (ODS) (7). The process consists of repeated fracturing and rewelding of powder particles by the application of high-energy compressive impact forces. The process is usually carried out in high-energy stirred ball mills (7). The mechanically alloyed powder is placed in a container and then hot extruded. The last step in processing consists of zone annealing, i.e. annealing in a steep temperature gradient, the hot extruded material. The resulting product is a recrystallized barstock with large elongated grain structure. The MA nickel-base alloys exhibit strong textures (7). For example, MA 6000 exhibits a <110> texture (7).

Creep Behavior of CC, DS & SC Nickel-Base Superalloys

The high temperature creep strength of nickel-base superalloys depends on such factors as solid solution hardening of the matrix, grain boundary strengthening by carbides and most importantly, on the ability of precipitates of the ordered phase to impede dislocation motion. Dislocations must overcome γ' particles by one of a variety of mechanisms. These mechanisms are namely: cutting the precipitates, looping between by Orowan mechanism or by diffusion controlled climb (8, 9). The operative mechanism will then depend on stress, temperature and the dispersion parameters, i.e. size, spacing and morphology of the γ' particles. It has become a normal procedure to represent creep data for most materials over a wide stress range by the power law relationship:

$$\dot{\varepsilon} = A \sigma^n \exp(-Q/RT) \qquad (1)$$

where $\dot{\varepsilon}$, σ, T, R, A, *n* and Q are the steady state creep rate, applied stress, temperature, gas constant and empirically determined constants respectively. For microstructurally complex materials such as nickel-base superalloys, the analysis of creep data by using equation (1) yields values of $n >> 4$ and $Q >> Q_{SD}$ (self-diffusion activation energy). Hence, various investigators have proposed the use of effective stress term i.e. $(\sigma - \sigma_o)$ where σ_o is a measure of the inherent resistance of the material to dislocation motion, in equation (1) (10). Hence, the proposed equation is:

$$\dot{\varepsilon} = A' (\sigma - \sigma_o)^m \exp(-Q'/RT) \qquad (2)$$

where A' is constant, m is a constant of the value ~4 and $Q' \sim Q_{SD}$. Stevens and Flewitt presented an extensive analysis of creep data for the nickel-base superalloy IN738, using the concept of effective stress (11). They reported that at 850°C and high stress > 315 MPa the dislocations may overcome γ' particles by cutting whereas at low stress by-pass of the γ' precipitates involves diffusion-controlled climb (11).

The principal creep strengthening mechanisms in DS superalloys are the same as in the conventionally cast alloys. Since the creep fracture of superalloys with equiaxed grain structures is generally associated with grain boundaries normal to the applied stress, hence, a reduction in density of the transverse grain boundaries, by DS process, will enhance the creep rupture ductility and life (12).

Several investigators have established that creep rupture of strengthened nickel-base superalloy single crystals is strongly orientation and temperature dependent, even at orientations lower than 15 degrees from <100>. In particular it has been shown that although the <001> oriented crystals have excellent creep resistance, the highest stress rupture lives are attained with crystals whose orientations are close to <111> (13).

The high temperature capability of the MA class of alloys is due to the stable oxide dispersion particles as well as to the large elongated grain structure exhibited by this class of alloys (7).

The MA nickel-base ODS superalloys exhibit a unique creep behavior, i.e. threshold stress high creep stress exponents and high activation energy values (14). These anomalies have

been rationalized by describing the stress dependence of the creep rates in terms of an effective stress (14). Transmission electron microscopy on crept oxide dispersion strengthened superalloys, revealed dislocation-particle configurations which suggest that an attractive interaction may exist. This effect of attractive interaction, between oxide particles and dislocations in MA nickel-base superalloys, has been used to model the threshold stress for dislocation climb (15). Recently, it has been reported that creep properties of the alloy MA 6000 exhibit a strong orientation dependence (16).

Figure 1 presents the results on creep rupture strength of different DS nickel-base superalloys as compared to CC IN738LC. In this figure one can observe the advantage in creep strength of the DS IN792 over that of CC IN738LC as well as the improved creep strength of DS CM247LC over both alloys. In figure 2, the creep rupture strength of the MA 760 ODS superalloy, SC CMSX4 and the base line of CC IN738LC, are presented. The creep advantage of the SC alloy over the CC IN738LC is obvious as well as the improved unique creep properties of the MA 760 at lower stress range.

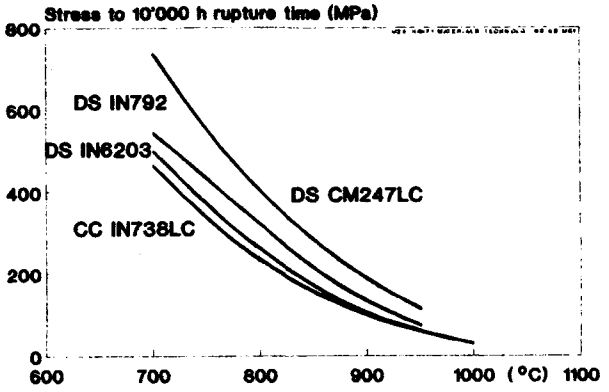

Figure 1 - Rupture stress vs. temperature of Ni-base superalloys

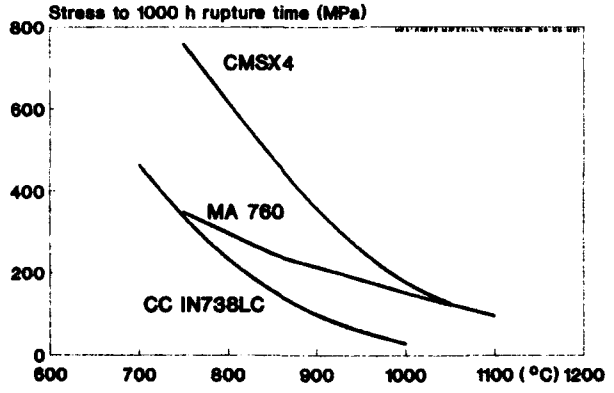

Figure 2 - Rupture strength of SC & ODS alloys

Development Approaches of Nickel-Base Superalloys

The multidimensional development approach is presented in figure 3. In principle, the chemistry modifications are applied to enhance the creep properties through solid solution and ' precipitation hardening mechanisms.
A recent trend in alloy design is the Re addition for further enhancement of the creep strength (17). It is known that Re partitions mainly to the matrix, retards coarsening of the γ' and increases γ/γ' misfit. In this study, Re was found to be an especially potent and necessary solid solution strengthening agent to achieve ultra high strength levels. Figure 4 presents a comparison between the creep rupture properties of DS CM247LC and DS CM186LC which contains 3% Re (18). The improved creep strength of the Re-containing CM186LC is clear.

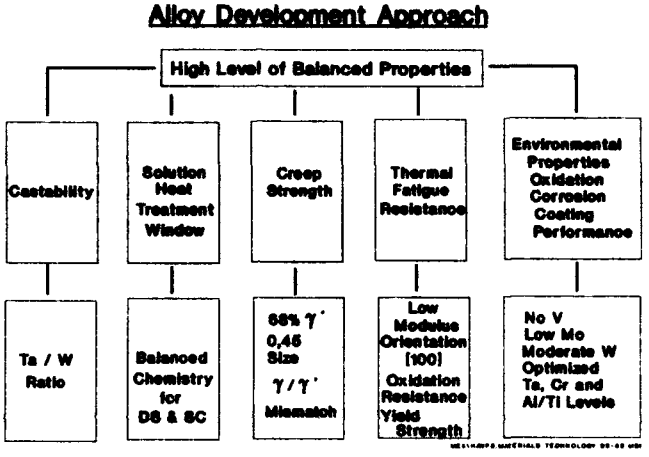

Figure 3 - Alloy development approach

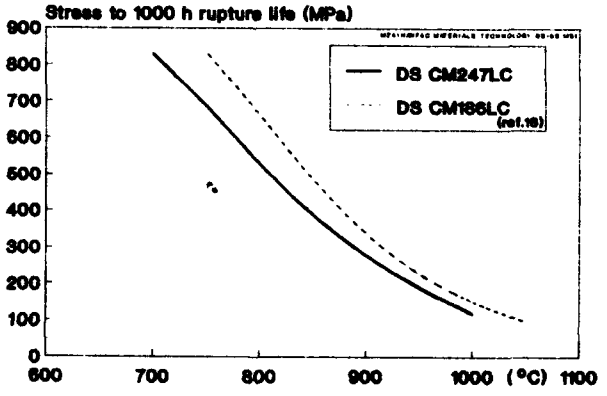

Figure 4 - Effect of Re on creep strength of DS Ni-base superalloys

Limitations on the Development of Nickel-Base superalloys

For industrial application of nickel-base superalloys, the hot corrosion resistance is considered to be important for specific components. Unfortunately, any enhancement in the creep strength is accompanied by a corresponding degradation in corrosion resistance. This is due to the need to reduce the chromium level of the alloy in order to replace it with other strengthening elements. Figure 5 shows how the creep strength varies with the alloy resistance to hot corrosion. The balance between corrosion resistance and creep strength is considered a limitation to further improvement in the creep strength of nickel-base superalloys.

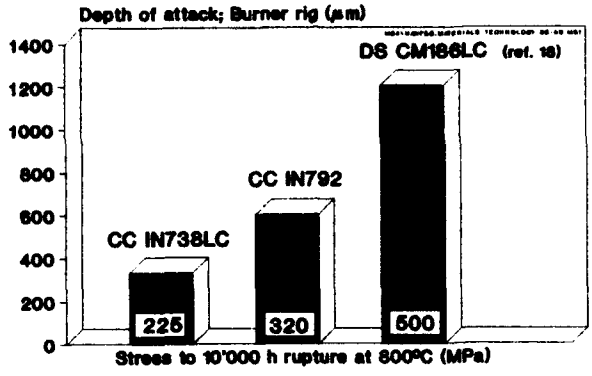

Figure 5 - Relationship between creep strength and corrosion resistance for Ni-base superalloys

The γ' solvus temperature and the incipient melting in nickel-base superalloys are considered the second limitation for their application at higher temperatures. Figure 6 presents the incipient melting of different alloy compositions. The process of SC and DS of gas turbine blades is relatively complex and it involves adjusting crucial parameters, such as growth rate and thermal gradient, in order to obtain the desired structure (19). Process modeling has been a useful tool not only in understanding the solidification but also to optimize its parameters. The real problems in this process modeling are tipically transient, three-dimensional and nonlinear in character and may involve fluid flow and stress analysis. With fine meshes required for accuracy, such problems can quickly take on the character of a grand challenge. This situation represents a technology barrier. The size of the component to be cast in SC or DS form is limited by the high temperature strength of the ceramic mold as well as by the dimensions of the casting facility. The second factor may be overcome by designing of a new larger facility, however the available ceramic materials have limited high temperature strength.

In the case of MA ODS superalloys, the limitation in applying them to different components is the maximum cross section that can be extruded. The extrusion ratio used for such materials ranges from 8 to 12. Hence, one can easily find out that the extrusion forces and the original cross section required to produce cross sections suitable for gas turbine components are getting unrealistically high.

The other limiting factor for MA superalloys is the zone annealing step. In this process one should attain a minimum temperature gradient and at a specific minimum temperture across the zone annealed cross section (7). Since the maximum attainable surface temperature is limited by the incipient melting of the material, hence there is a maximum cross section that can be properly zone annealed. This processing limitation hinders the application of ODS MA superalloys to usual sizes of gas turbine components.

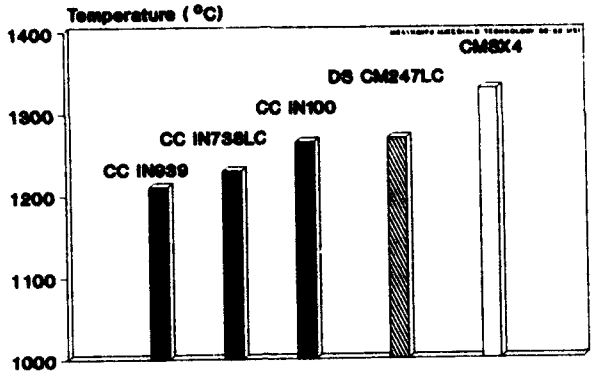

Figure 6 - Incipient melting temperature of CC, DS & SC alloys

Development of Creep Resistant Intermetallics

Creep Properties of Potential Candidate Intermetallics

In the past ten years, a sizable number of intermetallics have been studied for several applications (20, 21). At the time being, only few of these intermetallics can be defined as real potential candidates for applications in turbomachinery.
These intermetallics are γ-TiAl-base alloys and NiAl and to a lesser extent $MoSi_2$. Table 1 gives a summary of their physical and mechanical properties.

Table I Properties of Candidate Intermetallics

Alloy	Structure	Modulus [GPa]	Melting Point [°C]	Density [g/cm^3]
TiAl	LI_0	175	1460	3.9
NiAl	B_2	189	1640	5.9
$MoSi_2$	C_{11}	359	2030	6.3

The improved creep properties, based on density corrected stresses, of γ-TiAl base alloy Ti-48Al-2Cr-2Nb as compared with that of IN738LC are shown in figure 7 (22).
The creep strength capability of alloyed NiAl single crystals has been shown by Darolia and is illustrated in figure 8 (23). The stresses in this figure are not corrected for density, hence the corrected stresses will show the creep advantage of alloyed NiAl over René 80 superalloy.
In the case of $MoSi_2$, the creep strength of the monolithic material is not good at high temperature. Nevertheless, the composite versions may have a creep strength advantage as reported recently by Sadananda et al. (24).

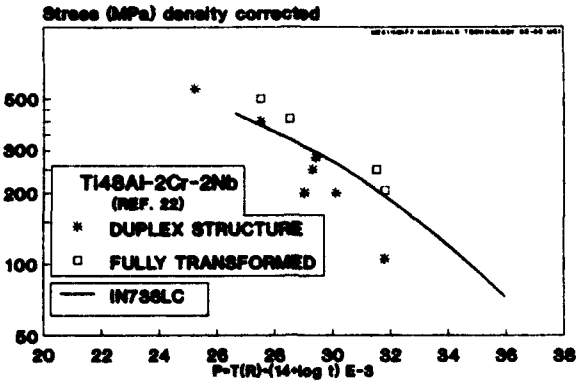

Figure 7 - Density corected creep properties of both structures of Ti48Al-2Cr-2Nb as compared with IN738LC

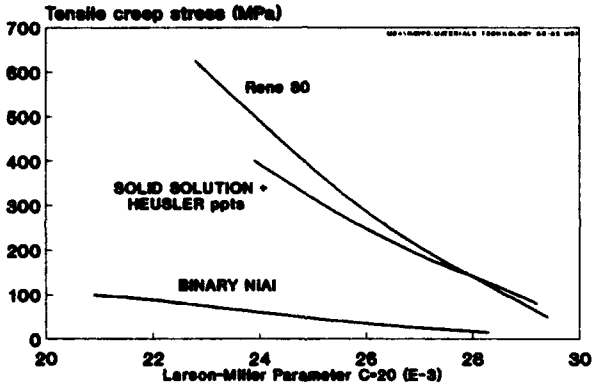

Figure 8 - Tensile stress rupture properties of NiAl intermetallics compared with superalloy Rene 80 (ref. 23)

Oxidation and Corrosion Behavior

The optimum oxidation and corrosion behavior of the material is an important factor to be considered for its applications at high temperature. The oxidation behavior of a large number of intermetallic systems have been summarized by Meier (25).

The oxidation behavior of γ-TiAl was studied by Meier et al. (26). They reported good oxidation resistance i.e. ability to form an Al_2O_3 layer, for γ-TiAl up to approx. 800°C, depending on the aluminum content. Oxidation resistance of γ-TiAl can be further improved by alloying additions such as Nb (27). The corrosion behavior of γ-TiAl at 800°C as determined in burner rig tests, has been found to be comparable to the corrosion resistant nickel-base superalloys IN739 and IN738LC as shown in figure 9.

It has been reported that the NiAl intermetallics exhibited good oxidation resistance up to approx. 1200°C, a temperature which is higher than the application range for nickel-base superalloys (26, 28). The hot corrosion behavior of unalloyed and alloyed NiAl have been reported by Darolia (28). He pointed out that the corrosion behavior of NiAl can be substantially improved by chromium and yttrium addition.

In the case of $MoSi_2$, the oxidation and corrosion behavior has been reported to be excellent by virtue of its ability to form a protective layer of SiO_2. Nevertheless, $MoSi_2$ can disintegrate catastrophically (pest) during oxidation at temperatures ¾ 600°C. Recently, Meschter has proposed that the "pest" effect can be avoided if the $MoSi_2$ intermetallic is not exposed to oxygen for long times in the immediate vicinity of 500°C or if all surfaces are covered by a SiO_2 layer formed by high temperature preoxidation (29).

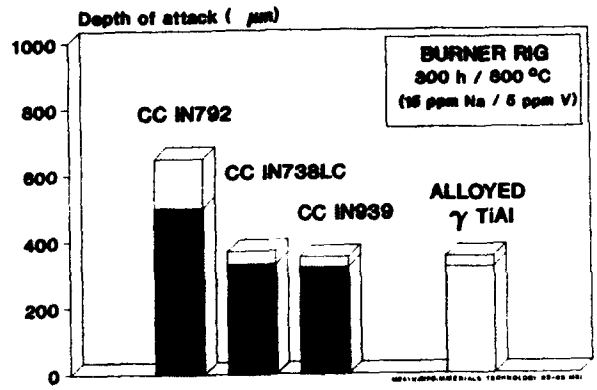

Figure 9 - Hot corrosion test (Burner rig) of selected Ni-base and intermetallic alloys

Limitations on the Development of Intermetallics

Ambient ductility is required for reducing local stresses at notches and other inhomogenities. The γ-TiAl base materials do not exhibit low temperature ductility of the same level as for the known nickel-base superalloys as presented in figure 11. Darolia has reported that with the appropriate microalloying, the ambient ductility of SC NiAl can be enhanced in the <110> direction (23). In figure 10, the maximum reported ductility for SC NiAl is also shown for comparison. From this comparison with nickel-base superalloys, it is apparent that one has to implement a relatively refined design procedures for the structural parts to be manufactured from intermetallics. This is in order to determine exactly the minimum level of ductility required for critical locations.

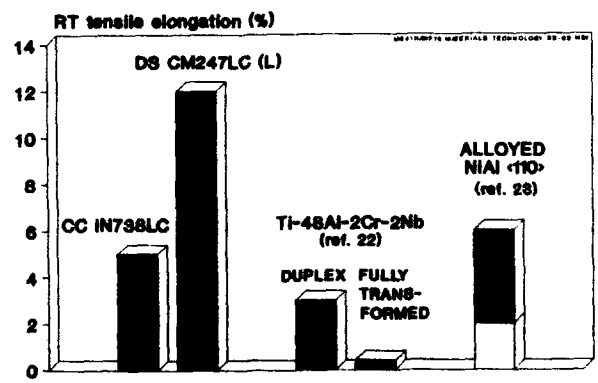

Figure 10 - RT tensile ductility of selected Ni-base and intermetallic alloys

Unfortunately, $MoSi_2$ exhibits brittle fracture at ambient temperature up to approx. 900°C. Hence, the only possibility to use this material in structural parts is by microstructural toughening.
The fracture toughness (K_{IC}) of these intermetallics, as shown in figure 11, is relatively lower than that for known nickel-base superalloys (30, 31) and can be considered one of the important limitations for their development.

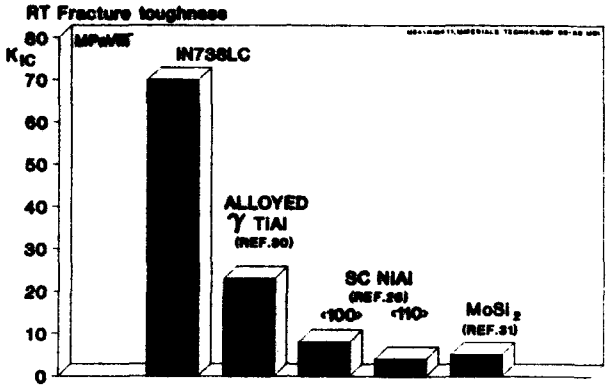

Figure 11 - Fracture toughness at RT of intermetallics compared with CO IN738LC

As well known, lower values of threshold stress intensity range (ΔK_{th}) and K_{IC} mean high sensitivity of the materials to defects and discontinuities in the structure. This is considered a limitation in applying these intermetallics, e.g. monolithic $MoSi_2$, to high temperature components. This brittle behavior of such intermetallics makes it essential to resort to structural toughening by ductile phases.
The size factor can be the limiting factor for applying alloyed SC NiAl to industrial gas turbine size components. As has been reported in literature, the SC NiAl should be grown and then processed to usable components e.g. blade shapes (23). It is not feasible at the moment to grow SC larger than few inches. Hence, large industrial gas turbine components of 10" to 20" in length cannot be manufactured in the near future from SC intermetallic NiAl.

Conclusions and Recommendations

For nickel-base superalloys:

- Their use will be limited to components that can be processed from SC and DS forms and see material temperature of maximum 1100°C.

- Process modeling can improve the cost effectiveness of the casting process but will not help to drastically change the maximum castable size.

- The compositional balance to offer a compromise between corrosion and creep resistance dictates that the primary requirement should be specified i.e. corrosion vs. creep strength.

For γ-TiAl, NiAl and $MoSi_2$ intermetallics:

- Design capability should be emphasized to construct with low ductility low fracture toughness materials.

- The γ-TiAl can be used to the limit of its oxidation resistance i.e. approx. 800°C-900°C. The main weight saving advantage can be made use of in the rotating components to replace nickel-base superalloys.

- The SC NiAl is limited to small components due to casting technology limitations.

- For $MoSi_2$ the "pest" effect, low temperature ductility and fracture toughness are the main limitations for the use of this material. Materials toughening and preoxidation can be considered as viable means to improve the possibility of materials applications.

Acknowledgements

The stimulating discussion with M. Staubli and C. Noseda and their help in preparing this paper are greatly appreciated. The financial award granted by the Engineering Foundation is highly appreciated.

References

1. H.E. Miller and W.L. Chamber, Superalloys II, Eds. C. Sims, N. Stoloff and W. Hagel, (Wiley-Interscience, New York, 1987), 27-57.

2. E. Ross and C. Sims, Superalloys II, Eds. C. Sims, N. Stoloff and W. Hagel (Wiley-Interscience,New York, 1987), 97-133.

3. F. Versnyder and M. Shank, Materials Science and Engineering, 6 (1970), 213-247.

4. F. Versnyder and M. Shank, Source Book on Materials for Elevated Temperature Applications, Ed. E.F. Bradley (ASM, Metals Park Ohio, 1979), 334-368.

5. J. Jackson, et al., Metall. Trans. A, 8A (1977), 1615-1620.

6. F. Versnyder, High Temperature Alloys for Gas Turbines 1982, Eds. R. Brunetaud et al., (D. Riedel Pub. Co., Dordrecht, Holland, 1982), 1-49.

7. R. Singer and G. Gessinger, Powder Metallurgy of Superalloys, Ed. G. Gessinger. (Butterworth, New York, 1984), 211-292.

8. N. Stoloff, Superalloys II, Eds. C. Sims, N. Stoloff and W. Hagel, (Wiley-Interscience, New York, 1987), 61-96.

9. S. Floreen, Superalloys II, Eds. C. Sims, N. Stoloff and W. Hagel, (Wiley-Interscience, New York, 1987), 241-262.

10. C. Ahlquist and W. Nix, Acta Metall., 19 (1971), 373-385.

11. R. Stevens and P. Flewitt, Acta Metall., 19 (9171), 373-385.

12. M. McLean, Directionally Solidified Materials for High Temperature Service, (The Metals Society, London, 1983), 151-205.

13. R. Mackay and R. Maier, Metall. Trans A, 13A (1982), 1747-1754.

14. T. Howson, D. Mervyn and J. Tien, Metall. Trans A, 11A (1980), 1609-1616.

15. E. Arzt and D. Wilkinson, Acta Metall., 34 (1986), 1893-1898.

16. M. Nazmy, M. Staubli and W. Ebeling, Material and Technik, 1 (1987), 9-13.

17. A. Cetel and D. Duhl, Superalloys 88, Eds. D. Duhl et al., (TMS, Warrendale, PA, 1988), 235-244.

18. K. Harris et al., Superalloys 92, Eds. R.A. Mackay et al. (TMS, Warrendale, PA, 1988), 297-306.

19. A. Giamei, J. of Metals, 45 (1) (1993), 51-53.

20. N. Stoloff, High Temperature Ordered Intermetallic Alloys, Eds. C. Koch, C.T. Liu and N. Stoloff. MRS Symp. Proc., 39 (1985), 3-27.

21. R. Fleischer, D. Dimiduk and H. Lipsitt, Annual Rev. Mat. Sci., 19 (1989), 231-263.

22. D. Shih et al., Microstructure/Property Relationships in Titanium Aluminides and Alloys, Eds. Y.-W. Kim and R. Boyer (TMS, Warrendale, PA, 1990), 135-148.

23. R. Darolia, J. of Metals, 43 (3) (1991), 44-47.

24. K. Sadananda et al., Materials Science and Engineering, A155 (1992), 27-239.

25. G. Meier, Oxidation of High-Temperature Intermetallics, Eds. T. Grobstein and J. Doychak, (TMS, Warrendale, PA, 1988), 1-29.

26. G. Meier et al., Oxidation of High-Temperature Intermetallics, Eds. T. Grobstein and J. Doychal, (TMS, Warrendale, PA, 1988), 189-193.

27. G. Welsch and A. Kahveci, Oxidation of High-Temperature Intermetallics, Eds. T. Grobstein and J. Doychak, (TMS, Warrendale, PA, 1988), 207-234.

28. C.A. Barrett, Oxidation of High-Temperature Intermetallics, Eds. T. Grobstein and J. Doychak, (TMS, Warrendale, PA, 1988), 67-82.

29. P. Meschter, Metall. Trans A,23A (1992), 1763-1772.

30. S. Kampe et al., Microstructure/Property Relationship in Titanium Aluminides and Alloys, Eds. Y.-W. Kim and R. Bayer (TMS, Warrendale, PA, 1990), 313-322.

31. D. Carter and P. Martin, Intermetallic Matrix Composites, Eds. D. Anton et al., MRS Symp. Proc., 194 (1990), 131-138.

CREEP AND DAMAGE PROCESSES IN MULTI-PHASE CERAMIC MATERIALS

D. S. Wilkinson
Department of Materials Science and Engineering
McMaster University
Hamilton, Ontario L8S 4L7, CANADA

Abstract

A brief review is presented of the creep and creep fracture behaviour of a range of multi-phase ceramic systems. Three main classes of material are considered, ranging from soft ceramic matrices reinforced with strong particles such as whiskers, through metal infiltrated ceramic compacts, to glass bonded ceramics. Thus a wide range of matrix volume fraction from 90 to 1%, is considered. The creep resistance is seen to depend generally on that of the soft phase, and on the rheological influence of the hard phase. At intermediate volume fractions, network formation plays a major role. The creep fracture behaviour in all classes of material shows two regimes - at high stress, failure is due to a single dominant crack emanating from a flaw; while at low stress, generalized damage is seen. A modified Monkman-Grant relationship is often found, suggesting that increasing creep resistance is the main route to improved lifetime at high temperatures.

Critical Issues in the Development of High Temperature Structural Materials
Edited by N.S. Stoloff, D.J. Duquette and A.F. Giamei
The Minerals, Metals & Materials Society, 1993

Introduction

The aim of this paper is to review our understanding of the processes which control creep and creep fracture in multi-phase ceramic materials. Attention will be focussed throughout on systems in which a hard reinforcing phase is embedded in a softer matrix. Such systems include ceramic materials to which particulates (in the form of particles, whiskers or platelets) have been added, ceramic powder compacts which have been infiltrated by a matrix phase, and ceramic systems which during processing produce a soft (usually amorphous) matrix. Thus the matrix phase can occupy a wide volume fraction range from near 100% down to about 1%. Because of space limitations, the treatment given here is somewhat selective, and only representative materials from each class of composite discussed will be presented. The discussion of creep phenomena is especially brief as a separate review in this area will appear shortly [1]. Likewise, only selected references to the available literature will be offered. A number of reviews which treat related topics have been prepared in recent years, and the reader may obtain further details in certain areas by reference to these [1-8].

Microstructural Classes

The discussion of creep and fracture behaviour will be based upon a division of materials into four microstructural classes. The distinction developed below is somewhat arbitrary, but there are several features which distinguish each class. We start, as a point of reference, with pure ceramic materials, i.e. those which do not contain amorphous or extensive second phase regions, focussing on the well documented behaviour of alumina. We will then consider systems which contain discrete second phase particles (primarily whiskers), fabricated by mixing two powders and sintering, with or without external pressure (class I). The most studied material in this class is alumina reinforced with silicon carbide whiskers, although a wide variety of similar systems have been recently developed. The volume fraction of the hard phase in such systems is usually low (up to about 30 vol%), and the particles are generally only in point contact with one another. Materials obtained by infiltration into a powder compact produce composites with a higher volume fraction of the hard phase (of order 50 vol%, class II), and in which particles make facet-to-facet contacts. The most important example in this class is siliconized silicon carbide. This material is made by infiltration of a SiC powder compact by liquid silicon. The silicon penetrates the contacts between particles, thus providing a thin silicon film along each SiC-SiC interface. Finally, we will consider materials in which the hard phase occupies a very large volume fraction (greater than 90%), with the particles bonded together by a soft phase (class III). Most silicon nitride ceramics fall within this class. These materials are typically sintered (with or without the aid of external pressure), using oxide and/or nitride additives which form a liquid phase and thus promote densification. On cooling, all or part of the liquid forms a glass which coats the silicon nitride particles. The glass exists in two forms. An equilibrium [9] film of nanometre scale thickness persists along boundaries between crystalline phases. For materials with a grain size of about 1 μm, this occupies 0.1-0.3 vol% of the composite. Any excess glass occupies larger pockets, either in wedge shaped regions between grains or as grain-sized regions throughout the body.

There are two important thresholds in volume fraction which need to be considered

in understanding the role of second phase additions on mechanical behaviour. The first is the percolation threshold, the volume fraction at which a network of touching particles extends throughout the solid. For spherical particles this occurs at about 18 vol%. For anisotropic particles (i.e. whiskers or platelets) percolation occurs at substantially lower volume fractions. Thus the class I materials straddle this threshold. The second threshold occurs when one can no longer pack additional particles into a given volume without modifying their shape. For spherical particles of uniform size this is given by the random close packing model, with a volume fraction of about 68%*. As one approaches this threshold the contacts betweenparticles change from predominantly point-to-point, which allows for particle rotation during flow, to primarily facet contacts, in which the deformation process within the facet boundary regions controls the composite properties. Thus, while class I and II materials can be densified by sintering of the soft phase alone, in class III materials it is the hard phase which must sinter.

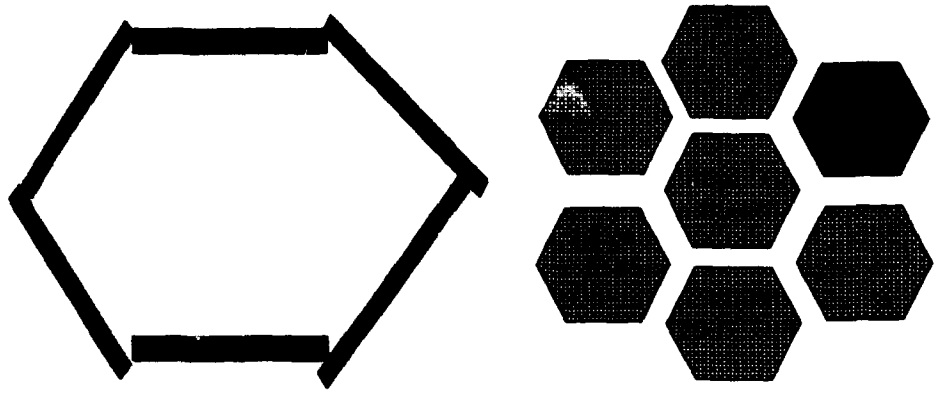

(a) (b)

Fig. 1: A schematic illustration of the important microstructural features of (a) class I and (b) class III materials. Class II materials contain some features of both.

Of course, this division of materials into distinct classes represents an oversimplification. More complex microstructures are possible in which, for example, a low volume fraction of whiskers are added to a class III material (such is the case with SiC-whisker-reinforced Si_3N_4) [10,11]. Alternatively, siliconized silicon carbide can be produced with a high volume fraction of SiC through the addition of graphite powder which reacts with silicon during processing and leads to a bimodal size distribution [12,13]. Nonetheless, this provides a useful way of classifying and distinguishing the creep and fracture behaviour of microstructurally different types of composites.

---

* Larger volume fractions can be obtained however, if powders of substantially different sizes are mixed together.

Creep

In many two-phase materials, the softening temperature of the individual phases is sufficiently different that one can assume that only one phase deforms while the harder phase remains essentially elastic. To a first approximation at least, this is the case with all of the systems under consideration here. Thus the creep response of the composite depends primarily on that of the softer matrix phase. However, this response is modified considerably by the rheological influence of the non-deforming particles. If the particles are assumed to be uniformly distributed and non-interacting (i.e. no network formation), then the response can be modelled by considering an isolated particle embedded within the matrix material. For a linear viscous matrix (which might be either a glass or a crystalline solid undergoing diffusional creep), this behaviour has been modelled by Dryden et al. [14], assuming a spherical particle sitting in a spherical shell of matrix material. This model is appropriate at low volume fraction ϕ, below the percolation threshold, in which case it yields the Einstein limit for the effect of particles on fluid viscosity,

$$\frac{\eta}{\eta_o} = 1 + 2.5\phi \qquad (1)$$

where η is the effective viscosity of the composite while η_o is that of the viscous phase. This predicts only a modest increase in creep resistance, about 25% for $\phi \approx 10\%$. This model is also effective at high volume fractions when the particles can no longer flow past each other but can only approach one another by squeezing the viscous medium which separates them. In this limit the model predicts an effective viscosity given by

$$\frac{\eta}{\eta_o} = \frac{10.8}{(1-\phi)^3} \qquad (2)$$

While this simple model overestimates the absolute magnitude of the viscosity increase, as predicted by a more exact model [14], it does contain the essential physics of the problem and predicts the correct dependence on ϕ. This suggests that the viscosity is a sensitive function of the volume fraction of the viscous phase. A careful analysis of these models however, indicates that $1-\phi$ should be thought of as the "effective" matrix volume fraction, given by the thickness of the interparticle soft layer, normalized by the grain size. In other words, the excess matrix material which occupies pockets throughout the structure do not significantly affect the creep response, although they do affect creep fracture, as discussed below. We therefore see that for a normalized thickness of 0.1%, as suggested above for silicon nitride, the effective viscosity of the composite will be about 10 orders of magnitude greater than that of the viscous matrix phase.

For intermediate volume fractions this approach is inadequate. Instead we need to recognize the role which a percolative network of non-deforming particles plays in the creep of the matrix. This problem has yet to be modelled adequately. However, to a first approximation we can recognize that as the body deforms the network must deform also. This occurs by rigid body motions (both translations and rotations) as the matrix deforms around the particles. If the matrix deforms by a

diffusional process, then the appropriate length scale for diffusion is increased from the grain size of the matrix material to that appropriate to the network. This is at least as large as the dominant length scale of the reinforcing particles. For whisker or platelet reinforced materials this can lead to an increase in the diffusion length of about one order of magnitude. Since grain boundary diffusion scales inversely as the third power of diffusion distance, this suggests that a strength increase of about 3 orders of magnitude can be anticipated for this process.

Single Phase Materials

The creep behaviour of single phase ceramics such as alumina has been well documented [2,3]. In the current context we need merely note those characteristics which distinguish it from that of the composite systems. For example it has been established that the creep rate in alumina is independent of the loading direction (i.e. tensile or compressive) [15]. Creep curves show a relatively short lived primary ($\approx$1% strain in tension) followed by a well defined steady-state regime, observed in both tensile and flexure geometries [15]. The stress exponent for creep varies between 1 and 2, with the higher exponents being more common for fine grained ($\approx 1\ \mu m$) materials. This is suggestive of creep controlled by grain boundary sliding processes leading to superplastic behaviour, and indeed, fine grained aluminas are known to be superplastic down to a relatively low temperature (e.g. 1250°C [15,16].

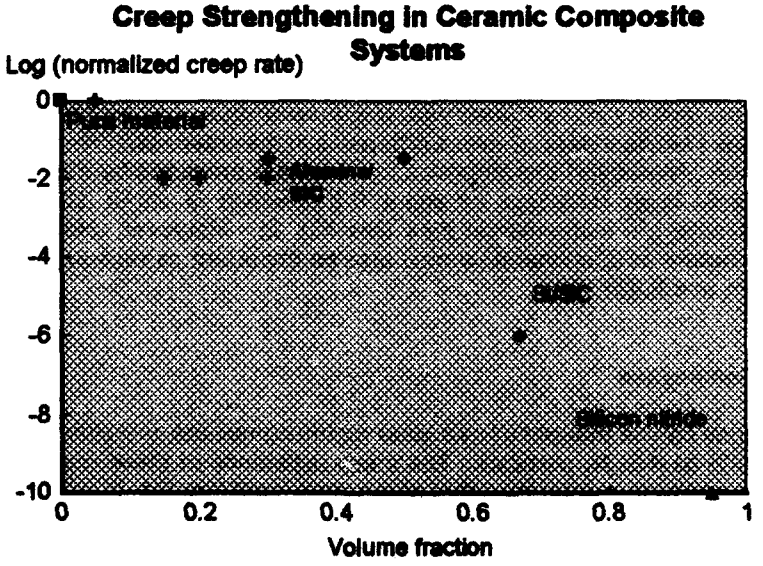

Fig. 2: The creep rate of a range of composites, normalized by the creep rate of the matrix phase is plotted as a function of the volume fraction of the non-deforming phase

Class I Composites

We will consider here only SiC-whisker-reinforced Al_2O_3. In common with the matrix, these materials exhibit a well defined steady state regime during creep. Analysis of the data is complicated somewhat by the effect of the whiskers on processing which leads either to the use of different sintering additives and processing conditions in the composites and the whisker-free materials, and/or differences in matrix grain size. The difficulty in densifying these materials is of course direct evidence for the formation of whisker networks, as noted by Lange [17]. Despite these concerns, some general conclusions can be reached about the creep of these materials. First, recent results have shown that the stress exponent for creep is between 1 and 2 at low stresses (i.e. the same as that of the matrix itself), and rises with increasing stress due to the onset of cavitation during creep [18]. There appears to be very little improvement in creep resistance for whisker loading less than about 10%. This is consistent with the model quoted above (see eq. 1) for non-interacting particles. For higher whisker loadings, the creep resistance increases by about 100 times and is then insensitive to volume fraction. This is shown in Fig. 2, in which the effect of reinforcement on matrix creep resistance is shown for a range of composite systems.

Class II Composites

Higher volume fractions can only be achieved by using equiaxed particles and modified processing routes, as in siliconized silicon carbide. The creep resistance of this material is characterized by a marked creep symmetry (i.e. the creep rate at a given stress is much higher in tension). At high stresses cavitation is important in tension while in compression, creep is controlled by deformation within the SiC particles themselves. At low stresses neither of these processes is seen. Instead, the creep asymmetry is associated with the viscous squeezing process. Models for viscous flow [14] do indeed predict a difference in the creep response in tension and compression. Moreover, the reduction in creep rate predicted by the models for a normalized Si layer thickness of about 0.01, which is about 10^{-7}, is broadly consistent with the experimental data (see Fig. 2). However, additional effects related to nature of dilational flow may also be important as recently proposed by Wiederhorn and Fuller [8].

Class III Composites

Silicon nitride can be thought of as a glass matrix composite containing between 90 and 99 vol% of β-Si_3N_4 particles. The creep resistance of these materials is 8-10 orders of magnitude greater than that of the glass itself (see Fig. 2), which is broadly consistent with the model for viscous flow presented earlier. Moreover, the marked creep asymmetry also suggests the presence of viscous flow. The clearest evidence for this process is found in a study of a Y_2O_3-Al_2O_3 doped material in which the creep rate is found to decrease dramatically as the glass is squeezed from between boundaries under compression [19]. However, a gradually decreasing strain rate is a commonly observed feature in silicon nitride creep studies [8]. Reference to eq. (1) suggests that creep strengthening of class III materials can be achieved by increasing the viscosity and reducing the volume fraction of the glassy phase.

Improvements of this nature over the past decade roughly, have led to about a 10^5 improvement in creep strength for silicon nitride ceramics, and it remains likely that further improvements can be achieved.

Damage Processes

Damage processes have received less attention than creep itself in multi-phase ceramics. In some cases this is simply a reflection of how recently materials have been developed. Most of our knowledge of whisker-reinforced ceramics for example, has been developed since about 1985, and creep studies of these systems have been undertaken only in the last 2-3 years. That creep should be studied before creep fracture is clear. First, the former is much easier to undertake, and since, at least to a first approximation, these materials obey a Monkman-Grant type of relationship, lowering the creep rate is the key to extending lifetime also.

In general, the creep fracture of all of the materials considered here occurs by a process involving crack propagation, often accompanied by generalized damage in the form of grain boundary cavitation. In many materials two distinct regimes are evident. At high stresses (and lower temperature) failure occurs by slow crack growth with the development of a single dominant crack and very little unconnected damage. This regime is connected with a very high stress exponent for creep life (typically of order 50), i.e. a distinct threshold stress for failure is observed. At lower stresses, a multitude of microcracks is observed which eventually link up to cause failure. A much lower stress exponent is observed in this regime, close to that for creep itself, thus leading to Monkman-Grant behaviour. This is exemplified by a relationship, valid over a wide range of applied stress and temperature, between the steady state strain rate and the time to failure of the form

$$\dot{\epsilon}^m t_f = C_{MG} \tag{3}$$

where C_M is the Monkman-Grant constant and is approximately equal to the failure strain unless primary creep is extensive. For true Monkman-Grant behaviour the exponent m should equal one, in which case both the stress exponents and the activation energies are the same for creep and fracture. This leads one to conclude that the same mechanism governs both processes. In many instances however, while a single curve is obtained for a range of temperatures (thus indicating a common activation energy), the exponent deviates from one. This suggests that a different mechanism but with the same temperature dependence governs creep and fracture. This is possible for example if creep is due to core diffusion-controlled dislocation climb, while fracture is controlled by grain boundary diffusion-controlled cavity growth. Thus care must be exercised in interpreting the mechanistic basis of the Monkman-Grant relationship.

In both failure regimes, cracks nucleate at flaws in the material. In many instance these are quite different from the flaws that lead to failure during fast fracture testing at lower temperatures. Indeed, the critical flaws may not even exist in the material as it enters service, but can develop as a result of environmental degradation. An example of such behaviour, a pit developed on the surface of a silicon nitride flexure bar is shown in Fig. 3.

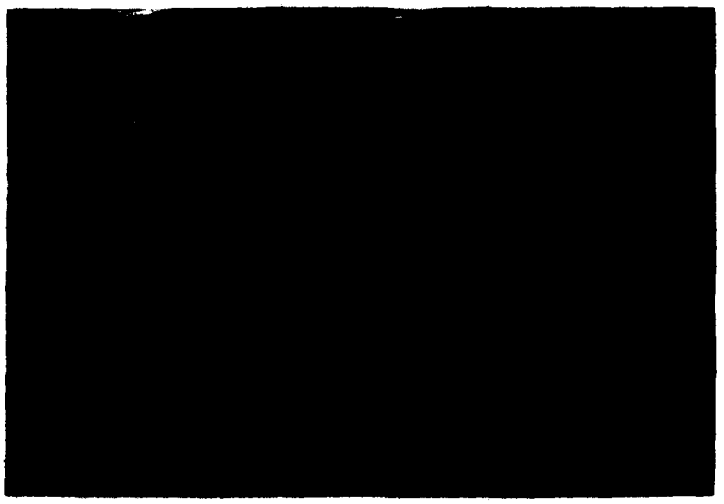

Fig. 3: A pit (about 40 μm wide) has developed on the surface of a silicon nitride flexure bar by oxidation during creep. Such pits can act as failure origins [20].

Single Phase Materials

The creep fracture behaviour of pure alumina has been extensively studied in recent years [15,16,21]. A typical stress rupture plot is shown in Fig. 4, which clearly shows the transition from slow crack growth to the generalized damage regime. This is accompanied by a marked increase in ductility from less than 1% to about 10%. Above the transition only a single crack is ever observed, while below it many microcracks are found on the surface of both flexure and tensile specimens. These are nucleated, in this material, in regions which have undergone abnormal grain growth. Such regions abound in hot-pressed aluminas due to incomplete mixing of sintering aids, and range from single large grains to large clusters of such. As the stress decreases diffusional accommodation makes crack nucleation more difficult. Thus, the size of the clusters which can nucleate cracks increases, and the crack density actually decreases. This is accompanied by a rapid increase in ductility and truly superplastic behaviour is observed, even at temperatures as low as 1200°C. However, even in this high ductility regime, it is not possible to rationalize creep fracture data in terms of cavity growth models. Instead failure is controlled by crack propagation in a creep-relieved C^* stress field [16].

Class I Composites

This class of material is typified by the Al_2O_3/SiC system, in which SiC whiskers are added to alumina matrices with volume fractions ranging from 5 to 30%. Creep fracture studies to date have involved flexure testing only. As shown in Fig. 5, for 20 vol% SiC, the two fracture regimes mentioned above are found only at

temperatures in excess of 1200°C [22]. The fracture surfaces and damage morphologies in both regimes are similar to those seen in pure alumina. The development of a threshold at 1100°C and below can be attributed to crack blunting due to environmental interactions involving both the oxidation of the SiC whiskers and reactions between SiC and alumina [22]. In summary, it appears from the limited data so far available, that creep fracture in whisker reinforced oxides is similar to that in the matrix materials themselves, although the stresses required to produce failure in a given time are increased.

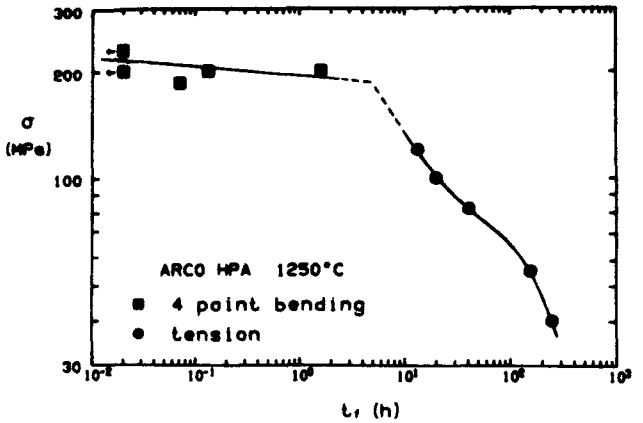

Fig. 4: A stress rupture plot for hot-pressed alumina at 1250°C. The high strength data is collected in flexure, while the longer term failures are the result of tensile testing. Since the high stress failures allow insufficient time for relaxation the strength is independent of stress state [15].

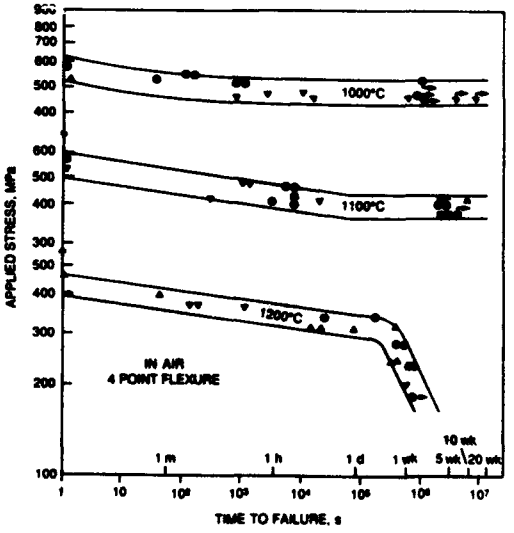

Fig. 5: A stress rupture plot for alumina reinforced with 20 vol% SiC whiskers. Slow crack growth controlled failure is observed at all temperatures, with the appearance of a generalized damage regime at 1200°C [23].

Class II Composites

When the volume fraction of the reinforcement rises to about 50%, then a well percolated network of second phase particles is developed such that interparticle contacts not only involve touching corners but shared faces. Such is the case for example with siliconized silicon carbide. Thus many SiC-SiC boundaries are found with relatively thin (i.e. 10-100 nm) films of silicon between them [24]. These highly constrained regions are the primary sites for damage in such materials [24,25]. This material cavitates readily and several quantitative studies of damage have shown that the level of damage (e.g. area fraction of cavities on a polished plane) increases linearly with strain beyond an incubation strain [24,26]. In fact, the cavitated volume fraction is almost equal to the strain leading some authors to suggest that the tensile strain is due almost entirely to that produced by cavity growth [27]. While this requires that all of the cavities grow on facets normal to the tensile stress and thus contribute only to the strain in the tensile direction (a somewhat extreme assumption), this behaviour does suggest that cavitation is controlled by deformation and that cavity growth contributes substantially to the tensile strain, and thus to the creep asymmetry noted in these materials. This explains the strong Monkman-Grant behaviour observed in this system, as illustrated in Fig. 6. This plot shows that the time to failure and steady state strain rate are well correlated over a range of temperature and stress. Note however, that the exponent is not one but closer to 1.2, i.e. creep has a stronger stress dependence than does fracture.

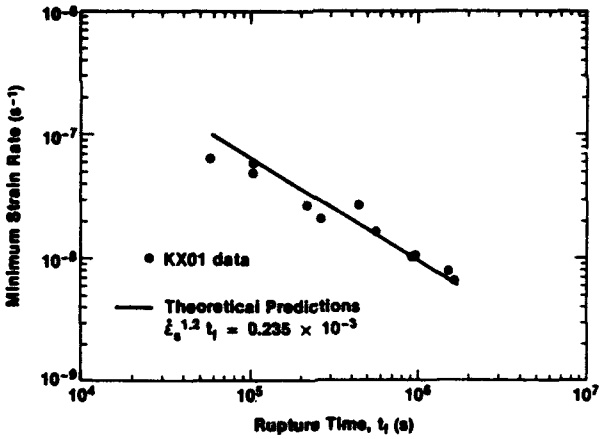

Fig. 6: The time to failure is correlated to the steady state strain rate over a range of temperature through the Monkman-Grant relationship with an exponent of 1.2. The material is Sohio KX01, a Si-SiC composite containing about 67% SiC particles [28].

Class III Composites

We now turn to ceramic systems in which a large volume fraction of hard particles is held together by a small amount of a binder phase. The prototypical example of this class of material is the silicon nitride family. A large body of creep rupture data

has been collected on a range of silicon nitride materials. The most studied material is Norton NC-132, a hot pressed material containing MgO as the additive [4,29]. Quinn has used this data to develop a fracture mechanism map which differentiates the regimes of stress and temperature in which failure occurs either by slow crack growth of by generalized damage [29,30]. This is shown in Fig. 7. This behaviour is then broadly similar to that observed in other ceramic systems. However, the slow crack growth regime persists out to longer times in these materials, and thus relatively little data is available on the generalized damage regime (referred to on the map as "creep fracture"), even in the most heavily studied systems.

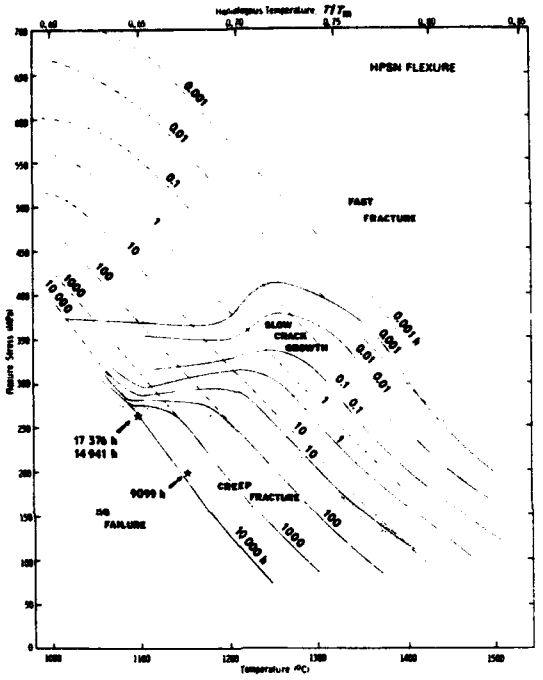

Fig. 7: A fracture mechanism map for an MgO-doped hot-pressed silicon nitride. This map summarizes the results of about 1,000 flexural tests over a wide range of temperature and stress [4].

The development of this class of materials over the last twenty years has led to an decrease in the volume fraction of the glassy phase and an increase in its refractoriness. Thus, early materials (such as NC-132) were prone to the development of microcracks from wedge shaped amorphous regions. These were replaced by materials with Y_2O_3 and Al_2O_3 as additives. These materials can be densified without external pressure and produce a more refractory amorphous phase, thus raising the temperature for the onset of creep fracture [20]. However, the relatively large volume fraction of glass (about 8-10 vol%) still leads to wedge cracking, making these materials also susceptible to slow crack growth. More recently this problem has been relieved by eliminating Al_2O_3. The resulting materials need to be HIPed or hot pressed, but much lower glass contents (on the order of 3 vol%) can be achieved. In these materials cavities can form along the silicon nitride junctions. The appearance of these cavities is similar to that observed in some pure materials such as alumina. Cavity formation and propagation in these regions is

highly constrained thus leading to longer creep lives [27], although with reduced ductility.

Despite the changes in damage tolerance and ductility brought about changes in processing, the greatest improvement in creep life is due to enhanced creep resistance through the Monkman-Grant relationship. Wiederhorn and Fuller [8] have recently shown that the creep rupture data for a wide range of silicon nitrides fall on almost the same curve (Fig. 8). However, materials densified with Y_2O_3 alone generally show about a 10^6 decrease in strain rate for a given stress as compared with an MgO-doped material of a decade ago [8]. They therefore exhibit much longer lives for a given stress and temperature. The scatter in failure time of about one order of magnitude represents differences in creep ductility brought about by differences in processing and microstructure (i.e. more damage-tolerant and flaw-free materials). It is interesting to note that the most recent materials fall to the left of the scatter band, suggesting these materials have generally lower failure strains. While this is secondary to lifetime, it suggests that such materials may be susceptible to enhanced crack growth from large defects and may be prone to cyclic fatigue damage at elevated temperatures.

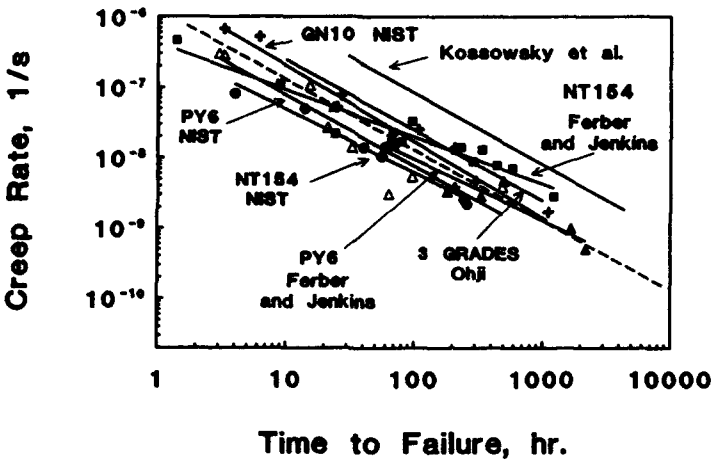

Fig. 8: The Monkman-Grant relationship is obeyed by a wide range of silicon nitride ceramics containing different sintering aids and using a range of processing routes. The variability in lifetime using this plot covers about one order of magnitude, indicative of the variation in creep ductilities [8]. For original references, see original paper [8].

An additional feature of this class of materials is the instability of the amorphous phase. In particular, glass in larger pockets is particulary susceptible to devitrification [20]. This can affect both the creep resistance and damage tolerance of the material. In some systems devitrification is nearly complete and the composition of any remaining glass is substantially more refractory than the initial glass. In this case the creep resistance is dramatically improved and by virtue of the Monkman-Grant relationship the creep life extended. This is the case for example with glass-bonded aluminas in which devitrification leads to a 100-fold increase in lifetime. In some materials however, devitrification is incomplete. This occurs for some sintered silicon nitrides in which the glass composition is close to that for a

stable glass. In the Y_2O_3-Al_2O_3-SiO_2 system for example, a stable glass exists at a composition of about 1:1:4. In Kyocera SN220 for example we have found that the glass reaches this composition when about 1/3 of the glass remains. Thus full devitrification is not possible in this system (Fig. 9). Moreover, the creep resistance of this material is essentially unchanged by devitrification. This is because there is ample glass in large intergranular pockets, while creep is controlled by the thickness and viscosity of the glass in intergranular films. Thermodynamic considerations[9,20] suggest that this will be unchanged by devitrification in the pockets. The result of this process is unchanged creep resistance accompanied by a loss of damage tolerance provided by the large glass pockets. Thus in this system, devitrification leads to a dramatic reduction of creep life (by more than a factor of 10, Fig. 10). This example makes clear that while Monkman-Grant behaviour gives guidelines on the control of lifetime through creep resistance there are additional factors which play an important role in the fracture behaviour of these materials.

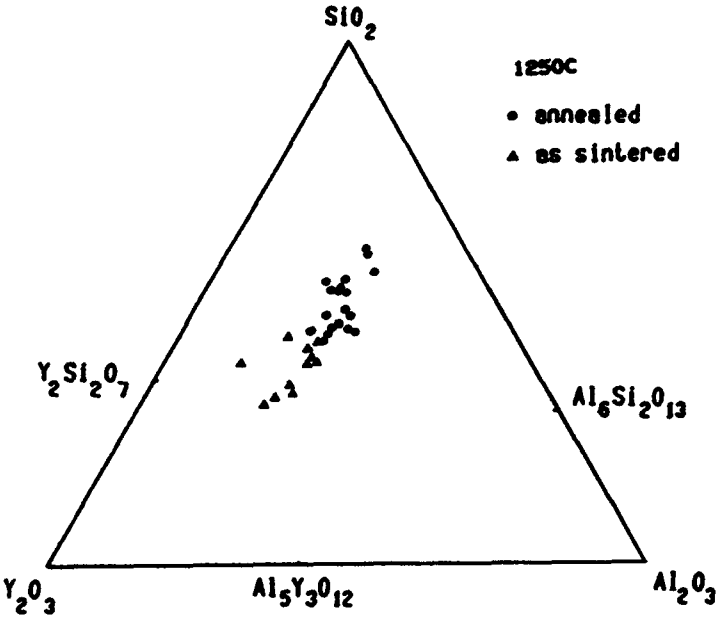

Fig. 9: The Y_2O_3-Al_2O_3-SiO_2 phase diagram showing the composition of the intergranular pockets in Kyocera SN220 before and after annealing (400 hrs. at 1250°C).

Conclusions

In this brief review of the creep and creep fracture behaviour of a range of multi-phase ceramic systems, one can see how the creep resistance changes dramatically as the volume fraction of the hard phase is increased. A range of strategies have been developed in which creep resistance is improved by both increasing the creep resistance of the softer matrix phase and by decreasing the volume fraction of this phase. Thus small volume fractions of a hard phase have been added to relatively strong matrices such as alumina, while large volume fractions of a hard phase are needed when a soft matrix such as a glass is used. Dramatic improvements in creep resistance of such systems have been achieved in recent years. While differences

in details exist amongst the materials considered, the damage mechanisms exhibited by a wide range of composites are broadly similar. At high stresses cracks are nucleated at large flaws in the most highly stressed region of the structure. The lack of additional damage suggest that once nucleated, cracks propagate rapidly leading to failure. Below a transition stress, the development of generalized damage is found. A much lower stress exponent for failure, comparable to that observed for creep itself is found. Cracks are still nucleated at flaws, but these are now often generated during service. Failure in this regime generally obeys the Monkman-Grant relationship. However, as improved processing leads to increased creep resistance and lifetime, this is often accompanied by a loss of ductility. This may lead to an increased susceptibility to high temperature fatigue.

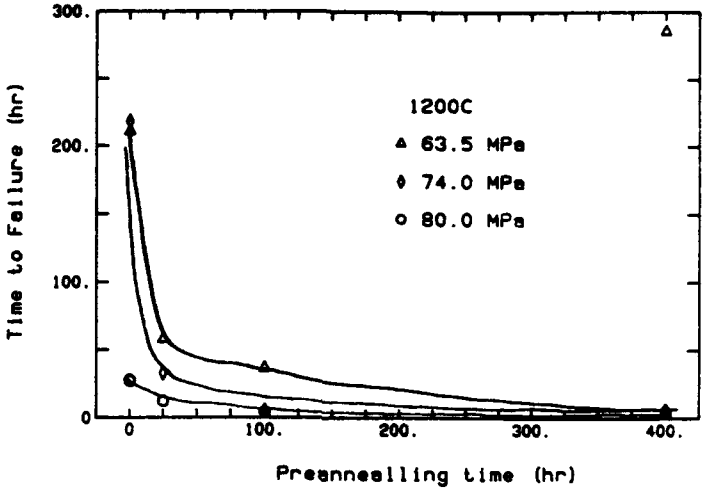

Fig. 10: The creep life of Kyocera SN220 at 1200°C, as a function of the annealing time (also at 1200°C) prior to creep. A 24 hour anneal is sufficient to dramatically reduce the creep life (at 64 MPa for example, by about 160 hours).

References

1. D. S. Wilkinson, "Feature Article: Creep Mechanisms in Multi-Phase Ceramic Materials", J. Am. Ceram. Soc., in preparation (1993)

2. W. R. Cannon and T. G. Langdon, "Review: Creep of ceramics. Part 1 - Mechanical charactersistics", J. Mat. Sci, **18**, 1-50 (1983)

3. W. R. Cannon and T. G. Langdon, "Review: Creep of ceramics. Part 2 - An examinations of flow mechanisms", J. Mat. Sci, **23**, 1-20 (1988)

4. G. D. Quinn, "Fracture mechanism maps for advanced structural ceramics, Part 1 - Methodology and hot-pressed silicon nitride results", J. Mat. Sci., **25**, 4361-76 (1990)

5. G. D. Quinn and W. R. Braue, "Fracture mechanism maps for advanced structural ceramics, Part 2 - Sintered silicon nitride", J. Mat. Sci., **25**, 4377-92 (1990)

6. K. S. Chan and R. A. Page, "Creep damage development in structural ceramics", J. Am. Ceram. Soc., in press (1993)

7. R. Raj, "Fundamental research in structural ceramics for service near 2000°C", J. Am. Ceram. Soc., in press (1993)

8. S. M. Wiederhorn and E. R. Fuller Jr. "Creep deformation of particulate reinforced ceramic matrix composites", in Elevated Temperature Mechanical Behaviour of Ceramic Matrix Composites, eds. S. V. Nair and K. Jakus (Butterworth Heinnema, 1993), in press

9. D. R. Clarke, "On the equilibrium thickness of intergranular glass phases in ceramic materials", J. Am. Ceram. Soc., **70**, 15-22 (1987)

10. B. J. Hockey, S. M. Wiederhorn, W. Liu, J. G. Baldoni and S. T. Buljan, "Tensile creep of whisker-reinforced silicon nitride", J. Mater. Sci., **26** 3931-39 (1991)

11. D. A. Koster, K. L. More and R. F. Davis, "Deformation and microstructural changes in SiC whisker-reinforced Si_3N_4 composites", J. Mater. Res., **6**, 2735-46 (1991)

12. A. J. Whitehead, T. F. Page and I. Higgins, "Novel siliconized mixed-phase ceramics", Ceram. Engin. & Sci. Proc., **10** [9-10], 1108-20 (1989)

13. S. M. Wiederhorn, B. J. Hockey and T. J. Chuang, "Creep and creep rupture of structural ceramics", in Toughening Mechanisms in Quasi-Brittle Materials, ed. S. P. Shah, 555-76 (Kluwer Academic Publishers, Netherlands, 1991)

14. J. R. Dryden, D. Kucerovsky, D. S. Wilkinson and D. F. Watt, "Creep deformation due to a viscous grain boundary phase", Acta metall., **37**, 2007-15 (1989)

15. A. G. Robertson, D. S. Wilkinson and C. H. Cáceres, "Creep and creep fracture in hot-pressed alumina", **74**, 915-21(1991)

16. D. S. Wilkinson, C. H. Cáceres, and A. G. Robertson, "Damage and fracture mechanisms during high temperature creep in hot-pressed alumina", J. Am. Ceram. Soc., **74**, 922-33 (1991)

17. F. F. Lange, "Constrained network model for predicting densification behaviour of composite powders", J. Mater. Res., **2**, 59-65 (1987)

18. A. R. de Arellano-López, A. Domínguez-Rodríguez, K. C. Goretta and J. L. Routbort, "Plastic deformation mechanisms in SiC-whisker-reinforced Al_2O_3", J. Am. Ceram. Soc., in press (1993)

19. M. M. Chadwick, R. S. Jupp and D. S. Wilkinson, "Creep behaviour of a sintered silicon nitride", J. Am. Ceram. Soc., **76**, 376-84 (1993)

20. M. M. Chadwick and D. S. Wilkinson, "Microstructural evolution in annealed and crept silicon nitride", J. Am. Ceram. Soc. **76**, 385-96 (1993)

21. B. J. Dalgleish, E. B. Slamovich and A. G. Evans, "Duality in the creep rupture of a polycrystalline alumina", J. Am. Ceram. Soc., **68**, 575-81 (1985)

22. P. F. Becher, P. Angelini, W. H. Warwick and T. N. Tiegs, "Elevated-temperature-delayed failure in alumina reinforced with 20 vol% silicon carbide whiskers", J. Am. Ceram. Soc. **73**, 91-96 (1990)

23. A. R. de Arellano-López, F. L. Cumbrera, A. Domínguez-Rodríguez, K. C. Goretta and J. L. Routbort, "Compressive creep of SiC-whisker-reinforced Al_2O_3", J. Am. Ceram. Soc., **73**, 1297-300 (1990)

24. D. F. Carroll and R. E. Tressler, "Accumulation of creep damage in a siliconized silicon carbide", J. Am. Ceram. Soc., **71**, 472-77 (1988)

25. S. M. Wiederhorn, L. Chuck, E. R. Fuller Jr. and N. J. Tighe, "Creep rupture of siliconized carbide", in Tailoring Multiphase and Composite Ceramics, eds, R. E. Tressler, G. L. Messing, C. G. Pantano and R. E. Newnham, 755-73 (Plenum, 1986)

26. D. F. Carroll and R. E. Tressler, "Effect of creep damage on the tensile creep behaviour of a siliconized silicon carbide", J. Am. Ceram. Soc., **72**, 49-53 (1989)

27. W. Luecke, S. M. Wiederhorn, B. J. Hockey and G. G. Long, "Cavity formation during tensile creep of Si_3N_4", Proc. MRS, vol. 287, Symp. on Silicon Nitride Ceramics - Scientific and Technological Advances, in press (1993)

28. T. J. Chuang, D. F. Carroll and S. M. Wiederhorn, "Creep rupture of a metal-ceramic perticulate composite", Proc. 7th Intl. Conf. on Fracture, eds. K. Salama, K. Ravi-chandar, D. M. R. Taplin and P. Rama Rao, 2965-76 (Pergamon, Oxford, 1989)

29. G. D. Quinn and J. B. Quinn, "Slow crack growth in hot-pressed silicon nitride", Fracture Mechanics of Ceramics, vol. 6, eds. R. C. Bradt, A. G. Evans, D. P. H. Hassleman and F. F. Lange, 603-36 (Plenum, 1983)

30. G. D. Quinn, "Fracture mecahnism maps for silicon nitride", Proc. 2nd Intl. Symp. on Ceramic Materials and Components for Engines (Deutsche Keramische Gesellschaft, 1986)

Acknowledgements

Several stimulating discussions over several years with Dr. S. Wiederhorn, NIST, have contributed signifigantly to this work. Funding for this research has been provided by Alcan, Intl., the Technology Fund of Ontario and the Natural Sciences and Engineering Research Council of Canada.

DESIGNING FOR IMPROVED HIGH TEMPERATURE STRENGTH, CREEP, OXIDATION, AND FATIGUE RESISTANCE IN Si_3N_4

Gareth Thomas*

Department of Materials Science and Mineral Engineering
University of California, Berkeley, CA 94720, and
Center for Advanced Materials, Lawrence Berkeley Laboratory, Berkeley, CA 94720

Abstract

One of the critical issues in many covalently bonded ceramics such as Si_3N_4 is that of grain boundary control. Grain boundaries can be engineered to avoid retention of the intergranular glassy phases which form as a result of sintering with oxide densifying additives. Long-range research on intergranular glassy phases and glass crystallization, using high resolution characterization, has led to a sintering process that forms intergranular crystalline rare-earth disilicates. The resulting "composite" is not 100% crystalline at grain boundaries, but shows great improvements in high temperature flexural strength (retention of ~90% of the room temperature strength at 1300° C) as well as oxidation and creep resistance compared to conventional silicon nitrides, without adversely affecting room temperature fatigue behavior.

*Currently on leave as Director of Technology Transfer Centre, Hong Kong University of Science and Technology, Clear Water Bay, Kowloon, Hong Kong.

Critical Issues in the Development of High Temperature Structural Materials
Edited by N.S. Stoloff, D.J. Duquette and A.F. Giamei
The Minerals, Metals & Materials Society, 1993

Introduction

To achieve more efficient research towards the improvement of materials, it is necessary to understand the relationships between synthesis and processing-structure (characterization) properties and performance by iterative theory and experiment. Processing determines microstructure and chemical distribution of components and impurities, which in turn greatly influence most of the mechanical properties desirable for high temperature applications. In the case of many ceramics whose bonding characteristics require processing with sintering aids to achieve densification, the resulting materials often contain residual, glassy phases at grain boundaries (Fig. 1). Si_3N_4 is a typical example (Fig. 2a). These phases, depending on composition, viscosity, etc., deteriorate mechanical, electrical and magnetic properties (Fig. 1). A basic understanding of such intergranular and interphase interfaces is therefore essential if improvements in performance are to be achieved. A program towards this end has been under way at Berkeley for some 15 years. In the course of this program, techniques were developed for high resolution electron optical characterization of intergranular phases [1,2] (morphologies, composition), studies of crystallization of glasses [3,4], and, finally, successful processing to obtain mostly crystalline intergranular phases [5]. Similar efforts have been made by other researchers (references 6-14). However, the use of the heavy RE lanthanide oxides (Sm → Yb) has received little attention outside our current research. Such problems are not limited to ceramics, as the case of aluminum alloy intergranular embrittlement illustrates (Fig. 2b). This paper summarizes our current microstructural research [5,15,16] and fatigue studies [17] in Si_3N_4. In all materials studied, sintering with RE oxide additives has been successful in obtaining $RE_2Si_2O_7$ crystalline grain boundary phases.

Grain boundaries / interfaces	Examples	Properties limited
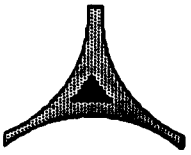 Amorphous films	Si_3N_4	Creep
Partly crystalline films	Some Sialons	Creep
	Ferrites	Magnetic: permeability
	Varistors	Voltage drop required
Additives / impurities	ß Na alumina	Na^+ conduction
	ZrO_2 / mullite composites	Varied (creep, etc.)
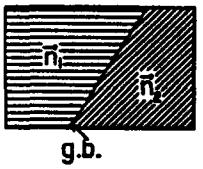 Lattice defects	Superconductors (high T_c):	
Faulting	$YBa_2Cu_3O_{7-x}$ (RE)	Defects limited; poor g.b. conduction
Transformation defects	(Pb)Bi-Sr-Ca-Cu-O Tl compounds	Polytypoids of variable T_c; poor g.b. conduction
Polytypoids		

Figure 1 - Schematic diagram illustrating some generic problems of properties, both mechanical and electronic, associated with grain boundary phases developed during processing.

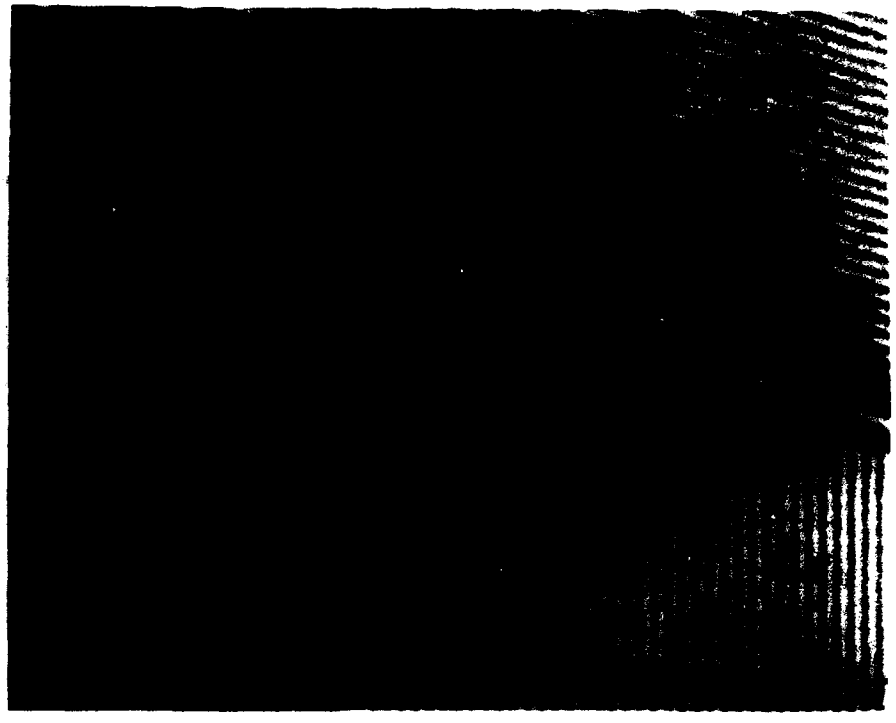

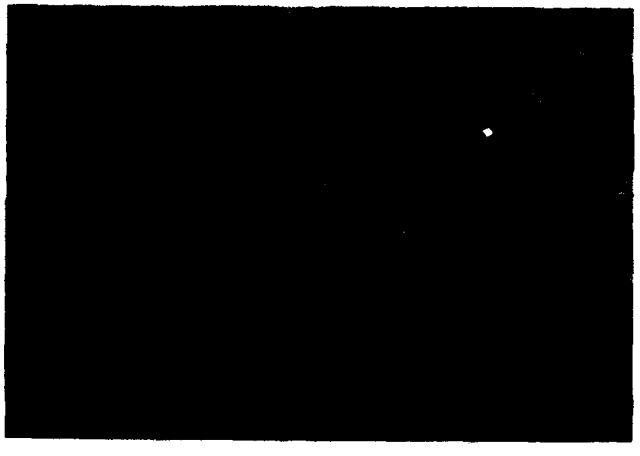

Figure 2 - (a) Lattice image of Si_3N_4 hot-pressed with Al_2O_3 and MgO, showing glassy phase at grain boundaries and triple point (Ref. 1, courtesy J. Am. Ceram. Soc.) (b) Aged Al-Zn-Mg base alloy to maximize tensile strength; the intergranular precipitate-free zone (PF2) is responsible for embrittlement (courtesy J. Inst. Metals). Such structures were responsible for the catastrophic failure of the first comet jet aircraft, i.e., before the concepts of fracture toughness were developed.

Experimental

The materials processing and testing procedures used in the work summarized here are given in detail in references 4, 11, 15 and 16. For processing with the rare-earth oxides, controlled cooling through 1400° C from the sintering temperature (1600° C) results in almost complete crystallization to form the $RE_2Si_2O_7$ crystalline phase at the grain boundaries. The choice of additives is based on the phase diagram work of Lange [7,18]. We assume that the phase relations for Si_3N_4 - Y_2O_3 - SiO_2 are similarly obtained in the other systems Si_3N_4 - RE_2O_3 - SiO_2, where RE represents Y, Sm, Gd, Dy, Er, and Yb currently under study. Figure 3 illustrates the compatibility diagram for the Si3N4 - SiO_2 - RE_2O_3 - $RE_2Si_2O_7$ phases. The only RE-containing phase stable with respect to SiO_2 (the oxidation product of Si_3N_4) is $RE_2Si_2O_7$. The ratios of SiO_2 : RE_2O_3 used for sintering aids to form $RE_2Si_2O_7$ are obviously 2 :1 and a volume fraction of ~0.2, as given at the Si_3N_4 - $RE_2Si_2O_7$ tie line, is chosen so as to "cover" all grain boundaries. Figure 3 also illustrates the trend in properties found using Y_2O_3 - SiO_2 as sintering aids and illustrates the need to control compositions very carefully. Previous researchers have used Y_2O_3 - Al_2O_3 sintering aids [6], but later work [4,5] indicated that the glassy phase was stabilized by partitioning of Al and N during crystallization Fig. 4).

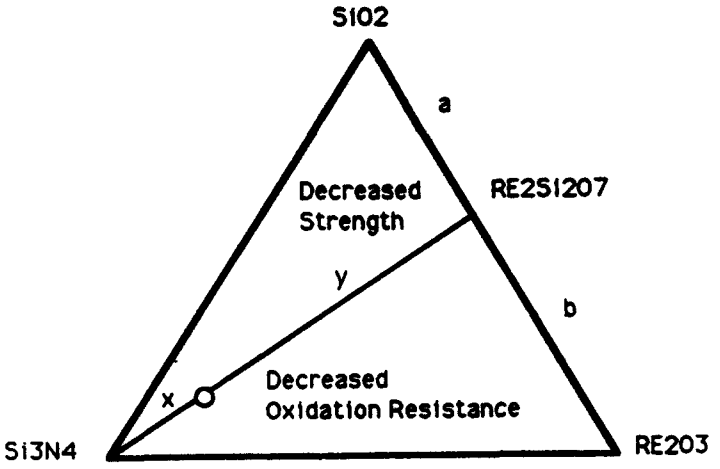

Figure 3 - Isothermal section of the Si_3N_4 - SiO_2 - $RE_2Si_2O_7$ - RE_2O_3 phase diagram illustrating grain boundary design.

Thus, Al_2O_3 has been eliminated as an additive in our subsequent research. However, even macroscopically low levels of impurities (< 200 ppm Fe + Ca + Al) in our Ube Si_3N_4 starting powder can concentrate in the glass. When this occurs, stable low-melting-point glass layers can remain. Calcium seems to be particularly deleterious in this regard. The detection of impurities thus requires careful high resolution electron microscopy and spectroscopic analyses.

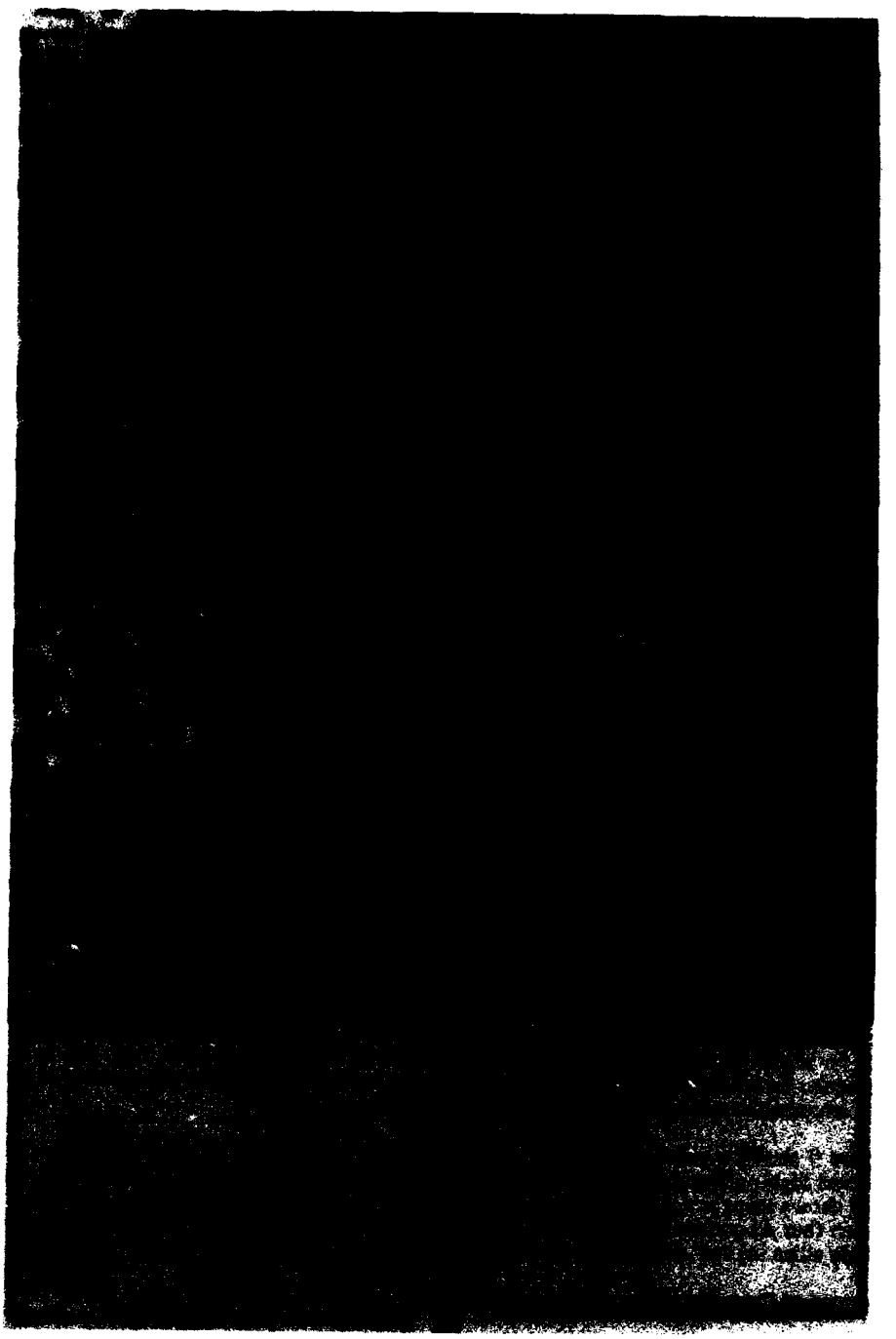

Figure 4 - Showing partitioning of Al + N into the glassy phase; chemical analyses performed by analytical electron microscopy.

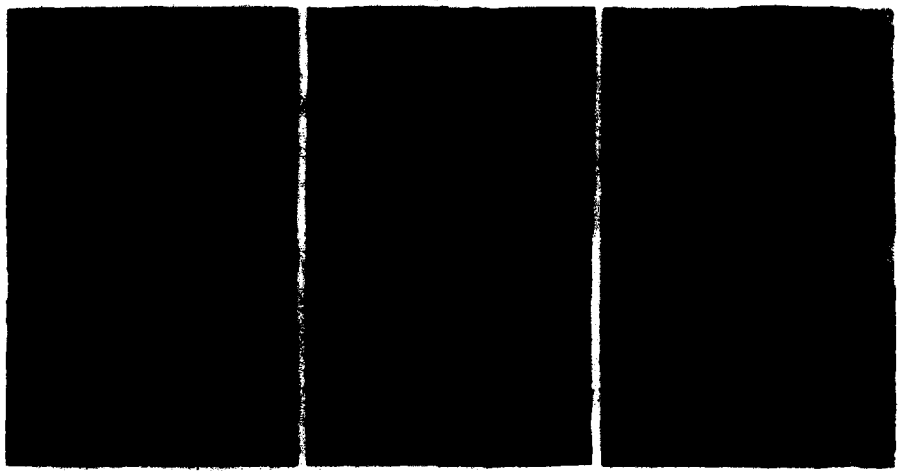

Figure 5 - Bright field electron micrographs showing the crystallized RE oxide sintered Si_3N_4. Note the large aspect ratio of matrix grains and the intergranular disilicate phases (ref. 5, courtesy J. Am. Ceram. Soc.).

Summary of Results

Microstructures

Figure 5 shows the bright field electron micrographs of the sintered products using the six RE oxides indicated. High aspect ratio grains of Si_3N_4 are surrounded by the $RE_2Si_2O_7$ phase (dark contrast) shown at higher magnification in Figure 6. The disilicate phases were characterized by x-ray and electron diffraction [5]. These high aspect ratio matrix grains are important in crack deflection, and such materials gave reasonably good K_{IC} fracture toughness values, e.g., ~ 8 MPa$\sqrt{m}$ in compact tension tests. The diffuse dark field images in Figures 7 and 8 show that some residual glass remains at grain boundaries, and at the interfaces between $RE_2Si_2O_7$ crystal phases and Si_3N_4 at triple points. Preliminary analytical electron microscopy indicates these glassy regions contain several cationic impurities, notably Ca. Thus, whilst it has been proposed from thermodynamic arguments [19] that a thin glassy layer will always be present, it appears that impurities (from the Si_3N_4, SiO_2 and RE_2O_3 starting powders) also play an important role in glass retention. Although such glasses are often only two to three molecular layers thick, their viscosity and thus composition could still be the limiting factor in high temperature mechanical behavior and performance.

Figure 9 shows typical microstructures and microchemical analyses of the "traditionally" sintered Si_3N_4 using Al_2O_3:Y_2O_3 sintering aids, usually [6] in the ratio 2:5. The diffuse dark field shows there is a glassy phase separating all Si_3N_4, and the only crystalline region is the Y-rich (but Al-containing) oxynitride phase at triple points. The residual glass appears to be mostly silica [4] and separates all crystalline interfaces.

Mechanical Properties (Flexural Strength : Creep)

Since it is possible to achieve 99% theoretical density by sintering with RE_2O_3, and since the resultant sintering product is nearly all crystalline (Figures 5-7), it is anticipated that the high temperature flexural strength and creep resistance will be greatly enhanced. This is indeed the

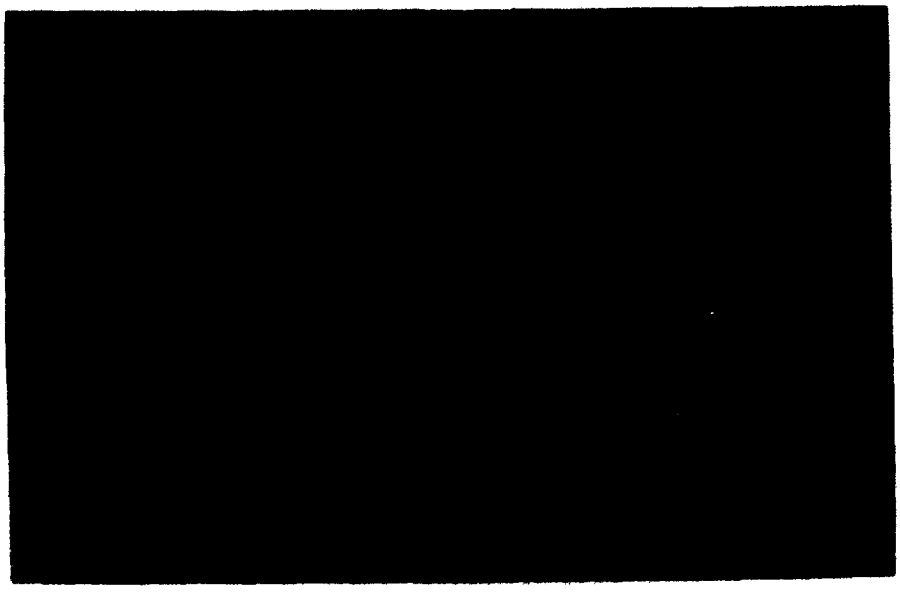

Figure 6 - Higher magnification TEM showing dark (absorption) contrast at all grain boundaries and triple junctions. The intergranular phase is $Yb_2Si_2O_7$ in this case.

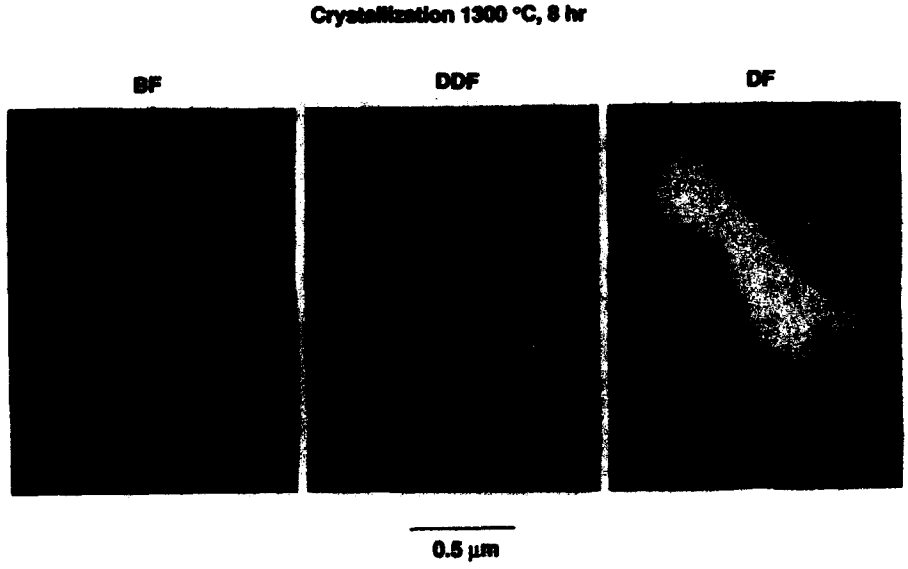

Figure 7 - As Fig. 6, showing large crystals of the $(RE)_2Si_2O_7$ phase, but in the diffuse dark field (DDF) image a thin glassy layer is resolved at grain-grain boundaries. The DF image (right) is taken using a disilicate reflection. It is seen that the crystalline phase has nucleated and grown rapidly at the expense of the matrix, and that the silicate phase is mostly in a single crystalline condition. (Courtesy M. Cinibulk.)

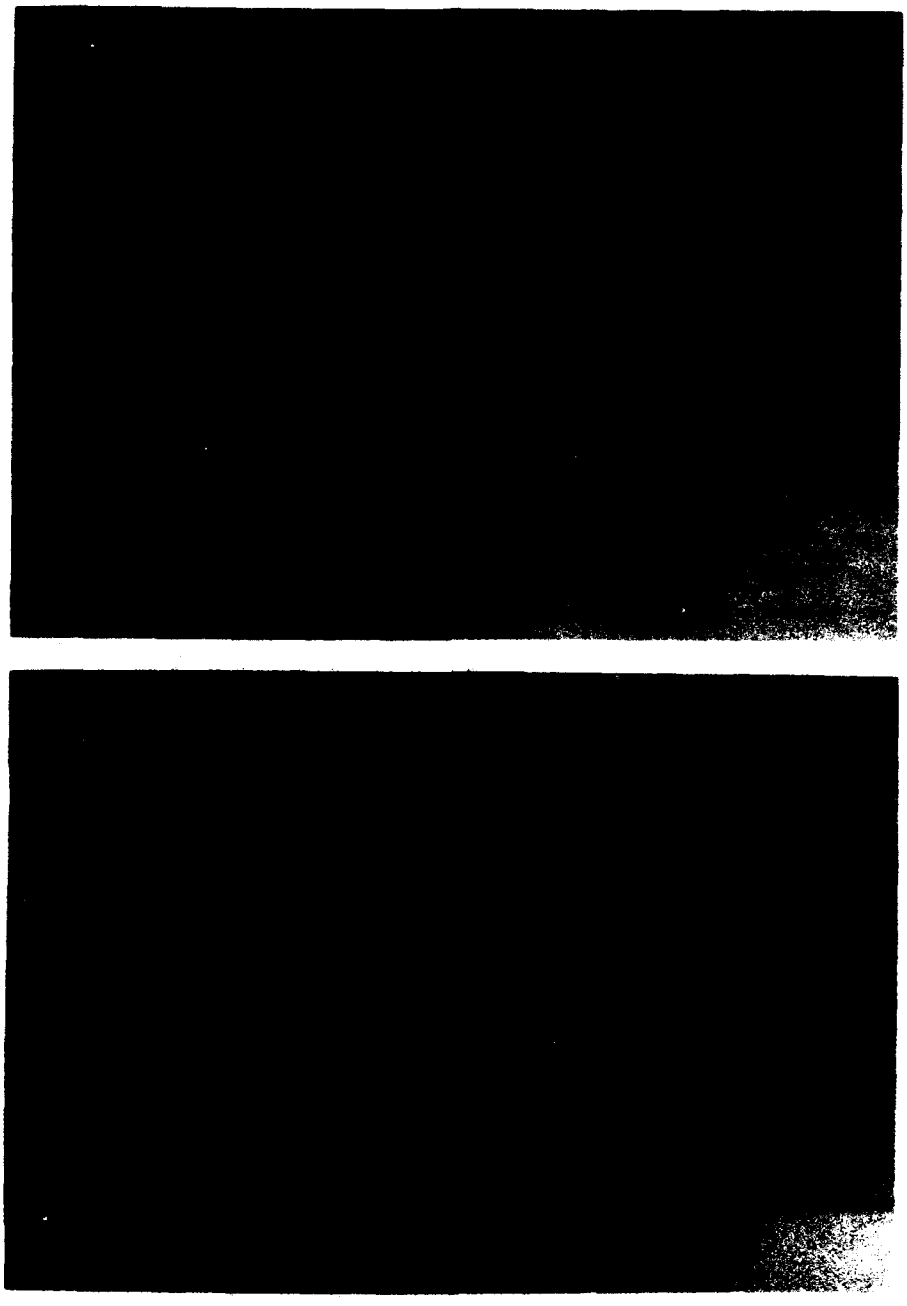

Figure 8 - Bright field-DDF pair showing that even at triple points there is also glassy phase between the matrix and disilicate phases. Impurities, especially Ca, are detected in these glasses by x-ray microanalysis (EDS) in the TEM. (Courtesy B. Cornelissen.)

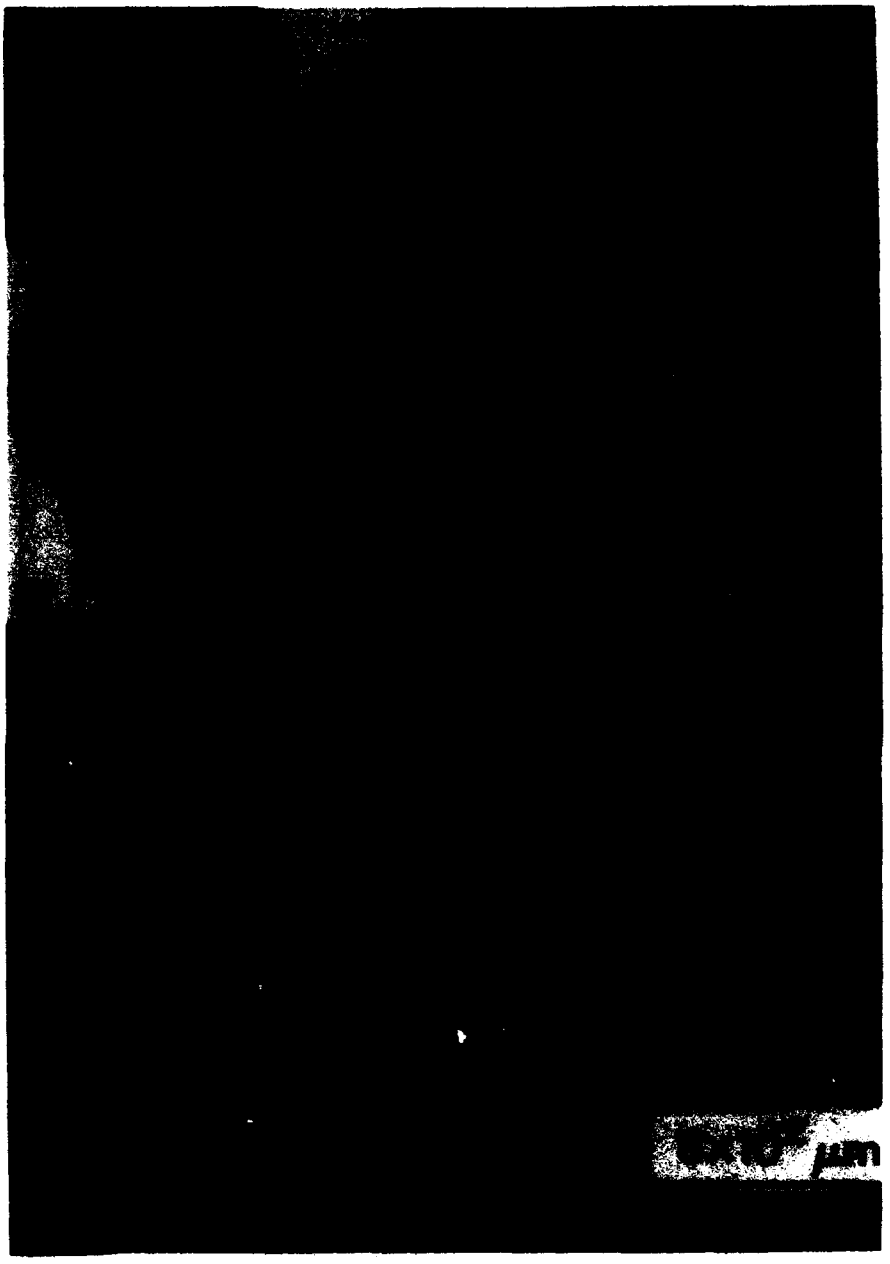

Figure 9 - Bright field (top) and diffuse dark field TEM images with the x-ray microanalysis data from the regions indicated. The crystalline Y-containing phase exists only at triple points and all crystalline interfaces are surrounded by a silica-rich glass.

case, as shown in Figure 10, for Si_3N_4 sintered with SiO_2 and Yb_2O_3. It should be noted that 91% of the room temperature strength is retained up to 1300° C. This is to be compared to Si_3N_4 sintered with Y_2O_3 and Al_2O_3, which fails to retain strength beyond ~1000° C. The latter behavior is now known to be due to glassy intergranular phases of relatively low viscosity, as shown by Figure 9. That is, the properties of the sintered compact are *determined by the grain boundary phase rather than by Si_3N_4 itself.* Strength-temperature results similar to that of Figure 10 were found for the other RE-sintered compacts [16]. These flexural strength data were obtained using standards and procedures set by the U.S. Army Materials Technology Laboratory [20]. It is important to specify the testing conditions because the flexural strengths of ceramics depend on specimen size, porosity, defects, etc. This is the reason for the differences in the room temperature strength data in Figure 10.

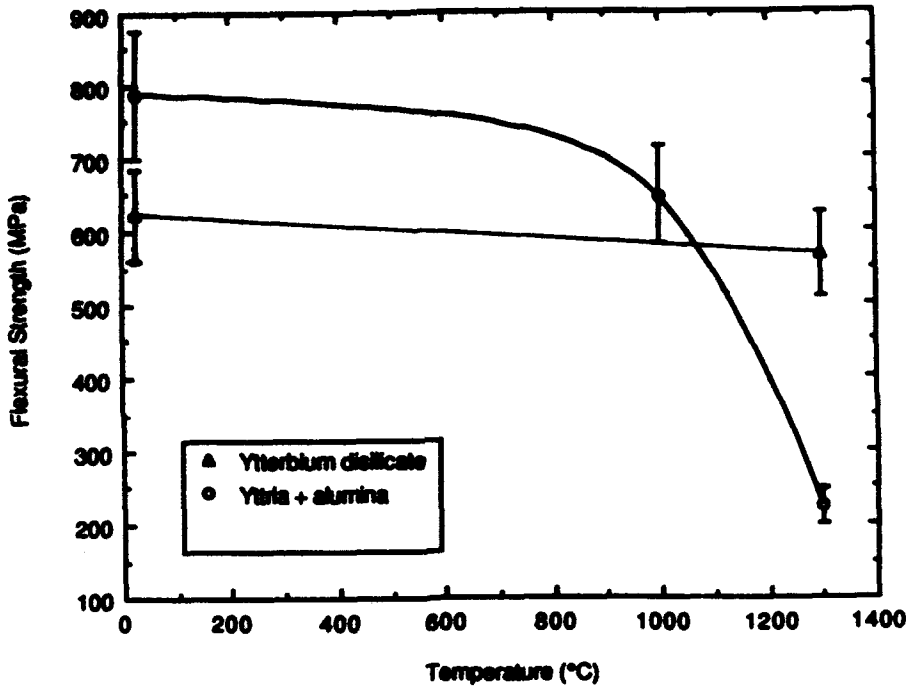

Figure 10 - Plot of flexural strengths from 25° C to 1300° C. Standard deviations are ~10% and ~5% of mean strengths at 25° C and 1300° C. The curve which shows a marked decrease in strength > 1000° C is for Al_2O_3 - Y_2O_3 sintered materials. (Courtesy M. Cinibulk.)

The creep strain versus time behavior showed a continuously decreasing creep rate. This has also been reported for Si_3N_4 by others [14,21-26]. Steady-state creep conditions are attained only after 70 hours. Figure 11 shows the creep strain rate-applied stress data, which are similar for all the materials. The creep exponents are small and correspond to creep mechanisms involving grain boundary cavitation. This has been verified by fractographic analyses [16]. *These creep rates are amongst the lowest reported in the literature.* The creep behavior is strongly dependent on the residual glass phase distribution and morphology, and on the oxidation behavior (section 2.3). Oxidation initiates at glassy phases with impurity diffusion to the surface. This results in "purification," increased viscosity, and even

devitrification of the glass. Cavitation occurs at the glassy interfaces with diffusive mass transport causing cavity growth at the expense of $RE_2Si_2O_7$. Although coalescence of cavities occurs, microcrack formation was not observed [16].

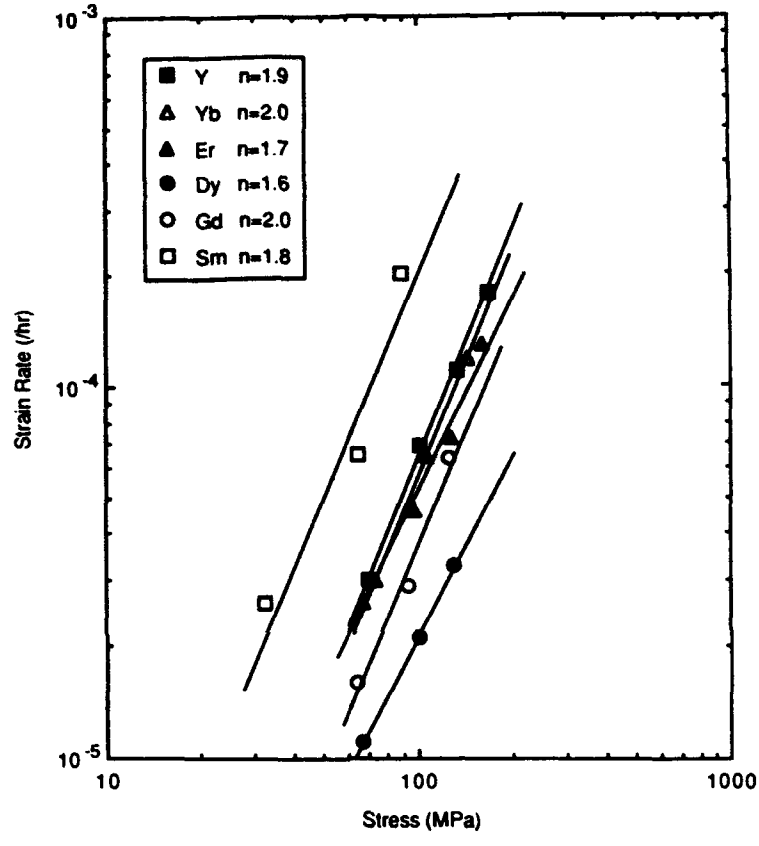

Figure 11 - Plot of "steady state" creep strain rates with applied stress at 1400° C in air. Creep exponents are given in the inset. (Courtesy J. Am. Ceram. Soc.)

Oxidation

The RE oxide-sintered materials were oxidized in air at 1400° C for over 200 hours; details are given in reference 15. The results in Fig. 12 show that the kinetics are parabolic with a rate constant of from 3.3×10^{-4} ($Er_2Si_2O_7$ - Si_3N_4) to 6.1×10^{-4} ($Gd_2Si_2O_7$ - Si_3N_4). The data indicate that a diffusional process corresponding to motion of RE^{3+} ions is the rate controlling factor.

During oxidation, disilicates crystallize at the surfaces in morphologies depending on crystal structures determined from x-ray analyses [15]. Figure 13 shows the results of scanning electron microscopy studies. The observations are consistent with previous results showing that outward diffusion of cations and inward diffusion of oxygen results in a compositional

gradient beneath the surface oxide layer. This condition results in a parabolic oxidation behavior [26-28]. The effect is not due to a protective oxide film.

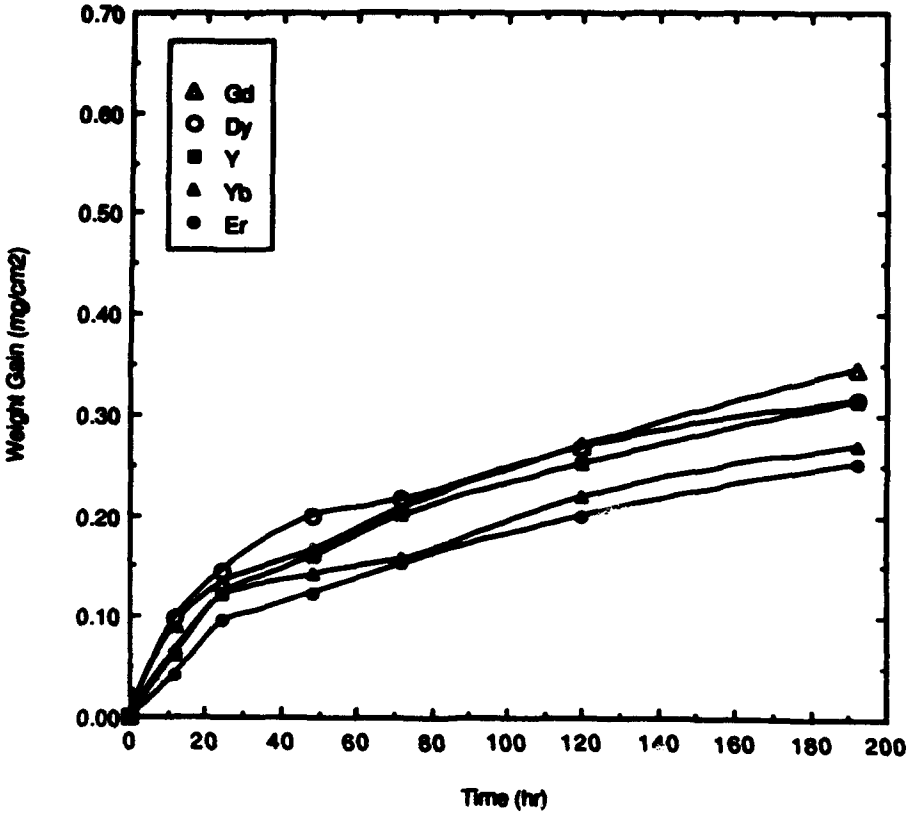

Figure 12 - Plot of oxidation rates (specific weight gain) at 1400° C (after ref. 15).

The importance of the existing disilicate phase and the devitrification of residual glass is significant in these materials, since *the oxidation rates are better by about a factor of x10 than previously reported* for Si_3N_4 prepared with "conventional" oxide sintering aids (e.g., references 26-28). The data of Figure 12 indicate that the relative rates of oxidation are roughly proportional to the eutectic temperatures of the RE_2O_3 - SiO_2 systems, indicating that a lower viscosity residual amorphous phase results in a higher rate of oxidation, as the rate-limiting step is diffusion of additive and impurity cations through the amorphous phase to the oxidized surface.

Fatigue

Although much attention has been paid to toughening ceramics, fatigue behavior can be an important, indeed limiting, condition for use of ceramics under cyclic loading conditions. Dauskardt et al. [29] indicate that the threshold stress intensity for fatigue crack propagation in ceramics is on the order of one-half of the corresponding K_{IC} values. Current work [17] on RE_2O_3 sintered Si_3N_4 is consistent with this observation. Very little difference in fatigue

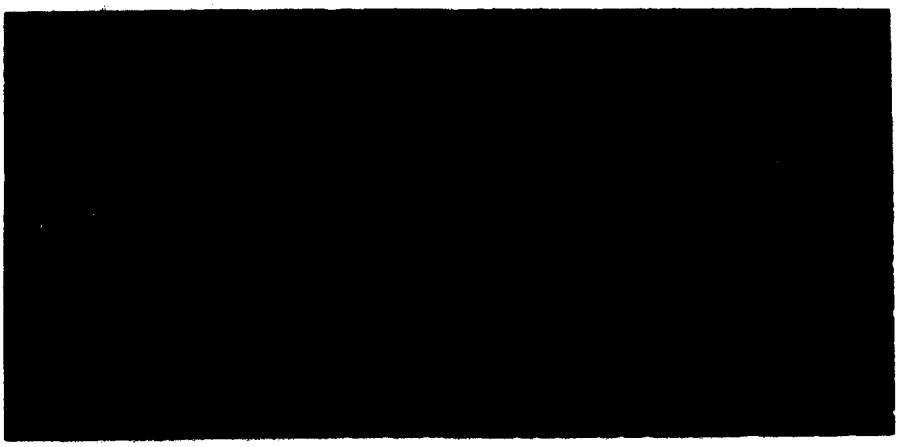

Figure 13 - Secondary electron image showing RE disilicate phases formed by oxidation at the surface. The needle morphology is associated with Ca impurities in the Gd- and Dy-containing ceramics (ref. 15, courtesy J. Am. Ceram. Soc.).

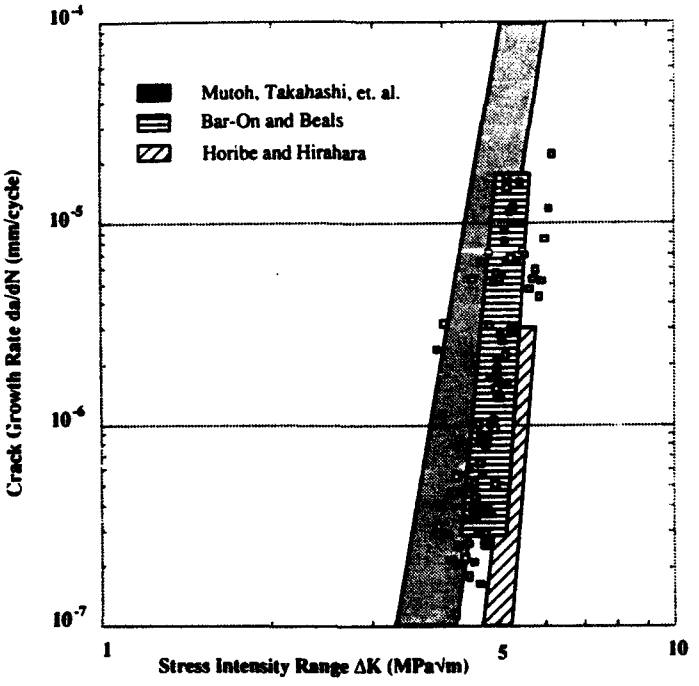

Figure 14 - Fatigue data for $RE_2Si_2O_7$ - Si_3N_4 samples (data points) plotted with previous data (shaded) indicating very little differences in crack growth (courtesy B. Cornelissen).

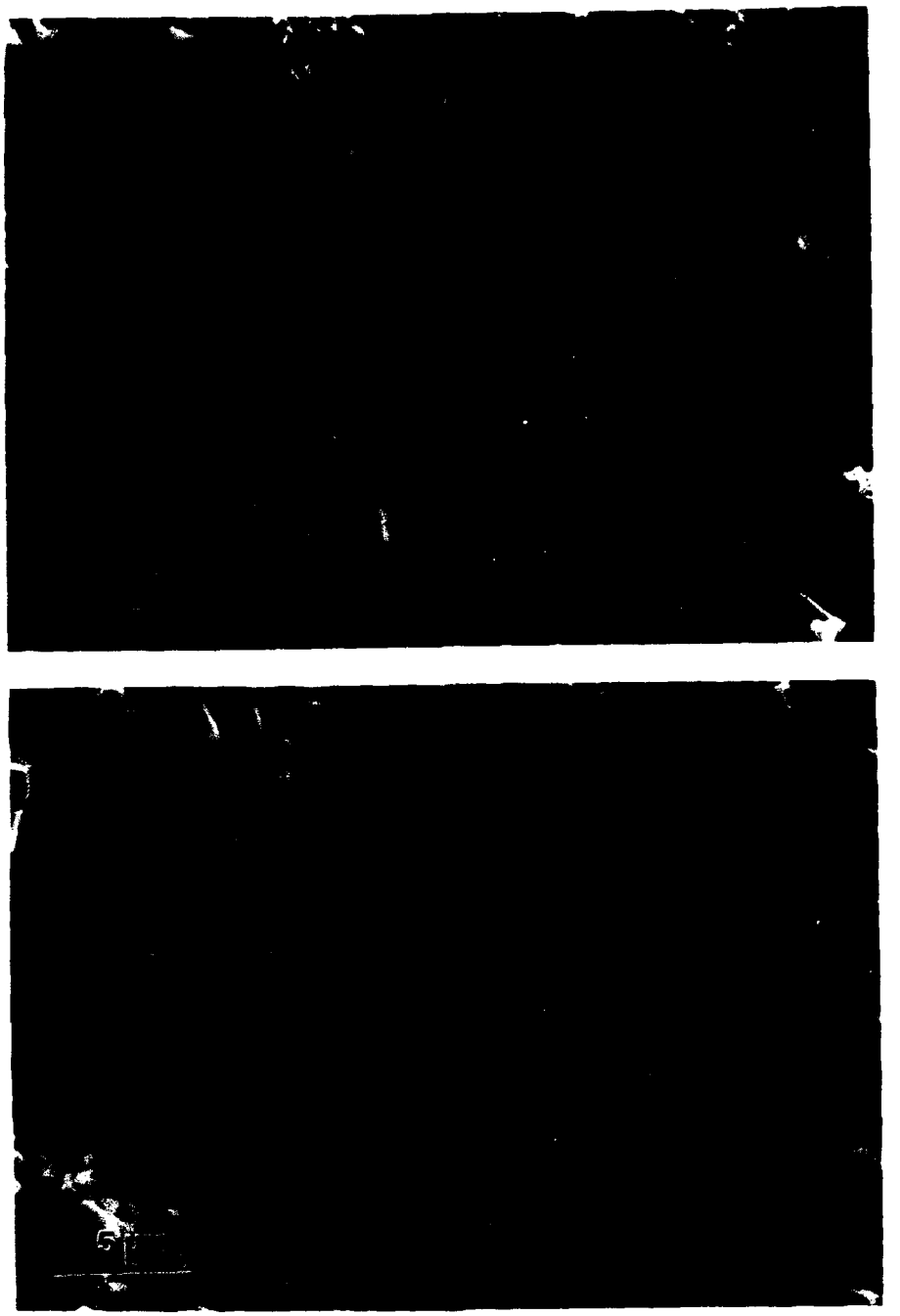

Figure 15 - Fatigue fractured surfaces imaged by scanning electron microscopy, showing intergranular failure in RE_2O_3 sintered samples (courtesy B. Cornelissen).

behavior at room temperature is noted between RE_2O_3 sintered Si_3N_4 and "conventional" Si_3N_4 containing appreciable amounts of residual intergranular glass. An example is shown in Figure 14. Stable crack propagation under cyclic loads could be terminated by holding at the maximum load, proving that true fatigue rather than an environmentally-assisted cracking mechanism was responsible for the observed crack growth. The exponent m in the classical Paris power law equations [30] generally varies from 24 to 28, consistent with results for other ceramics [31]. The results of Figure 14 can be understood by considering that fatigue fracture propagation in Si_3N_4 is mostly intergranular (Figure 15), and that amorphous material is retained at the boundaries between Si_3N_4 grains (Figure 8) even after bulk crystallization. The immediate crack tip environment is therefore not altered significantly compared to conventional Si_3N_4. Compact-tension fracture toughness tests of fatigue-cracked specimens yielded K_{IC} values of ~8 $MPa\sqrt{m}$.

These fatigue studies will continue with efforts to carry out comparison testing on well-characterized glassy Si_3N_4 at room temperature, and similar tests on crystalline "composites" at higher temperatures.

Conclusions

The results of sintering silicon nitride with heavy rare-earth oxides to produce stable $RE_2Si_2O_7$ crystalline phases at grain boundaries are very encouraging. Greatly improved high temperature strength, creep and oxidation resistance have been achieved. Long range research has resulted in the ability to "tailor" or "engineer" grain boundaries. Initial results of fatigue behavior show no detrimental effects of the intergranular crystalline phase on fatigue behavior. The research is continuing, with emphasis on optimizing the sintered microstructures and more controlled fatigue experiments, especially at high temperatures.

Acknowledgments

This work was initially supported by the National Science Foundation but is now supported by the Director, Office of Energy Research, Office of Basic Energy Sciences, Materials Sciences Division of the U.S. Department of Energy under Contract No. DE-AC03-76SF00098. I am especially grateful for the excellent work and support of the students and postdoctoral fellows who have contributed so much to the understanding and development of silicon nitride ceramics during the past 16 years or so. I also thank Bastiaan Cornelissen for providing his unpublished thesis data, and Professor R. O. Ritchie and Dr. R. H. Dauskardt for collaborating in the fatigue effort.

References

1. D. R. Clarke and G. Thomas, J. Am. Ceram. Soc., 61 (1978), 114.

2. G. Thomas, "Grain Boundaries and Interfaces," in J. A. Pask, and A. G. Evans, eds., Ceramic Microstructures '86 (Plenum Publishing Corporation, 1988), 55-72.

3. G. Thomas, C. Ahn, and J. Weiss, J. Am. Ceram. Soc., 65 (1982), C185.

4. T. R. Singer, R. S. Rai, and G. Thomas, J. Am. Ceram. Soc., 71 (1988), 236.

5. M. K. Cinibulk, G. Thomas, and S. M. Johnson, J. Am. Ceram. Soc., 75 (1992), 2037.

6. A. Tsuge, K. Nishida, and M. Komatsu, J. Am. Ceram. Soc., 58 (1975), 323.

7. F. F. Lange, S. C. Singhal, and R. C. Kuznicki, J. Am. Ceram. Soc., 60 (1977), 249.

8. R. E. Lochman, J. Non-Cryst. Solids, 56 (1983), 411.

9. D. R. Clarke, F. F. Lange, and G. D. Schnittgrund, J. Am. Ceram. Soc., 65 (1982), C51.

10. D. A. Bonnell, T.-Y. Tien, and M. Rühle, J. Am. Ceram. Soc., 70 (1987), 460.

11. M. K. Cinibulk, G. Thomas, and S. M. Johnson, J. Am. Ceram. Soc., 73 (1990), 1606.

12. W. A. Sanders and D. M. Mieskowski, J. Am. Ceram. Soc., 64 (1985), 304.

13. J. T. Smith and C. L. Quackenbush, Am. Ceram. Soc. Bull., 59 (1980), 529.

14. S. M. Wiederhorn and N. J. T Ceram. Soc., 66 (1983) 884.

15. M. K. Cinibulk, G. Thomas and S. M. Johnson, J. Am. Ceram. Soc., 75 (1992), 2044.

16. M. K. Cinibulk, G. Thomas and S. M. Johnson, ibid., 2050.

17. B. E. Cornelissen, "Cyclic Fatigue Behavior and Fracture Toughness of Silicon Nitride Ceramics Sintered with Rare-Earth Oxides," M.S. thesis, University of California, Berkeley, 1992.

18. F. F. Lange, Am. Ceram. Soc. Bull., 59 (1980), 239.

19. R. Raj and F. F. Lange, Acta Metall., 29 (1981), 1993.

20. Report MIL-STD-1942A, U.S. Army Mat. Tech. Lab. (Watertown, MA, 1990).

21. R. Kossowsky, D. A. Miller, and E. S. Diaz, J. Mater. Sci., 10 (1975), 987.

22. R. M. Arons and J. K. Tien, J. Mater. Sci., 15 (1980), 2046.

23. M. K. Ferber, M. G. Jenkins, and V. J. Tennery, Ceramic Eng. Sci. Proc., 11 (1990).

24. F. F. Lange, B. I. Davis, and D. R. Clarke, J. Mater. Sci., 15 (1980), 601.

25. B. S. B. Karunaratne and M. H. Lewis, J. Mater. Sci., 15 (1980), 449.

26. A. C. Singhal, J. Mater. Sci., 11 (1976) 500.

27. G. N. Babini, A. Bellosi, and P. Vincenzini, J. Mater. Sci., 19 (1984), 3487.

28. D. Cubicciotti and K. H. Lau, J. Am. Ceram. Soc., 61 (1978), 512.

29. R. H. Dauskardt, D. B. Marshall, and R.O. Ritchie, J. Am. Ceram. Soc., 73 (1990), 893.

30. P. Paris and F. Erdogan, Trans. AIME, 85 (1963), 528.

31. R. O. Ritchie and R. H. Dauskardt, J. Ceram. Soc. Japan, 99 (1991), 1047.

SESSION VII

Fatigue Resistance

Fatigue of Superalloys and Intermetallics

N.S. Stoloff

Rensselaer Polytechnic Institute
Materials Engineering Department
Troy, New York 12180-3590

Abstract

The fatigue behavior of intermetallic alloys and their composites is contrasted to that of nickel-base superalloys. The roles of microstructure and slip planarity are emphasized. Obstacles to use of intermetallics under cyclic loading conditions are described and future research directions are suggested.

Critical Issues in the Development of High Temperature Structural Materials
Edited by N.S. Stoloff, D.J. Duquette and A.F. Giamei
The Minerals, Metals & Materials Society, 1993

Introduction

The objective of this paper is to review our current understanding of the fatigue behavior of nickel base superalloys, and to compare their behavior with that of ordered intermetallics. Such comparisons are useful in helping to determine whether intermetallics can successfully replace superalloys in applications that may be fatigue limited. However, there is a much larger data base available for superalloys, inasmuch as studies of fatigue behavior of intermetallics have lagged investigations of monotonic behavior. Further, superalloys are multiphase alloys with large volume fractions of one or more strengthening precipitates, while the intermetallics that have been studied to date are typically single phase or two phase with only a small volume fraction of the second phase. Nevertheless, some useful guidelines for improving fatigue lives and fatigue crack growth resistance of both superalloys and intermetallics have been developed and are described in this review. The fatigue behavior of intermetallic matrix composites also will be described briefly in this paper.

Overview of Superalloy Behavior

High Cycle Fatigue

High cycle fatigue (HCF) is not considered to be a predominant failure mechanism in gas turbines, since it typically involves a resonance condition which is easily designed away. Therefore, relatively few studies have been carried out on the influence of metallurgical variables on HCF. A recent study of HCF behavior of P/M Astroloy confirmed that γ' size has virtually no effect on HCF life at 25°C even though strength is increased appreciably (1). This is somewhat surprising, since in a stress-controlled test the yield strength should affect crack initiation. When the data were normalized for yield strength, the coarse γ' produced a higher endurance ratio, about 0.7 compared to about 0.5 for fine γ', see Fig. 1. In most cases, HCF endurance ratios relative to yield stress at 25°C are of the order of 0.55-0.6, as shown in Table I (2). Therefore, when comparing different alloys, HCF resistance will increase with increasing strength (3). As temperature increases to 725°C, the endurance ratio of Astroloy rises steadily, to a maximum value of 1.0 for coarse γ', also shown in Fig. 1. These values are still lower than for intermetallics at comparable temperatures, as seen in Table I and as will be discussed later.

Cyclic Hardening and Low Cycle Fatigue

Nickel-base superalloys are characterized by planar slip, due to a combination of shearable, coherent γ' or γ'' precipitates in a low stacking fault energy Ni-Cr-X matrix. Coarse planar slip is favored by small γ' size, large grain size, low temperature, low inelastic strain and high strain rates (4). Cyclic hardening is lowest in the underaged or peak aged conditions. Cyclic hardening followed by softening is noted both in γ' and γ'' strengthened superalloys such as Nimonic PE 16 (5) and IN 718 (6,7) respectively and in several single phase intermetallics (8) (Ni_3Al, FeCo-V, Ni_3Fe); however, one intermetallic in which appreciable cyclic softening has not been seen is NiAl (9,10).

Apart from effects on cyclic hardening, coarse planar slip associated with peak aged superalloys lead to early crack initiation. For the peak aged condition the maximum shear measured in any slip band can be three to four times higher than for underaged or overaged conditions, due to rapid softening of peak aged material.

The low cycle fatigue behavior of polycrystalline PE16 has been studied at room temperature as a function of γ' particle size and total strain amplitude (5). The cyclic hardening response was very dependent on strain amplitude, with a much smaller dependence upon γ' particle size, see Fig. 2 (5). Similarly, the Coffin-Manson plots are not significantly affected by aging condition.

Unlike HCF, where strength is the most important factor, LCF behavior is controlled by ductility. Thus the most ductile alloys display long lives in LCF, while the strongest alloys are the most resistant to HCF when the data are plotted on the basis of total strain range (3).

Table I High Cycle Fatigue (HCF) Data, T=25°C, R≈0 (2,22,23)

Alloy	$\frac{\Delta\sigma_{10^6}}{\sigma_{ys}}$
Aluminides	
Ni-24Al HIP	1.79
Fe-24Al (DO_3)	0.84
Fe-24Al (B2)	0.76
Ti-25Al-10Nb-3V-1Mo	0.83
Ti-25-11Nb	0.85
TiAl	0.80 (R=-1)
NiAl+0.28a%Fe (400°C)	1.7
NiAl+0.28a%Fe (550°C)	1.2
Superalloys	
Waspaloy	0.57
Udimet 700	0.60
Mar M 200	0.55
Astroloy	0.45-0.6
Astroloy (550°C)	0.6-0.9
Titanium Alloys	
Ti-24%V	0.71
Ti-32%V	0.36
Ti-6Al-4V (ß-Annealed)	0.45

Crack Propagation

Fatigue crack propagation is a critical factor in the selection of superalloys for turbine disks, due to the severe consequences of failure arising from a small flaw. Extensive experimental work, therefore, has been carried out on nickel base superalloys. For relatively high values of crack growth rates the data are well characterized by the Paris-Erdogan equation:

$$da/dN = A\Delta K^m \qquad (1)$$

where A and m are material constants dependent upon frequency, temperature and load ratio, R. Certain trends in the crack growth behavior of commercial superalloys have been reported. Crack growth rates tend to decrease with increasing strength (11) and increasing grain size (12). The influence of strength is to be expected since fatigue crack growth tests

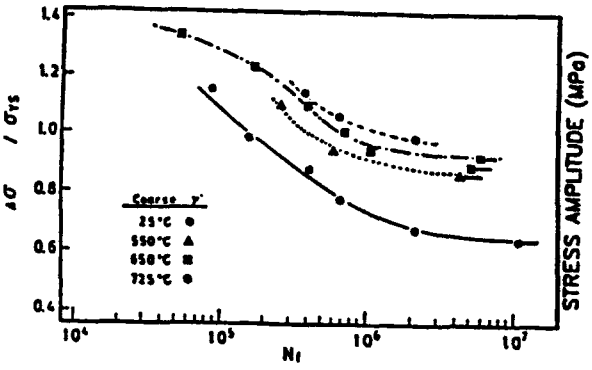

Fig. 1 Influence on temperature on HCF lives of P/M Astroloy normalized by yield stress. γ' size ≈ 1μm (1).

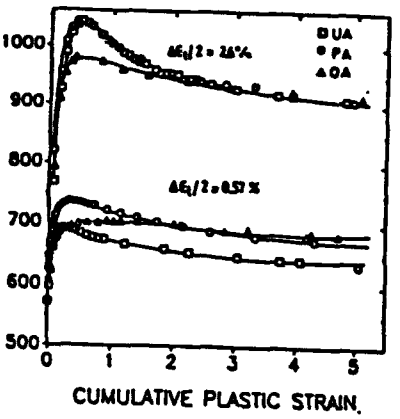

Fig. 2 Cyclic response curves for the UA, PA, and OA conditions of Nimonic PE 16 as a function of cumulative plastic strain tested at $\Delta\epsilon_t/2$=0.60 and 2.60 pct. UA=under-aged, PA=peak aged, OA=overaged (5).

are usually conducted under stress control conditions. The explanation for the effect of increased grain size is not so clear; some researchers suggest that increased surface roughness and consequent closure effects are responsible, while others cite factors such as slip reversibility (13) and lower average strains in the critical process zone at the crack tip (14). The most detailed investigation of microstructural effects have been carried out on Waspaloy, an alloy with a relatively low volume fraction (25%) of coherent γ' precipitates (15). These studies have shown that coarse grained material is more resistant to crack growth than fine grained material, independent of precipitate size. The influence of precipitate size is not as clear, but there is a tendency for reduced crack growth rates with decreasing precipitate size.

Temperature effects on crack growth rate are very significant, with both creep (16,17) and environmental interactions playing a role at elevated temperatures (16,18).

Crack growth studies on single crystals show that the rate of growth is dependent on the relative orientations of the load axis and the direction of crack propagation. Fatigue cracks propagate along {111} in MarM 200 (19), but may also propagate along {001} in MarM 002 at elevated temperatures (20).

A recent study of fatigue crack propagation in the single crystal alloy René N4 was carried out on [001] and [110] oriented samples in the range 21°C to 1093°C (21). Temperature had no significant effect on growth rates at or below 927°C, but at 1038° and 1093°C the growth rates were about 10x higher, as shown in Fig. 3 (21). At 21°C cracks propagated along {111} planes at low ΔK, but for $\Delta K > \sim 30 MPam^{1/2}$ a less crystallographic mode was observed. At all temperatures cracks followed a path through the matrix or the γ/γ' interface, rather than through the γ' particles.

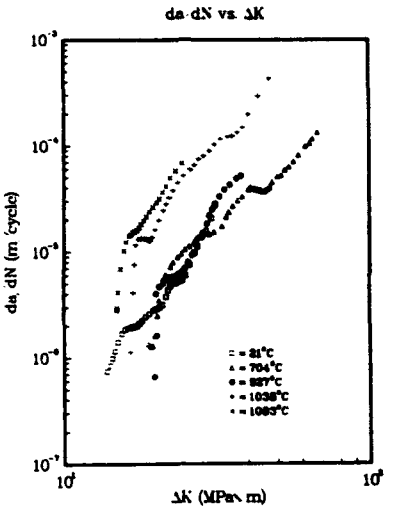

Fig. 3 The effect of temperature on the fatigue crack growth rate (R = 0.1) of single crystal superalloy René N4 (21).

Overview of Intermetallics Behavior

High Cycle Fatigue

Table I (2,22,23) shows that whereas superalloys display endurance ratios of 0.55-0.6 at room temperature, intermetallics show much higher ratios, in one case reaching 1.79. At 500°C an endurance ratio of 0.98 was reported for P/M Ni-24at%Al in the HIP + extruded condition, tested in air (22). Recent work on NiAl polycrystals doped with 0.28a%Fe showed that the endurance ratio at 400°C (below the brittle to ductile transition) was about 1.9 while at 550°C (above the brittle to ductile transition) the ratio was about 1.5, see Fig. 4 (23). By comparison, Udimet 700 has an endurance ratio of only 0.6 (24). The high endurance ratios of intermetallics at both room and elevated temperatures arises from the very rapid cyclic hardening in these alloys, which tends to delay crack initiation. However, many intermetallics (e.g. Ti_3Al, TiAl, Fe_3Al) display very rapid crack propagation, so that failure may soon follow the initiation of a crack. This may explain the very poor high cycle fatigue resistance of α_2 alloys compared to IN 100 at 650°C, see Fig. 5 (25). Even when α_2 is reinforced with continuous SiC fibers, IN 100 is superior.

Low Cycle Fatigue

Low cycle fatigue studies are difficult to carry out with many intermetallics due to lack of appreciable tensile ductility. Nevertheless, the LCF behavior of several high temperature intermetallics, including Ni_3Al, NiAl, Ti_3Al and TiAl, has been reported.

Ni_3Al polycrystals. Strain-life data for Ni_3Al alloy IC-218 (Ni-16.5a%Al-8Cr-0.4Zr-0.1B) prepared by hot extrusion of powders, are shown in Fig. 6 (2). Note that the LCF performance of IC-218 is superior to that of several other structural alloys, including steels and Ti-6Al-4V, especially at high strain amplitudes. These results were attributed to high tensile ductility of the fine grained microstructure and good crack growth resistance of a similar Ni_3Al alloy, IC-221 (34).

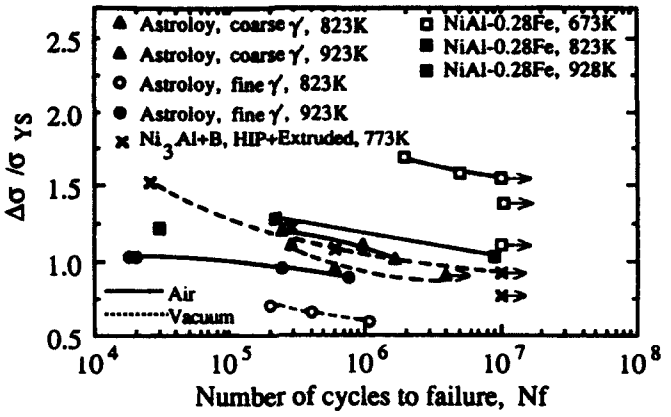

Fig. 4 High cycle lives of P/M Astroloy Ni_3Al+B and NiAl+0.6%Fe normalized for yield stress (1,22,23).

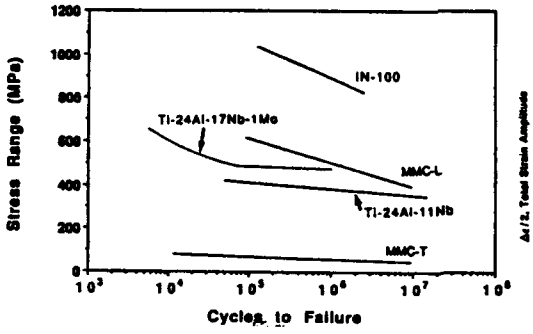

Fig. 5 High cycle fatigue of continuous Ti_3Al composites reinforced with SCS 6 fibers, compared to superalloy IN 100, 650°C, 0.2Hz, R=0. MMC-L is longitudinal MML-T is transverse orientation (25).

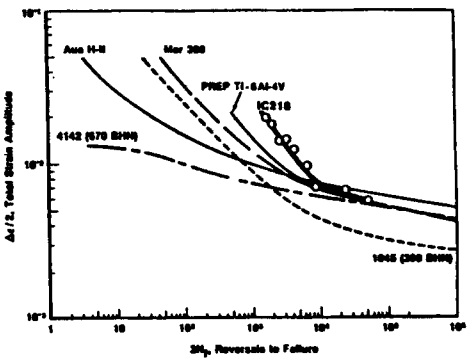

Fig. 6. Comparison of LCF behavior of Ni_3Al alloy IC-218 with several commercial alloys (2).

NiAl Polycrystals. Recently there have been several reports of LCF behavior of NiAl. Lerch and Noebe (9,26) have compared the fatigue behavior of powder-processed (P/M) and cast + extruded (C+E) polycrystals of equiatomic NiAl. Two temperature regimes were selected: above and below the ductile to brittle transition temperature. At room temperature a Coffin-Manson plot was obtained for C+E material (9). The data obeyed the equation $\Delta\epsilon_p = 0.003N_f^{-0.14}$. The influence of processing technique and environment on the fatigue life at 727°C also was investigated. At low temperatures cyclic hardening is continuous to failure and fracture always initiated at fabrication defects (e.g. inclusions or pores). At 727°C NiAl displayed higher fatigue lives than superalloys on a strain range basis, see Fig. 7 (27), but had shorter lives on a stress range basis. Interestingly, C+E material was superior to the P/M alloy based on strain range, but was inferior based on stress range. However, when the P/M samples were tested in strain control at 727°C in $1x10^{-6}$ torr (Pa) vacuum, lives improved by a factor of three, Fig. 8 (27), so that lives were comparable to those of C+E samples at high strain ranges.

Cullers and Antolovich (28,29) report that powder processed Ni-49.5a%Al displays cyclic hardening at 600 and 700K that resembles the room temperature behavior: i.e. hardening is continuous until final fracture and there is little stable crack growth. (At 1000K, on the other hand, a maximum in hardening was noted by Noebe and Lerch (27) after a few cycles followed by slight cyclic softening until failure). Lives increased substantially between 600 and 700K, but considerably less than expected from the large increase in monotonic ductility that occurs over the same temperature range (29). At 1000K, on the other hand, lives increased by about 100 times relative to room temperature for a plastic strain range of 0.2% (26).

NiAl-single crystals. Bain et al (30) have studied the cyclic deformation of <001> single crystals of Ni-49.9Al-0.1Mo at 298 and 1033K. At the higher temperature, fatigue lives of the single crystals were nearly identical to those for polycrystalline stoichiometric NiAl, and the Coffin-Manson relation was obeyed.

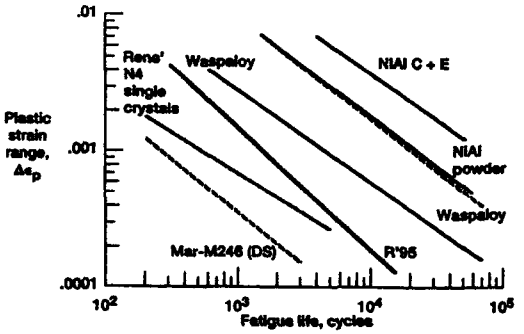

Fig. 7 Comparison of NiAl and superalloy fatigue life (27).

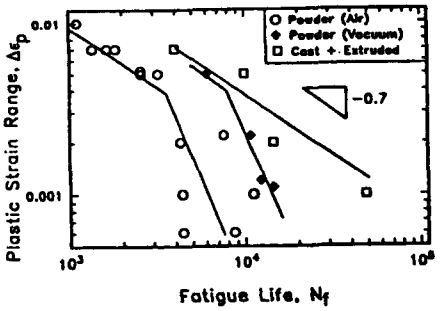

Fig. 8 Fatigue life of polycrystalline NiAl at 1000K (27).

Smith et al (10) have provided preliminary room temperature fatigue data for <121> oriented equiatomic single crystals. At room temperature single crystals as well as polycrystals harden and fracture with little or no stable crack growth.

At high temperatures, e.g. 1000K, the fatigue lives of <100> oriented NiAl single crystals in air resemble those of P/M polycrystals (Fig. 7 (27). However, fracture mechanisms are dissimilar in the two materials. In single crystals, cracks initiated and propagate approximately parallel to the loading direction until crosslinking occurs, just prior to failure. In polycrystals, on the other hand, cracks grow intergranularly.

Crack Initiation

A variety of crack initiation sites is observed in polycrystalline intermetallics. Crack initiation at 25°C is intergranular in wrought Fe_3Al (31) and C+E NiAl (9). In the latter case specific crack initiation sites (e.g. voids) always were observed. The same defects do not influence cracking in this material at 1000K, probably because of the high ductility above the brittle to ductile transition temperature of about 773K (27).

In most other reported cases in polycrystals crack initiation is along slip bands (e.g. $FeNi_3V$ and Ni_3Al+B at room temperature and Ni_3Al+B and NiAl at elevated temperatures (32). However, some intergranular cracks also were observed in NiAl at 700°K (28). Also, cracks initiated at casting pores in a directionally solidified Ni_3Al alloy (56).

Single crystal studies have shown that persistent slip bands form readily in Ni_3Al (33) and NiAl (10), with intrusions and extrusions developing after a few hundred cycles. The development of surface damage in these and other intermetallics such as FeCo-V and Ni_3Fe closely resembles that seen in conventional metals such as copper and iron (32,33) as well as superalloys (17). However, internal substructures are different in the intermetallics.

Crack Propagation

Ni_3Al Alloys. We have carried out detailed studies of crack propagation in two aluminides, a Ni_3Al base alloy, IC-221 (34,35) and Fe_3Al (36). In both alloy systems environmental effects are very important: for Ni_3Al due to oxygen and for Fe_3Al due to moisture and/or hydrogen. Crack growth rates for Ni_3Al alloys as well as other $L1_2$ alloys are lower than for nickel-base superalloys at room temperature and at 600°C, see Fig. 9 (34). Also, crack growth rates increase with increasing temperature in spite of a rise in flow stress over the same temperature range. Crack tip embrittlement by oxygen seems to be a major factor, although creep processes also influence growth rates at temperatures above about 700°C (34,35). Crack growth rates, da/dN, increase with decreasing frequency in both vacuum and air for alloy IC 221 (Ni-9w%Al-8%Cr,1.8%Zr,0.02%B) at 800°C but the rates always are higher in air (35). While increased growth rates at low frequency in vacuum are indicative of a creep effect, the higher growth rates in air undoubtedly reflect a contribution of environmental embrittlement. Intergranular fracture occurs in air at all test frequencies, while transgranular fracture is noted in vacuum. Secondary cracking is enhanced at lower frequencies, suggesting that diffusion of oxygen is required for such cracks to appear.

Fe_3Al Alloys. Although Fe_3Al alloys are not intended for service above about 500°C, it is instructive to use this sytem to illustrate the potent effects of ordering and of external environments on the crack growth behavior or ordered intermetallics.

Binary Fe_3Al alloys generally are intermediate in growth rates (in air) between superalloys and Ll_2 intermetallics, e.g. Ni_3Al or $(Fe,Ni)_3V$, at low ΔK levels; at high ΔK, crack growth is more rapid in Fe_3Al (32).

Recent work has shown that hydrogen (36,37) or moisture (38) is very detrimental to fracture ductility of iron aluminides. Our own research has extended the study of environmental effects to cyclic loading. Crack growth rates for an Oak Ridge-developed Fe_3Al alloy, 28.6%Al,4.8%Cr,0.5%Nb,0.21%C, bal Fe (FA-129), are shown in Fig. 10a) for the partially disordered B2 condition, and in Fig. 10b) for the fully ordered DO_3 condition, both at room temperature. Note that the lowest crack growth rates are observed with oxygen for both ordered conditions. Values for the slopes as well as apparent threshold and critical stress intensities for fracture for each environment and ordered condition may be found in Table II. Values of ΔK_{TH} and ΔK_c are lower than reported previously (36,37), because of a machine error in the previous work. In every respect the DO_3 condition is less resistant to cyclic crack growth and fracture, especially in each of the aggressive environments: air and hydrogen gas. It is now generally considered that moisture in contact with iron aluminides (Fe_3Al and FeAl) breaks down by chemical reaction at the surface of the sample, thereby liberating hydrogen, which is the specific embrittling agent (38).

Chromium reportedly improves the ductility of Fe_3Al in monotonic tension tests in air (39), but offers no benefit under cyclic loading conditions. Growth rates are actually higher for FA-129 than for a binary alloy with similar Al content, both tested in the DO_3 condition (32,36). This unexpected result may be due to the influence of chromium on the repeated formation and rupture of the oxide film on a freshly exposed crack surface.

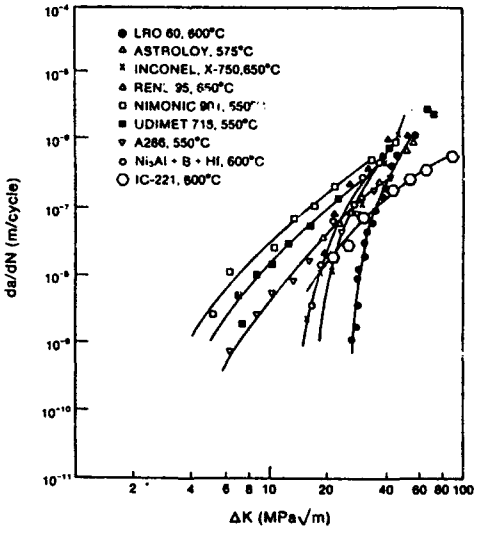

Fig. 9. Comparative crack propagation rates as a function of ΔK for Ni_3Al alloy IC-221 and a number of commercial and experimental alloys between 550°C and 650°C (34).

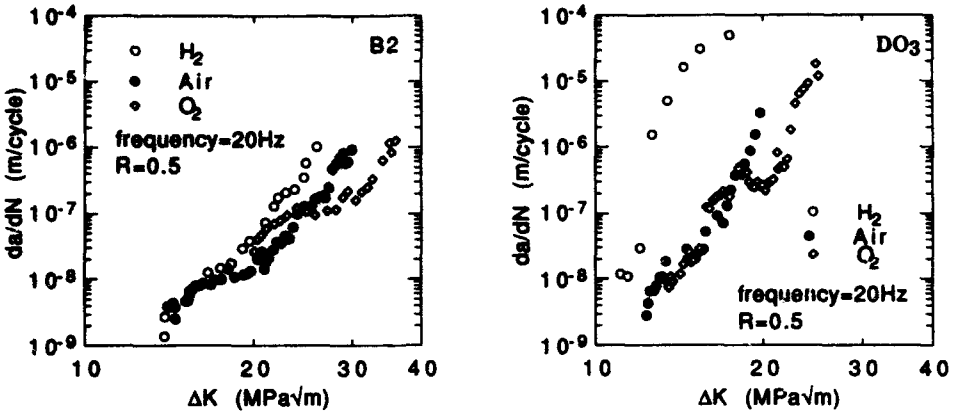

Fig. 10 Crack growth of Fe_3Al alloy FA-129, 25°C.
a) B2 condition b) DO_3 condition

Table I I Fatigue Crack Growth Data for FA-129 at 25°C

Condition	Fracture Surface	m	ΔK_{TH} (MPa√m)	ΔK_C (MPa√m)
B2 Oxygen	Dimpled, few striations	3.0	20.0	35.9
B2 Air	TG, many striation	6.9	14.5	29.9
B2 Gas	TG, few striations	8.8	13.8	25.9
DO_3 Oxygen	Dimpled + cleavage	8.5	13.5	25.1
DO_3 Air	Mixed, few striations	11.2	13.3	19.8
DO_3 Gas	Mixed, no striations	25.1	11.1	17.4

The influence of temperature on crack growth rates of FA-129 also has been studied (36). Growth rates decrease between 25°C and 150°C in the B2 and DO_3 conditions. However, at higher temperatures growth rates rise again for the DO_3 condition. (Tests of the B2 condition are limited to low temperatures due to the occurrence of DO_3 ordering). Even at 450°C, crack growth rates are lower than at room temperature, presumably due to the fact that hydrogen diffuses too rapidly at high temperatures to cause embrittlement. Therefore, it appears that hydrogen embrittlement is maximized near room temperature, as is the case for structural steels.

Ti3Al and Ti3Al Composites. Although crack growth phenomena in Ti3Al alloys have been studied extensively, little had been published prior to a series of recent papers on Ti-24Al-11Nb ($\alpha 2$) and Ti-25Al-10Nb-3Mo-1V (super $\alpha 2$). One of the most interesting aspects of crack growth behavior is the potent effect of microstructure, see Fig. 11 (40).

Note that a coarse Widmanstätten microstructure provides the greatest resistance to crack growth. A similar strong effect of microstructure on HCF behavior of super α_2 at 600°C has been reported by Luetjering et al (41) and has been attributed to the resulting yield stresses. A bi-model microstructure produces higher yield stresses and longer lives than an equiaxed or lamellar structure. Fatigue crack growth resistance improves when the alloy is cycled in vacuum.

Evidence for environmental effects on crack growth of α_2 at both room and elevated temperature has been provided by several groups. There is an effect of frequency on crack growth rates in laboratory air and in vacuum (10^{-5} torr) for Ti-24-11 with coarse Widmanstatten α_2 surrounded continuously by transformed ß (42) (this is a microstructure with relatively high FCG resistance). Crack growth is much more rapid in air than in vacuum. Similar observations have been made at temperatures in the range 650-800°C (43,44). Crack growth rates of Ti-24Al-11Nb decrease between 25°C and 250°C, but then increase at higher temperatures (44). Crack growth rates in air decreased with increasing frequency, and were further decreased by testing in vacuum. Crack growth rates for super α_2 are considerably lower in vacuum than in air at 700°C; m increases from 2.3 in vacuum to 4.0 in air (45). Growth rates of Ti-24Al-11Nb increase by about ten times at 649°C when frequency is lowered from 100Hz to 0.01Hz, see Fig. 12 (46). In general, fatigue crack growth rates in α_2 increase with moist environments (probably due to the release of hydrogen), lowered test frequency, increased hold times and increased test temperature (47,48).

Small crack behavior in Ti_3Al alloys has been reported (49,50). Long crack and short crack data for cast, forged and rolled super α_2 correlate well with ΔK^*_{eff} which is defined as:

$$\Delta K^*_{eff} = \Delta K_i + \Delta K - \Delta K_c \qquad (2)$$

where ΔK_i is the value of ΔK^*_{eff} at $\Delta K=0$ and ΔK_c is the closure level for small cracks and is about $0.4\Delta K$ for super α_2. Comparison of the growth rate of small cracks in super

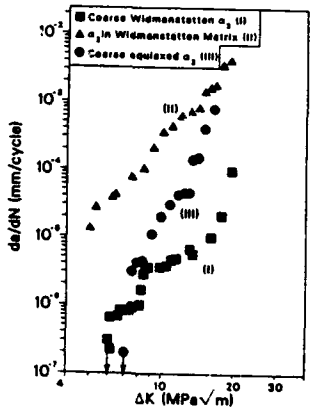

Fig. 11 Effect of microstructure on crack growth of Ti_3Al at 25°C (40).

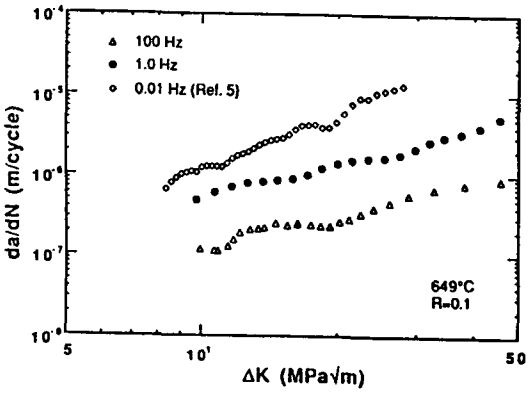

Fig. 12 Variation of fatigue crack growth rates of Ti-24-Al-11Nb with frequency at 649°C (46).

α_2 with those in 7075 Al and in the superalloy Astroloy is shown in Fig. 13 (49). Note that super α_2 has a growth rate slightly higher than for Astroloy but about 10-100x slower than for 7075 Al. Some small cracks arrest in each of the three alloys.

For Ti-24Al-11Nb small cracks develop arbitrary shapes that are influenced by microstructure and texture; the shapes in turn affect crack growth rates. With a basketweave microstructure as well as with two other microstructures, small and long crack data correlate well when crack closure is accounted for (50). However, for an aligned colony structure small crack growth rates were always higher than those for long cracks.

Perhaps the single factor most likely to influence the fatigue crack growth resistance of titanium aluminides is the use of fibrous reinforcements. Fig. 14 (25) shows that although the crack growth rates of α_2 and γ are higher than for the P/M Ni base superalloy IN 100, the longitudinally oriented composite of α_2 (Ti-24Al-11Nb) with continuous SCS-6 SiC fibers is far more crack growth resistant than is IN 100. Unfortunately, the transversely oriented α_2 composite displays the highest growth rate of all. (Note: the specimen geometry differed in that thin tubes of Ti-48Al-1V (γ) were utilized; also, the frequency of tests of the α_2 composite was 3.33 Hz, which would be expected to result in a somewhat lower growth rate than at 0.2 Hz).

TiAl. Data for TiAl(γ) alloys are even more limited than for Ti_3Al. Due to the low toughness of γ, ΔK values rarely reach 20 MPa$\sqrt{m}$ prior to fracture. Note in Fig. 14 that the growth rate of Ti-48Al-1V is comparable to that of super α_2 (25). Soboyejo et al (51) have reported the influence of microstructure and temperature on fatigue crack growth behavior of a P/M Ti-48%Al alloy tested in air. Crack growth at room temperature was slightly slower than for a Ti-6Al-4V alloy. At 700°C, crack growth was even slower, probably due to oxide-induced crack closure.

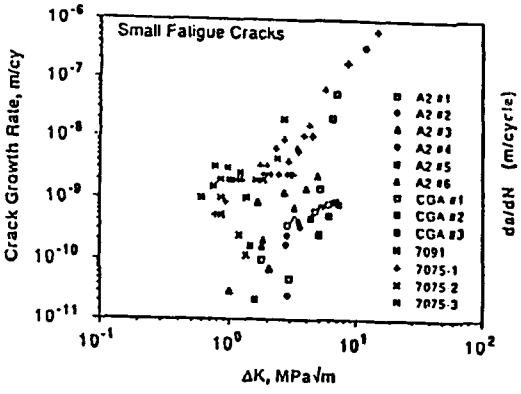

Fig. 13 Comparison of crack growth rates for small fatigue cracks in Super Alpha 2 (A2), coarse-grained Astroloy (CGA), and the aluminum alloys 7075-T651 and 7091 (49).

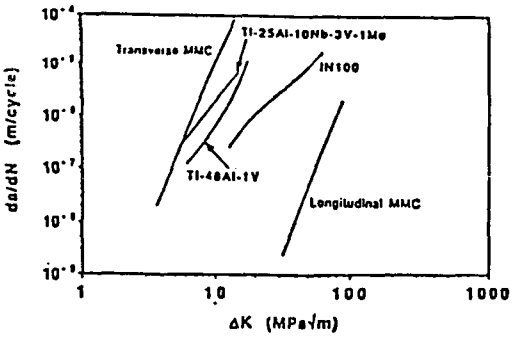

Fig. 14 Comparative plot of fatigue crack propagation rates for tests at 650°C, frequency ≈ 0.2 Hz, and R = 0.1 (25). MMC are Ti-24Al-11Nb/SCS-6.

The constants A and m in Eq. 1 are extremely sensitive to test conditions for Ti-48Al-2Mn-2Nb, see Table III (52). The slope m varies from 8.2 for as-cast material tested at 700°C in vacuum to as high as 56.2 for a sample heat treated for 2h at 1200°C and tested at 700°C in air. (This range of slopes is similar to that noted with Fe_3Al alloy FA-129 as a function of long range order and environment, as was shown in Table II (36). James and Bowen (52) point out that "static failure modes": transgranular cleavage of allotriomorphic γ grains at room temperature or transgranular decohesion at 700 or 800°C contribute to high values of m. Therefore, microstructures containing large amounts of γ grains are not resistant to cyclic loading at elevated temperatures. Rather, a two phase lamellar α_2/γ microstructure is preferred. Although this alloy displays no change in crack growth rates between 700°C and 800°C, vacuum decreases the crack growth rates by about an order of magnitude.

Ductile-Phase Toughened Composites

With the exception of the α_2-SCS-6 system, crack growth data have been reported only for composites reinforced with ductile phases; data have been published only for tests at room temperature in air. As in the case of monotonic tests, particles do not confer much advantage due to the lack of crack-stopping ability of low aspect ratio reinforcements. For example, sub-critical cracks grow at stress intensities as low as 2-3 MPa$\sqrt{m}$ in $MoSi_2$-Nb composites (53). For this reason it has been suggested that increasing the aspect ratio, together with a reduction in particle-matrix interface strength, is necessary for improved crack growth resistance in these composites (54).

The most detailed study of crack growth in ductile-phase toughened composites has been carried out on γ-TiAl reinforced with 25 or 50μm TiNb particles (54,55). As in the case of $MoSi_2$-Nb composites, cracks can propagate subcritically at very low stress intensities, less than 6MPa$\sqrt{m}$, see Fig. 15 (55), compared to a fracture toughness of 25MPa$\sqrt{m}$. However, the Paris slopes, m, are considerably reduced by TiNb, from 29.4 to about 9.6 for 20v%TiNb. A particularly striking observation was that the crack growth resistance of monolithic TiAl appears to be diminished by the particles, particularly at near-threshold levels, as shown in Fig. 15 (55).

Table III Grack Growth Data for Ti-48Al-2Mn-2Nb (52)

Heat Treatment	Test Conditions	A mm/cycle	m
as cast	800°C/vac.	1.62×10^{-15}	9.4
as cast	700°C/vac.	3.36×10^{-14}	8.2
as cast	700°C/air	7.34×10^{-15}	10.0
2h/1200°C	800°C/vav.	7.21×10^{-26}	22.8
2h/1200°C	700°C/air	2.33×10^{-57}	56.2
24h/1200°C	800°C/vac.	1.88×10^{-25}	22.8
24h/1200°C	700°C/air	1.47×10^{-31}	29.2

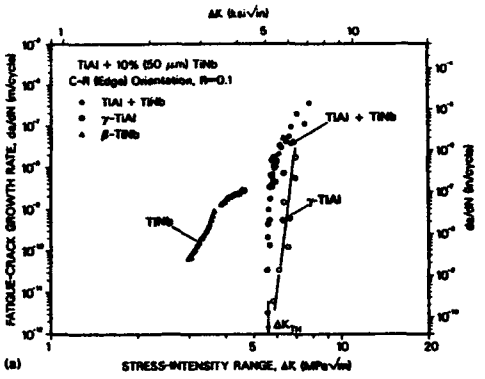

Fig. 15 Crack growth rates of γ TiAl and TiAl+TiNb particulate composites (55).

Discussion

Intermetallics with Ll_2 structure are the easiest to compare with superalloys because of the common crystal structure. It is clear that crack initiation under stress control is relatively difficult in single phase Ll_2 alloys, in spite of the planar slip associated with intermetallics. Further, crack growth rates at both 25° and 600° are lower than for either single phase or precipitation hardened nickel base alloys, as was shown in Fig. 9 (34). It is doubtful that planarity of slip is the decisive factor, since slip is planar in both the single phase intermetallics and in the precipitation hardened superalloys.

The titanium aluminides are extremely sensitive to microstructure, test temperature and frequency. The crack growth rates of both TiAl and Ti_3Al show a high value of m, see Table III, especially at low temperature and in air (52). Short crack data for α_2 alloys generally correlate well with long crack data when crack closure effects in long cracks are subtracted out. However, microstructure does affect short crack behavior of Ti-24Al-11Nb.

Strong effects of temperature, environment and microstructure also are found in crack growth data for Fe_3Al (31,36,37) and Ni_3Al (34,35) alloys. As in the case of titanium aluminides, Fe_3Al alloy FA-129 displays Paris exponents that range from "normal" values of about 3-4 for B2 material tested in vacuum to as high as 40 for the fully ordered DO_3 condition tested in hydrogen gas, as was shown in Table II (36). Temperature is extremely important, as the detrimental effects of water vapor and hydrogen on Fe_3Al disappear above about 100°C. However, at high temperatures factors such as decreasing yield stress, creep-fatigue interactions or environmental interaction of oxygen with fatigue cracks can sharply increase crack growth rates in Ni_3Al alloys.

Summary and Conclusions

On the basis of fairly limited data for intermetallics, the following conclusions may be drawn:

1) High cycle fatigue endurance ratios are higher for nickel and titanium aluminides than for superalloys. However, this may be at least in part due to the very high strengths of the superalloys, so that absolute values of endurance limit may be comparable.
2) Cyclic hardening followed by softening occurs in superalloys as well as in most intermetallics, the only exception being NiAl.
3) Low cycle fatigue behavior of Ni_3Al and NiAl is superior to that of superalloys when expressed on the basis of strain range.
4) Crack growth rates of $L1_2$ alloys are lower than for superalloys. Intermetallics are extremely sensitive to environment, frequency and temperature.
5) Hydrogen and moisture adversely affect fatigue crack growth resistance in Ni_3Al, Ti_3Al and Fe_3Al alloys at low temperatures; oxygen has a similar detrimental effect at high temperatures for Ni_3Al and Ti_3Al alloys, as well as superalloys.
6) Microstructure strongly influences crack growth behavior of Ti_3Al alloys.
7) Crack initiation in Ni_3Al and NiAl single crystals occurs after the development of the same pattern of surface damage as seen in conventional alloys.
8) Ductile phase toughening of intermetallics under monotonic loading does not lead to improved fatigue resistance.
9) Additional research on fatigue of intermetallics needs to be performed in the following areas:

a) LCF as a function of temperature, especially for Ni_3Al, Ti_3Al and TiAl.
b) environmental effects on crack initiation and growth.
c) short crack behavior
d) influence of surface modification on fatigue behavior.
e) all aspects of fatigue behavior of "newer" intermetallics such as $MoSi_2$, Laves phases, Al_3Ti and Nb_3Al.

Acknowledgements

The author is grateful to the National Science Foundation for support under Grant No. DMR-8911975 and to the Department of Energy Fossil Energy Program for support under Oak Ridge National Laboratory Subcontract No. 19X-SF521C.

References

1. T. Isomoto and N.S. Stoloff, Mat. Sci. and Eng., A124 (1990), 171-181.

2. D.E. Gordon and C.K. Unni, General Dynamics, Fort Worth, TX, 1990, unpublished.

3. B.A. Cowles, J.R. Warren and F.K. Hooke, (NASA Cr-165123, July 1980).

4. R.V. Miner, Superalloys II, eds, C.T. Sims, N.S. Stoloff and W.C. Hagel, (New York, Wiley, 1987) 263-287.

5. V. Singh, M. Sandararaman, W. Chen and R.P. Wahi, Metall. Trans A., 22 (1991), 499-506.

6. H.F. Merrick, Metall. Trans. A, 5, (1974), 891-897.

7. D. Fournier and A. Pineau, Metall. Trans. A, 8 (1977), 1095-1105.

8. N.S. Stoloff, Ordered Intermetallics - Physical Metallurgy and Mechanical Behavior, eds. C.T. Liu, R.W. Cahn and G. Sauthoff (Dordrecht, Netherlands, Kluwer Acad. Publ., 1992), 257-277.

9. R.D. Noebe and B.A. Lerch, Scripta Metall., 27 (1992). 1161-1166.

10. T.R. Smith, C.G. Kallingal, K. Rajan and N.S. Stoloff, Scripta Metall., 27 (1992), 1389-1393.

11. R. Miner and J. Gayda, Metall. Trans. A, 14 (1983), 2301-2308.

12. H.F. Merrick and S. Floreen, Metall. Trans. A, 9 (1978), 231-233.

13. J. Lindyheit, G. Terlinde, A. Gysler and G. Luetjering, Acta Metall., 27 (1979), 1717-1726.

14. G.R. Chanani, S.D. Antolovich and W.W. Gerberich, Metall. Trans. A, 3 (1972) 2661-2672.

15. B. Lawless, S.D. Antolovich, C. Bathias and B. Boursier, Fracture: Interactions of Microstructure, Mechanisms and Mechanics, eds. J.M. Wells and J.D. Landes, (Warrendale, PA, TMS, 1985) 285-301.

16. S. Golwalker, N.S. Stoloff and D.J. Duquette, Proc. 7th Int. Conf. on Strength of Metals and Alloys, v. 2, (Oxford: Pergamon, 1983) 379-384.

17. K.M. Nikbin, Superalloys 1992, Proc. 7 Springs Conf. on Superalloys, eds. S.D. Antolovich et al, (Warrendale, PA, TMS 1992) 637-646.

18. V. Lupini, G. Onofrio and G. Vimercati, Superalloys 1992, Proc. 7 Springs Conf. on Superalloys, eds. S.D. Antolovich et al, (Warrendale, PA, TMS 1992) 717-726.

19. K.S. Chan and G.R. Leverant, Metall. Trans. A, 18 (1987) 593-602.

20. J.S. Crompton and J.W. Martin, Metall. Trans. A, 15 (1984) 1711-1719.

21. S.D. Antolovich and B. Lerch, Superalloys, Supercomposites and Superceramics, eds. J.K. Tien and T. Caulfield, (Boston, Academic Press 1989) 363-411.

22. G.E. Fuchs and N.S. Stoloff, Scripta Metall., 21 (1987) 863-868.

23. K. Matsugi and N.S. Stoloff (1993) unpublished.

24. D.E. Gordon and C.K. Unni (Presented at TMS-AIME Fall Meeting, Indianapolis, IN, Oct. 2-5, 1989).

25. J.M. Larsen, K.A. Williams, S.J. Balsone and M.A. Stucke in High Temperature Aluminides and Intermetallics, eds. S.H. Whang et al, Warrendale, PA, TMS (1990) 521-556.

26. B.A. Lerch and R.D. Noebe, HITEMP Review 1992, NASA Conf. Publ., 10104, v. II, 47-1-47-15.

27. R.D. Noebe and B.A. Lerch, High Temperature Ordered Intermetallic Alloys II, MRS Symp. Proc., v. 288, (1993) in press.

28. C.L. Cullers and S.D. Antolovich, Superalloys 1992, Proc. 7 Springs Conf. on Superalloys, (Warrendale, PA, TMS 1992) 351-359.

29. C.L. Cullers and S.D. Antolovich, High Temperature Ordered Intermetallic Alloys V, MRS Symp. Proc., v. 288 (1993) in press.

30. K.R. Bain, R.D. Field and D.F. Lahrman, (Presented at TMS Fall Meeting, Cincinnati, OH, 1991) unpublished.

31. G.E. Fuchs and N.S. Stoloff, Acta Metall., 36, (1988) 1381-1387.

32. N.S. Stoloff, G.E. Fuchs, A.K. Kuruvilla and S.J. Choe, High Temperature Ordered Intermetallic Alloys II, Mat. Res. Soc. Symp. Proc. 81, (1987) Pittsburgh, PA, MRS, 247-261.

33. L.M. Hsiung and N.S. Stoloff, High Temperature Ordered Intermetallic Alloys III, Mat. Res. Soc. Symp. Proc. 133 (Pittsburgh, PA, MRS, 1988) 261-267.

34. W. Matuszyk, G. Camus, D.J. Duquette and N.S. Stoloff, Metall. Trans. A, 21 (1990) 2967-2976.

35. G. Camus, D.J. Duquette and N.S. Stoloff, J. Mater. Res. 5, (1990) 950-954.

36. A. Castagna and N.S. Stoloff, High Temperature Ordered Intermetallic Alloys V, Mat. Res. Soc. Proc. (1993) in press.

37. A. Castagna, M. Shea and N.S. Stoloff, High Temperature Ordered Intermetallic Alloys IV, Mat. Res. Soc. 213, (Pittsburgh, PA, MRS, 1991) 609-616.

38. C.T. Liu, C.G. McKamey and E.H. Lee, Scripta Metall., 24, (1990) 385-390.

39. C.G. McKamey, J.A. Horton and C.T. Liu, Scripta Metall., 22, (1988) 1679-1684.

40. P.B. Aswath and S. Suresh, Metall. Trans. A 22, (1991) 817-828.

41. G. Luetjering, G. Proske, J. Albrecht, D. Helm and M. Daeubler, Intermetallic Compounds-Structure and Mechanical Properties, eds. O. Izumi, (Sendai, Japan Inst. of Metals, 1991) 536-541.

42. K.A. Williams, S.J. Balsone, M.A. Stucke and J.M. Larsen, (presented at Aeromat 90, Long Beach, CA, May 21-24, 1990).

43. P.B. Aswath and S. Suresh, Mat. Sci. and Eng., A114, (1989) L5-L10.

44. S.J. Balsone, D.C. Maxwell, M. Khobaib and T. Nicholas, Fatigue 90, eds., H. Kitagawa and T. Tanaka, (Warley, U.K., Materials and Components Eng. Publ. Ltd., III, 1990) 1905-1910.

45. R.J.T. Penton, M.T. Cope and P. Bowen, Mat. Sci. and Eng. A, 153 (1992) 508-513.

46. B.K. Parida and T. Nicholas, Mat. Sci. and Eng. A, 153 (1992) 493-498.

47. J.F. Wessels, B.J. Marquardt and D.D. Krueger (presented at TMS-AIME Symp. on Creep and Fracture of Titanium Aluminides, TMS, Indianapolis, IN, 1989).

48. S. Vekaturaman, AFWAL-TR-87-4103, Air Force Materials Lab, Wright Patterson Air Force Base, Ohio, (1987).

49. D.L. Davidson, J.B. Campbell and R.A. Page, Metall. Trans. A, 22A, (1991) 377-391.

50. K.S. Ravichandian and J.M. Larsen, Mat. Sci. and Eng., A153 (1992) 499-507.

51. W.O. Soboyejo, P.B. Aswath and J.E. Deffeyes, Mat. Sci. and Eng., A138 (1991) 95-102.

52. A.W. James and P. Bowen, Mat. Sci. and Eng., A153 (1992) 486-492.

53. K.T. Venkateswara Rao, W.O. Soboyejo and R.O. Ritchie, submitted to Metall. Trans. A, (1992).

54. K.T. Venkateswara Rao, G.R. Odette and R.O. Ritchie, Acta Metall. 40, (1992) 353-361.

55. K.T. Venkateswara Rao and R.O. Ritchie, Mat. Sci. and Eng., A153, (1992) 479-485.

56. M. Nazmy and M. Staubli, Scripta Metall., 25, (1991) 1305-1308.

CREEP FRACTURE AND CREEP–FATIGUE FRACTURE IN CERAMICS AND CERAMIC COMPOSITES

S. Suresh

Division of Engineering, Brown University
Providence, Rhode Island 02912, U.S.A.

Abstract

This paper summarizes recent advances in the area of subcritical crack growth in ceramics subjected to static and cyclic loads at elevated temperatures. Attention is devoted to the specific role of pre-existing and in-situ-formed glass films in influencing creep fracture and creep–fatigue fracture. Experimental results on the effects of cyclic frequency and load ratio, along with detailed transmission electron microscopy of crack-tip damage, are presented. The differences between the mechanisms of crack-tip and crack-wake damage are highlighted. Some general conclusions are drawn about the dependence of high-temperature damage tolerance on interfacial glass films and about the susceptibility of ceramic materials to cyclic fatigue fracture.

Introduction

The increasing need for strong, oxidation-resistant, and tough materials in high-temperature and high-performance propulsion systems has led to enhanced interest in the elevated-temperature mechanical properties ceramics and ceramic composites. The new generation of ceramics and ceramic-matrix composites are now candidate materials for replacing conventional alloys, such as nickel-base superalloys, for a range of high-temperature structural applications, in competition with intermetallics and structural silicides. Considerable work has been done in the past decade to identify the mechanisms which can potentially improve the resistance to crack initiation and subcritical crack growth at low temperatures (typically below 1000°C). However, the micromechanisms of fracture and slow crack growth in ceramics subjected to sustained and cyclic loads in the elevated-temperature environment have remained largely unexplored.

A limited number of experimental studies (e.g., [1, 2]) conducted in the 1970's led to the notion that the mechanisms responsible for failure under static and cyclic loads at high temperatures were the same for ceramic materials. Consequently, it was inferred that high-temperature cyclic crack growth rates could be uniquely derived from sustained-load crack growth rate data. However, more recent experimental work encompassing a broader variety of materials, test conditions and microstructures has shown that cyclic crack growth, in general, cannot be predicted solely on the basis of static fracture results, and that some ceramic materials do exhibit intrinsic differences in the

Critical Issues in the Development of High Temperature Structural Materials
Edited by N.S. Stoloff, D.J. Duquette and A.F. Giamei
The Minerals, Metals & Materials Society, 1993

micromechanisms of crack-tip damage under static and cyclic loads, as evidenced by transmission electron microscopy of crack-tip region (e.g., [3–9]).

This paper briefly summarizes work on crack growth, over the temperature range 1050–1400°C, in some monolithic ceramics and ceramics reinforced with SiC whiskers. Particular attention is devoted to the examination of the effects of glass phase on subcritical crack growth under sustained and cyclic loads in the elevated temperature environment. It is shown that intergranular and interfacial glassy films, which form *in situ* ahead of the crack tip as a consequence of the oxidation of Si-containing phases in the material, promote an overall crack growth response that is similar to that arising from glassy films introduced during the processing of the ceramic. Transmission electron microscopy of crack-tip damage as well as electron/optical microscopy of crack-wake morphology and contact are presented in an attempt to elucidate the influence of cyclic loading on high-temperature fracture. Specific examples discussed in this paper focus exclusively on oxide ceramics with and without reinforcements, primarily because of the large amount of exprimental information which has become available on these systems in recent years. Furthermore, the experimental conditions described here pertain to situations where creep–fracture and creep–fatigue fracture are amenable to characterization on the basis of linear elastic fracture mechanics.

Role of Pre-Existing Glass Phase on High-Temperature Crack Growth

Figure 1 shows the variation in tensile crack propagation rates per fatigue cycle, da/dN, in 1050°C air as the function of the stress intensity factor range, ΔK, for a 90% pure alumina, which is commerically available as AD90 from Coors Ceramic, Golden, CO. (This material has an average grain size of 4 μm, tensile and compressive strengths of 221 MPa and 2482 MPa, respectively, at room temperature, and a tensile strength of 103 MPa at 1000°C.) The results shown in Fig. 1 were obtained by Ewart and Suresh [6] using four-point bend specimens pre-cracked in uniaxial cyclic compression. Depsite the normal scatter in data, some distinct trends emerge. At fixed ΔK and load ratio, R, the fatigue crack subjected to a loading frequency $\nu = 0.13$ Hz exhibits a significantly faster growth rate than at 2 Hz. Figure 2 shows the results of Fig. 1 replotted in terms of crack velocity, $da/dt = (da/dN) \times \nu$, versus the maximum stress intensity factor, $K_{max} = \Delta K/(1-R)$. Also included here are the crack velocity versus nominal K under static loads in 1050°C air. At comparable values of maximum stress intensity factor, the crack velocity under static loads is up to two orders of magnitude higher than that under cyclic loads, with the difference being particularly more pronounced at lower stress intensity levels. Figure 3 also includes predictions of cyclic crack growth rates on the basis of static fracture data based on the expression

$$\left[\frac{da}{dt}\right]_{\text{cyclic}} = \nu \int_0^{1/\nu} \left[\frac{da}{dt}(K)\right]_{\text{static}} dt.$$

It is evident that the predicted growth rates deviate significantly from experimental values, especially at low stress intensity factor levels.

The AD90 ceramic contains impurities of silica and magnesia, and trace amounts of iron-, sodium- and potassium-oxide which are introduced as amorphous films at grain boundaries from the sintering aids added during processing. During high temperature deformation, the grain boundary films undergo viscous flow which results in the nucleation

and growth of cavities along grain boundary facets [6]. Ligaments of glass films bridging the faces of an intergranular crack in the alumina are shown in Fig. 3(a). Although viscous deformation of amorphous grain boundary films and the attendant intergranular fracture process are essentially the same under both static and cyclic loading, distinct differences also exist between the two cases which provide at least a qualitative explanation for the apparently lower grwoth rates seen under cyclic loading [6–9]. (1) The deformation of glassy intergranular films in the crack-tip region and in the crack wake is highly sensitive to the loading rate (i.e., cyclic frequency and waveform). As a result, the rate of fracture along grain boundary facets populated with the glass phase would be expected to be affected by whether the loading is static or cyclic, and by the frequency and waveform of cyclic loading. Experimental work has conclusively shown that both cyclic frequency and waveforms have a pronounced effect on crack growth rates; lower frequencies and waveforms with longer hold times at the peak stress (e.g., square wave form) promote higher crack growth rates [6, 8]. (2) Microscopically tortuous crack profiles are seen under both static and cyclic loads as a result of intergranular fracture. However, several differences have been identified between the two cases. First, repeated loading and unloading in cyclic fatigue creates debris particles of the ceramic within the crack walls, which enhance roughness-induced fatigue crack closure (e.g., [7]) over and above that created by the micro-tortuosity of crack path. Second, the pumping action of the crack walls under cyclic loads can "squeeze out" the glass film from the crack, as shown in Fig. 3(b). (3) When the concentration of glass film is significantly reduced (as, for example, in high-purity aluminum alloys such as the 99.9% pure AD999 alumina), the aforementioned effects contributing to apparent differences between static and cyclic load failures are also essentially suppressed [6]. Consequently, very little subcritical crack growth is observed for both sustained and cyclic loads at elevated temperature for the high-purity ceramic.

Role of In-Situ-Formed Glass Phase on High-Temperature Crack Growth

We now consider examples of materials which, during high-temperature deformation, form large amounts of glassy films in the crack tip region as a result of environmental interactions. The material selected for illustrating such effects is aluminum oxide reinforced with 33 vol.% of SiC whiskers, which is a laboratory version of a commerically available Grade WG300 composite from Greenleaf Corporation, Saegertown, PA. The material, which is uniaxially hot-pressed in the form of plates with practically full density, has matrix alumina grains with an average diameter of 1.5 μm, α-SiC whiskers of 0.1–1.0 μm diameter and a whisker aspect ratio of 10–100 [3, 10]. The whiskers were randomly oriented in the as-received material. Figure 4 is a transmission electron micrograph of the as-received microstructure of this ceramic composite. Here, perfect mechanical bonding between the matrix and SiC whiskers is evident. Note also the absence of any intergranular or interfacial cavities in Fig. 4. Transmission electron microscopy of the untested material exhibited very little pre-existing glass phase, with only trace amounts of Si, K, Fe, S, Ca, Y, and Mo [10].

When the SiC-containing alumina is subjected to deformation or fracture in air at temperatures typically in excess of 1200°C, the oxidation of SiC occurs initially according to the reaction [4, 10–13]:

$$2SiC + 3O_2 \rightarrow 2SiO_2 + 2CO.$$

In an unnotched and/or uncracked test specimen exposed to such high-temperature oxidation with or without an applied stress, the oxidation products leading to the formation of silica glass will be confined only to the near-surface region because of the paucity of oxygen in the interior sections of the specimen. However, when the specimen contains a through-thickness notch or crack, the availability of oxygen uniformly through the thickness of the specimen in regions ahead of the crack-tip results in the formation of glass phase at SiC–alumina interfaces uniformly ahead of the crack-tip. Detailed transmission electron microscopy of crack-tip region by Han and Suresh [3] show that the amount of in-situ-formed glass phase increases with increasing applied K or K_{max}, decreasing loading rate, increasing concentration of glass-forming phase (in this case, SiC concentration), and increasing temperature. Although full details of the above reaction are still not fully understood, available experiments indicate that silica glass is the primary reaction product influencing deformation in the early stages of creep ahead of the crack tip [10–14]. However, SiO_2–Al_2O_3 reaction can also result in the formation of alumino-silicate glasses and, given sufficient time, of mullites. In the high-temperature environment, melting of the glass films is followed by stress-assisted viscous flow in the crack-tip region leading to profuse cavitation. Creep deformation arising from the formation of interfacial cavities is more pronounced when the viscosity of the glass is low and when the glass phase wets or penetrates the grain facets.

High-temperature crack growth experiments have been conducted in the Al_2O_3-33% SiC composite in the air environment over the temperature range 1300–1500°C using fatigue-pre-cracked four-point bend specimens. Subcritical crack growth has been observed over distances of several millimeters under both static and cyclic loading conditions over a wide range of stress intensity factor values. Figure 5(a) is an example of a cyclic fatigue crack profile in the composite subjected to tension fatigue in 1400°C at ΔK = 3.2–5 MPa$\sqrt{\text{m}}$, R = 0.15 and ν = 0.1 Hz. Diffuse microcracking is visible along the crack wake in addition to periodic deflections/bifurcations of the crack tip. Figure 5(b) shows the development of a diffuse microcrack zone in the same material after unloading from a tensile load in 1500°C air.

A detailed understanding of the microscopic mechanisms of damage during stable crack growth can be obtained from transmission electron microscopy (TEM) of the deformation zone immediately ahead of the crack tip. For TEM studies in the Al_2O_3–SiC whisker composite, thin sections from the crack-tip region were prepared using the following procedure. A close-fitting wedge was introduced into the notch in the specimen using a thermosetting plastic. The specimen was then cut into thin slices about 100 μm thick, along planes perpendicular to the plane of the notch. Circular discs, 3 mm in diameter and covering the region of interest around the crack tip, were cut from these slices using an ultrasonic vibratory drill (Gatan model 601). The discs were then thinned further by glueing them to a glass slide and polishing them with a dimpler using a diamond compound. They were subsequently thinned to perforation by ion beam milling with a single gun at a voltage of 5 kV and a current of 1 mA [3, 10].

It is important to ensure that the aforementioned technique for thin foil preparation prior to TEM observation does not lead to damage in the sample, which may be misconstrued as damage occurring during high-temperature fracture or fatigue test in the ceramic composite. Therefore, TEM observations of crack-tip damage made on the ceramic composite specimen (which were subjected *a priori* to elevated-temperature fracture) were compared with similar observations made on as-received (untested) material (for which TEM foils were prepared using the same thinning, polishing and ion

milling procedure). Figure 4, which is a typical transmission electron micrograph of the as-received (untested) microstructure of the Al_2O_3–SiC composite, does not reveal damage.

Figure 6a is a TEM picture showing examples of cavities formed at the interface between a SiC whisker and the alumina matrix. The cavities grow along the interface (Figure 6b). The viscous flow of glass along the interfaces and matrix grain boundaries results in debonding of the SiC from the surrounding matrix and in the complete separation of the alumina grain facets, as illustrated in Figure 6c.

The kinetics of SiC oxidation and the geometrical changes in the SiC whiskers in the crack-tip region are also determined by whether the ceramic composite is subjected to static or cyclic loading at high temperatures. Under sustained loads, a significant fraction of the SiC whisker can be converted to glass pocket in the vicinity of the crack tip. Figure 7a shows examples of glass pockets formed within SiC whiskers (regions indicated by the arrows) in the Al_2O_3–SiC composite subjected to slow crack growth under a sustained stress intensity factor of approximately 3.5 $MPa\sqrt{m}$ at 1400°C. However, if the ceramic composite is subjected to cyclic loads (even with the maximum stress intensity factor being the same as that in the static tests), such extensive oxidation of SiC is not observed because of periodic unloading. On the other hand, cyclic loading causes the SiC whiskers (in the crack-tip region) to break. Figure 7b shows a broken whisker from a cyclic fatigue test. Note the meniscus of the molten glass phase (indicated by the arrow) flowing inside the broken whisker [3].

Figure 8 shows the variation of fatigue crack propagation rates, da/dN, with the stress intensity factor range, ΔK, for the Al_2O_3–SiC composite subject to load ratios of 0.15, 0.40 and 0.75 in 1400°C air at a frequency of 0.1 Hz. Similar to the trend seen in the fatigue of metals at room temperature, increasing the load ratio causes an apparent reduction in the threshold ΔK for crack growth and an apparent increase in the rates of fatigue crack growth. At $R = 0.15$, an increase in test frequency leads to slower crack growth rates, similar to the trend seen in AD 90 alumina at 1050°C.

The variation of crack velocity, da/dt, in the alumina–SiC composite is plotted in Figure 9 as a function of the applied stress intensity factor K_I for static crack growth experiments conducted in 1400°C air (open symbols). Also indicated in this figure are the fatigue crack velocities, $(da/dt) = (da/dN) \times \nu$, as a function of the maximum stress intensity factor, K_{max}, for the cyclic fatigue tests conducted on the ceramic composite in 1400°C at $R = 0.15$ and $\nu = 0.1$ Hz and 2 Hz. Similar to the trend seen in the alumina ceramic, the cyclic crack growth rates in the ceramic composite are significantly lower than those seen under static loads. Furthermore, an increase in test frequency results in a reduction in the rates of fatigue crack growth. It is found that the predictions of cyclic crack growth rates, on the basis of static crack growth data, deviate significantly from the experimenal results. These differences between static and cyclic crack growth rates have been attributed to (i) the differences in the microscopic mechanisms of deformation ahead of the main crack-tip (e.g., Figures 7a and 7b), (ii) enhanced levels of crack closure, frictional sliding along interfaces, and bridging of the crack faces by whiskers under cyclic loading conditions and (iii) rate-sensitivity of deformation of the viscous glass phase along interfaces. Note the similarity of the effects of static and cyclic loading on high-temperature crack growth in the ceramic composite to those seen earlier for the monolithic alumina. Figure 10 schematically summarizes the effects of various mechanical loading variables on static and cyclic fatigue crack growth in ceramic materials whos

high-temperature crack growth response is influenced by the presence of interfacial glass films.

In both monolithic ceramics (such as polycrystalline alumina) and ceramic composites (such as alumina reinforced with SiC whiskers), pre-existing or in-situ-formed glass films at interfaces accommodate deformation at the crack-tip by the nucleation and growth of cavities. The predominant role of this cavitation process in controlling crack-tip damage also results in the suppression of any dislocation plasticity within the matrix grains. In this context, it is interesting to examine recent experiments on molydisilicide-matrix composites with SiC reinforcements. $MoSi_2$ and $MoSi_2$–50 mol.% WSi_2 alloys are known to undergo a brittle–ductile transition at approximately 1000°C. These intermetallics also contain silica glassy films at interfaces as a result of the reaction (e.g., [15]):

$$5(Mo,W)Si_2 + 7O_2 \rightarrow (Mo,W)_5Si_3 + 7SiO_2.$$

During high-temperature crack growth in $(Mo,W)Si_2$ alloys with SiC reinforcements, the presence of the glass film promotes intergranular and interfacial cavitation in the crack-tip region in much the same way as that seen for the ceramic materials. The presence of the glass also appears to suppress dislocation plasticity and slip within the matrix. As a result, the high-temperature subcritical fracture characteristics of the silicide-matrix composites are qualitatively similar to those of the alumina–SiC composites schematically sketched in Fig. 10 [15]. Since carbon reduces the extent of glass by aiding in the following reaction,

$$2SiO_2 + 6C \rightarrow 2SiC + 4CO,$$

attempts are currently underway [16, 17] to develop high-temperature silicides with reduced amounts of glass phase through proper additions of carbon.

Discussion and Concluding Remarks

In this review, it is demonstrated that the presence of glassy films, either pre-exising or forming *in situ* in the high temperature environment, can have a profound effect on the subcritical crack growth response of ceramics and ceramic composites. Experimental evidence available in the literature indicates that interfacial glass films generally have the following effects on creep fracture and creep–fatigue fracture in ceramics and ceramic composites:

- An increase in the apparent differences in crack growth response between static and cyclic fracture at elevated temperature, as compared to brittle solids with little or no amorphous intergranular phases.
- An increase in the sensitivity of high-temperature crack growth to cyclic frequency, waveform and hold times as a consequence of the strain-rate-sensitivity of the glass phase to deformation.
- A noticeable increase in the tendency of the material to develop interfacial cavitation and microcracking.

- A decrease in the thresholds for creep crack growth and creep fatigue crack growth.
- Expanded range of subcritical crack growth (i.e., greater spread of K or ΔK values over which subcritical fracture occurs) during static and cyclic fatigue at high temperatures.
- Suppression of dislocation activity within the matrix.

It has traditionally been assumed that ceramic materials do not exhibit true cyclic fatigue effects due to the absence of cyclic plasticity. However, the results reviewed in this paper and those reported elsewhere [18–21] clearly show that cyclic fatigue effects can occur in ceramic materials in many different ways:

1. A mechanical (cyclic) fatigue effect wherein the macroscopic mode of fracture under cyclic loads is distinctly different from that seen under monotonic loads. The mode I fatigue fracture of notched ceramic materials in cyclic compression [18, 19] is an example of this mechanical fatigue effect and it is distinctly different from the splitting mode of failure (parallel to compression axis) under monotonic compression.
2. A microscopic fatigue effect wherein the mechanisms of deformation and failure under cyclic loads is distinctly different from that seen under static loads. The differences between failure mechanisms observed under static and cyclic loads in the elevated-temperature failure of the Al_2O_3–SiC composite (Figures 7a and 7b) under cyclic tension are examples of this microscopic fatigue effect.
3. A *micromechanical fatigue effect* wherein kinematically irreversible cyclic deformation arises in ceramic materials as a consequence of microcracking, phase transformations, creep, interfacial sliding or crack bridging, analogous to slip irreversibility in metal fatigue. The generation of localized residual tensile stresses and the nucleation of compression fatigue cracks [18, 19] is an outcome of this kinematically irreversible microscopic deformation.
4. A mechanical fatigue phenomenon arising from crack-wake effects wherein differences in crack closure, crack bridging, or grain bridging result in apparently different crack growth rates between static and cyclic fatigue, even though the basic micromechanisms of deformation and failure are similar [20, 21]. The differences between static and cyclic fatigue crack growth rates at high temperatures in the polycrystalline alumina ceramic are an example of this type of fatigue effect.

Acknowledgements: This review is based on work sponsored by the Basic Science Division of U.S. Department of Energy under Grant DE-FG02-84ER-45167.

References

[1] A.G. Evans, L. R. Russell and D.W. Richardson, *Metall. Trans. A*, **6A** (1975) 707.

[2] A.G. Evans, *Int. J. Fract.*, **16** (1980) 485.

[3] L.X. Han and S. Suresh, *J. Amer. Ceram. Soc.*, **72** (1989) 1238.

[4] S. Suresh, *Int. J. Fract.*, **42** (1990) 41.

[5] S. Suresh, *J. Hard Mater.*, **2** (1991) 29.

[6] L. Ewart and S. Suresh, *J. Mater. Sci.*, **27** (1992) 5181.

[7] S. Suresh, ***Fatigue of Materials***, Cambridge University Press, Cambridge, UK (1991).

[8] C.-K.J. Lin and D.F. Socie, *J. Amer. Ceram. Soc.*, **74** (1991) 1511.

[9] C.-K.J. Lin, D.F. Socie, Y. Xu and A.V. Zangvil, *J. Amer. Ceram. Soc.*, **75** (1992) 637.

[10] L.X. Han, R. Warren and S. Suresh, *Acta Metall. Mater.*, **40** (1992) 259.

[11] P.F. Becher and T.N. Tiegs, *Adv. Ceram. Mater.*, **3** (1988) 148.

[12] J.R. Porter, *Mater. Sci. Eng.*, **A107** (1989) 127.

[13] S.R. Nutt, P. Lipetzky and P.F. Becher, *Mater. Sci. Eng.*, **A126** (1990) 165.

[14] R.L. Tsai and R. Raj, *Acta Metall.*, **30** (1982) 1043.

[15] U. Ramamurty, A.S. Kim, S. Suresh and J.J. Petrovic, *J. Amer. Ceram. Soc.*, **76** (1991) in press.

[16] J.J. Petrovic and F. Gac, this volume.

[17] S.R. Srinivasan, R.B. Schwartz and J.D. Embury, *MRS Symp. on Intermetallics*, Fall Meeting, 1992, in press.

[18] L. Ewart and S. Suresh, *J. Mater. Sci.*, **22** (1987) 1173.

[19] S. Suresh and J.R. Brockenbrough, *Acta Metall.*, **36** (1988) 1455.

[20] R.H. Dauskardt, D.B. Marshall and R.O. Ritchie, *J. Amer. Ceram. Soc.*, **73** (1990) 893.

[21] J.F. Tsai, C.S. Yu and D.K. Shetty, *J. Amer. Ceram. Soc.*, **73** (1990) 2992.

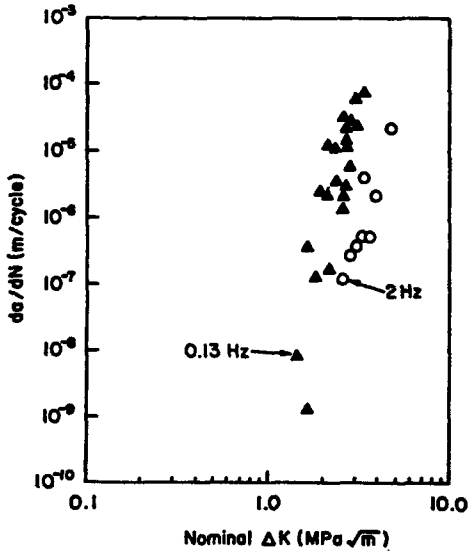

Fig. 1. Fatigue crack growth behavior of polycrystalline alumina in 1050°C air.

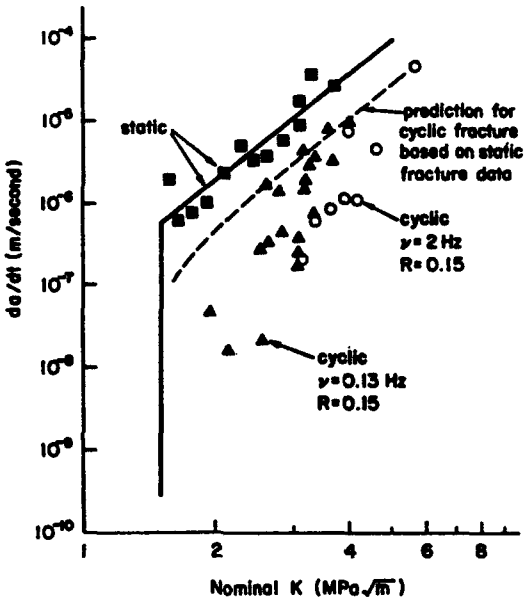

Fig. 2. A comparison of experimental results on static and cyclic fatigue fracture in alumina in 1050°C air. Also shown is a comparison of predicted cyclic response with experiments. See text for details.

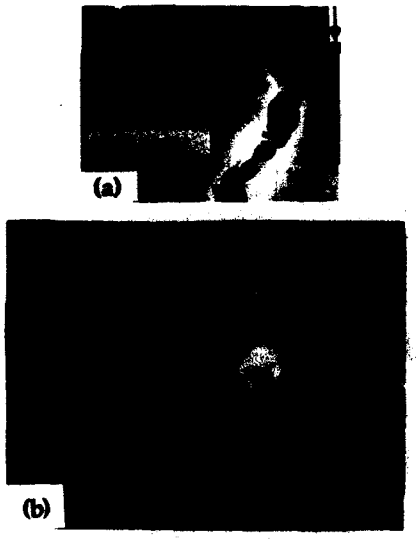

Fig. 3. (a) Ligaments of glass bridging the faces of the fatigue crack. (b) Films squeezed out of the crack by the pumping action of crack walls.

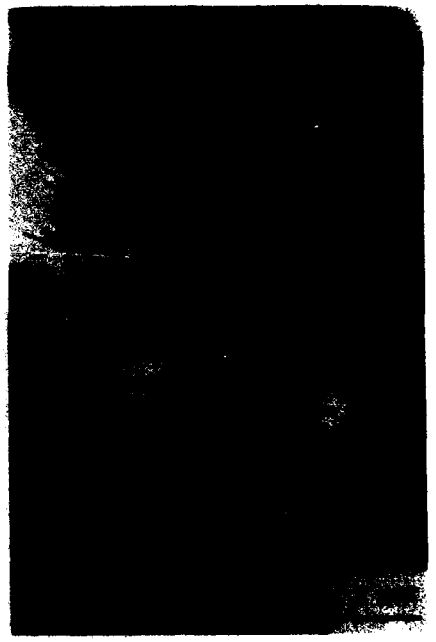

Fig. 4. As-received microstructure of the alumina–33 vol.% SiC whisker composite.

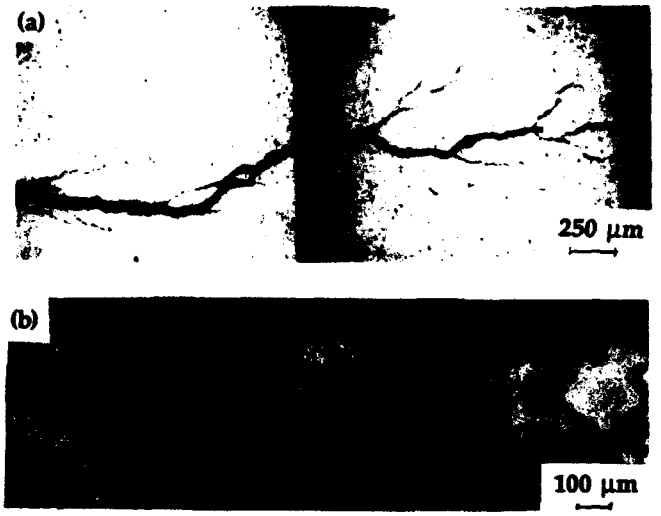

Fig. 5. Fatigue crack profiles in air. (a) 1400°C and (b) 1500°C.

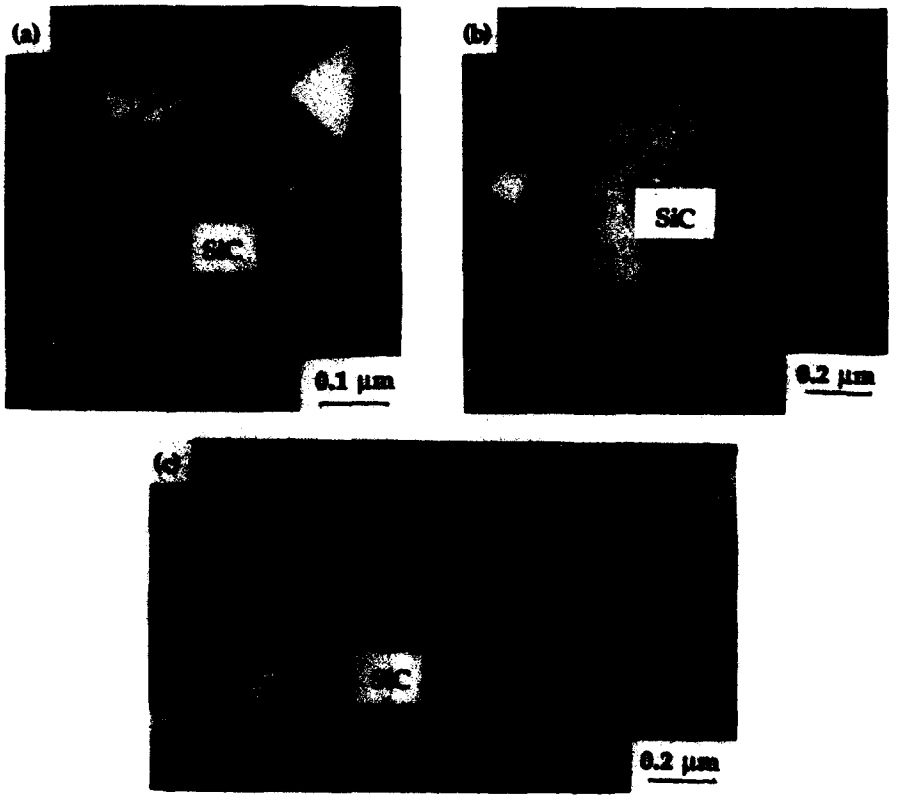

Fig. 6. (a)–(c) Examples of the growth of cavities along grain boundaries and interfaces in the immediate vicinity of a fatigue crack tip in the alumina–SiC composite in 1400°C air.

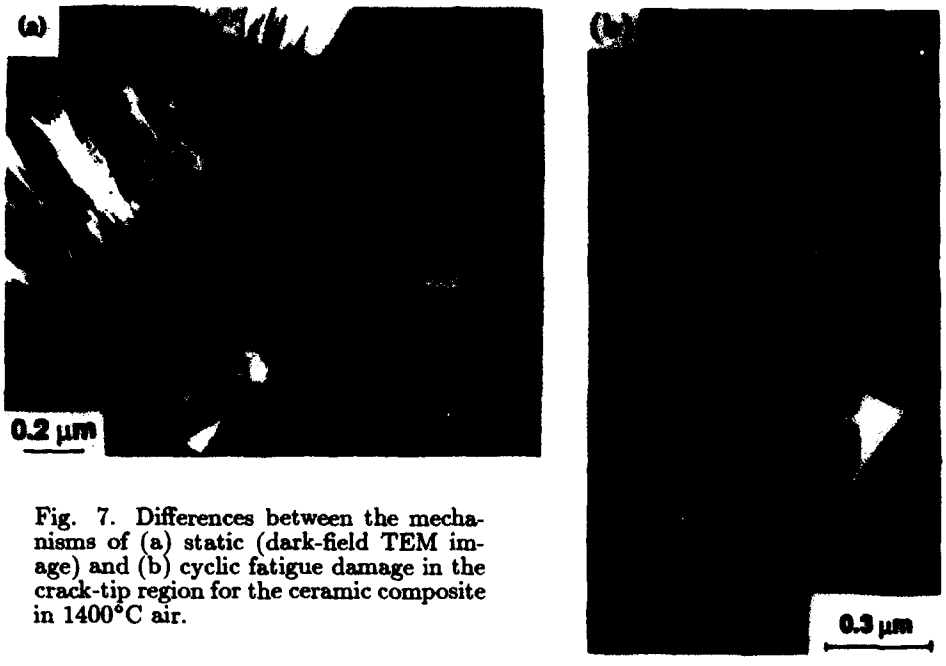

Fig. 7. Differences between the mechanisms of (a) static (dark-field TEM image) and (b) cyclic fatigue damage in the crack-tip region for the ceramic composite in 1400°C air.

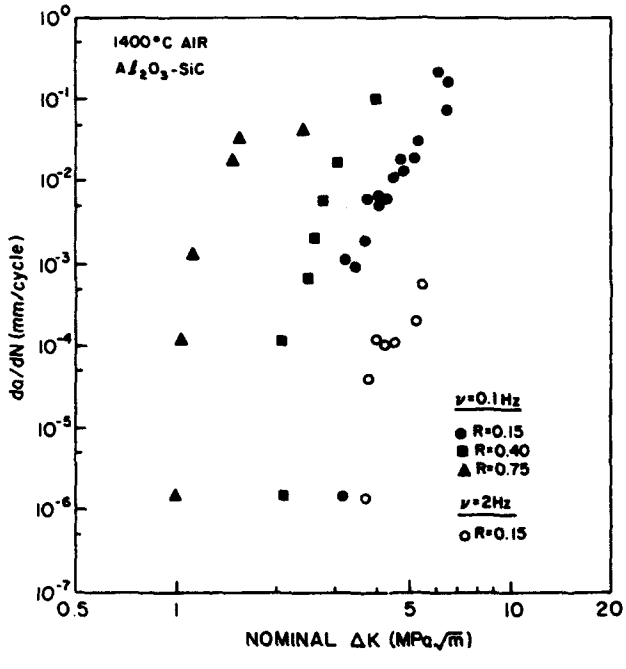

Fig. 8. Fatigue crack growth behavior of the ceramic composite at different load ratios in 1400°C air environment.

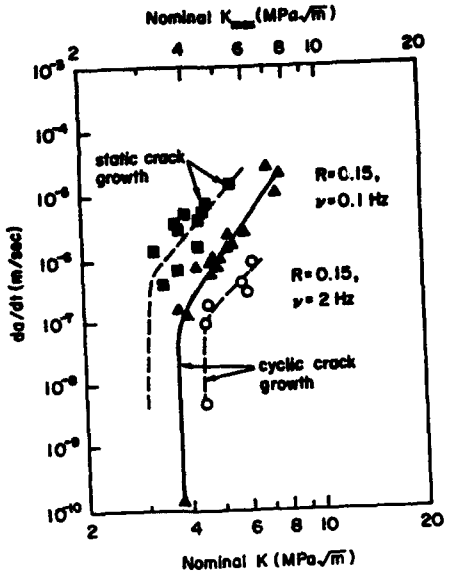

Fig. 9. A comparison of experimental results on static and cyclic fatigue fracture in alumina-matrix composite in 1400°C.

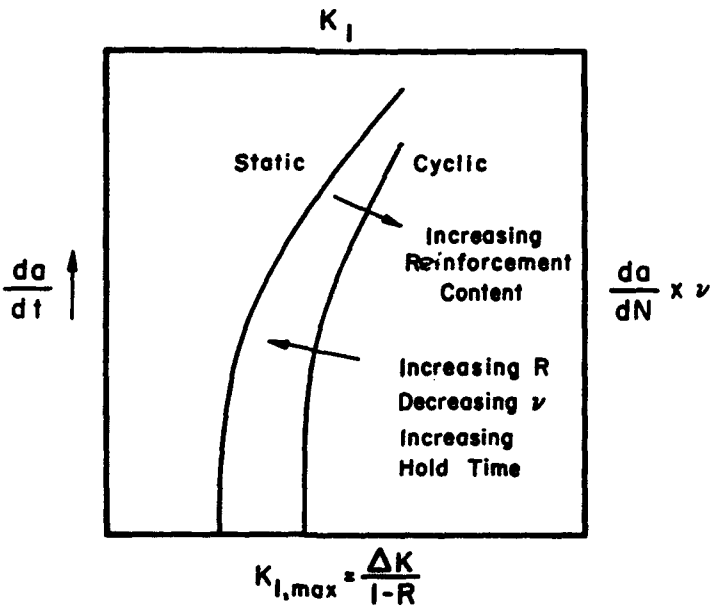

Fig. 10. A schematic representation of the effects of various loading variables on high-temperature fatigue in ceramics and ceramic-matrix composites.

SESSION VIII

Environmental

ENVIRONMENTAL EMBRITTLEMENT OF ORDERED INTERMETALLICS AT AMBIENT TEMPERATURES

Takayuki Takasugi

Institute for Materials Research
Tohoku University
Katahira 2-1-1, Aoba-ku, Sendai 980 Japan

Abstract

It is demonstrated that the environmental embrittlement of ordered intermetallics, which is caused by hydrogen released from moisture in air or hydrogen gas in environment at ambient temperatures, takes place in various kinds of crystal structures, alloys and microstructures. First, the phenomenology of the environmental embrittlement, i.e. atmosphere, temperature and strain rate dependencies, as well as alloying, doping and microstructural effects, is presented in terms of mechanical properties, fractography and microstructural features. Next, possible mechanisms of embrittlement involving the kinetics (i.e. decomposition, migration and condensation of hydrogen) and the bond breaking are discussed. Finally, some evidence indicating suppression of the embrittlement through selection of deformation condition, alloying and microstructural modification is presented.

Critical Issues in the Development of High Temperature Structural Materials
Edited by N.S. Stoloff, D.J. Duquette and A.F. Giamei
The Minerals, Metals & Materials Society, 1993

Introduction

It has been believed that a number of ordered intermetallics, which possess attractive high-temperature structural properties, have superior environmental resistance because they generally have a high melting point, good thermal, chemical and microstructural stability. Also, the poor ductility and brittle fracture of ordered intermetallics which have limited their use as engineering materials, were overcome by the substantial recent efforts. However, as many observations on their mechanical properties are reported, it is clear that the environmental resistance of most ordered intermetallics is not always high under the dynamical condition, such as in loading and also in ordinary atmosphere, such as air. It has been demonstrated during the last and this decades that the environmental embrittlement of ordered intermetallics, which is caused by hydrogen released from moisture in air or hydrogen gas in environment at ambient temperatures, occurs severely in various kinds of crystal structures, alloys and microstructures.

In this article, the phenomenological features of the environmental embrittlement of ordered intermetallics, which are evaluated by mechanical property and fractography, are summarized in terms of testing condition (i.e. atmosphere, temperature and strain rate dependencies) as well as of material condition (i.e. alloying, doping and microstructural effects whether polycrystal or single crystal). The mechanisms responsible for the environmental embrittlement, which involve a number of processes such as decomposition, permeation, migration and condensation of hydrogen and the bond breaking, are presented. Also, strong evidence indicating suppression of the embrittlement through alloying, doping and microstructural modification, and some attempts to control the embrittlement through modifying the surface composition and selecting the appropriate deformation condition are presented. Finally, it is demonstrated that the environmental embrittlement of ordered intermetallics is a major cause and an extrinsic factor for their low ductility and brittle fracture. Another kind of environmental embrittlement, which is operative at elevated temperatures and is associated with oxygen released from air, is excluded from this article.

Phenomenological Features

Just as traditional materials such as high strength-low alloy steels and titanium base alloys, it has been known that some $L1_2$ ordered intermetallics of $(Fe,Ni)_3V$ [1], Ni_3Fe [2], boron-doped Ni_3Al [3], and Co_3Ti [4] alloys are embrittled by electro-charging of hydrogen at low temperatures, and Ti_3Al [5,6] and TiAl [7] alloys are embrittled by hydrogen gas exposure at high temperatures (Table I also lists other materials showing such hydrogen embrittlement). This kind of embrittlement is due to the compulsorily injected hydrogen into materials. However, the fact that these ordered intermetallics are more susceptible to hydrogen embrittlement and more critical than traditional materials was first shown in $L1_2$-type Co_3Ti polycrystal which has been known to be intrinsically ductile [4,8]. Figure 1 shows that when Co_3Ti polycrystals are tensile-tested in vacuum, air and hydrogen charging obtained elongation value was lower in air than in vacuum, and the lowest value was observed in hydrogen-charging. This result reveals that the embrittling species is hydrogen and also the embrittlement in air is due to the moisture or hydrogen gas in a low level in air. Since this finding, a number of alloys were shown to be simply embrittled in air at ambient temperatures, as summarized in Table I. It is demonstrated from Table I that the environmental embrittlement is operative in various kinds of crystal structures, alloy systems and microstructures, one limiting form of which is single crystal. Table I also indicates that the environmental embrittlement has been observed in ordered intermetallics which were ductilized by alloying or found to be intrinsically ductile.

The effect of testing atmosphere

As shown in Figure 1, the elongation strongly depends on the environment. A number of $L1_2$ ordered intermetallics of Co_3Ti and their alloys [4,8-11], $(Co,Fe)_3V$ alloys [12,13], Ni_3Al and their alloys [14-19], Ni_3Si and their alloys [20-23] in both of polycrystal and single crystal form were tensile tested in various atmospheres (including liquid medium) such as vacuum, air, oxygen gas, Ar gas, hydrogen gas, distilled water, mixture of Ar and hydrogen gas.

Table I Ordered intermetallics showing the environmental (and hydrogen) embrittlement

Type	Single/ polycrystal	Alloys	Environmental embrittlement	Hydrogen embrittlement	Beneficial addition
$L1_2$	polycrystal	Ni_3Al	o		
		Ni_3Al+B	o	o	o
		Ni_3Al+Be	o		
		$Ni_3(Al,Mn)$	o	o	
		$Ni_3Al+Zr+B$	o		o
		Ni_3Si	o		
		Ni_3Si+B	o		o
		$Ni_3(Si,Ti)+B$			o
		$Ni_3(Si,Ti)+C$			o
		Co_3Ti	o	o	
		Co_3Ti+X	o		
		Co_3Ti+Fe			o
		Co_3Ti+Al			o
		Co_3Ti+B	o		
		Co_3Ti+C	o		
		Co_3Ti+Be	o		
		$(Co,Fe,Ni)_3V$	o		
		Ni_3Fe		o	
	single	$Ni_3(Al,Ti)$	o	o	
		$Ni_3(Al,Ti)+B$	o	o	o
		$Ni_3(Si,Ti)$	o	o	
		$Ni_3(Si,Ti)+B$	o	o	
		$(Co,Ni)_3Ti$	o	o	
$L1_0$	polycrystal	TiAl	o	o	
		TiAl+Cr	o		o
DO_{19}	polycrystal	Ti_3Al	o	o	
B2	polycrystal	FeAl	o	o	
		FeCo+V		o	
		NiAl	o	o	
DO_3	polycrystal	Fe_3Al	o	o	
		Fe_3Al+Cr	o	o	o
Others	polycrystal	Ni_2Cr		o	

"Environmental embrittlement" means the embrittlement occurring in air or in other atmosphere while "Hydrogen embrittlement" means the embrittlement occurring by cathodic charging or by hydrogen gas exposure. Note that "Beneficial addition" means doping or alloying elements resulting in the suppression of the environmental (or hydrogen) embrittlement. Also, the blanks in the column of "Hydrogen embrittlement" mean that the effect has not been investigated.

Observed result was that the tensile elongation is generally the highest in vacuum, low in air or distilled water, and the lowest in hydrogen gas or cathodic charging. However, the yield stress and the strain hardening were insensitive to the testing atmosphere.

Testing atmosphere effect on the tensile ductility was also observed in bcc-derivative crystal structures such as DO_3-type Fe_3Al and B2-type FeAl [24,25]. Trend is quite similar to that in $L1_2$ ordered intermetallics. When samples were tested in air, these alloys were severely embrittled, although the yield stress was again insensitive to testing environment. CuZn also showed the apparent environment embrittlement in distilled water, but may be categorized as stress-cracking in a solution [26].

Figure 2 shows another example where environmental (and also hydrogen) embrittlement was observed in monolithic γ–TiAl alloy with $L1_0$ structure; the elongations were lower in air and in hydrogen gas than in vacuum [27]. Quite the same environmental effect was observed in TiAl base ordered intermetallics, the ductility of which was evaluated by three-point bending

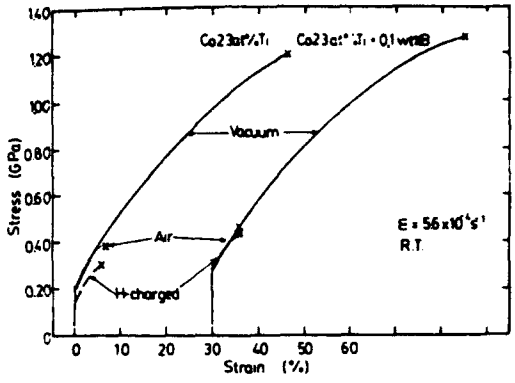

Figure 1 Stress-strain curves of $L1_2$-type Co_3Ti polycrystals with and without boron which were tensile tested at room temperature in various atmospheres.

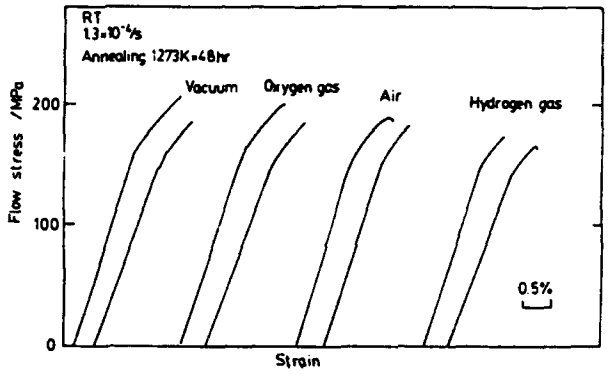

Figure 2 Stress-strain curves of $L1_0$-type TiAl polycrystals which were tensile tested at room temperature in various atmospheres. Two sets of tensile deformations were performed to confirm reproducibility.

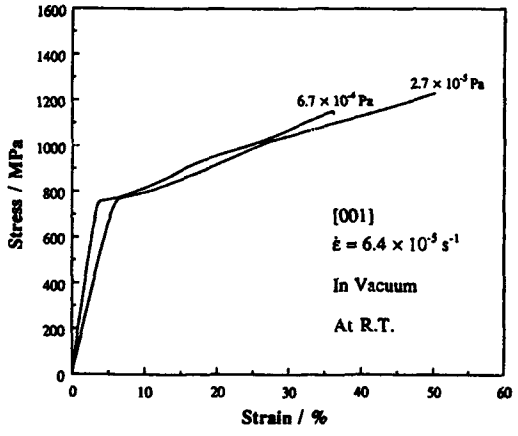

Figure 3 Comparison of the stress-strain curves of $Ni_3(Si,Ti)$ single crystals with [001] orientation deformed under two vacuum degrees of 2.7×10^{-5} Pa and 6.7×10^{-4} Pa.

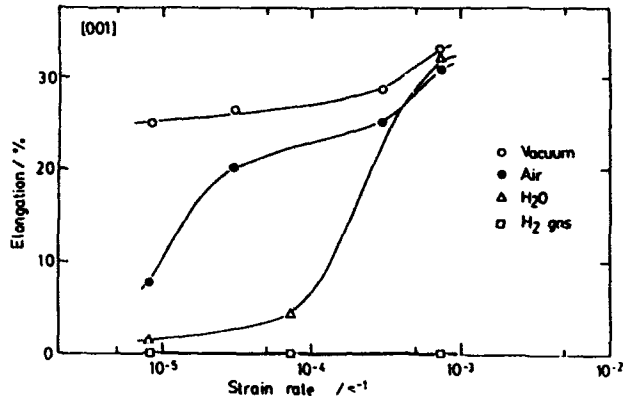

Figure 4 Variation of the tensile elongation with strain rate for $Ni_3(Al,Ti)$ single crystals with [001] orientation which were doped with a trace amount of boron and tensile-tested in various atmospheres.

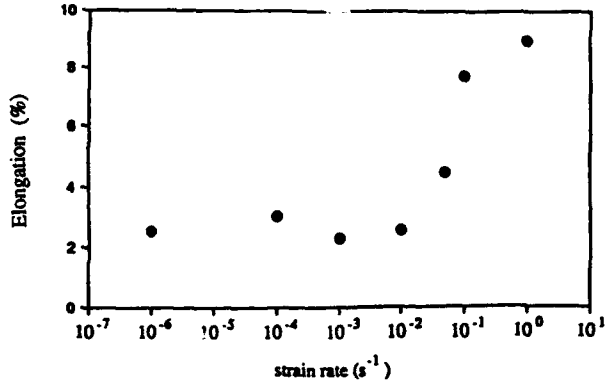

Figure 5 Variation of the tensile elongation with strain rate for B2-type FeAl polycrystals deformed in air.

[28]. It was recently reported that γ–TiAl titanium aluminide consisting of a lamellar structure, that is, *polysynthetic twinned crystal* (PST) shows the apparent environmental effect on their mechanical properties [29]; it was higher when tested in vacuum or in dry air than in air or in hydrogen gas.

Interesting result was shown in DO_3-type Fe_3Al and B2-type FeAl [23,24], and $L1_2$-type Ni_3Al alloyed with Zr [18] and $(Co,Fe)_3V$ [12,13]; the highest elongation value was not obtained in samples tensile-tested in vacuum but in oxygen gas, indicating evidence that the environmental embrittlement is suppressed.

Figure 3 shows the effect of vacuum degree on the tensile elongation of $L1_2$-type $Ni_3(Si,Ti)$ single crystal with [001] orientation [30]. The tensile elongation of sample tested in vacuum degree of 2.7×10^{-5} Pa was higher than that of sample tested in vacuum degree of 6.7×10^{-4} Pa. This result suggests that the ductility of this material is still affected under this range of vacuum degree, meaning that the environmental embrittlement in ordered intermetallics is so severe in contrast to ordinary materials such as iron and steel.

Strain rate dependence

The strain rate dependence on the tensile ductility was investigated in a number of $L1_2$ type [4-11,15,16,21,22,30] and B2-type [31,32]-type ordered intermetallics. As examples, Figures 4 and 5 show the results on $Ni_3(Al,Ti)$ single crystals with [001] orientation which were doped with a trace amount of boron and tested in a variety of atmospheres [33], and the result on FeAl polycrystals deformed in air [31], respectively. Tensile elongation generally decreased with decreasing strain rate, depending on the testing atmosphere, although the yield stress and the strain hardening were primarily independent of strain rate. In some cases, an apparent ductile-brittle transition was observed. Figure 5 demonstrates that the tensile elongation of FeAl (B2 structure), which has been believed to be intrinsically brittle, rapidly increased in a strain rate range beyond 10^{-1}/sec. Thus, the strain rate effect indicates that the environmental embrittlement is dynamic effect due to the competitive process of hydrogen with the applied deformation rate.

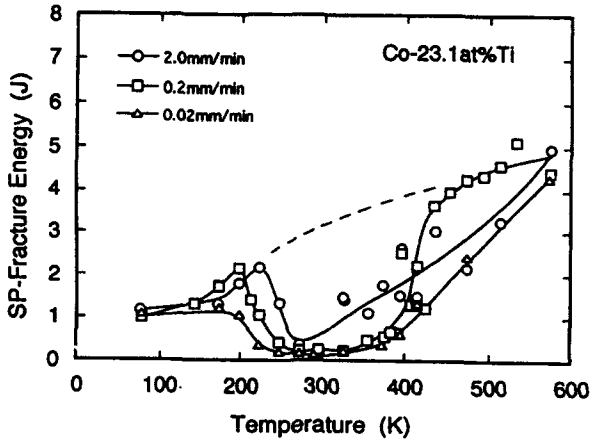

Figure 6 Variations of small punch fracture energy (SPEE) with temperature for Co_3Ti polycrystals deformed in air.

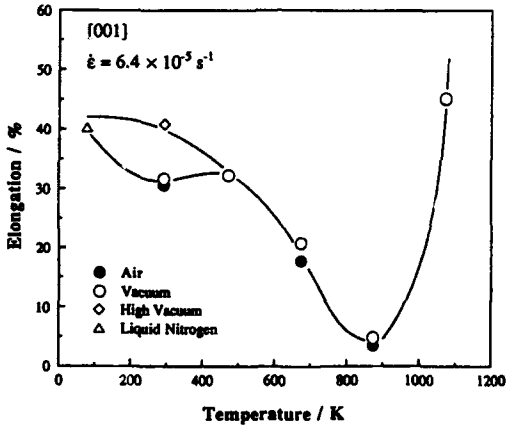

Figure 7 Variations of the tensile elongation with temperature for $L1_2$-type $Ni_3(Si,Ti)$ single crystals with [001] orientation which were deformed in air and in vacuum, respectively.

In addition to the above, some ordered intermetallics like TiAl PST with a lamellar structure was shown to be sensitive to strain rate [29]; the tensile elongation increased with increasing the strain rate. Thus, it is noted that the strain rate effect was observable whenever alloy shows the effect of the testing atmosphere on the tensile ductility.

Temperature dependence

The effect of temperature on the embrittlement has been reported in some $L1_2$ ordered intermetallics of Co_3Ti base alloys in polycrystalline form [9,34], $Ni_3(Al,Ti)$ in single crystalline form [33], $Ni_3(Si,Ti)$ in both polycrystal [21,22] and single crystal [30] form, and in B2 ordered intermetallics of FeAl (36.5%Al) polycrystals [35]. Figure 6 shows the variation of toughness (i.e. fracture energy) of Co_3Ti polycrystals which was evaluated in air by the compressive punch test as a function of temperature [34]; the minimum in toughness was observed around room temperature (i.e. 300 K), indicating that the toughness loss is limited to ambient temperature. With an increase in test temperature to 400 K and also with a decrease in test temperature below 200 K, the toughness was recovered to high values. As an another example, Figure 7 shows the variation of elongation with temperature for $L1_2$-type $Ni_3(Si,Ti)$ single crystals with [001] orientation which were deformed in air and vacuum[30]; the elongation minimum appears around room temperature when samples are deformed in air and low degree of vacuum (6.7×10^{-4} Pa). As already described in a previous section (Fig. 3), when sample is deformed in high degree of vacuum (2.7×10^{-5} Pa), the elongation increased and consequently the minimum in the curve of the elongation vs. temperature disappeared. This result means that the minimum of the elongation, i.e. the embrittlement at room temperature therefore can be attributed to the hydrogen embrittlement. However, there were some cases at which even when samples were deformed in high degree of vacuum the elongation displayed the minimum around room temperature [9,33] (for an example, see Figure 8). This result indicates that *residual* hydrogen contained in the sample may affect the elongation property. Otherwise, vacuum degree may be not high enough. More work is needed to know the roles of hydrogen from environment and residual hydrogen in the material.

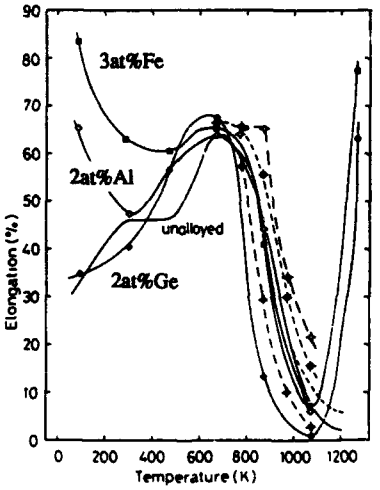

Figure 8 Variations of the elongation with temperature for $L1_2$-type Co_3Ti alloys containing various additive elements which were deformed in vacuum.

Besides $L1_2$ and B2 (or DO_3) ordered intermetallics, the testing temperature effect on the embrittlement has been observed in γ-TiAl [27]; in this case, the discrepancy of the tensile elongation between air and vacuum was larger at 673 K than at room temperature. However, whether the environmental embrittlement observed at 673 K is associated with hydrogen or with oxygen is not identified yet [27].

Recovery in ductility at cryogenic temperature can be attributed to the lowering of the mobility of hydrogen into the near tip region of propagating micro-crack [8,11], or to a combined effect of (a) reduction in the kinetics of decomposition of moisture, and (b) lowering of the equilibrium moisture content in air at this temperature [35]. On the other hand, the ductility recovery at high temperatures can be attributed to the reduction in the capability of hydrogen condensation into the associated place [8,11], or to a rapid in-situ formation of protective oxide scales on sample surfaces [23,24].

Here, it must be noted that the reduction of the tensile ductility by hydrogen charging is generally recovered after a degassing treatment and then stressing under a high vacuum environment; the recovery has been established simply at room temperature in the case of Co_3Ti polycrystals [8], 473 K in the case of $(Fe, Ni)_3V$ [1], at 673 K in the case of boron-doped Ni_3Al [3] and 673 K in the case of $Ni_3(Al,Mn)$ [15]. These results suggest that the reduced ductility in these alloys is not due to the permanent damage such as a hydride or swelling void, and also that hydrogen can be penetrated into the sample interior or degassed into the outer environment, in a reversible way.

Figure 9 The effect of the testing atmosphere and strain rate on the fracture pattern observed in $Ni_3(Al,Ti)$ single crystals with [001] orientation.

Fracture mode

In response to the embrittlement, i.e. with decreasing the tensile ductility, the fracture mode changed from "ductile" mode to "brittle" mode, depending on crystal structures, alloys and microstructures. In the case of polycrystals of $L1_2$ ordered intermetallics of Co_3Ti [4,8-11], Ni_3Al [14,15,17-19], $(Fe,Ni)_3V$ [12,13], Ni_3Si [20-23] and their alloys, the fracture mode changed from transgranular fracture to intergranular fracture. Thus, hydrogen promoted brittle fracture separating grain boundaries, which are the (inherent) weakest defect path. In the case of single crystals of $L1_2$ ordered intermetallics of Co_3Ti [11], $Ni_3(Al,Ti)$ [16,33] and $Ni_3(Si,Ti)$ [30], the fracture mode changed from the dimple pattern or the ripple pattern, to the

river pattern with decreasing the tensile ductility. Figure 9 shows the fracture patterns observed in $Ni_3(Al,Ti)$ single crystals with [001] orientation as functions of testing atmosphere and strain rate [16]. In the embrittled situation, the fracture plane consisted of featureless smooth facets accompanied with river patterns. Corresponding to the change in fracture pattern (i.e. mode), measured fracture planes also changed depending on alloys; with decreasing the ductility, fracture plane changed, from {111} plane (or non-crystallographic plane) which is usually inclined to the stress axis, that is, along highest applied resolved shear stress, to {001} plane which is usually normal to stress axis, that is, has the maximum resolved normal stress [11,16,30,33]. In the case of the severest embrittlement of $Ni_3(Al,Ti)$ single crystals which were deformed in hydrogen gas and also at a very slow strain rate, {011} and {111} fracture planes were observed [16]. However, the fracture pattern on {111} plane in this case was quite distinct from the fracture pattern on {111} plane observed in vacuum. The fracture patterns in the former case showed the river patterns, revealing fracture by the brittle manner. Thus, these results indicate that the cohesive strength is affected by hydrogen and also depends on alloys.

To summarize the fractography of the embrittled $L1_2$ ordered intermetallics it may be remarked that even though certain amount of plastic deformation precedes before fracture of sample, fracture mode is quite brittle, i.e. showing the river pattern in the case of single crystals and grain boundary facets in polycrystals. This result is in contrast to the fracture patterns in embrittled iron and steel, where certain amount of plastic deformation is not expected whenever embrittlement occurs.

In the case of polycrystal of B2 FeAl ordered intermetallic [24,25], with decrease in ductility, the fracture mode changed from mainly intergranular fracture (e.g. in oxygen), through mixed mode fracture (e.g. in vacuum), to mainly transgranular (cleavage) fracture (e.g. in air). Thus, in this alloy, the brittle fracture mode is not intergranular fracture but transgranular (cleavage) fracture. The cleavage plane in the embrittled condition was determined to be {001} plane [36].

In the case of monolithic γ-TiAl, the fracture mode was mainly transgranular cleavage with river pattern and basically insensitive to the testing atmosphere [27,28]. The corresponding cleavage plane has not been determined yet. In TiAl PST with a lamellar structure, it was found that they fail in a cleavage-like mode with a habit plane parallel to lamellar boundaries between α_2 phase and γ phase. Otherwise, fracture occurs across lamellar boundaries [29]. It was suggested that the lamellar boundaries with higher interfacial energy have large free volume and thereby provide preferential site (or diffusion path) for hydrogen atoms, resulting in easier separation [29].

Mechanisms

The environmental (i.e. hydrogen) embrittlement is caused via some microscopic processes involving hydrogen diffusion (and reaction) kinetics and bond breaking. Process of diffusion kinetics furthermore may involve some processes consisting of (1) the reaction (or decomposition) of moisture, hydrogen gas or distilled water (or a solution), (2) penetration (or injection) into sample interior, (3) migration and (4) condensation into the corresponding region (or defect). Understanding the mechanism for these processes is important to control or to suppress the environmental embrittlement of ordered intermetallics. It has been demonstrated that each process and the associated mechanism involve specific feature which is not always similar to the hydrogen embrittlement observed in conventional materials such as iron and steel.

Kinetics

As shown in Table I, the major components in most ordered intermetallics are reactive elements, such as aluminum, silicon, titanium and vanadium. These elements (M_{active}) may strongly react with moisture in air or water in solution, as shown in below [24];

$$M_{active} + H_2O \rightarrow MO + 2H \qquad (1)$$

In other words, the element M_{active} generally has very high affinity with oxygen and thereby atomic hydrogen (H) can be released from H_2O into the material interior. Based on this reaction, it was demonstrated that the highest ductility obtained in samples deformed in oxygen gas [12,13,18,23,24] is due to the reaction of the element M_{active} with oxygen gas competing with the moisture reaction in eq. (1), therefore reducing the generation of atomic hydrogen from the moisture in air [24].

Table I also shows that other major components in most ordered intermetallics are the transition elements, such as nickel, iron and cobalt. These elements ($M_{transition}$) may play an important role as surface reactive element, i.e. catalysis, as shown in below [8,22,37]:

$$H_2 \underset{\uparrow}{\rightarrow} 2H \qquad (2)$$

$M_{transition}$ (catalysis)

It has been well known that the transition metals, particularly VIII elements, are very surface active elements and therefore expected to be very effective as catalyst. This reaction results in easier decomposition of molecular (i.e. gaseous) hydrogen (H_2) into atomic hydrogen, although eq. (2) may proceed via some metastable reactive products (processes).

Thus, it is predicted that a number of ordered intermetallics consisting of M_{active} in minority of content and $M_{transition}$ in majority of content are susceptible to two kinds of environmental embrittlements, i.e. the moisture-induced and hydrogen-induced embrittlements. However, in both cases, it is very likely that slip steps or free surface of microcrack freshly exposed during deformation work as catalyst and thereby promote both the reactions by eqs. (1) and (2) [8,22,37]. Some experimental facts that the environmental embrittlement is operative under loading, that is, in a stage of plastic deformation after yielding of materials support this idea.

Hydrogen generated by eqs. (1) or (2) must migrate (or permeate) to the region where hydrogen condenses and the breaking takes place. Dislocations, grain boundaries, interfaces and also crack surface linked to the free surface are able to provide rapid diffusion paths for hydrogen. Dislocations in ordered intermetallics mostly move in the form of a pair of superpartials bounding with antiphase boundary (APB) or stacking fault (SF). This characteristic of dislocations may provide very rapid diffusion path of hydrogen or collects sufficient amount of hydrogen during their sweeping, although the exact mechanisms are not understood. Grain boundaries which are inherently the weakest links in polycrystals with $L1_2$ structure also may provide rapid diffusion path. However, it is suggested that hydrogen migration along free surface, grain boundaries or dislocations in the very vicinity of propagating crack tips are very important because the phenomenon is so rapid, spontaneous and caused by a trace amount of moisture or hydrogen gas. *In-situ* observation using the transmission electron microscope (TEM) observation is helpful to further understand this subject.

Various kinds of defects such as grain boundaries, phase interfaces (e.g. lamellar interface, matrix-inclusion interface and so on) and micro-cracks produced by intersection of two slip systems are possible condensation sites for hydrogen because their interfaces generally have high interfacial energies and high free volumes. The condensation is also promoted by stress concentration introduced around these defects and combined with high stresses piled up in front of propagating crack tips. There exists the *hierarchy* for the hydrogen condensation and the associated hydrogen embrittlement. For example, in $L1_2$ structure, the environmental embrittlement is caused by intergranular fracture in the case of polycrystals, but by cleavage fracture in the case of single crystals. It appears that the embrittlement due to the former fracture mode occurs under a low level of applied stress, i.e. in low content of hydrogen.

Bond breaking

Basically three micromechanisms can be considered for the bond breaking due to hydrogen embrittlement of ordered intermetallics as well as traditional materials such as iron and steel:

(1) associated with hydride formed before deformation or under loading,
(2) due to locally enhanced plasticity, i.e. "ductile" mechanism,
(3) due to the decohesion, i.e. "brittle" mechanism.

When γ-TiAl or Ti_3Al is exposed in high concentration of hydrogen, the alloys were shown to be embrittled by the formation of hydrides [5,6,7]. Therefore, the mechanism (1) may be applicable to ordered intermetallics consisting of, or containing Ti (or Zr, Hf) element. The hydrides themselves can be cracked, or introduce lattice cracking under stress concentrations formed around them. However, hydride formation has not been detected when γ-TiAl is embrittled in air and even in hydrogen gas at ambient temperature [22]. This result reveals that the environmental embrittlement in these alloys is not due to hydrides, but to atomic hydrogen.

There is some evidence supporting that mechanism (3) is applicable to embrittlement in a number of ordered intermetallics. Many $L1_2$ polycrystals including Ni_3Al, Ni_3Si, Co_3Ti and their alloys showed very featureless patterns on their fractured grain boundary facets. On the other hand, $L1_2$ single crystals including $(Co,Ni)_3Ti$ [11], $Ni_3(Al,Ti)$ [16] and $Ni_3(Si,Ti)$ [30] fractured on low index crystallographic planes, accompanied with the river patterns, indicating the reduction of the lattice bonding. Also, in an *in-situ* TEM study in $(Co,Ni)_3Ti$, it was found that hydrogen accumulated at the tip of propagating crack introduced a large number of stacking faults which hindered the emission and motion of dislocations and thereby decreased the associated plastic work at the crack tip [11]. Similarly, *in-situ* TEM observation in Ni_3Al with and without boron showed that hydrogen causes the embrittlement by decreasing the cohesive strength of grain boundaries [38].

Table II Fracture stress of $L1_2$-type $Ni_3(Si,Ti)$ single crystals which had crystal orientations [001] and [$\bar{1}$23] and were deformed in water and in vacuum, respectively.

	Testing atmosphere			
	Vacuum		Water	
	[001]	[$\bar{1}$23]	[001]	[$\bar{1}$23]
Fracture stress (MPa)	1150	1022	802	885
Resolved normal fracture stress on (001) plane (MPa)	1150	853	802	739
Relative ratio of [$\bar{1}$23] to [001]	0.74		0.92	
Resolved shear fracture stress on (111) plane (MPa)	470	509	328	441
Relative ratio of [$\bar{1}$23] to [001]	1.08		1.34	

Recent study using $L1_2$-type $Ni_3(Si,Ti)$ single crystals provided good insight on the decohesion mechanism [30]. Fracture stress of their single crystals was investigated as a function of crystal orientation, i.e. on two orientations of [001] and [$\bar{1}$23]. Both orientations showed {001} cracking in distilled water, indicating hydrogen embrittlement, while both orientations showed {111} fracture plane in vacuum, indicating no embrittlement [30]. Table II represents the corresponding fracture stress, and calculated resolved normal fracture stress on {001} plane and resolved shear fracture stress on {111} plane, respectively. The fact that resolved normal fracture stress on {001} plane was primarily independent of crystal orientation when deformed in water indicates that fracturing was controlled by the cohesion strength on {001} plane. Similarly, the fact that resolved shear fracture stress on {111} plane was independent of crystal orientation when deformed in vacuum indicates that fracture was

controlled by shearing along {111} plane. Thus, it is concluded that the cohesion stress on {001} plane in $L1_2$ structure was, under the influence of hydrogen, reduced below the fracture strength on {111} plane.

It was shown in a previous section that the embrittled FeAl (B2 structure) fractures on {001} plane [36]. This result also supports a possible reduction of the cohesive strength by hydrogen injected from environment [24,25,39],which is also consistent with the calculation by Fu [40]; the charge transfer from Fe to H results in the weakening of d-bonding and is then mostly effective on the lattice bonding between {001} atomic planes. Measurement of fracture strength in FeAl polycrystals containing 35%Al also supports the cohesion mechanism [39]; the fracture strength in air was insensitive to, and then lower than the maximum strength obtained by prestraining in oxygen gas. This result, thus, demonstrates that hydrogen released from moisture reduces atomic bonding and causes crack initiation (or propagation) at a relatively lower strength.

Thus, the environmental embrittlement in most ordered intermetallics is caused by dynamic and atomistic mechanism by which the cohesive strength and the associated plastic flow around a crack tip are affected. The details of this embrittlement due to hydrogen can be understood in terms of the electronic concept for fracturing, as argued by Eberhart et al.[41].

Control and Suppression

Control and suppression of the environmental embrittlement is the technologically important subject to use ordered intermetallics as engineering structural materials. First, from the point of view of experimental (or testing) condition, discussion in the foregoing section proposes the following ways:

(1) to deform materials in vacuum, inert gas or dry air,
(2) to deform at high temperatures (mostly 300°C~400°C), otherwise at cryogenic temperature,
(3) to deform at high deformation rate.

Indeed, based on above ways, the present author has been able to fabricate a number of ductile ordered intermetallics which have been known to be very brittle in ambient air environment [42-44].

From the point of view of material condition, some ways to control the embrittlement are possible and indeed have been demonstrated:

(1) modification of surface composition by which reactions by eqs. (1) and (2) can be reduced,
(2) alloying method,
(3) microstructural modification.

Concerning method (1), surface film coating or protective oxidation scales on surface which have definite interface to matrix may be not successful because cracking of surface film introduced during deformation does not deserve the suppression of reactions by eqs. (1) and (2). Diffused alloying layer appears to be effective in suppressing the decomposition and penetration of hydrogen from environment.

Recent attempts to control or suppress the environmental embrittlement by alloying have been shown to be very promising. Table I summarizes some examples whose alloying is beneficial to suppress the losses of the tensile ductility in air or in hydrogen gas. First finding was shown in $L1_2$ Co_3Ti polycrystals [9]; among variety of alloying elements (V, Ta, Cr, Mo, W, Fe, Al and Ge) to Co_3Ti (23 at%Ti), the elements of Fe and Al at a few atomic % level showed a tendency to suppress the embrittlement in air, as shown in Figure 10 [45]. The beneficial effect of the element Fe may be attributed to a more homogeneous electronic distribution at grain boundaries where some of the Co-Ti bonds are replaced by Co-Fe bonds

[42-44]; the effect of Al is yet to be explored. In this alloy, the control of stoichiometric composition was found to be effective in reducing the environmental embrittlement [8]; Co_3Ti alloys containing low Ti content showed small amount of reduction in the tensile elongation in air, in comparison with Co_3Ti alloys containing high Ti content [8]. Most striking result was found on Ni_3Al polycrystals doped with boron [46] and on $Ni_3(Si,Ti)$ polycrystals doped with boron and carbon [21,22]. The tensile elongation of boron-doped Ni_3Al polycrystals were basically insensitive to the test environment and test strain rate [46] although this alloy has been known to be embrittled by compulsory injected hydrogen [3]. This result indicates that boron is the beneficial element in suppression of the environmental embrittlement of Ni_3Al. Figure 11 shows the environmental effect on the tensile elongation for $Ni_3(Si,Ti)$ polycrystals with and without boron and carbon [21,22]. It was found that the room temperature tensile elongation of $Ni_3(Si,Ti)$ polycrystals with boron (and also carbon) was insensitive to testing atmosphere and were then higher than those of undoped $Ni_3(Si,Ti)$ polycrystals. Whereas, the room temperature elongation of undoped $Ni_3(Si,Ti)$ polycrystals was sensitive to the testing atmosphere and thus lower in air than in vacuum. Beneficial effect of boron on the environmental effect was also reported in Ni_3Si binary alloys [23]. These results clearly indicate that boron (and also carbon) is very effective in alleviating the environmental embrittlement in some $L1_2$ alloys. Also, these results indicate that the environmental embrittlement may be a major cause of low ductility and brittleness in these alloys. In other words, it may be demonstrated that the boron effect in these alloys is not an ***intrinsic*** effect that improves the grain boundary cohesion, but an ***extrinsic*** effect that kills the harmful effect of hydrogen. As a responsible mechanism to this alloying effect, it is very likely that these elements segregate strongly to grain boundaries, compete with hydrogen for site occupation, and thereby reduce grain boundary diffusion of hydrogen or suppress the harmful effect of hydrogen on grain boundary decohesion [21,22,42-44]. In $L1_2$-type $(Co,Fe)_3V$ alloys, control of grain size, i.e. refinement of grains was shown to be effective in improving the room temperature tensile elongation in air [13].

It has been observed that boron doping of Ni_3Al single crystals is slightly beneficial for the room temperature tensile elongation in air although its effect is not so remarkable [47], in comparison to that in Ni_3Al polycrystals. Also, it was shown that {111} fracturing, which is intrinsic fracture mode under no hydrogen, is more dominating in boron-doped $Ni_3(Al,Ti)$ single crystals than in undoped $Ni_3(Al,Ti)$ single crystals [48]. It is anticipated from these results that boron in the grain interior, i.e. within the lattice is also beneficial to suppress the harmful action of hydrogen, by reducing the solubility of hydrogen in the lattice, scavenging the hydrogen atoms, or affecting core structure of dislocations.

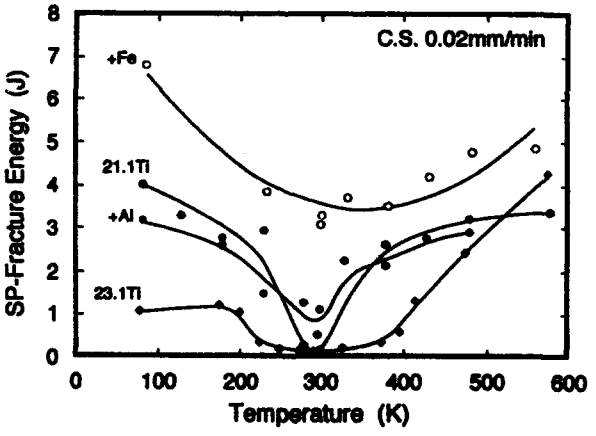

Figure 10 Variation of the fracture toughness (evaluated by fracture energy) with temperature for Co_3Ti (23 at%Ti) polycrystals alloyed with Fe and Al which were deformed in air.

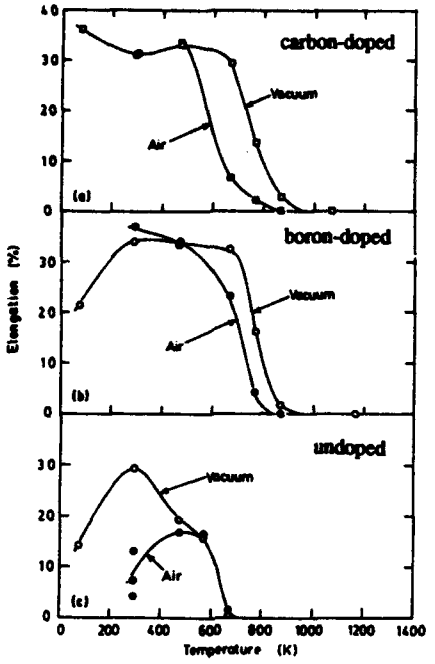

Figure 11 Variations of the elongation with temperature for $L1_2$-type $Ni_3(Si,Ti)$ polycrystals with and without boron and carbon which were deformed in vacuum and in air, respectively.

In Fe_3Al and FeAl alloys, recent efforts show that the ductility of these alloys in air can be substantially improved by increasing Al content and by adding Cr at a level of 2 to 6% [24,25]. The Cr additions doubled the tensile ductility and their effect was attributed to the oxide scales formed on material surfaces during fabrication in air [49]. Also in Fe_3Al, refinement of grains has been proven to be effective in enhancing the ductility in moist air [39].

Recent observation using γ-TiAl PST showed that some transition metals, particularly Cr elements, were very effective in suppressing the environmental embrittlement in air [50]. In vacuum TiAl alloyed with 0.6at%Cr showed an identical elongation value to that of binary TiAl, while in air TiAl alloyed with Cr showed higher elongation value than that of binary TiAl, accompanied with the reduced propensity of fracturing along lamellar boundaries between α_2 phase and γ phase.

Summary and Concluding Remarks

During the last and this decades, a large number of ordered intermetallics were shown to be intrinsically ductile or can be ductilized by some metallurgical techniques, such as alloying, microstructural modification and also adequate selection of deformation conditions. Many recent studies associated with such ductilization showed that the environmental embrittlement takes place when ordered intermetallics are simply tensile tested in conventional testing (and also fabrication) conditions, e.g. in air at slow deformation rates at ambient temperatures. It has been observed that this kind of embrittlement occurs in a variety of crystal structures including $L1_2$, B2, DO_3 and $L1_0$, and also a variety of alloy systems. The process is dynamic

involving the kinetics of hydrogen and bond breaking in the front of a propagating crack. Also, it was demonstrated that principal cause of the environmental embrittlement in ordered intermetallics is due to the extremely high reaction of moisture (i.e. H_2O) in air with reactive elements (such as Al, Si, Ti, V) and/or of H_2 with surface reactive elements (such as Ni, Co and Fe) in environment.

is article, the environmental embrittlement was shown to be principal cause of the low ity and the associated brittle fracture in many ordered intermetallics. In Ni_3Al, Ni_3Si, Fe_3Al and TiAl base alloys, it has been demonstrated that the alloying effect, by which le ductility in air at room temperature was improved, can be attributed to hindering of the ironmental embrittlement. Recent observations reporting ductility improvement in Ni_3Al without boron doping, all of which were carefully prepared by alloying or unidirectional solidification and then tensile-deformed in well controlled experimental conditions [17,18,51,52], are coherent to notions that environmental embrittlement is the major cause of the low ductility and extrinsic effect. Finally it must be noted that data for solubility limit, diffusion and site occupation of hydrogen is required to further understand the environmental embrittlement in ordered intermetallics.

Acknowledgment

This work was supported in part by the Grant-In-Aid of Scientific Research from the Ministry of Education, Science and Culture.

References

1. A. K. Kuruvilla, S. Ashok and N. S. Stoloff, Proceedings of the Third International Congress on Hydrogen in Metals, Pergamon, Paris, p. 629, (1982).
2. G. M. Camus, N. S. Stoloff and D. J. Duquette, Acta Metall., **37** (1989), 7.
3. A. K. Kuruvilla and N. S. Stoloff, Scripta Metall., **19** (1985), 83.
4. T. Takasugi and O. Izumi, Scripta Metall., **19** (1985), 903.
5. E. Manor and D. Eliezer, Scripta Metall., **23** (1989), 1313.
6. E. Manor and D. Eliezer, Scripta Metall. Mater., **24** (1990), 129.
7. W. -Y. Chu and A. W. Thompson, Scripta Metall. Mater., **25** (1991), 1369.
8. T. Takasugi and O. Izumi, Acta Metall., **37** (1986), 607.
9. Y. Liu, T. Takasugi, O. Izumi and H. Suenaga, J. Mater. Science, **24** (1989), 4458.
10. T. Takasugi, M. Takazawa and O. Izumi, J. Mater. Science, **25** (1990), 4239.
11. Y. Liu, T. Takasugi, O. Izumi and T. Yamada, Acta Metall., **37** (1989), 507.
12. C. Nishimura and C. T. Liu, Scripta Metall. Mater., **25** (1991), 791.
13. C. Nishimura and C. T. Liu, Acta Metall. Mater., **40** (1992), 723.
14. T. Takasugi, N. Masahashi and O. Izumi, Scripta Metall., **20** (1986), 1317.
15 N, Masahashi, T. Takasugi and O. Izumi, Metall. Trans. A, **19A** (1988), 353.
16. T. Takasugi, Acta Metall. Mater., **39** (1991), 2157.
17. C. T. Liu, Scripta Metall. Mater., **27** (1992), 25.
18. E. P. George, C. T. Liu and D. P. Pope, Scripta Metall. Mater., **27** (1992), 365.
19. C. T. Liu and B. F. Oliver, J. Mater. Research, **4** (1989), 294.
20. T. Takasugi, M. Nagashima and O. Izumi, Acta Metall. Mater., **38** (1990), 747.
21. T. Takasugi, H. Suenaga and O. Izumi, J. Mater. Science, **26** (1991), 1179.
22. T. Takasugi and M. Yoshida, J. Mater. Science, **26** (1991), 3032.
23. C. T. Liu and W. C. Oliver, Scripta Metall. Mater., **25** (1991), 1933.
24. C. T. Liu, H. E. Lee and C. G. McKamey, Scripta Metall., **23** (1989), 875.
25. C. T. Liu, C. G. McKamey and H. E. Lee, Scripta Metall., **24** (1990), 385.
26. I. R. Kramer, B. Wu and C. R. Feng, Mater. Science and Engin., **82** (1986), 141.
27. T. Takasugi, M. Yoshida and S. Hanada, J. Mater. Research, **7** (1992), 2739.
28. M. Nakamura, K. Hashimoto and T. Tsujimoto, J. Mater. Research, **8** (1993), 68.
29. M. H. Oh, H. Inui, M. Misaki and M. Yamaguchi, to appear in Acta Metall. Mater.
30. T. Nakayama, Master thesis, Tohoku University, (1993).
31. P. Nagpal and I. Baker, Scripta Metall. Mater., **25** (1991), 2577.
32. A. Shan and D. Lin, Scripta Metall. Mater., **27** (1992), 95.

33. T. Takasugi, to be published.
34. A. Kimura, H. Izumi, Y. Igarashi, T. Misawa and T. Takasugi, 6th JIM International Symposium on Intermetallic Compounds - Structure and Mechanical Properties -, ed. by O. Izumi, JIM, p. 737, (1991).
35. C. T. Liu, 6th JIM International Symposium on Intermetallic Compounds - Structure and Mechanical Properties -, ed. by O. Izumi, JIM, p. 703, (1991).
36. K. -M. Chang, R. Darolia and H. A. Lipsitt, Acta Metall. Mater., 40 (1992), 2727.
37. X. J. Wan, J. H. Zhu and K. L. Jing, Scripta Metall. Mater., 26 (1992), 473.
38. G. M. Bond, I. M. Robertson and H. K. Birnbaum, Acta Metall., 37 (1989), 1407.
39. C. T. Liu, Ordered Intermetallics - Physical Metallurgy and Mechanical Behavior, ed. by C. T. Liu et al., Kulwer Academic Publishers, p. 321, (1992).
40. C. L. Fu and G. S. Painter, J. Mater. Research, 6 (1991), 719.
41. M. E. Eberhart, R. M. Latanison and K. H. Johnson, Acta Metall., 33 (1985), 1769.
42. T. Takasugi, MRS Symp. Proc. Publication, ed. by Johnson et al., MRS, vol. 213, p. 403, (1991).
43. O. Izumi and T. Takasugi, J. Mater. Research, 3 (1988), 426.
44. T. Takasugi and O. Izumi, Materials Forum, 12 (1988), 8.
45. H. Izumi, A. Kimura, T. Misawa and T. Takasugi, to be published.
46. N. Masahashi, T. Takasugi and O. Izumi, Acta Metall., 36 (1988), 1823.
47. F. E. Heredia and D. P. Pope, Acta Metall. Mater., 39 (1991), 2017.
48. M. S. Kim, S. Hanada, S. Watanabe and O. Izumi, Trans. JIM, 29 (1988), 790.
49. C. G. McKamey and C. T. Liu, Scripta Metall., 24 (1990), 219.
50. H. Inui, M. Kobayashi, M. H. Oh, H. Inui, M. Misaki and M. Yamaguchi, Collected Abstract of Fall Meeting of Japan Institute of Metals, p. 278, (1992).
51. C. T. Liu and E. P. George, Scripta Metall., 24 (1990), 1285.
52. T. Hirano, Scripta Metall. Mater., 25 (1991), 1747.

HIGH TEMPERATURE CORROSION OF INTERMETALLICS, CERAMICS, AND CARBON-CARBON COMPOSITES

G. H. Meier and F. S. Pettit

Department of Materials Science + Engineering
University of Pittsburgh
Pittsburgh, PA 15261

Abstract

There is continuing interest in the development of materials which can increase the specific strength of components, compared to conventional superalloys, for a variety of high temperature applications. A number of ceramics and intermetallic compounds, as well as carbon-carbon composites have the high melting points and low densities to potentially meet these requirements. However, these materials must further demonstrate adequate toughness and environmental resistance if they are going to achieve widespread use. This paper deals with environmental resistance. The corrosion mechanisms of these three classes of materials are described and compared. Current and potential protection schemes for each class of material are described and critical problems are identified.

Acknowledgement: The work described in this paper was supported in large part under ONR Contract Number N0014-89-J-1087, DARPA Contract Number 6155, and the University of Pittsburgh Materials Research Center.

Critical Issues in the Development of High Temperature Structural Materials
Edited by N.S. Stoloff, D.J. Duquette and A.F. Giamei
The Minerals, Metals & Materials Society, 1993

Introduction

The oxidation behavior of the "advanced materials" (ceramics, intermetallics, and carbon-carbon composites) spans the spectrum from inert materials to those which undergo catastrophic oxidation (See Figure 1). As a result the applications for which they are suitable and the methods required to protect them differ markedly. In discussing the oxidation behavior of advanced materials it is necessary to mention that the oxidation resistance of state-of-the-art materials, such as nickel-base superalloys, has been improved. For example, in Figure 2 the cyclic oxidation resistance of some advanced nickel-base superalloys are compared before and after treatments to remove sulfur. These treatments result in very substantial improvements in the cyclic oxidation resistance of these alloys as the result of the formation of more adherent alumina scales. Alloys in the pretreated condition have oxidation resistance better than untreated alloys with aluminide coatings.

The following describes the oxidation and corrosion behavior of three classes of "advanced" materials: ceramics, intermetallics, and carbon-carbon composites.

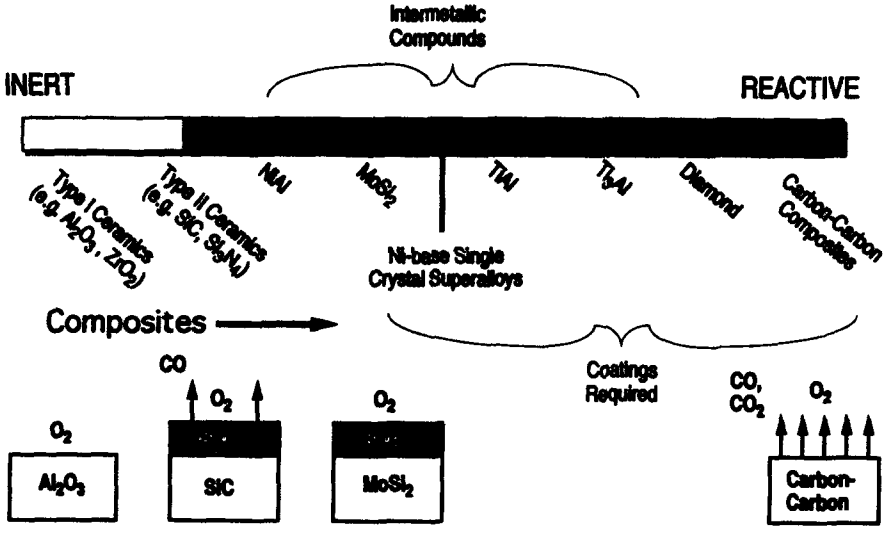

Figure 1. Schematic showing the relative corrosion resistance of various materials relative to that for nickel base superalloys.

Oxidation and Corrosion of Ceramics

In most gaseous environments ceramics are more resistant than metallic systems. Nevertheless, depending upon the ceramic and the environment, oxidation and hot corrosion can occur. The degradation of ceramics in corrosive environments is often sensitive to the impurities in the ceramic. Grain boundaries are frequently preferred sites for attack. Such preferential attack can be expected to deleteriously affect the mechanical properties of structural ceramics. In discussing the corrosion of ceramics it is convenient to first examine the attack of ceramics in corrosive gases and then consider hot corrosion where molten deposits such as Na_2SO_4 are present to influence the degradation processes.

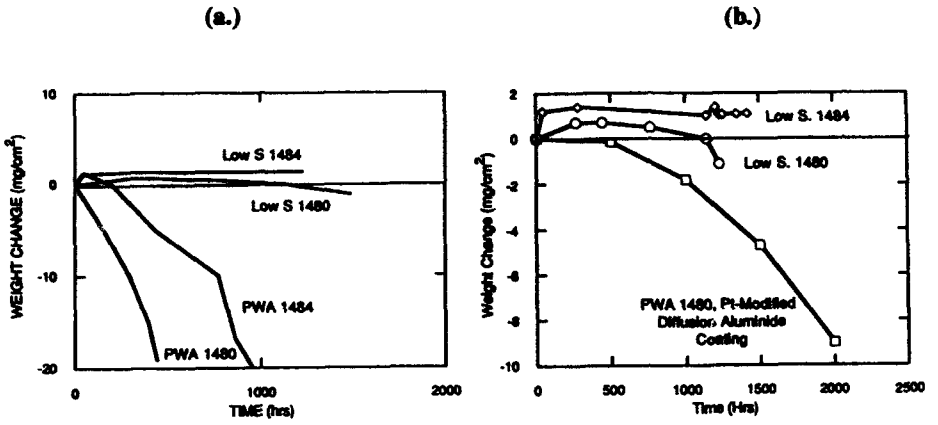

Figure 2. Cyclic oxidation resistance of single crystal nickel base superalloys in air at 1100°C. (a.) Effect of sulfur removal. (b.) Comparison of low-sulfur alloys to untreated alloy with a conventional coating.

A material is considered to be immune to a particular environment when it is in equilibrium with the environment. Total or complete immunity is rare in practice but in some cases the amount of reaction required for equilibrium to be achieved is very small, and consequently the changes in properties are very small. There are a number of ceramics which can be considered immune to those gaseous environments encountered in practice which contain oxygen. Typical examples of such Type I ceramics are Al_2O_3, SiO_2 and ZrO_2. Type II ceramics are those which react with the gaseous environments and require the formation of a protective reaction product barrier to inhibit attack. SiC and Si_3N_4 are typical of this second category where SiO_2 scales provide protection against subsequent attack. The factors which control the oxidation resistance of Type II ceramics are the same as those affecting alloys that develop oxidation resistance via selective oxidation (1). An adherent barrier of oxide reaction product must cover the surface of the ceramic and diffusion of reactants through this barrier must occur as slowly as possible. In cases where the protective barrier cracks or spalls, the barrier must reform over the exposed area of the ceramic. Layers of silica on ceramics such as Si_3N_4 can be extremely protective. For example, the parabolic rate constant for the growth of silica on Si_3N_4 is 1×10^{-12} g^2/cm^4sec at 1400°C in air compared to a rate constant of 2×10^{-12} g^2/cm^4sec for alumina growth at 1200°C.

In gases that contain reactants in addition to oxygen other reactions are possible. For example, in a gas mixture containing oxygen and SO_2 sulfates can be formed. As can be seen in the stability diagram shown in Figure 3, the SO_3 pressure must be high to form $Al_2(SO_4)$ but much smaller pressures are required to form $MgSO_4$ or $CaSO_4$. When Al_2O_3 containing MgO or CaO as impurities is exposed to such gases, $MgSO_4$ or $CaSO_4$ can be formed. Impurities also may play an important role in the oxidation of Type II ceramics. It has been shown that MgO in SiO_2 (2) causes transport through SiO_2 to be increased, and hence its protectiveness can be significantly reduced.

Ceramics which are resistant to a gas environment can be substantially degraded when exposed to the same gas and a molten deposit such as Na_2SO_4 or $NaVO_3$ (3). While

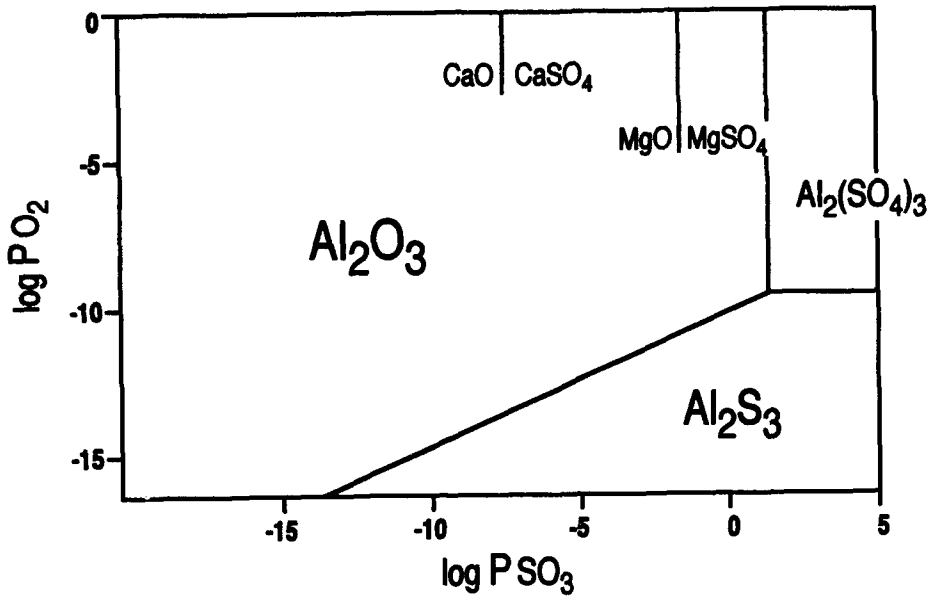

Figure 3. **Stability diagram for Al_2O_3 in SO_2-SO_3 atmospheres at 1000°C. The boundaries for CaO and MgO are also shown.**

specific processes and reactions that cause the corrosion depend intimately upon the melt composition, most melts exhibit characterisitcs that are essentially equivalent. In particular, there are reactions where components from the gas phase are incorporated into the melt, the reactants and products diffuse in the melt, and there are reactions by which the ceramics are degraded. The reaction by which the ceramics are degraded may involve the bulk ceramic (e.g. Al_2O_3), or a normally protective barrier on a ceramic (e.g. SiO_2 on SiC). These reactions can be broadly classified as either basic or acidic in character as illustrated in Figure 4 (4). Furthermore, certain ions in the melt can be much more effective in causing attack than others. For example, Na_2SO_4 melts containing $NaVO_3$ produce more severe degradation of oxides such as Al_2O_3 and stabilized ZrO_2 than pure Na_2SO_4, Figure 5. The increased attack by such melts has been found to be caused by the acidic component, V_2O_5.

The rates at which ceramics are degraded depend upon the ceramic, the gas composition, and especially the composition of the deposit. The hot corrosion rates are normally smaller than those for metallic alloys but not negligible. The nature of the degradation usually consists of a minimum of attack at some intermediate composition with more accelerated rates as the melt becomes either more basic or more acidic, which is consistent with solubility considerations. Silica is one ceramic that appears to be resistant to acidic melts but is very susceptible to attack induced by basic melts due to the formation of silicates in basic deposits. Some typical results obtained for the hot corrosion and oxidation of SiC and Si_3N_4 are presented in Figure 6.

Composites with exceptional levels of strength and toughness, such as silicon carbide reinforced lithium aluminosilicate, are beginning to be considered for elevated temperature applications. While such materials are usually considered to be oxidation resistant, oxidation reactions can occur and hot corrosion degradation will definitely be

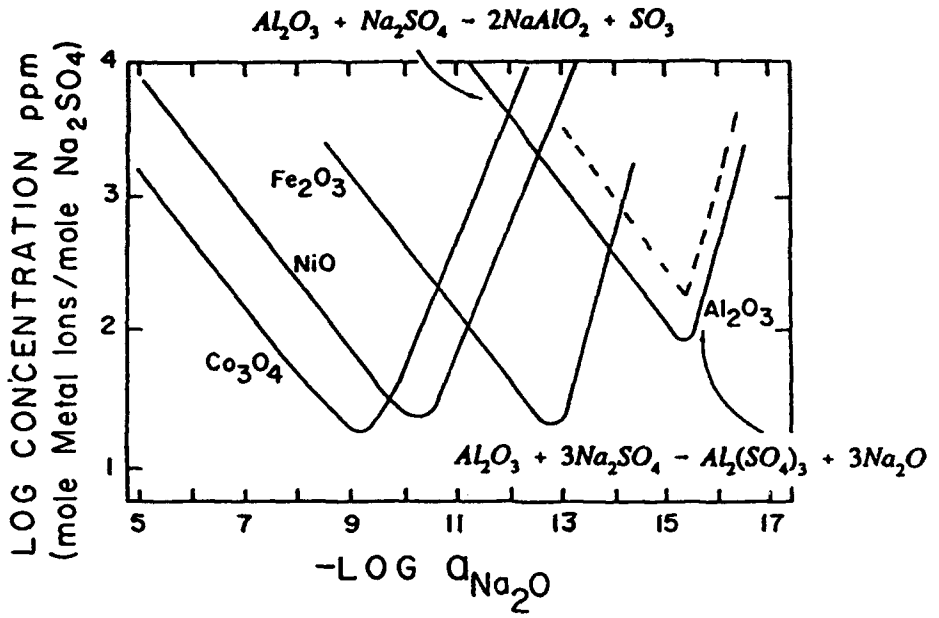

Figure 4. **Solubilities of some oxides in Na_2SO_4 at 1200K as determined by Rapp and coworkers. The dashed lines give calculated solubilities using Temkins model for ionic melts.**

a factor in determining performance. For example, as shown in Figure 7, oxidation does occur at 800°C and hot corrosion attack causes significant degradation.

Oxidation of Intermetallic Compounds

The subject of oxidation of intermetallic compounds has been reviewed in 1988 by one of the authors (5). The reader is directed to the excellent review by Aitken (6) for details of work prior to 1967.

The development of oxidation resistance in intermetallic compounds is similar to that for conventional high temperature alloys and for Type II ceramics. It is based on the selective oxidation of an element from the intermetallic to produce a protective surface oxide. The formation of this surface layer requires that the oxide be more stable than the lowest oxide of the other elements in the alloy. The oxides Al_2O_3 and SiO_2 are of principal interest because they exhibit low diffusivities for both cations and anions as well as being highly stable. Thus the addition of Al to Ni, as in the case of aluminide coatings on nickel-base alloys, or Si to Mo, as in the case of $MoSi_2$ heating elements, clearly satisfy the stability requirements. However, in the case of Nb-, Ti-, or Zr-base alloys the oxides of the base metal are nearly as stable as those of Al or Si. This can result in conditions for which selective oxidation is not possible. It should be emphasized that the determination of which oxide is more stable must take into account the prevailing metal activities. Detailed analyses of this situation are presented by Rahmel and Spencer (7) for Ti-Al and Ti-Si alloys and Luthra (8) for Ti-Al alloys. These analyses predict that alumina scales

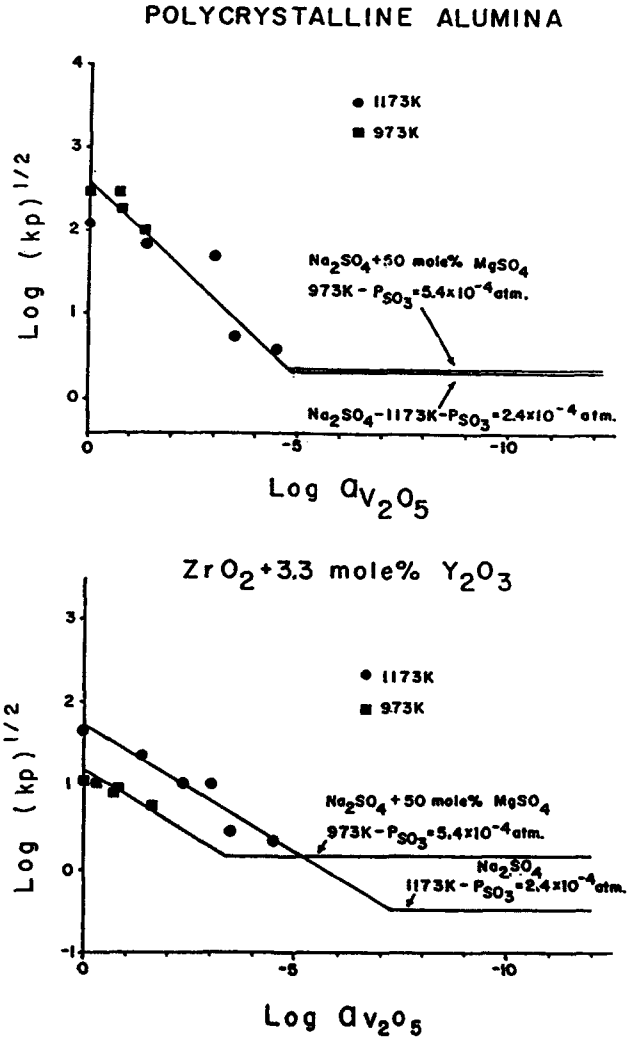

Figure 5. **Dependence of the parabolic rate constants for hot corrosion of alumina and yttria-stabilized zirconia on activity of V_2O_5 in the deposits. The horizontal lines indicate the rate constants for a sulfate deposit.**

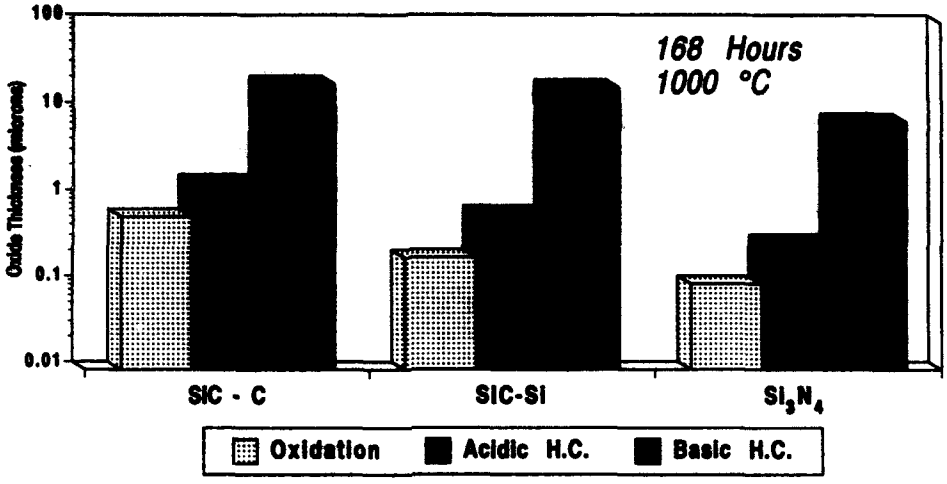

Figure 6. **Thickness of layers formed for the oxidation, acidic and basic hot corrosion of C-side and Si-side single crystal SiC and CVD Si_3N_4. Note that oxide thickness increases as O<A<B.**

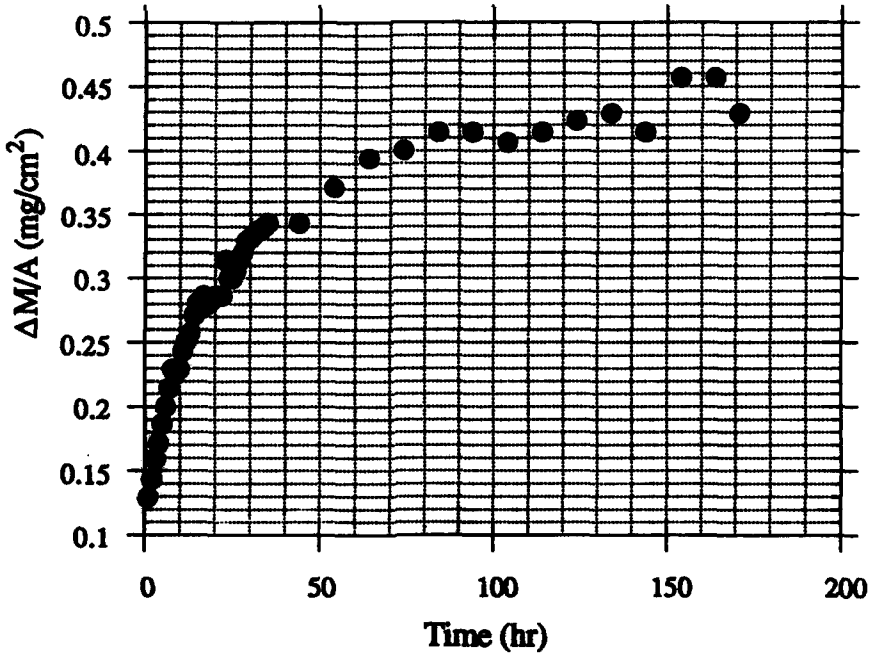

Figure 7. **Oxidation rate of a lithium aluminosilicate-SiC composite in air at 800°C.**

are not stable in contact with Ti-Al alloys containing less than 50 at% Al. This prediction has been verified experimentally by Misra (9)

A second requirement is that the concentration of the element added for oxidation resistance is sufficient for the formation of its oxide as a continuous external layer rather than as internal precipitates. The two possibilities are illustrated in Figure 8. Alloys with low solute concentrations allow inward diffusion of oxygen which results in internal oxidation, Fig. 8a., while for high solute contents the outward diffusion of solute results in the formation of a continuous external layer of oxide, Fig. 8b. The critical solute concentration for the transition from internal to external oxidation has been expressed by Wagner(10) as

$$N_B^* = \left(\frac{\pi g^* N_O D_O V_M}{2 D_B V_{OX}} \right)^{1/2} \quad (1)$$

Here $N_O D_O$ is the oxygen permeability in A, D_B is the solute diffusivity, g^* is a factor determined by the volume fraction of oxide required for the transition(often near 0.3), and V_M and V_{OX} are the molar volumes of the alloy and oxide, respectively. The solute content required for external scale formation is seen to increase with the solubility and diffusivity of oxygen and decrease with an increase in the solute diffusivity in the alloy. However, for most systems of interest, the oxide of the base metal can also form in the ambient atmosphere and grows until the more stable oxide of the solute B becomes continuous and stops the growth of the "transient oxide", Figure 8b. The effect of transient oxidation on the transition from internal to external oxidation of B has been analyzed by Gesmundo and Viani(11) who found that an excess of solute above that predicted by equation 1. is required in the presence of transient oxides. The amount of excess solute required is predicted to increase as the growth rate of the transient oxide increases.

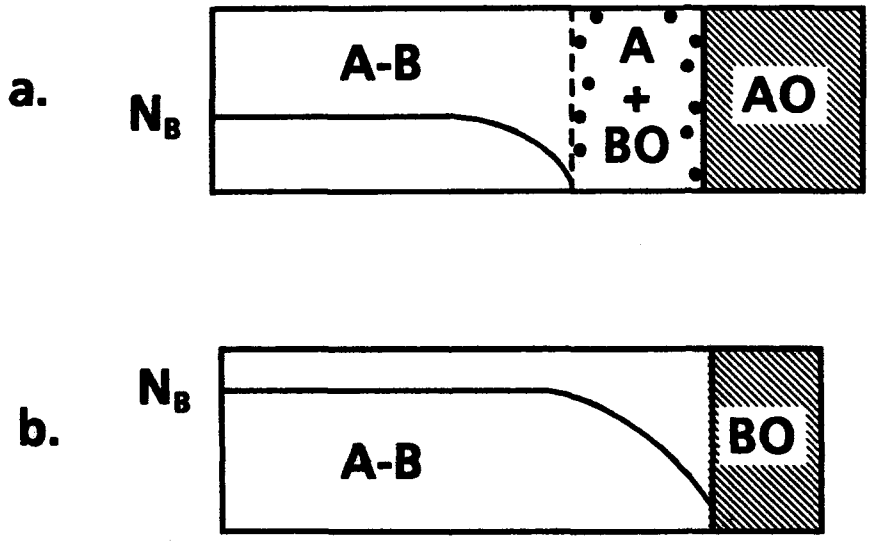

Figure 8. Schematic diagram of the oxidation of an alloy A-B with both AO and BO stable (BO more stable). a.) Dilute alloy showing internal oxidation of B under a layer of AO. b.) Concentrated alloy forming an external layer of BO.

Long term stability of the protective scale requires that the flux of solute to the alloy/scale interface remains large enough to prevent oxides of A from becoming stable. Pettit(12), for example, found there were two critical concentrations for the formation of alumina scales on Ni-Al alloys: one required for development of the alumina scale and a larger one required to maintain its stability. Wagner(13) has derived an approximate equation for the concentration of solute required to maintain the growth of an external scale as:

$$N_B = \frac{V_M}{16 z_B}\left(\frac{\pi k_p}{D_B}\right)^{1/2} \quad (2)$$

Here k_p is the parabolic rate constant for the growth of the protective scale and z_B is the valence of B. Thus, the long term stability of a protective scale depends on the thermodynamic and diffusional properties of the alloy immediately beneath the scale. This can be particularly significant for the oxidation of intermetallic compounds with small homogeneity ranges. Here the removal of the scale-forming element to form an external layer immediately results in the formation of a layer of the next lower compound adjacent to the oxide. This situation, which is in contrast to the smooth concentration gradient in the alloy depicted in Figure 8b, means that the properties of the lower compound determine the ability of the alloy to maintain the growth of the protective oxide. Apparently some compounds, such as Mo_5Si_3, provide a sufficient flux of Si to the oxide/alloy interface to maintain the growth of a silica layer on $MoSi_2$, as is illustrated schematically in Figure 9. This is not the case, however for many systems as is illustrated for the oxidation of $NbAl_3$ in Figure 9. The initial exposure of this compound results in the formation of a continuous alumina layer on the surface but the depletion of Al causes the next lower aluminide, Nb_2Al, to form beneath the oxide. This compound has been shown to be incapable of forming continuous alumina (14) and, indeed, the alumina scale becomes discontinuous as the oxide forms within and beneath the Nb_2Al layer. Consequently oxides of niobium are also formed and the oxide scale consists of a mixture. Repetition of these processes results in a layered scale. This process has been studied by Steinhorst and Grabke (15) using acoustic emission which indicated cracking associated with each successive layer. It is not yet clear, however, if the cracking is the cause of the breakdown of the alumina layer or the result of the formation of Nb-Al mixed oxides which have become more stable in contact with the alloy as Al is depleted.

The effect of temperature on the selective oxidation process is determined by the temperature dependence of all of the terms in equations 1 and 2 and that of the growth rate of the transient oxides. Therefore, some systems form protective external scales more readily at higher temperatures while others form them more efficiently at lower temperatures. For example, Ni-Al alloys form protective alumina scales more readily at high temperatures (12) whereas γ-TiAl forms alumina scales at low temperatures in oxygen but forms mixed Ti-Al scales above about 1000°C (16). The refractory-metal di-silicides generally form protective silica scales more readily at high temperatures. For example, the oxidation rates of $MoSi_2$ at temperatures between 600 and 1200°C are extremely slow as the result of the formation of a protective silica film. However, the oxidation rates at 500°C show rapid, breakaway kinetics. This breakaway can result in disintegration of the specimen. This disintegration was first studied for $MoSi_2$ by Fitzer(17) who termed it "pesting".

The composition of the oxidizing atmosphere can also effect the oxidation behavior of intermetallic compounds. For example, silicides can undergo accelerated oxidation at low oxygen partial pressures as the result of SiO gas formation. Additional effects of the

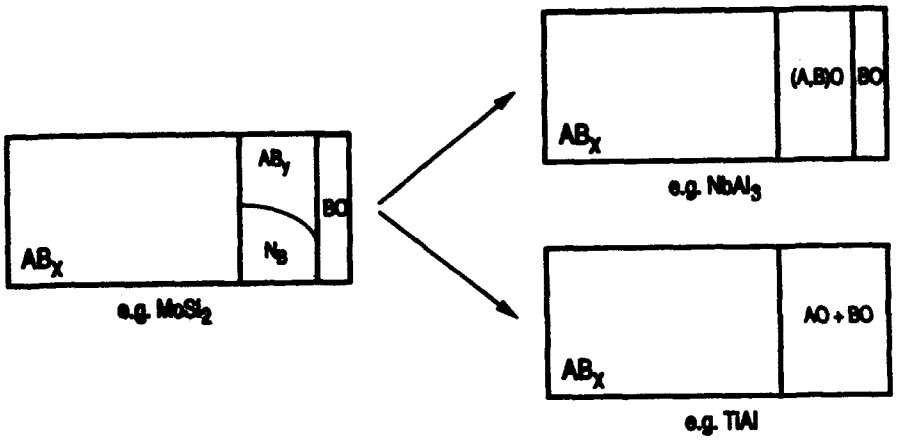

Figure 9. Schematic diagram illustrating the special features involved in the oxidation of intermetallic compounds with narrow ranges of stoichiometry.

atmosphere can occur if it contains a second reactive component, even the nitrogen in air. This effect is most striking for the oxidation of Ti-aluminides. Protective alumina scales are formed on TiAl, exposed in oxygen, up to temperatures near 1000°C. However, the same exposures conducted in air result in the formation of TiO_2-rich scales which grow at rates orders of magnitude faster than the alumina scales (16). This effect was originally shown by Choudhury et al (18) to be associated with the presence of nitrogen as opposed to any other variable such as oxygen pressure. The detailed mechanisms of the effect of nitrogen and the extent that it applies to other intermetallic systems is in need of further study. However, it appears that the effect involves the nucleation and initial growth of the scale on TiAl since preoxidation in pure oxygen develops an alumina scale which remains protective when nitrogen is added to the gas. Kobayashi et al (19) have reported that such preformed scales remain protective even under cyclic oxidation conditions.

There is an increasing amount of data which indicates that many intermetallic compounds are susceptible to embrittlement in oxidizing atmospheres. The ductility of FeAl, Fe_3Al, and Co_3Ti have been found to be much lower when tested in air at room temperature as compared with testing in vacuum (20). This effect has been ascribed to the introduction of atomic hydrogen into the compound from water vapor in the test atmosphere. Similarly, Ni_3Al (20,21) and Ti_3Al (22) have been shown to be embrittled by oxygen at elevated temperatures. Perkins (23) studied the deformation of Nb-modified α_2 deformed in three-point bending after exposure in various atmospheres at elevated temperatures. The alloy was completely embrittled by annealing 2 hours at 900°C in vacuum, however, the ductility could be recovered when approximately 100μm of material was polished from the specimen surfaces. The alloy showed greatly reduced ductility after annealing in various oxidizing atmospheres at temperatures between 600 and 900°C. This indicates that oxygen diffusion into the alloy results in severe embrittlement. Furthermore, those atmospheres which contained water vapor (in the range of 30 to 40 vol%) showed the lowest ductilities. This suggests that the release of hydrogen when water vapor reacts with the alloy results in embrittlement similar to that proposed for other compounds deformed at room temperature (20).

Intermetallic composites, such as $MoSi_2$ reinforced with SiC. Al_2O_3, or TiB_2 possess many of the oxidation characteristics discussed previously for intermetallics. Complications arise as a result of the oxidation of the reinforcing phase which can compromise the the protectiveness of the oxide scale forming on the intermetallic matrix phase.

Oxidation of Carbon-Carbon Composites

Carbon-carbon composites are the antitheses of most ceramics in that they have no intrinsic oxidation resistance. This results from the formation of gaseous oxidation products (CO and CO_2) which do not provide a barrier to further oxidation. Previous attempts to reduce the oxidation rates of carbon-carbon composites have involved two approaches: inhibitors, such as B and P, and protective coatings based primarily on SiC.

The oxidation kinetics for both carbon-carbon composites and inhibited composites in dry oxygen consist of linear weight losses as a function of time. Typical results are presented in Figure 10 for oxidation in dry flowing oxygen. (The mass changes represent the amount of carbon consumed.) Such reactions have been observed for temperatures as low as 300°C. At temperatures up to about 600°C, Figure 11, the oxidation rate is controlled by a chemical reaction involving the adsorption of oxygen and the desorption of CO. At temperatures above 800°C the oxidation rate is controlled by diffusion in the gas, but the transition from chemical reaction control to diffusion control is affected by the specimen size and the gas flow rate.

The use of inhibitors attempts to protect the carbon-carbon composite by forming a liquid oxide layer (e.g. B_2O_3) which separates the composite from the gas. Such liquid oxides were observed not to be effective in protecting the carbon matrix. They were, however, effective in protecting the carbon reinforcing phases. The oxidation kinetics for the inhibited specimens, therefore, contained a final stage after the linear stage where the matrix had been completely oxidized and the fibers were coated with the liquid oxide. The presence of water vapor accelerated the oxidation of carbon-carbon evidently by increasing the rate of the chemical reaction. Water vapor also removed B_2O_3 from the surfaces of the carbon fibers due to the formation of volatile species such as orthoboric acid (H_3BO_3) and metaboric acid (HBO_2).

Carbon-carbon composites can be protected by using coatings of SiC or Si_3N_4 where these coatings are formed by different chemical vaporization techniques (24). Due to differences between the coefficients of expansion cracks are developed in these coatings. Typical results obtained in cyclic oxidation tests are presented in Figure 12. In this figure results with coatings containing glass glazes to fill the cracks have also been included. Most of these glazes improve the cyclic oxidation resistance of these coatings but eventually failure of the coating does occur. In Si_3N_4 coatings on carbon-carbon the formation of SiO_2 seals the cracks in the coating at temperatures above about 1300°C (25), but extended cyclic oxidation tests indicate cracking may still be a problem.

Jorgenson (26) and others have examined an electrolytic concept proposed a number of years ago by C. Wagner to prevent high temperature oxidation. This approach consists of passing a flux of electrons through an oxide scale to cause the electro-chemical potential gradient of the mobile ionic species to be zero. It has been attempted to apply this concept to prevent or inhibit the oxidation of carbon-carbon composites coated with stabilized ZrO_2 coatings. Such coatings formed on carbon-carbon via plasma spray were not sufficiently free of porosity to test this approach. Moreover, the coatings may also be susceptible to cracking from thermally induced stresses. The concept has been tested,

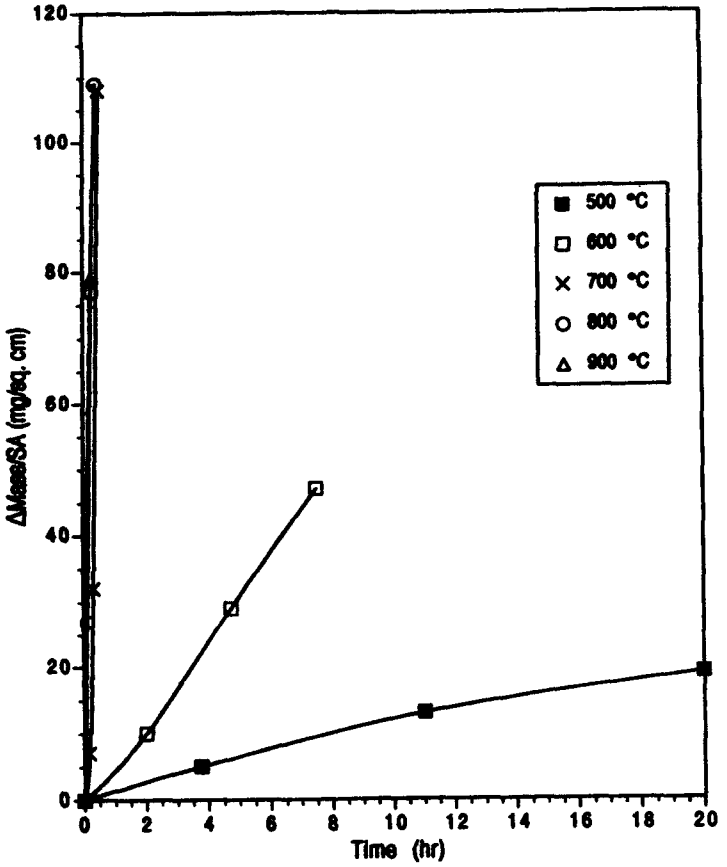

Figure 10. **Isothermal oxidation kinetics for uninhibited carbon-carbon over the temperature range 500 to 900°C in a dry oxygen flow of 100 cm^3/min.**

however, by using a Y_2O_3 stabilized ZrO_2 tube containing carbon as shown in Figure 13. The results obtained show that the oxygen pressure at the ZrO_2 carbon interface can be controlled to limit CO pressures to less than one atmosphere.

Diamond coatings formed using chemical vapor deposition are now being considered for elevated temperature applications. As shown in Figure 14, diamond begins to degrade in oxidizing environments at temperatures above about 500°C. This attack has been found to occur at preferential sites and it may be possible to obtain more oxidation resistant films in this temperature range by controlling the orientation of the grains in these coatings.

Summary

The corrosion behavior of ceramics, intermetallics, and carbon-carbon composites have been described. It is clear that the intermetallics and, particularly, carbon-carbon composites are susceptible to severe oxidation. Ceramics are generally more corrosion resistant but are also susceptible in certain environments.

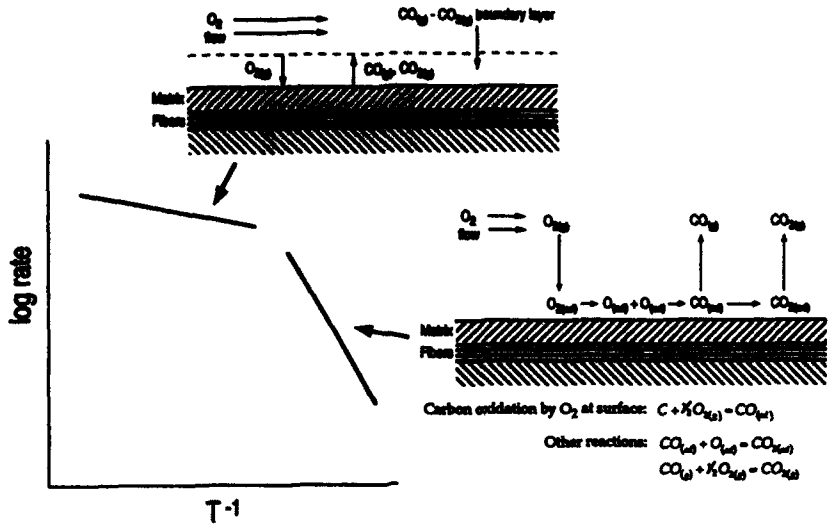

Figure 11. **Schematic illustrations of adsorption-dissociation-desorption and gas phase diffusion mechanisms of uninhibited carbon-carbon composite oxidation in dry oxygen.**

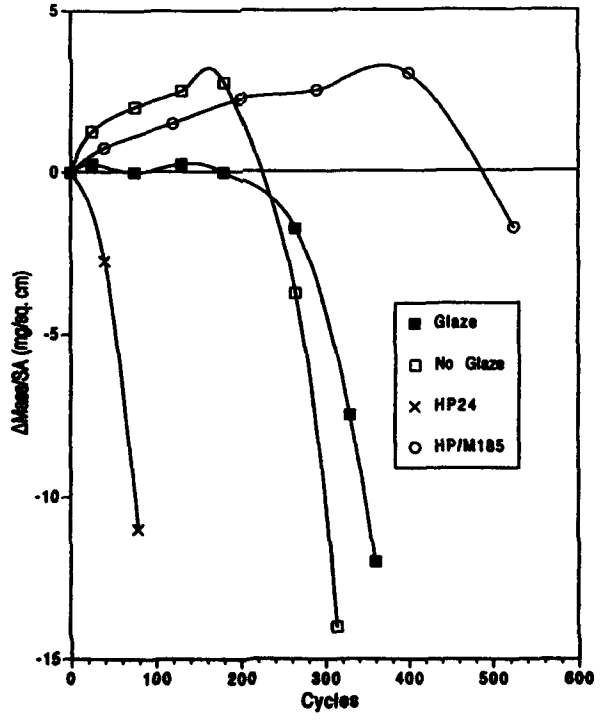

Figure 12. **Cyclic oxidation results for coated carbon-carbon composites in still air at 1125°C.**

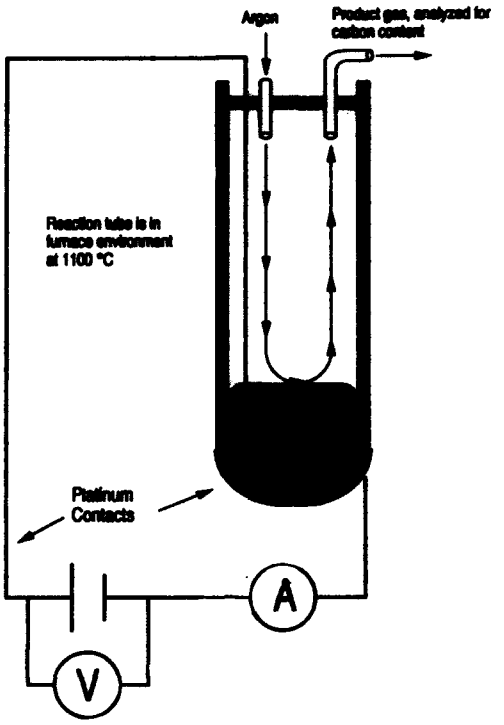

Figure 13. **Schematic diagram of the use of an electrical potential gradient across a zirconia tube to control the oxidation rate of carbon.**

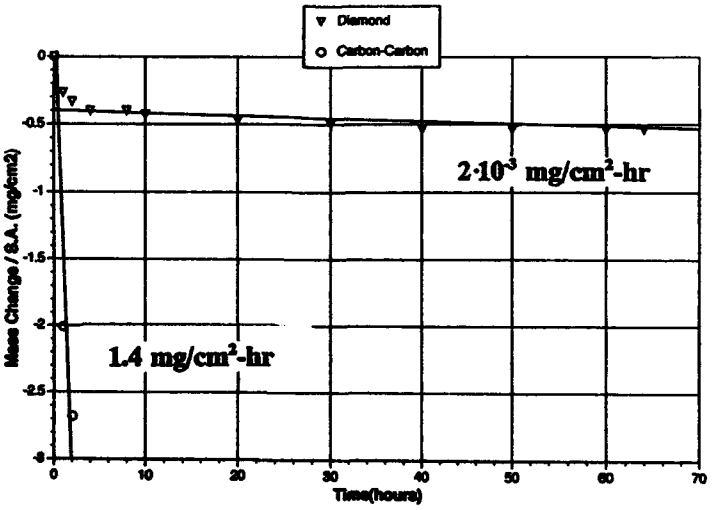

Figure 14. **Comparison of the oxidation rates of a carbon-carbon composite and a CVD diamond film at 500°C**

References

1. G. H. Meier and F. S. Pettit, Surface Coatings and Technology, 39/40 (1989), 1.

2. S. C. Singhal, J. Mat. Sci., 11 (1976), 500.

3. B. M. Warnes, S. Y. Hwang, J. R. Caola, F. S. Pettit, and G. H. Meier, "Hot Corrosion Of Metallic and Ceramic Coatings in Heat Engines" in Proc. of the 1990 Coatings for Advanced Heat Engines Workshop, J. Fairbanks ed., U. S. DOE, Aug. 6-9, 1990, Castine, ME, pp. iv-1 to iv-37.

4. R. A. Rapp, "Hot Corrosion of Materials" in Selected Topics in High Temperature Chemistry, O. Johannesen and A. Anderson, eds., Elsevier, 1989, pp. 291-329.

5. G. H. Meier, "Fundamentals of the Oxidation of High-Temperature Intermetallics" in Oxidation of High-Temperature Intermetallics, T. Grobstein and J. Doychak eds., TMS, Warrendale, PA, 1989, p. 1.

6. E. A. Aitken, "Corrosion Behavior", in Intermetallic Compounds", J.H. Westbrook ed., Wiley, 1967, Chap. 25.

7. A. Rahmel and P. J. Spencer, Oxidation of Metals, 35 (1991), 53.

8. K. L. Luthra, Oxidation of Metals, 36 (1991), 475.

9. A. K. Misra, Met. Trans. A., 22A (1991), 715.

10. C. Wagner, Z. Elektrochem., 63 (1959), 772.

11. F. Gesmundo and F. Viani, Oxid. Metals, 25 (1986), 269.

12. F. S. Pettit, Trans. TMS-AIME, 239 (1967), 1296.

13. C. Wagner, J. Electrochem. Soc., 99 (1952), 369.

14. R. Svedberg, "Oxides Associated with the Improved Air Oxidation Performance of some Niobium Intermetallics and Alloys", in Properties of High Temperature Alloys, Z. A. Foroulis and F. S. Pettit eds., The Electrochem Soc., 1976, p. 331.

15. M. Steinhorst and H. J. Grabke, J. Mater. Sci. Eng., A120 (1989), 55.

16. G. H. Meier, D. Appalonia, R. A. Perkins, and K. T. Chiang, "Oxidation of Ti-Base Alloys", in Oxidation of High-Temperature Intermetallics, T. Grobstein and J. Doychak eds., TMS, Warrendale, PA, 1989, p. 185.

17. E. Fitzer, Plansee Proc., 2nd Seminar, Reutte/ Tyrol, Pergamon Press, 1956, p.56.

18. N. S. Choudhury, H. C. Graham, and J. W. Hinze, "Oxidation Behavior of Titanium Aluminides", in Properties of High Temperature Alloys, Z. A. Foroulis and F. S. Pettit eds., The Electrochem Soc., 1976, p.668.

19. E. Kobayashi, M. Yoshihara, and R. Tanaka, High Temp. Tech., 8 (1990), 179.

20. C. T. Liu and C. G. McKamey, "Environmental Embrittlement - A Major Cause for Low Ductility of Ordered Intermetallics" in S. H. Whang, C. T. Liu, D. P. Pope, and J. O. Stiegler, eds., High Temperature Aluminides and Intermetallics, TMS, 1989, p.133.

21. J. H. DeVan and C. A. Hippsley, "Oxidation of Ni_3Al Below 850°C and Its Effect on Fracture Behavior", in Oxidation of High Temperature Intermetallics, T. Grobstein and J. Doychak eds., TMS, Warrendale, PA, 1989, p.31.

22. S. J. Balsone, "The Effect of elevated Temperature Exposure on the Tensile and Creep Properties of Ti-24Al-11Nb" in Oxidation of High Temperature Intermetallics, T. Grobstein and J. Doychak eds., TMS, Warrendale, PA, 1989, p. 219.

23. R. A. Perkins, Private Communication, 1991.

24. J. R. Strife and J. E. Sheehan, Ceramic Bulletin, 67 (1988), 369.

25. J. R. Strife, R. D. Veltri, and E. J. Brambani, "Si_3N_4 Coated C-C for Advanced Turbopropulsion Applications" in Proc. 14th Conference on Composite Materials and Structures, Cocoa Beach, FL (1990).

26. P. J. Jorgenson, J. Chem. Phys., 37 (1962), 874.

ENVIRONMENTAL RESISTANCE OF INTERMETALLIC COMPOUNDS AND COMPOSITE MATERIALS

D. J. Duquette

Rensselaer Polytechnic Institute
Troy, New York 12180-3590

Abstract

Intermetallic compounds and composite are candidate materials for high temperature structural applications. However both elevated temperature and ambient temperature resistance to the environment pose potential problems for these materials. For example, minor alloying elements have been shown to have significant influences on the static and cyclic oxidation resistance. Additionally, at ambient temperatures, virtually all of the alloys which have been examined show considerable susceptibility to hydrogen embrittlement. A brief overview of these phenomena is presented.

Critical Issues in the Development of High Temperature Structural Materials
Edited by N.S. Stoloff, D.J. Duquette and A.F. Giamei
The Minerals, Metals & Materials Society, 1993

Introduction

Intermetallic compounds, alloys based on those compounds, and composite materials utilizing intermetallic compounds or alloys as matrix materials have been identified as potential high technology materials for structural applications. However, most intermetallics lack inherent ductility, often exhibit poor creep resistance and, since many are line or near line compounds, do not lend themselves to alloying without precipitating second phases which are usually deleterious. Nevertheless, several promising intermetallics are currently being developed, either for use as monolithic materials, or as components of composite materials. In the latter case, the inherent lack of ductility, and associated lack of significant toughness are overcome by controlled interfacial bonding between the matrix and the reinforcing phases. From an environmental point of view, those intermetallics which are line or near line compounds, in some instances, exhibit phase transformations when one of the elements in the compound is selectively oxidized at elevated temperatures. In addition, they are often sensitive to hydrogen embrittlement, oxygen induced embrittlement, and many oxidize catastrophically at intermediate temperatures. While these disadvantages are certainly substantial, the development of a number of interesting systems is currently underway, with potential applications for both ambient and elevated temperatures.

Alloy Systems

While there are a great number of interesting alloy systems which have been explored, only those systems which appear to be close to commercial application will be examined in this presentation. These alloys include the nickel aluminides (Ni_3Al and NiAl), the iron aluminides (Fe_3Al and FeAl), the titanium aluminides (Ti_3Al, TiAl and $TiAl_3$), niobium aluminide ($NbAl_3$), and molybdenum disilicide ($MoSi_2$). Some of the known properties of these materials are shown in Table I.

Table I Properties of Selected Intermetallic Compounds

Compound	Crystal Structure	Melting Point °C	Density g/cm^3	Modulus GPa	Specific Modulus $GPa/g/cm^3$
Ni_3Al	$L1_2$	1390	7.50	178	23.7
NiAl	B2	1640	5.86	200	34.1
TiAl	$L1_0$	1460	3.91	175	44.8
$NbAl_3$	DO_{22}	1600	4.54	----	----
$MoSi_2$	C11	2030	6.3	359	57.0
Al_3Ti	DO_{22}	1325	3.40	----	----
Fe_3Al	DO_3	*	6.72	141	21.1

*Disorders at approx 550°C

The discovery that small amounts of boron (~0.1%), added to Ni_3Al resulted in a significant increase in room temperature ductility has initiated a significant amount of research into other alloying elements (1) which might enhance ductility in other alloy systems. However, with the exception of a very few specific alloying additions it is generally conceded that the boron effect is rather selective. Boron has been shown to enhance the ductility of other $L1_2$ compounds including Ni_3Si (2) and Ni_3Ga (2), although neither of these alloys is currently being extensively developed. Ni_3Al also shows some enhanced ductility when alloyed with manganese, chromium, iron or palladium (3-6). However, except for the palladium and beryllium effects, ductility is achieved with the other alloying additions due to the formation of ductile second phases. Fe_3Al and FeAl show a significant amount of ductility in dry air, but moisture is sufficient to induce embrittlement. This phenomenon will be addressed in a later section of this paper. No significant room temperature ductility has been achieved for other intermetallic alloys of interest for advanced technological applications, except for TiAl, which has been alloyed with chromium and vanadium to yield room temperature ductilities of approximately 3% (7). These alloys are two phase materials - gamma + alpha-2 (8), and the alloying additions generally decrease the melting temperatures of the alloys as well as increase their density; both effects reducing the advantages of the intermetallic alloys when compared with conventional high technology alloys. It should be noted that the alloys of most interest to technological applications contain significant amounts of aluminum or in the case of $MoSi_2$, silicon. Since these alloys are generally intended for elevated temperature use, it is imperative that they form protective oxide scales. An exception to the use of these alloys for intermediate to high temperature applications is the development of the iron aluminides which are currently being studied as potential replacements for stainless steels.

Elevated Temperature Resistance

The intermetallic compound, NiAl, has already been widely utilized as a coating material for conventional nickel base alloys in aerospace applications. In conventional oxidizing atmospheres it forms a continuous aluminum oxide film which resists further oxidation by inhibiting cationic diffusion through the film. It is somewhat susceptible to spalling due to cyclic oxidation. This drawback has been addressed by the addition of rare earth elements to the aluminide which has been shown to improve the adherence of the oxide film. As a monolithic material it undergoes a ductile to brittle transition at approximately 400°C (9). This transition results in inferior creep properties, and it is unlikely that the compound can be used at elevated temperatures without composite reinforcing. Single crystals of the compound have been developed (10), and in order to improve the low temperature toughness of the alloy, iron or cobalt have been added to provide crack-blunting second phases (11). Other alloying additions have resulted in improving the elevated temperature strength of the compounds to a level where they compete successfully with conventional nickel-base superalloys, with a density reduction of some 40% (12).

Even Ni_3Al shows a significant amount of oxidation resistance, through the formation of alumina; the oxidation resistance being even

better than that of pure silicon, and considerably better than that of nickel or of the nickel chromium alloys (Figure 1) (13). Unfortunately, the relatively low melting temperature of the compound, combined with its relatively high density will probably inhibit its use for aerospace applications. On the other hand, it is currently being developed as a possible candidate for land based turbines, for internal combustion engine applications, for incinerator components, etc.

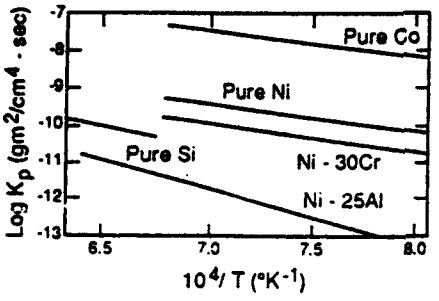

Fig. 1 Parabolic oxidation rate constants for aluminides and conventional alloys (13)

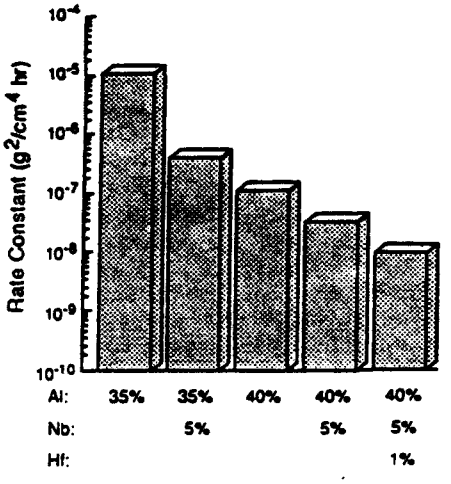

Fig. 2 Effect of Niobium on the parabolic rate constant of TiAl (14)

The titanium aluminides show increasing oxidation resistance with increasing aluminum content. $TiAl_3$ shows the best oxidation resistance, but has the lowest melting temperature of the Ti-Al alloys, which may limit its elevated temperature use. However its low ductility and outstanding oxidation resistance may make it a suitable coating material for titanium and its alloys for intermediate temperature applications. TiAl is considerably less oxidation resistant than $TiAl_3$, even with 50% aluminum in the compound. The inferior oxidation resistance arises because rutile (TiO_2) is a significant component of the oxidation products produced at temperatures in the vicinity of 1000 °C (14). Cationic diffusivity is considerably higher in rutile than in alumina. Recent results indicate that the addition of niobium to TiAl can result in significantly improved oxidation resistance. The oxidation rate constant is reduced by at least two orders of magnitude with the addition of 5w% niobium to a 40 w% aluminum alloy. Further additions of a small amount of hafnium results in a further decrease in the static oxidation rates of TiAl based alloys (Figure 2) (14). Ti_3Al has undergone a considerable amount of development with significant additions of niobium reported to improve ductility, and small amount of vanadium and molybdenum added to impart strength without sacrificing ductility (15). However, the relatively low melting temperature

limits the useful operating temperature to approximately 800°C and the alloy shows a marked tendency toward hydrogen embrittlement (see following section). In any event, the alloy is not resistant to oxidation, due to the formation of rutile as its primary reaction product, and would probably only be successfully utilized in a coated condition.

The niobium aluminide of perhaps the most technological interest, $NbAl_3$, exhibits an interesting high temperature oxidation phenomenon (16). While this alloy contains a considerable amount of aluminum, an abnormally high rate of oxidation is observed. This behavior can be ascribed to the fact that this material is a line compound, allowing virtually no variation in either the niobium or the aluminum content. Depletion of aluminum from the original aluminide due oxidation results in a phase transformation from $NbAl_3$ to Nb_2Al. This compound exhibits significantly lower oxidation resistance and in fact, oxidizes so rapidly that it is virtually consumed by the oxidative process. This in turn results in the original compound being exposed to oxidation, forming alumina, being depleted in aluminum with a subsequent phase transformation. The final result is a banded reaction product zone consisting of alternate layers of alumina, niobium aluminate and, in some instances, niobia.

$MoSi_2$ is among the most oxidation resistant compounds being considered for elevated temperature applications. The reaction product on this compound is silica (SiO_2), and the "pest" phenomenon described below does not occur in fully dense, crack-free material (17).

In addition to static oxidation considerations, thermal cycling also affects the elevated temperature environmental resistance of intermetallic compounds and alloys. The differences between coefficients of thermal expansion of the oxides and of the base materials can result in significant tensile or compressive stresses in the oxides with the result that the oxide film will fail in tension or by buckling. For superalloys and superalloy coatings this phenomenon can be alleviated by alloying with trace amounts of zirconium, hafnium or, more commonly, yttrium. A similar alloying scheme has been also successful for niobium aluminides as well as for nickel aluminides. Figure 3 shows cyclic oxidation results for these alloys containing either yttrium or zirconium and, in one case, the addition of silicon (18). Similar results have been reported for TiAl, and for monolithic NiAl where such additions have been traditionally applied to coating materials (14,19).

At intermediate temperatures intermetallics suffer from two rather distinct phenomena which are not usually observed in conventional alloys. These are the so-called "pest" phenomenon and oxygen induced embrittlement. The "pest" phenomenon results from rapid internal oxidation of the intermetallics, generally along grain boundaries. These internal oxidative processes generally generate large internal volumetric expansions, virtually always resulting in serious degradation of mechanical properties and, in some cases, total destruction of the material in an almost explosive manner. While the specific mechanisms of this phenomenon have not been quantitatively established, it appears that surface oxide films, which are formed at intermediate temperatures, are not sufficient diffusion barriers to oxygen ingress. Grain boundaries, with their inherent defect structures, act as short circuit diffusion paths in

preference to the usually ordered matrix. This phenomenon has been reported for virtually all of the aluminides with the possible exception of TiAl. Oxygen induced embrittlement, which has been reported for cases where internal oxidation has not had sufficient time to form, is still another, recently observed phenomenon in some intermetallic compounds at intermediate temperatures. It has been observed in polycrystals and single crystals of Ni_3Al and in polycrystals of Ni_3Si (20,21). The phenomenon is gene not observed in vacuum and, while it has generally been associ with oxygen, some recent results suggest that it may also be related to water vapor, and accordingly to hydrogen embrittlement. For Ni_3Al, this intermediate temperature embrittlement may be somewhat alleviated by alloying with chromium, as shown in Figure 4 (20).

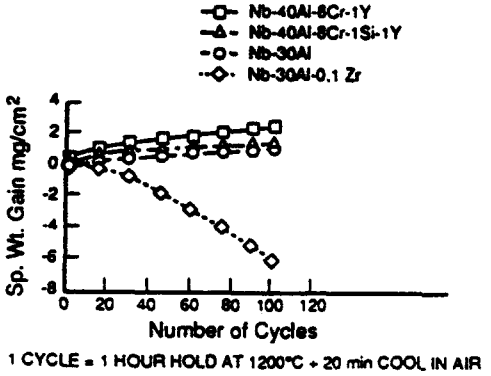

Fig. 3 Cyclic oxidation behavior of intermetallics alloyed with minor element additions (18)

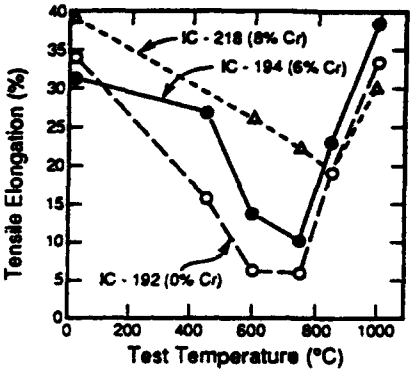

Fig. 4 Intermediate temperature embrittlement of Ni_3Al alloys in air, showing beneficial effect of Cr additions (20)

The effects of compositing on any of the phenomena described above have not been extensively studied. However, in a series of experiments conducted on TiAl as well as on NiAl, it has been shown that the chemistry of the reinforcing phases appears to play a significant role in the static and cyclic oxidation behaviors. For example, the introduction of a zirconia stabilized alumina reinforcing phase in TiAl results in significant increases in the static oxidation rates, and results in otherwise unobserved internal oxidation processes. Substitution of the zirconium stabilized reinforcing phase with pure alumina results in only slightly increased oxidation rates, the increase being associated with a rapid diffusion path in the interface between the reinforcing phases and the matrix material. The presence of reinforcing phases in TiAl virtually always results in enhanced oxide adherence on this compound during cyclic oxidation, although the exact causes for the enhanced adherence are still not well understood (14). For NiAl, reinforcing phases of either HfB_2 or TiB_2 result in abnormally high static oxidation rates (16). In this case the enhanced oxidation is associated with the inclusion of boron oxide in the alumina film which results in a non-protective barrier film, and may even result in the fluxing

of the otherwise protective alumina. The inclusion of alumina reinforcing phases in NiAl has no effect on the intrinsic oxidation resistance of the compound. Thus, while research in the area of oxidation studies of composites based on intermetallic compounds is still in its infancy, it is apparent that the nature of the reinforcing phases can exert a profound effect on their oxidation resistance.

Ambient Temperature Resistance

In addition to elevated temperature considerations, many intermetallic compounds suffer from room temperature degradation, particularly by solid state dissolved hydrogen. Table II shows a brief summation of some of the intermetallic compounds and alloys which have been shown to be affected by this phenomenon.

Table II Alloys Embrittled by Hydrogen

B2	$L2_0$	DO_{19}	$L1_2$	Orthorhombic	DO_3
FeCo-V FeAl	TiAl	Ti_3Al	Ni_3Al+B Ni_3Fe $(Fe,Ni)_3V$ Co_3Ti $Ni_3Al_{0.4}Mn_{0.6}$	Ni_2Cr	Fe_3Al

The $L1_2$ compounds appear to be exceptionally susceptible, although perhaps only because they generally exhibit more inherent ductility than those exhibiting other crystal structures (22-26). For example, Figure 5 shows the results of slow strain rate tests for annealed and cold worked Ni_3Al in several environments (27).

These data show that only acidic environments have any appreciable effect on the ductility of this compound, and that annealed samples show a larger reduction in ductility than cold worked samples. The implications of these experiments are that hydrogen, produced by electrochemical reaction with the compound, is responsible for the marked reduction in ductility. Further, sulfuric acid has a more damaging effect than nitric acid. This result is reasonable if it is assumed that sulfuric acid, being a reducing acid, can be expected to generate more hydrogen under freely corroding conditions than nitric acid, which is an oxidizing acid. The beneficial role of cold work is presumably to provide trapping sites for electrochemically generated hydrogen.

Figure 6 shows the results of applied electrochemical potentials on the ultimate tensile strength ratios for tests performed on an Ni_3Al alloy containing boron (27). It is clear that only when hydrogen is actively generated does embrittlement occur. It has also been shown that cathodic precharging of a similar alloy results in large losses of ductility, while simultaneous charging of the alloy with cathodic hydrogen results in virtually no ductility, indicating that dynamic hydrogen effects are more

damaging than simply introducing hydrogen into the alloy matrix (23). Similar effects have been observed for Ni_3Fe compounds except that, for this compound, which can be ordered or disordered at room temperature, the ordered compound showed considerably more embrittlement when tensile testing and cathodic charging were applied simultaneously (23). In both the Ni_3Al and the Ni_3Fe, the presence of hydrogen resulted in grain boundary separation.

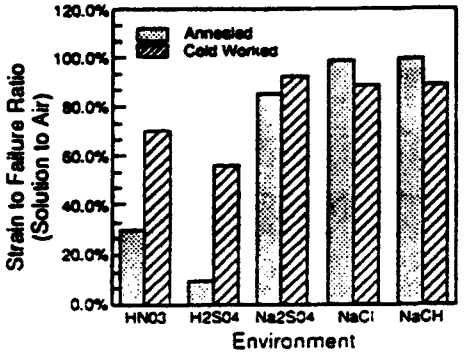

Fig. 5 Effect of environment on the ductility of Ni_3Al (27)

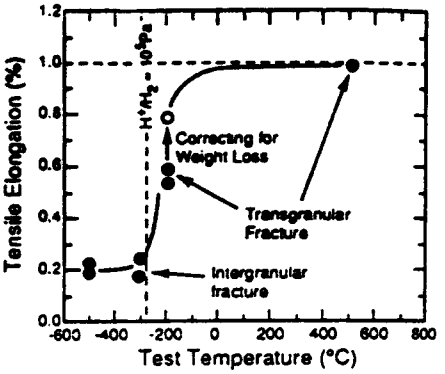

Fig.6 Effect of potential on the ductility of Ni_3Al (27)

Iron aluminides are also susceptible to hydrogen embrittlement. In fact, for these alloys it appears that laboratory air is a sufficiently embrittling medium for either Fe_3Al or for FeAl (28,29). For example, Table III shows the results of exposure to a variety of environments including air, vacuum, dry oxygen, dry hydrogen and water vapor. These data indicate that air and water vapor are extremely damaging to the ductility and strength of these materials, but that hydrogen *per se* is only slightly damaging. Vacuum or dry oxygen had virtually no effect on the mechanical properties of the compound. These data also showed that the embrittling effect is not a function of the crystal structure of the compound, the B2 and the DO_3 structures (controlled by heat treatment) yielding essentially the same dependence on the environment. Similar results have been observed for FeAl, except that a vacuum of $<10^{-4}$ Pa or Argon + 4% hydrogen were apparently not sufficiently inert to inhibit at least some degree of embrittlement. The role of dry oxygen in virtually completely inhibiting hydrogen embrittlement is not completely understood but it has been suggested that, since it appears to be stronger in the case of the higher aluminum alloy, the formation of alumina may prevent the ingress of hydrogen.

It is perhaps interesting to note that, in the case of the iron aluminides, Fe_3Al exhibits cleavage cracking when it is hydrogen embrittled, while FeAl exhibits intergranular separation. This observation suggests that there is nothing intrinsic about hydrogen induced intergranular failure, but that hydrogen embrittlement simply follows the

line of least resistance with respect to fracture path. Some recent results regarding the Fe_3Al alloy indicate that the hydrogen embrittlement phenomenon is similar to that for more conventional alloy systems. For example, decreasing strain rates result in decreased ductilities in air or in water vapor containing environments, but have no effect on ductility in dry oxygen (30). The addition of 5% chromium to the Fe_3Al compound has been reported to inhibit cracking under conditions of cathodic charging when samples were statically loaded (U-bend tests) (31). However, when dynamically tensile tested in air or after precharging with hydrogen, severe embrittlement was observed, the ductility being reduced to less than 2%, compared to a value of 13% in vacuum (32). Compositing of chromium alloyed Fe_3Al with Al_2O_3 fibers had no significant effect on the susceptibility to hydrogen embrittlement of the alloy (30).

Table III Effects of Environment on the Room Temperature Tensile Properties of Fe_3Al (25)

Test environment	Elongation (%)	Yield strength (MPa)	Tensile Strength MPa
		B2	
Air	4.1	387	559
Vacuum	12.8	387	851
Ar + 4% H_2	8.4	385	731
Oxygen	12.0	392	867
H_2O Vapor	2.1	387	475
		DO_3	
Air	3.7	279	514
Vacuum	12.4	316	813
Oxygen	11.7	298	888
H_2O Vapor	2.1	322	439

Hydrogen embrittlement has also been reported for titanium aluminides, including some relatively highly alloyed materials. In contrast to most of the intermetallics which have been studied, these materials have been shown to precipitate hydrides for those alloys which contain more than 50a% titanium (34). Embrittlement due to hydrogen gas has been reported for Ti-24Al-11Nb (34) and for Ti-25Al-10Nb-3V-1Mo (35). For the former alloy the ductility was reduced from 3% to 0% when the alloy was annealed in hydrogen. For the latter alloy, ductility in tests performed in hydrogen was reduced from 2.8% to 1.7% *vs* a test performed in helium. Interestingly a loss of ductility was also observed for this alloy when the tests were performed at 204°C, in contrast to many other hydrogen embrittled alloys which show susceptibility only near room temperature. This can be interpreted as evidence that hydrides are associated with embrittlement in these alloys since the hydrides have been shown to be stable to relatively high temperatures (depending on the hydrogen content of the alloys). TiAl also appears to be susceptible to hydrogen

embrittlement. A reduction in tensile strength has been reported for a Ti-48Al-2.5Nb-0.3Ta alloy after pre exposure to hydrogen gas at 815°C for 30 min (36,37).

With the exception of the titanium compounds and alloys, where a distinct possibility of hydride formation may provide an explanation for the observed ductility losses, the mechanisms for hydrogen embrittlement of intermetallic compounds and alloys of those compounds appear to be similar to those which have been suggested for other alloy systems. Those include hydrogen enhanced plasticity and/or decohesion of either cleavage planes or of grain boundaries. Direct experimental evidence for either of these mechanisms (with the possible exception of a few experiments performed in-situ in an electron microscope) are still to be obtained.

Summary

While there is considerable effort being devoted to the development of intermetallic compounds and alloys of these compounds for structural applications, it is likely that most of these materials will be utilized for elevated temperature applications under conditions where conventional structural materials cannot be used. Additionally it is quite probable that, given the intrinsic lack of ductility exhibited by most of the intermetallics, they will have to be composited in order to provide sufficient toughness for structural applications. However, independent of the attractive elevated temperature capabilities shown by these materials, considerations of static and cyclic oxidation will have to be addressed, particularly since it has been shown that reinforcements may have significant effects on elevated temperature environmental resistance. Finally it has been shown that virtually every intermetallic compound or alloy of an intermetallic compound which has been examined is embrittled by hydrogen. While it is unlikely that this phenomenon will be of direct importance for elevated temperature applications (with the possible exception of titanium compounds), each of the systems to be considered must resist hydrogen embrittlement at ambient temperatures. As a minimum, if resistance to hydrogen embrittlement cannot be realized, sufficient engineering data, related to the properties of alloys in the presence of hydrogen, must be generated to ensure successful utilization of these materials.

Acknowledgement

The author is grateful to DARPA and ONR for financial support through a University Research Initiative, under Contract N00014-86-K-0770.

References

1. K. Aoki and O Izumi, Nippon Kinzaku Gakkaishi, 43, (1979), 1190.

2. A. I. Taub and C. L. Briant, High Temperature Aluminides and Intermetallics, S. H. Whang, *et al*, eds., (Warrendale, PA.:TMS-AIME, 1990), 183.

3. T. Takasugi, O. Izumi and N. Masahashi, Acta Metall., 33, (1985), 1259.

4. G. E. Fuchs and N. S. Stoloff, Acta Met., 36, (1988), 138.

5. A. Chiba, S. Hanada and S. Watanabe, Proc. Int. Symp., on Intermetallic Compounds (JIMIS-6), O. Izumi, ed., (Sendai: Japan Inst. of Metals, 1991), 445.

6. T. Takasugi, N. Masahashi and O. Izumi, Scripta Metall., 20 (1986), 1317.

7. Y.-W. Kim, High Temperature Ordered Intermetallic Alloys IV, L. Johnson, *et al*, eds., MRS Symposia, vol.213, (Pittsburgh, PA: MRS, 1991),777.

8. J. M. Larsen, K. A. Williams, S. J. Balsone and M. A. Stuckie, High Temperature Aluminides and Intermetallics, S. H. Whang, et al eds., (Warrendale, PA.: TMS-AIME, 1990), 521.

9. R. N. Noebe, R. R. Bowman, C. L. Cullers and S. V. Raj, High Temperature Ordered Intermetallic Alloys IV, L. Johnson, et al, eds., MRS Symposia, vol.213, (Pittsburgh, PA.: MRS, 1991), 589.

10. R. Darolia, J. of Metals, 43(3), (1991), 44.

11. K. Ishida, R. Kainuma, N. Ueno and T. Nishizawa, Metall. Trans, 22A, (1991), 441.

12. R. Darolia *et al*, Ordered Intermetallics - Physical Metallurgy and Mechanical Behavior, NATO Workshop on Advanced Intermetallics, (Dordrecht, Netherlands: Kluwer Academic Publ., 1992), 679.

13. F. S. Pettit and G. W. Goward, Metallurgical Treatises, (Warrendale, PA.: TMS-AIME, 1981), 603.

14. J. Fish and D. J. Duquette, Rensselaer Polytechnic Institute, Troy, New York, 1992, unpublished.

15. M. J. Blackburn and M. P. Smith, Titanium Alloys of the Ti_3Al Type, U.S. Patent No. 4,292,077, Sept.29, 1981.

16 P. Korinko and D. J. Duquette, Rensselaer Polytechnic Institute, Troy, New York, 1992, unpublished.

17. J. Petrovic, Los Alamos National Laboratory, 1991, private communication.

18. M. G. Hebsur, J. R. Stevens, J. L. Smialek, C. A. Barrett and D. S. Fox, Oxidation of High Temperature Intermetallics, T. Grobstein and J. Doychak, eds., (Warrendale, PA.: TMS-AIME, 1989),171.

19. S. Mrowec and J. Jeddinski, Oxidation of High Temperature Intermetallics, T. Grobstein and J. Doychak, eds, (Warrendale, PA.: TMS-AIME, 1989), 57.

20. C. T. Liu, C. L. White and E. H. Lee, Scripta Metall., 19, (1985), 1247.

21. W. C. Oliver and C. L. White, High Temperature Ordered Intermetallic Alloys II, MRS Symposia, 81, (Pittsburgh, PA.: MRS, 1987).

22. A. K. Kuruvilla and N. S. Stoloff, Scripta Metall., 19, (1985) 83.

23. G. M. Camus, N. S. Stoloff and D. J. Duquette, Acta Metall., 37, (1989), 7.

24. T. Takasugi and O. Izumi, Acta Metall., 34, (1986), 607.

25. Y. Liu, T. Takasugi, O. Izumi and T. Yamada, Acta Metall., 37, (1989), 507.

26. A. K. Kuruvilla, S. Ashok, and N. S. Stoloff, Proc. 3rd Int. Cong. on Hydrogen and Materials Vol. 2, (Oxford: Pergamon Press, 1982), 629.

27. R.E. Ricker, D. E. Hall and J. L. Fink, Scripta Metall. 24, (1990), 291.

28. C. T. Liu, C. G. McKamey, and E. H. Lee, Scripta Metall., 24, (1990), 385.

29. C. T. Liu, E. H. Lee and C. G. McKamey, Scripta Metall., 23, (1989), 875.

30. J. Scott, N. S. Stoloff and D. J. Duquette, Rensselaer Polytechnic Institute, Troy, New York, 1992, unpublished research.

31. R. A. Buchanan and J.G. Kim, Proc. 4th Annual Conf. on Fossil Energy Materials, Oak Ridge, TN, May 1990, ORNL/FMP-90/1, 383.

32. M. Shea, A. Castagna and N. S. Stoloff, High Temperature Ordered Intermetallics IV, MRS Symposia,213, (Pittsburgh, PA.: MRS, 1991), 609.

33. D. S. Shih, G.K. Scarr and G. E. Wasielewski, Abstract, J. of Metals, 39(7), (1987), 7.

34. T. Fox, D. B. Knorr and N. S. Stoloff, Rensselaer Polytechnic Institute,1991, unpublished research.

35. D. E. Matejczyk, and P. R. Jewett, Summary, Proc. of 2nd workshop on Hydrogen Materials Interactions, NASA Workshop Publ 1004, (Nov 1988), 137.

36. J. H. Holbrook, H. J. Cialone and M. S. Majumdar, Abstract, 3rd NASP Workshop on Hydrogen Materials Interactions, Scottsdale, AZ, May ,1989.

37. L. G. Fritzemeier, M.A. Jacinto and G. D. Schnittgrund, Abstract, 3rd NASP Workshop on Hydrogen Materials Interactions, Scottsdale, AZ May, 1989.

ENVIRONMENTAL EFFECTS ON ELEVATED TEMPERATURE

SUBCRITICAL CRACK GROWTH OF SiC/SiC COMPOSITES

C. H. Henager, Jr. and R. H. Jones

Pacific Northwest Laboratory*
Battelle Blvd.
Richland, WA 99352

Abstract

Time-dependent crack growth measurements of ceramic composites in varying PO_2 environments were conducted on materials consisting of chemical vapor infiltration (CVI) SiC reinforced with Nicalon fibers having C-interfaces. Crack velocities are determined as a function of applied stress intensity and time for varying O_2 levels. Results are presented for crack velocity-stress intensity relationships in pure Ar and in Ar plus 2000-, 5000-, 10,000-, and 20,000-ppm O_2 atmospheres at 1100°C. A 2D micromechanics model is used to represent the time-dependence of observed crack bridging events and is able to rationalize the observed phenomena.

*Pacific Northwest Laboratory is operated for the U.S. Department of Energy by Battelle Memorial Institute under Contract DE-AC06-76RLO 1830.

Critical Issues in the Development of High Temperature Structural Materials
Edited by N.S. Stoloff, D.J. Duquette and A.F. Giamei
The Minerals, Metals & Materials Society, 1993

Introduction

Most ceramics are chemically stable and resistant to corrosion in many environments. Ceramic matrix composites are expected to also exhibit similar corrosion resistance; however, the stability of the fiber and interface may differ from monolithic ceramics and the method of manufacturing CMCs, i.e. CVI, can result in a relatively porous matrix that does not protect the fibers from the environment. The fiber/matrix interface through which CMCs gain their strength and toughness is of particular concern.

Time-dependent crack growth, referred to as subcritical crack growth or slow crack growth (SCG), likely controls the long-term life of ceramic matrix composite (CMC) structural materials at elevated temperatures when preexisting flaws are present. Using CMCs in systems where long-term stability is required demands resistance to time-dependent crack growth, as well as high-temperature corrosion (1-8). No prior data exists, to the best of our knowledge, on the subcritical crack growth rates of typical CMC materials at elevated temperatures under static or cyclic loads as a function of temperature or environment. Therefore, a fundamental research study was begun at Pacific Northwest Laboratory (PNL) to determine important aspects of SCG in ceramic composite materials (1,2).

This initial study has acquired crack velocity data as a function of stress intensity at elevated temperature in an inert environment to obtain baseline data for these CMC materials and to explore the phenomenon of SCG in CMC materials. Data are presented for SCG measured in a chemical-vapor infiltrated (CVI) β-SiC matrix material containing eight laminates of Nicalon fiber cloth at 1100°C in pure Ar. Results are also presented for SCG in Ar plus 2000-, 5000-, 10,000-, and 20,000-ppm O_2 to explore the effects of an aggressive environment.

Crack-wake bridging by long fibers in continuous-fiber-reinforced CMCs dominates the mechanical response of these materials (9). Therefore, it is reasonable to expect the time-dependent response of the bridging zone at elevated temperatures to dominate SCG in CMCs. Crack bridging reinforcements will be highly stressed and may exhibit a variety of time-dependent deformation behaviors including creep, time-dependent interface fracture, time-dependent interface creep, and possibly visco-elastic effects at the interface. In addition, the bridging reinforcements will be exposed directly to the external environment. Thus, environmental effects on SCG are also concerns for CMC materials. The environment can affect the bridging reinforcements by penetrating down the reinforcement-matrix interface or by directly degrading the reinforcements.

High Temperature Corrosion of SiC/SiC

Silicon carbide is thermodynamically unstable in O_2, H_2 and H_2O environments and will react with them in the following manner:

$$SiC(s) + O_2(g) = SiO(g) + CO(g) : \text{Low } PO_2 \qquad (1a)$$

$$SiC(s) + 3/2\ O_2(g) = SiO_2(s) + CO(g) : \text{High } PO_2 \qquad (1b)$$

$$SiC(s) + 2\ H_2(g) = Si + CH_4(g) \qquad (2)$$

$$SiC(s) + 2\ H_2O(g) = SiO(g) + CO(g) + 2\ H_2(g) \quad (3)$$

The stability of SiC depends on the formation of a stable "passive" layer of SiO_2 (10). Active oxidation of SiC occurs at around 10^{-8} atm of O_2 at 900°C. Oxidation of C to CO or CO_2 is a concern for C/C and C/SiC as well as for SiC/SiC composites relying on a C interfacial layer for fracture toughness. Jacobson, Eckel, Misra and Humphrey (11) have calculated the stability of SiC in an $Ar/H_2O/5\%\ H_2$ mixture. Their data illustrate that SiH, SiH_4, SiO, CH_4, CO and CH_4 are thermodynamically stable at various H_2/H_2O ratios ranging from 10^2 to 10^7 and total pressures of 1 atm. This analysis gives no information regarding the kinetics of these reactions.

The major reaction between alkali metals and Si-based ceramics is the formation of a low melting temperature salt such as Li_2O-SiO_2. Reaction with SiO_2 is of concern because of its presence at grain boundaries and surfaces (i.e. reaction of SiC with O_2). Degradation of the protective "passive" SiO_2 layer and accelerated crack growth caused by the decreased viscosity of grain boundary glass phases in contact with alkali metals are two of the possible chemical compatibility concerns for SiC/SiC composites in contact with a Li coolant or Li ceramic. If the Li is at a very low O_2 activity, the possibility of forming these eutectic phases is greatly reduced.

The corrosion and fracture behavior of SiC in molten Li has been evaluated by Curran and Amateau (12) and Cree and Amateau (13). Both studies were conducted on α-SiC exposed to a thin layer of molten Li in contact with the sample surface. A decrease in the room temperature fracture strength from about 350 MPa to about 150 MPa was found in both studies for exposures exceeding 500°C. The strength loss was related to Li penetration down SiC grain boundaries. Reaction with the glass phase in the SiC grain boundaries was considered to be the primary cause of the rapid intergranular penetration. Uniform corrosion rates were reported as being extensive but with no apparent effect on the fracture strength.

Experimental Procedures

Composites consisting of Nicalon fiber cloth (0°/90°) and CVI β-SiC with carbon (C) interfaces were tested. The composites are 8-ply material, 4 mm thick, fabricated by Refractory Composites, Inc. of Whittier, CA. Interfaces of 1.0 μm C were deposited on the Nicalon fibers before the β-SiC CVI fabrication step. Single-edge-notched bend bar (SENB) specimens with dimensions of 4 mm x 5.5 mm x 50 mm were prepared. The SENB specimens were tested in 4-point bending using a fully articulated SiC bend fixture. Other test details have been discussed previously (1,2).

The SCG studies were performed using constant load tests for long times, up to 7×10^4 s, and using stepped load tests with load holding carried out at 1100°C in Ar and Ar plus varying PO_2. The specimens were typically loaded at an applied stress intensity of 7-8 $MPa\sqrt{m}$ to begin the test. The test continued until a load drop was observed. Specimens that were tested in Ar plus O_2 were brought up to temperature in pure Ar.

Each SCG test consisted of either a series of 1000-s constant-load tests or a long-term hold at constant load in 4-point bending at a constant temperature. The displacement-time curves for the 1000-s exposures at constant load in Ar indicate that the specimen displacement, and thus the crack opening displacement, undergoes a transient period of displacement that is logarithmic in time and does not exhibit a true steady-state over the 1000-s hold time. The slope of the displacement-time curve over the final 600 s of the load step,

however, was fairly linear and was taken as proportional to the crack velocity for each 1000-s period. The longer term hold displacement-time data were fit to polynomial functions and differentiated to give $\partial\delta/\partial t$.

Writing $\delta = P\,C(\alpha)$, where δ is the displacement, P is the load, C is the specimen mid-point compliance, and α is equal to a/W normalized crack length) can be used to give

$$\frac{\partial\delta}{\partial t} = \frac{\partial}{\partial t}(PC(\alpha)) = P\frac{\partial C}{\partial \alpha}\frac{\partial \alpha}{\partial t} = \frac{P}{W}\frac{\partial C}{\partial \alpha}\frac{da}{dt} \tag{4}$$

which is then used to derive the following expression for da/dt V_c

$$\frac{da}{dt} = V_c = \frac{\frac{\partial\delta}{\partial t}W}{PC'(\alpha)} \tag{5}$$

where V_c is the crack velocity and W is the specimen thickness. An expression was determined for the mid-point compliance of a SENB specimen in 4-point bending and was used to calculate crack length and $C'(\alpha)$ (2). The slope of the displacement-time curve at a given load is $\partial\delta/\partial t$.

Fatigue crack growth tests were performed similarly to the static load subcritical crack growth tests with the load cycled 5 or 25 times at each of the constant loads used for the static load tests. The load was held for 1000s between each load cycle and the load ratio, R, was 0.1. Tests were conducted in both Ar and Ar plus 2000 ppm O_2. The crack velocity was determined during each of the 1000s hold periods between load cycles and compared to the crack velocity obtained with the statically loaded samples.

Experimental Results

The data for the C-interface materials, when plotted as crack velocity versus applied stress intensity (V-K curves), reveal a stage-II region where the crack velocity is essentially independent of the applied stress intensity (Figure 1) followed by a stage-III, or power-law crack growth region, at high stress intensities.

The power-law region exhibits a strong dependence, but the stage-II region exhibits a weak dependence, on the applied stress intensity. The data reveal a pronounced increase in stage-II crack velocity because of O_2 in the gas. The crack velocity increases with increasing O_2 content of the Ar (Figure 1). Also, the stress intensity required for the onset of stage-III is shifted to a lower value of the applied stress intensity.

When the crack velocity is plotted as a function of time (V-t curves), the effects of O_2 become more pronounced (Figure 2). The time-dependence of V_c in Ar shows a decreasing velocity with time while V_c in the varying $^cPO_2$ environments show either a constant V_c or increasing V_c with time. The curves for 10,000- and 20,000-ppm O_2 indicate that the crack velocity increases quite rapidly and that those tests were much shorter in duration than the 5000- and 2000-ppm O_2 tests.

SCG data for monolithic ceramics that do not exhibit a large-scale bridging zone do not show stage-II behavior; rather, the crack velocity is observed to

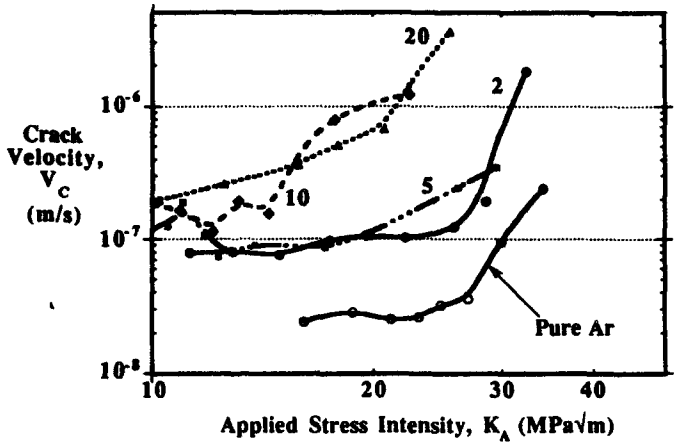

Figure 1 - V-K Curves as a Function of O_2 Partial Pressure and Applied Stress Intensity. Curve Labels Indicate PO_2 in Units of 10^3 ppm.

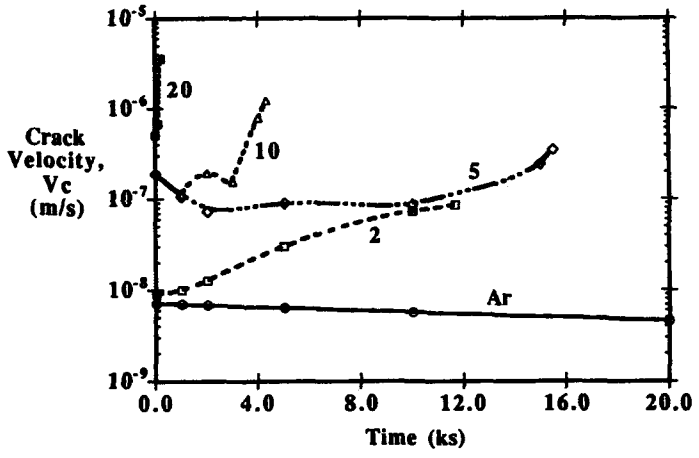

Figure 2 - Crack Velocity as a Function of Time in Pure Ar and in Varying O_2 Partial Pressures for Long Times. Curve Labels Indicate PO_2 in Units of 10^3 ppm.

be a power-law function of applied stress intensity (K_A) (3,5,7,8). The observed stage-II region in the present data reveals a weak dependence on K_A. This behavior suggests that SCG in CMCs is controlled by crack-bridging by the continuous fibers in the crack wake. The bridging zone screens, or shields, the crack-tip from the applied stress intensity. Over the region of increasing K_A as a function of increasing crack length, a bridging zone is established for these materials, and it screens the crack-tip from K_A. A nearly constant crack-tip stress intensity, K_{tip}, is established as the bridging zone develops and R-curve behavior is observed. Eventually, the bridging zone saturates and cannot continue to shield the crack-tip.

Comparison of Figures 1 and 3 reveals that the cyclic crack velocities are lower than the static crack growth rates for Ar and Ar + 2000 ppm O_2. This effect is revealed by comparing the crack velocities after 1 cycle and after

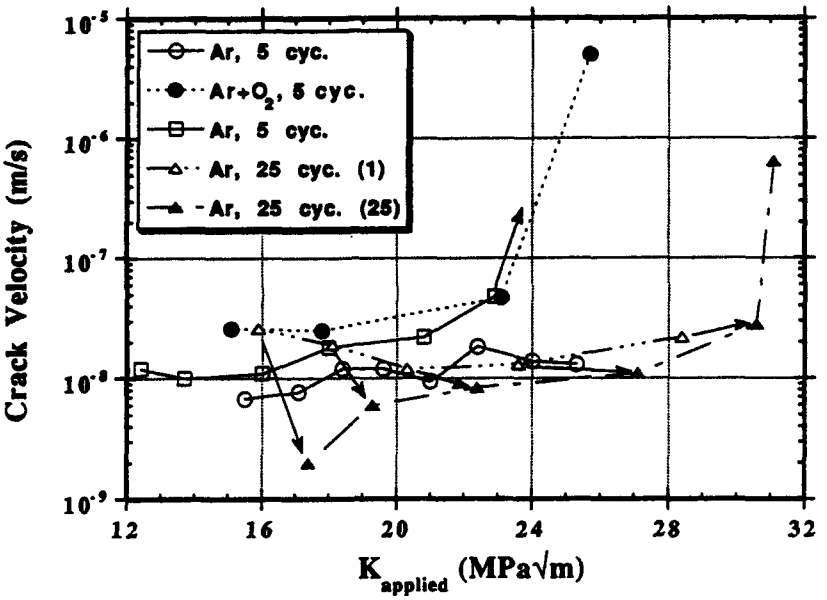

Figure 3 - Crack velocity as a function of applied stress intensity (V-K) for C-interface material at 1100°C in pure Ar and Ar + 2000 ppm oxygen and with cyclic stresses at a R of 0.1.

25 cycles, Figures 3. Clearly the crack velocity decreases with increasing number of cycles; however, the decrease in crack velocity is greatest at low K values at the beginning of the test with less of a decrease at higher K values. Stage II crack velocities ranged from 7×10^{-9} in Ar to about 3×10^{-8} m/s in Ar 2000 ppm O_2.

The effect of cyclic stresses on the transition from stage II to rapid fracture, stage III, is difficult to identify with this data set. For the tests in Ar + O_2, the transition occurs at a lower value of K for cyclic than static loading while the data for tests conducted in Ar is less conclusive. A transition from stage II to stage III occurred at about 28 MPa√m with static loading, Figure 1, but for two tests conducted with cyclic loading the transition occurred at about 24 MPa√m in one test while the other survived to 25 MPa√m without failing. The test was terminated at this stress intensity because of equipment failure.

Discussion and Modeling of Results

The evidence for bridging zone domination of SCG is suggested from the experiments using Ar plus O_2 in comparison with pure Ar and also from a micromechanical model developed to rationalize SCG in CMC materials (1, 2). Adding O_2 to the 1100°C Ar environment increases the crack velocity in the stage-II regime and shifts the stage-II-to-stage-III transition to lower K_A values (Figure 1). The shift to lower K_A values for the transition to stage-III crack growth is consistent with a reduction in the closure forces imparted on the crack faces by the bridging fibers. Scanning electron photomicrographs (not shown here) of the CMCs exposed to the O_2 reveal the partial removal of the C-interfaces due to oxidation at 1100°C. Removing this interface material reduces the shear strength of the interface, reduces the ability of the matrix to transfer load to the fibers, and reduces the bridging zone effectiveness.

These effects are rationalized using a 2D-micromechanical model of a crack in a CMC material (1,2). The model places a semi-infinite crack in a linear-elastic body and simulates the bridging fibers by crack closure forces placed along the crack face. The forces applied by the fibers to the crack face are calculated using an explicit frictional bridging model that calculates the fiber load transfer as a function of distance from the crack-tip. A basic result of the model is to predict crack-tip screening over a range of crack extension (R-curve behavior) when high-strength fibers and weak interfaces are present (1,2).

The model is used to explore the time-dependence of crack growth by allowing the crack-closure forces to undergo time-dependent relaxation. Available creep data for Nicalon fibers at 1100°C in pure Ar (14) were used to construct a constitutive equation for the stress- and time-dependence of creep in Nicalon fibers at 1100°C. Based on this approach, the discrete micromechanics model is used to calculate the crack velocity using a quasi-static approach (2).

Using a definition for the stress intensity for an equilibrium bridging zone, an expression was derived for the velocity of a crack in a composite at equilibrium, which gives a quasi-static approximation to the crack velocity. For this approximation, it is assumed that the bridging zone is in equilibrium by virtue of a balance between crack advance and relaxation of bridging zone stresses. As the crack advances, it bridges additional fibers, which retards its growth. As the stresses in the bridging zone relax, the crack-tip screening is reduced, and the crack tends to advance.

The quasi-static approximation assumes that K_{tip} is a constant such that

$$K_{tip}(a,t) = C \rightarrow dK_{tip} = 0 \tag{6}$$

Therefore, one can write the total differential of K_{tip} as

$$dK_{tip} = \frac{\partial K_{tip}}{\partial a} da + \frac{\partial K_{tip}}{\partial t} dt \tag{7}$$

which was used to derive an expression for crack velocity, V_c, as

$$V_c = \frac{da}{dt} = -\left(\frac{\frac{\partial K_{tip}}{\partial t}}{\frac{\partial K_{tip}}{\partial a}} \right) \tag{8}$$

where the crack velocity is expressed as the ratio between the time-dependence of K_{tip} due to stress relaxation of bridging forces, $\partial K_{tip}/\partial t$, and the change in K_{tip} due to crack advance, $\partial K_{tip}/\partial a$. Reducing the crack-closure (fiber bridging) forces as a function of time, due to either stress relaxation in the fibers (Figure 4) or removal of the interface, allows the crack to extend during the load step. The agreement of the predicted velocities, as well as the time-dependence, suggests that fiber creep is controlling SCG in the pure Ar environment at 1100°C. Other relaxation processes, such as interface removal, would be expected to occur in O_2. This relaxation process would be faster than for fiber creep alone because the fiber/matrix interface is simultaneously being removed by oxidation. This process would reduce the fiber/matrix interfacial shear strength as a function of time. A faster stress

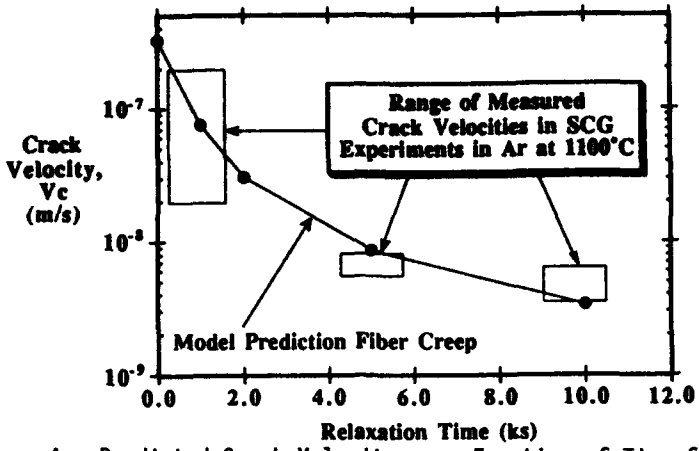

Figure 4 - Predicted Crack Velocity as a Function of Time for the Case of Stress Relaxation Due to Fiber Creep.

relaxation shifts the onset of accelerated cracking (stage-III) to lower K_A values and increases the relative crack velocities in the stage-II region.

The crack velocity-time data in O_2 (Figure 2) indicates that velocities are increasing with time, which cannot be accounted for using a logarithmic function for $K_{tip}t$, such as that used for fiber creep. A linearly increasing $K_{tip}(t)$ will give a constant crack velocity, while a power-law function would be required to account for increasing velocities with time. Such a result would have to come from a model of interface removal and subsequent bridging zone relaxation, which remains to be accomplished.

Summary and Conclusions

SCG in continuous-fiber CMC materials at 1100°C in pure Ar exhibits a stage-II region where crack velocity depends weakly on the applied stress intensity. At higher stress intensities, the crack velocity is accelerated, and a power-law (stage-III) region is observed where crack velocity depends strongly on stress intensity. The stage-II region corresponds to the development of the fiber bridging zone in the wake of the crack. It was observed that crack velocities increase at 1100°C in Ar plus O_2 compared to pure Ar. It was also observed that O_2 shifted the onset of stage-III to lower values of applied stress intensity. These observations were rationalized using a 2D-micromechanical model developed to simulate cracks bridged by continuous fibers. Fiber creep relaxation predicted the correct crack velocity and time-dependence in Ar, but other mechanisms, such as interface removal, are required to rationalize the data in Ar plus O_2.

Acknowledgments

This work was supported by Basic Energy Sciences under U.S. Department of Energy (DOE) Contract DE-AC06-76RL0 1830 with Pacific Northwest Laboratory, which is operated for DOE by Battelle Memorial Institute.

References

1. C. H. Henager, Jr. and R. H. Jones, "The Effects of an Aggressive Environment on the Subcritical Crack Growth of a Continuous-fiber Ceramic Composite," Ceramic Eng. Sci. Proc., 13 (7-8) (1992), 411-419.

2. C. H. Henager, Jr. and R. H. Jones, "High-Temperature Plasticity Effects In Bridged Cracks and Subcritical Crack Growth in Ceramic Composites" (Accepted for publication in Mater. Sci. and Engr.

3. J. L. Henshall, "The Mechanism and Mechanics of Subcritical Crack Propagation in Hot-Pressed SiC Above 1000°C," Advances in Fracture Research (Fracture 81), D. Francois, ed., Pergamon Press, NY (1981), 1541-1549.

4. D. C. Larsen, J. W. Adams, S. A. Bortz, and R. Ruh, "Evidence of Strength Degradation by Subcritical Crack Growth in Si_3N_4 and SiC," Fracture Mechanics of Ceramics, Vol. 6, R. C. Bradt et al., eds., Plenum Press, NY (1983), 571-585.

5. H. Cao, B. J. Dalgleish, C. Hsueh, and A. G. Evans, "High Temperature Stress Corrosion Cracking in Ceramics," J. Am. Ceram. Soc., 70 (1987), 257-264.

6. J. L. Smialek and N. S. Jacobson, "Mechanism of Strength Degradation for Hot Corrosion of α-SiC," J. Am. Ceram. Soc., 69 (1986), 741-752.

7. C. H. Henager, Jr. and R. H. Jones, "Environmental Effects on Slow Crack Growth in Silicon Nitride," Ceramic Eng. Sci. Proc., 9 (9-10) (1988), 1525-1530.

8. C. H. Henager, Jr. and R. H. Jones, "Molten Salt Corrosion of Hot-Pressed Si3N4/SiC-Reinforced Composites and Effects of Molten Salt Exposure on Slow Crack Growth of Hot-Pressed Si_3N_4," in Corrosion and Corrosive Degradation of Ceramics, Ceramic Transactions, V. 10, R. E. Tressler and M. McNallen, eds., American Ceramics Society, Westerville, OH (1990), 197-210.

9. A. G. Evans, "Perspective on the Development of High-Toughness Ceramics," J. Am. Ceram. Soc., 73 (1990), 187-206.

10. E. A. Gulbransen and S. A. Jansson, Oxid. Met., 4 (1972), 181.

11. N. S. Jacobson, A. J. Eckel, A. K. Misra and D. L. Humphrey, J. Am. Ceram. Soc., 73 (1990), 2330.

12. D. R. Curran and M. F. Amateau, Am. Ceram. Bull., 65 (1986), 1419.

13. J. W. Cree and M. F. Amateau, J. Am. Ceram. Soc., 70 (1987), C-318.

14. G. Simon and A. R. Bunsell, "Creep Behavior and Structural Characterization at High Temperatures of Nicalon SiC Fibres," J. Mater. Sci., 19 (1984), 3658-3670.

HYDROGEN AND TITANIUM BASE MATERIALS

Howard G. Nelson

NASA Ames Research Center
MS 213-3
Moffett Field, CA 94035-1000

Abstract

Titanium base materials in intermetallic form and/or as a fiber reinforced composite are extremely attractive for high temperature structural applications where high specific strength and stiffness are required. Significant problems arise with these materials when hydrogen is present in the service environment. Unlike most other structural materials, titanium will absorb more hydrogen at low temperatures than at high and can readily form embrittling titanium hydride phases. The degrading effects of hydrogen on the presently available high temperature, titanium base structural materials are reviewed. The critical issue of the present lack of a reliable, light weight, high temperature structural material for aerospace applications when hydrogen is present is discussed.

Critical Issues in the Development of High Temperature Structural Materials
Edited by N.S. Stoloff, D.J. Duquette and A.F. Giamei
The Minerals, Metals & Materials Society, 1993

Introduction

Titanium base materials are very attractive for structural applications in advanced aerospace vehicles. Because of titanium's low density, the elevated temperature specific strength, stiffness, and creep behavior of these materials far exceed those of the superalloys and even exceed the advanced carbon-carbon composite materials and the ceramic matrix composite materials up to reasonably high temperatures (1). For example, the silicon carbide fiber reinforced, beta phase titanium matrix composite has a maximum useful operating temperature of about 800°C, the Ti_3Al (alpha-2 phase) intermetallic base alloys can operate up to about 900°C, and the TiAl (gamma phase) intermetallic base alloys up to about 1000°C.

When these titanium base materials are considered for structural applications on airbreathing, hot structured, hypersonic vehicles, however, difficulties are encountered. High speeds at low altitudes result in extremely high structural temperatures. Outer skin temperatures can approach 2000°C (2). Additionally, propulsion systems are complex and can require a combination of rockets, ramjets, and scramjets. Ramjets can operate effectively to between Mach 3 and 5 but above Mach 5 scramjets (supersonic combustion ramjets) or rockets are required. To attain these hypersonic velocities, only hydrogen as a fuel has the required propulsive efficiency. Specific impulse (a measure of propulsive efficiency) of hydrogen-fueled propulsion systems is always greater than that of hydrocarbon-based fuels and, above about Mach 5, only a hydrogen-fueled propulsion system is capable of attaining the velocity required for orbital insertion (3).

Unfortunately, it has been known for years that the interaction of hydrogen with most titanium base alloys can be extreme (4). Equilibrium hydrogen solubility in titanium decreases with increasing temperature (5). In the relatively open (bcc), elevated temperature, beta phase of titanium, hydrogen solubility can be large, approaching 60 atomic % at 600°C. Hydrogen will stabilize the beta phase and can reduce the beta-transus temperature from 885°C to 350°C. In contrast, the more closed (hcp), low temperature, alpha phase of titanium exhibits a maximum hydrogen solubility of only about 10 atomic % (at 350°C,) becoming nearly negligible at room temperature. When the hydrogen concentration exceeds these solubility limits, titanium hydrides will begin to precipitate (6). Even with the inherent incompatibilities between hydrogen and titanium, titanium base alloys have been used extensively to contain hydrogen in critical applications such as in the Space Shuttle Main Engine (6). Such applications usually involve hydrogen at cryogenic temperatures where insufficient thermal energy is present to dissociate the hydrogen molecule or about room temperature where the normally present oxide film on the titanium can act as an effective hydrogen barrier to isolate the titanium from the active hydrogen environment (4).

Although titanium base materials have been used extensively in a variety of aerospace structural applications, consideration of their use as high temperature structures has only been recent. In advanced hypersonic vehicles, it is highly desirable to take advantage of the excellent high temperature specific properties of titanium base alloys for hydrogen containment during fuel handling, in actively cooled structures, and as primary airframe structure exposed to a casual or residual hydrogen environment. The purpose of this paper is to review our present understanding of the hydrogen interactions with titanium base materials. We will first consider the hydrogen interaction with both monolithic beta phase titanium and silicon carbide fiber reinforced beta titanium matrix composites, potential hot structure airframe materials. Next, we will consider the Ti_3Al (alpha-2 phase) titanium aluminide intermetallic base alloys as potential hydrogen plumbing and actively cooled structures. Finally, we will consider the TiAl (gamma phase) titanium aluminide intermetallic base alloys for heat exchanger applications along the propulsion flow path. Based on our present understanding, we will conclude that presently available high temperature titanium base materials can not be reliably used in direct contact with a hydrogen containing environment. Therefore, the development of a reliable, light weight, high temperature structural material for aerospace applications where hydrogen is present is a critical issue that is begging for our attention.

Hydrogen and the Beta Titanium Phase

In the past, beta phase titanium alloys have been thought to be fairly resistant to hydrogen since hydride formation requires large hydrogen concentrations (8). At elevated temperatures, hydrogen diffusion in the open bcc beta titanium lattice becomes very rapid (9) and large amounts of hydrogen can be absorbed in the beta phase even at very low hydrogen pressures (much less that one atmosphere pressure) (6) in very short times (10). Hydrogen in a beta alloy will further stabilize the beta phase at the expense of any remaining alpha phase (6). The precipitation of fine, acicular alpha phase is the primary strengthening mechanism in most beta alloys and thus, the strength of these alloys decrease with increasing amounts of absorbed hydrogen (11). Recently, it has been observed that hydrogen in beta titanium lattice can have a significant influence on the ductile-to-brittle fracture transition in the beta phase alloys (10-12).

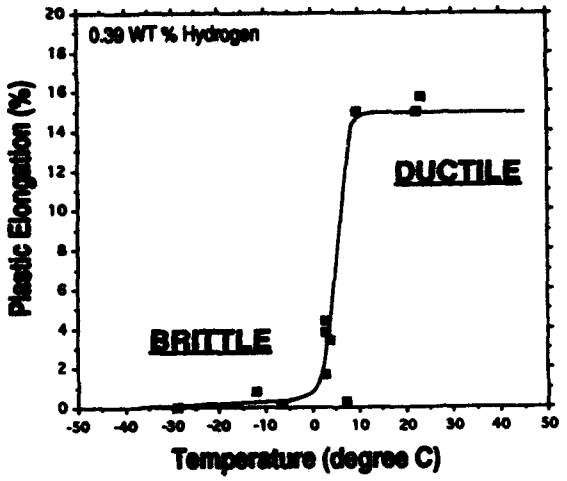

Figure 1 - Ductile-to-brittle fracture transition observed in the Beta 21S titanium alloy containing 0.39 wt percent hydrogen.

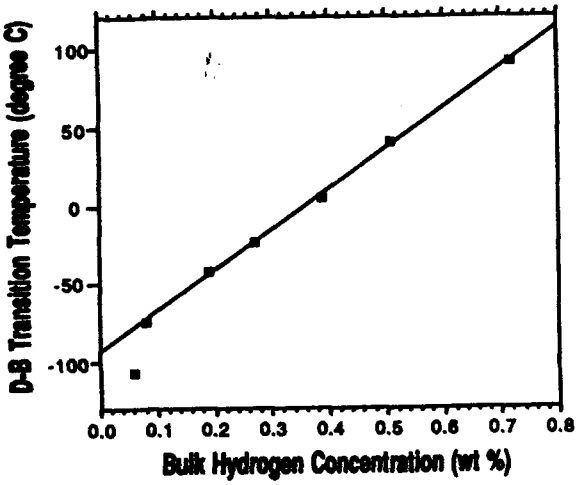

Figure 2 - The influence of bulk hydrogen concentration on the ductile-to-brittle fracture transition in the Beta 21S titanium alloy.

A typical example of the hydrogen influence on ductile-to-brittle fracture transition is shown in Fig. 1. These data were obtained on 0.063 cm (0.025 in.) thick, monolithic Beta 21S (Ti-15Mo-2.6Nb-0.2Si-3Al) titanium alloy sheet that had been exposed at 704°C to a 2.7 kPa (20 torr) hydrogen environment for a sufficient length of time 18 ks (5 hours) to establish equilibrium between hydrogen in the environment and that in the bulk (total pick-up of 0.39 wt percent hydrogen). The ductile-to-brittle transition is sharp and exhibits a corresponding change in fracture mode from transgranular, ductile, microvoid coalescence at the higher test temperatures to nearly complete transgranular, brittle cleavage at the lower temperatures. The temperature of this ductile-to-brittle transition can be changed significantly by the amount of hydrogen in the bulk of the alloy, as shown in Fig. 2. Uncharged material exhibits a transition temperature of around -130°C but can be raised to about 100°C with a bulk hydrogen concentration about 0.72 wt percent.

The effect of hydrogen on the ductile-to-brittle transition temperature appears to be the result of restricting slip behavior to increase the yield stress (13) and/or lowering the fracture stress of

the material (11). Equilibrium hydrides would not be expected to form at these bulk hydrogen concentrations in the beta phase (14) and have not been observed using the X-ray diffraction technique at hydrogen concentrations up to 49 atomic percent (11). What appear to be metastable hydrides have been found within the grains of this beta alloy at these hydrogen concentrations, but there appears to be little or no correlation to the occurrence of the ductile-to-brittle transition (15, 16).

Hydrogen has been found to affect the beta phase titanium matrix of a silicon carbide fiber reinforced composite in much the same manner as it does the monolithic material. An elevated temperature pre-exposure to a low pressure hydrogen environment can cause a severe degradation in room temperature tensile behavior (10). Degradation in the composite appears to be the result of the hydrogen interaction with the bulk, beta matrix. Figure 3 shows the tensile behavior of a beta matrix, silicon carbide reinforced composite laminate after long-time exposures (sufficient time to allow equilibrium to be established between hydrogen in the environment and hydrogen in the beta lattice) at 650°C and three hydrogen pressures. As can be seen, the severity of embrittlement is dependent on hydrogen pressure. Equilibrium absorption under 533 Pa (4 torr) hydrogen is seen to be insufficient to cause a significant change in room temperature tensile behavior. After equilibrium exposure to 1.333 kPa (10 torr) hydrogen, room temperature behavior is significantly degraded, with the primary effects being a change in the modulus of the composite and a reduction in strength. After equilibrium with a 8.36 kPa (62 torr) hydrogen environment, the laminate is severely degraded, with matrix cracking beginning on initial loading and ultimately resulting in a nearly complete loss in the structural integrity of the composite laminate.

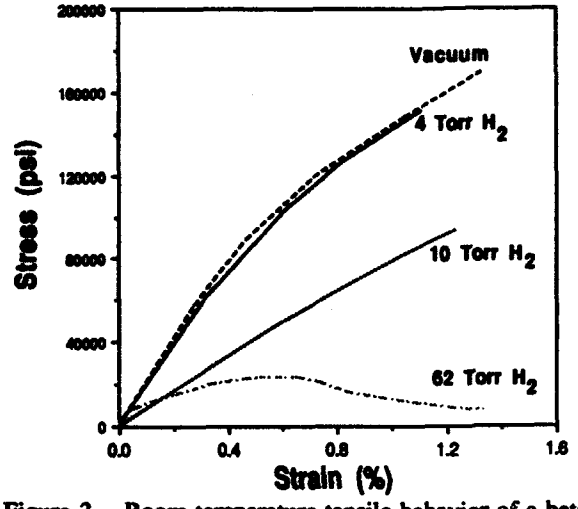

Figure 3 - Room temperature tensile behavior of a beta titanium matrix, silicon carbide fiber reinforced composite following equilibrium exposures at 650°C to three different hydrogen pressures.

As would be expected, the fracture surfaces of the composite laminate reflect the degree of hydrogen degradation occurring in the beta phase matrix. As shown in Fig. 4, the laminate exposed to a vacuum environment exhibits ductile, transgranular failure of the beta matrix by microvoid coalescence. After a 1.333 kPa (10 torr) hydrogen exposure at 650°C (Fig. 4), the fracture morphology of the beta matrix material is brittle with transgranular fracture occurring by cleavage.

Hydrogen and the Alpha-2 (Ti_3Al) Titanium-Aluminide Phase

Alpha-2 titanium-aluminide (nominally Ti_3Al) is an ordered intermetallic phase having a modified hcp (DO_{19}) crystal structure. Like many other intermetallics, the titanium aluminides can exhibit low ductility and poor fracture toughness at low temperatures (1). Low temperature ductility in alpha-2 base alloys has been improved significantly by the addition of alloying elements such as Nb, V, and Mo and the selection of heat treatments that force the retention of the more ductile transformed beta titanium phase in the primarily alpha-2 microstructure (1).

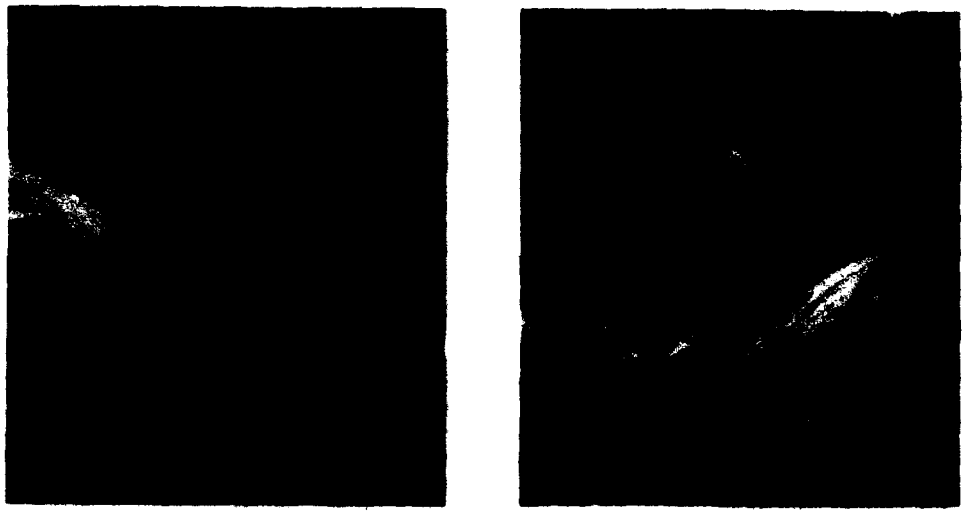

Figure 4 - A comparison of room temperature matrix fracture morphology of a silicon carbide fiber reinforced Beta 21S titanium matrix composite after equilibrium exposure at 650°C to (a) a vacuum environment and (b) a hydrogen environment at 1.333 kPa.

Hydrogen interactions with alpha-2 base alloys are similar to those observed in other titanium base alloys. Hydrogen has the potential to influence microstructural stability of the alpha-2 base alloys and to produce damaging hydride phases. Although hydrogen has been shown to stabilize the beta phase, its influence appears to be less than that exhibited on the alpha containing titanium alloys (17). Additionally, in alpha-2 based alloys that contain the beta stabilized phase, hydrogen has been thought to assist the formation of an orthorhombic phase (Ti_2AlNb) (18). Thus far, there is little evidence that these hydrogen-induced changes in microstructure have a significant effect on the mechanical behavior of alpha-2 base alloys. The primary influence of hydrogen on the titanium aluminide intermetallics appears to be the formation of degrading titanium hydride phases.

Although the hydrogen solubility limit in alpha-2 is quite large at elevated temperatures, approaching 15 atomic percent at 650°C in the Ti-24Al-11Nb alloy (19), essentially all of this hydrogen will precipitate upon cooling as some form of titanium hydride. The fcc delta hydride phase has been observed in alpha-2 alloys as have more complex hydride phases (20-22).

The effects of hydrogen on the mechanical behavior of the modified hcp alpha-2 titanium aluminide base alloys are much like those observed in the hcp alpha titanium base alloys (4). If hydrogen is allowed to enter the bulk of the material at elevated temperature, hydrides will precipitate on cooling and will degrade the mechanical behavior of the alloy. Significant changes in critical properties such as fracture toughness, threshold stress intensity for the initiation of cracking, and fracture stress have been observed (23). Further, large hydrogen pressures are not required. Significant degradation can result from an elevated temperature exposure to a hydrogen environment at pressures of much less than one atmosphere. Under extreme conditions of high pressure or long times, sufficient hydrogen can be absorbed into the alpha-2 phase to cause the complete disintegration of the material (essentially the complete conversion of the alpha-2 base alloy to titanium hydride). Additionally, like the alpha base alloys (4), embrittlement of alpha-2 base alloys can occur as the result of exposure to a hydrogen environment at low temperatures as well (24).

Finally, the microstructural details of alpha-2 base alloy play an important role in determining the severity of hydrogen-induced degradation. It has been shown that the Ti-24Al-11Nb alloy will exhibit a complete loss in tensile ductility at a bulk hydrogen concentration as low as 300 weight ppm when the microstructure is equiaxed. When the microstructure is in the form of a course basketweave, a bulk hydrogen concentration of about 500 weight ppm is required for complete embrittlement. A fine basketweave microstructure exhibits a tolerance to hydrogen contents up to about 1500 weight ppm (25). These observations are most probably due to the variation in the amount and distribution of the more hydrogen soluble beta phase in these microstructures.

Hydrogen and the Gamma (TiAl) Titanium-Aluminide Phase

The gamma titanium aluminaide intermetallic phase (TiAl) has an ordered fct ($L1_0$) lattice structure. Gamma base alloys are either single phase gamma (TiAl) or alloys with some retained alpha-2 (Ti_3Al) phase. The metallurgy of these alloys is not yet well understood and, as a consequence, no mechanism has been identified to effectively reduce the severe loss in ductility at low temperatures. Initial studies on the effects of hydrogen indicate that the amount of hydrogen absorbed into gamma base alloys was small, and thus, these alloys appeared be resistant to degradation from a hydrogen environment. However, this is not the case. It now appears that these initial results were due to the ability of the oxide film on these higher aluminum containing alloys to serve as a partial hydrogen barrier. Although hydrogen absorption in gamma is less than in alpha-2, it can be significant (26, 27). The solid solution solubility limit for hydrogen in gamma has not been reported; however, the total hydrogen uptake (hydrogen in solution and as a hydride) in gamma base alloys has been shown to be large at elevated temperatures and pressures (27). It appears that at room temperature very little hydrogen can be held in solution in the gamma lattice and extensive precipitation of a hydrides will occur (28, 29). The fcc delta hydride has been observed as have far more complex hydrogen containing phases, some exhibiting significant volume contraction compared with the host gamma phase (30).

Hydrogen degradation in the mechanical properties of gamma base alloys can occur at an elevated temperature in a high pressure (≈13.8 MPa) hydrogen environment (31) and at room temperature after elevated temperature hydrogen charging (31-34). Like the alpha-2 intermetallic base alloys, the primary cause of degradation in gamma appears to be the formation of hydride phases. Somewhat conflicting studies have been reported on the effect of a low pressure hydrogen environment on the gamma phase intermetallic. No significant degradation of a near alpha-2 alloy was observed either after an elevated temperature pre-exposure to a low pressure (≈0.1 MPa) hydrogen environment or during testing in a low pressure hydrogen environment at room temperature (31). In contrast, tensile tests performed on polysynthetically twinned crystals of TiAl indicate a significant reduction in ductility when tests were conducted in a low pressure (≈0.1 MPa) hydrogen environment (35). In the latter study, the mechanism of degradation was suggested to be decohesion rather than the presence of titanium hydrides.

Summary

Without question, titanium base materials are important aerospace structural materials because of their low density, good mechanical properties, and superior corrosion resistance. In the form of fiber reinforced composites and as titanium aluminide intermetallics, they show promise as high temperature structural materials. For some advanced, hot structure, aerospace vehicle applications, their use can be considered critical. No other structural material offers such high specific strength and stiffness up to temperatures approaching 1000°C in combination with good oxidation resistance. Problems arise, however, when hydrogen comes in contact with titanium base materials. Titanium has a great affinity for hydrogen. Unlike most other common structural materials, hydrogen has a greater solubility in titanium at low temperatures than at high. Consequently, it is difficult to remove hydrogen from a titanium structure once it has been absorbed. Structures that are thermally cycled, if hydrogen saturation is not achieved during the first cycle, will continue to pick-up additional hydrogen with each thermal cycle until saturation is achieved. Great quantities of hydrogen can be absorb by some titanium

alloys, particularly at moderate temperatures. Once hydrogen is present in the titanium lattice, titanium hydrides can be precipitated. Generally speaking the hydrides are brittle and can degrade the mechanical behavior of titanium base alloys, particularly at lower temperatures.

Beta phase titanium, a common matrix material for fiber reinforced titanium matrix composites, has been shown be severely degraded by the exposure to an elevated temperature hydrogen environment. Although beta phase titanium can hold large quantities of hydrogen (≈50 atomic %) in solid solution before hydrides begin to precipitate, equilibrium hydrogen solubility under low hydrogen pressures (≈0.1 MPa) is very large and hydrogen pick-up at elevated temperatures is very rapid. The precipitation of titanium hydride in beta titanium can cause severe cracking and the ultimate disintegration of the material. Hydrogen concentrations in the beta lattice at levels below the hydride solvus has also been shown to degrade this material. The presence of hydrogen has a strong effect on the ductile-to-brittle fracture transition temperature in this bcc titanium phase. It appears that hydrogen can lower the fracture stress and raise the transition temperature from below about -130°C in a hydrogen free material to above 100°C following a high temperature, low pressure hydrogen exposure. An exposure of a silicon carbide fiber reinforced beta matrix composite laminate to a 1.33 kPa (10 torr) hydrogen environment at 650°C is sufficient to significantly degrade room temperature tensile behavior.

The titanium aluminide intermetallics (Ti_3Al and TiAl), although originally thought to be fairly resistant to degradation from a hydrogen environment, have been shown to be significantly degraded by hydrogen as well. The primary mechanism of degradation appears to be the formation of titanium hydride phases. The alpha-2 intermetallic (Ti_3Al) appears to behave in a manner similar to alpha phase titanium. Hydrides readily form in the alpha-2 phase and can cause severe loss in ductility both during exposure to a low pressure (≈0.1 MPa) hydrogen environment at low temperatures and after low pressure hydrogen charging at elevated temperatures. The gamma intermetallic (TiAl) appears more resistant to hydrogen than the alpha-2 phase, but still can be degraded by the formation of hydride phases. Degradation has been demonstrated at elevated temperatures during exposure to a high pressure (13.8 MPa) hydrogen environment and at room temperature after an elevated temperature, high pressure hydrogen pre-exposure. Presently, it is not clear whether or not gamma base materials will be degraded by the presence of a low pressure hydrogen environment.

At present, titanium base materials whether in the form of a metallic matrix composite or as a titanium aluminide intermetallic, when used in hot structure applications, appear to be incompatible with a hydrogen containing environment. The availability of a light weight structural material having good thermal-mechanical behavior and a demonstrated compatibility with hydrogen appears critical to the success of many future, advanced, hydrogen-fuel, aerospace vehicles. Without question, the development of such a material offers a significant challenge to the high temperature materials technologist.

References

(1) R. E. Anderson et al, "High Temperature Titanium Alloys," NASP Contractor Report 1130 (Wright-Patterson AFB, OH: NASP Joint Program Office, 1992).

(2) Morris A. Steinberg, "Materials for Aerospace," Scientific American, October (1986), 67-72.

(3) "NASP: Expanding Space Launch Opportunities," Aerospace Engineering, November (1991), 15-17.

(4) Howard G. Nelson, "Hydrogen Embrittlement," Treatise on Materials Science and Technology, Vol. 25, Embrittlement of Engineering Alloys, ed. C. L. Briant and S. K. Banerji, (New York, NY: Academic Press, 1987), 275-359.

(5) A. D. McQuillan, "An Experimental and Thermodynamic Investigation of the Hydrogen Titanium System," Proc. Roy. Soc. London, 204 (1950), 309-323.

(6) S. L. Ames and A. D. McQuillan, "The Resistivity-Temperature-Concentration Relationships in β-Phase Titanium-Hydrogen Alloys," Acta Metallurgica et Materiala, 4 (1956), 602-610.

(7) R. P. Jewett et al, "Hydrogen Environment Embrittlement of Metals," A NASA Technology Survey, NASA CR-2163 (Washington, DC: NASA, 1993).

(8) N. E. Paton et al, "The Effect of Hydrogen and Temperature on the Strength and Modulus of Beta Phase Ti Alloys," Hydrogen Effects in Metals, ed. M. Bernstein and A. Thompson (Warrendale, PA: The Metallurgical Society, 1980), 269-279.

(9) W. R. Holman et al, "Hydrogen Diffusion in a Beta-Titanium Alloy," Metallurgical Transactions, 233 (1965), 1836-1839.

(10) H. G. Nelson, "Hydrogen Environment Effects on Advanced Alloys and Composites in Aerospace Structures," Thermal Structures and Materials for High Speed Flight, ed. E. A. Thornton, (Washington, DC: American Institute of Aeronautics and Astronautics, 1992), 383-399.

(11) D. A. Hardwick and D. G. Ulmer, "Effect of Hydrogen Exposure on the Microstructure and Mechanical Properties of the Titanium Alloy, Beta 21S," Second Workshop on Hydrogen Effects on Materials in Propulsion Systems, eds. B. N. Bhat, R. L. Dreshfield, and E. J. Vesely, Jr., NASA Conference Publication 3182, (Washington, DC: NASA, 1992), 227-234.

(12) H. G. Nelson, "Hydrogen Effects in Advanced Aerospace Materials," Second Workshop on Hydrogen Effects on Materials in Propulsion Systems, eds. B. N. Bhat, R. L. Dreshfield, and E. J. Vesely, Jr., NASA Conference Publication 3182, (Washington, DC: NASA, 1992), 2-11.

(13) L. M. Hartman and R. P. Gangloff, "Hydrogen Environment Embrittlement of Beta Titanium Alloys," to be published in the Proceedings of the Seventh World Conference on Titanium, ed. S. H. Froes, (Warrendale, PA: The Metallurgical Society, 1992).

(14) G. A. Young, Jr., and J. R. Scully, "Effects of Hydrogen on the Mechanical Properties of a Ti-Mo-Nb-Al Alloy," Scripta Metallurgica et Materiala, 28 (1993), 507-512.

(15) I. M. Robertson, private communication with author, University of Illinois at Urbana-Champaign, IL, October 1991.

(16) D. S. Schwartz, private communication with author, McDonnell Douglas Research Laboratories, St. Lois, MO, October 1991.

(17) W.-Y. Chu and A. W. Thompson, "Effect of Hydrogen as a Temporary b Stabilizer on Microstructure and Brittle Fracture Behavior in a Titanium Aluminide Alloy," Metallurgical Transactions A, 22A (1991), 71-81.

(18) D. Banerjee et al, "A New Ordered Orthorhombic Phase in a Ti_3Al-Nb Alloy," Acta Metallurgica et Materiala, 36 (1988), 871-882.

(19) W.-Y. Chu, A. W. Thompson and J. C. Williams, "Hydrogen Solubility in a Titanium Aluminide Alloy," Acta Metallurgica et Materiala, 40 (1992), 455-462.

(20) D. S. Shih, G. K. Scarr and G. E. Wasielewski, "On Hydrogen Behavior in Ti_3Al," Scripta Metallurgica et Materiala, 23 (1989), 973-978.

(21) D. B. Allen and A. W. Thompson, "Hydrides in Ti_3Al Alloys," Second Workshop on Hydrogen Effects on Materials in Propulsion Systems, eds. B. N. Bhat, R. L. Dreshfield, and E. J. Vesely, Jr., NASA Conference Publication 3182, (Washington, DC: NASA, 1992), 243-251.

(22) D. S. Schwartz et al, "A Novel Hydride Phase in Hydrogen Charged Ti_3Al," Acta Metallurgica et Materiala, 39 (1991), 2799-2803.

(23) W.-Y. Chu and A. W. Thompson, "Hydrogen Effects on Brittle Fracture of the Titanium Aluminide Alloy Ti-24Al-11Nb," Metallurgical Transactions A, 32A (1992) 1299-1312.

(24) D. E. Matejczyk and R. P. Jewett, "Effect of Microstructure on Hydrogen Environment Embrittlement of Alpha-2 Titanium Aluminides," Summary Proceedings of the 2nd Workshop on Hydrogen-Material Interactions, ed. H. G. Nelson, NASP Workshop Publication 1004, (Wright-Patterson AFB, OH: NASP Joint Program Office, 1988), 137-139.

(25) K. S. Chan, "Developing Hydrogen-Tolerant Microstructures for an Alpha-2 Titanium Aluminide Alloy," Metallurgical Transactions A, 23A (1992), 497-507.

(26) A. W. Thompson, W.-Y. Chu, and J. C. Williams, "Hydrogen in Titanium Aluminides," Summary Proceedings of the 2nd Workshop on Hydrogen-Material Interactions, ed. H. G. Nelson, NASP Workshop Publication 1004, (Wright-Patterson AFB, OH: NASP Joint Program Office, 1988), 133-135.

(27) B. S. Majumdar, H. J. Cialone, and J. H. Holbrook, "Solubility of High Pressure Hydrogen in TiAl, Ti_3Al, and Be at Elevated Temperatures, and Effects on Microstructures," Summary Proceedings of the 3rd Workshop on Hydrogen-Material Interactions, ed. H. G. Nelson, NASP Workshop Publication 1007, (Wright-Patterson AFB, OH: NASP Joint Program Office, 1990), 73-87.

(28) W.-Y. Chu and A. W. Thompson, "Effect of Microstructure and Hydrides on Fracture of TiAl," Scripta Metallurgica et Materiala, 25 (1991), 2133-2138.

(29) D. Legzdina, I. M. Robertson, and H. K. Birnbaum, "Hydride Structures in Ti-Aluminides Subjected to High Temperature and Hydrogen Pressure Charging Conditions," Summary Proceedings of the 4th Workshop on Hydrogen-Material Interactions, ed. H. G. Nelson, NASP Workshop Publication 1007, (Wright-Patterson AFB, OH: NASP Joint Program Office, 1993), 139-154.

(30) D. E. Matejczyk and C. G. Rhodes, "Second Phase Formation in Gamma Titanium Aluminide During High-Pressure Hydrogen Charging," Scripta Metallurgica et Materiala, 24 (1990), 1369-1373.

(31) A. A. Sheinker and S. M. El-Soudani," Gaseous Hydrogen Effects on Tensile Properties of Gamma Titanium Aluminide Alloys," Summary Proceedings of the 3rd Workshop on Hydrogen-Material Interactions, ed. H. G. Nelson, NASP Workshop Publication 1007, (Wright-Patterson AFB, OH: NASP Joint Program Office, 1990), 169-190.

(32) S. M. L. Sastry, W. O. Soboyejo, and R. J. Lederich, "Hydrogen Effects in Gamma Titanium Aluminides," Summary Proceedings of the 3rd Workshop on Hydrogen-Material Interactions, ed. H. G. Nelson, NASP Workshop Publication 1007, (Wright-Patterson AFB, OH: NASP Joint Program Office, 1990), 191-200.

(33) D. G. Ulmer and D. E. Matejczyk, "Fracture Behavior of Gamma Titanium Aluminides in Hydrogen," Summary Proceedings of the 3rd Workshop on Hydrogen-Material Interactions, ed. H. G. Nelson, NASP Workshop Publication 1007, (Wright-Patterson AFB, OH: NASP Joint Program Office, 1990), 201-203.

(34) R. J. Lederich, S. M. L. Sastry, and W. O. Soboyejo, "Effects of Internal Hydrogen on the Mechanical Properties of Titanium Aluminides," Summary Proceedings of the 4th Workshop on Hydrogen-Material Interactions, ed. H. G. Nelson, NASP Workshop Publication 1013, (Wright-Patterson AFB, OH: NASP Joint Program Office, 1993), 55-70.

(35) M. H. Oh et al, "Environmental Effects on the Room Temperature Ductility of Polysynthetically Twinned (PST) Crystals of TiAl," accepted in October 1992 for publication in Acta Metallurgica et Materiala.

PLASTICITY ENHANCEMENT MECHANISMS IN REFRACTORY METALS AND INTERMETALLICS

R. Gibala, H. Chang, C.M. Czarnik, K.M. Edwards and A. Misra

Department of Materials Science and Engineering
University of Michigan, Ann Arbor, Michigan 48109-2136 USA

Abstract

Plasticity enhancement associated with surface films and precipitates or dispersoids in bcc refractory metals is operative in ordered intermetallic compounds. Some results are given for NiAl- and $MoSi_2$-based materials. The monotonic and cyclic plasticity of NiAl at room temperature can be enhanced by surface films. Ductile second phases also enhance the plasticity of NiAl. $MoSi_2$ exhibits similar effects of surface films and dispersoids, but primarily at elevated temperatures. The plasticity enhancement is associated with enhanced dislocation generation from constrained deformation at the film-substrate or precipitate/ dispersoid-matrix interface of the composite systems.

Critical Issues in the Development of High Temperature Structural Materials
Edited by N.S. Stoloff, D.J. Duquette and A.F. Giamei
The Minerals, Metals & Materials Society, 1993

Introduction

The bcc refractory metals Nb, Ta, Mo, and W and ordered intermetallic compounds such as NiAl and $MoSi_2$ possess many desirable engineering properties, especially potentially high strength at elevated temperatures. However, a major difficulty in applications as structural materials has been a lack of adequate toughness at relatively low temperatures (1-3). These materials undergo brittle-to-ductile fracture transitions at temperatures from well below room temperature to above 1000°C that are dislocation-mobility limited, dislocation-density limited, or both. The brittle-to-ductile transition temperature (BDTT) can be associated with thermal-to-athermal dislocation glide transitions or with the onset of dislocation climb and/or diffusional creep processes(1-4).

Many approaches have been taken to reduce the BDTT of these materials, to enhance plastic flow, and to obtain increased toughness at relatively low temperatures(5,6). We examine two methods of plasticity enhancement, viz. surface film coatings and second phase particles(3). Such results have demonstrated that the ductility of bcc refractory metals can be greatly enhanced by these methods because a combination of dislocation-mobility and dislocation-density limitations can be overcome. The dislocation-mobility limitation follows from the large difference in intrinsic mobility between edge and screw dislocations in the bcc structure, whereas the dislocation-density limitation arises from a lack of surface or internal dislocation sources(3,7). For NiAl, there does not appear to be a large difference in edge and screw dislocation mobility for <001> glide dislocations(8-10), although <111> dislocations in <001>-oriented single crystals are characterized by a large mobility difference(11). For $MoSi_2$, insufficient knowledge exists concerning the relative mobilities of edge and screw dislocations or of the different dislocation types <100>, <110>, $\frac{1}{2}$ <111>, and $\frac{1}{2}$ <331>(12). However it is clear that there is negligible dislocation plasticity below ~900°C at normal strain rates(13), except under hardness indentations(14).

Experimental

Most experimental procedures have been described in other papers or theses given as references. Only brief descriptions of procedures pertaining to results described in this paper are given.

Stoichiometric polycrystalline NiAl for fatigue studies was prepared by hot extrusion of mild-steel-canned castings to an extrusion ratio of 6:1 at 1150°C. The equiaxed grain size was 100 μm. Texture analysis indicated a <111> fiber texture of 2 to 3 times random. Surface film coatings involved electroless Ni plating at 85°C to a thickness of 170 nm(9,15). Specimens of a Ni-30 at.% Al alloy used to demonstrate second-phase toughening of NiAl-based alloys were prepared by directional solidification (DS) to produce a two-phase β matrix of composition Ni-37 at.% Al with either discontinuous or continuous aligned γ' rods of composition Ni-27 at.% Al. The β phase matrix was single crystalline with a [001] orientation parallel to the growth direction. The γ' was aligned such that the Kurdjumov-Sachs orientation relationship existed. The bulk alloy contained about 40% β and 60% γ'. The DS Ni-30 at.% Fe-20 at.% Al alloy has been reported on in other papers(1,16-18). It is a lamellar $\beta+(\gamma+\gamma')$ single crystal composite with the same [001] growth-oriented β phase and Kurdjumov-Sachs orientation relationship between the β and γ phases. The $\gamma+\gamma'$ reinforcements constitute approximately 35 vol.% of the composite and have a composition Ni-38% Fe-13% Al. The β phase has a composition Ni-20% Fe-30% Al.

Experiments on monolithic $MoSi_2$ were done on powder processed materials. Most experiments were performed on -325 mesh powder obtained from Cerac, Incorporated, with some work on high purity, oxide-free powders prepared by mechanical alloying by Dr. R. Schwarz of Los Alamos National Laboratory (LANL). Most materials were tested in the hot-pressed condition, although some materials were additionally HIPed. The approximately equiaxed grain size was about 30 μm, and the materials were about 95-98% of theoretical density. No preferential texture was noted. Surface film coating experiments utilized PVD

electron beam deposition of ZrO_2 films 100 nm thick at 50°C. $MoSi_2$-TiC particulate composites were prepared by powder processing. TiC powders of 2.5-4 μm size with the stoichiometry $TiC_{0.95}$ were dry blended in a ball mill with commercial $MoSi_2$ powders in proportions to produce various $MoSi_2$-TiC composites. These materials were given identical hot pressing/HIPing treatments given to the monolithic $MoSi_2$ materials. The composites were usually 92 - 98% dense. The grain size of the $MoSi_2$ matrix was approximately 15-25 μm in these materials. The TiC particles were well distributed throughout the composite volume, but because of agglomeration varied from 5 μm to 45 μm, with a mean size of 10 μm.

Plastic strain controlled fatigue experiments were performed on polycrystalline NiAl using a MTS Model 810 servohydraulic machine and experimental methods described elsewhere(9,15). The specimens were 70 mm in length, with a 8 mm grip diameter, 3 mm gauge diameter, and 10 mm gauge length. Plastic strain ranges of 0.0002 - 0.0016 were used. The total strain rate during cyclic deformation was 10^{-4} s^{-1}. All tensile and compression tests of NiAl and Ni-30% Al and Ni-30% Fe-20% Al alloys were performed on an Instron Model 1137 machine at cross head speeds to give strain rates of 2-5 x 10^{-4} s^{-1}. Tensile specimens had gauge diameters of 2-3 mm, gauge lengths of 6-10 mm, and length-to-diameter ratios of at least 3. Compression specimens had similar gauge diameters, but lengths were cut to maintain a length-to-diameter ratio of 2. Most mechanical testing of $MoSi_2$ and $MoSi_2$-TiC composites was done in compression at an initial strain rate of 10^{-4} s^{-1} on specimens that were 6 mm x 3 mm x 3 mm in dimensions. Tests were done on an Instron Model 4507 machine in argon at 950-1200°C. Yttria was used as a platen lubricant to minimize friction. To examine surface film effects in ZrO_2-coated $MoSi_2$, we used microhardness indentation techniques. Diamond Vickers indentations at loads of 1 kgf were made at temperatures of 25-1300°C with a Nikon QM hot hardness tester, with at least five measurements made at each temperature. The $MoSi_2$ specimens were coated over one half of the indentation surface so that hardness measurements of uncoated and coated materials could be made on the same specimen at the same time.

Materials were examined by light optical, scanning electron, and transmission electron microscopies. Optical and SEM methods were employed to determine grain size, grain shape, second phase structure and distribution and deformation and fracture path morphologies on fracture surfaces and side surfaces. Conventional TEM on a JEOL 2000FX microscope was used to determine orientation relationships between phases in the two-phase microstructures and to analyze the dislocation substructures in each phase. High-resolution TEM (HRTEM) observations of the atomic structure of interfaces in two-phase alloys were made on a JEOL 4000EX microscope.

Results and Discussion

This paper illustrates that surface films and second phase particles enhance the plasticity of ordered intermetallic alloys in the manner observed for bcc refractory metals(3,7). We present new results on low-cycle fatigue of NiAl and on monotonic deformation of NiAl-based two-phase alloys, plus new observations on $MoSi_2$ and its alloys. The intent is to demonstrate that elastic and plastic constraint afforded by strong and adhering interfaces can generate dislocations into quasi-brittle matrix materials and afford plasticity that would not ordinarily occur in the uncoated or unalloyed matrix(3).

Surface Film Effects: NiAl

Several papers have demonstrated that surface films on NiAl and FeAl, in single crystal or polycrystalline form, can enhance the plasticity of the substrate material at room temperature(1,3,9,19-21). These effects can be manifested in tension, compression, cyclic deformation, and (in the present paper for $MoSi_2$) hardness experiments. The usual manifestation takes the form of reduced yield and flow stresses and increased strain to failure(19-21). Figure 1 illustrates an additional effect of surface films on the cyclic stress asymmetry of polycrystalline NiAl, which has a room-temperature tensile ductility of 1%. Ni

films have little effect on the monotonic tensile or compression deformation behavior, but do change the magnitudes of the tensile and compressive peak stresses during low-cycle fatigue. Note in Fig. 1 that the sign of the stress asymmetry is changed by the application of the surface film. In general, the effect of these Ni films, which induce a tensile stress in the substrate material(9), is to introduce a more negative stress asymmetry. The mechanism by which the stress asymmetry is changed has not been determined.

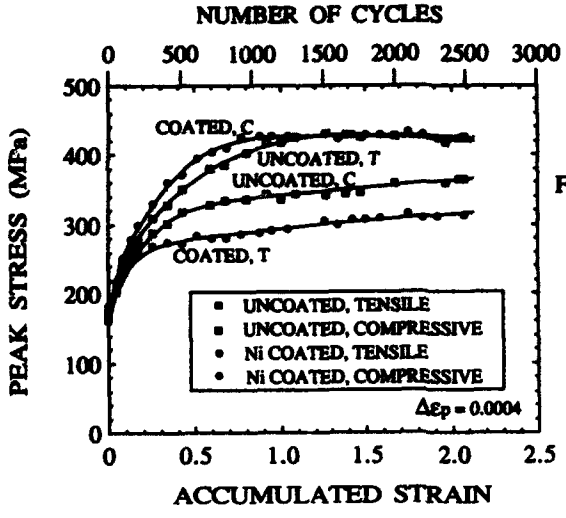

Fig. 1. Peak stress vs. accumulated strain for polycrystalline NiAl (100 μm grain size) illustrating the effect of a 170 nm electroless Ni film on the stress asymmetry.

Two other effects of cyclic deformation were noted in experiments on uncoated materials(15,22). [1] Step testing of NiAl indicates that cycling at lower plastic strain amplitudes can improve the cyclic life achievable at higher amplitudes. [2] Low amplitude cyclic prestrain can also significantly increase the monotonic yield and ultimate strength of the material, as shown in Fig. 2 for monotonic tension. Note that most of the tensile ductility of the unprestrained material is retained in the prestrained material, even though the strength is nearly doubled by cyclic prestrain and there is fractographic evidence of accumulated intergranular damage from the cyclic prestrain(15). Compressive strengths are similarly enhanced by cyclic prestrain without loss of monotonic plasticity.

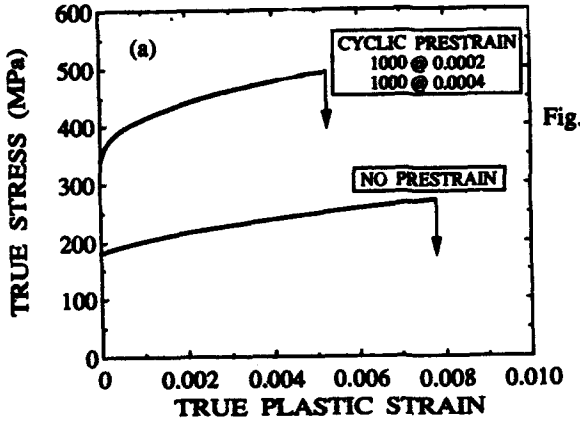

Fig. 2. The effects of cyclic prestrain on the tensile behavior of polycrystalline NiAl. The cyclic prestrain is given as the number of cycles at the plastic strain ranges employed.

Plasticity Enhancement from Second-Phase Interfaces: NiAl

The low ductility of ß-NiAl alloys near room temperature reflects the inability to generate and move a sufficient density of dislocations. We have found that interphase boundaries between the brittle ß-phase matrix and ductile γ' and $\gamma+\gamma'$ reinforcing phases in Ni-30%Al and Ni-30% Fe-20% Al DS alloys, respectively, are effective in enhancing plastic flow of the ß phase. The result is substantial tensile plasticity of the composite. Figure 3 demonstrates that both the binary and the ternary two-phase microstructures exhibit of the order 10% tensile elongation to fracture, even though the unconstrained matrix materials exhibit no tensile plasticity, as given for the Ni - 40% Al ß-phase alloy.

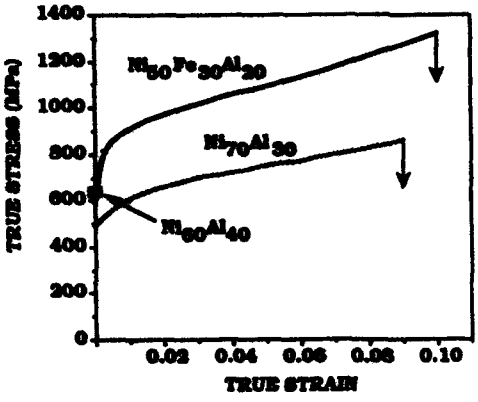

Fig. 3. True stress - true strain curves in tension at room temperature for a ß + γ' Ni-30 at.% Al alloy and a ß + ($\gamma+\gamma'$) Ni-30 at.% Fe-20 at.% Al alloy. For both materials, the ß phase matrix is brittle in the unconstrained state, as shown for the Ni-40 at.% Al alloy.

Observations of slip traces and dislocation substructures illustrate the effectiveness with which the normally brittle ß phase undergoes extensive plastic deformation during constrained deformation it receives during mechanical testing of these alloy composites. During deformation of the composite, the plastically softer γ' or $\gamma+\gamma'$ phases deform first. Slip impinges on the interface with ß and is transferred into the ß phase, which undergoes appreciable plastic deformation that it ordinarily would not have in monolithic form. The slip transfer process is greatly facilitated by the favorable alignment of slip planes and slip directions in the two phases afforded by the Kurdjumov-Sachs orientation relationship.

TEM observations of the interface structures in the NiAl-base alloys show that the ledge and facet structure of the interfaces can play a significant role in facilitating dislocation nucleation into the ß phase. This is demonstrated in Fig. 4, in which extensive dislocation pile-ups occur at the interface and cause nucleation of dislocations into the ß phase. Although dislocation nucleation and generation into the ß phase occur quasi-uniformly along the interface, there is particularly effective nucleation at the interfacial facets, afforded by the local stress concentration such steps produce under an applied stress.

Surface Film Effects: $MoSi_2$

In many respects, NiAl and $MoSi_2$ are similar types of dislocation-mobility and/or dislocation-density limited materials. Thus we also investigated possible surface-film and second-phase sources for dislocation generation processes in $MoSi_2$.

Surface film softening was investigated in polycrystalline $MoSi_2$ which was coated with 0.1 µm thick PVD-deposited ZrO_2. The two different substrate materials are a hot-pressed material of commercial powder from Cerac and a hot-pressed high purity material prepared by mechanical alloying at LANL (23). ZrO_2 was chosen as a surface film because it forms adherently on $MoSi_2$ by low-temperature PVD. Petrovic and co-workers (24) have also demonstrated that $MoSi_2$ composites containing ZrO_2 particles exhibit toughening that is not observed in ZrO_2-free materials.

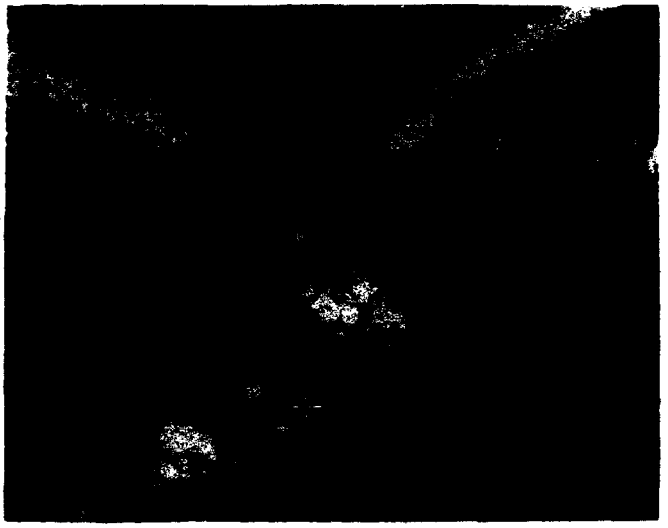

Fig. 4. Bright field TEM of dislocation substructures in the ß + (γ +γ') Ni-30 at.% Fe-20 at.% Al alloy deformed 2% in compression, showing dislocation nucleation in the brittle ß phase ahead of a dislocation pile-up in the (γ +γ') phase mixture. Dislocation nucleation is seen at the interfacial facets.

The experiments to investigate surface film softening of $MoSi_2$ by ZrO_2 films employed hot-hardness indentation testing at 25-1300°C. Hardness testing utilizes deformation under a large, essentially hydrostatic compressive stress state at large effective stresses and strain rates. Hence dislocation glide plasticity is operative throughout this temperature range of hardness measurements(25). Such conditions are optimum for observation of film softening, which has usually been observed in bcc refractory metals and B2 ordered alloys at relatively low homologous temperatures where the temperature dependence of the flow stress is very large and where dislocation glide predominates (3,7,19,20). In $MoSi_2$, the temperature dependence of the flow stress in compression is very large over the temperature range 900-1400°C, but the dominant dislocation mechanism changes from glide, to glide/climb, to climb, to diffusional creep with increasing temperature for slow strain rate monotonic testing(4). Consequently, hardness testing offers mechanistic simplicity that other testing does not.

The results of experiments on the two hot-pressed $MoSi_2$ materials are given in Fig. 5. Both uncoated materials exhibit a large temperature-dependent decrease in hardness as a function of temperature, and both coated materials exhibit a much smaller hardness relative to that of the respective uncoated materials. The amount of film-induced softening is larger for the higher purity material, as expected(3). Note that the ZrO_2 films are 0.1 µm in thickness compared to hardness indentation depths of 10 ± 5 µm. Hence the hardness test samples almost entirely the plastic zone of the substrate and not film properties. Experiments on single crystals are underway to elucidate the role of film properties in the hardness behavior in the film-coated materials.

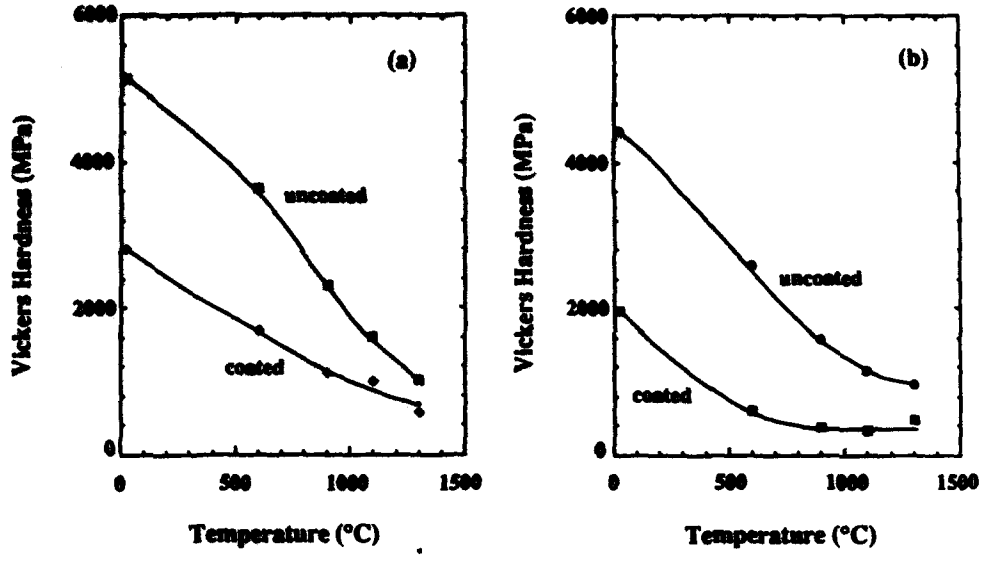

Fig. 5. Temperature dependence of the Vickers hardness of uncoated and ZrO_2-coated $MoSi_2$. (a) Commercially pure hot-pressed $MoSi_2$. (b) Mechanical alloyed $MoSi_2$.

Plasticity Enhancement from Second-Phase Interfaces: $MoSi_2$

Internal interfaces associated with second-phase precipitates or dispersoids in $MoSi_2$ should be capable of acting as effective dislocation sources in the same manner as for bcc refractory metals and B2 ordered alloys(1,3). We have been successful in observing enhanced dislocation generation and plasticity by TiC particles in $MoSi_2$(26). TiC is extremely hard at room temperature, but deforms appreciably with increasing temperature above 600-800°C. At temperatures above 900°C as a particulate addition to $MoSi_2$, it undergoes deformation prior to the $MoSi_2$ matrix and can lead to enhanced dislocation generation into the $MoSi_2$ in the manner illustrated for the two-phase NiAl-base alloys. An example of dislocation generation into the $MoSi_2$ matrix from the $MoSi_2$-TIC interface is given in Fig. 6 for a 10% TiC composite deformed 5% at 1150°C. The diffraction conditions preferentially disclose dislocations in the $MoSi_2$ matrix. Most of these dislocations are of the <100> type. Note the formation of an extensive low-angle boundary produced by dislocation recovery processes in the vicinity of the TiC particle. These boundaries form to a much greater extent in the composites than in monolithic $MoSi_2$ deformed under similar conditions and are associated with more effective dislocation generation in the $MoSi_2$-TiC composites. Such processes allow plastic deformation of the composites at lower temperatures than the monolithic material(26).

Some representative mechanical behavior data for $MoSi_2$ and a $MoSi_2$-10% TiC composite are given in Fig. 7. These materials have been prepared by hot pressing and HIPing to produce 98% of theoretical density and nearly the same grain sizes (28 μm and 25 μm, respectively)in both materials. The composite has a larger strength, exhibits greater total plasticity in compression, and reaches a steady-state of zero work hardening at smaller strains than the monolithic $MoSi_2$. The $MoSi_2$-TiC composites exhibit some plasticity at temperatures as low as 950°C, whereas comparable $MoSi_2$ exhibits completely brittle fracture with no plasticity at temperatures below 1050°C(26).

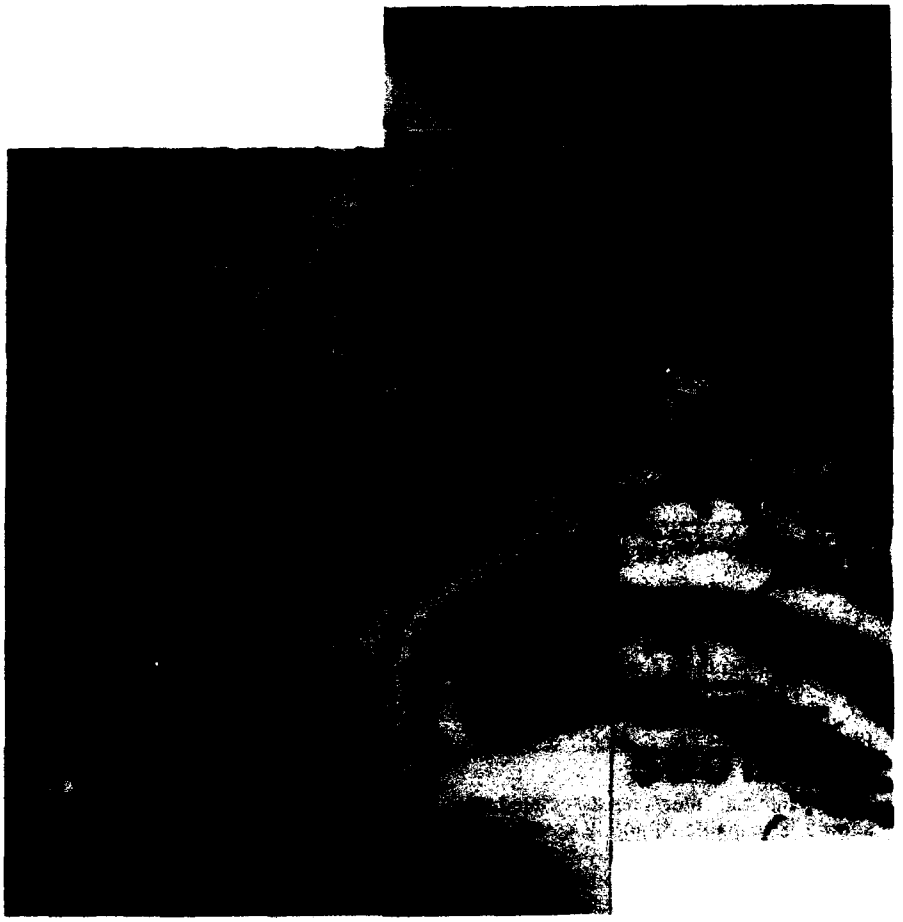

Fig. 6. TEM observation of dislocation substructures in the $MoSi_2$ matrix of a $MoSi_2$-10 vol.% TiC particulate composite deformed 5% at 1150°C. B = [331], g = $\bar{1}10$.

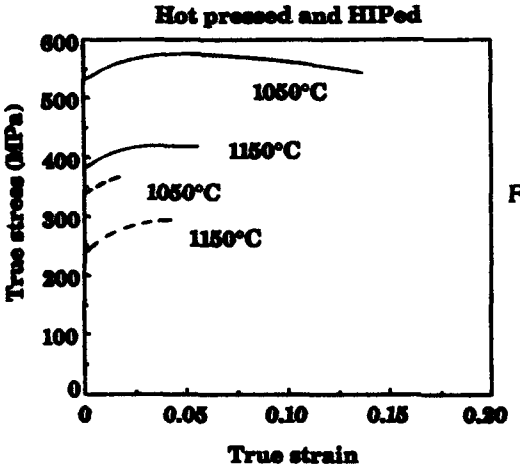

Fig. 7. True stress-true strain curves for hot pressed and HIPed $MoSi_2$ (dashed curves) and $MoSi_2$ - 10% vol.% TiC composites (solid curves) deformed at 1050°C and 1150°C. Initial strain rate is 10^{-4} s^{-1}.

Summary

We have demonstrated enhanced plasticity of NiAl, $MoSi_2$, and selected alloys by surface films and internal interfaces associated with second-phase precipitates or dispersoids. For NiAl, additional effects of surface films on cyclic stress asymmetry and of cyclic prestrain on monotonic yield and tensile strengths and ductility have been observed. The observed enhancements of plasticity by surface films and second phases occur because of the conditions of constrained deformation at the film-substrate and particle-matrix interfaces which are effective in introducing glissile dislocations into the otherwise brittle substrate/matrix material. These observations, made initially on bcc refractory metals, offer hope that optimized microstructural control of such systems will lead to enhanced toughness in future engineering applications.

Acknowledgments

Various parts of this research were individually supported by the U.S. National Science Foundation, Grant No. DMR 9102414, Dr. Bruce A. MacDonald, Program Director, and by the Air Force Office of Scientific Research, Grant No. DoD-G-AFOSR-90-0141, Dr. Alan H. Rosenstein, Program Manager. We also acknowledge the Department of Energy for fellowship support that enabled two of us (R.G., C.M.C.) to do major portions of the research on surface film softening of $MoSi_2$ in the Center for Materials Science at Los Alamos National Laboratory.

References

1. R.D. Noebe, A. Misra and R. Gibala, ISIJ International 31, 1172 (1991).

2. R.M. Aikin, Jr., Scripta Metall. Mater. 26, 1025 (1992).

3. R.D. Noebe and R. Gibala, Structure and Deformation of Boundaries, K. Subramanian and M.A. Imam, eds., The Metallurgical Society, AIME, Warrendale, PA, p. 89, 1986.

4. R. Gibala, A.K. Ghosh, D.C. Van Aken, D.J. Srolovitz, A. Basu, H. Chang, D.P. Mason and W. Yang, Mater. Sci. Eng. A155, 147 (1992).

5. I. Baker and P.R. Munroe, High Temperature Aluminides and Intermetallics, S.H. Wang, C.T. Liu, D.P. Pope, and J.O. Stiegler, eds, TMS, Warrendale, PA, p. 425 (1990),

6. A.K. Vasudevan and J.J. Petrovic, Mater. Sci. Eng. A155, 1 (1992).

7. V.K. Sethi and R. Gibala, Phil. Mag. 37, 419 (1978).

8. J.T. Kim and R. Gibala, High Temperature Ordered Intermetallic Alloys IV, L.A. Johnson, D.P. Pope and J.O. Stiegler, eds., MRS Symposium Proceedings 213, 261 (1991).

9. S.E. Hartfield-Wünsch, Ph.D. Thesis, University of Michigan, Ann Arbor, MI, 1991.

10. T.A. Parthasarathy, S.I. Rao and D.M. Dimiduk, Phil. Mag., in press.

11. M. Yamaguchi, Mechanical Properties of BCC Metals, M. Meshii, ed., The Metallurgical Society, AIME, Warrendale, PA, p. 31, 1982.

12. S.A. Maloy, A.H. Heuer, J.J. Lewandowski and T.E. Mitchell, Acta Metall. Mater. 40, 3159 (1992).

13. Y. Umakoshi, T. Sakagami, T. Hirano and T. Yamane, Acta Metall. Mater. 38, 909 (1990).

14. P.H. Boldt, J.D. Embury, and G.C. Weatherly, Mater. Sci. Eng. A155, 251 (1992).

15. K.M. Edwards, M.S. Thesis, University of Michigan, Ann Arbor, MI, 1992.

16. A. Misra, S.E. Hartfield-Wünch and R. Gibala, Proc. Sixth JIM International Symposium (JIMIS-6), Intermetallic Compounds: Structure and Mechanical Properties, O. Isumi, ed., p. 597, 1991.

17. A Misra and R. Gibala, Structure and Properties of Interfaces in Materials, W.A.T. Clarke, U. Dahmen, and C.L. Briant, eds., MRS Symposium Proceedings 238, 369 (1992).

18. A. Misra, R.D. Noebe and R. Gibala, Intermetallic Matrix Composites II, D.B. Miracle, I. Baker, R. Darolia, J.D. Whittenberger and M.H. Yoo, eds., MRS Symposium Series 273, 205 (1992).

19. R.D. Noebe and R. Gibala, Scripta Metall. 20, 1635 (1986).

20. K.J. Bowman, S.E. Hartfield-Wünsch and R. Gibala, Scripta Metall. Mater. 26, 1529 (1992).

21. S.E. Hartfield-Wünsch and R. Gibala, High Temperature Ordered Intermetallic Alloys IV, L.A. Johnson, D.P. Pope, and J.O. Stiegler, eds., MRS Symposium Proceedings, 213, 575 (1991).

22. K.M. Edwards and R. Gibala, High Temperature Ordered Intermetallic Alloys V, I. Baker, R. Darolia, J.D. Whittenberger, and M.H. Yoo, eds., MRS Symposium Proceedings 288, 665 (1993).

23. R.B. Schwarz, S.R. Srinivasan, J.J. Petrovic and C.J. Maggiore, Mater. Sci. Eng. A155, 75 (1992).

24. J.J. Petrovic, A.K. Bhattacharya, R.E. Honnell, T.E. Mitchell, R.K. Wade, and K.T. McClellan, Mater. Sci. Eng. 155A, 259 (1992).

25. W.B. Li, J.L. Henshall, R.M. Hooper and K.E. Easterling, Acta Metall. Mater. 39, 3099 (1991).

26. H. Chang, H. Kung and R. Gibala, Intermetallic Matrix Composites II, D.B. Miracle, I. Baker, R. Darolia, J.D. Whittenberger and M.H. Yoo, eds., MRS Symposium Series 273, 253 (1992).

SESSION IX

Governmental Programs

Japanese National Project on Intermetallics

Tomohiko Maruo and Makoto Tomita

R&D Institute of Metals and Composites for Future Industries (RIMCOF)
Tokyo, 105 Japan

Abstract

A group of national laboratories, universities and member companies have been challenging a series of tough research areas concerning advanced materials used by, for example, space planes, and hypersonic aircraft to withstand the severest of environments. This project was initiated in 1989 as an eight-year national project. Two kinds of intermetallic compounds, Ti-Al and Nb-Al have been studied in the following areas:

Ti-Al
- the compound's fundamental characteristics,
- design of the material,
- technologies for sheet-casting, isothermal-rolling and superplastic deformation.

Nb-Al
- the compound's fundamental characteristics,
- design of the material,
- precision casting technique
- technologies for alloy powdering and forming.

The authors briefly review all R&D activities and achievements obtained so far, focusing on these intermetallics.

Critical Issues in the Development of High Temperature Structural Materials
Edited by N.S. Stoloff, D.J. Duquette and A.F. Giamei
The Minerals, Metals & Materials Society, 1993

Introduction

Towards realization in the early part of the 21st century, various research and development projects are just under way in Japan; in the field of aeronautics and space, space plane, supersonic transport (SST) and high speed civil transport (HST), in the field of energy, integrated coal gasification combined cycle (IGC) and thermonuclear power plants.

These projects obviously require a variety of advanced materials which can withstand extremely severe environments, for example high temperatures (1,000 ~ 2,000℃) in an oxidizing atmosphere. Furthermore, high specific strength and high rigidity are also prerequsite in the field of aeronautics and space, while conventional materials can not provide all these characteristics at the same time. In order to develop these types of materials, enormous funds for R&D and great divergence in long-term R&D such as in material design, evaluation technology , application technology, etc. are necessary. Moreover, this type of research is so risky that we strongly need R&D conducted under close cooperation between industry, government, national laboratories and universities, and international cooperation.

The "high performance materials for severe environments" project started as an eight-year national project in October,1989, based in part on MITI's (Ministry of International Trade and Industry) Research and Development Program on Basic Technologies for Future Industries, known by its Japanese acronym "JISEDAI".

In this paper, we will outline the project and the achievements obtained so far, focusing primarily on intermetallics.

Organization of R&D

In 1987 the Agency of Industrial Science and Technology (AIST), a division of MITI, studied 46 basic technologies which are expected to flourish in the 21st century. There was also a proposal that some intermetallics and composites should be developed, and processes for near-net shaping and joining should also be researched. This sparked a study meeting on the materials. RIMCOF played a major role in forming a feasible study group of industry, government and national laboratories, and universities in the latter half of 1987. The group published a report in Japanese entitled "The state of the art and issues on high performance materials for severe environments". The Materials Process Technology Center of Japan and RIMCOF also issued a book reviewing fundamentals and possible applications of intermetallics for structures and R&D achievements in March 1989.

After the study and public relations, dozens of R&D organizations showed a strong desire to be involved and they were evaluated as potential members of the project. Thus, the national project was initiated under the auspices of AIST, by the organization stated below, in fiscal year 1989 (Fig.1).

Following is a list of R&D groups and their research themes.

(1) Mechanical Engineering Laboratory :
Stirring synthesis and microstructural control of Ti-Al
(2) Government Industrial Research Institute, Nagoya :
Injection molding of Ti-Al
(3) National Research Institute for Metals :
Microstructure and properties of Ti-Al, and fundamentals of Nb-Al
(4) Kyoto University : Fundamentals of rolling Ti-Al
(5) Institute for Materials Research, Tohoku University :
Fundamentals of Nb-Al alloy
(6) Crucible Materials Corporation :
Fundamentals of HIP and pressing media for Nb-Al powder
(7) Daido Steel Co.,Ltd. :
Fundamantals of ceramic mold materials under HIP consolidation for

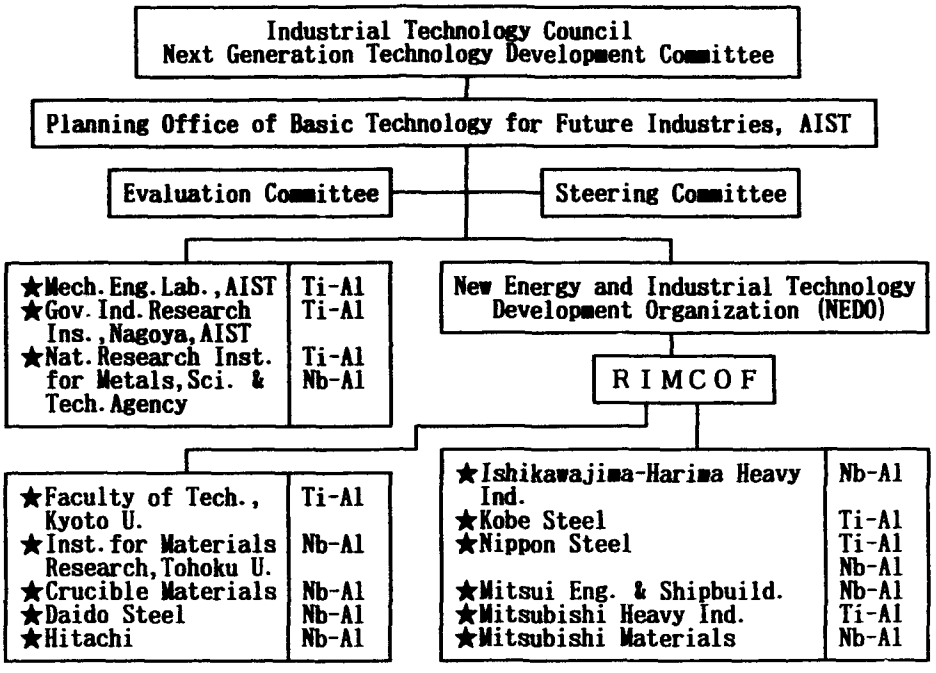

Figure 1 - Organization for the Project

Table I Schedule for R&D

Intermetallic	1989 1990 1991 1992	1993 1994 1995 1996
Ti-Al	Development of material design, manufacture and processing technologies ←----------→	Establishment of technologies for better material design, material manufacture and processing ←----------→
Nb-Al	Basic studies on material design, material manufacture and processing technology ←----------→	Establishment of technologies for material design, material manufacture and processing ←----------→

Nb-Al

(8) Hitachi, Ltd. :
Fundamantals of surface treatment and processing for Nb-Al

(9) Ishikawajima-Harima Heavy Industries Co., Ltd. :
Powder Rolling of Nb-Al

(10) Kobe Steel, Ltd. :
Sheet-casting and isothermal rolling of Ti-Al

(11) Nippon Steel Corporation :
Material design of Ti-Al and Nb-Al

(12) Mitsui Engineering & Shipbuilding Co., Ltd. :
Melting and casting of Nb-Al

(13) Mitsubishi Heavy Industries, Ltd. :
Plastic deformation and heat-treatment of Ti-Al

(14) Mitsubishi Materials Corporation :
Plasma-melt-gas atomization of Nb-Al

A long-term schedule has been also determined for the project - see Table 1. The eight-year period consists of the first phase (FY 1989-1992) and the second phase (FY 1993-1996). In the former, along with material design of intermetallics, (Ti-Al and Nb-Al systems), technologies for casting, powdering and processing of the designed intermetallics were developed. In the latter, based upon the achievements of the first phase, material design will be refined and the technologies will be established.

Target of Research and Development

Taking into account competition and the kinds of materials already under development, the following intermetallics and research targets have been chosen.

(1) Intermetallics with high specific strength (Ti-Al system)
- Specific strength(strength/specific gravity) of more than 100MPa/g/cm^3 at 1100℃
- Elongation of more than 3% at room temperature

(2) Intermetallics with high melting point (Nb-Al system)
- Tensile strength of more than 75MPa at 1800 ℃
- Elongation of more than 3% at room temperature

Interim Findings of R&D

Four years of research on the high level of targets of the project have brought forth various findings. The following are brief reviews.

1. Intermetallics with high specific strength:Ti-Al system

(1) Stirring synthesis and microstructural control

Firstly, the microstructural control of intermetallics for structural applications was studied by stirring synthesis of Cu-Al alloys (Cu-37wt%Al and Cu-46wt%Al). The melts of the alloys were allowed to flow down onto a polygonal rotor rotating at a high speed of max. 167s^{-1} around the horizontal shaft in a heat-controlled vessel. As the rotor spattered the melts, many primary crystals formed in the spattered droplets were refined with repeated collisions against the rotor surface and the inner wall of the vessel by the stirring action of the rotor, rotating at high speeds. Then, the slurry alloys of gathered semi-solidified droplets were poured down into a metallic mold through a taphole at the bottom of the vessel. Microstructural observation revealed extreme refinement of the alloys.

Based on the preparatory experiment, a new vacuum stirring synthesis apparatus was made for the Ti-Al system. The modified rheocasting process of the rotation of the stirrer at a speed of max.70s^{-1} produced another extreme homogeneous refinement of primary grains in an intermetallic compound Ti-44at%Al, under a pressure of 0.1MPa argon gas. The grain size was 2.2 ±1.3 μm in major axis and 1.0±1.3 μm in minor axis (Fig.2).

The microstructural control of titanium aluminides was also studied by powder metallugy.

(2) Injection molding

In the first place, pellets bound by a binder consisting of wax and acrylic resin, confirmed the possibility of injection molding TiAl powder for near- net shape of the intermetallics. Dewaxing in an inactive atmosphere such as argon or nitrogen improved sintering for the green body of the intermetallics. Under a 10^{-4} torr vacuum at around 1400℃, sintering was made with few deformations. The relative density, however,

Figure 2 - Microstructure of Ti-44at%Al ingot stircast at a high rotation speed[6]

was around 90%, which indicates the necessity of some further treatment like HIP in order to obtain better sintering and higher density. Adoption of finer powder, addition of third alloying elements, and so forth are also prerequsites for better mechanical properties of the sintered body.

Furthermore, addition of a small amount of the third elements, Cr and Ni, to the Ti-Al powder were tried, resulting in unsatisfactory densities and tensile strength.

(3) Microstructure and properties

An as-cast Ti-48at%Al with lamellar and γ grains changed its volume fraction of the γ grains from 0 to 80% with heat-treatment in a temperature range of 1473K to 1673K. The ductility at room temperature increased with the γ grain volume fraction, but not with the grain size. The tensile elongation of 1.2% was obtained for the specimen with the γ volume fraction of 80%. When the alloy homogenized at 1473K was reheated at 1623K, α phase precipitated in γ grains in Widmannstatten configuration and the tensile elongation increased to 1.8%.

A three-step isothermal forging was carried out for Ti-43 ~ 52at%Al : firstly at 1473K, secondly at 1273K changing the loading direction of the specimen by 90°, and lastly at 1273K changing once more the loading direction by 90°. By combination of the three-step forging and subsequent heat-treatment, equiaxial α_2 and γ grains with a diameter of 5 to 300 μm were obtained. The yield strength of these alloys was as follows: at room temperature it increases with decreasing grain size and an increasing volume fraction of α_2 phase. At 1273K it decreases with decreasing grain size, and its maximum is estimated to be about 190MPa. Superplastic elongation attaining several hundred percent was observed at elevated temperatures in the Ti-46at%Al alloy with the finest grain size.

Strengthening by alloying was studied (Fig.3). The addition of a small amount of Sb (0.5%) increased the yield strength at 1273K to about 230MPa.

A new electrolytical etching technique which dissolves only γ phase was developed. Although this method scarcely indicated any distinct difference in microstructure for the Ti-48 ~52at%Al which contained 400 ~2000wt.ppm of oxygen, the α_2 phase of the the oxygen-rich ingots generally tended to have coaser and more peculiar configuration, and form more divided dendrite.

Si-added Ti-50at%Al showed better oxidation behavior at elevated temperatures (1173 and 1223K). When 1%Cr, 1%Y and 1%Mn were added to Ti-50at%Al, degradation of oxidation resistance was generated. The study of the effect of the surface condition on the specimens on oxidation behavior in air, revealed an improvement by the existence of deformed layers on the surface at temperatures up to 1123K. However, the effect completely vanished at higher temperatures (Fig.4).

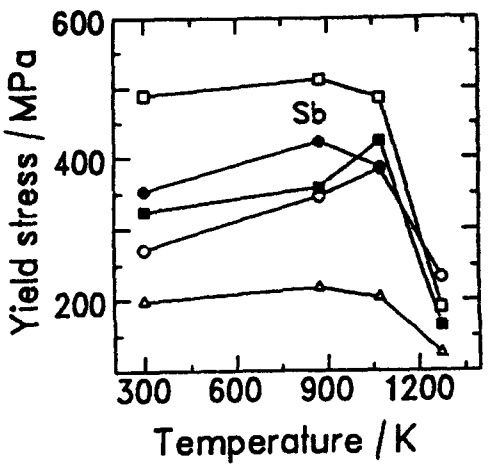

Figure 3 - Temperature dependence of yield strength[6]
△:Ti-50at%Al
○:Ti-49.5at%Al-0.5at%Sb
●:Ti-49at%Al-1.0at%Sb
□:Ti-48at%Al-2.0at%Sb
■:Ti-50at%Al-1at%Sb

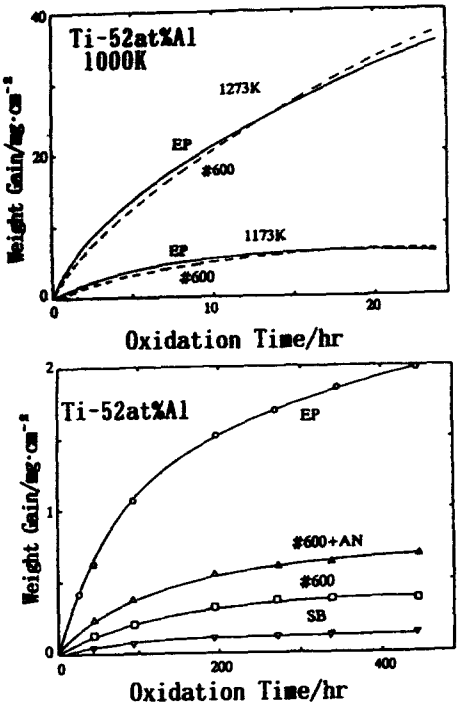

Figure 4 - Effect of surface condition on oxidation behavior in air[6]

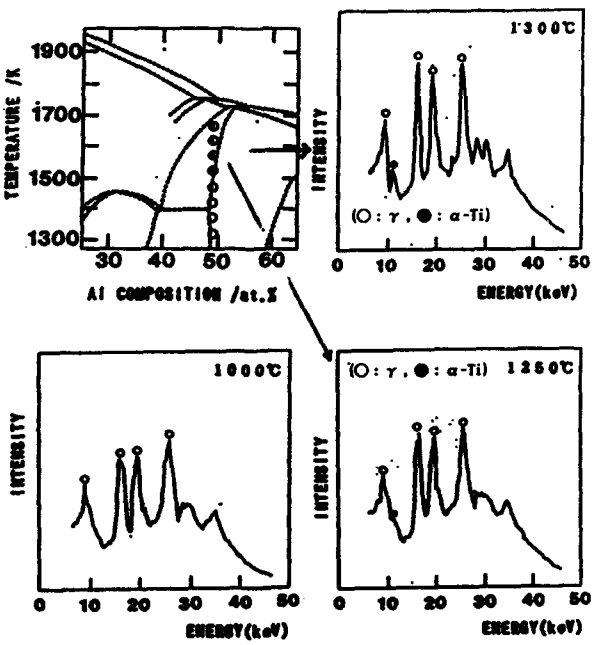

Figure 5 - Successive phase change at high temperature in Ti-49at%Al[4]

(4) Material design

For the study on fundamental mechanical properties of TiAl, the compositions of Al in the intermetallics were changed systematically to examine phase stability, microstructure and mechanical properties. High temperature X-ray analysis revealed that α phase appeared at a temperature above 1250℃ in Ti-49at%Al, which concurs with a recently revised Ti-Al phase diagram (Fig.5). Furthermore, it was found that morphology of TiAl strongly depends on its composition and affects the mechanical properties. Among the Ti-Al intermetallics, Ti-48at%Al showed relatively good overall properties.

The addition of a third element X (X=V, Cr, Mn, Nb, Mo and Ta) caused a change in phase equilibria among the γ, α_2(Ti_3Al) and β (bcc-Ti) phases; the β phase is stabilized by the addition (except X=Ta), resulting in a drastic change in microstructure. The Ti-Al-Mo system showed a unique behavior; the β phase region protrudes toward the α phase region around 1200 ℃ in the ternary phase diagram. The β phase contained in specimens quenched from high temperature has a long-range ordering structure, which is different from the B2 structure.

Utilization of phase diagrams is essential to understanding the effects of microstructure on the mechanical properties of the intermetallics. Based on the experimental results, Ti-Al-Mo and Ti-Al-Nb ternary phase diagrams have been proposed. Consideration on the binary and ternary phase diagrams leads to accurate information about phase stability and microstructural control.

The relationship between microstructure and tensile elongation of the TiAl has been examined in detail. Most of the specimens showed cleavage-like fractures at room temperature. It was revealed that plastic elongation increased proportionally with decreasing cleavage facet size. Crack initiation sites, which correspond to catastrophic failure later, were found mostly on the surface of tensile specimens. At high temperatures, microstructure and morphology of a secondary phase played an important role in improvement of elongation and strength. Preliminary results of mechanical properties of the Ti-Al-X suggest that Ta and Nb addition would increase the high temperature strength of TiAl. Furthermore, the precipitated β phase at grain boundary considerably improved high temperature deformability. These results strongly suggest that the mechanical properties of TiAl can be greatly improved by microstructural control.

(5) Sheet-casting and isothermal rolling

Fundamental aspects of melting, solidification and high temperature deformation of TiAl have been studied in order to develop the manufacturing process of TiAl sheet using isothermal rolling.

The test result suggests that a skull melting process be adopted for the TiAl because the use of the crucible made from CaO resulted in a high oxygen content of 800～1400 ppm. The melting process using the "sheet-caster", which adopts the cold crucible induction method gives good uniformity of the TiAl due to little contamination from the crucible.

Dendrite arm spacing of ingots is reduced with an increased cooling rate from a molten state. Microstructure in dendrite arms in an as-cast state is a lath structure irrespective of Al- content. The interdendrite consists of only γ phase in the high Al alloys and $\gamma + \alpha_2$ phase in the low Al alloys. Heat-treatment at 1523K produces a massive γ structure. The reduction of Al-content and/or the addition of Cr, Mn and V suppress the formation of a massive structure, resulting in a mostly lath microstructure.

High temperature flow stress is greatly affected by composition, morphology of microstructure, deformation temperature and strain rate. The increase in Al content brings about the decrease of peak stress and the increase in m-value and recrystallization rate. These lead to the improvement of hot workability of the alloy. However, the effect of dendrite arm spacing on the flow stress is rather small.

According to another fundamental study of microstructural control of TiAl, grain refinement of γ single phase easily takes place through thermo-mechanical processing. However, the lamellar structure composed of $\gamma + \alpha_2$, which is observable in the Ti-rich composition is very stable, even when heated up to 1473K. The two phase structure of $\gamma + \alpha_2$ rarely recrystallizes because of its thermal stability.

The rolling technology is now under development using an isothermal rolling mill which has been specially designed and installed (Fig.6).

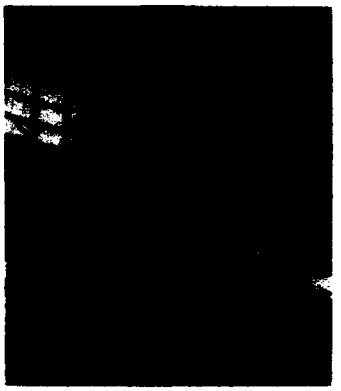

Fig.6. Isothermal rolling mill

(6) Plastic deformation and heat-treatment

It is important to improve the plastic formability of TiAl by optimizing the manufacturing process of the sheets. Plastic deformation behavior of the intermetallics was studied from the view points of chemical compositions and microstructures in order to understand the main factors to be controlled for manufacturing TiAl sheets. As a result, plastic deformation characteristics of TiAl are strongly affected by chemical compositions in the as-cast condition, because the microstructures are different from each other. Refinement of the microstructures, which brings about an increase in m-value and a decrease in deformation stress, is a most effective factor for improving formability of TiAl sheets, as compared with as-cast and as-forged.

Grain size dependence of plastic flow properties and tensile strength at elevated temperature is studied for TiAl with equiaxed grain structures. Along with the initial grain size, grain size stability during deformation is a significant factor in improving the plastic flow property. For Ti-48at%Al-1%Mn, the grain size stability during deformation is so poor that the plastic flow property is not good even with a very fine initial micro- structure. For example, the plastic flow property of a fine grain material (d=20μm) was quite similar to that of coarse grain one (d=100μm). On the other hand, Ti-46at%Al exhibits better grain size stability and superior plastic flow property to the Ti-48at%Al-1%Mn. The former contains considerable amounts of α_2 phase which presumably contributes grain size stability. High temperature tensile strength is significantly affected by grain size. The larger the grain size, the higher the tensile strength above 800℃. Therefore, the grains of TiAl, which are initially controlled to be finer for better formability, should be coarsened for high temperature service.

The effects of chemical composition on superplasicity were studied by using binary TiAl (Ti-45, 46, 47, 48 and 49 at%Al), whose microstructures were finely controlled by thermo-mechanical treatment. Among the materials, the plastic flow properties of the Ti-46at%Al was best due

to the finest dual phase equiaxial structure ($d < 6\mu m$) which was sustained during deformation.

Microstructures of TiAl after heat-treatment are significantly affected by the temperature of the heat-treatment, while tensile properties depend on the microstructures. The materials heat-treated just above the α-transus temperature showed high tensile strength at 1000 ℃ and good ductilities at room temperature, 290MPa and 2.9%, respectively (Fig.7).

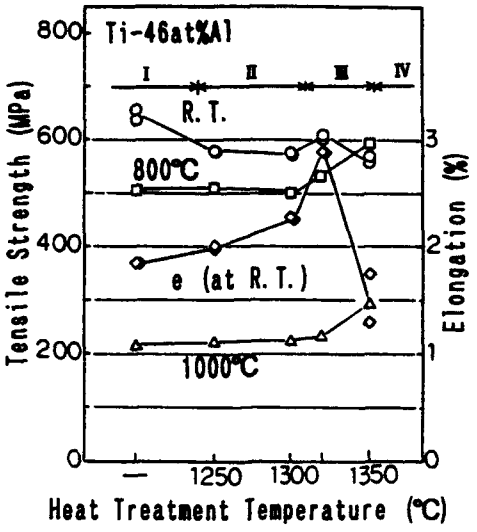

Figure 7 - Effect of heat-treatment on tensile properties of Ti-46at%Al [6]

2. Intermetallics with high melting point:Nb-Al system

(1) Fundamentals on Nb-Al alloy

Preliminary experiments were carried out to obtain information on the various effects from alloying elements. Sound buttons were procured for Nb-20at%Al alloys alloyed with Mo, Ta, and W and Nb-16at%Al alloys alloyed with Co, Ni and Si, respectively. Nb-24at%Al alloy and Nb-20at%Al alloys alloyed with Hf or Cr were found to suffer. A small piece of 96% theoretical density was successfully produced by HIP-consolidation of a commercial powder (Nb-8.41wt%Al). The powder of under 100 mesh started to oxidize at about 400℃ and ignited at about 800℃ in the oxygen gas of normal pressure.

Further systematic studies were carried out on effects of alloying elements on melting behavior, the phase boundary between A15-one-phase and A15/A2-two-phase regions, hardness and vulnerability to gases of the Nb-rich side of Nb-Al binary system. The original phase boundary of the binary system is located nearer the Nb side than reported in other literature (Fig.8). Alloying with Ta and W stabilized the two-phase structure, while alloying with Mo stabilized the single phase structure. The two-phase structure is more resistant to crack propagation than the one-phase structure. Weight change of Nb-Al binary alloys with various Al-contents is observed in a thermobalance at various temperatures in oxygen, in commercial nitrogen, or in a N_2-20%O_2 gas mixture. The alloys are far more vulnerable to chemical attack by these gases as compared with TiAl or Ni_3Al.

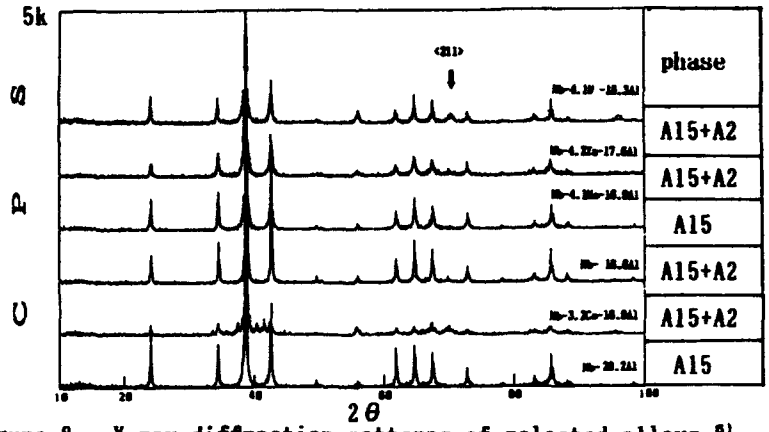

Figure 8 - X-ray diffraction patterns of selected alloys [6]
(see arrow at θ=70 ° ; (211) peak of the A2 phase)

(2) Material design of Nb-Al

A new type of X-ray system was installed for exclusively determining the phase diagram of the Nb-Al system at high temperature. It consists of a high-temperature heating system (max. 2000 ℃) and an atmosphere controller. Structural analysis is carried out by an improved X-ray diffraction technique which combines angle dispersion with energy dispersion in measurement.

Some Nb-Al compounds were prepared in combination with melting and heat-treatment, and then examined by an optical microscope and the X-ray diffraction. It is revealed that Nb-29.2at%Al is composed of Nb_3Al and Nb_2Al and that the atomic ratio Nb_3Al/ Nb_2Al is over 6. It was also found that the Nb_3Al intermetallic compound (A15 structure) appeared as a stable single phase between 20at%Al and 23at%Al after annealed at 1600 ℃. This indicates that the stable Nb_3Al phase exists off stoichiometry composition at room temperature. Based on the current experiment, a tentative Nb-Al binary phase diagram was proposed. The single phase is narrower than the ones ever reported and does not contain a stoichiometry composition of A15-type structure, Nb-25at%Al.

The mechanical properties of the Nb-Al alloys were also examined. According to a high temperature hardness test, single phase Nb_3Al which was produced by plasma arc melting is very brittle between room temperature and 1000 ℃, and it becomes deformable above 1100℃. Brittleness changes with Al content. By means of a hardness test at room temperature, the composition of ductile brittle transition of the Nb-Al system was found to be Nb-16at%Al. By increasing Al content from 16 to 25at%, the value of microhardness showed a remarkable increase up to 1100Hv (Fig.9).

(3) Melting and casting of Nb-Al

Concerning the manufacturing process of Nb-Al, precision casting and powder metallurgy can be applied to the intermetallics. Melting methods, mold materials and fundamentals of the intermetallics for precision casting were studied.

For the melting of Nb-Al, high purity, homogeneity and accurate control of composition are required. In this respect, various skull melting processes for the intermetallics were studied. As a result, an advanced Induction Skull Melting(ISM) furnace with a capacity of max. 5kg (iron equivalent) has been developed. Using the ISM, homogeneity of Nb-Al ingots and the possibility of melting achieving accurate control of composition were confirmed.

Thermodynamic stability for the molten Nb-Al and high-temperature

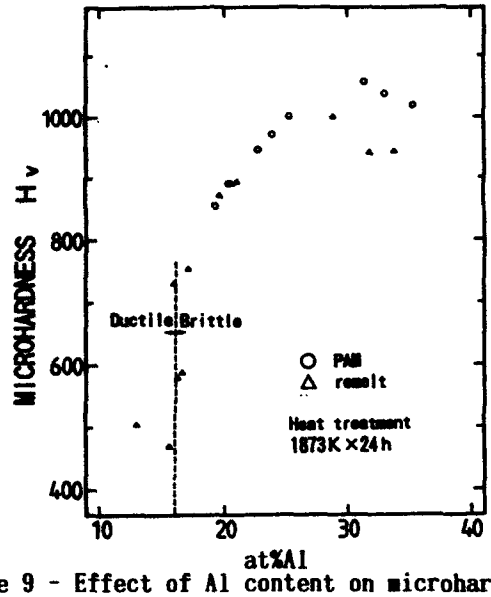

Figure 9 - Effect of Al content on microhardness in Nb-Al [6]

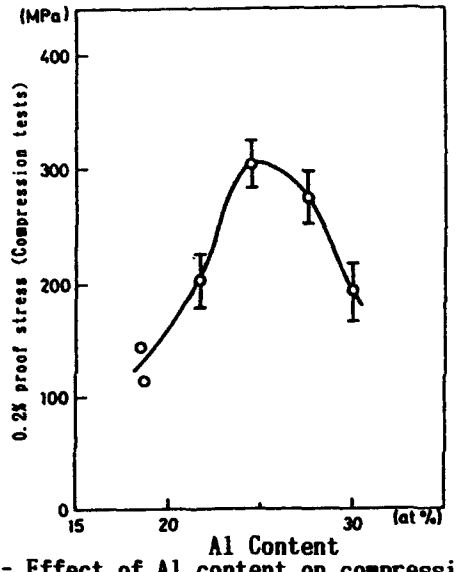

Figure 10 - Effect of Al content on compression 0.2% proof stress of Nb-Al binary compounds (1500℃) [6]

stability are required in the mold materials for the intermetallics. High melting point oxides such as CaO, MgO, ZrO_2, and graphite were prepared as mold materials to investigate reactions with the molten Nb-Al. As a result, Y_2O_3, HfO_2, and CaO proved to be most suitable as mold materials owing to their thermodynamic stability for the molten Nb-Al.

Another fundamental study on the intermetallics was carried out to understand the basic properties of the molten Nb-Al and the solid phase of Nb-Al by changing Al content in the binary alloy systematically. As a result, a stoichiometric Nb-25at%Al showed 300MPa of 0.2% proof stress on a compression test at 1500 ℃ as the highest value (Fig.10).

(4) Plasma-melt-gas atomization of Nb-Al

To start the work for rapidly soldified niobium-aluminides (near Nb_3Al), sophisticated plasma-skull-melting equipment has been installed for the production of melting stock. The equipment can be pressurized up to 0.3MPa of argon, helium and/or their mixture to eliminate Al vaporization during melting. It was confirmed that pressurizing the melting atmosphere to approximately 0.25MPa can minimize Al vaporization during the melting. After a series of studies, a unique Plasma-Melt-Gas-Atomization process (PMGA) was established in a laboratory scale of 30kW plasma and 100g/charge. In this technique, only water-cooled copper is used as a tundish for bottom-pouring, instead of conventional refractories or refractory metals. The crystal structure of PMGA'ed Nb_3Al powder consists of a mostly Al-saturated solid solution of Nb(bcc), with a mean diameter of around 100 μm (Fig.11). The gas content was sufficiently low, and besides the PMGA'ed Nb_3Al powder was soft and ductile, while a plasma-melted ingot was hard and very brittle. This fact mean that the solidification rate of the process is extremely high.

To confirm capabilities of the process and to supply the members of the project with necessary amounts of the powder, a pilot-scale facility with a bottom-pouring nozzle made of graphite and heated by induction was installed (450kW, 5kg/charge), and has been tested for atomization. Since a fair amount of carbon was detected in the powders, it is urgently necessary to change it to a water-cooled type copper nozzle, which is currently available only for laboratory-scale PMGA equipment.

Figure 11 - SEM image of PMGA'ed powders of pure Nb_3Al produced by pilot-scale atomizer

(5) Powder Rolling of Nb-Al

In order to fabricate sheets of Nb-Al using an isothermal powder rolling process, sintering properties of powders and oxidation properties of compacted specimens were studied on Nb-Al and Nb-Al-W powders. The powders were prepared by mechanically crushing ingots and by mechanically alloying prealloyed powders and element powders. The oxidation test indicated the necessity of improving the oxidation resistance of the mechanically alloyed and sintered specimens.

With the mechanically alloyed powders, 100% density was obtained by sintering under a hot press condition of 1623K and 49MPa, while the as-crushed powders were not fully consolidated under the same condition. The fine grain structure of $NbAl_3$ reduced sintering temperature by more than 350K. Before studying the Nb-Al powder rolling technique, a preliminary test was carried out using irregular shapes of Cu powders to investigate roll speed effects on density, thickness and rolling load, etc.

Non-equilibrium structures with nanocrystals, formed by ball milling, were characterized by differential scanning calorimetry (DSC), X-ray diffraction and thin-foil TEM. Fine grain structures of about 10nm in size

were formed by ball milling in Nb_3Al and Al_3Nb compounds. The ball-milled Nb_3Al powders released heat of 2kJ mol^{-1} with a peak temperature of around 0.45Tm (Tm:melting temperature). An X-ray diffraction study revealed the DSC peak as an annihilation process of a bcc Nb phase formed during ball milling. Atomic diffusion is considered to become significant at the DSC peak temperature to restore an equilibrium state. A die-press test was conducted for the ball-milled powders. Enhanced consolidation by milling was found for both compounds to occur at temperatures as low as 0.4Tm to 0.5Tm. Compacts with 90% density were obtained at 0.5Tm under 600MPa. Extremely fine grain structures rather than small sizes are considered to have contributed to the enhancement of consolidation at relatively low temperatures and high stress.

The rolling technology is now under development using an electric current powder rolling mill which has been specially designed and installed (Fig.12).

Figure 12 - Electric current powder rolling mill

Conclusions

The Japanese national project on the intermetallics as advanced structural materials has been briefly introduced, focusing on the two kinds of intermetallics, Ti-Al and Nb-Al. The R&D activities for the past about four years have brought forth various interesting, useful findings.

We hope steady further R&D for the remaining four years by all concerned will lead us to passing our targets, along with obtaining a lot of findings and stimulating the study on intermetallics in a wider range.

Acknowledgements

The authors wish to thank all concerned with the project for quoting their contributions. Every part of this work was supported by the New Energy and Industrial Technology Development Organization (NEDO).

References

1. Yasuhiko Kondoh,"R&D of the Intermetallics"(Paper presented at the 10th Anniversary of "Research and Development Program on Basic Technologies or Future Industries,Tsukuba,Japan,19 Feburuary 1992)

2. Yoshinori Nakazawa, "The State of the Art and Future of the Jisedai Project-High Performance Materials for Severe Environments" (Paper presented at the First Workshop on the Intermetallics, Tokyo, Japan, 8 May 1992)
3. Masaharu Yamaguchi, "High temperature intermetallics-with particular emphasis on TiAl," Materials Science and Technology, 8(4) (1992), 299-307
4. "Symposium Proceedings for Basic Technologies for Future Industries High-performance Materials for Severe Environments First Meeting" (Japan Industrial Technology Association and RIMCOF, October 24-25, 1990)
5. "Symposium Proceedings for Basic Technologies for Future Industries High-performance Materials for Severe Environments Second Meeting" (Japan Industrial Technology Association and RIMCOF, November 28-29, 1991)
6. "Symposium Proceedings for Basic Technologies for Future Industries High-performance Materials for Severe Environments Third Meeting" (Japan Industrial Technology Association and RIMCOF, November 25-26, 1992)

Advanced Structural Materials and Processes

Alan H. Rosenstein

Air Force Office of Scientific Research
Bolling Air Force Base
Washington, DC 20332-6448

Abstract

Basic research toward a fundamental understanding of the processing and properties of metals, intermetallics, ceramics, carbon, polymers, and their composites greatly supports the Air Force need for advanced structural materials for aircraft and space applications. The scientific objective of the research is to investigate techniques to obtain advanced structural materials that are often controlled by nanoscale, microscale, and/or macroscale microstructural characteristics; and to determine the mechanical property/microstructure dependence of these materials on processing techniques. Research of this nature will have great potential for applications in advanced aircraft engines where high temperature is a critical design factor, and for high temperature skins of hypersonic vehicles. Operating temperatures of advanced materials could potentially double the operating temperature of conventional Ni-base superalloys, thereby doubling engine thrust-to weight ratios. The expertise for these advances lies with government, university and industrial laboratory scientists.

The next generation of high temperature materials will almost certainly have many of the following characteristics:

- Heterogeneous in nature - some hybrids of metals-ceramics-polymers.
- Delicate balance of equilibrium and non-equilibrium microstructural elements, (phases, dispersions, precipitates).
- Many of these microstructural elements will be on the nanoscale. Dispersion strengthening and/or toughening will be key.
- Morphology of the microstructure will be important.
- Geometric distribution of the microstructure may be critical.

The need for these property-determining characteristics will result in difficult processing problems that will require innovative concepts.

Some of the scientific issues that will have to be addressed include:

- Composite materials with dispersed phases produced in-situ.
- *Ductile phase toughening through phase transformation control.*
- Mechanical alloying to synthesize unique systems.
- Solidification concepts in presence of reinforcements or dispersions.
- Production, control, tailoring of nanoscale microstructures.
- Control and tailoring of interfacial structure.
- Processing under non-equilibrium conditions.
- In-situ processing sensors to monitor chemistry and quality.
- Innovative processes that control energy input.
- Development of knowledge-based processing strategies.
- Computer simulation to model processes to:

  Control microstructure.
  Avoid fiber or phase damage.
  Control residual stresses in composites.
  Avoid interface damage.
  Obtain desired mechanical/physical properties.
  Determine thermal cycles, thermomechanical processing.

Summary

Although most of the above is perceived as research that is driven by material needs to improve performance of systems (i.e., higher operating temperature engines resulting in greater thrust and power), there are additional legitimate objectives. Range and efficiency of systems, durability and life cycle costs, and affordability and lead time issues are objectives that also will be served by informed research on advanced structural materials and processes.

SUBJECT INDEX

Alloy content 137
Alloy design 67
Alpha phase 174

Bond breaking 409
Bonding charge density 30

Carbon-carbon composites 415
Casting 137
Ceramic-metal composite 151
Ceramic coatings 304
Ceramic composite 2, 120, 151, 239, 333
Ceramic reinforcements 71
Ceramics 385
Chemical corrosion 194
Combustion synthesis 151
Compact tension specimen 219
Computational analysis 29, 109
Corrosive gases 415
Crack propagation 369
Crack-tip 386
Crack velocity 448
Creep resistance 73, 204, 297, 321, 336, 354, 385
Crystallographic structure 280
CTE 304
Cyclic oxidation 431

Deformation 175
Diffusion 15, 45
Directional solidification 94, 161, 322
Dislocation motion 75, 279, 465
Dislocation strengthening 203
Ductile phase toughening 205
Ductile-to-brittle transition 457, 466
Ductility 217, 227, 404, 432
Duplex microstructure 173

Elastic constants 31
Environmental degradation 127

Fatigue 360, 367, 385, 468
Fibers 44, 120, 445
Finite difference method 110
Floating zone method 161
Fracture mechanics 244
Fracture surface morphology 220
Fracture toughness 217

Gamma phase 174
Gas turbine 2
Glass bonded ceramic 333
Grain boundaries 349

High temperature corrosion 446
Hot corrosion 416
Hot pressing 151
Hydrogen embrittlement 406, 431, 455

Interface 44, 303
Interfacial glass phase 385
Intergranular fracture 162
Interstitial elements 57

J-integral 220

Lamellar structure 173
Lattice defects 30
Liquid metal infiltration 151

Matrix cracks 243
Mechanical erosion 194
Mechanical properties 57, 120, 137, 164, 173, 291, 310, 400, 480
Metal composite 2, 43, 71, 455
Metal infiltrated ceramic 333
Microstructural control 109
Microstructure 15, 57, 91, 137, 162, 203, 227, 292, 322, 367, 481
Molybdenum alloy 189
Molybdenum disilicide 279
Molybdenum disilicide composites 291
Monkman-Grant constant 339

Ni-base superalloys 2, 87, 321, 367
Nickel alun alloy 161, 203, 227
Niobium al ie 477

Ordered structure 2, 400
Ordering energy 227
Oxidation 359, 416, 446

Particle reinforcement 291
Phase diagram 15
Powder metallurgy 137
Precipitate formation 206
Processing 2, 109, 124, 137, 480
Protective barrier 417
Pull-out 3

Rapid solidification 57
Rare earth disilicates 349
Rare earth dopants 433
Reaction kinetics 16
Recrystallization structure 227
Refractory metal alloy 189

Second phase precipitates 471
Silicon carbide 239
Single crystal 322
Single crystal casting 98
Slip planarity 367
Slip system 280
Static oxidation 431
Strengthening mechanisms 32
Substitutional element 227
Surface film effects 467

Tensile behavior 458
Thermal barrier 303
Thermal degradation 192
Thermal gradient 110
Thermal shock 81
Thermal stress 192
Ti-base alloy 455
Titanium aluminide alloy 217, 477
Transport 45
Turbine blade 89
Two dimensional micromechanical model 445

Whiskers 291

Yield stress 282

AUTHOR INDEX

Basu, A., 291

Chang, H., 465
Chiba, A., 227
Czarnik, C.M., 465

Domergue, J.-M., 239
Duquette, D.J., 431

Edwards, K.M., 465
Erickson, G.L., 87
Evans, A.G., 239

Feng, H.J., 151
Flinn, J.E., 57
Fu, C.L., 29
Fuchs, G.E., 137

Ghosh, A.K., 291
Giamei, A.F., 109
Gibala, R., 465
Gnanamoorthy, R., 217
Guo, H.Z., 227

Hanada, S., 227
Henager, C.H., Jr., 445
Hillig, W.B., 119
Hirano, T., 161

Inui, H., 173

Jones, R.H., 445

Kelley, T.F., 57

Maloy, S.A., 279
Maru, T., 477
Masahashi, N., 217
Meier, G.H., 415
Misra, A., 465
Mitchell, T.E., 279
Mizuhara, M., 217
Mutoh, Y., 217

Nazmy, M., 321
Nelson, H.G., 455
Nemoto, M., 203
Nieh, T.G., 189
Norman, J.H., 43

Perepezko, J.H., 115
Pettit, F.S., 415

Raj, R., 71
Reynolds, G.H., 43
Rigdon, M.A., 1
Rosenstein, A., 491

Shiota, I., 303
Stoloff, N.S., 367
Suresh, S., 385

Takasugi, T., 399
Thomas, G., 349
Tomita, M., 477

Vaggagini, E., 239

Wadsworth, J., 189
Watanabe, S., 227
Wilcox, B., 1
Wilkinson, D.S., 333
Wittenauer, J., 189

Yamaguchi, M., 173
Yoo, M.H., 29